



ARISTOTLE
UNIVERSITY
THESSALONIKI

SCHOOL OF
PHYSICS

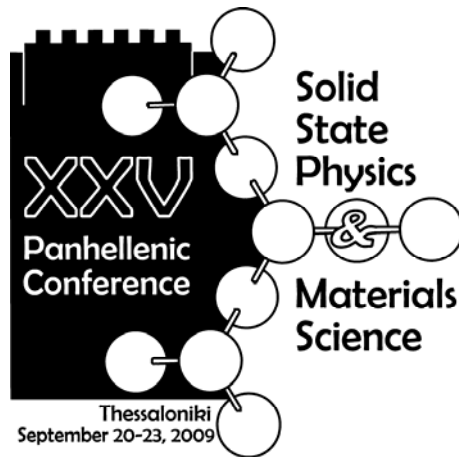


XXV Panhellenic Conference on Solid State Physics & Materials Science extended abstracts

September 20-23, 2009

Teloglion Foundation of Art
Thessaloniki





XXV Panhellenic Conference on Solid State Physics & Materials Science

Program & Extended Abstracts

Thessaloniki, September 20-23, 2009

Teloglion Foundation of Art
Aristotle University of Thessaloniki

Under the auspices of



ARISTOTLE UNIVERSITY OF THESSALONIKI



SCHOOL OF PHYSICS (AUTH)



FACULTY OF SCIENCES (AUTH)



DEPARTMENT OF SOLID STATE PHYSICS
SCHOOL OF PHYSICS



POST-GRADUATE COURSE PROGRAM
"MATERIALS PHYSICS & TECHNOLOGY"



RESEARCH COMMITTEE (AUTH)

Sponsors



NATIONAL BANK OF GREECE



HELLENIC INSTITUTE OF METROLOGY



ION PLUS, ST. GOUNTROMICHOS & CO



SOTIRIA ARGYROPOULOS REPRESENTATIONS
INTERNATIONAL TECHNOLOGY CORPORATION



REPRESENTATION & TRADE OF
SCIENTIFIC INSTRUMENTS



ANALYTICAL INSTRUMENTS S.A.
DR. C. J. VAMVAKAS



L'ORÉAL
HELLAS



Committees

Local Organizing Committee

Chair: Eleni C. Paloura, *Professor*

Vice-Chair : Philomela Komninou, *Professor*

Secretary : Maria Katsikini, *Lecturer*

Treasurer: Makis Angelakeris, *Lecturer*

Members: Konstantinos G. Efthymiadis, *Associate Professor*

Eleni Pavlidou, *Assistant Professor*

George Dimitrakopoulos, *Assistant Professor*

Maria Gioti, *Assistant Professor*

Fani Pinakidou, *Post-Doctoral Researcher*

Konstantinos Simeonidis, *Post-Doctoral Researcher*

Steering Committee

Professor **T. Bakas** (University of Ioannina)

Professor **P. Kelires** (Cyprus Univ. of Technology, IESL/FORTH & Univ. of Crete)

Professor **S. Kennou** (University of Patras)

Professor **S. Logothetidis** (Aristotle University of Thessaloniki)

Dr. **D. Niarchos** (NCSR Demokritos)

Professor **C. Soukoulis** (Iowa State University & IESL/FORTH & Univ. of Crete)

Professor **N. Stefanou** (University of Athens)

Foreword

The “*XXV Panhellenic Conference on Solid State Physics and Materials Science*” will take place in Thessaloniki, at the facilities of the Teloglion Foundation of Art. The aim of this annual conference is to provide a forum for the discussion of current experimental and theoretical issues in solid state physics & materials science. To reinforce the extraverted character of the Conference, a number of distinguished scientists from Europe are invited to give plenary and invited talks. Another important task of the conference is to encourage and promote interaction among senior and junior scientists from the academia and research institutions. To encourage the participation of young scientists the organizing committee provided ample financial support. In addition to that the Conference will award young scientists for excellence in their presented work.

The topics that will be discussed in 2009 include Photonics & optoelectronics (8 contributions); Structural, mechanical & optical properties of condensed matter (50 contributions); Electronic transport, semiconductors & devices (22 contributions); Magnetism & superconductivity (35 contributions); Nanoscale & surface science (42 contributions); Inhomogeneous & disordered materials, polymers & biomaterials (29 contributions); Cultural heritage materials & interdisciplinary physics (22 contributions).

The 2010 Conference will take place in Ioannina while the recent past conferences were held in Heraklion, Crete (2008), Athens (2007), Patras (2006), Nicosia (2005) and Ioannina (2004). For historical reasons it should be mentioned that the first one in the series took place in Thessaloniki in 1982 and was chaired by Dr. Eleni Gamari-Seale of NCSR “Democritos”. The organizing committee decided to honor Dr. Gamari-Seale for her contribution in the longevity of the conference and solid state research.

During this Conference we shall honor the memory of Prof. G. Kanellis of Physics Department, A.U.Th., Dr. A. Simopoulos of NCSR-“Demokritos” and Dr. Th. Kostikas of NCSR-“Demokritos”. Brief obituaries of the distinguished scientists, who passed away during the past year, are included in the proceedings volume.

A few pieces of information about the program of the Conference: a total of 208 abstracts were submitted from 15 Greek Universities and 16 Greek Research Institutions. The program consists of 55 oral (4 plenary, 13 invited and 38 contributed) and 153 poster presentations. The international character of the Conference is reflected in the large number of cooperations among the Greek and foreign scientists who coauthor the submitted papers. For example, 95 foreign addresses appear in the author’s list.

Last but not least, the Organizing Committee wishes to thank the Sponsors whose contributions were critical for the realization of the extraverted character of the Conference.



Prof. Eleni C. Paloura, Chairperson

In memory of Prof. George Kanellis

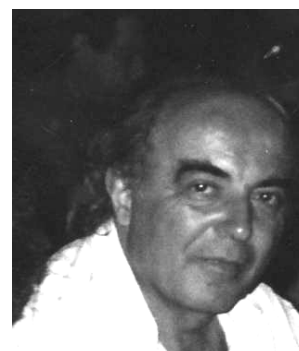
George Kanellis (1942- 2008) was born in Zagora of mount Pilion, Greece in 1942. After finishing the high school in Volos in 1960, he sat successfully entry examinations for University and was registered in the Department of Physics of the Aristotle University of Thessaloniki, from which he was awarded the Diploma of Physics in 1969. After completing his national service, he taught Physics for a short period at a state high school and then in 1970 was appointed Assistant in the Physics Chair A of the Physics and Mathematics (Science) Faculty of University of Thessaloniki, from which he was awarded the Doctorate (PhD) degree in 1977 for his contribution in the study of Lattice Dynamics of compounds with the chalcopyrite structure. Following successive promotions to higher positions, he retired in 2007 as Associate Professor. During his over 30 year service in the Department of Physics, George Kanellis taught a large number of undergraduate and postgraduate courses and was distinguished for the complete and precise transfer of knowledge to his students, as well as for the frequent and thorough discussions he had with his colleagues for the clarification of ambiguous concepts. He was characterized by an exhausting consideration in his pioneering research studies which were carried out either in the Department of Physics (Lattice Dynamics of Ag Chalcopyrites) or in top, recognized European Research Institutes, such as the Max Planck Institut für Festkörperforschung in Stuttgart (Professor M. Cardona, superstructures Si/Ge και H. Bilz, Lattice Dynamics of CuCl) and the Laboratory of Solid State Physics of the University Pierre et Marie Curie in Paris (Professor M. Balkanski, Lattice Dynamics in a thin rod). His published work amounts to more than 50 articles in international journals and is still cited regularly having accumulated a total number of citations over of 550. Without any exaggeration, he is reputed among the best recognized researchers in analytical studies of Lattice Dynamics of solids. George Kanellis served the Department of Physics also from other capacities, either as an active member of the General Assembly or as elected Chairman over the period 1997-2001 with essential contribution to the drafting of the existing Programme of Studies (Syllabus) of the Department of Physics. Unfortunately, his unexpected death in October 2008 interrupted his plans to give more time to his family and himself after retirement. His colleagues in the Section of Solid State Physics, in the Department of Physics and in other Departments of the University who highly respected him, as well as colleagues and friends belonging in relevant scientific areas will remember him with love and respect.



*Professor Sotirios Ves
School of Physics, AUTH*

In memory of Dr. Athanasios Simopoulos

Athanasios Simopoulos (1936- 2009) was born in Arta, Greece, in June 1936. He graduated from the 2nd High School of Athens in 1954 and then studied Physics in the University of Athens from 1955 until 1960. He was among the first young scientists who attended graduate courses in the Graduate School of the Demokritos National Center for Scientific Research in the period 1961-1964. In between, with the encouragement of the Demokritos administration he visited the Research Center A.E.R.E. Harwell, England with a two month scholarship (1962) and the Nuclear Research Center in Stockholm E.N.E.A. with a one month scholarship.



In 1964 Athanasios Simopoulos went to the Weizmann Institute of Science, Israel, specializing in Mössbauer effect γ -ray spectroscopy, where he completed his Ph.D. “Mössbauer Studies of ^{57}Fe impurities bound in non-magnetic crystals”. He returned to “D” and together with Athanasios Kostikas who had just returned from U.S.A. with a similar scientific experience they established the Mössbauer laboratory of Demokritos and developed the field of low temperature research in Greece. The Mössbauer laboratory earned national and international reputation through the collaboration of the practical and excellent experimental skills of Dr A. Simopoulos with those of the theoretician - experimentalist, Dr A. Kostikas.

Apart from the rich research work in the field of Solid State Physics A. Simopoulos is distinguished for his important contribution to the scientific education of young researchers through many doctoral dissertations, hundreds of publications in international journals, and announcements in scientific conferences. He visited many laboratories abroad as a specialist and participated in the organization of many conferences. His contributions to the application of Mössbauer spectroscopy in magnetism, superconductivity, inorganic chemistry, biology and archaeometry were fundamental. His scientific output was rich and of high quality (over 150 publications in peer-reviewed journals, over 2500 citations, $h = 27$).

He served “Demokritos” in a period where the research in Greece, especially in the area of Solid State Physics, was in its infancy. Beyond his rich educational and scientific contributions, A. Simopoulos contributed to the development and running of the Institute of Materials Science and NCSR “Demokritos” in general. He served as vice president of Demokritos and he was the first director of the Institute of Materials Science (1988).

All of those who were lucky to collaborate with him will remember him as a hard working, excellent scientist, with a gentle, wise and modest character.

Dr. Dimitris Niarchos
NCSR “Demokritos”

In memory of Dr. Thanasis Kostikas

Thanasis Kostikas (1933- 2008), was one of the first researchers at the Demokritos National Centre for Scientific Research in the early 60's where he worked until his retirement in 1993.



He was a graduate of the National Technical University of Athens in electrical engineering, but his scientific interests pushed him to continue with postgraduate studies in physics at Purdue University in the USA. After Purdue he went to Illinois Polytechnic where he taught and completed his doctorate titled “The Photoequilibrium between F and F' Centers in Potassium Chloride” (1962). After his return to Greece his scientific worth was soon evident in both his research and his teaching commitments. At first in the Physics Dept., and later in the Institute for Materials Science he made important contributions both to the development of the laboratories and the postgraduate research at Demokritos. In 1973 he traveled to South Korea as a representative of the International Atomic Energy Agency (IAEA), successfully setting up the Mössbauer Spectroscopy laboratory in Seoul. His most important achievement though may have been his inspiration of new generations of young scientists to begin scientific research, something which was in a formative stage in the 60's and 70's in Greece.

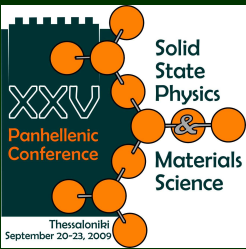
In his own research area, solid state physics, he made significant contributions in the introduction of new materials characterization techniques, bringing international recognition to the centre's laboratories. His internationally recognized research achievements are reflected in his more than 130 publications and 2500 citations (h-factor of 25). In Greece he was one of the first researchers to study material properties at low temperatures i.e down to 1.2K. He was also responsible for the installation of the liquid helium liquefier at Demokritos which currently supplies the entire country.

He taught physics both in the postgraduate program of Demokritos as well as in the University of Crete where he was a member of the executive committee in its early years. That he was an excellent teacher is recorded in the preface of the standard physics textbook of S. Trachanas, ‘Quantum Mechanics vol. I’. At Demokritos he worked administratively on many bodies, committees etc.

His close colleagues and students will always remember a man of principles and with characteristic deep scientific thought and judgment.

*Dr. Dimitris Niarchos
NCSR “Demokritos”*

XXV Panhellenic Conference on Solid State Physics and Materials Science
Scientific Program



Program & Proceedings
also available on the web
<http://xxv.physics.auth.gr>
xxv@physics.auth.gr
Tel. & Fax: +302310-998036

Sunday, Sept. 20

17⁰⁰ - 18³⁰ Registration

18³⁰ - 19⁰⁰ Opening Ceremony (*Chair: E. Paloura*)

19⁰⁰ - 20⁰⁰ Ple1 E. Dooryhee - CNRS, Grenoble, France
Looking into Art and Cultural Heritage with Synchrotron X - rays

20⁰⁰ Welcome Reception

Monday, Sept. 21

09⁰⁰ - 11⁰⁰ Session MO1: STRUCTURAL, MECHANICAL & OPTICAL PROPERTIES OF CONDENSED MATTER - 1

In memory of G. Kannelis (Chair: S. Ves & C. Raptis)

- 09⁰⁰ - 10⁰⁰ **Ple2** **K. Syassen (Max Plank Institut für Festkörperforschung, Stuttgart) - High - pressure studies of transition metal compounds located near the insulator - metal borderline**
- 10⁰⁰ - 10¹⁵ **O1** **A. Antonakos (NTUA, Dept. of Physics) - Controlling phase separation in manganite thin films**
- 10¹⁵ - 10³⁰ **O2** **D. Kastanis (FORTH/ICE-HT, Patras) - Plasma oxidation of multi - walled carbon nanotube sheets**
- 10³⁰ - 10⁴⁵ **O3** **Ch. Lekka (Univ. of Ioannina, Dept. of Mat. Sci. & Eng.) - Ultra fine structure of the short range order of the Cu₆₅Zr₃₅ and Cu₃₅Zr₆₅ metallic glasses**
- 10⁴⁵ - 11⁰⁰ **O4** **P. Kavouras (TEI Thessaloniki, Dept. of Applied Sciences) - The effect of In implantation on the structural and nano - mechanical properties of GaN**

11⁰⁰ - 11³⁰ Coffee break

11³⁰ - 13⁰⁰ Session MO2: POSTER SESSION: STRUCTURAL, MECHANICAL & OPTICAL PROPERTIES - 1 / ELECTRONIC TRANSPORT, SEMICONDUCTORS & DEVICES / PHOTONICS & OPTOELECTRONICS (Chair: G. Kourouklis, K.Syassen, E. Dooryhee)

13⁰⁰ - 14⁰⁰ Lunch break

14⁰⁰ - 16³⁰ Session MO3: ELECTRONIC TRANSPORT, SEMICONDUCTORS & DEVICES, PHOTONICS & OPTOELECTRONICS - 1

(Chair: G. Papavassiliou & C. Dimitriadis)

- 14⁰⁰ - 14³⁰ **I1** **E. Iliopoulos (Univ. of Crete, Dept. of Physics & FORTH, IESL) - Advancing III - nitrides epitaxy: from kinetics to new device applications**
- 14³⁰ - 14⁴⁵ **O5** **V. Constantoudis (NCSR "Demokritos", IMEL) - The role of gate width in transistor performance: Effects of gate sidewall roughness**
- 14⁴⁵ - 15⁰⁰ **O6** **A. Tsormpatzoglou (AUTH, Dept. of Physics, & IMEP, MINATEC, Grenoble) - Electrical characterization and design optimization of finfets with TiN/HfO₂ gate stack**
- 15⁰⁰ - 15¹⁵ **O7** **N. Kelaidis (NCSR "Demokritos", IMEL) - Electrical and structural characteristics of strained - Si MOS structures as a function of strained - Si overlayer**
- 15¹⁵ - 15⁴⁵ **I2** **E. Monroy (CEA -INAC/SP2M/PSC, Grenoble) - Polar and semipolar GaN/AlN nanostructures for optoelectronic applications**
- 15⁴⁵ - 16⁰⁰ **O8** **S. F. Galata (NCSR "Demokritos", IMS) - Stabilization of a very high - k tetragonal phase in Ge - doped ZrO₂ films grown by direct doping with Germanium**
- 16⁰⁰ - 16¹⁵ **O9** **G. Leftheriotis (Univ. of Patras, Dept. of Physics) - Electrochromic devices based on electrodeposited WO₃ films with modified surface morphology**
- 16¹⁵ - 16³⁰ **O10** **G. Mitrikas (NCSR "Demokritos", IMS) - Ultrafast control of nuclear spins using only microwave pulses: towards switchable solid state gates for quantum information processing**

16³⁰ - 17⁰⁰ Coffee break

17⁰⁰ - 18⁴⁵ Session MO4: ELECTRONIC TRANSPORT, SEMICONDUCTORS & DEVICES, PHOTONICS & OPTOELECTRONICS - 2

(Chair: P. Keliris & S. Logothetidis)

- 17⁰⁰ - 17³⁰ **I3** **M. Kafesaki (Univ. of Crete, Dept. of Mat. Sci. & Tech. & FORTH, IESL) - Manipulating light with optical left - handed metamaterials**
- 17³⁰ - 17⁴⁵ **O11** **C. Tserkezis (Univ. of Athens, Dept. of Physics) - Coupled plasmons and resonant effective permeability of metal - dielectric - metal nanosandwich assemblies**
- 17⁴⁵ - 18⁰⁰ **O12** **L. Mouchliadis (Cardiff Univ., School of Physics & Astronomy) - Exciton polaritons in resonant Bragg gratings**
- 18⁰⁰ - 18¹⁵ **O13** **Z. Viskadourakis (Univ. of Cyprus, Dept. Mechanical and Manufacturing Eng. & Univ. of Crete, Dept. of Mat. Sci. & Tech.) - Power factor enhancement in composite Ag - Bi - Ag planar thin film thermoelectric structures**
- 18¹⁵ - 18⁴⁵ **I4** **L. Palilis (NCSR "Demokritos", IMEL) - Molecular and polymeric organic semiconductors and their applications in plastic optoelectronic and photonic devices**

19⁰⁰ - 21⁰⁰ Round Table: RESEARCH PERSPECTIVES IN EUROPE & GREECE

Tuesday, Sept. 22

09⁰⁰ - 11⁰⁰ Session TU1: STRUCTURAL, MECHANICAL & OPTICAL PROPERTIES OF CONDENSED MATTER - 2

(Chair: S Kennou & A. Lappas)

- 09⁰⁰ - 10⁰⁰ **Ple3 F. Boscherini (Univ. of Bologna, Dept. of Physics) - New opportunities to study defects in semiconductors by soft X-ray absorption spectroscopy**
- 10⁰⁰ - 10¹⁵ O14 **G. Apostolopoulos (NCSR "Demokritos", INT-RP) - Neutron Compton scattering from LiH and LiD**
- 10¹⁵ - 10³⁰ O15 **Ch. B. Lioutas (AUTH, Dept. of Physics) - Identification of new nano-scale phases in AgPb₁₈SbSe₂₀ crystals by electron crystallography methods**
- 10³⁰ - 11⁰⁰ **I5 A. Erko (BESSY II, Helmholtz Zentrum Berlin für Materialien und Energie GmbH) - Ultra-high time-resolved XAS**

11⁰⁰ - 11³⁰ Coffee break

11³⁰ - 13⁰⁰ Session TU2: POSTER SESSION: STRUCTURAL, MECHANICAL & OPTICAL PROPERTIES - 2 / MAGNETISM & SUPERCONDUCTIVITY / CULTURAL HERITAGE MATERIALS & INTERDISCIPLINARY PHYSICS (Chair: T. Bakas, F. Boscherini, M. Farle)

13⁰⁰ - 14⁰⁰ Lunch break

14⁰⁰ - 16³⁰ Session TU3: MAGNETISM & SUPERCONDUCTIVITY - 1

In memory of A. Simopoulos & A. Kostikas (Chair: D. Niarchos & O. Kalogirou)

- 14¹⁵ - 15¹⁵ **Ple4 M. Farle (Univ. Duisburg – Essen, Dept. of Physics & Center for Nanointegration) - Magnetism at the nanoscale**
- 15¹⁵ - 15³⁰ O16 **E. Hristoforou (NTUA, School of Mining and Metallurgy Engineering) - New sensors based on the magnetostrictive delay line technique**
- 15³⁰ - 15⁴⁵ O17 **E. Th. Papaioannou (Uppsala Univ., Dept. of Physics & Mat. Sci.) - Magnetic and magneto-optical properties of transition metal films with sub-wavelength antidot arrays**
- 15⁴⁵ - 16⁰⁰ O18 **O. Crisan (National Inst. for Materials Physics, Bucharest) - Exchange spring effects in FePt/Fe(Co)/⁵⁷Fe multilayers**
- 16⁰⁰ - 16¹⁵ O19 **V. Tsakaloudi (CPERI, Lab. of Inorganic Materials) - New magnetic ferrite materials for innovative RFID concepts**
- 16¹⁵ - 16³⁰ O20 **A. Andriotis (FORTH, IESL) - Defect-induced defect-mediated magnetism in diluted magnetic semiconductors**

16³⁰ - 17⁰⁰ Coffee break

17⁰⁰ - 18⁰⁰ Session TU4: MAGNETISM & SUPERCONDUCTIVITY - 2

In memory of A. Simopoulos & A. Kostikas (Chair: E. Hristoforou & K. G. Efthymiadis)

- 17⁰⁰ - 17³⁰ **I6 P. Pouloupoulos (Univ. of Patras, Dept. of Mat. Sci.) - Magnetic force microscopy on thin films and nanostructures**
- 17³⁰ - 17⁴⁵ O21 **A. Kaidatzis (Université Paris Sud, CNRS, Lab. de Physique des Solides) - Hot electron transport and high resolution magnetic imaging on Co/Cu/Co and Co/Cu/NiFe spin valves**
- 17⁴⁵ - 18⁰⁰ O22 **K. N. Trohidou (NCSR "Demokritos", Inst. of Mat. Sci.) - Exchange bias effects in Co nanoparticles dispersed in a Mn matrix**

18⁰⁰ - 19³⁰ Session TU5: CULTURAL HERITAGE MATERIALS & INTERDISCIPLINARY PHYSICS

(Chair: K.M. Paraskevopoulos & E.K. Polychroniadis)

- 18⁰⁰ - 18³⁰ **I7 Th. Samaras (AUTH, Dept. of Physics) - The use of iron oxide nanoparticles in hyperthermia**
- 18³⁰ - 18⁴⁵ O23 **P. Papanikolaou (AUTH, Dept. of Chemistry) - Study of the effect of a uniform electric field on the bond lengths and the electronic distribution of diatomic and polyatomic molecules**
- 18⁴⁵ - 19⁰⁰ O24 **E. Pavlidou (AUTH, Dept. of Physics) - Wall painting materials and technique: the case of famous iconographer Onoufrios**
- 19⁰⁰ - 19¹⁵ O25 **M. Maragakis (AUTH, Dept. of Physics) - Random walk in complex systems with the particle diffusion model**
- 19¹⁵ - 19³⁰ O26 **B. Subedi (AUTH, Dept. of Physics & CETI Archaeometry Lab.) - Towards luminescence dating of turquoise gemstone using TL and OSL methods**

21⁰⁰ - Conference Dinner

Wednesday, Sept. 23

09⁰⁰ - 11⁰⁰ Session WE1: INHOMOGENEOUS & DISORDERED MATERIALS, POLYMERS & BIOMATERIALS

(Chair: S. Messoloras & A. Andriotis)

- 09⁰⁰ - 09³⁰ I8 I. Margiolaki (ESRF, Grenoble) - *Complementary methods for the study of biomaterials*
- 09³⁰ - 09⁴⁵ O27 G. Soras (NHRF, Theoretical & Physical Chemistry Inst. & Univ. of Athens, Chemistry Dept) - *Synthesis of novel transition metal dithiolenes: Synthesis, experimental and theoretical investigation*
- 09⁴⁵ - 10⁰⁰ O28 E. Karakosta (NCSR "Demokritos", IMS) - *In situ monitoring of cement gel growth dynamics. The use of a miniaturized permanent Halbach magnet for precise ¹H NMR studies*
- 10⁰⁰ - 10³⁰ I9 N. Papageorgiou (Univ. de la Méditerranée & Univ. de Provence, CNRS) - *Transmission electron microscopy of proteins and single particle 3D reconstruction*
- 10³⁰ - 10⁴⁵ O29 K. Chrissopoulou (FORTH, IESL) - *Effect of inorganic additive on the chain crystallization in polymer / layered silicate nanohybrids*
- 10⁴⁵ - 11⁰⁰ O30 G. Kalosakas (Univ. of Patras, Dept. of Mat. Sci.) - *Tight Binding Parameters for Charge Transport in DNA*

11⁰⁰ - 11³⁰ Coffee break

11³⁰ - 13⁰⁰ Session WE2: POSTER SESSION: INHOMOGENEOUS & DISORDERED MATERIALS, POLYMERS & BIOMATERIALS/ NANOSCALE & SURFACE SCIENCE (Chair: M. Calamiotou, E. Liarokapis, C. Galiotis)

13⁰⁰ - 14⁰⁰ Lunch break

14⁰⁰ - 15³⁰ Session WE3: NANOSCALE & SURFACE SCIENCE - 1

(Chair: A. Vomvas & Th. Karakostas)

- 14⁰⁰ - 14³⁰ I10 D. Christofilos (AUTH, School of Technology) - *Optical spectroscopy of nanoobjects: carbon nanotubes and metallic nanoparticles*
- 14³⁰ - 14⁴⁵ O31 T. Leontiou (Cyprus Univ. of Technology, Dept. of Mech. & Mat. Sci. Eng.) - *Thermodynamics and kinetics of dislocated Ge/Si and InAs/GaAs thin layers*
- 14⁴⁵ - 15⁰⁰ O32 A. P. Douvalis (Univ. of Ioannina, Dept. of Physics) - *Synthesis and characterization of novel carbon nanotubes - iron oxide nanoparticles hybrids*
- 15⁰⁰ - 15¹⁵ O33 J. Kioseoglou (AUTH, Dept. of Physics) - *The nonpolar - semipolar boundaries in III - nitrides: Atomic structure and influence on defect introduction*
- 15¹⁵ - 15³⁰ O34 A. Skarmoutsou (NTUA, School of Chem.Eng.) - *Nanomechanical properties of hydroxyapatite (HA) with DAB dendrimers (poly propylene imine) coatings onto Ti surfaces*

15³⁰ - 16⁰⁰ Coffee break

16⁰⁰ - 17³⁰ Session WE4: NANOSCALE & SURFACE SCIENCE - 2

(Chair: Ph. Komninou & M. Kamaratos)

- 16⁰⁰ - 16³⁰ I11 P. Patsalas (Univ. of Ioannina, Dept. of Mat. Sci. & Eng.) - *Complex conducting nitrides: Synthesis, structure, properties and applications*
- 16³⁰ - 16⁴⁵ O35 E. Symianakis (Univ. of Patras, Dept. of Chem. Eng. & ICE/HT-FORTH) - *On the substrate - driven oxidation of Ni/NiO(001) by X - ray photoelectron spectroscopy and molecular dynamics simulations*
- 16⁴⁵ - 17⁰⁰ O36 A. Kostopoulou (FORTH, IESL, Un. Of Crete, Dept. of Chemistry) - *Magneto - optical properties of iron oxide nanoclusters*
- 17⁰⁰ - 17¹⁵ O37 N. Galanis (Univ. of Crete, Dept. of Mat. Sci. & Tech.) - *Mechanical properties of nanocrystalline Copper*
- 17¹⁵ - 17³⁰ O38 D. Vlachos (Univ. of Ioannina, Dept. of Physics) - *Indium adsorption on the reconstructed Si(111)√3×√3 and 4×1 - In surfaces at room and low temperature*

17³⁰ - 18³⁰ Session WE5: SPECIAL SESSION ON RENEWABLE ENERGY RESOURCES – HYDROGEN (UNDER THE AUSPICES OF HELLENIC SOCIETY FOR SCIENCE AND TECHNOLOGY OF CONDENSED MATTER (H.S.S.T.C.M)) (Chair: H. Gamari-Seale)

- 17³⁰ - 18⁰⁰ I12 A. G. Konstandopoulos (CPERI/CERTH, & AUTH, Dept. of Chem. Eng.) - *Solar thermochemical water-splitting for Hydrogen production: The Hydrosol Process*
- 18⁰⁰ - 18³⁰ I13 E. Varkaraki (CRES-Center for renewable energy sources & hydrogen technologies-Pikermi) - *Perspectives and challenges of hydrogen storage in metal hydrides. The case of the CRES wind-hydrogen plant*

18³⁰ - 19⁰⁰ Awards - Closing Ceremony

19⁰⁰ - 19³⁰ Annual Meeting of the Hellenic Society for Science and Technology of Condensed Matter

Monday, Sept. 21

11³⁰ - 13⁰⁰ : Session MO2: Poster Session

STRUCTURAL, MECHANICAL & OPTICAL PROPERTIES - 1 / ELECTRONIC TRANSPORT, SEMICONDUCTORS & DEVICES / PHOTONICS & OPTOELECTRONICS

MO2-P1	J. Parthenios (FORTH, ICE- HT, Patras) - <i>The effect of temperature on aramid fibre phonons</i>
MO2-P2	A. E. Lagogianni (Univ. of Ioannina, Dept. of Physics) - <i>Microstructure evolution in Cu_xZr_{100-x} metallic glasses under tensile deformation</i>
MO2-P3	Ch. Argiris (NTUA, School of Chemical Engineering & Technische Universität Clausthal, Inst. für Metallurgie) - <i>Water and carbon dioxide as sources for oxygen incorporation into acceptor Doped SrTiO₃ single crystals</i>
MO2-P4	K. Vartzelis – Nikakis (NTUA, Dept. of Physics) - <i>Molecular dynamics in intercalated poly (propylene oxide) amines/layered silicate nanocomposites</i>
MO2-P5	E. Almpanis (NCSR “Demokritos”, IMEL) - <i>Optical response of plasmonic nanoantenna arrays</i>
MO2-P6	K. Pomoni (Univ. of Patras, Dept. of Physics) - <i>Structure and photoconductivity of modified TiO₂ sol-gel coatings</i>
MO2-P7	E. Kalesaki (AUTH, Dept. of Physics) - <i>Structural and electronic properties of InN a-edge threading dislocations</i>
MO2-P8	H. Zoubos (Univ. of Ioannina, Dept. of Materials Science and Engineering)- <i>Optical properties of AlN-based nanocomposite films</i>
MO2-P9	I. Efthimiopoulos (Max Plank Inst. für Festkörperforschung, Stuttgart) - <i>High pressure studies of the perovskite isotopes Re¹⁶O₃ and Re¹⁸O₃</i>
MO2-P10	I. Efthimiopoulos (Max Plank Inst. für Festkörperforschung, Stuttgart) - <i>Structural and spectroscopic studies of the multiferroic spinel CdCr₂S₄ under pressure</i>
MO2-P11	I. Efthimiopoulos (Max Plank Inst. für Festkörperforschung, Stuttgart) - <i>High pressure structural investigations of Fe-based superconductors</i>
MO2-P12	S. M. Souliou (AUTH, Dept. of Physics & School of Technology) - <i>Probing the pressure-induced structural deformation of carbon nanotubes through carotene encapsulation in their interior</i>
MO2-P13	C. A. Londos (Univ. of Athens, Dept. of Physics) - <i>The effect of germanium doping on the annealing characteristics of the VO and VO₂ defects in silicon.</i>
MO2-P14	V. Likodimos (NCSR “Demokritos”, IPC) - <i>Micro-Raman investigation on the long term stability of dye-sensitized solar cells under light and thermal stress</i>
MO2-P15	V. Likodimos (NCSR “Demokritos”, IPC) - <i>Micro-Raman spectroscopy on self-assembled anodized TiO₂ nanotube arrays</i>
MO2-P16	M. Dimitrijevic (Univ. of Belgrade, Faculty of Technology and Metallurgy) - <i>Use of image analysis for characterisation of thermal shock behaviour of improved ceramic matrix composites</i>
MO2-P17	M. Posarac (Inst. of Nuclear Sciences “Vinca”, Belgrade) - <i>Influence of microstructure on mechanical properties of porous SiC/cordierite composite materials</i>
MO2-P18	Th. A. Goutziotis (Univ. of Ioannina, Dept. of Materials Science and Engineering) - <i>Structural and electronic properties of metal nitrides</i>

Monday, Sept. 21

11³⁰ - 13⁰⁰ : Session MO2: Poster Session

STRUCTURAL, MECHANICAL & OPTICAL PROPERTIES - 1 / ELECTRONIC TRANSPORT, SEMICONDUCTORS & DEVICES / PHOTONICS & OPTOELECTRONICS

MO2-P19	Ch. Motsanos (Univ. of Crete, Dept. of Materials Science and Technology) - <i>A maximum in the strength of superhard Rhenium Borides</i>
MO2-P20	Th. Ch. Hasapis (AUnTh, Dept. of Physics) - <i>Far infrared spectra and structure of $(K_2S)_x(Sb_2S_3)_{100-x}$ glasses</i>
MO2-P21	E. Ramou (Univ. of Patras, Dept. of Physics) - <i>On the measurement of the instability thresholds of nematic liquid crystal</i>
MO2-P22	E. M. Pechlivani (AUnTh, Dept. of Physics) - <i>Interaction between heterostructural interfaces and structural faults in GaN / $Al_xGa_{1-x}N$ on Al_2O_3 thin films</i>
MO2-P23	Th. Kehagias (AUnTh, Dept. of Physics) - <i>Mechanisms of indium segregation in MOVPE and MBE grown InAlN epilayers</i>
MO2-P24	M. Gioti (AUnTh, Dept. of Physics) - <i>Evaluation of the optical properties, stoichiometry and composition of SiO_x films on PET by ellipsometry</i>
MO2-P25	D. Georgiou (AUnTh, Dept. of Physics) - <i>Effect of thickness on the optical properties of CuPc and C60 thin films for organic photovoltaic applications</i>
MO2-P26	A. Laskarakis (AUnTh, Dept. of Physics) - <i>Effect of thickness in the optical properties of organic thin films deposited via organic vapor phase deposition</i>
MO2-P27	E. D. Vanidhis (AUnTh, Dept. of Physics) - <i>Theoretical calculations to determine the electro-gyration coefficients in point group of $CaCO_3$</i>
MO2-P28	E. Kalesaki (AUnTh, Dept. of Physics) - <i>Morphological and structural characterization of polar and semipolar GaN quantum dots in AlN</i>
MO2-P29	M. Marinova (AUnTh, Dept. of Physics) - <i>Typical structural defects in 3C-SiC layers grown by various methods on different substrates</i>
MO2-P30	A. Lotsari (AUnTh, Dept. of Physics) - <i>Structural and mechanical properties of AlN:Ag nanocomposite coatings grown by pulsed laser deposition</i>
MO2-P31	C. Aris Chatzidimitriou-Dreismann (Technical Univ. of Berlin, Inst. of Chemistry) - <i>Scattering of fast neutrons from protons in solids ($NbH_{0.80}$ and LiH): New quantum effects in the attosecond timescale</i>
MO2-P32	D. Berdekas (Direction of High Schools Education of Larissa) - <i>The influence of the disorder in the Raman spectra of GaSb/AlSb (001) superlattices</i>
MO2-P33	G. Mitrikas (NCSR "Demokritos", IMS) - <i>Probing the electronic structure of molecular magnets by pulse EPR methods</i>
MO2-P34	<i>Withdrawn</i>
MO2-P35	A. Vomvas (Univ. of Patras, Dept. of Physics) - <i>Dark conductivity and photoconductivity behavior of sol-gel S-doped TiO_2, thermally treated at different temperatures</i>

Monday, Sept. 21

11³⁰ - 13⁰⁰ : Session MO2: Poster Session

STRUCTURAL, MECHANICAL & OPTICAL PROPERTIES - 1 / ELECTRONIC TRANSPORT, SEMICONDUCTORS & DEVICES / PHOTONICS & OPTOELECTRONICS

MO2-P36	M. Dimakogianni (Univ. of Athens, Dept. of Physics) - <i>Field and temperature dependence of the small polaron hopping electrical conductivity in 1D disordered systems</i>
MO2-P37	C. Paraskeva (AUTH, Dept. of Physics) - <i>Study of LiMgVO₄ ionic conductivity mechanisms</i>
MO2-P38	S. D. Pappas (Univ. of Patras, School of Engineering) - <i>Photoluminescence from SiO₂ thin films produced by Reactive Radio Frequency Magnetron Sputtering</i>
MO2-P39	K. T. Zorbass (AUTH, Dept. of Physics & Univ. of Cyprus, Dept. of Mechanical and Manufacturing Engineering) - <i>Study of an in-car refrigerator using commercial Bi₂Te₃ thermoelectric modules</i>
MO2-P40	V. Vargiamidis (AUTH, Dept. of Physics) - <i>Fano resonances in electronic transport through quantum wires</i>
MO2-P41	V. N. Petoussis (Univ. of Thessaly, Dept of Electrical & Computer Engineering) - <i>A novel Hall effect sensor using elaborate offset cancellation method</i>
MO2-P42	V. N. Petoussis (TEI of Lamia, Dept. of Electronics) - <i>Semiconductor spintronics</i>
MO2-P43	G. Kitis (AUTH, Dept. of Physics) - <i>Correlation between TL And OSL signals in KMgF₃:Ce³⁺; Bleaching study of individual glow peaks</i>
MO2-P44	G. S. Polymeris (C.E.T.I., R.C "ATHENA", Archaeometry Lab., Xanthi) - <i>Thermally assisted photo transfer OSL from deep traps in Al₂O₃:C</i>

Tuesday, Sept. 22

11³⁰ - 13⁰⁰ : Session TU2: Poster Session

STRUCTURAL, MECHANICAL & OPTICAL PROPERTIES - 2 / MAGNETISM & SUPERCONDUCTIVITY / CULTURAL HERITAGE MATERIALS & INTERDISCIPLINARY PHYSICS

TU2-P1	D. Tsitrouli (NCSR "Demokritos", IMS) - <i>In vitro and in vivo efficient magnetic heating with polymer-dressed Fe₂O₃ nanoparticles</i>
TU2-P2	P. Pandis (NTUA, School of Chemical Engineering) - <i>Oxygen permeation study through dense ceramic membranes with perovskite structure (Ba_{0.8}Sr_{0.2}M_xB_{1-x}O_{3±δ}, M=Co, Al, B=Mn, Fe, Ni)</i>
TU2-P3	F. Noli (AUTH, Dept. of Chemistry) - <i>Surface characterisation of nitrogen-implanted steel and corrosion behaviour in aggressive environment</i>
TU2-P4	K. Kosmas (NTUA, Lab. of Physical Metallurgy) - <i>On the magnetic properties of plastically deformed Armco steel</i>
TU2-P5	P. Apostolopoulos (AUTH, Dept. of Physics) - <i>Designing composite panels for minimum cost and weight</i>
TU2-P6	F. Pinakidou (AUTH, Dept. of Physics) - <i>Nanostructural characterization of TiN-Cu films using EXAFS spectroscopy</i>
TU2-P7	F. Pinakidou (AUTH, Dept. of Physics) - <i>Micro-XRF and micro-EXAFS studies of an Al matrix Fe-Ni composite</i>
TU2-P8	D. Moussadakos (Univ. of Athens, Dept. of Physics) - <i>Magnetic properties of Nd-Fe-B/3:29 and Sm(CoFeCuZr)_{7.5}/3:29 nanocomposite permanent magnets</i>
TU2-P9	N Pistofidis (AUTH, Dept. of Physics) - <i>Effect of the steel composition on the morphology of zinc hot-dip galvanized coatings</i>
TU2-P10	N. Pistofidis (AUTH, Dept. of Physics) - <i>Effect of the cooling time on the morphology of zinc hot-dip galvanized coatings</i>
TU2-P11	N. Pistofidis (AUTH, Dept. of Physics) - <i>Thermodynamic evaluation of zinc hot-dip galvanizing</i>
TU2-P12	N. Pistofidis (AUTH, Dept. of Physics) - <i>Evaluation of Fe-Zn diffusion coefficient during hot-dip galvanizing</i>
TU2-P13	M. Papazoglou (AUTH, Dept. of Physics) - <i>Comparative examination on structure and oxidation behavior of pack cementation zinc coated and not coated copper alloys substrates</i>
TU2-P14	M. Papazoglou (AUTH, Dept. of Physics) - <i>Influence of Al and Cr alloying elements on the structure and corrosion resistance of zinc coatings formed by pack cementation process</i>
TU2-P15	D. Hadjiapostolidou (Imperial College London, Dept. of Materials) - <i>Coarsening in René 80 Ni-based superalloy</i>
TU2-P16	K. Mergia (NCSR "Demokritos", INT-RP) - <i>Residual stress measurements on CuCrZr/W brazed alloy using neutron diffraction</i>
TU2-P17	N. Moutis (NCSR "Demokritos", INT-RP) - <i>Brazing of Nimonic superalloy to carbon-based ceramic composites</i>
TU2-P18	Y. Keremi (AUTH, Dept. of Physics) - <i>Effect of indium implantation on the bonding environment of GaN</i>
TU2-P19	E. Siranidi (NTUA, Dept. of Physics) - <i>Pressure-induced phase separation in the Y123 superconductor</i>

Tuesday, Sept. 22

11³⁰ - 13⁰⁰ : Session TU2: Poster Session

STRUCTURAL, MECHANICAL & OPTICAL PROPERTIES - 2 / MAGNETISM & SUPERCONDUCTIVITY / CULTURAL HERITAGE MATERIALS & INTERDISCIPLINARY PHYSICS

TU2-P20	C. Simserides (NCSR "Demokritos", IMS) - <i>Influence of antiferromagnetic interactions and of alloy disorder on the ferromagnetic properties of p-type (Cd,Mn)Te quantum wells</i>
TU2-P21	M. Vasilakaki (NCSR "Demokritos", IMS) - <i>Numerical study of the exchange bias effect in nanoparticles with ferromagnetic core / ferrimagnetic shell morphology</i>
TU2-P22	N. Panopoulos (NCSR "Demokritos", IMS) - <i>Structural investigation of optimal doped manganites at high temperature NMR</i>
TU2-P23	D. Koumoulis (NCSR "Demokritos", IMS) - <i>¹³⁹La NMR study reveals peculiar spin ordering and antiferromagnetism in the overdoped region of La_{1-x}Ca_xMnO₃ phase diagram</i>
TU2-P24	V. Likodimos (Univ. Of Athens, Dept. Of Physics) - <i>Matrix effects in carbon nanotube polymer composites</i>
TU2-P25	V. Likodimos (Univ. Of Athens, Dept. Of Physics) - <i>Magnetic properties of single-wall carbon nanotubes</i>
TU2-P26	N. Ntallis (AUTH, Dept. of Physics) - <i>Study of a magnetic NDT method with finite elements analysis</i>
TU2-P27	P. Arampatzis-Ziamos (AUTH, Dept. of Physics) - <i>Optimization of time response in electromechanical systems with iron core</i>
TU2-P28	C. Serletis (AUTH, Dept. of Physics) - <i>Experimental errors in magnetic viscosity measurements and activation volume calculations</i>
TU2-P29	G. Litsardakis (AUTH, Dept. of Electrical and Computer Engineering) - <i>Electromagnetic properties and absorption of new La substituted Sr W-type hexaferrite in the 2-18 GHz frequency range</i>
TU2-P30	D. Sakellari (AUTH, Dept. of Physics) - <i>Study of the mechanism through which microstructural characteristics affect the impedance of NiCuZn ferrites</i>
TU2-P31	A. Markou (Univ. of Ioannina, Dept. of Materials Science and Engineering) - <i>Magnetic thin films deposited on PDMS nanotemplates</i>
TU2-P32	A. Kotoulas (AUTH, Dept. of Physics) - <i>Controllable synthesis and characterization of hcp and fcc nickel nanoparticles</i>
TU2-P33	I. Giannarakis (AUTH, Dept. of Physics) - <i>The beneficiary role of intentional alloying in noble metal-Cobalt multilayered systems</i>
TU2-P34	Th. Gkinis (AUTH, Dept. of Physics) - <i>Evaluation of iron oxide nanoparticles prepared by high-energy ball milling in drinking water treatment</i>
TU2-P35	A. Gaki (NTUA, School of Chemical Engineering) - <i>Synthesis and magnetic properties of LaCO_{3-δ} and La_{0.8}Sr_{0.2}CoO_{3-δ}</i>
TU2-P36	N. Sheloudko ("St. Kl. Ohridski" Univ. of Sofia, Faculty of Physics) - <i>Magnetic anisotropy of Ho-Fe-Co-Cr intermetallic compounds</i>

Tuesday, Sept. 22

11³⁰ - 13⁰⁰ : Session TU2: Poster Session

STRUCTURAL, MECHANICAL & OPTICAL PROPERTIES - 2 / MAGNETISM & SUPERCONDUCTIVITY / CULTURAL HERITAGE MATERIALS & INTERDISCIPLINARY PHYSICS

TU2-P37 **K. Simeonidis** (AUTH, Dept. of Physics)- *Structural, morphological and magnetic features in exchange-biased Co nanoparticles*

TU2-P38 **P. Vlachos** (Democritus Univ. of Thrace, Dept. of Electrical and Computer Engineering) - *A quantum circuit for quantum key expansion from 6 to 24 Qubits*

TU2-P39 **K. Chrissafis** (AUTH, Dept. of Physics) - *Thermal degradation kinetics of in-situ prepared PET nanocomposites containing fumed silica nanoparticles (SiO₂)*

TU2-P40 **K. Chrissafis** (AUTH, Dept. of Physics) - *Thermal degradation kinetics of in-situ prepared PET nanocomposites containing organically modified montmorillonite (MMT) nanoparticles*

TU2-P41 **P. Argyrakis** (AUTH, Dept. of Physics) - *Scientific collaboration in Europe, and the Overlapping Tree Network*

TU2-P42 **A. Kittas** (AUTH, Dept. of Physics) - *Trapping in complex networks*

TU2-P43 **E. Filippaki** (NCSR "Demokritos", IMS) - *Optical emission spectroscopy in a glow discharge plasma during the restoration of iron corroded objects*

TU2-P44 **E. Filippaki** (NCSR "Demokritos", IMS) - *Effect of the Hydrogen-reductive plasma on underwater oxidized objects. Chaotic plasma configuration*

TU2-P45 **S. K. Papadopoulou** (AUTH, Dept. of Physics) - *Efficacy of hydrophobic polymeric coatings and superhydrophobic nanoparticle based composite films for the protection of stone*

TU2-P46 **E. Anagnostopoulou** (AUTH, Dept. of Physics) - *Magnetically induced hyperthermia: Size, phase and concentration-dependent heating power of magnetic nanoparticles*

TU2-P47 **E. Pavlidou** (AUTH, Dept. of Physics) - *Technique and painting materials characterization of St. Athanasius Church in Moschopolis, Albania (18th Century)*

TU2-P48 **E. Pavlidou** (AUTH, Dept. of Physics) - *Study of the painting materials from 4th century B.C. Vergina Tomb*

TU2-P49 **A. Chalkidou** (AUTH, Dept. of Physics & Theagenio Cancer Hospital, Molecular Oncology Lab.) - *Preparation, characterization and in-vitro toxicity test of nanoparticle-based system for magnetic hyperthermia of cancer tissues*

TU2-P50 **E. Sakellariou** (AUTH, Dept. of Physics) - *Studying technique and pigments of wall paintings in the Byzantine Church of "40 Holy Martyrs" in Veliko- Turnovo in Bulgaria*

TU2-P51 **A. Lappas** (FORTH, IESL) - *Order Against Frustration in a Spin-2 Triangular Lattice System α -NaMnO₂*

Wednesday, Sept. 23

11³⁰ - 13⁰⁰ : Session WE2: Poster Session

INHOMOGENEOUS & DISORDERED MATERIALS, POLYMERS & BIOMATERIALS / NANOSCALE & SURFACE SCIENCE

WE2-P1	D. Chasoglou (Chalmers Univ. of Technology, Gothenburg) - <i>Evaluation of surface characteristics of prealloyed Cr-Mo-steel powder</i>
WE2-P2	Z. Sompolos (Univ. of Patras, Dept. of Physics) - <i>Study of thin YSZ coatings deposited by e-beam evaporation</i>
WE2-P3	G. E. Vantarakis (Univ. of Crete, Dept. of Materials Science and Technology & Cyprus Univ. of Technology, Dept. of Mechanical and Materials Science Engineering) - <i>Atomistic simulations of carbon nanofoams</i>
WE2-P4	G. C. Hadjisavvas (Cyprus Univ. of Technology, Dept. of Mechanical and Materials Science Engineering) - <i>Theory of defects in Si nanocrystals embedded in α-SiO₂</i>
WE2-P5	G. Syrrokostas (Univ. of Patras, Dept. of Physics) - <i>Nanostructured thin films for dye sensitized solar cells</i>
WE2-P6	I. Spanos (Univ. of Patras, Dept. of Physics) - <i>Electrolytic Hydrogen production using ternary and quaternary Nickel based coatings</i>
WE2-P7	K. T. Kleovoulou (Univ. of Crete, Dept. of Physics) - <i>Interacting Si nanocrystals in α-SiO₂: a Monte Carlo study</i>
WE2-P8	D. Georgakaki (AUniv, Dept. of Physics) - <i>Application of time-series analysis methods for the study of nonlinear dynamical phenomena during nanosurface characterization in AFM metrology</i>
WE2-P9	Ch. B. Lioutas (AUniv, Dept. of Physics) - <i>Structural characterization of Ti / TiB₂ multi-nano-layer films by means of electron microscopy techniques</i>
WE2-P10	D. Lafatzis (NCSR "Demokritos", INT-RP) - <i>Oxidization behaviour of amorphous SiC coatings</i>
WE2-P11	G. Bokas (Univ. of Ioannina, Dept. of Physics) - <i>CuZr nanoclusters by ab-initio calculations</i>
WE2-P12	M. Gialampouki (Univ. of Ioannina, Dept. of Materials Science and Engineering) - <i>Structural and electronic properties of octahedral Titanium Oxide on Graphene by ab-initio calculations</i>
WE2-P13	O. Crisan (National Inst. for Materials Physics, Bucharest) - <i>Magnetic nanoclusters synthesized by a new gas-stabilised aggregation technique</i>
WE2-P14	E. P. Koumoulos (NTUA, School of Chemical Engineering)- <i>Effect of the adhesive forces and time-dependent response of polydimethylsiloxane elastomer on the nanomechanical properties determination by nanoindentation</i>
WE2-P15	A. Skarmoutsou (NTUA, School of Chemical Engineering) - <i>Nanoindentation studies and high stress sensitivity of fatigue life of rolled AZ31 Magnesium alloy</i>
WE2-P16	J. N. Remediakis (Univ. of Crete, Dept. of Materials Science and Technology) - <i>Shape and properties of gold nanoparticles</i>
WE2-P17	A. Delimitis (CERTH, CPERI, Thessaloniki) - <i>Electron microscopy studies of the structural transformation of VOHPO₄.1/2H₂O precursors to (VO)₂P₂O₇ catalysts</i>

Wednesday, Sept. 23

11³⁰ - 13⁰⁰ : Session WE2: Poster Session

INHOMOGENEOUS & DISORDERED MATERIALS, POLYMERS & BIOMATERIALS / NANOSCALE & SURFACE SCIENCE

WE2-P18	A. Zora (Univ. of Athens, Dept. of Physics) - <i>Temperature dependence of photoluminescence in individual self-assembled quantum dots</i>
WE2-P19	M. Filippousi (AUn, Dept. of Physics) - <i>Preparation and characterization of palladium supported on zeolites</i>
WE2-P20	A. Skarmoutsou (NTUA, School of Chemical Engineering) - <i>Nanomechanical and structural properties of deposited binary nitrides thin films grown by Pulsed Laser Deposition</i>
WE2-P21	C. Georgiou (NTUA, School of Chemical Engineering) - <i>Mechanical and electrical properties of epoxy resin filled with multi walled Carbon nanotubes</i>
WE2-P22	G. A. Tritsarlis (Technical Univ. of Denmark, Dept. of Physics) - <i>Theoretical investigation of model non-Platinum cathode catalysts for low temperature fuel cells</i>
WE2-P23	N. Tsakiris (AUn, Dept. of Physics) - <i>Crystal growth model with stress development and relaxation</i>
WE2-P24	C. Batistakis (AUn, Dept. of Physics) - <i>Percolation theory and phase transitions in granular ferromagnets</i>
WE2-P25	L. Skarpalezos (AUn, Dept. of Physics) - <i>Simulation of non classical coarsening mechanism in Pb/Si</i>
WE2-P26	K. Brintakis (FORTH, IESL & AUn, Dept. of Physics) - <i>Fe₃O₄@Au core-shell nanocrystals: magnetic and optical properties</i>
WE2-P27	A. P. Douvalis (Univ. of Ioannina, Dept. of Physics) - <i>Structural and magnetic properties of colloidal Iron oxide magnetic nanoclusters</i>
WE2-P28	A. Tsimpliaraki (AUn, Dept. of Chemical Engineering) - <i>Organomodification of nanoclays and its role on the porous structure of polymer nanocomposites produced by supercritical CO₂</i>
WE2-P29	J. Kioseoglou (AUn, Dept. of Physics) - <i>Atomic scale modelling by the use of a III-species environment approach: Implementation on threading dislocations and (Al,In)N/GaN interfaces</i>
WE2-P30	D. Tsikritzis (Univ. of Patras, Dept. of Chemical Engineering - FORTH/ICE-HT) - <i>The electronic structure of Ni-phthalocyanine on ITO/flexible interface studied by photoelectron spectroscopies</i>
WE2-P31	I. Tsiaoussis (AUn, Dept. of Physics) - <i>Structural characterization of ZnO/Mg_xZn_{1-x}O and ZnO/MgO thin films grown on sapphire by using HRTEM</i>
WE2-P32	V. Kouloukakis (Univ. of Western Macedonia) - <i>Hydrogen storage in the pseudobinary system of TiMn_{0.4}Fe_{0.2}V_{0.4}, TiMn_{0.1}Fe_{0.2}V_{0.7} and Ti_{0.4}Zr_{0.6}Mn_{0.4}Fe_{0.2}V_{0.4}</i>
WE2-P33	A. Ioannidou (Univ. of Western Macedonia, Dept. of Mechanical Engineering) - <i>Structural properties of the effect of V substitution on the composite Zr-Ti-Cr-V-Ni intermetallic hydrides</i>
WE2-P34	T. E. Karakasidis (Univ. of Thessaly, School of Engineering) - <i>Transport properties of flows at the nanoscale</i>
WE2-P35	T. E. Karakasidis (Univ. of Thessaly, School of Engineering) - <i>Flow in periodically grooved nanochannels studied by computer simulation</i>

Wednesday, Sept. 23

11³⁰ - 13⁰⁰ : Session WE2: Poster Session

INHOMOGENEOUS & DISORDERED MATERIALS, POLYMERS & BIOMATERIALS / NANOSCALE & SURFACE SCIENCE

WE2-P36	E. Pavlopoulou (FORTH, IESL & Univ. of Crete, Dept. of Materials Science and Technology) - <i>Following the synthesis of metal nanoparticles within pH-responsive micelles and microgels by SAXS</i>
WE2-P37	C. Grigoriadis (Univ. of Ioannina, Dept. of Physics) - <i>Self-assembly and molecular dynamics of nanographenes</i>
WE2-P38	A. Z. Stimoniaris (Univ. of Ioannina, Dept. of Chemistry & TEI of Western Macedonia, Lab. of Physics and Materials Technology) - <i>Absorption and diffusion of commercially available cleaning liquids in epoxy resin nanocomposites</i>
WE2-P39	A. Z. Stimoniaris (Univ. of Ioannina, Dept. of Chemistry & TEI of Western Macedonia, Lab. of Physics and Materials Technology) - <i>Fluid absorption effects on the dynamics of epoxy resin nanocomposites</i>
WE2-P40	C. G. Delides (TEI of Western Macedonia, Lab. of Physics and Materials Technology) - <i>Epoxy composites filled with amine modified carbon nanotubes: High voltage corona discharge studies</i>
WE2-P41	H. Zois (TEI of Lamia) - <i>Thermogravimetric properties of epoxy resin/carbon nanotubes nanocomposites</i>
WE2-P42	G. Ioannou (Univ. of Patras, Dept. of Materials Science) - <i>Dielectric and functional properties of polymer matrix/ZnO/BaTiO₃ hybrid composites</i>
WE2-P43	A. Patsidis (Univ. of Patras, Dept. of Materials Science) - <i>Dielectric response and functionality of polymer matrix BaTiO₃ nanocomposites</i>
WE2-P44	A. Delimitis (CERTH, CPERI, Thessaloniki) - <i>Development of metallic Ag nanowires and nanoparticles on mesoporous silicas: Effect of pore structure and size of the silica support</i>
WE2-P45	G. Kalosakas (Univ. of Patras, Dept. of Materials Science) - <i>Statistical distributions of bubble lengths in DNA</i>
WE2-P46	K. S. Andrikopoulos (TEI of Thessaloniki, Dept. of Applied Science) - <i>Nanoindentation studies of phase separated glasses: The ternary Ag-As-S system</i>
WE2-P47	A. Angelopoulou (NCSR "Demokritos", IMS & Univ. of Patras, Dept. of Materials Science) - <i>About the mixed alkali effect</i>
WE2-P48	V. Gountsidou (AUTH, Dept. of Physics) - <i>Modelling Indentation of porous and inhomogenous materials</i>
WE2-P49	T. P. Biros (AUTH, Polytechnic School) - <i>Mechanical properties of collagen fibrils</i>
WE2-P50	E. Vitoratos (Univ. of Patras, Dept. of Physics) - <i>The influence of thermal treatment and ambient atmosphere on the electrical conductivity of polypyrrole and polypyrrole/5%w/w TiO₂ nanocomposite</i>
WE2-P51	P. Gamaletsos (Univ. of Athens, Faculty of Geology and Geoenvironment) - <i>Spectroscopic (Mössbauer, XANES and FTIR) and thermal investigation of Greek bauxites from the Parnassos- Ghiona active mining area</i>
WE2-P52	E. Mavromati (AUTH, Dept. of Physics) - <i>Fe distribution and speciation in human nails</i>
WE2-P53	A. K. Nikolaidis (AUTH, Dept. of Chemistry) - <i>Mechanical properties of PMMA/organomodified montmorillonite nanocomposites prepared by in situ bulk polymerization</i>

Wednesday, Sept. 23

11³⁰ - 13⁰⁰ : Session WE2: Poster Session

INHOMOGENEOUS & DISORDERED MATERIALS, POLYMERS & BIOMATERIALS / NANOSCALE & SURFACE SCIENCE

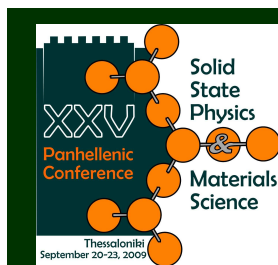
WE2-P54 **O. M. Goudouri** (AUTH, Dept. of Physics) - *Bioactivity studies of hydroxyapatite based glass-ceramics synthesized by Transferred Arc Plasma (TAP)*

WE2-P55 **D. Bikiaris** (AUTH, Dept. of Chemistry) - *Comparative study of the effect of different nanoparticles on the UV stability of HDPE*

WE2-P56 **G. Theodorou** (AUTH, Dept. of Physics) - *Bioactivity studies of bioactive glasses in different environments: the case of the 45S5 bioglass*

WE2-P57 **D. Afouxenidis** (C.E.T.I., R.C "ATHENA", Archaeometry Lab., Xanthi & AUTH, Dept. of Physics) - *Preliminary TL/OSL characterization on synthetic bioactive materials*

WE2-P58 **A. M. Pashou** (AUTH, Dept. of Physics) - Raman characterization of psoriatic and healthy nails



Program & Proceedings
also available on the web

<http://xxv.physics.auth.gr>

xxv@physics.auth.gr

Tel. & Fax: +302310-998036

TABLE OF CONTENTS

<i>SUNDAY, 20 SEPTEMBER 2009</i>		<i>Page</i>
Opening Ceremony	18 ³⁰ - 20 ⁰⁰	1
<hr/>		
<i>MONDAY, 21 SEPTEMBER 2009</i>		
Session MO1	09 ⁰⁰ - 11 ⁰⁰	5
	STRUCTURAL, MECHANICAL & OPTICAL PROPERTIES OF CONDENSED MATTER - 1 <i>In memory of G. Kannelis</i>	
Session MO2 POSTER SESSION	11 ³⁰ - 13 ⁰⁰	15
	STRUCTURAL, MECHANICAL & OPTICAL PROPERTIES - 1 / ELECTRONIC TRANSPORT, SEMICONDUCTORS & DEVICES / PHOTONICS & OPTOELECTRONICS	
Session MO3	14 ⁰⁰ - 16 ³⁰	85
	ELECTRONIC TRANSPORT, SEMICONDUCTORS & DEVICES, PHOTONICS & OPTOELECTRONICS - 1	
Session MO4	17 ⁰⁰ - 18 ⁴⁵	103
	ELECTRONIC TRANSPORT, SEMICONDUCTORS & DEVICES, PHOTONICS & OPTOELECTRONICS - 2	
<hr/>		
<i>TUESDAY, 22 SEPTEMBER 2009</i>		
Session TU1	09 ⁰⁰ - 11 ⁰⁰	113
	STRUCTURAL, MECHANICAL & OPTICAL PROPERTIES OF CONDENSED MATTER - 2	
Session TU2 POSTER SESSION	11 ³⁰ - 13 ⁰⁰	123
	STRUCTURAL, MECHANICAL & OPTICAL PROPERTIES - 2 / MAGNETISM & SUPERCONDUCTIVITY / CULTURAL HERITAGE MATERIALS & INTERDISCIPLINARY PHYSICS	
Session TU3	14 ⁰⁰ - 16 ³⁰	221
	MAGNETISM & SUPERCONDUCTIVITY - 1 <i>In memory of A. Simopoulos & A. Kostikas</i>	
Session TU4	17 ⁰⁰ - 18 ⁰⁰	233
	MAGNETISM & SUPERCONDUCTIVITY - 2 <i>In memory of A. Simopoulos & A. Kostikas</i>	
Session TU5	18 ⁰⁰ - 19 ³⁰	241
	CULTURAL HERITAGE MATERIALS & INTERDISCIPLINARY PHYSICS	
<hr/>		
<i>WEDNESDAY, 23 SEPTEMBER 2009</i>		
Session WE1	09 ⁰⁰ - 11 ⁰⁰	253
	INHOMOGENEOUS & DISORDERED MATERIALS, POLYMERS & BIOMATERIALS	
Session WE2 POSTER SESSION	11 ³⁰ - 13 ⁰⁰	265
	INHOMOGENEOUS & DISORDERED MATERIALS, POLYMERS & BIOMATERIALS/ NANOSCALE & SURFACE SCIENCE	
Session WE3	14 ⁰⁰ - 15 ³⁰	371
	NANOSCALE & SURFACE SCIENCE - 1	
Session WE4	16 ⁰⁰ - 17 ³⁰	381
	NANOSCALE & SURFACE SCIENCE - 2	
Session WE5	17 ³⁰ - 18 ³⁰	393
	SPECIAL SESSION ON RENEWABLE ENERGY RESOURCES – HYDROGEN (UNDER THE AUSPICES OF HELLENIC SOCIETY FOR SCIENCE AND TECHNOLOGY OF CONDENSED MATTER (H.S.S.T.C.M))	
<hr/>		
<i>AUTHOR INDEX</i>		399

*OPENING
CEREMONY*

Sunday, 20 September 2009, 18³⁰-20⁰⁰



Looking into Art and Cultural Heritage with Synchrotron X-Rays

E. Dooryhee^{1,2*}, M. Anne¹, J-L. Hodeau¹, P. Martinetto¹, P. Walter³, M. Menu³

¹ *Neel Institute, CNRS-UPR2940, Joseph Fourier University, 25 av. des Martyrs, BP 166, 38042 Grenoble Cedex 9, France*

² *Brookhaven National Laboratory, National Synchrotron Light Source 2 (NSLS II), Upton, NY 11973 USA*

³ *Centre de Recherche et de Restauration des Musées de France, CNRS-UMR 171, Palais du Louvre, 14, quai François Mitterrand 75001 Paris, France*

*dooryhee@bnl.gov

Cultural heritage objects inspire through their artistic merit and through their encapsulation of the art, science and technology of past and present cultures. The microstructure and composition of many archaeological objects are a direct or indirect record of ancient ways of life, know-how and trade routes. As a consequence, there is an increased demand for the scientific characterization of objects that are part of our cultural heritage, such as paintings, ceramics, books, sculptures and utensils to name but a few. One looks forward to unveiling the secrets that lie within these artifacts such as their origin, history, manufacturing processes and about the specific societies from which they emerged. One also often questions the authenticity of these objects.

Moreover it is essential to preserve this cultural heritage for future generations. The diagnosis of degradation/aging mechanisms of artifacts and the development of repair or stabilization strategies are areas of central importance. This can only be accomplished by means of multidisciplinary analysis of complex systems and innovative problem solving, and also leads to the development of new noninvasive or microsampling examination technologies.

It is thus desirable to implement non-destructive experimental techniques that preserve the “real character” of the objects, without contaminating or damaging them. Synchrotron radiation (SR) covers a very wide range of wavelengths, from infrared up to x-rays. It offers many well-established experimental techniques capable of providing elemental analysis, internal structural analysis and even in some cases atomic structure analysis. It can allow non-destructive imaging of the surfaces and also 3D structural information of the artifacts, since x-rays can penetrate through the materials without leaving a trace of the investigation process.

Applications of physics and chemistry in archaeology thus emerge as a part of materials science and the needs for SR-based techniques are ever increasing, including x-ray imaging, x-ray diffraction, x-ray fluorescence and FTIR spectroscopy. This is also an opportunity to exploit the appeal of this cross-disciplinary field to engage the public and train students in science.

As an example among many, Fig. 1 shows the combined fluorescence-diffraction work carried out over several paint samples of Matthias Grünewald, a major painter at the beginning of the German Renaissance. Chemical and phase mappings of the cross-sections, keeping the stratigraphy intact, are an essential step towards the description of the artist’s paint palette and know how [1].

Ancient materials often are complex, heterogeneous samples with a hierarchical arrangement which is related with the artifact manufacturing. Different structural probes covering different scale lengths are required. X-ray diffraction is one of the prime structural methods but suffers from a relatively poor detection limit, whereas transmission electron analysis involves destructive sample preparation. In a second example (Fig. 2), we show the potential of coupling pencil-beam tomography with x-ray diffraction to examine unidentified phases in ill-ordered and poly-phased materials [2].

I shall present a brief overview of the different aspects of SR “archaeometry”, in terms of diversity and complexity of historically and/or artistically interesting samples, as well as SR technical and instrumental requirements. The present contribution outlines the new but still fragile interface between art, archaeology and synchrotron science.

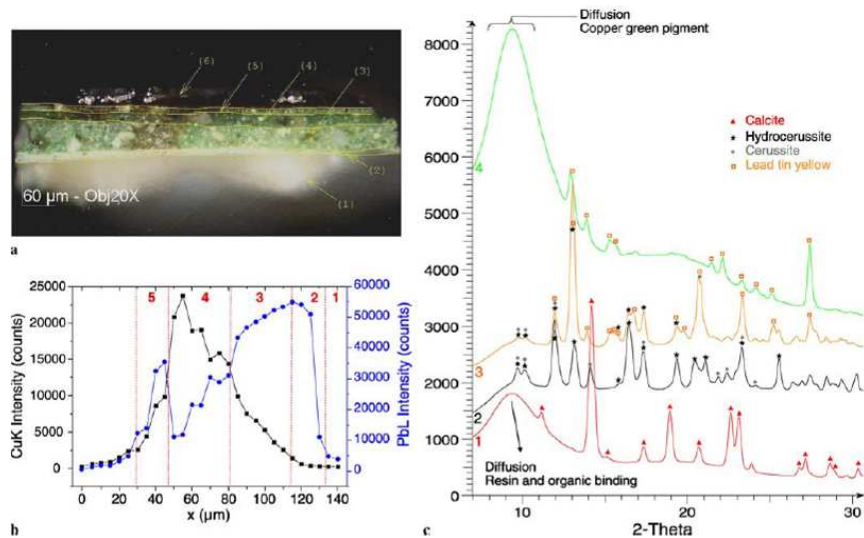


Figure 1 from ref. [1]: SR micro-beam diffraction (XRD) and fluorescence (XRF). (a) Optical microscope observation of a cross section embedded in resin, magnification: $\times 20$. (b) XRF transverse line-scan across the stratigraphy of the cross section, from the outer to the inner layer. The intensities of the Cu K and the Pb L emission rays are plotted as a function of depth. (c) SR x-ray micro-XRD patterns from the four distinct layers 1,2,3 and 4. Layer 1: calcium carbonate preparation layer; layer 2: priming layer made of lead carbonates (hydrocerussite and cerussite); layers 3,4,5: green copper pigments composed of lead tin yellow and lead carbonates; layer 6: organic layer, varnish.

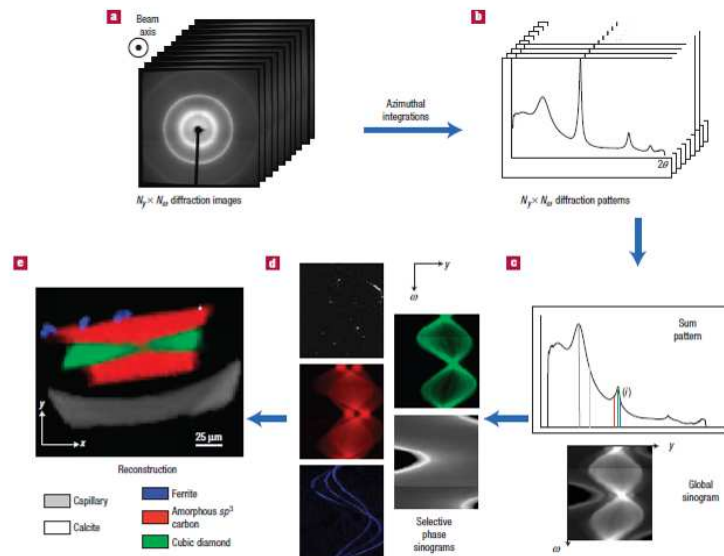


Figure 2 from ref. [2]: The successive steps and principles of the reconstruction scheme of the Diffraction-Tomography direct analysis are illustrated here. **a,b**, For every position (y, ω) , the 2D scattering pattern is integrated over the azimuthal angle and produces the respective 1D scattering pattern $f(2\theta)$. **b,c**, On the one hand, all the 1D patterns are summed up over y and ω , to construct the scattering sum pattern of the entire sample. On the other hand, each 1D $f(2\theta)$ pattern is integrated over the diffraction angle 2θ , and the resulting total scattering intensity is plotted as a function of (y, ω) to build up the global sinogram. **d**, a ROI over a selected 2θ angle range, corresponding to a given scattering contribution or a diffraction peak, can be defined to extract the relevant sinogram of the corresponding individual phase. **e**, Finally, a reconstruction from these sinograms provides axial slices of the corresponding phases. This cross-section image reveals the spatial distribution of the different phases inside the sample and the surrounding glass capillary holder.

[1] E. Welcomme, P. Walter, P. Bleuet, J.-L. Hodeau, E. Dooryhee, P. Martinetto, M. Menu, Appl. Phys. A 89, 825 (2007).
 [2] P. Bleuet, E. Welcomme, E. Dooryhee, J. Susini, J.-L. Hodeau, P. Walter, Nature Materials 7, 468 (2008).

Session MO1

STRUCTURAL, MECHANICAL & OPTICAL PROPERTIES OF CONDENSED MATTER

PART 1

in memory of G. Kanellis

Monday, 21 September 2009, 09⁰⁰-11⁰⁰



**High-pressure studies of transition metal compounds
located near the insulator-metal borderline**

K. Syassen

Max Plank Institut für Festkörperforschung, D-70569 Stuttgart, Germany

**k.syassen@fkf.mpg.de*

Experimental high pressure studies of crystalline phases take advantage of numerous recent developments in diamond-anvil-cell techniques. Major advances have occurred in microscopic analytical methods that utilize synchrotron x-ray radiation (diffraction and inelastic scattering), optical spectroscopies, and synchrotron infrared spectroscopy. Concerning correlated electron systems, the subjects of interest range from pressure-induced structural changes to illuminating the interplay between more subtle changes in atomic arrangements, electron delocalization, magnetism, and superconductivity. Some recent results will be highlighted in this presentation. The main focus will be on structural and electronic properties of perovskite-related transition metal oxides located near the insulator-metal borderline, specifically titanates and vanadates. New findings for cuprate superconductors and Fe-based pnictides will be addressed briefly.

Work performed in collaboration with X. Wang, I. Loa, S. Karmakar, I. Efthimiopoulos (MPI/FKF Stuttgart), M. Hanfland, M. Merlini (ESRF Grenoble), and Y.-L. Mathis (ANKA Karlsruhe).

Controlling Phase Separation in Manganite Thin Films

A Antonakos^{1*}, D. Lampakis, D. Palles, E Liarokapis¹, M Filippi², W Prellier², G. H. Aydogdu³ and H-U Habermeier³

¹Department of Physics, National Technical University of Athens, GR-15780 Athens, Greece

²Laboratoire CRISMAT, CNRS UMR 6508, ENSICAEN, 6 Bd Marechal Juin, F-14050 Caen Cedex, France

³Max-Planck-Institute for Solid State Research, Stuttgart, D-70569, Germany

*tantonak@central.ntua.gr

The very interesting complex physics, the discovery of colossal magnetoresistance (CMR) effect [1] and the possible applications [2] of the rare-earth manganites $R_{1-x}Ca_xMnO_3$ (R: a trivalent rare-earth ion; A: a divalent alkaline-earth ion) [3], have attracted much attention during past decades. The complex phase diagram of the manganites with doping can be described by a Jahn-Teller (JT) induced charge-localization competing with the magnetic interactions (double exchange-DE model [4]), charge, orbital and spin ordering [5]. The control of the transport and magnetic properties is crucial for the application of manganites to devices.

We have investigated methods for tuning the charge ordered state and controlling the phase separation in manganite [$R_{1-x}Ca_xMnO_3$ (R = La, Pr)] thin films grown on different substrates (SrTiO₃ (STO), LaAlO₃ (LAO), SrLaGaO₄ (SLGO) and SrLaAlO₄ (SLAO)). By our systematic Raman and IR studies under varying external (temperature, pressure and magnetic field) and internal (interfacial strains and doping) conditions, we have analyzed certain phonon modes and extracted direct information about the amount of the Jahn-Teller distortions, the charge ordered state, and the strain or the pressure induced phase separation in the manganite thin films.

A full assignment of the observed modes in LCMO and PCMO has been achieved and the results obtained by several perturbations were combined with polarization-dependent scattering [6, 7] and compared with previously published theoretical and experimental works on manganites.

The effect of epitaxial strains on the Raman and IR spectra were studied at room temperature for the $Pr_{1-x}Ca_xMnO_3$ and $La_{0.5}Ca_{0.5}MnO_3$ thin films of varying thickness deposited on different substrates that induce tensile or compressive strains. The Raman scattering scanning of the cross section area of the film demonstrates that the $A_g(2)$ tilting mode, which is related with the rotation of the MnO_6 octahedra, is highly sensitive to local changes and distortions in the lattice caused by the variations in epitaxial strains and can be used as a measure of strains [7].

The low temperature phase diagram of the $Pr_{1-x}Ca_xMnO_3$ thin films has been studied systematically as a function of doping and epitaxial strains. It appears that both doping and the strains from the substrate can alter the charge ordered state, as detected by the JT modes, and tune the electrical properties of the compound. The distortion of the structure can be measured by the shift of the $A_g(2)$ tilting mode frequency, which is a soft mode and couples with the structural and the phase transitions [7]. The compounds were also studied under hydrostatic pressure [8] and the application of a magnetic field for various doping levels in order to induce a delocalization of the carriers and destroy the charge ordered state [9]. Based on the spectral analysis and the coexistence of modes and the characteristics of the metallic phase with others attributed to the Jahn-Teller distortions that identify an insulating charge-ordered behavior, we conclude that the compound has undergone a phase separation into metallic and insulating domains.

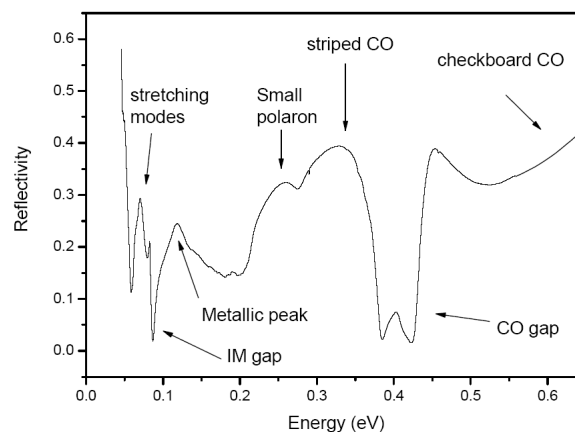


Fig. 1. The assignment of the MIR reflectivity features to several phases. Reproduced from [11].

The strain effects on the low temperature optical spectra of $\text{La}_{0.5}\text{Ca}_{0.5}\text{MnO}_3$ thin films were also investigated [6, 10]. It is demonstrated that different substrates can be exploited as a tool to obtain thin films with adjustable electronic and magnetic properties even if chemical compositions and thicknesses of the films remain unchanged [10]. The differences between the Raman spectra of the bulk and the strained thin films compounds are analyzed in terms of a phase separation scenario. The appearance of new modes in superposition with several broad bands in the reflectivity IR spectra (Fig. 1) are correlated with the magnetotransport results and strongly suggest that phase separation between coexisting charge/orbitally ordered/disordered phases is an intrinsic property of the $\text{R}_{1-x}\text{Ca}_x\text{MnO}_3$ manganite compounds [11]. We have identified distinct phases, namely the insulating or the metallic one and two or more charge ordered phases (checkerboard and stripes). The strain effects on the LCMO/STO(100) thin film destroy the ferromagnetic phase and the charge ordered phase is more robust than in the bulk compound, leading to the charge/orbital ordered insulating phase at LT. On the contrary, the ferromagnetic metallic clusters grow and start to coalesce until the percolation limit is reached on the LCMO/SLGO, LCMO/STO(111) and the LCMO/SLAO thin films, and the system behaves as a metal due to the strain effect [12].

These findings provide important information for a comprehensive theoretical model that will understand the complex physics of the orthorhombic manganite thin films. Furthermore, they demonstrate that the proper selection of film thickness, substrate, and orientation can manipulate the film properties. These results contribute to the control of phase separation and the creation of functional materials with selected subphases for technological applications.

- [1] S. Jin, H. Tiefel, M. McCormack, R. Ramesh, L.H. Chen, *Science* 264, 413 (1994).
- [2] R. vonHelmolt, J. Weckberg, B. Holzapfel, L. Schultz, K. Samwer, *Phys. Rev. Lett.* 71 (1993) 2331.
- [3] A. P. Ramirez, *J. Phys. Cond. Matter* 9, 8171 (1997).
- [4] C. Zener, *Phys. Rev.* 82, 403 (1951).
- [5] A.J. Millis, P.B. Littlewood, B.I. Shraiman, *Phys. Rev. Lett.* 74, 5144 (1995).
- [6] A. Antonakos, E. Liarokapis, G. H. Aydogdu, H.-U. Habermeier, *Materials Science and Engineering: B* 144, 83 (2007).
- [7] A. Antonakos, D. Palles, E. Liarokapis, M. Filippi, W. Prellier, *Journal of Applied Physics* 104, 063508 (2008).
- [8] Antonakos A., Lampakis D., Liarokapis E., Filippi M., Prellier W., Auban-Senzier P., Pasquier C.: *J. Phys. Condensed Matter* 20, 485202 (2008).
- [9] Filippi, M., Auban-Senzier, P., Pasquier, C., Prellier, W.: *Appl. Phys. Lett.* 93, 142110 (2008).
- [10] A. Antonakos, E. Liarokapis, G. H. Aydogdu, H.-U. Habermeier, unpublished.
- [11] A. Antonakos, E. Liarokapis, M. Filippi, W. Prellier, G. H. Aydogdu and H.-U. Habermeier, *unpublished*.
- [12] A. Antonakos, D. Lampakis, M. Filippi, G. H. Aydogdu, H.-U. Habermeier, W. Prellier, and E. Liarokapis, *Physica Status Solidi (b)* 246, 635 (2009).

Acknowledgments Work funded by the Grant of NTUA "PEVE2008".

Plasma Oxidation of Multi-walled Carbon Nanotube Sheets

D. Kastanis^{1*}, M. Nitschke³, F. Simon³, M. Stamm³ and C. Galiotis^{1,2}

¹ FORTH/ICE-HT, Stadiou St., Platani Achaïas, 26504, Greece

² Department of Materials Science, University of Patras, Rio Achaïas, 26500, Greece

³ Leibniz-Institute of Polymer Research Dresden, Hohe Str. 6, 01069 Dresden, Germany

*kastanis@iceht.forth.gr

Carbon nanotube (CNT) based materials are gaining new trend at the materials science field due to their extraordinary properties [1]. Such kind of materials as carbon nanotube yarns [2] forests [3] and sheets [4] have many applications as reinforcements in polymer composites [5], actuators [6], catalyst supports [7] and scaffolds for biomineralization assays [8]. Our work is focused on Carbon Nanotube sheets (so called buckypapers) which are nano-porous, self-standing materials made by randomly distributed MWCNTs. MWCNT sheets are produced by vacuum filtration process and their average thickness is in the range of 50-150µm. Common functionalization techniques of CNTs' surface are chemical and electrochemical treatments. The technique that used in this work is oxygen plasma treatment. Plasma treatment has advantages of low treatment time (seconds as compared to hours of chemical oxidation) and of a non-wet process that makes plasma treatment ideal for industrial grade processing. Thus we managed to oxidize MWCNTs sheets' surface by oxygen plasma treatment. A study by Raman spectroscopy revealed that plasma oxidation degrades the graphitic structure of MWCNTs. A full XPS and TGA study occurred to examine the defect production for different exposure times and to specify oxidation degree. Morphological study by SEM showed that flattening of MWCNT sheet rough surface is analogous to plasma exposure time. Also maximum etching of MWCNT sheets' surface was carried out at first minute of plasma exposure process. Additionally TEM pictures of degraded MWCNTs, contact angle measurements and surface topography analysis of MWCNT sheets will be presented at conference.

[1] P. Moriarty et al, *Reports on Progress in Physics*, 64 (2001).

[2] K. R. Atkinson et al, *Physica B*, 394 (2007).

[3] M. Zhang et al, *Science*, 309 (2005).

[4] D. Kastanis et al, *Advanced Composites Letters*, 16 (2007).

[5] Z. Wang et al, *Composites:Part A*, 35 (2004).

[6] U. Vohrer et al, *Carbon*, 42 (2004).

[7] E. Munoz et al, *Chemical Physics Letters*, 359 (2002).

[8] D. Tasis et al, *Physica Status Solidi (b)*, 243 (2006).

Ultra Fine structure of the short range order of the $\text{Cu}_{65}\text{Zr}_{35}$ and $\text{Cu}_{35}\text{Zr}_{65}$ Metallic Glasses

G. Almyras¹, Ch. E. Lekka^{2*} and G. A. Evangelakis¹

¹ *Department of Physics, University of Ioannina, Ioannina 45110, Greece*

² *Department of Materials Science and Engineering, University of Ioannina, Ioannina 45110, Greece*

**chlekk@cc.uoi.gr*

We present Molecular Dynamics simulations (MD) results referring to the microstructure of two representatives CuZr Metallic Glasses (MG) ($\text{Cu}_{65}\text{Zr}_{35}$ and $\text{Cu}_{35}\text{Zr}_{65}$). From the microscopic analysis of the glassy structures of both systems we found that they are mainly composed by small Icosahedral-like clusters (ICO) that are interconnected and/or interpenetrating, in agreement with previous studies. The detailed exploration of their possible interconnections revealed that the structural characteristics of the systems may be satisfactorily reproduced by considering only 13 and 15-atom ICO clusters that are interpenetrating with predefined ways, thus explaining the existence of the short range order which is a typical characteristic of these MGs. The approach is based on geometrical considerations for the possible combinations of the ICO-like clusters in conjunction with the restriction of the systems' composition. Several polyicosahedral superclusters (PSC) are thus predicted and subsequently verified by the analysis of the MD equilibrium configurations. It turns out that there are "magic" numbers for the PSCs that are dictated from the combination of both the geometry of the interpenetrating ICOs and the stoichiometry of the system and that these numbers are identical for both compositions, the only difference being their relative amplitudes. Interestingly, the radial distribution function calculated by considering only the central atoms of the participating ICOs in the PSCs reproduces very well the experimental data. The energetic and electronic stability of some representative small free standing PSCs were further investigated and verified by means of calculations based on the Density Function Theory. We believe that the present results elucidate the microstructure of these MGs and that they could be of use for the description of more complex systems and possibly for the design of new MGs with improved properties.

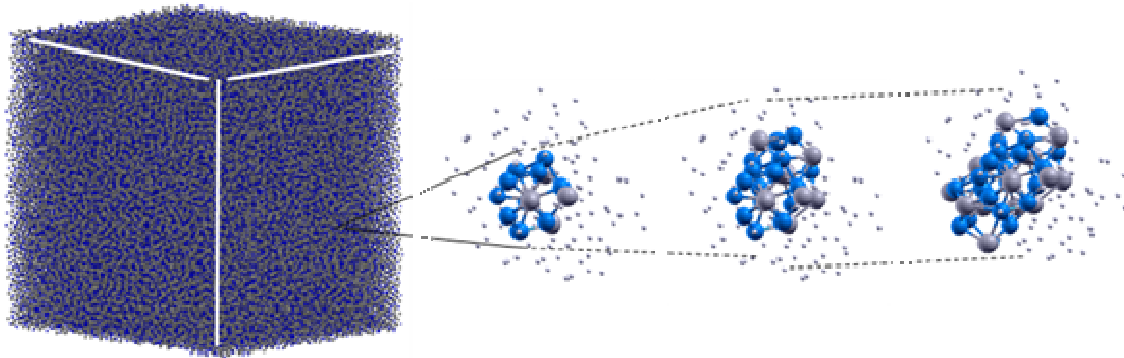


Figure 1. Polyicosahedral superclusters within the metallic glass

- [1] I.D.B. Miracle, Nat. Mater. 3 (2004), p. 697.
- [2] Ch.E. Lekka, A. Ibenskas, A.R. Yavari and G.A. Evangelakis, Appl. Phys. Lett. 91 (2007).
- [3] M. Wakeda, Y. Shibutani, S. Ogata and J. Park, Intermetallics 15 (2007), p. 139.
- [4] A.E. Lagogianni, G.A. Almyras, Ch.E. Lekka, D.G. Papageorgiou, G.A. Evangelakis, J. Alloys and Comp. in press.
- [5] H.W. Sheng, W.K. Luo, F.M. Alamgir, J.M. Bai and E. Ma, Nature 439 (2006), p. 419.

The Effect of In Implantation on the Structural and Nano-Mechanical Properties of GaN

P. Kavouras^{1*}, J. Arvanitidis¹, E. Fournou¹, B. Kargas¹, M. Katsikini²,
E. C. Paloura², S. Ves², W. Wesch³ and E. Wendler³

¹ Department of Applied Sciences, Technological Educational Institute of Thessaloniki, 57400 Sindos, Greece

² Physics Department, Aristotle University of Thessaloniki, 54124 Thessaloniki, Greece

³ Institut für Festkörperphysik, Friedrich-Schiller-Universität Jena, Max-Wien-Platz 1, Jena D-07743, Germany

* pkavo@physics.auth.gr

In implantation of GaN is a promising method for the fabrication of InGaN/GaN nanostructures. The large scale implementation of this method requires the study of the effects induced by the implantation of In projectiles on the physical properties of GaN. In the present work, we study the structural and the mechanical properties, at the nano-scale, of n-type GaN grown on Al₂O₃ implanted with 700 keV In ions and fluences ranging from 5×10^{13} ions/cm² to 1×10^{16} ions/cm². The disorder degree of the films has been probed by means of Raman spectroscopy, while the mechanical properties were obtained by the quasi-static nano-indentation technique.

The Raman spectra were recorded in the backscattering geometry using a DILOR XY micro-Raman system equipped with a cryogenic charge coupled device (CCD) detector. For excitation, the 514.5 nm line of an Ar⁺ laser was focused on the sample by means of a 100× objective lens with a laser power of ~5 mW. Mechanical properties were obtained by the Hysitron Ubi-1 Tribolab modular instrument. The nanomechanical characterization techniques applied gave quantitative results concerning the nanohardness value. Qualitative results about the elasto-plastic response and crack initiation were obtained by the shape of the load-unload curves.

The Raman spectra of the implanted GaN samples with varying In fluences are illustrated in figure 1 along with that of the as-grown material. For wurtzite GaN, factor group analysis predicts at Γ point the symmetry species $A_1 + E_1 + 2B_1 + 2E_2$. The A_1 , E_1 (which are polar and split into longitudinal, LO, and transverse optical, TO, components), and the two E_2 modes are Raman active, while the B_1 modes are silent [1]. In the backscattering geometry used here the two in-plane E_2 modes are favoured, observed in the as-grown sample at ~143 (E_2^+ , Ga sublattice) and ~571 (E_2^- , N sublattice), while the totally symmetric along c -axis A_1 (LO) Raman mode expected at ~739 cm⁻¹ is completely damped due to plasmon-phonon coupling. The relatively narrow E_2^- Raman peak (FWHM: ~5.1 cm⁻¹) reflects the good crystalline quality of the as-grown material. The frequency of the E_2^- mode is strongly affected by biaxial stress induced in the GaN epilayer mainly due to the different thermal expansion coefficients of the epilayer (smaller) and the Al₂O₃ substrate (larger coefficient) and in the as-grown sample is upshifted by ~4.6 cm⁻¹ compared to that in strain-free GaN [2]. From this blue shift, and taking into account that $\Delta\omega(\text{cm}^{-1}) = 6.2 \sigma(\text{GPa})$ [3], we estimate a value of $\sigma \sim 0.74$ GPa for the compressive biaxial strain in pristine GaN.

In the implanted GaN with 5×10^{13} and 5×10^{14} cm⁻² In fluences the E_2^- peak attenuates and broadens significantly (FWHM: ~9.6 and ~11.2 cm⁻¹, respectively). Moreover, in both samples this Raman peak is blue shifted, compared to the as-grown sample, and is located at 573.3 cm⁻¹ ($\sigma \sim 1.15$ GPa) for the lower and at 572.6 cm⁻¹ ($\sigma \sim 1.03$ GPa) for the higher ion fluence, revealing that In implantation enhances initially the compressive strain of the GaN films, most probably due to the large atomic radius of In compared to that of Ga and N atoms. This is contrast to the situation encountered in the case of

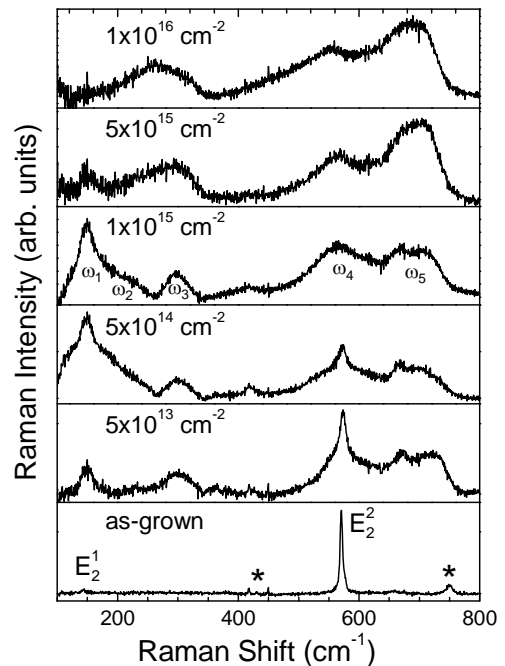


Fig. 1: Raman spectra -after background subtraction- of the In implanted (the numbers on the left refer to the In fluences) and the as-grown GaN samples. Asterisks mark peaks due to the Al₂O₃ substrate.

heavy ion implantation of GaN, where a partial stress relaxation is observed [4]. In these two samples, apart from the E_2^2 peak new broad bands appear (marked by ω_1 - ω_5 in the figure), rendering the Raman spectrum similar to that of amorphous GaN [5]. In amorphous materials, the q -selection rules -limiting Raman activity to zone-center modes- relax significantly, permitting every mode to contribute in the Raman spectrum. Thus, the spectrum reflects, in a certain degree, the phonon density of states of the material. In our case, the ω_1 - ω_3 peaks could be attributed to the acoustic band of GaN dominated by the Ga atomic motions, while the ω_4 and the ω_5 peaks to the transverse and the longitudinal optic band, respectively dominated by the N atomic motions [6]. At higher fluences (5×10^{15} and 1×10^{16} cm^{-2}), the E_2^2 peak disappears, revealing the complete amorphization of GaN after implantation.

Table 1: Nanohardness value of In implanted and the as-grown GaN samples.

In fluence (cm^{-2})	H (GPa)	Structure
1×10^{16}	4.0 ± 0.4	amorphous
5×10^{15}	5.5 ± 0.5	amorphous
1×10^{15}	32.5 ± 5.0	heavily damaged
5×10^{14}	36.5 ± 4.0	heavily damaged
5×10^{13}	34.0 ± 3.0	damaged
as-grown	28.5 ± 3.5	wurtzite

results [7]. Normal ISE is connected to primarily elastically deformed films, while reverse ISE is connected to primarily plastic behavior. In this case, the material does not offer resistance or exhibit elastic recovery, but undergoes relaxation involving a release of the indentation stress away from the indentation site [8]. Study of the loading-unloading curves (figure 2) showed that for fluences up to 1×10^{15} cm^{-2} the behavior of the samples is indeed mainly elastic, with higher elastic recovery. In the above cases all load-unload curves can be barely distinguished. For the two amorphized samples the unloading curve is markedly different and characteristic of primarily plastic behavior. As a result, it is possible that the markedly different nanohardness values (not presented here), for shallower than 60 nm indentations, are a manifestation of an Indentation Effect.

The analyses made by both Raman spectroscopy and Quasi-static nano-indentation techniques have given results that comply with each other, concerning the effect of In implantation. The combination of structural and mechanical response to In implantation was also compatible with the effect of heavy ion implantation on GaN films reported in previous studies [4,9].

The nanohardness value of In implanted samples together with that of the as-grown GaN sample are listed in Table 1. For fluences up to 1×10^{15} cm^{-2} the nanohardness value is increased with respect to that of the unimplanted GaN film. For higher fluences, an abrupt decrease in the nanohardness value was monitored. The errors shown in Table 1 represent the standard deviations obtained from five indentations. The respective indentation loads were high enough in order to produce indentation events with maximum depth approximately equal to half of the radius of curvature of the indenter tip, i.e. ≈ 60 nm.

Additionally, unimplanted GaN and implanted samples for fluences up to 1×10^{15} cm^{-2} showed normal Indentation Size Effect (ISE), while for higher fluences they showed reverse ISE. These results should be treated with caution, since the nanohardness values for indentation depths lower than half of the indenter tip radius of curvature can give rise to misleading

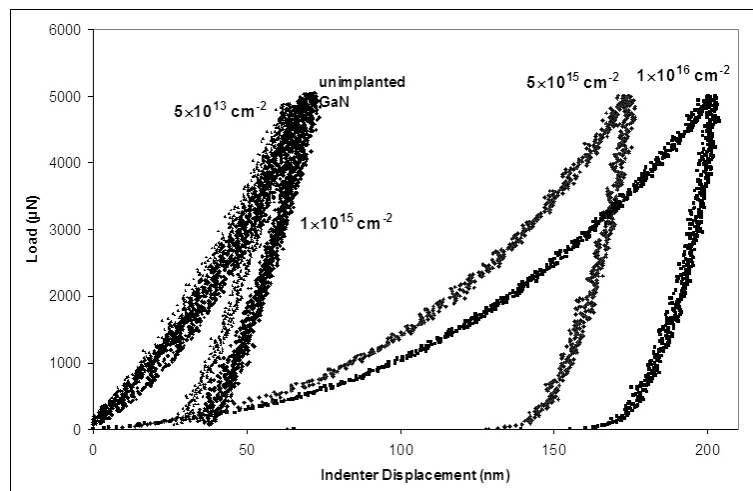


Fig. 2: Load-unload curves of the In implanted and the as-grown GaN samples. The numbers in the diagram correspond to the In fluences in cm^{-2} .

- [1] Zhang J. M., Ruf T., Cardona M., O. Ambacher, M. Stutzmann et al., Phys. Rev. B 56, 14399 (1997).
- [2] Kisielowski C., Kruger J., Ruvimov S., Suski T., Ager III J.W. et al., Phys. Rev. B 54, 17745 (1996).
- [3] Kozawa T., Kachi T., Kano H., Nagase H., Koide N. and Manabe K., J. Appl. Phys. 77 (1995) 4389.
- [4] Katsikini M., Arvanitidis J., Paloura E. C., Ves S., Wendler E. and Wesch W., Optical Materials 29, 1856 (2007).
- [5] Bittar A., Trodahl H. J., Kemp N. T. and Markwitz A., Appl. Phys. Lett. 78, 619 (2001).
- [6] Pollard W., J. Non-Cryst. Solids 283, 203 (2001).
- [7] Fischer-Cripps A.C., Surf. Coat. Technol. 200, 4153 (2006).
- [8] Sangwal K., Chem. Phys. 63, 145 (2000).
- [9] Kavouras P., Kominou Ph. and Karakostas Th., Thin Solid Films 515, 3011 (2007).

Session MO2

POSTER SESSION

*STRUCTURAL, MECHANICAL &
OPTICAL PROPERTIES – 1*

ELECTRONIC TRANSPORT

*SEMICONDUCTORS &
DEVICES*

*PHOTONICS &
OPTOELECTRONICS*

Monday, 21 September 2009, 11³⁰-13⁰⁰



The Effect of Temperature on Aramid Fibre Phonons

J. Parthenios^{1*}, K. Papagelis² and C. Galiotis^{1,2}

¹ Institute of Chemical Engineering and High Temperature Chemical Processes, Foundation of Research and Technology-Hellas, P.O. BOX 1414, Patras 265 00, Greece

² Department of Materials Science, University of Patras, Patras 265 04, Greece

*jparthen@iceht.forth.gr

Raman microscopy has been successfully used to follow the micromechanics of both the deformation of high-performance fibres as well as the fibres within composites[1]. The technique has also been applied to a wide range of systems including aramid, carbon, ceramic and natural fibres. In each case well-defined Raman spectra are obtained and the position of the Raman bands shift on the application of mechanical deformation (stress or strain) or Temperature. This is due to the macroscopic deformation giving rise to stretching/bending of the atomic bonds in the materials. A particularly important aspect of the Raman technique is that it is possible to obtain Raman spectra from individual fibres inside a transparent matrix during deformation. From the stress-induced Raman band shifts it is possible to determine the point-to-point variation of axial fibre stress or strain along an individual fibre under any general state of deformation [2]. High-performance polymer fibers such as the poly(p-phenylene terephthalamide) (PPTA) hereafter referred as aramid, are ideal candidates for stress/ strain and temperature measurements in composites. A characteristic spectrum of aramid fibre is presented in fig.1

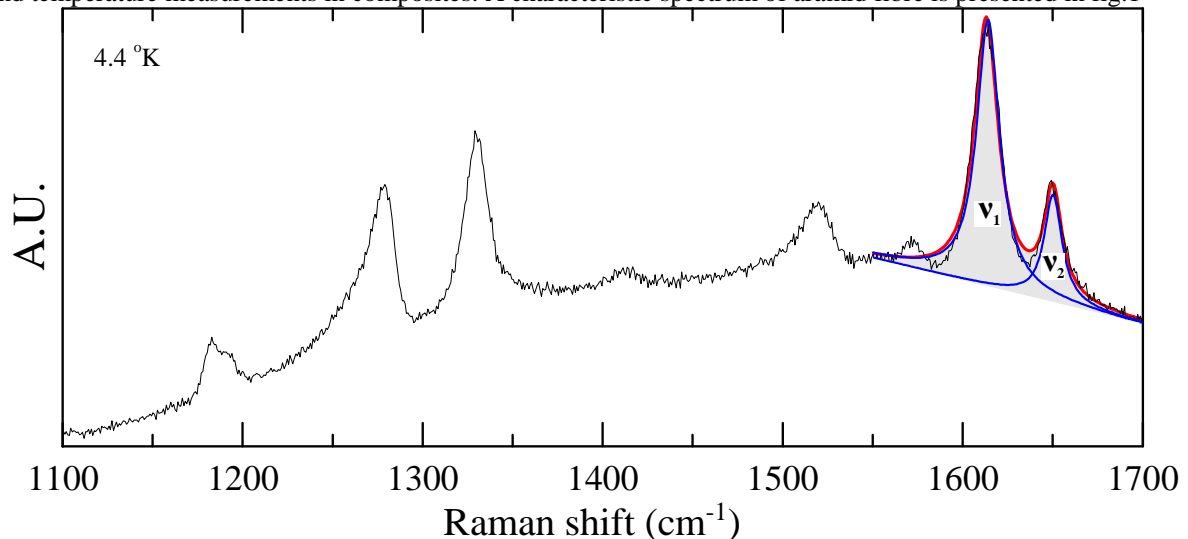


Figure 1 A characteristic Raman spectrum of Kevlar 29[®] fibers at 4.4 K. The red line is a fitted curve consisted of two Lorentzian components corresponding to ν_1 and ν_2 peaks

The Raman vibrational modes recorded at the 1611 and 1648 cm^{-1} , hereafter referred to as phonons ν_1 and ν_2 , respectively, shift to lower values under tension and to higher values under compression [2]. The first phonon corresponds mainly to ring/C–C stretching of the aromatic groups which are placed on the backbone of the molecular chain, while ν_2 corresponds mainly to amide/C=O stretching, which is a side group mode[3]. It has been shown that both phonons shift linearly as a function of the applied stress/strain, with the value of the slope of the ν_1 phonon shift to be twice as large as the value of the corresponding slope of the ν_2 phonon. Thus, stress or strain calibration curves (phonon shift vs axial stress or strain) can be constructed, leading to a potential use of the aramid fibers as stress/strain sensors in composite materials.[1]

The temperature dependence of the ν_1 and ν_2 Raman phonons of a certain class of aramid fibers (Kevlar 29[®]) has been determined recently by Bollas et al [4] in the temperature range of 218 to 473 K. The knowledge of the Raman shift with temperature of the two bands, as above, would also allow their use as *in situ* temperature diagnostic tools. However, inverse stress and temperature measurements are problematic as the corresponding values of stress and temperature cannot be easily deconvoluted from a given wavenumber shift. This manifests itself particularly in the case where axial stress measurements are conducted in composites that incorporate aramid fibers at elevated temperatures.

In this work, we have conducted a systematic experimental study of the temperature dependence of the ν_1 and ν_2 Raman phonons of Kevlar 29[®] fibers in the temperature range of 4 to 473 K. The peak position of ν_1 and ν_2 as

a function of temperature is presented in fig. 2. It is clear that the two phonons exhibit different behaviour above 100 K: phonon ν_1 softens considerably while phonon ν_2 is hardened slightly with a lower rate. The dependence of phonon ν_1 on temperature is explained through the formula[5]

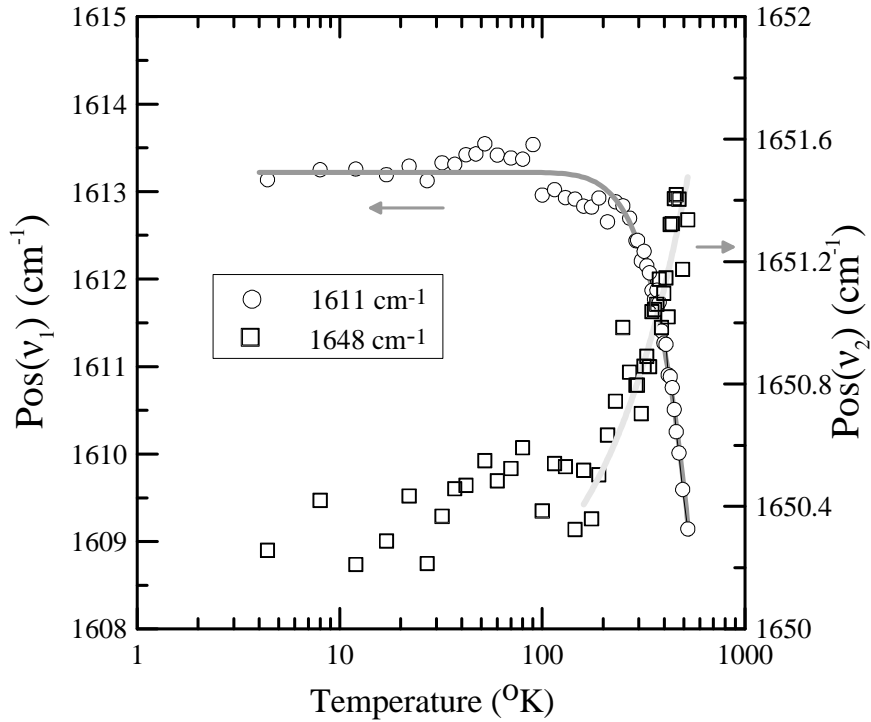


Fig. 2 Temperature dependence of ν_1 and ν_2 Raman phonons of Kevlar 29[®] fibers. The solid lines are a linear fit for ν_2 and the Balkanski formula for ν_1

$$\nu(T) = \nu_0 + A \left(1 + \frac{2}{e^x - 1} \right) + B \left(1 + \frac{3}{e^y - 1} + \frac{3}{(e^y - 1)^2} \right)$$

όπου $x = \hbar \nu_0 / 2k_B T$ and $y = \hbar \nu_0 / 3k_B T$.

The formula quantifies the anharmonic decay of a phonon to other phonons of lower frequencies (three and four phonon process). The results show that the $\nu_1(T)$ dependence can be described as a mixture of 3 and 4-phonon processes ($A = -7.15 \text{ cm}^{-1}$, $B = -2.03 \text{ cm}^{-1}$). On the other hand, phonon ν_2 remains stable in the temperature range of 4.4K – 100K and increases almost linearly with increasing temperature having a slope of $+0.003 \text{ cm}^{-1}/\text{°K}$. In contrast with its normal behavior as the strain/stress is increasing (softening), the $\nu_2(T)$ dependence can be related on its origin corresponding to a vibration of the side group (amide/C=O) perpendicular to polymer backbone.

- [1] Galiotis C., Parthenios J., “Stress/ Strain measurements in Fibers and Composites using Raman Spectroscopy” in “Vibrational spectroscopy of biological and polymeric Materials”, ed. V. G.Gregoriou and M. S. Braiman, Taylor & Francis, Boca Raton, London, New York 2006.
- [2] Young R.J., Eichhorn S.J., Polymer 48 2 (2007).
- [3] Kim P. K., Chang C., Hsu S. L., Polymer 27, 34 (1986).
- [4] Bollas D., Parthenios J. and Galiotis C., Phys. Rev. B, 73, 094103 (2006)
- [5] Balkanski M., Wallis R., Haro E., Phys. Rev. B, 28, 1928 (1983).

Microstructure Evolution In $\text{Cu}_x\text{Zr}_{100-x}$ Metallic Glasses Under Tensile DeformationA.E. Lagogianni¹, G.A. Almyras¹, Ch.E. Lekka^{2,*}, G.A. Evangelakis¹¹ *University of Ioannina, Department of Physics, Ioannina 45110 Greece*² *University of Ioannina, Department of Materials Science and Engineering, Ioannina 45110 Greece*

*chlekk@cc.uoi.gr

We present results from large scale Molecular Dynamics simulations based on a semi-empirical potential model in analogy to the Tight-Binding scheme in the Second Moment Approximation on the microstructural alterations occurring during mechanical solicitation of the $\text{Cu}_x\text{Zr}_{100-x}$ Metallic Glasses (MG). We found that in all compositions studied the systems are composed by Icosahedral-like tiny clusters (ICO), the stoichiometries of which depend on the system's composition, while their number exhibits significant temperature dependence, in agreement with previous studies[1,2]. In addition, we found that although in all cases the ICO number decreases upon tensile deformation, the rate of decrease is correlated with the systems composition, while systems with conjugated stoichiometries having with the same number of ICOs at different temperatures exhibiting practically identical rates of ICO destruction[3]. Interestingly, the same systems when analyzed at the same temperatures (either at room or in the supercooled temperature region) exhibit fundamentally different ICO destruction rates. These findings indicate that the ICO-like clusters in conjunction with their stability play important role in the mechanical responses of these metallic glasses.

[1] M. Wakeda, Y. Shibutani, S. Ogata, J. Park, *Intermetallics* 15 (2007) 139-144.[2] H.W.Sheng, W.K.Luo, F.M.Alamgir, J.M.Bai, E.Ma, *Nature* 439 (2006) 419.[3] Ch.E. Lekka, A. Ibenskas, A.R. Yavari, G.A. Evangelakis, Submitted to *Appl. Phys. Lett.*

MO2

P2

Water and Carbon Dioxide as Sources for Oxygen Incorporation into Acceptor Doped SrTiO₃ Single Crystals

Christos Argiris^{1,2*}, Jana Grosse-Brauckmann², Florian Voigts³, Wolfgang Maus-Friedrichs³

¹*School of Chemical Engineering, National Technical University of Athens, Iroon Polytechniou 9, Zografou 157 80, Athens, Greece*

²*Institut für Metallurgie, Technische Universität Clausthal, Robert-Koch-Str. 32, 38678 Clausthal-Zell., Germany*

³*Institut für Physik und Physikalische Technologien, Technische Universität Clausthal, Leibnizstrasse 4, 38678 Clausthal-Zell., Germany*

**christos.argiris@tu-clausthal.de*

SrTiO₃ is a model oxide for electroceramics. It is a typical ABO₃ type perovskite material with remarkable thermal and chemical stability and easy fabricability. As a result of that SrTiO₃ has found applications in a wide range of technologically relevant fields like capacitors, oxygen sensors, dielectrics as well as substrate for superconducting materials. Moreover, depending on the conditions it can show ionic conduction or p- or n-type electronic conduction. The key point that enables one to render this material with a specific conductivity is its suitability to dope this material with aliovalent dopants without changing its crystal structure [1,2]. Defect chemical basics of this material can be found in the literature [3,4] and in the references therein. Recently Merkle and Maier [5] discussed the oxygen incorporation in oxides on the example of SrTiO₃ as a model material.

One use of SrTiO₃ is its application as resistive high temperature oxygen sensor [6,7], with the analysis of combustion engine exhaust being one important utilisation.

The most convenient way of studying oxygen incorporation in a crystalline solid is by the means of tracer isotope exchange. In this process the oxygen incorporation consists of a surface reaction at the gas solid interface which is characterized by the surface exchange rate constant and a subsequent bulk transport which is characterized by the diffusion coefficient. The objective of this investigation is to see whether different gaseous contaminants influence oxygen incorporation reaction in acceptor doped SrTiO₃. Results for oxygen incorporation from ²H₂¹⁸O sources are here reported.

Single crystals of SrTiO₃(100) were supplied by CrysTec GmbH (Berlin, Germany). First, each of the three differently doped SrTiO₃ single crystals (0.13, 0.039 and 0.013 at.% Fe) were cut from one boule each with the dimension of 5×5×1 mm³ and have been polished down to optical finish with the dimension 0.1 μm.

For the diffusion experiments, all samples were first heated at 1000 °C for 24 hours in 200 mbar of ¹⁶O₂. The samples were equilibrated at any temperature for about ten times the estimated subsequent diffusion time in an oxygen partial pressure similar to the subsequent diffusion. Three sets of samples were then annealed separately in ²H₂¹⁸O (Campro Scientific, Berlin, Germany) at various temperatures

The oxygen incorporation from H₂O or CO₂ into Fe-doped SrTiO₃ (100) single crystals (0.013 at.% Fe, 0.039 at.% Fe and 0.13 at.% Fe) was investigated. Oxygen incorporation processes using ²H₂¹⁸O or ¹³C¹⁸O₂ as gas source were studied by isotope exchange depth profiling (IEDP) and subsequent Secondary Ion Mass Spectroscopy (SIMS). The interaction of ²H₂¹⁸O or ¹³C¹⁸O₂ with SrTiO₃(100) surfaces was further studied with different surface analytical techniques like Metastable Induced Electron Spectroscopy (MIES), Ultraviolet Photoelectron Spectroscopy (UPS) and X-Ray Photoelectron Spectroscopy (XPS).

²H₂¹⁸O acts as an incorporation source of ¹⁸O into the Fe-doped crystals. The results of the diffusion profile evaluation confirm that oxygen and hydrogen migrate independently in the bulk. This oxygen incorporates into the material at high incorporation rates, practically comparable with the ones resulting from an oxygen atmosphere.

The results on the interaction of ¹³C¹⁸O₂ with SrTiO₃(100) surfaces indicate that CO₂ interaction with SrTiO₃(100) surfaces does not change the surface at all. It seems that CO₂ provides a very low sticking probability on the surface as it is not traced by valence band spectroscopy even at room temperature. Nonetheless, ¹³C¹⁸O₂ acts as an incorporation source of ¹⁸O into the Fe-doped crystals.

Tracer diffusion coefficients and tracer surface oxygen exchange coefficients for the oxygen incorporation into Fe doped SrTiO₃ from CO₂ dissociation are found to be strongly dependent on Fe concentrations. The diffusion probability increases with decreasing Fe concentration. CO₂ is believed to be dissociated into CO and oxygen. This oxygen incorporates into the material at high incorporation rates, practically comparable with the ones resulting from an oxygen atmosphere. The CO molecules are desorbed quite quickly. Further dissociation of CO into C and O is not conclusive from our study. Neither any trace of carbon is found on the

surface of SrTiO₃ by examining the surface by means of XPS, MIES and UPS nor could any CO dissociation fragments be detected by TPD. The SrTiO₃ surface remains unchanged by the CO₂ exposure in terms of surface electronic structure and stoichiometry.

References

- [1] R. Moos, T. Bischoff, W. Menesklou and K. H. Härdtl, *J. Mat. Sci.*, 32 (1997) 4247.
- [2] S. Steinsvik, R. Bugge, J. Gjønnnes, J. Taftø and T. Norby, *J. Phys. Chem. Solids*, 58 (1997) 969.
- [3] G. M. Choi and H. L. Tuller, *J. Am. Ceram. Soc.*, 71 (1988) 201.
- [4] R. Moos and K. H. Härdtl, *J. Am. Ceram. Soc.*, 80 (1997) 2549.
- [5] R. Merkle and J. Maier, *Angew. Chem. Int. Ed.*, 47 (2008) 2.
- [6] W. Menesklou, H. J. Schreiner, K. H. Härdtl and E. Ivers-Tiffée, *Sensors and Actuators B*, 59 (1999) 184.
- [7] R. Meyer and R. Waser, *Sensors and Actuators B*, 101 (2004) 335.

Molecular Dynamics in Intercalated Poly (propylene oxide) Amines/Layered Silicate Nanocomposites

A. Kyritsis^{1*}, S. Kriptou¹, A. Panagopoulou¹, K. Vartzelis-Nikakis¹, P. I. Xidas²
and K. S. Triantafyllidis²

¹*Department of Physics, National Technical University of Athens, Zografou Campus, 15780, Athens, Greece*

²*Department of Chemistry, Aristotle University of Thessaloniki, 54124 Thessaloniki, Greece*

*akyrits@central.ntua.gr

The dynamics of poly (propylene oxide) amines intercalated in montmorillonite clays, have been investigated by means of Differential Scanning Calorimetry (DSC), Thermally Stimulated Depolarization Currents (TSDC) and broadband Dielectric Relaxation Spectroscopy (DRS) methods. The amines of interest were the commercially available α , ω -diamines known as Jeffamine D-series amines with a molecular weight of 2000, direct incorporated in the galleries of montmorillonite clays via ion-exchange process [1].

The intercalated polymeric chain motions are restricted between successive clay platelets, thus providing a true confined system where diamines are actually confined in one dimension related to the gallery height. It is well established that in confined systems the resulting molecular mobility is controlled mainly by two opposite acting factors: interfacial interactions and geometrical (spatial) restriction. In this work we study comparatively the dynamics of intercalated chains of similar lengths hosted in galleries of comparable heights but exhibiting different interfacial interactions. More specifically, by varying the number of diamines' head groups of each chain which interact electrostatically with the negatively charged surface of the clay platelets, both chain ends, one or none chain ends are effectively anchored to the walls. Dielectric Spectroscopy can provide especially valuable information on the chain dynamics of intercalated Jeffamines, monitoring both short length molecular motions (local relaxation processes) and longer scale cooperative molecular motions (segmental relaxation process). In addition, the polymeric chains under study possessing electrical dipole moment along the chain contour exhibit the dielectric normal mode (nm) relaxation due to the fluctuation of the end-to-end chain vector (dipole inversion occurs about the middle of the chains). Therefore, information on the global chain mobility can also be provided by dielectric studies.

Concerning the local relaxation process (mechanism β) our experimental results indicate that no significant changes occur in the intercalated chains compared to the mechanism β in bulk polymeric chains. Concerning longer length scale processes the experimental results show that at temperatures slightly higher than the glass transition temperature, T_g , the segmental mobility of all intercalated chains has not been changed, as compared with the segmental mobility in the bulk, whereas the global chain mobility has been dramatically changed: the nm process of the net chains in the bulk is not activated, instead a new relaxation process, slower than the segmental but faster than the nm process in the bulk, appears and dominates to relaxation spectra. No remarkable differences among the three intercalated systems have been observed. Surprisingly, by decreasing temperature and approaching T_g our results indicate that for the systems with both chain ends attached to the walls, i.e. with stronger interfacial interactions, the segmental dynamics becomes faster compared to that of net chains and to other intercalated systems. The results are discussed in terms of interfacial interactions and contact points, chain orientations / chain layering and fluctuations of polymer density.

Aiming at studying the effects of geometrical restrictions on the dynamics of the intercalated chains we investigated comparatively intercalated chains which have both chain ends attached to the walls but are hosted in galleries of two different heights, namely 4 and 1 nm. Our results show that whereas the time scale of the slower relaxation process, which is related with large scale chain segments, is similar in the two systems, the segmental dynamics becomes remarkably faster for the chains with the stronger spatial confinement, as the temperature decreases approaching T_g (pure confinement effect).

Investigation of intercalated chain dynamics after following hydration / dehydration procedures allow us to reveal the role of existent water traces on the various relaxation modes exhibited by the intercalated chains. The DSC results imply that calorimetric T_g is sensitive on water content whereas DRS measurements show that adsorbed water molecules affect mainly the global chain relaxation process.

[1] Triantafyllidis C.S, LeBaron P.C., Pinnavaia T.J., *Journal of Solid State Chemistry* 167, 354 (2002).

Acknowledgements. A.K, S.K. and A.P acknowledge financial support of NTUA via program «PEVE 2007». K.S.T acknowledges partial support of EU and Greek Ministry of Development via program EPAN-PENED2003.

Optical Response of Plasmonic Nanoantenna Arrays

E. Almpanis^{1*}, N. Papanikolaou¹, C. Tserkezis² and N. Stefanou²

¹ Institute of Microelectronics, NCSR “Demokritos”, Ag. Paraskevi, GR-153 10 Athens, Greece

² Section of Solid State Physics, University of Athens, Panepistimioupolis, GR-157 84 Athens, Greece

*almpanis@imel.demokritos.gr

Optical antennas, operating through the excitation of plasmon modes localized at properly designed metallic nanoparticles [1], are fundamental devices for directing an incoming light wave to subwavelength dimensions. Moreover, optical antennas characterized by strong plasmon resonances provide an important mechanism for locally amplifying the electromagnetic field. This characteristic is of particular interest to enhance a weak optical response, e.g., in single molecule fluorescence and Raman scattering, or trigger nonlinear effects. In the simple case of noble-metal nanospheres, the extinction spectrum is dominated by strong dipole plasmon resonances at visible wavelengths. For elongated particles, the threefold degeneracy of these modes is lifted and one obtains a predominant nondegenerate longitudinal mode at longer wavelengths and a doubly degenerate transverse mode at shorter wavelengths. The longitudinal resonance can be easily tuned by properly choosing the particle aspect ratio [2]. Therefore, elongated metallic nanoparticles, such as spheroids or cylinders, can be used as efficient and tunable optical antennas for manipulating light at the nanoscale and tailoring the light-matter interaction.

In the present communication, we report on the optical response of planar periodic arrays of gold nanocylinders by means of full electrodynamic calculations using the extended layer-multiple-scattering method [3]. This method provides an efficient computational framework for fast and accurate calculations of the optical properties of complex inhomogeneous systems consisting of successive, possibly different, layers of scatterers arranged with the same two-dimensional periodicity. The method proceeds at a given frequency, i.e., it is an “on-shell” method; therefore, it can be directly applied to structures made of strongly dispersive and absorptive materials such as real metals. Here, for the dielectric function of gold we interpolate to the bulk values measured by Johnson and Christy [4]. The properties of the individual scatterers enter through the corresponding T matrix which, for scatterers of arbitrary shape, is calculated numerically by the extended boundary condition method.

We first consider isolated gold nanorods in water (refractive index of water: 1.33), and compare the calculated variation of the position of the longitudinal resonance versus the particle aspect ratio, for three different particle shapes: spheroids, cylinders and cylinders with hemispherical caps, with available experimental data [5-9]. The particle diameter in the experiments was varying between 10 nm and 20 nm; therefore, in our calculations we assumed a constant diameter $d = 17$ nm and varied the aspect ratio by changing the length, L , of the particles. As can be seen from Fig. 1, the resonance wavelength, λ_{\max} , increases almost linearly with the particle aspect ratio, for all three particle shapes. Most of the experimental data agree with the theoretical results for the cylinders with hemispherical caps, which is consistent with TEM micrographs of the fabricated samples [5]. Interestingly, the fundamental longitudinal resonance appears at wavelengths much longer than those of an ideal half-wave dipole antenna ($L = \lambda/2$). This is explained as follows. At optical frequencies the simple wavelength scaling $L = \lambda/2$ breaks down because incident radiation is no longer perfectly reflected from the metal’s surface. Instead, the

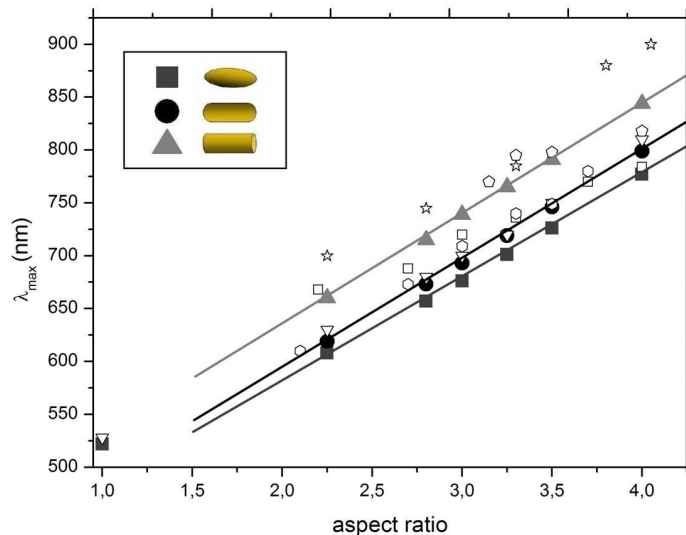


Fig. 1. Position of the fundamental longitudinal resonance of single gold nanorods versus their aspect ratio. The results for aspect ratio equal unity refer to a sphere. Filled symbols: Calculated results for spheroids (squares), cylinders (triangles), and cylinders with hemispherical caps (circles). Particle diameter is fixed at 17 nm. Open symbols: Experimental data from Refs. [5] (triangles), [6] (squares), [7] (stars), [8] (circles), and [9] (pentagons).

wave field penetrates into the metal and gives rise to surface-plasma oscillations. Hence, at optical frequencies an antenna does not respond to the external wavelength, λ , but to an effective wavelength, λ_{eff} , which depends on the material properties [10].

We next consider square arrays of gold nanocylinders, of diameter $d = 10$ nm and length $L = 30$ nm, with different lattice constants: $a = 25, 50,$ and 100 nm, in air (refractive index of air: 1). Interaction between plasmons of the individual particles gives rise to corresponding collective plasmon modes, which manifest themselves as peaks in the extinction spectra of these arrays. Expectedly, under illumination at normal incidence or at an angle with s-polarized light, the longitudinal modes are not excited since, in these cases, the electric field of the incident electromagnetic wave oscillates perpendicularly to the particle axis. At off-normal incidence, a p-polarized wave excites both longitudinal and transverse collective plasmon modes, as can be seen in Fig. 2. It is worth noting that the peak positions do not vary much with the angle of incidence, thus implying a relatively weak dispersion of the corresponding collective plasmon modes. However, as the lattice constant decreases and the nanocylinders approach each other, their interaction increases and leads to large shifts of the long-wavelength collective longitudinal plasmon modes. For $a = 100$ nm, the extinction peaks at about 620 nm and 510 nm (the short-wavelength peak is barely discernible in the scale of Fig. 2) essentially correspond to the longitudinal and transverse plasmon modes, respectively, of the isolated nanocylinder. For $a = 50$ nm the peaks become more pronounced. Interparticle coupling leads to a blue shift of the long-wavelength resonance that now appears at about 600 nm, while the position of the short-wavelength resonance remains almost unchanged. Finally, if the particles come very close to each other ($a = 25$ nm), the long-wavelength resonance is further shifted and the two peaks are merged into one pronounced peak at about 510 nm. Our results are in line with recent experimental and theoretical studies on arrays of longer gold nanorods, fabricated by electrodeposition into thin nanoporous anodized aluminum oxide templates [11, 12].

It becomes clear from the above that ordered arrays of metallic nanocylinders provide the opportunity for engineering collective plasmon modes that can be easily tuned throughout the spectrum of visible and infrared wavelengths by a proper choice of the geometric parameters of the structure.

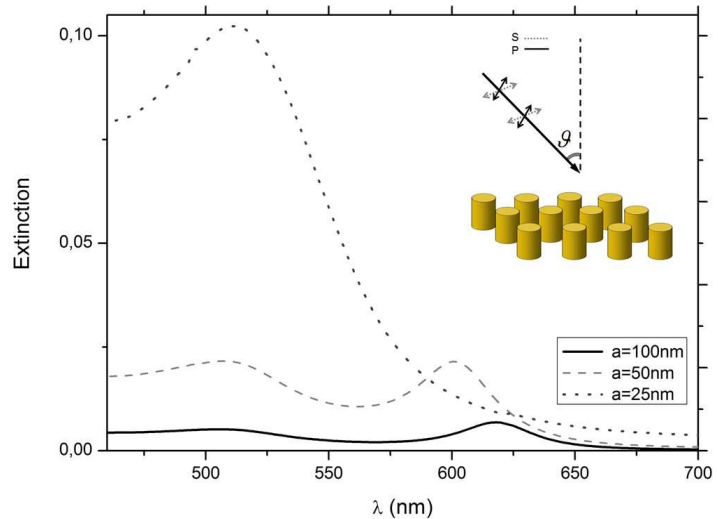


Fig. 2. Extinction spectra of square arrays of gold nanocylinders ($d = 10$ nm, $L = 30$ nm), with lattice constant $a = 25$ nm (dotted line), 50 nm (dashed line), and 100 nm (solid line), under illumination with a p-polarized plane wave incident at an angle $\theta = 10^\circ$.

- [1] Mühlischlegel P., Eisler H. J., Martin O. J. F., Hecht B., Pohl D. W., Science 308, 1607 (2005).
- [2] Eustis S. and El-Sayed M. A., Chem. Soc. Rev. 35, 209 (2006).
- [3] Gantzounis G. and Stefanou N., Phys. Rev. B 73, 035115 (2006).
- [4] Johnson P. B. and Christy R. W., Phys. Rev. B 6, 4370 (1972).
- [5] Al-Sherbini A.-S. A.-M., Colloids Surf. A 246, 61 (2004)
- [6] Brioude A., Jiang X. C., Pileni M. P., J. Phys. Chem. B 109, 13138 (2005).
- [7] Pérez-Juste J., Pastoriza-Santos I., Liz-Marzán L. M., Mulvaney P., Coord. Chem. Rev. 249, 1870 (2005).
- [8] Link S., Mohamed M. B., El-Sayed M. A., J. Phys. Chem. B, 103, 3073 (1999).
- [9] Jiang X. C., Brioude A., Pileni M. P., Colloids Surf. A 277, 201 (2006).
- [10] Novotny L., Phys. Rev. Lett. 98, 266802 (2007).
- [11] Wurtz G. A., Dickson W., O'Connor D., Atkinson R., Hendren W., Evans P., Pollard R., Zayats A. V., Opt. Express 16, 7460 (2008).
- [12] Kullock R., Hendren W., Hille A., Grafström S., Evans P., Pollard R., Atkinson R., Eng L., Opt. Express 16, 21671 (2008).

Acknowledgments This work was supported by the research programme “Kapodistrias” of the University of Athens.

Structure and Photoconductivity of Modified TiO₂ Sol-Gel Coatings

K. Pomoni¹, A. Vomvas¹, N. Todorova², C. Trapalis^{2*}

¹Department of Physics, University of Patras, 26 500 Patras, Greece

² Institute of Materials Science, National Centre for Scientific Research "Demokritos" 153 10, Ag. Paraskevi Attikis, Greece

*trapalis@ims.demokritos.gr

MO2
P6

Abstract

Thick transparent TiO₂ coatings were prepared by sol-gel route on SiO₂ pre-coated soda lime glass substrates. Polyethylene glycol (PEG) with various average molecular weights and Fluorine-containing acid (CF₃COOH) were used as modifiers and their influence on the crystallinity, hydrophilicity and photoconductivity of the coatings was investigated. It was established that the addition of F modifier improves the anatase phase crystallization when PEG with lower molecular weight is used. In addition, CF₃COOH modification leads to formation of superhydrophilic TiO₂ coatings with contact angle $\theta \leq 3^\circ$. The conductivity measurements revealed that the increase of the PEG's molecular weight does not influence significantly the dark conductivity in air nor in vacuum. The photoconductivity measurements demonstrated that the addition of fluorine containing precursor results in the increase of photoconductivity in air and in vacuum when low-mass PEG 2000 was added.

Keywords: TiO₂; Sol-gel; PEG; photoconductivity, superhydrophilicity

Introduction

TiO₂ films are materials of great technological importance with various photocatalytic applications for purification of water and air, ultraviolet filters for optics and packing materials, photo-electrochemical solar cells, self cleaning coatings on windows, buildings and tiles, gas and humidity sensors, etc. Nanostructured TiO₂ photoactive coatings are gaining a growing interest due to their simple low cost preparation, promising photocatalytic activity and variety of potential applications [1, 2]. In this paper the effect of PEG and CF₃COOH modification on structure, hydrophilicity and photoconductivity properties was investigated.

Experimental details

For the TiO₂ coating procedure two groups of solutions containing 10% PEG with average molecular weight 2000, 10000 and 20000 were prepared. The first group of solutions did not contain CF₃COOH while the second group contained CF₃COOH in quantity 20 at.% F toward Ti. TiO₂ gel coatings were deposited on the SiO₂-coated substrates by dip-coating and treated at 450°C for 1 hour. The dip-coating and the heating procedures were repeated 5 times. The samples obtained were designated as F20-PEG_w and F0-PEG_w (w=2000, 10000 and 20000) for the TiO₂ films originated from solutions with and without CF₃COOH addition, respectively.

The X-Ray Diffraction patterns were obtained on Siemens D500 diffractometer with secondary graphite monochromator and CuK α radiation. The thickness of the films was measured on a Talystep instrument. Horizontal microscope with a protractor eyepiece type II-P Leitj, Germany, was used for the measurement of the contact angle of water drop after illumination.

For the electrical conductivity and photoconductivity measurements coplanar silver electrodes were vacuum deposited on the samples. A vacuum cryostat was used and the temperature was adjusted by a temperature controller. The used light source was a 100 W (white light) Xenon lamp and the full light intensity at the samples surface was adjusted to 500 W/m². The light was switched on and off every 20 min and the photocurrent response was measured by an electrometer and recorded every 10 s [3]. For the elimination of persisting effects of previous light exposure, before any measurement, the samples were annealed at 440 K for 90 min and were left to cool down slowly. Then the photoconductivity was measured only after the samples rested in the dark for 24 h at room temperature.

Results and Discussion

The 5-layered TiO₂ coatings had thickness of ~500nm (Table 1) and consisted of anatase crystalline phase (Fig.1). In the absence of trifluoroacetic acid modifier the intensity of anatase diffraction peak (101) becomes stronger with the increase of the PEG's molecular weight indicating the enhancement of crystallization and formation of larger TiO₂ crystallites. The opposite tendency is observed for the CF₃COOH modified samples. With the increase of the PEG's molecular weight the crystallite size decreases (Table 1). The modified coatings exhibited superhydrophilic behavior after illumination with UV light for 20 min (Fig 2). The photoconductivity (σ_p) of F20-PEG_w modified TiO₂ samples versus time, in vacuum, at 300 K is presented in Fig. 3. The rise is slow, it reaches high values and a steady-state photoconductivity is not attained for the 20 min intervals of illumination and the intensity used. The σ_p value after the first 20 min of illumination, are more than seven

orders of magnitude higher than their dark conductivity ones and in the case of the sample PEG 2000 photoconductivity reaches the value of $3.54 \Omega^{-1}\text{m}^{-1}$.

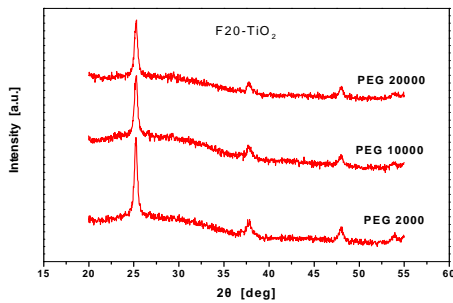


Fig.1. XRD diffraction patterns of PEG and CF₃COOH modified TiO₂ coatings

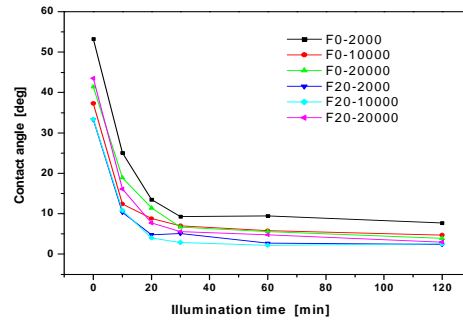


Fig.2. Contact angle values of studied coatings versus illumination time

Table1. Films thickness and crystallites average size d calculated using the Scherrer equation

Nominal Name	F0 PEG ₂₀₀₀	F0PEG ₁₀₀₀₀	F0 PEG ₂₀₀₀₀	F20 PEG ₂₀₀₀	F20 PEG ₁₀₀₀₀	F20P EG ₂₀₀₀₀
d [nm]	16.28	22.49	22.50	22.49	20.87	16.79
Film thickness [nm]	451	463	504	425	486	536

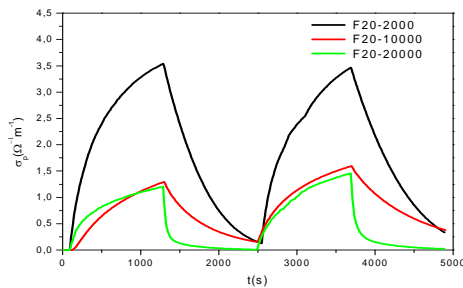


Fig.3. The photoconductivity response at 300 K, in vacuum, of F20 TiO₂ coatings.

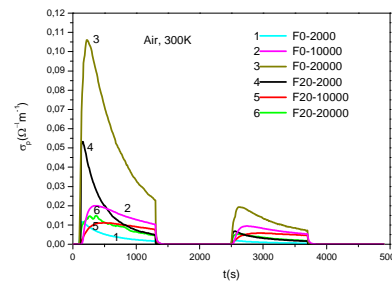


Fig.4. The photoconductivity response at 300 K, in air, of modified TiO₂ coatings.

In Fig. 4 the photoconductivity (σ_p) behavior for F0 and F20 TiO₂ samples in air, at 300 K, is presented. The σ_p , after 20 min of illumination, reaches in the case of PEG 2000, for non-modified and modified with CF₃COOH coatings the values $1.66 \times 10^{-3} \Omega^{-1}\text{m}^{-1}$ and $4.94 \times 10^{-3} \Omega^{-1}\text{m}^{-1}$, respectively, that is more than three orders of magnitude lower than in vacuum. The oxygen in air, when adsorbed at the surface of the samples, causes the creation of scavengers (O_2^-) for the photogenerated electrons, resulting in the decrease of photoconductivity. At the early stages of the illumination a fast increase of σ_p for the case of PEG 2000 is shown ($1.16 \times 10^{-2} \Omega^{-1}\text{m}^{-1}$ for the F0 and $5.3 \times 10^{-2} \Omega^{-1}\text{m}^{-1}$ for the F20 samples) followed by a decrease, which is more pronounced in the case of the trifluoroacetic acid modified sample.

Conclusions

The influence of PEG and CF₃COOF modifiers on the structure and properties of TiO₂ coatings has been investigated. The crystallite size of TiO₂ coatings is proportional to the increase of PEG molecular weight in absence and reverse proportional in presence of trifluoroacetic acid respectively. The trifluoroacetic acid modified coatings exhibited superhydrophilicity after 20 min of illumination. In vacuum, the photoconductivity decreases with the increase of PEG's molecular weight for the F20 coatings. In air, the photoconductivity increases with the increase of PEG molecular weight for F0 coatings while the opposite tendency is observed for the F20 coatings.

References

- [1] Hoffmann M., Martin S., Choi W., et al. Chemical Reviews, 95, 1, 69, (1995).
- [2] Todorova N., Giannakopoulou T., Vaimakis T., Trapalis C. Materials Science and Engineering: B, 152, 1-3, 50 (2008).
- [3] Pomoni K., Vomvas A., Trapalis C. Thin Solid Films 479, 160 (2005).

Structural and Electronic Properties of InN *a*-Edge Threading Dislocations

E. Kalesaki¹, J. Kioseoglou¹, Ph. Komninou^{1,*} and Th. Karakostas¹

¹ *Department of Physics, Aristotle University of Thessaloniki, GR-54124 Thessaloniki, Greece*

**komnhnoy@auth.gr*

MO2

P7

Threading dislocations have a detrimental effect on semiconductor optoelectronic properties, such as luminescence. It is commonly expected that the core region will induce deep gap states within the band gap thus making the dislocation electrically active.

Among III- N semiconductors, InN is the least studied mainly due to its low thermal stability. Threading dislocations of edge character (ETDs) are the dominant defects in InN [1]. High electron concentration [2, 3] and decrease of Hall mobility [4] are attributed to ETDs. Recent experimental studies also imply that they act as non-radiative recombination centers [5] or attribute to them resonant donor states [6]. Theoretical calculation methods can provide valuable feedback to experimental results but also suggest new methods and foresee characteristics that will assist growth and achievement of maximum efficiency.

The work reported here focuses on the structural characteristics of *a*-ETD cores and their effect on the electronic properties of InN. We performed density functional theory (DFT) calculations, using the ESPRESSO code [7], in single edge dislocations of full (5/7), four (4) and open (8) core structures with Burgers vector $\mathbf{b} = \frac{1}{3}[\bar{1}210]$. The core configurations were constructed following elasticity theory and relaxed initially in supercell-

clusters of 30.000 atoms by Tersoff interatomic potential. The relaxed core regions were then extracted in form of cluster hybrids comprising 152, 150 and 158 atoms respectively and the surface dangling bonds were saturated by additional fractionally charged hydrogenlike atoms (Fig. 1 (a)-(c)). Additional calculations were performed on a 5/7 core cluster hybrid of 156 atoms (Fig.1 (d)), in order to make a straightforward comparison to the 8-atom core. Our results suggest that the 5/7 core structure is more stable than the 4- and 8-atom rings by 0.28 eV/Å and 0.34 eV/Å respectively. At this point though, we should note that these results do not prohibit the presence of the 4- and 8-atom rings core configurations in the grown material. The strain and the low coordinated atoms at the core regions designate them as chemically active positions for impurity incorporation. Thus the core structure and energetics may be altered.

Our electronic structure calculations using the PBE-GGA pseudopotential approach resulted in a zero band gap value and by the use of the cluster hybrid approach it reached the value of 0.07 eV. As can be observed in Fig. 2 (a) a σ_p bond is formed between the 2 and 4 nitrogen atoms of Fig. 1 (a) (distance 1.5118 Å), which results in the formation of a deep band state. The In-In wrong bond formed at the dislocation core between atoms 1-3 (Fig. 1 (a)), which are in a distance of 2.86 Å, induces a state in the conduction band of InN (Fig. 2 (b)).

The four core structure is characterized by an In-In interaction between atoms 1 and 3 (2 and 4), shown in Fig. 1(b), which lie in a distance of 3.0505 Å. This interaction results in a state in the conduction band of InN (Fig. 2 (c)). In the case of the 8-atom dislocation core no localized state is observed in the band gap. The dangling bond orbitals of In atoms induce states in the conduction band (Fig. 2 (d)), suggesting that this configuration should be electrically inactive. These results are in agreement to those of Segev and Van de Walle [8] on polar and nonpolar InN surfaces, where both surface In-In and In dangling bonds induce states above the conduction band minimum thus not disturbing the InN band gap.

[1] Lu C. J., Bendersky L. A., Lu H., and Schaff W. J., *Appl. Phys. Lett.* 83, 2817 (2003).

[2] Wang X., Che S. -B., Ishitani Y., and Yoshikawa A., *Appl. Phys. Lett.* 90, 151901 (2007).

[3] Lebedev V., Cimalla V., Baumann T., Ambacher O., Morales F. M., Lozano J. G., and Gonzalez D., *J. Appl. Phys.* 100, 094903 (2006).

[4] Wang H., Jiang D. S., Wang L. L., Sun X., Liu W. B., Zhao D. G., Zhu J. J., Liu Z. S., Wang Y. T., Zhang S. M., and Yang H., *J. Phys. D: Appl. Phys.* 41, 135403 (2008).

[5] Muto D., Naoi H., Araki T., Kitagawa S., Kurouchi M., Na H., and Nanishi Y., *Phys. Stat. Sol. (a)* 203, 1691 (2006).

[6] Plesiewicz J., Suski T., Dmowski L., Walukiewicz W., Yu K. M., Korman A., Ratajczak R., Stonert A., Lu H., and Schaff W., *Semicond. Sci. Technol.* 22, 1161 (2007).

[7] Baroni S., Dal Corso A., Gironcoli S., and Giannozzi P., <http://www.pwscf.org>.

[8] D. Segev and C. G. Van de Walle, *Europhys. Lett.* 76, 305 (2006).

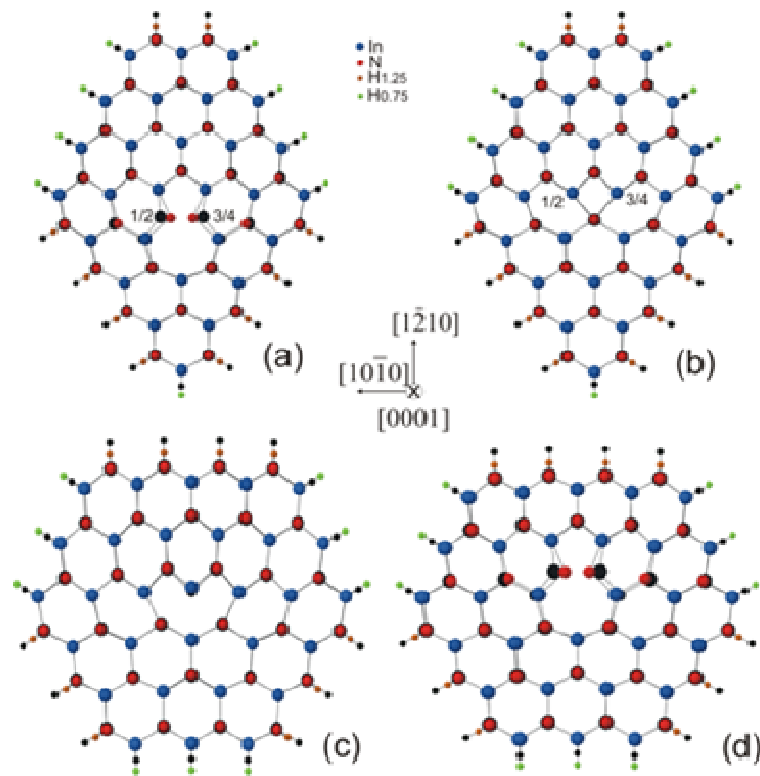


Figure 1. Projection along the [0001] direction of the (a) 5/7 (152 atoms), (b) 4 and (c) 8 relaxed core configurations. (d) corresponds to a 5/7 (156 atoms) relaxed core configuration used for comparison with the 8 dislocation core. Shading denotes level $c/2$ along the projection direction.

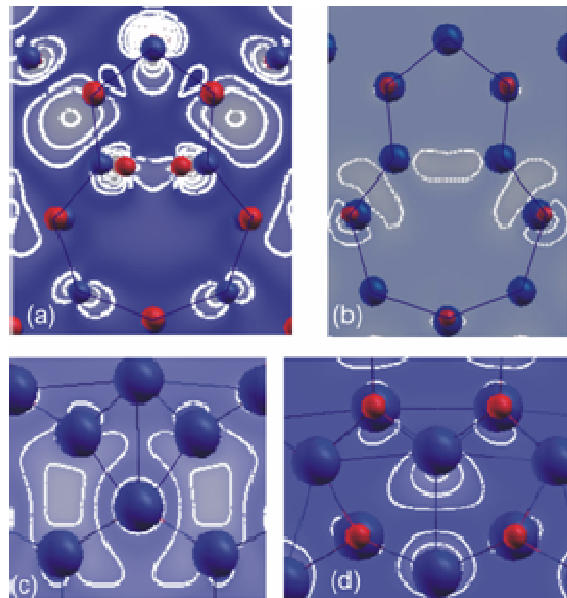


Figure 2. Charge density contour plots of: (a) 5/7 core structure, depicting the strained σ_p bond formed between the N atoms of the core, (b) 5/7 core structure depicting the wrong bond formed between the In atoms of the core, (c) 4-atom core corresponding to the state induced in the conduction band due to the In-In interaction. (d) corresponds to the state induced in the conduction band due to the In dangling bonds of the 8 atom core. Larger, blue spheres correspond to In while smaller, red spheres correspond to N atoms.

Acknowledgments

Support under the 7th European Framework Project DOTSENSE (Grant No. STREP 224212) and the MRTN-CT-2004-005583 "PARSEM" project is gratefully acknowledged.

Optical Properties of AlN-based Nanocomposite Films

H. Zoubos, E. Lidorikis and P. Patsalas*

University of Ioannina, Department of Materials Science and Engineering, GR-45110, Ioannina, Greece

*ppats@cc.uoi.gr

MO2

P8

AlN is a very well known wide bandgap semiconductor which exhibits absorption in the far UV spectral range, while being purely transparent in the visible spectral region. In addition, it has excellent mechanical properties and substantial chemical and metallurgical stability. The combination of its properties makes AlN a promising matrix material for durable optical sensors based on metal nanoparticles embedded into AlN and exhibiting surface plasmon resonance (SPR).

In this work we present AlN nanocomposite films with Ag inclusions (AlN:Ag) suitable for optical coatings. The growth has been performed using Pulsed Laser Deposition (PLD) or dual-cathode confocal magnetron sputtering on Si and sapphire substrates. Optical reflection and transmission spectroscopy (ORS/OTS) were employed in order to determine the films' and the optical properties, respectively. *In-situ* Auger Electron Spectroscopy (AES) and X-Ray Diffraction (XRD) have been used for the chemical and crystallographic analysis, respectively, of the grown films.

ORS/OTS has revealed that strong SPR exist in films with well defined metal inclusions of narrow size distribution. The spectral position of SPR is blue-shifted compared to the anticipated position considering the refractive index of pure AlN. This indicates alteration of the matrix's effective refractive index when the Ag nanoparticles are incorporated. Supporting evidence is also provided by finite difference time domain (FDTD) calculations.

High Pressure Studies of the Perovskite Isotopes Re^{16}O_3 and Re^{18}O_3

I. Efthimiopoulos^{1*}, S. Karmakar¹, X. Wang¹, K. Syassen¹, R. K. Kremer¹, F. S. Razavi¹, M. Hanfland² and Y.-L. Mathis³

¹ Max-Planck-Institut für Festkörperforschung, D-70569 Stuttgart, Germany

² European Synchrotron Radiation Facility (ESRF), F-38043 Grenoble, France

³ Forschungszentrum Karlsruhe GmbH, Institut für Synchrotronstrahlung (ISS), D-76344 Eggenstein, Germany

* I.Efthimiopoulos@fkf.mpg.de

The metallic perovskite ReO_3 (SG $Pm-3m$) is one of the most extensively studied transition metal oxides, with its behavior under pressure still not fully clarified [1]. Even though several works have been reported regarding its structural evolution under pressure (both for the bulk and nanocrystalline ReO_3), there has been a discrepancy in the literature over the number of the observed phase transitions [1- 4]. In particular, and for the bulk ReO_3 , it is generally observed that the initial $Pm-3m$ cubic structure transforms into another, more compressible cubic phase ($Im-3$) at ~ 0.5 GPa, while another phase transition into a rhombohedral phase ($R-3c$) takes place at ~ 13 GPa. However, there has been observed a tetragonal phase ($P4/mbm$) at ~ 0.52 GPa and a monoclinic phase ($C2/c$, MnF_3 -type) between 3 and 13 GPa. In addition, a high pressure study of nanocrystalline ReO_3 suggests that the ambient $Pm-3m$ phase first transforms into a monoclinic ($C2/c$) phase at ~ 0.6 GPa and then adopts the $R-3c$ phase at ~ 5 GPa. Strangely enough, no high pressure vibrational study has been reported so far.

Aiming at clarifying the sequence (and eventually the number) of the structural phase transitions, we have high-resolution synchrotron-based x-ray powder diffraction (XRD) studies on bulk Re^{16}O_3 under pressure. In addition, we have performed Raman investigations on both Re^{16}O_3 and the oxygen-substituted Re^{18}O_3 compounds, in order to elucidate the lattice dynamics of these compounds under pressure for the first time.

Our XRD results indicate that the sequence of the pressure-induced phase transitions depends on the viscosity of the pressure transmitting medium (PTM) used in the experiment. In the low viscosity environment (mixture of methanol-ethanol 4:1 as PTM), the original cubic phase ($Pm-3m$) transforms into the $P4/mbm$ phase at ~ 0.4 GPa. Upon further pressure increase, another phase transition into the monoclinic $C2/c$ phase takes place at ~ 3 GPa, and at ~ 13.5 GPa the transformation to the $R-3c$ phase occurs. Under high viscosity conditions (Si oil as PTM), the ambient $Pm-3m$ phase transforms initially into the $P4/mbm$ phase at ~ 0.3 GPa and then into the $Im-3$ phase at ~ 0.5 GPa. Upon further pressure increase, the transformation to the $R-3c$ phase is initiated at ~ 6 GPa. These findings helped to understand the controversial results reported in the literature [1-4].

Raman studies (mixture of methanol-ethanol 4:1 as PTM) have been performed on Re^{16}O_3 and the oxygen-substituted Re^{18}O_3 with two different laser wavelengths. The study of the ^{18}O isotope, which exhibits the same pressure-induced behaviour as Re^{16}O_3 , allowed us to assign all of the observed Raman modes. Regarding the structural transitions, the $P4/mbm$ and the $R-3c$ high pressure modifications are clearly resolved in our Raman investigation. However, the $P4/mbm$ to $C2/c$ transformation cannot be discerned. The most remarkable feature in our Raman spectra is the appearance of two high-intensity and low-frequency ($\sim 50 \text{ cm}^{-1}$) modes at ~ 0.5 GPa, where ReO_3 becomes Raman-active. Both of these modes exhibit an exceptionally large increase of their frequencies at moderate pressure. Actually, this remarkable frequency increase against pressure appears to be the highest observed in inorganic compounds so far. This unusual feature can be rationalized within the framework of Landau theory of second-order phase transitions ($\omega \sim P^{1/2}$). Our high-pressure synchrotron-based mid-infrared reflectance study on this compound (KCl as PTM) indicates that it remains metallic throughout the investigated pressure range.

[1] Biswas K., Muthu D. V. S., Sood A. K., Kruger M. B., Chen B. and Rao C. N. R., J. Phys.: Cond. Mat. 19, 436214 (2007) and references therein.

[2] Jorgensen J. E., Olsen J. S. and Gerward L., J. Appl. Cryst. 33, 279 (2000).

[3] Suzuki E., Kobayashi Y., Endo S. and Kikegawa T., J. Phys. Cond. Mat. 14, 10589 (2002).

[4] Jorgensen J. E., Marshall W. G., Smith R. I., Olsen J. S. and Gerward L., J. Appl. Cryst. 37, 857 (2004).

Structural and Spectroscopic Studies of the Multiferroic Spinel CdCr₂S₄ under pressure

I. Efthimiopoulos^{1*}, S. Karmakar¹, X. Wang¹, K. Syassen¹, P. Lemmens², V. Tsurkan³, M. Hanfland⁴
and Y.-L. Mathis⁵

¹ Max Plank Institut für Festkörperforschung, D-70569 Stuttgart, Germany

² Inst. for Condensed Matter Physics, TU Braunschweig, D-38106 Braunschweig, Germany

³ Inst. of Applied Physics, Academy of Sciences of Moldova, MD-2028 Chisinau, R. Moldova

⁴ European Synchrotron Radiation Facility, F-38043 Grenoble, France

⁵ Forschungszentrum Karlsruhe GmbH, Institut für Synchrotronstrahlung (ISS), D-76344 Eggenstein, Germany

* I.Efthimiopoulos@fkf.mpg.de

The behavior of spinels under non-ambient conditions has been the subject of extensive investigations, since the spinel structure and its high-pressure modifications play an important role in modelling major mineral phases of the upper mantle [1]. Within condensed matter physics, several spinels have recently attracted considerable interest because of the intimate interplay of structural, magnetic and ferroelectric properties. One of the most recent examples is the cubic CdCr₂S₄ spinel compound (SG *Fd-3m*), which was reported to exhibit relaxor ferroelectric behavior, displaying a particularly large magneto-capacitive effect at ~130 K [2]. In addition, CdCr₂S₄ becomes ferromagnetic at $T_{\text{Curie}}=85$ K. Clear evidence for a strong coupling between lattice, electrical polarization and magnetism comes from temperature-dependent studies of infrared- and Raman-active phonon modes of CdCr₂S₄ and similar chalcogenides [3]. This raises the question on how the tuning of elasticity by pressure affects its physical properties.

Here we report the results of our high pressure (HP) investigations on CdCr₂S₄. We have performed Raman spectroscopy, synchrotron-based infrared (IR) reflectance measurements, and x-ray diffraction experiments at room temperature. Overall, three structural phase transitions are clearly resolved: at ~13 GPa the ambient cubic structure adopts a tetragonal phase, at ~23 GPa an orthorhombic distortion occurs, while at ~39 GPa amorphization takes place. The amorphous phase persists after full decompression. Our HP IR study reveals that the structural transitions are accompanied by changes in the electronic properties. In particular, at ~12 GPa, a reversible insulator-to-metal transition occurs.

The findings are compared with the pressure-induced behavior of other spinel compounds. The interplay between structure and multiferrocity will also be discussed within a thermodynamic framework.

[1] Levy D., Pavese A., Sani A. and Pischedda V., Phys. Chem. Miner. 31, 122 (2004) and references therein.

[2] Hemberger J., Lunkenheimer P., Fichtl R., Krug-von-Nidda H.-A., Tsurkan V. and Loidl A., Nature 434, 364, (2005).

[3] Rudolf T., Kant Ch., Mayr F., Hemberger J., Tsurkan V. and Loidl A., Phys. Rev. B 76, 174307 (2007) and references therein.

High Pressure Structural Investigations of Fe-based Superconductors

I. Efthimiopoulos^{1*}, S. Karmakar¹, X. Wang¹, K. Syassen¹, J.S. Kim¹, R. K. Kremer¹, C. T. Lin¹ and M. Hanfland²

¹ *Max Plank Institut für Festkörperforschung, D-70569 Stuttgart, Germany*

² *European Synchrotron Radiation Facility, F-38043 Grenoble, France*

* *I.Efthimiopoulos@fkf.mpg.de*

The recent discovery of superconductivity at 26 K in the doped quaternary iron oxy-pnictide LaFeAsO attracted tremendous scientific interest [1]. More recently, the ternary iron-pnictide family AFe₂As₂ (R = Ba, Sr, Ca, Eu), adopting the ThCr₂Si₂ structure (SG *I4/mmm*), has also been shown to become high-*T_c* superconductors upon doping [1]. Structural building blocks common to these compounds are square layers built of edge-sharing FeAs₄ tetrahedra. These findings indicated the potential for superconductivity in other compounds of similar structure. Subsequently, FeSe (anti-litharge type structure) and LiFeAs were found to be superconducting, even without doping [1].

At ambient pressure, both the AFe₂As₂ and FeSe compounds exhibit a simultaneous structural (tetragonal to orthorhombic) and anti-ferromagnetic transition upon lowering *T* [1, 2]. Pressure has been found to be an important variable in these compounds, since it can induce superconductivity (e.g. *T_c* ~30 K at 4 GPa for BaFe₂As₂) or raise *T_c* (*T_c* ~37 K at ~7 GPa for FeSe) and suppress the aforementioned structural and magnetic transitions [2, 3]. The effect of pressure resembles that of doping, but without the chemical complexity. However, controversial results have been reported [3]. In addition, a novel “collapsed” tetragonal (c-T) phase was found to exist in the superconducting regime of CaFe₂As₂ (structure adopted at ~1.5 GPa at room temperature) [3]. All of the above indicate the strong interplay between the structural and the electronic properties in these compounds. Hence, the pressure-induced modification of the structural parameters becomes an important ingredient for the interpretation and modelling of the superconducting properties.

Here we report the high-pressure structural behavior of two Fe-based superconductors, namely BaFe₂As₂ and FeSe, investigated at room temperature by means of Raman spectroscopy and synchrotron-based x-ray powder diffraction. For BaFe₂As₂, the tetragonal *I4/mmm* phase was found to be stable up to ~25 GPa. The c-T phase was not detected. As for FeSe, we find that the tetragonal phase transforms irreversibly into a hexagonal NiAs-like phase at ~12 GPa, where *dT_c/dP* becomes negative [2]. We do not find any high-pressure orthorhombic phase of FeSe, as reported elsewhere [2]. In both compounds, the FeAs₄ (FeSe₄) tetrahedra become more distorted under pressure. We compare our results with the findings reported in the literature. We also discuss the correlation between the structural and the electronic/ superconducting properties in these two compounds.

[1] M. V. Sadovskii, arXiv:0812.0302 (unpublished) and references therein.

[2] D. Braithwaite et al., arXiv: 0904.1816 (unpublished) and references therein.

[3] C. W. Chu and B. Lorenz, arXiv:0902.0809 (unpublished) and references therein.

Probing the pressure-induced structural deformation of carbon nanotubes through carotene encapsulation in their interior

S. M. Souliou^{1,2*}, D. Christofilos¹, J. Arvanitidis^{1,3},
K. Yanagi⁴, H. Kataura⁴, G. A. Kourouklis¹ and S. Ves²

¹Physics Division, School of Technology, Aristotle University of Thessaloniki, 54124 Thessaloniki, Greece

²Physics Department, Aristotle University of Thessaloniki, 54124 Thessaloniki, Greece

³Department of Applied Sciences, Technological Educational Institute of Thessaloniki, 57400 Sindos, Greece

⁴Nanotechnology Research Institute, National Institute of Advanced Industrial Science and Technology (AIST), 1-1-1 Higashi, Tsukuba, Ibaraki, 305-8562, Japan

* msouliou@physics.auth.gr

Carotene molecules have been recently encapsulated in single-wall carbon nanotubes (SWCNTs), permitting the combination of the unique properties of carbon nanotubes and the light harvesting function of the carotene molecule, overcoming the molecule's instability at ambient conditions [1]. In the present work, we study the pressure response of carotene encapsulating single-wall carbon nanotubes (carotene@SWCNTs) by means of Raman spectroscopy, demonstrating the pressure screening effect provided to the carotene molecules by the tubes and the use of carotene molecules as internal probes in carbon nanotubes for the study of their structural modifications.

For the carotene encapsulation in SWCNTs, 1 mg of purified bundled SWCNTs, with diameters 1.26-1.50 nm, and 100 mg of all-trans- β -carotene were dissolved in 100 ml of hexane, following the procedure in Ref. [1]. Raman spectra were recorded in the back-scattering geometry using a micro-Raman triple grating system (DILOR XY), equipped with a cryogenic CCD detector. High pressure Raman measurements were carried out using a Mao-Bell type diamond anvil cell (DAC) with 4:1 methanol-ethanol mixture as the pressure transmitting medium and the ruby fluorescence technique for pressure calibration. The 514.5 nm line of an Ar⁺ laser, which is in resonance with both the carotene molecule and the E_{33} transition energy branch of the semiconducting tubes, was focused on the sample by means of a 20x objective, while the laser power was kept below 2 mW.

Figure 1 illustrates Raman spectra of carotene@SWCNTs, solid β -carotene and β -carotene solution in 4:1 methanol-ethanol mixture recorded at room temperature and various pressures in the frequency region 900 to 1600 cm^{-1} . The most characteristic Raman bands of the carotene molecule appear in this spectral region: ν_1 (in-phase C=C stretching vibration), ν_2 (C-C stretching and C-H bending modes), ν_3 (in plane rocking of the CH₃ groups) and ν_4 (out-of-plane C-H wagging modes). In the case of carotene@SWCNTs, the band frequencies at ambient conditions are located more closely to those of the carotene solution. In carotenoids, the vibronic coupling (interaction between the vibrational and electronic degrees of freedom) causes the frequency shift of the ν_1 mode. In carotenoid solutions, there is an additional frequency shift and diverse pressure dependencies for different solvents due to carotene-solvent interactions [2].

The ν_4 band is absent in solid carotene and carotene solution, however it is clearly observed in the case of carotene@SWCNTs (Fig. 1). This mode is forbidden for planar carotenoid molecules, while it becomes active upon molecular twisting [3]. Thus, the appearance of this mode in carotene@SWCNTs suggests that the carotene molecule inside the tube is forced to adopt a twisted trans conformation.

With increasing pressure, all the observed Raman bands shift to higher frequencies and broaden significantly. Figure 2 illustrates the pressure evolution of the frequency and the full width at half maximum (FWHM) of the carotene ν_1 band in carotene@SWCNTs, solid β -carotene and β -carotene solution in methanol-ethanol 4:1 mixture. Downstroke measurements (solid symbols in the figure) demonstrate that all

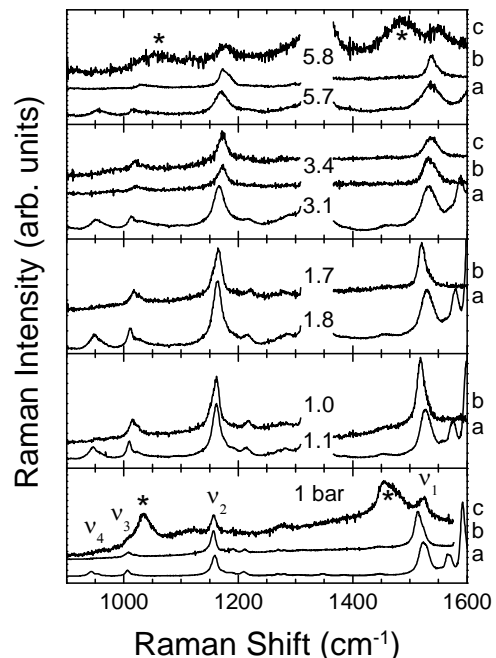


Fig. 1. Raman spectra of (a) carotene@SWCNTs, (b) solid β -carotene and (c) β -carotene solution in 4:1 methanol-ethanol mixture recorded at various pressures. Numbers denote the corresponding pressure in GPa. The asterisks mark bands of the methanol-ethanol mixture.

the pressure induced frequency shifts are fully reversible and the original frequencies are restored upon total pressure release. The pressure dependence of the ν_1 frequency in solid and in solution is linear without any slope change in the pressure region investigated. The slope of this band in 4:1 methanol-ethanol mixture and in a 1:1 mixture of n-pentane and isopentane [4] are close to each other ($4.1 \text{ cm}^{-1}/\text{GPa}$ and $3.6 \text{ cm}^{-1}/\text{GPa}$, respectively), whereas inside the SWCNTs it is $\sim 32\%$ smaller ($2.8 \text{ cm}^{-1}/\text{GPa}$ for pressures up to 2 GPa) than those in the former solutions. This indicates a pressure screening effect similar to that observed for the inner tubes in double-wall carbon nanotubes [5]. Interestingly, the pressure coefficient of the ν_1 band in carotene@SWCNTs exhibits an abrupt reduction and becomes even smaller above 2 GPa ($1.9 \text{ cm}^{-1}/\text{GPa}$).

Theoretical calculations for SWCNTs predict a diameter dependent pressure induced cross-section deformation of the tubes from circular to oval or polygonized and eventually to flattened shapes [6,7]. For nanotubes with diameters 1.3-1.5 nm these deformations are expected at $\sim 2 \text{ GPa}$ [6], suggesting that the pressure slope change of the ν_1 mode frequency can be attributed to the surrounding tube deformation. This deformation affects the carotene molecule both by modifying the distortion degree of its twisted trans conformation and by altering the pressure transmission in the interior of the nanotube, resulting to a differentiation of the pressure dependence of the carotene's mode frequencies. Since the pressure coefficient above 2 GPa is smaller compared to the one below that pressure, it is demonstrated that the tube deformation results in a stronger pressure screening effect for the carotene molecule.

As illustrated in figure 2(b), the FWHM of the carotene's ν_1 band is broader in carotene@SWCNTs than that in solid carotene and carotene solution, possibly due to the twisted trans conformation of the carotene molecule. While the pressure response of the FWHM of ν_1 in solid β -carotene and β -carotene solution exhibits a linear behavior, in carotene@SWCNTs, a deviation from the linear pressure response is observed and the pressure coefficient decreases at elevated pressures (sublinear behavior), suggesting that the tube deformation diminishes the pressure effect on the carotene molecule.

Consequently, the changes in the pressure response of the carotene molecule underline its possible use as a sensitive probe of the nanotube structural stability. It is important to note, that the small molecular size of carotene molecule and the rather weak carotene-tube interaction do not alter significantly the pressure response of the encapsulating nanotubes and the Raman spectra of the carotene@SWCNTs system are identical to the corresponding of the pristine (empty) SWCNTs in the whole pressure range studied (not shown).

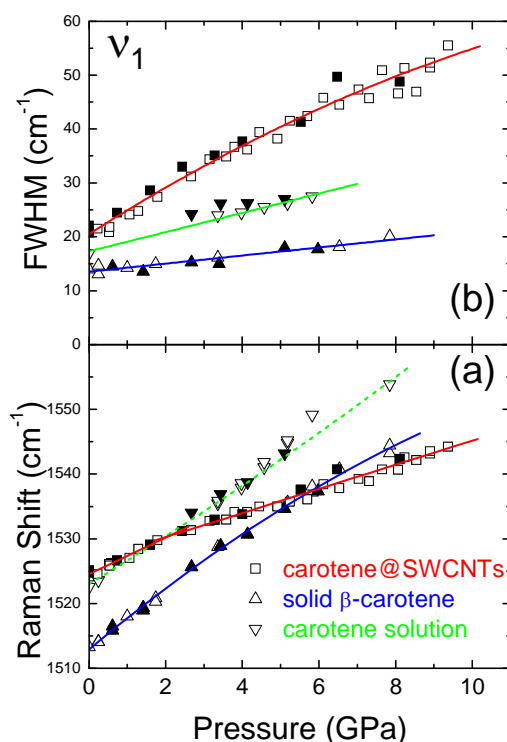


Fig. 2. Pressure dependence of (a) the frequency and (b) the FWHM of the carotene's ν_1 band in carotene@SWCNTs (squares), solid β -carotene (up triangles) and β -carotene solution in 4:1 methanol-ethanol mixture (down triangles). The open (solid) symbols denote data obtained for increasing (decreasing) pressure. The solid lines in (a) and (b) are least square fittings to the experimental data, while the dashed line in (a) is obtained from the literature and refers to the β -carotene solution in a 1:1 mixture of n-pentane and isopentane [4].

- [1] Yanagi K., Miyata Y. and Kataura H., *Adv. Mater.* 18, 437 (2006).
- [2] Liu W.-L., Zheng Z.-R., Zhu R.-B., Liu Z.-G., Xu D.-P., Yu H.-M., Wu W.-Z., Li A.-H., Yang Y.-Q. and Su W.-H., *J. Phys. Chem. A* 111, 10044 (2007).
- [3] Robert B., *The Photochemistry of Carotenoids* (Eds: Frank H. A., Young A. J., Britton G. and Cogdell R. J.), Kluwer, Dordrecht, The Netherlands (1999).
- [4] Ho Z. Z., Hanson R. C. and Lin S. H., *J. Phys. Chem.* 89, 1014 (1985).
- [5] Arvanitidis J., Christofilos D., Papagelis K., Takenobu T., Iwasa Y., Kataura H., Ves S. and Kourouklis G. A., *Phys. Rev. B* 72, 193411 (2005).
- [6] Chan S.-P., Yim W.-L., Gong X. G. and Liu Z.-F., *Phys. Rev. B* 68, 075404 (2003).
- [7] Elliott J. A., Sandler J. K. W., Windle A. H., Young R. J. and Shaffer M. S. P., *Phys. Rev. Lett.* 92, 095501 (2004).

The Effect Of Germanium Doping On The Annealing Characteristics Of The VO And VO₂ Defects In Silicon

C.A. Londos^{1*}, A. Andrianakis¹, V. Emtsev², H. Ohyama³

¹ University of Athens, Solid State Physics Section, Panepistimiopolis Zografos, Athens 157 84, Greece

² Ioffe Physicotechnical Institute of the Russian Academy of Sciences, Politekhnicheskaya ul. 26, 194012, St. Petersburg, Russia

³ Kumamoto National College of Technology, 26592, Nishigoshi, Kumamoto 861-1102, Japan

*hlontos@phys.uoa.gr

Nowadays, silicon is the most important material in electronic industry. It is employed in a wide variety of applications. However, modern electronics and microelectronics face problems with corresponding Si-based devices especially concerning high speed operation, low noise level, high operating frequencies, as well as the increased demand for higher radiation hardness and thermal resistance. All these problems, coupled with the need of low manufacturing costs, pose the necessity of creating new materials. In this context, doping of silicon with isovalent impurities attract considerable interest. These impurities are electrically inactive and they do not exert strong influence on initial parameters of materials. However, the elastic strains introduced in materials due to their different atomic size than that of regular atoms can effectively change interactions of impurities with intrinsic defects such as vacancies and self-interstitials. This property of isovalent impurities can be used to affect and somehow control interactions between point defects during crystal growth as well as under irradiation and annealing.

Oxygen is the most important impurity in commercial Czochralski grown silicon. It is electrically inactive. However, during irradiation or/and heat treatment various oxygen-related defects, especially multioxygen-multivacancy complexes V_nO_m, are formed. The majority of these defects are electrically active, exerting strong effects on electrical properties of Si materials. On the other hand, it is known that the introduction of Ge into silicon gives rise to compressive strains in the lattice, since the isovalent Ge atoms are larger in atomic size. As a result, they are effective traps for vacancies. Therefore, the formation and annealing of V_nO_m defects is expected to be influenced by the Ge presence. The aim of this work is to investigate these effects.

To this goal, Ge-doped Si samples (table 1) with various Ge concentrations up to $2 \times 10^{20} \text{ cm}^{-3}$ were used. They were irradiated with 2 MeV electrons at a dose of $5 \times 10^{17} \text{ e}^-/\text{cm}^2$. The irradiation temperature was 95°C. After the irradiation, the samples were subjected to isochronal annealing up to 650°C, in steps of $\Delta T = 10^\circ\text{C}$ and $\Delta t = 20 \text{ min}$. After each annealing step, IR absorption spectra were recorded by means of a FTIR spectrometer.

Sample name	[Ge] cm ⁻³	[O _i] _o 10 ¹⁷ cm ⁻³	[C _s] _o 10 ¹⁶ cm ⁻³	[VO] 10 ¹⁶ cm ⁻³
Cz-Si	0	9.56	<2.0	2.35
Ge-1	1·10 ¹⁷	9.60	2.0	3.40
Ge-2	7·10 ¹⁷	6.50	<2.0	2.50
Ge-3	1·10 ¹⁸	10.00	3.0	3.50
Ge-4	4·10 ¹⁸	5.55	10.0	3.60
Ge-5	1·10 ¹⁹	6.74	20.0	5.00
Ge-6	5·10 ¹⁹	7.60	<2.0	3.10
Ge-7	1·10 ²⁰	8.77	3.7	3.75
Ge-8	2·10 ²⁰	7.70	18.0	4.25

Table 1 The initial germanium oxygen and carbon concentrations as well as the VO defects concentration in the Ge-doped Si samples used.

As can be seen from table 1, the used samples can be separated into three groups. Group 1 contains samples with initial carbon concentration below the detection limit namely Cz-Si, Ge-2 and Ge-6. Group 2 contains samples with low initial carbon concentration up to $1 \cdot 10^{17} \text{ cm}^{-3}$ including the samples Ge-1, Ge-3, Ge-4 and Ge-7. Group 3 contains samples with high initial carbon concentration up to $2 \cdot 10^{17} \text{ cm}^{-3}$ including the samples Ge-5 and Ge-8. As a result of irradiation, vacancy-oxygen (VO) pairs are formed. Their presence in the spectra is verified by the 830 cm^{-1} IR band. The VO defect concentration versus Ge content in the used samples is shown in Fig.1. It is clearly seen

from this figure that in group 1 samples VO concentration is slightly increased versus Ge content for Ge up to $5 \cdot 10^{19} \text{ cm}^{-3}$. This can be explained by the fact that Ge atoms in the temperature of irradiation act as temporary traps for vacancies reducing thus the annihilation rate with self-interstitials ($V + (\text{Si})_I \rightarrow (\text{Si})_s$). As a consequence, more vacancies are available to be captured by O_i atoms to form VO defects. In group 2 samples, VO concentration also increases versus Ge content for Ge up to $1 \cdot 10^{20} \text{ cm}^{-3}$ being sufficiently higher from the values of group 1. The observed increase can be explained taking into account that during irradiation carbon atoms captures self-interstitials while Ge atoms act as temporary traps for vacancies. Both carbon and germanium impurities result in a reduction of the annihilation rate of vacancies and self-interstitials, leading more vacancies to be captured by O_i atoms. In group 3 samples, VO concentration is enhanced in comparison

with the samples of group 2, but for $[Ge]=2 \cdot 10^{20} \text{ cm}^{-3}$ a decrease is observed in relation with the corresponding

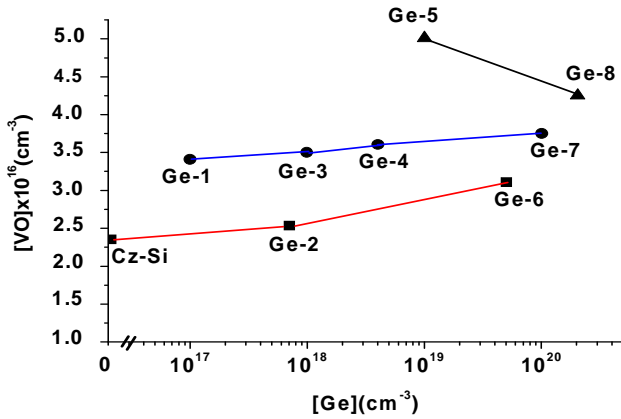


Fig.1 The VO defect concentration versus Ge content in the Ge-doped Si samples used.

value for $[Ge]=1 \cdot 10^{19} \text{ cm}^{-3}$. The enhancement in the VO concentration can be explained by the presence of carbon in high concentration that results in a suppress of the annihilation rate of vacancies and self-interstitials although Ge impurity in high concentration ($2 \cdot 10^{20} \text{ cm}^{-3}$) seem to enhance this rate due to the clusters of Ge atoms formed, which act as sites for annihilation of primary defects [1].

Upon annealing this band begins to decay and another band at 888 cm^{-1} , attributed to the VO_2 defect, begins to grow in. The relevant reaction is $\text{VO} + \text{O}_i \rightarrow \text{VO}_2$. It has been established that the temperature of the VO_2 defect formation is markedly reduced due to the presence of Ge atoms [2]. This reduction is relatively small for $[Ge]$ up to $\sim 4 \cdot 10^{18} \text{ cm}^{-3}$, and more pronounced for higher; (Fig. 2.(a))

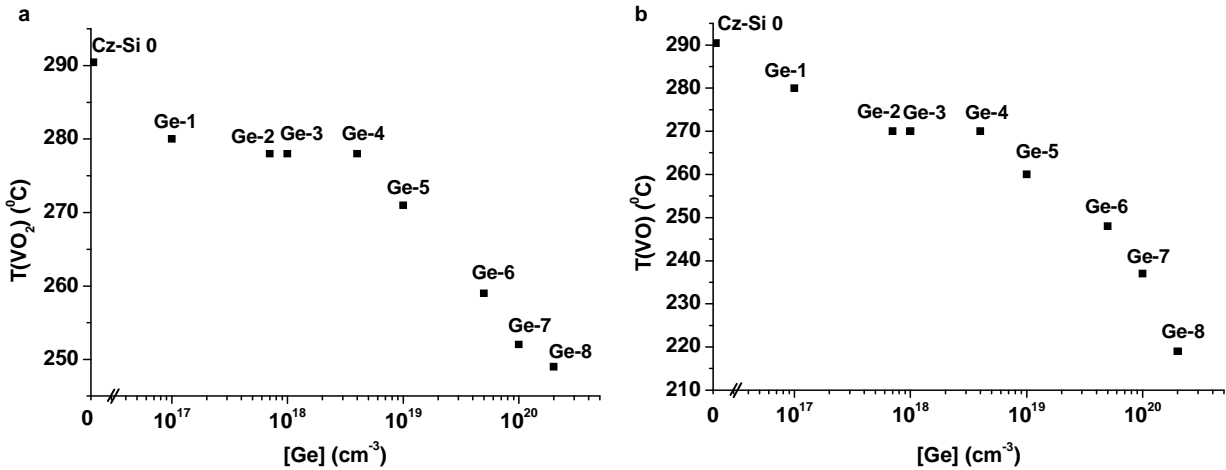


Fig.2. The annealing temperature of VO defect (a) and the formation temperature of the VO_2 defect (b) versus $[Ge]$.

On the other hand, the annealing temperature of VO defects, especially in materials with high $[Ge]$, it was found to be even lower than the corresponding temperature of the VO_2 defect formation (Fig. 1(b)), indicating that another defect reaction ($\text{VO} + (\text{Si})_i \rightarrow \text{O}_i$) is also running in the annealing processes of VO complexes. These phenomena could be reasonably explained if one takes into account an influence of elastic strains due to Ge atoms in the Si lattice on the rates of both principal reactions, i.e. $\text{VO} + \text{O}_i \rightarrow \text{VO}_2$ and $\text{VO} + \text{Si}_i \rightarrow \text{O}_i$ which govern the annealing of the VO defects. The migration energy of VO defects in the first reaction and the binding energy of self-interstitials at large agglomerates in the second reaction are believed to be sensitive to the Ge concentration in Si [2,3]. More specifically, they are reduced as $[Ge]$ increases, leading the above reactions to occur at lower temperatures .

References

[1] Londos C.A., Andrianakis A., Emtsev V.V., Ohyama H. , Semicond. Sci. Technol. 24, (2009) to be published.
 [2] Londos C.A., Andrianakis A., Emtsev V.V., G. A. Oganessian, Ohyama H. , Mat. Sci. and Eng. B 154-155, 133, (2008)
 [3] Londos C.A., Andrianakis A., Aliprantis A., Ohyama H., Emtsev V.V., G. A. Oganessian, Physica B 401-402, 487,(2007)

Micro-Raman investigation on the long term stability of dye-sensitized solar cells under light and thermal stress

V. Likodimos^{1*}, T. Stergiopoulos¹, P. Falaras¹, R. Harikisun², J. Desilvestro², G. Tulloch²

¹ Institute of Physical Chemistry, NCSR Demokritos, 153 10, Aghia Paraskevi Attikis, Athens, Greece
² Dyesol Limited Company, Queanbeyan, NSW 2620, Australia

*likodimo@chem.demokritos.gr

Mesoscopic dye solar cells (DSCs) have been attracting much attention due to their unique potential as a viable alternative to current silicon-based photovoltaics that offers the prospect of efficient, clean and low cost solar energy conversion [1]. Mimicking the principles of natural photosynthesis for the separation of light harvesting and charge carrier transport, the operation mechanism of DSCs relies upon the synergistic function of the three major cell components, the light absorbing antenna (the most effective being Ru(II) polypyridyl complexes) the electron transporting system involving a wide band gap semiconductor of mesoporous structure (typically the anatase TiO₂) and the electrolyte/hole-transporter subsystem (the most frequent being the I⁻/I₃⁻ redox couple) [2].

Systematic studies of the DSCs' components and their complex interdependence have established marked efficiency improvements of the underlying physicochemical processes including fast electron injection from the photo-excited state of the dye into the TiO₂ conduction band with near unity photon-to-electron conversion efficiency, rapid dye regeneration, weak interfacial recombination losses as well as efficient collection of the photo-generated electrons and hole transport at the counter electrode through the redox couple, leading to power conversion efficiencies over 11% under standard air mass AM 1.5 solar illumination [2]. However, apart from the requirement of high device efficiency, long-term stability of the DSC operation is a key aspect in view of practical applications, especially on industrial modules of larger area (efficiencies ranging from 7-8% at 1/3 sun and 5.8-7% at 1 sun) [3]. Despite the significant progress in the long-term performance of these DSC devices, detailed spectroscopic information on aging phenomena, besides monitoring through current-voltage characteristics and electrochemical impedance spectroscopy, has been limited.

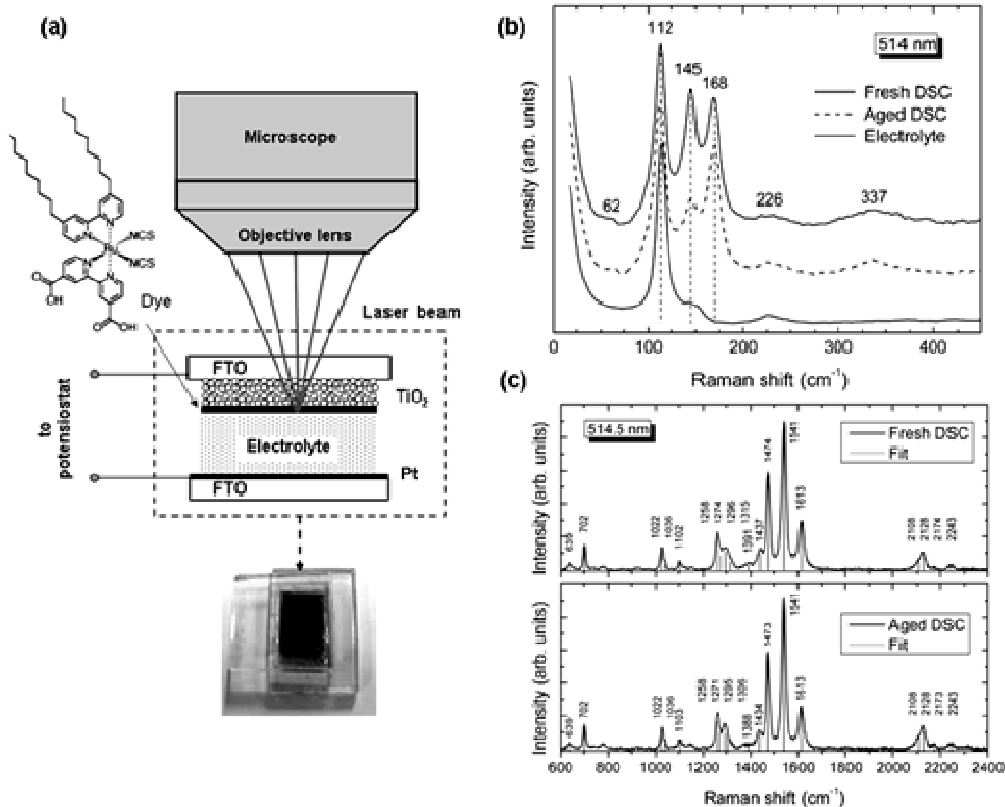


Figure 1. (a) Schematic diagram of the micro-Raman setup for the *in situ* measurements on DSC devices under operating conditions. (b) Micro-Raman spectra of the fresh and aged DSCs in comparison with the electrolyte solution at low frequencies. (c) Resonance Raman of the fresh and aged DSCs in the dye vibration region.

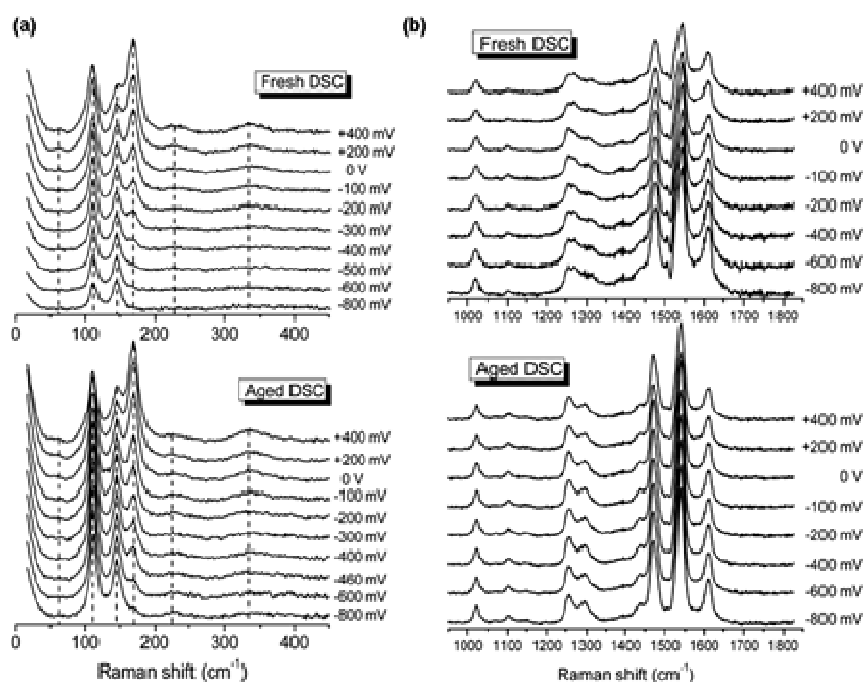


Figure 2. *In-situ* Raman spectra as a function of the polarization bias of the fresh and aged DSCs in the (a) low frequency region and (b) the dye vibration region, at 514.5 nm.

Micro-Raman spectroscopy has been proved to be a sensitive experimental technique offering high spectral and spatial resolution to probe the vibrational properties and coordinative interactions of the individual cell components and the corresponding interfaces and most importantly investigate *in-situ* the DSC response under operating conditions [4]. In this work, resonance micro-Raman spectroscopy is exploited as a site-specific spectroscopic probe to evaluate the stability of DSCs under prolonged exposure to light soaking and thermal stress, involving continuous illumination over 6450 hours at 55-60 °C.

Micro-Raman measurements at different excitation wavelengths of 514.5 nm and 785 nm are employed to study the vibrational properties of the individual cell components, including the TiO₂/conducting glass photoelectrode, the hydrophobic ruthenium dye and its chemisorption on the mesoporous TiO₂ film as well as the electrolyte components. Subsequently, resonance Raman at 514.5 nm, close to the metal-to-ligand charge transfer transition (~530 nm) of the dye complex, is used to resolve aging effects in the fresh and aged DSC test devices under both *ex-situ* and *in-situ* (applying a polarization bias) conditions, Fig. 1(a). Comparative *ex-situ* resonance Raman measurements on the fresh and stressed solar cells show minor differences in the spectral response of both the triiodide and dye molecules as well as the triiodide/dye adduct at the electrode/electrolyte interface implying a marked chemical stability and the absence of any major variation of the corresponding interfaces, Fig 1(b) and (c). The anatase Raman spectrum shows an intensity decrease and broadening of its spectral width for the aged cells, indicating a modification of the semiconductor electronic state through electron accumulation on the TiO₂ nanoparticles after long term stress. *In-situ* resonance Raman measurements, implemented via the application of an external bias voltage, allow a comparative spectroscopic evaluation of the fresh and aged DSCs under operating conditions (Fig. 2). In that case, a relatively small decrease of the initially high bias dependence of the Raman intensity of the triiodide, dye and triiodide/dye bands is detected for the aged cells. This behaviour along with the variation of the anatase Raman modes imply a modification of the interfacial electric field at the TiO₂/dye/electrolyte junction. The absence of any distinct chemical modification/degradation process on industrial DSC devices after prolonged light and thermal stresses is thus established for the first time in the literature by a direct Raman investigation of the cell components and interfaces.

[1] Grätzel M., Nature 414, 338 (2001).

[2] Kroon J. M., Bakker N. J., Smit H. J. P., Liska P., Thampi K. R., Wang P., Zakeeruddin S. M., Grätzel M., Hinsch A., Hore S., Würfel U., Sastrawan R., Durrant J. R., Palomares E., Pettersson H., Gruszecki T., Walter J., Skupien K., Tulloch G. E., Prog. Photovoltaics 15, 1, (2007).

[3] Desilvestro J., Harikisun R., Moonie P., Ball D., Au F., Duong H., Evans G., Bertoz M., 17th Int. Conf. Photochem. Conv. and Storage of Solar Energy, Sydney, Australia, 2008. http://www.dyesol.com/index.php?element=Desilvestro_IPS-17.

[4] Stergiopoulos T., Bernard M.-C., Hugot-Le Goff A., Falaras P., Coord. Chem. Rev. 248, 1407 (2004).

Micro-Raman spectroscopy on self-assembled anodized TiO₂ nanotube arrays

V. Likodimos^{1*}, A. G. Kontos¹, T. Stergiopoulos¹, P. Falaras¹, J. Kunze²

¹ Institute of Physical Chemistry, NCSR Demokritos, 153 10, Aghia Paraskevi Attikis, Athens, Greece

² Department of Materials Science, WW4-LKO, University of Erlangen-Nuremberg, Erlangen, Germany

*likodimo@chem.demokritos.gr

Controlled growth of TiO₂ nanotube (NT) arrays by electrochemical anodization of metallic titanium has been recently realized, providing a straightforward synthetic route to a robust, vertically oriented architecture that is being actively investigated for various applications, where the advantages of the self-organized layers combined with the intrinsic properties of nanocrystalline TiO₂ can be effectively exploited [1,2]. Micro-Raman spectroscopy has emerged as a sensitive local probe of the phase composition, crystallographic orientation, lattice dynamics and polarization effects in nanostructured materials, while based on the spatial confinement of optical phonons in nanosized systems, where translational invariance is broken by the interrupted lattice periodicity, it has been applied to determine the particle size of metallic and semiconductor nanomaterials [3].

In this work, we present a systematic polarized micro-Raman investigation on the phase composition, crystallite size, crystallographic orientation and “antenna” polarization effects in self-organized TiO₂ NT arrays with tailored morphologies produced by variable electrochemical anodization in both aqueous buffered (phosphate) and highly viscous organic (ethylene glycol) electrolytes as well as in perchlorate/chloride electrolytes under the rapid breakdown anodization (RBA) conditions [1]. Figure 1(left) shows representative SEM micrographs of the TiO₂ NTs arrays, where a marked variation of the tube morphology is evidenced for the samples grown under different conditions. Comparative Raman measurements of the as-grown and thermally annealed NTs reveal that post-growth thermal treatment results in severe reduction of the concentration of organic species encapsulated in the as-grown NT matrix by the anodization bath and the transformation of the amorphous TiO₂ to nanocrystalline anatase, Fig. 1(right), with minor amounts of the rutile phase persisting for the shorter TiO₂ NTs anodized in phosphate electrolytes.

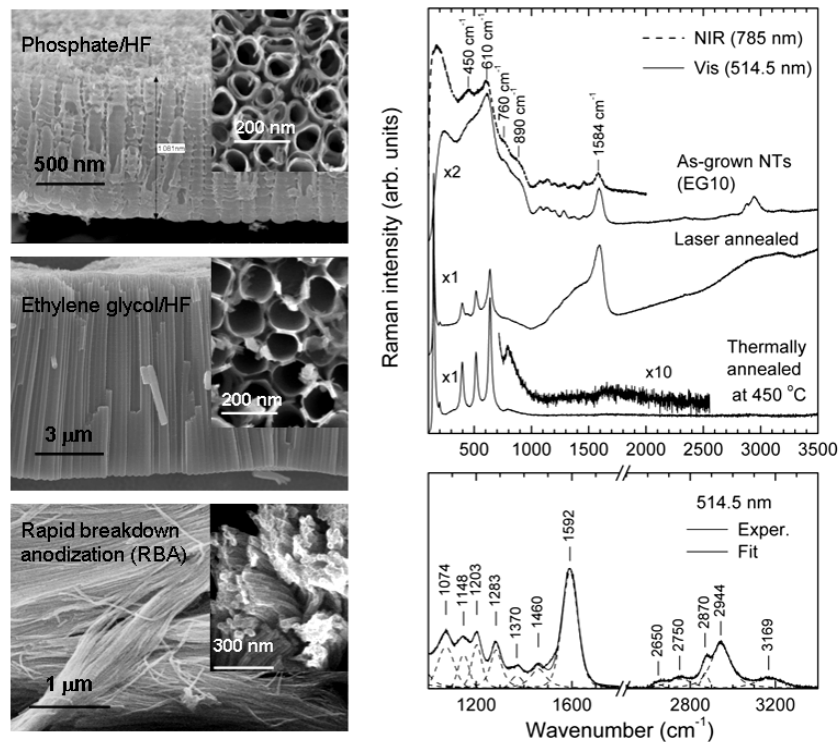


Figure 1. (left) Cross-sectional and top surface (inset) SEM images of TiO₂ NT arrays grown in phosphate, ethylene glycol and perchlorate/chloride (RBA) electrolytes. (right) Micro-Raman spectra of TiO₂ NTs synthesized in ethylene glycol electrolytes in the as-grown state and after laser and post-growth thermal annealing at wavelengths of 785 and 514.5 nm.

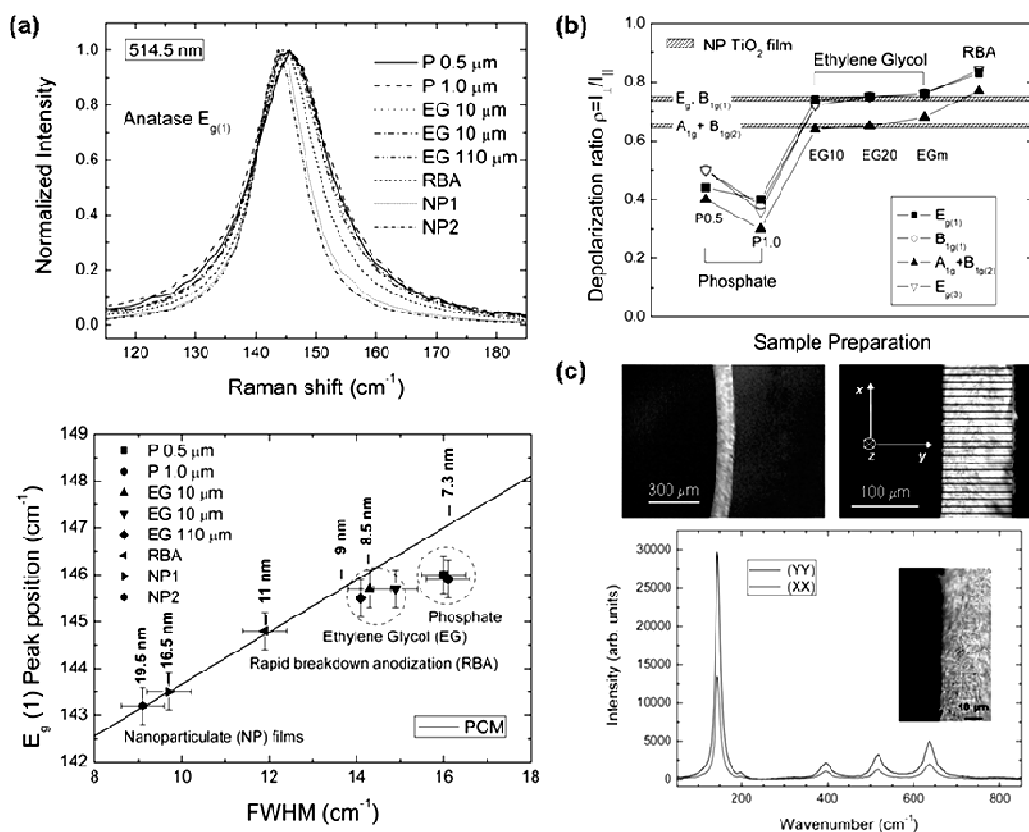


Figure 2. (a) Normalized Raman lineshape and peak position vs peak width (FWHM) of the $E_{g(1)}$ anatase mode for the annealed TiO₂ NTs compared to that of nanoparticulate (NP) TiO₂ films at 514.5 nm. The solid line shows the PCM behavior and the vertical bars depict the corresponding anatase particle sizes. (b) Depolarization ratios of the anatase modes for the TiO₂ NT arrays and the NP TiO₂ films (hatched bands). (c) Optical images of the NT membrane cross section at different magnifications and polarized micro-Raman spectra in parallel (XX) and (YY) polarizations at 514.5 nm.

Depending on the specific electrochemical preparation route and the concomitant variation of the NT morphology, a variation of the particle size/shape and possibly oxygen stoichiometry as well as the degree of preferential crystallographic orientation of the anatase nanocrystallites is inferred. The E_g anatase mode follows closely the size-dependent variation predicted by the phonon confinement model (PCM) for nanoparticulate anatase [Fig. 2(a)], though, a small but systematic discrepancy from the PCM behavior is observed for the TiO₂ NT arrays produced in ethylene glycol and phosphate electrolytes. Significantly smaller crystallite sizes are predicted by phonon confinement model than those estimated by X-ray diffraction data for the phosphate TiO₂ NTs, a discrepancy that can arise from the contribution of shape effects imposed by the formation of cylindrical crystallites or oxygen non-stoichiometry. Polarized micro-Raman measurements reveal that partial orientation effects pertain only for the phosphate TiO₂ NTs, most probably due to the relatively short length of these arrays that allows preferential (101) growth, Fig. 2(b). On the other hand, a predominant random orientation of the anatase crystallites is found for the ethylene glycol and RBA NTs, consisting of long individual NTs, their length exceeding 10 microns, Fig. 2(b). Most importantly, polarized Raman spectra on the cross section of a free standing TiO₂ NT membrane reveal substantial enhancement of the Raman intensity, when the incident electric field of the laser beam is parallel to the nanotube axis [Fig. 2(c)], suggesting an “antenna” effect [4], attributed to the polarization dependent light scattering by the cylindrical NT structure and the high dielectric constant of the anatase TiO₂ NTs. These effects provide insight to the enhanced optoelectronic properties, light transmittance and electron transport of anodic TiO₂ nanotube materials and justify their particular significance for light-induced applications.

- [1] Macak J. M., Tsuchiya H., Ghicov A., Hahn R., Bauer S., Schmuki P., *Curr. Opin. Solid State Mater. Sci.* 11, 3 (2007).
- [2] Shankar K., Basham J. I., Allam N. K., Varghese O. K., Mor G. K., Feng X., Paulose M., Seabold J. A., Choi K.-S., Grimes C. A., *J. Phys. Chem. C* 113, 6327 (2009).
- [3] Gouadek G., Colomban P., *Prog. Cryst. Growth Charact. Mater.* 53, 1 (2007).
- [4] Chen G., Wu J., Lu Q., Gutierrez H. R., Xiong Q., Pellen M. E., Werner D. H., Eklund P. C., *Nanolett.* 8, 1341 (2008).

Use of Image Analysis for Characterisation of Thermal Shock Behaviour of Improved Ceramic Matrix Composites

M. Dimitrijevic^{*}, R. Jancic Heinemann, T. Volkov Husovic

Faculty of Technology and Metallurgy, University of Belgrade, Karnegijeva 4, Belgrade, Serbia

** mdimitrijevic4@yahoo.com*

Refractory materials need to maintain good mechanical properties at high temperatures and to exhibit good thermal shock resistance. Thermal shock resistance is measured using the water quench test. After every cycle of heating and quenching the specimen surface is examined and the quantitative results are obtained using image analysis. Surface destruction is determined by observing the damaged parts of the surface and shape and area of the damage are observed and used for analysis.

Specimens consisted of composite materials having short fibres as reinforcement. Lengths to diameter ratio of fibres used as reinforcement in the composite was 10 and 20 respectively. In this paper the surface area and shape of damaged parts were determined using image analysis. Obtained results were compared to strengths degradation and to dynamic modulus of elasticity of specimens.

MO2

P16

Influence of Microstructure on Mechanical Properties of Porous SiC/Cordierite Composite Materials

M. Posarac^{1*}, T. Volkov-Husovic², B. Matovic¹

¹*Institute of Nuclear Sciences "Vinca", P.O. Box 522, 11001 Belgrade*

²*Faculty of Technology and Metallurgy, Karnegijeva 4, POB 3503*

* *milicap@vinca.rs*

SiC/cordierite porous composite ceramics with weight ratio of 70:30 were prepared by a mechanical mixing of commercial SiC and cordierite from two different sources. In the one case mixture of commercially available spinel, quartz (SiO₂) and alumina (Al₂O₃) corresponding to a cordierite stoichiometry was attrition milled using Al₂O₃ balls and ethyl alcohol as media for four hours. The second source of cordierite was Mg-exchanged zeolit, quartz (SiO₂) and alumina (Al₂O₃) mixed according to the chemical composition of cordierite, attrition milled using Al₂O₃ balls and ethyl alcohol as media for five hours. Graphite powder used as the pore former to change the porosity of the specimens. The mixture was heated in air so that graphite was burned out. The weight fraction of graphite had a strong influence on porosity and strength so we used 10, 20 and 30 wt% of graphite powder. Microstructure was investigated with SEM. Pore size and pore distributions was determined by Image ProPlus program for image analysis. Vickers hardness test was performed and influence of porosimetry on hardness of composite materials was investigated. Young's modulus of samples was calculated using measured values of ultrasonic velocities obtained by ultrasonic pulse velocity technique.

Structural and Electronic Properties of Metal Nitrides

Th. A. Goutziotis, L. E. Koutsokeras, P. Patsalas and Ch. E. Lekka *

Department of Materials Science and Engineering, University of Ioannina, Ioannina 45110, Greece

*chlekk@cc.uoi.gr

MO2

P18

We present ab-initio calculations and experimental data of selective group IV-VI binary metal nitrides (TiN, ZrN, HfN, NbN, TaN, MoN and WN) referring to their structural and electronic properties. Theory and experiment indicate that there is correlation of lattice constant with the atomic number and their corresponding period [1]. In all cases the nitrides exhibit enhanced bulk modules compared to the simple metal cases rendering the nitrides harder, in agreement with previous studies [1-4]. Aiming in obtaining insight of the origin of this behavior we conducted a detailed study of their electronic properties as well as of the role of N. It is well known that e.g. for Nb the majority of electronic states are situated from -4eV up to the Fermi level whereas for NbN these states that present the metallic character of the nitride are depleted; other states emerge between -9eV and 4eV due to the presence of N. This dominant localized energy state is characterized by the contribution of both Nb and N and gives covalent-like features to the nitride rendering it harder; however, the crystal field splitting of the metal's d -band (t_{2g} , e_g states) indicate a partially ionic character, as well. Thus, these nitrides exhibit a mixed covalent-ionic bonding. In addition, another energy state is found around -17eV up to -15eV that is mainly occupied by N. Similar behavior is exhibited for all cases with the characteristic energy states slightly shifted compared to NbN. These results could be used for a deeper understanding of the metal nitrides' behavior in order to design new ternary, quaternary or even nanostructured metal nitrides for specific applications in electronics and microelectromechanical systems.

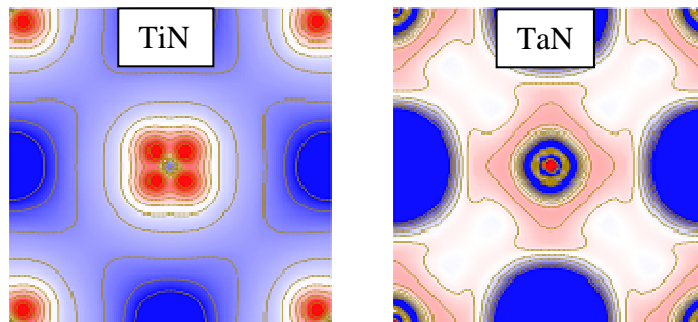


Figure. Charge density of TiN and TaN.

- [1] G. M. Matenoglou, L.E. Koutsokeras, P. Patsalas, Appl. Phys. Lett. 94 (2009) 152108.
- [2] L.E. Koutsokeras, G. Abadias, Ch.E. Lekka, G.M. Matenoglou, D.F. Anagnostopoulos, G.A. Evangelakis and P. Patsalas Appl. Phys. Lett. 93 (2008) 011904.
- [3] G.M. Matenoglou L.E. Koutsokeras, Ch.E. Lekka, G. Abadias, S. Camelio, G.A. Evangelakis, C. Kosmidis, and P. Patsalas, J. Appl. Phys. 104 (2008) 124907.
- [4] P. Patsalas, C. Charitidis, S. Logothetidis, Surf. Coat. Technol. 125 (2000) 335.

A maximum in the strength of Superhard Rhenium Borides

Ch. Moutsanos* and I. N. Remediakis

Department of Materials Science and Technology, University of Crete, Heraklion, Crete, Greece

**moutsanos@materials.uoc.gr*

Rhenium diboride (ReB_2) is a superhard material that was recently synthesized at ambient pressure and temperature. We use Density Functional Theory (DFT) to calculate the mechanical response of ReB_2 as well as other rhenium borides. We compare our findings to similar properties for pure Re and B as well as ReB_2 , Re_7B_3 and Re_3B . Our results allow us to compare properties of $\text{Re}_x\text{B}_{1-x}$ as a function of B content. We discuss the hardness of these materials, and its correlation to their enthalpy of formation, density, bulk and shear moduli, as well as the electronic density of states. Our calculations provide new insight for the properties of the crystal structure and the boron concentration that yields maximum strength of the material.

At low B concentrations, the high electron density of Re gives rise to high incompressibility of the material, resulting at a large bulk modulus. At high B concentrations materials consist of a network of directional bonds between $2p$ orbitals of B, which gives rise to small Poisson ratios for B-rich materials. The strongest material lies in between the two extreme cases, at the optimum mixture of high bulk modulus and small Poisson ratio. We find a clear maximum in the strength of these materials for B concentration of $2/3$ (ReB_2). Our results explain the experimental findings for the high hardness of ReB_2 , and can be used to guide the design of new superhard materials.

Far Infrared Spectra and Structure of $(K_2S)_x(Sb_2S_3)_{100-x}$ Glasses

Th. Ch. Hasapis^{1*}, E. Hatzikraniotis¹, K. M. Paraskevopoulos¹, K. S. Andrikopoulos², S. N. Yannopoulos³

¹*Solid State Physics, Dept. of Physics, Aristotle University of Thessaloniki, 54124 Thessaloniki, Greece*

²*Physics Division, School of Technology, Aristotle University of Thessaloniki, 54124 Thessaloniki, Greece*

³*FORTH /ICE-HT, P.O. Box 1414, GR-26504, Rio, Patras*

**thasa@physics.auth.gr*

MO2

P20

Abstract

The structure of chalcogenide glasses $(K_2S)_x(Sb_2S_3)_{100-x}$ with $x=0, 10, 16.67$ and 30 was studied by infrared reflectance spectroscopy. Polycrystalline Sb_2S_3 was also studied for comparison and the oscillator fit revealed the main vibrations of the mineral stibnite structure. The reflectivity spectra of alkali doped compositions showed broad features representative of glassy structures and the oscillator fit yielded vibrations of $SbS_{3/2}$ pyramidal molecules. For the $x=10$ and 30% the analysis showed probably a two phase glass structure with different Sb-S distances, while the $x=16.67$ the compound KSb_5S_8 composition, was found to consist of a homogeneous pyramidal network.

Introduction

Mineral stibnite Sb_2S_3 crystallizes in the orthorhombic space group D_{2h} . It is composed of infinite chains $(Sb_4S_6)_n$ parallel to the b axis. Sb atoms occupy trivalent or quivalent sites, while S atoms occupy divalent or trivalent sites [1]. The structure of glassy Sb_2S_3 , which is difficult to obtain (very high cooling rates are necessary), mainly consists of trigonal pyramids SbS_3 linked via Sb-S-Sb bonds [2], being therefore isostructural to the well-known glass As_2S_3 .

Introduction of alkali metals as Li, Na, K modifies the glass network formed by a glass former. Addition of Li_2S in As_2S_3 causes the creation of nonbridging sulfurs (NBS), which are bonded to one As (As-S) instead of two, maintaining the pyramidal geometry [3]. The number of NBS increases with increasing modifiers' content.

In this work we present infrared reflectivity spectra of $(K_2S)_x(Sb_2S_3)_{100-x}$ glasses for $x=10, 16.67$ and 30 in order to study the effect of potassium doping on the structure of the stoichiometric glass matrix. This work has been motivated by recent studies which have revealed that K-Sb-S compounds have the advantages (fast crystallization rate and appreciable contrast in the refractive index between crystalline and glassy phases) of phase change materials with potential applications to optical data storage [4].

Experimental

Glasses were prepared by mixing appropriate amounts of high purity elements. Due to the hygroscopic and explosive properties of the alkali metals (K) the procedure took place in an Ar-filled glove bag. Batches of several grams were prepared and heated at ~ 750 °C for several hours to ensure homogenization. Quenching took place in water. Infrared spectra were recorded at nearly normal incidence in the $70-500\text{cm}^{-1}$ spectral region, at room temperature, with a Bruker 113V FTIR spectrometer. The reflection coefficient shown in Fig. 1 for different K_2S compositions was determined by typical sample-in-sample-out method with a gold mirror as the reference. The absorption coefficient spectra (Fig. 2) were calculated from reflectance by Kramers-Kronig analysis, using the expression $\alpha(\omega)=2\pi\cdot\omega\cdot\epsilon_2(\omega)/n(\omega)$, where $\epsilon_2(\omega)$ is the imaginary part of the complex dielectric function, $\epsilon=\epsilon_1+i\epsilon_2$ and $n(\omega)$ the real part of the refractive index.

Results-Discussion

Figure 1 presents the infrared reflectivity spectra of $(K_2S)_x(Sb_2S_3)_{100-x}$ glasses and Fig. 2 the respective optical conductivity spectra. The insets of Figs. 1 and 2 show the reflectivity and absorption coefficient spectra of the Sb_2S_3 crystal. It is obvious that the alkali free composition yields mainly a polycrystalline structure as can be seen by the narrow band shapes of the reflectivity and the absorption coefficient spectra, in contradiction with the broad features spectra of the alkali doped samples, characteristic of a glassy structure. Two distinct broad peaks in the spectral regions $70-190\text{cm}^{-1}$ and $200-350\text{cm}^{-1}$ are resolved for the three compositions containing alkali metal. As x increases the first broad region becomes stronger, while at the composition $x=30$ an extra broad peak in the high frequency region, at $\sim 400\text{cm}^{-1}$, appears.

Dispersion analysis in terms of a three-parameter model was applied for all the composition range. In particular for the stoichiometric composition, the obtained frequencies coincide with the observed ones for the natural mineral of stibnite with C_{3v} symmetry, originating from the stretching vibrations of the longer Sb-S distances' bonds at ~ 240 and 270cm^{-1} and from the stretching vibrations of the shorter Sb-S distances at $\sim 330\text{cm}^{-1}$. The bands below 200cm^{-1} can be assigned to the S-Sb-S bending vibrations [5].

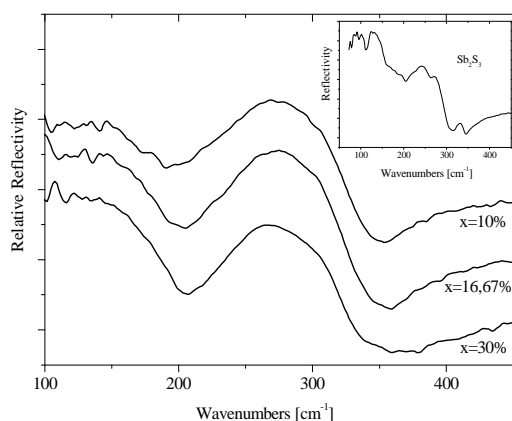


Figure 1: Infrared reflection spectra of $(K_2S)_x(Sb_2S_3)_{100-x}$. For clarity the spectra are shifted vertically against each other

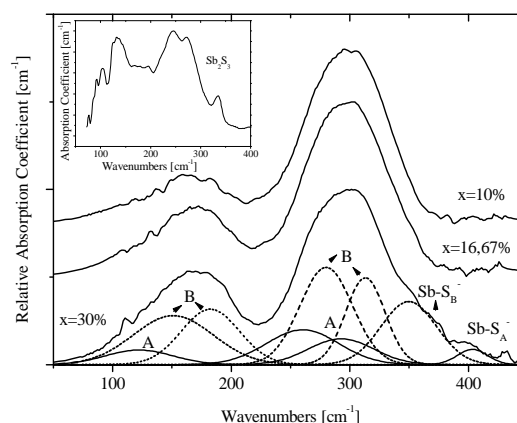


Figure 2: Absorption coefficient spectra of $(K_2S)_x(Sb_2S_3)_{100-x}$. Spectra have been off-set to facilitate comparison.

The introduction of 10% K_2S gives rise to a broad strong feature peaked at 280cm^{-1} in the high frequency region and a second broad band centered at 160cm^{-1} . The vibrational properties of glassy Sb_2S_3 in the infrared region are attributed to two intramolecular vibrations of $SbS_{3/2}$ pyramids and two intermolecular vibrations of Sb-S-Sb bridges. The strongest ir band attributed to the antisymmetric stretching mode $\nu_3(E)$ of the C_{3v} symmetry, occurs in the range $\sim 270\text{-}290\text{cm}^{-1}$ and the symmetric stretching $\nu_1(E)$ in the range $\sim 300\text{-}335\text{cm}^{-1}$. The $\nu_2(E)$ and $\nu_1(E)$ bending vibrations of the pyramids are situated in the region $\sim 120\text{-}180\text{cm}^{-1}$ [6, 7]. For the high frequency envelop the fit with the use of two oscillators was poor and it was further improved with the use of four oscillators at frequencies $268, 288, 307$ and 327cm^{-1} . Among them the 268 and 288cm^{-1} vibrations were stronger. For the lower frequency region three oscillators at $119, 160$ and 180cm^{-1} were resolved. This fact probably indicates that alkali introduction causes a two phase glassy structure with two $SbS_{3/2}$ pyramidal networks with different Sb-S distances giving rise to two different antisymmetric-symmetric doublets at $268\text{-}307\text{cm}^{-1}$ and $288\text{-}327\text{cm}^{-1}$.

The $x=16.67\%$ K_2S is the stoichiometric KSb_5S_8 compound which is a potential phase-change material with rapid and reversible glass-to-crystal transition [4]. In the crystalline form it consists of SbS_n coordination polyhedra. The oscillator fit yielded two stretching vibrations at frequencies 272 and 302cm^{-1} , which can be attributed to the antisymmetric and symmetric vibrations of $SbS_{3/2}$ pyramids, with bending vibrations centered at 120 and 165cm^{-1} .

The two phases found for the $x=10\%$ K_2S are retained in the $x=30\%$ K_2S composition and are indicated as phase A and phase B in the deconvoluted absorption coefficient spectrum of Fig. 2. The spectral features associated with phase B are more intense relative to those for $x=10\%$. For $x=30\%$ there is one NBS per pyramid and the proposed structure is $[Sb_3S_6]^-$, i.e. a pyramidal network with two bridging sulfurs per pyramid, for each phase. Therefore, the bands centered at 350cm^{-1} and 400cm^{-1} can be assigned to $Sb-S^-$ terminal vibrations. The bending vibrations were found to coincide in frequency with the respective ones of the $x=10\%$ composition and probably assigned to bending vibrations of pyramids with one NBS.

References

- [1] Bayliss P. and Nowacki W., Z. Kristallogr. 135, 308 (1972)
- [2] Cervinka L. and Hruba A., J. Non-Cryst. Solids 48, 231 (1982)
- [3] Shastry M. C., Couzi M., Lévassieur A. and Menetrier M., Philos. Mag. B, 68, 551 (1993)
- [4] Kyrtasi Th., Chrissafis K., Parskevopoulos K.M. and Kanatzidis M.G., Adv. Mater., 15, 1428 (2003)
- [5] Minceva-Sukurova B., Jovanofski G., Makreski P., Soptrajanov B., Griffith W., Willis R., Grzeetic I., J. of Mol. Struct. 651-653, 181 (2003)
- [6] Kato M., Onari S. and Arai T., Jpn. J. Appl. Phys., 22, 1382 (1983)
- [7] Kamitsos E. I., Kapoutsis J. A., Culeac I. P. and Iovu M.S., J. Phys. Chem. B, 101, 11061 (1997)

Acknowledgment We acknowledge financial support from GSRT (Ministry of Development) in the framework of the program PENED 2003 (03EΔ887). The Hellenic Telecommunications Organization (OTE S.A.) is also thanked for support.

On the Measurement of the Instability Thresholds of Nematic Liquid Crystal

E. Ramou¹, P. K. Karahaliou², H. M. Zenginoglou^{1*}, P. L. Papadopoulos¹, J. A. Kosmopoulos¹, N. T. Tsiberis¹

¹ *Department of Physics, University of Patras, Patras 265004, Greece*

² *Department of Materials Science, University of Patras, Patras 26504, Greece*

**harzeng@physics.upatras.gr*

When an AC electric field in the acoustic frequency range is applied perpendicularly to a nematic liquid crystal layer, with a thickness of the order of 10 μ m to 100 μ m, a reorientation of the director of the nematic layer is observed. This is the case of the one dimensional Fredericksz instability as well as of the, two or three, dimensional electrohydrodynamic instability [1, 2]. Due to the birefringence of any nematic material, the onset of the instability in both cases causes a monochromatic light beam illuminating the nematic layer to change its intensity and/or its phase resulting in spectacular optical effects.

On the other hand the instabilities are observed when the applied AC voltage is larger than a threshold value, the determination of which is of major importance for the potential electro-optical applications of nematic liquid crystals. As a rule, the instability threshold is determined by observing its optical effect on the incident of the monochromatic light beam: When the applied voltage is lower than or equal to its threshold value the optical effect is zero. Upon further increasing of the applied voltage the optical result increases gradually [3]. The measurement of the threshold voltage based on the above experimental behavior leads to a subjective estimation of the experimental result: One has to decide which optical result has to be considered to mark the onset of the instability.

In what follows we present a completely objective method for the experimental determination of the instability threshold based on the dependence of the decay time τ of the director field on the value of the electric field applied across the nematic layer: When the applied voltage tends to its threshold value the decay rate $1/\tau$ of the director field tends to zero. Thus, plotting $1/\tau$ as a function of the applied voltage enables us to graphically determine the threshold value of the latter [4].

[1] Collings P. J., Hird M., Introduction to Liquid Crystals: Chemistry and Physics, Taylor and Francis, London UK (1997).

[2] Rigopoulos R. A., Zenginoglou H. M., Mol. Cryst. Liq. Cryst. 35, 307 (1976).

[3] Zenginoglou H. M., Kosmopoulos J. A., Applied Optics 27, 3898 (1988).

[4] Papadopoulos P. L., Zenginoglou H. M., Kosmopoulos J. A., Tsiberis N. T., J. Nanostructured Polymers and Nanocomposites 2, 96 (2006).

Interaction Between Hetrostructural Interfaces and Structural Faults in GaN / $\text{Al}_x\text{Ga}_{1-x}\text{N}$ on Al_2O_3 Thin Films

E.M. Pechlivani*, Ch. B. Lioutas, N.Z. Vouroutzis

Solid State Physics Section, Department of Physics, Aristotle University of Thessaloniki, GR-54124 Thessaloniki, Greece

*epechl@physics.auth.gr

GaN, AlN, and their ternary alloy $\text{Al}_x\text{Ga}_{1-x}\text{N}$, have emerged as the leading materials for a variety of applications due to their high electron saturation velocity, high critical field, high thermal and mechanical stability, and good thermal conductivity. $\text{Al}_x\text{Ga}_{1-x}\text{N}$ layers were grown using metal-organic vapor phase epitaxy (MOVPE) on top of low temperature buffer layers of AlN or GaN with a thickness of 10 or 25 nm (Table 1).

Electron Diffraction, Conventional and High Resolution Transmission Electron Microscopy (HRTEM) were used for the structural study of the films. A typical electron diffraction patterns is shown in Fig. 1 It is clear the epitaxial growth of the films. In all cases the [0001] Al_2O_3 substrate direction is parallel to the [0001] $\text{Al}_x\text{Ga}_{1-x}\text{N}$ and [11 $\bar{2}$ 0] Al_2O_3 to the [1000] $\text{Al}_x\text{Ga}_{1-x}\text{N}$.

The striking of the GaN or $\text{Al}_x\text{Ga}_{1-x}\text{N}$ spots along the [0001] direction in ED patterns taken close to the substrate suggests the existence of large number of planar defects parallel the hexagonal plane of the films. That is clearly proved from HRTEM micrographs. Fig.2 and 3 reveal that the structure of the buffer layer is highly disordered and retains the perfect crystal structure only in small areas extended in few nanometres. From the same micrographs it was possible to estimate the buffer layer thickness^[2] given in Table-1.

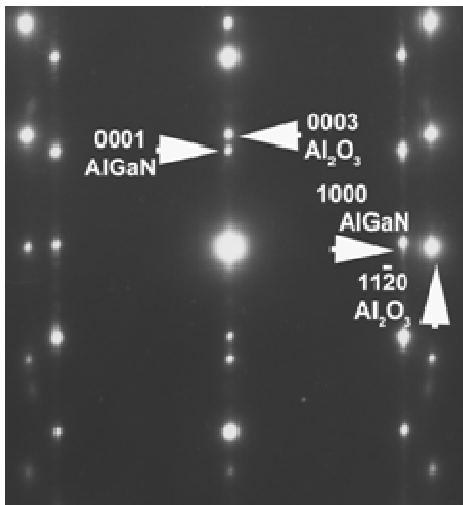


Fig. 1 Electron diffraction pattern from the specimen X 633($\text{Al}_{0.15}\text{Ga}_{0.85}\text{N}$). It is typical for all the films showing the perfect epitaxial growth of the films.

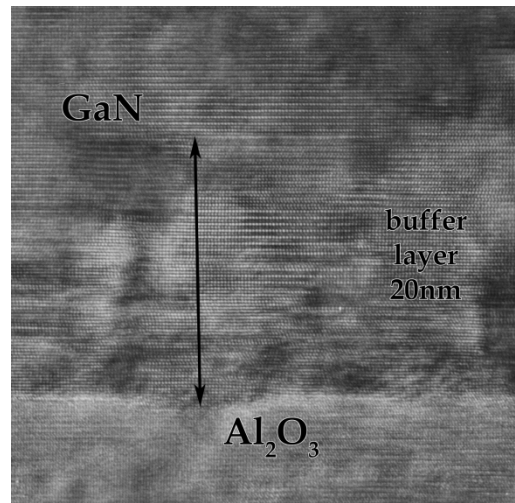


Fig. 2 HRTEM micrograph from X631 specimen. It is obvious the highly disordered region of the buffer layer mainly presenting areas separated by planes perpendicular to the hexagonal c GaN axis.

The Inversion domain Boundary density is also measured from CTEM high magnification images (Table 1). It is clear that is not strongly affected from the Al-Ga content and the epitaxial growth of films with different stoichiometry would not have a considerable influence of IDB density.

Table 1

Sample	Buffer Layer	Thickness [nm]	AlGa _x N Film	Thickness [μm]	IDB density 10 ⁶ m ⁻¹
X 631	GaN	20	GaN	1.65	21.25
X 633	AlN	7.6	$\text{Al}_{0.15}\text{Ga}_{0.85}\text{N}$	1.25	35.48
X 635	AlN	13.2	$\text{Al}_{0.23}\text{Ga}_{0.77}\text{N}$	1.35	28.57
X 636	AlN	10.7	$\text{Al}_{0.30}\text{Ga}_{0.70}\text{N}$	1.37	40.11
X 638	AlN	10.5	$\text{Al}_{0.15}\text{Ga}_{0.85}\text{N}$	1.32	28.67

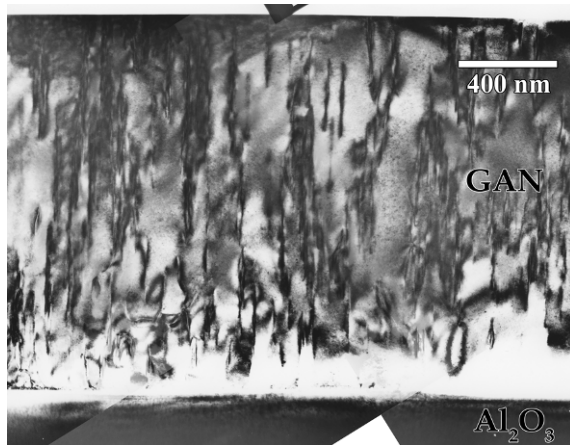


Fig. 3 CTEM high magnification image from the specimen X 631 (GaN).

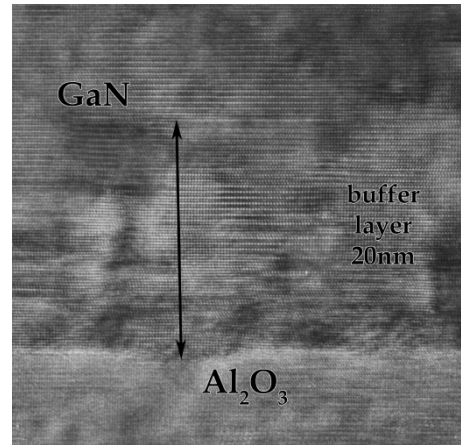


Fig. 4 HRTEM micrograph from X631 specimen. It is obvious the highly disordered region of the buffer layer mainly presenting areas separated by planes perpendicular to the hexagonal *c* GaN axis.

Fig. 5 shows the typical contrast observed in the area of a planar fault. The contrast alternation on successive dot arrays suggests that the observed defects are IDBs extended along the $[00.1]$ $\text{Al}_x\text{Ga}_{1-x}\text{N}$ hexagonal direction. A great number of these plains are originated on the interface between the buffer layer and the main film (Fig. 6) and run across the film (Fig. 3).

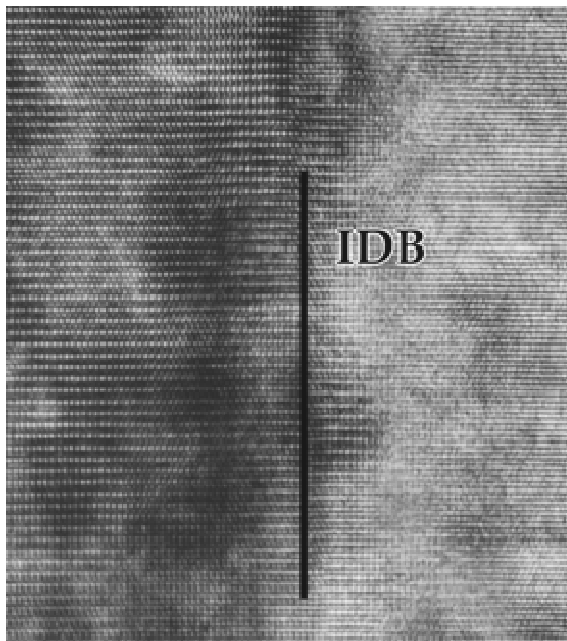


Fig. 5 HRTEM image from the specimen X635 ($\text{Al}_{0.23}\text{Ga}_{0.77}\text{N}$). The contrast alternation on successive dot arrays suggests the position of an IDB along $[00.1]$ direction.

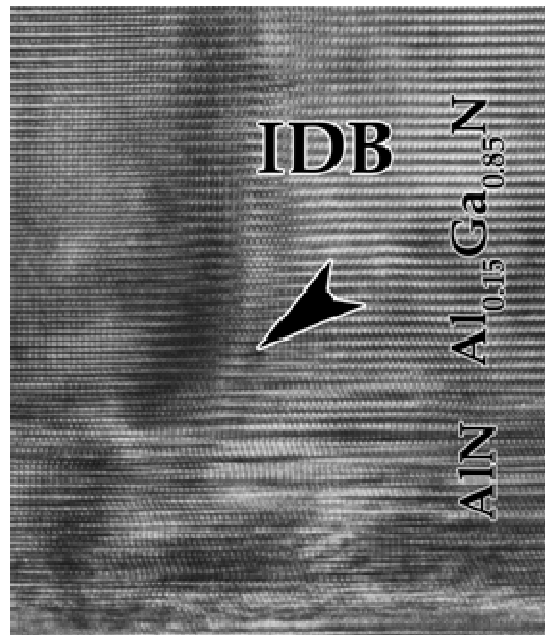


Fig. 6 HRTEM micrograph from X638 specimen. The arrow indicates the starting point of an IDB growth on the buffer layer, main film interface.

[1] M. Laugt, E. Bellet- Amalric, P. Ruterana, F. Omnes. *Phy.Stat.sol.b*.236.NO.3,729-739(2003).
 [2] Akasaki I, Amano H, 1994 *J. Electrochem. Soc.*141,2266-71.

Mechanisms of Indium Segregation in MOVPE and MBE Grown InAlN Epilayers

Th. Kehagias^{1*}, S.-L. Sahonta^{1,2}, G. P. Dimitrakopoulos¹, J. Kioseoglou¹, H. Kirmse³, W. Neumann³, C. Giesen⁴, M. Heuken⁴, A. Adikimenakis⁵, A. Georgakilas⁵, Th. Karakostas¹, and Ph. Komninou¹

¹ Department of Physics, Aristotle University of Thessaloniki, GR-54124 Thessaloniki, Greece

² Department of Materials Science and Metallurgy, University of Cambridge, Pembroke Street, Cambridge, CB2 3QZ, United Kingdom

³ Institute of Physics, Humboldt University of Berlin, Newtonstrasse 15, D-12489 Berlin, Germany

⁴ AIXTRON AG, D-52134 Herzogenrath, Germany

⁵ Microelectronics Research Group, Department of Physics, University of Crete, PO Box 2208, GR-71003 Heraklion, and IESL, FORTH, PO Box 1385, GR-71110 Heraklion, Crete, Greece

*kehagias@auth.gr

Indium incorporation mechanisms in $\text{In}_x\text{Al}_{1-x}\text{N}$ epilayers are studied and compared for the metalorganic vapor phase epitaxy (MOVPE) and molecular beam epitaxy (MBE) growth processes, employing atomic-scale transmission electron microscopy (TEM) techniques. Such alloys can be grown to be lattice-matched to GaN and AlN templates, leading to important benefits regarding defect reduction, while maintaining a large band-gap difference at the heteroepitaxial interfaces [1]. However, due to the poor miscibility between indium and aluminum, it is vital to elucidate different behaviors of indium regarding diffusion, segregation and clustering.

$\text{In}_x\text{Al}_{1-x}\text{N}$ epilayers were deposited by MOVPE and MBE on GaN/Al₂O₃ (0001) templates. The MOCVD growth experiments have been performed in a horizontal flow AIXTRON reactor with standard precursors and process gases. An initial low-temperature AlN nucleation and subsequent AlN deposited at 1250 °C is followed by 1.5 μm of Si-doped GaN grown at 1070 °C under H₂ ambient. The structure was continued by a 100 nm thick InAlN layer grown at 70 mbar under N₂ ambient. For the InAlN layer, the growth temperature was ramped down to an optimized surface temperature of ~790 °C. In MBE growth, the epilayers were grown using a RIBER 32P MBE system equipped with an OAR HD25 nitrogen RF plasma source. Growth was carried out between 610 °C and 620 °C, with the III/V flux ratio > 1 and varying In/Al flux ratios to control In incorporation.

In the compressively strained MOVPE grown film, V-shaped defects with a density of $7.5 \times 10^9 \text{ cm}^{-2}$ were observed. They consisted of hexagonal inverted pyramids, with six $\{10\bar{1}1\}$ sidewall facets, emerging on the (0001) surface (Figure 1). Conversely, MBE grown films exhibited columnar domains of 10-15 nm in diameter with increasing In content towards domain edges (Figure 2). The following physical understanding was developed to explain both phenomena.

In MOVPE growth, In induced changes in the surface energetics and built-in strain in the film enable the formation of inverted hexagonal pyramids having $\{10\bar{1}1\}$ sidewall facets at the termination of threading defects on the (0001) surface [2,3]. Indium seems to reduce the surface energy of $\{10\bar{1}1\}$ planes relative to (0001), promoting a V-defect with $\{10\bar{1}1\}$ sidewalls opening up from a threading dislocation. Z-contrast images and energy dispersive X-ray (EDX) analysis of V-defects showed an accumulation of In along the traces of the $\{10\bar{1}1\}$ sidewalls, the edges between the sidewalls and the surface, as well as the apex of the pyramid (Figures 3 and 4). These In-rich specific sites inside and around V-defects suggest preferential segregation of indium driven by the tendency the In adatoms to occupy low-coordinated III-sites [4]. Hence, indium incorporation is influenced by the formation of V-defects acting as In migration paths during diffusion of the In atoms along nanopipes, formed at the open-core threading dislocations.

In MBE growth, the $\text{In}_x\text{Al}_{1-x}\text{N}$ film growth initiates with the formation of dynamical platelets on the GaN (0001) surface, similarly to the growth of AlN on GaN [5]. These incorporate In according to the changing surface kinetics during growth, and owing to the generation of tensile strain between platelets at coalescence. At the early stages of growth, the continuous adsorption and evaporation of In atoms from the film growth surface results in dynamical $\text{In}_x\text{Al}_{1-x}\text{N}$ platelets being Al-rich. The rapid accumulation of a metallic In adlayer on the growing film improves adatom diffusion and stabilizes the incorporation of In atoms. At the onset of platelet coalescence, the relative relaxation at platelet edges, combined with momentary tensile strain generation between adjacent coalescing platelets [6], results in the preferential incorporation of In atoms at platelet boundaries. Indium incorporation at these boundaries sets up a concentration gradient, which is maintained throughout the film growth.

[1] R. Butté *et al.*, J. Phys. D: Appl. Phys. 40, 6328 (2007).

[2] J. E. Northrup, J. Neugebauer, Phys. Rev. B 60, R8473 (1999).

- [3] A. Cremades, V. Navarro, J. Piqueras, A. P. Lima, O. Ambacher, and M. Stutzmann, *J. Appl. Phys.* 90, 4868 (2001).
 [4] J. E. Northrup, L. T. Romano, J. Neugebauer, *Appl. Phys. Lett.* 74, 2319 (1999).
 [5] A. Bourret, C. Adelmann, B. Daudin, J.-L. Rouvière, G. Feuillet, and G. Mula, *Phys. Rev. B* 63, 245307 (2001).
 [6] W. D. Nix, *J. Mater. Res.* 14, 3467 (1999).

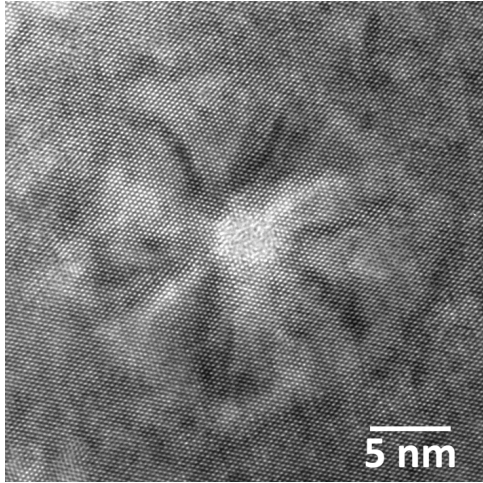


Figure 1. Plan-view high-resolution TEM image depicting a V-defect in MOVPE grown $\text{In}_{0.24}\text{Al}_{0.76}\text{N}$, consisting of a V-shaped inverted pyramid with $\{10\bar{1}1\}$ sidewall facets and apex the termination point of an open-core threading dislocation on the (0001) surface.

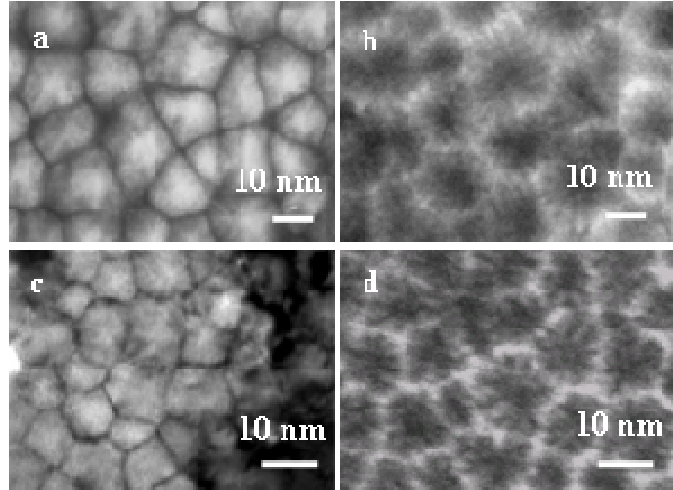


Figure 2. (a), (c) Plan-view TEM images of a compressively-strained and a nearly lattice matched MBE grown $\text{In}_x\text{Al}_{1-x}\text{N}$ films, showing columnar domains with an average diameter of 10-15 nm. Dark contrast suggests high In-content at domain edges. (b), (d) Corresponding Z-contrast images of (a) and (c) films, displaying heavy In atoms localized at domain edges with brighter contrast.

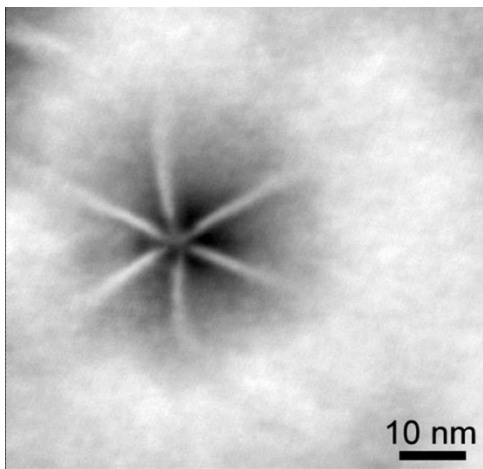


Figure 3. Z-contrast scanning TEM (STEM) image revealing high In concentration along the traces between the $\{10\bar{1}1\}$ sidewalls, the apex of the pyramid as well as the traces of the $(10\bar{1}1)$ planes with the (0001) surface. Away from the edges, the $\{10\bar{1}1\}$ facets exhibit a darker contrast.

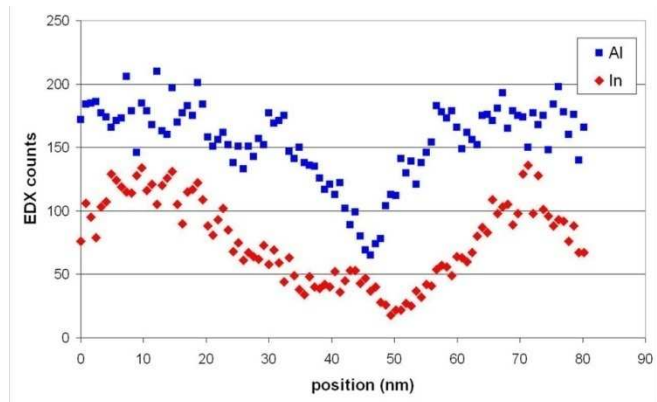


Figure 4. EDX line scan, illustrating the In and Al signals across a V-defect. Increased In concentration regions and consequently, reduced Al, are detected at positions around 10 nm and 70 nm, which correspond to the surrounding area of the traces between the $\{10\bar{1}1\}$ sidewalls of the pyramid and the (0001) surface, whereas the position of 45 nm to its apex.

Acknowledgement: Support under the EC FP6 MRTN-CT-2004-005583 project “PARSEM” and IST-FET project “UltraGaN”, Contract No. 006903 is greatly acknowledged.

Evaluation of the Optical Properties, Stoichiometry and Composition of SiO_x Films on PET by Ellipsometry

M. Gioti* and S. Logothetidis

Aristotle University of Thessaloniki, Department of Physics, GR-54124 Thessaloniki, Greece

**mgiot@physics.auth.gr*

The moisture and oxygen penetration through the organic opto-electronic devices controls their lifetime stability and consequently their use reliability. Thus, hermetic encapsulation of the devices is mandatory. Similarly, long term preservation of food, pharmaceutical and electronic products requires packaging with high diffusion-barrier performance materials. The use of inorganic oxide coatings on polymers as packaging materials has attracted a considerable interest due to their flexibility and cost-effective roll-to-roll production.

These coatings are especially interesting in the case that the barrier component has to be transparent. A barrier film fulfilling all the aforementioned demand is SiO_x [1,2]. It can be fabricated by a number of techniques, including Electron Beam Evaporation (EBE); an easily applicable method in industrial scale. The SiO_x films' thickness, stoichiometry and quality are the key parameters for the achievement of the final functional properties of the systems. The SiO_x films' quality is mainly determined by the coating defects, pinholes, grain boundaries and microcracks [3-5]. However, a very important role plays the film's composition and stoichiometry, which are strongly related to the applied deposition conditions. The methodology for the correlation of the optical properties, namely refractive index and Penn gap (the energy where the strong electronic absorption in amorphous materials takes place) with the SiO_x films' composition and stoichiometry is presented and evaluated.

The deposition of the SiO_x thin films carried out in an ultra high vacuum (UHV) deposition chamber, having a base pressure of about 10⁻⁹ Torr, and by applying the EBE technique. The working pressure was about 10⁻⁶ Torr, whereas the accelerating voltage and the beam current were close to 7 kV and 100 mA, respectively. The deposited SiO_x thin films exhibit an x varying between x=1 and x=2, covering all the range of different SiO_x stoichiometries. All the SiO_x coatings were grown onto flexible polymeric substrates of poly(ethylene terephthalate) (PET) with having a thickness of 12 μm [6,7].

The spectroscopic measurements and the real-time monitoring of the optical properties of the growing SiO_x thin films were realized using an Ellipsometer having a monochromator and an ultra-fast Multi-Wavelength (MWE) unit covering the energy range from Vis to far UV (1.5 – 6.5 eV). The ellipsometer is adapted on the UHV chamber with an angle of 70°. The MWE unit is equipped with a 32-fiber-optic array detector for the simultaneous measurements of the 32 different wavelengths. The integration time (IT), which is the time for the completion of one MWE spectrum, can be as low as 100 ms. Thus, the corresponding sampling time (ST), which is the total required time for the recording of one MWE spectrum, should be larger than 100 ms depending on the applied monitoring recipe and the number of spectra that are predefined to be collected per deposition run.

The SiO₂ exhibits transparency in the Vis-UV energy range having a fundamental optical band gap $\omega_g = 5.5$ eV., and its strong electronic absorption occurs at $\omega_0 \sim 12$ eV. The SiO is a more absorbing material with an $\omega_g = 3$ eV and $\omega_0 \sim 5.5$ eV. These differences in the electronic absorption between the two aforementioned materials are reflected to their dielectric function $\epsilon(\omega)$. However, in the case of thin films the measured quantity is the pseudodielectric function $\langle\epsilon(\omega)\rangle$ which carries information for the film thickness and the $\epsilon(\omega)$ of the substrate in addition to $\epsilon(\omega)$ of the film. Taking into account all the above ones expects that the $\langle\epsilon(\omega)\rangle$ of a SiO_x film, measured within the energy range 1.5 - 6.5 eV, will be dominated by multiple reflections for stoichiometries $x \rightarrow 2$, whereas strong electronic absorption will take place for stoichiometries $x \rightarrow 1$.

The optical parameter ω_g is an important one if we take into account that for the implementation of the SiO_x films as transparent barrier films onto polymeric substrates, the films should exhibit an optical transparency in the visible range. The latter can be testified by the ω_g values, since ω_g represents the photon energy where the electronic absorption of a material initiates. Thus, for ω_g values larger than 3.25 eV, which is the upper energy limit of the visible range, the required optical transparency has been achieved. On the other hand, ω_0 is directly correlated to the SiO_x film stoichiometry, which is one of the basic intermediate properties, and to the final barrier properties (such as oxygen permeation), which is the final functional property [2]. As it is demonstrated in the following, the changes in the ω_0 are correlated to alterations in the stoichiometry of the deposited SiO_x coating, which also presents variations during the deposition process. This means that the characteristics and the quality of the growing film can be easily controlled in real-time with the proper readjustments of the applied deposition conditions. We have to note here that ω_g values depend not only on the film's stoichiometry but also on the film's composition and microstructure. As a result of this, we can not easily deduce a clear correlation between this optical parameter and the SiO_x films' stoichiometry.

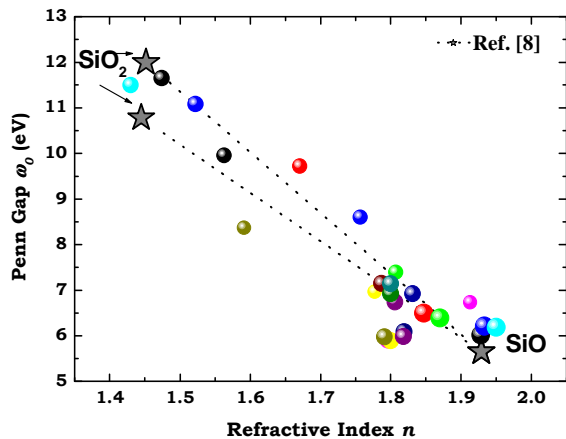


Figure 1. The correlation of ω_0 with the n calculated from spectroscopic ellipsometry data analysis for the SiO_x coatings produced with various evaporation source materials.

In Fig. 1 have been plotted comparatively these parameters corresponding to reference materials together with those derived through by the fitting analyses of the $\langle \varepsilon(\omega) \rangle$ experimental spectra for a number of SiO_x film/PET samples. If we take a linear-like dependence of ω_0 and n to the stoichiometry x , then all the intermediate stoichiometries $1 < x < 2$, are expected to lie close to the line that connect the reference stoichiometric materials. Indeed, from Fig. 1 we deduce more or less this expected relationship. The small deviations from the “rule” that are obtained can be justified by the SiO_x films’ composition. More specifically, ω_0 seems to be the more dependent optical parameter on stoichiometry comparing to n . This is because the energy position of the electronic absorption in an amorphous material is not diversified by the percentage of microvoids inclusions, which are prospective due to the amorphous microstructure. On the contrary, n exhibits a strong dependence on the microvoids inclusions, that is the larger the microvoids percentage the lower n values. In addition, inclusions of Si nanoclusters can cause significant increase in the n values, whereas the ω_0 values can be unaffected. The aforementioned conclusions are summarized in Fig. 2, where the final correlation of the optical parameters ω_0 and n with the SiO_x films’ stoichiometry and composition is presented.

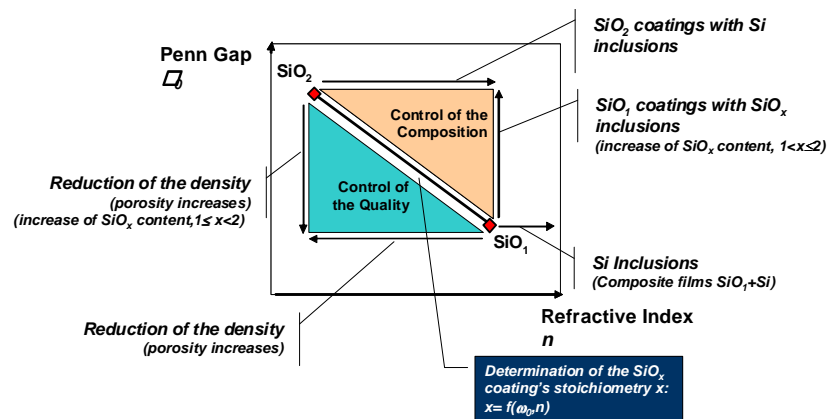


Figure 2. The correlation of ω_0 and n with the SiO_x films’ stoichiometry and composition.

- [1] H. Chatham, Surf. Coat. Technol. 78, 1 (1996).
- [2] M. Gioti, S. Logothetidis, J. Schroeder and G. Steiniger, Thin Solid Films in press (2009).
- [3] A. Grüniger, Ph. Rudolf von Rohr, Thin Solid Films 459, 308 (2004).
- [4] K. Mueller, H. Weisser, Packag. Technol. Sci. 15, 29 (2004).
- [5] G. Rossi, M. Nulman, J. Appl. Phys. 74, 5471 (1993).
- [6] S. Logothetidis, M. Gioti, and Ch. Gravalidis, Synth. Met. 138, 369 (2003).
- [7] M. Gioti, A. Laskarakis and S. Logothetidis, Thin Solid Films 455-456, 283 (2004).
- [8] E.D. Palik, “Handbook of Optical Constants of Solids”, edited by E.D. Palik (Academic Press, New- York NY, 1985).

Effect of Thickness on the Optical Properties of CuPc and C60 Thin Films for Organic Photovoltaic Applications

D. Georgiou¹, A. Laskarakis^{*1}, S. Logothetidis¹, C. Gravalidis¹, N. Meyer², M. Heuken², M. Rusu³, M. Ch. Lux-Steiner³, S. Wiesner³ and K. Fostiropoulos³

¹ Aristotle University of Thessaloniki, Department of Physics, Laboratory for Thin Films – Nanosystems and Nanometrology, GR-54124, Thessaloniki, Greece

² AIXTRON AG, Kaiserstr. 98, 52124 Herzogenrath, Germany

³ Institute Heterogeneous Material Systems, Helmholtz-Zentrum Berlin, Glienicker Str. 100, 14109 Berlin, Germany

*alask@physics.auth.gr

The development of organic photovoltaic cells (OPVs) onto flexible polymeric substrates is one of the most rapidly growing sectors and it is considered to improve our way of living. Among their unique advantages are the flexibility, low weight, low cost and potentiality for upscaling to roll-to-roll large-area production.[1,2] The use of small-molecular-weight organic layers has resulted in the fabrication of OPVs with efficiencies that reach up to 5% [3]. In order to increase the OPV efficiency, it is required to obtain a high degree of layer morphology and mixing of multiple materials and layer thickness. The accurate control of these parameters during the deposition process will also lead to the achievement of enhanced OPV performance.[3] Among the most important materials to be used for organic photovoltaics are the metal phthalocyanines, such as copper phthalocyanine (CuPc), and the fullerene (C₆₀).[4-6] These materials can be fabricated easily and are compatible with any flexible substrates and therefore can play an important role in the fabrication of low-cost OPVs [4-6]. The recently developed Organic Vapour Phase Deposition (OVPD[®]) process [4,7] is well suited for thin film deposition of such materials on large-area substrates. The principle of OVPD[®] combined with the close-coupled showerhead enables the efficient and reproducible deposition on large substrate sizes [4,7]. The precise control of nitrogen carrier gas by standard mass-flow controllers, the steady-state process temperature, and the process pressure are key parameters for industrial mass production.

In this work, we investigate the optical properties of CuPc and C₆₀ thin films that have been deposited by OVPD[®] process onto c-Si substrates, by the use of SE in the Vis-fUV spectral region. This detailed study will reveal the dependence of the optical response with the experimental parameters of the OVPD[®] process, such as the source flow (Q_{source}) during the thin film deposition. Also, the results can be also used as optical information for the study of CuPc:C₆₀ blends to be used as active materials in solar cells.

The CuPc and C₆₀ thin films have been deposited by the OVPD[®] process at Helmholtz Zentrum, Berlin, Germany. The organic materials are sublimed from specially designed source containers at temperatures between 200 and 500°C and then transported by a nitrogen gas stream to the cooled substrate. The gas-phase transport allows all organic sources to be decoupled from the deposition chamber. This design guarantees no cross contamination of the source material. Compared to other deposition technologies such as vacuum thermal evaporation (VTE), the OVPD[®] offers essential advantages such as high material yield, uniform deposition on large scale, well-defined doping with multiple dopants and low costs [4]. Both CuPc and the C₆₀ layers were deposited by maintaining a total gas flow (Q_{total}) of 1050 sccm. The values of the N₂ carrier gas source flux (Q_{source}) were varied between 50 and 500 sccm. The deposition time was in the range of 2160-3980 s. The CuPc and C₆₀ films were deposited onto 8 inch c-Si (100)-oriented wafers. The thickness of the C₆₀ sample with the lowest (highest) value of Q_{source} has been measured to be 30.7 (125.3) nm. On the other hand, the thickness values of the CuPc thin films are ranging from 30 nm (Q_{source}=50 sccm) to 130 nm (Q_{source}=500 sccm).

The optical properties of the C₆₀ and CuPc thin films have been investigated by SE covering the Vis-fUV (0.7-6.5 eV) spectral region.[8-10] The analysis of the measured $\langle \epsilon(\omega) \rangle$ spectra has revealed that the fundamental energy gap of the C₆₀ films is $\omega_g=1.95$ eV. Also, the existence of four individual electronic transitions has been found at energies $\omega_{01}\approx 2.5$ eV ($h_u \rightarrow t_{1g}$), $\omega_{02}\approx 3.5$ eV ($h_g+g_g \rightarrow t_{1u}$), $\omega_{03}\approx 4.4$ eV ($h_u \rightarrow h_g$), and $\omega_{04}\approx 5.6$ eV ($h_g+g_g \rightarrow t_{2u}$) in accordance with other published results.[6] As it has been found, the value of the energy gap of OVPD[®] deposited films is found to be lower than the reported values of C₆₀ thin films deposited by thermal evaporation, which are in the range between 2.02 eV (vacuum deposited films) and 2.24 eV (Ar deposited films).[6]

Concerning the CuPc films, from the analysis of the $\langle \epsilon(\omega) \rangle$ spectra, some distinct absorption bands have been found. These are at 1.71 eV, 2.12 eV and 3.59 eV. The first two are the know Q bands and the third is the B (or Soret) band, and they have been assigned to $\pi \rightarrow \pi^*$ transitions of the macrocyclic p-system consisting of C and aza-N atoms.[5] The results obtained here are in reasonably good agreement with previously reported

results.[5] The absorption bands in the region of 4.5 to 5.7 eV are due to $d \rightarrow \pi^*$ transitions. Similar behavior of the absorption spectra has been obtained by some workers for metal-derivative phthalocyanines [12].

These results indicate the potentiality of the OVPD[®] technique for the preparation of organic thin films for application in OPV applications and moreover, the results can be also used as optical information for the study of CuPC:C₆₀ blends to be used as active materials in OPVs.

- [1] Logothetidis S., Laskarakis A., European Physical Journal-Applied Physics 46 1 12502 (2009).
- [2] Siringhaus H., Tessler N., Friend R.H., Science 280, 1741 (1998).
- [3] Yang F., Shtein M., Forrest SR. J. Appl Phys. 98, 014906 (2005).
- [4] Rusu M., Wiesner S., Mete T., Blei H., Meyer N., Heuken M., et al., Renewable Energy 33 254 (2008).
- [5] Gordan O.D., Friedrich M., Zahn D.R.T., Organic Electron-ics 5, 291 (2004).
- [6] Zhang H., Ding Y., Zhong S., Wu C., Ning X., He Y., Liang Y., Hong J., Thin Solid Films 492, 41 (2005).
- [7] Heuken M., Meyer N. in: Organic electronics, Edited by H. Klauk, (Weinheim, Germany, Wiley, VCH).
- [8] Laskarakis A., Logothetidis S., J. Appl. Phys., 99, 066101, (2006).
- [9] R.M.A. Azzam, N.M. Bashara, Ellipsometry and Polarized Light, (North Holland, Amsterdam, 1977).
- [10] Irene G.E., Tompkins H.G., Handbook of Ellipsometry, William Andrew Publishing, Norwich, NY, 2005.
- [11] Jellison Jr. G.E., Modine F.A., Appl. Phys. Lett. 69, 371 (1996).
- [12] Bortchagovsky E.G., Kazantseva Z.I., Koshets I.A., Nespurek S., Jastrabik L., Thin Solid Films 460, 269 (2004).

Effect of Thickness in the Optical Properties of Organic Thin Films Deposited via Organic Vapor Phase Deposition

A. Laskarakis^{*1}, D. Georgiou¹, S. Logothetidis¹, C. Gravalidis¹, N. Meyer², D. Keiper², M. Heuken², M. Bösing³, F. Lindla³, H. Kalisch³ and R. H. Jansen³

¹ Aristotle University of Thessaloniki, Department of Physics, Laboratory for Thin Films – Nanosystems and Nanometrology, GR-54124, Thessaloniki, Greece

² AIXTRON AG, Kaiserstr. 98, 52124 Herzogenrath, Germany

³ Institute of Electromagnetic Theory, RWTH Aachen University, 52074 Aachen, Germany

*alask@physics.auth.gr

Organic semiconductors and their heterostructures have attracted considerable attention due to their application in organic light emitting devices (OLEDs) which are expected to play a significant role in various lighting and flat-panel displays applications. [1-4] These materials exhibit high brightness and low cost and large area fabrication onto flexible and rigid substrates.[5] One of the premier organic materials which used as light-emitting and electron transporter layer in OLED is the tris(8-hydroxyquinoline) aluminium (Alq3), which presenting excellent photoluminescent and electroluminescent properties. Another popular organic material which used in OLED as hole transport layer is the N,N'-di-1-naphthyl-N,N'-diphenyl-1,1'-biphenyl-4,4'-diamine (α -NPD). [3,6-10] However, OLEDs show relatively poor stability and improving the lifetime of these devices remains an important challenge. The optical response of single and multilayered structures can provide valuable information about the preparation quality, thickness and optical properties of materials (refractive index, absorption coefficient). In this way the deposition parameters of the fabrication process can be optimized and so that the final product has an improved quality. [1,4,11,12]

In this work, we investigate the optical properties of Alq3 and α -NPD layers deposited onto Si substrate by organic vapor phase deposition (OVPD[®]) process in various values of gas flows and deposition times. The optical properties were measured in an extended spectral region in the near IR-visible–far ultraviolet (NIR-Vis–fUV) spectral region in order to determine the effect of deposition conditions in the materials' optical response..

Single layers of Alq3 and α -NPD materials were deposited by the OVPD[®] process on Si and glass substrates by using various values of gas flows (Q_{source}) and deposition times. The OVPD[®] system offers the possibility to deposit large area single and multi-layers or to dope layers in a single deposition chamber. The organic materials are sublimed from specially designed source containers at temperatures between 200 and 400°C and then transported by a nitrogen gas stream to the cooled substrate. The Alq3 and α -NPD container temperatures were 288.6 °C and 270.9 °C, respectively. The Alq3 and α -NPD films were deposited onto 8 inch c-Si (100)-oriented wafers and onto glass substrates. Spectroscopic Ellipsometry (SE) covering an extended spectral region in the Visible-far UltraViolet (Vis-fUV) has been employed for the investigation of the optical properties of the Alq3 and α -NPD thin films. The NIR-Vis-fUV SE measurements were performed by a Phase Modulated Spectroscopic Ellipsometer covering the energy range 0.7-6.5 eV.

The Alq3 and α -NPD films were found to be transparent in the spectral range of 0.7–2.5 eV. In order to analyze the measured $\langle \varepsilon(\omega) \rangle$ of the Alq3 and α -NPD materials, we have considered a three layer model that consists of the ambient (air) (medium 1), the Alq3 (or α -NPD) thin film with a thickness d (medium 2) and the bulk substrate (medium 3), which can be either c-Si or glass. The optical response of medium 1 and 3 have been kept constant, whereas the optical response of the Alq3 films have been modelled by the Tauc–Lorentz (TL) oscillator model.[13] The thickness values that were determined by SE are in perfect agreement with the thickness values of the Alq3 and α -NPD samples that were measured by stylus profilometry. This support the validity of the performed analysis of the $\langle \varepsilon(\omega) \rangle$. Also, the analysis of the measured $\langle \varepsilon(\omega) \rangle$ spectra has revealed that the fundamental energy gap of the Alq3 films has the value of $\omega_g=2.7$ eV. Also, the existence of four individual electronic transitions has been found at energies $\omega_{01}\approx 3.0$ eV, $\omega_{02}\approx 4.6$ eV, and $\omega_{03}\approx 6.2$ eV in accordance with other published results.[1,2,10] Moreover, the optical response of the Alq3 films (energy position) has been found to be independent of thin film thickness..

Concerning the NPD films, from the analysis of the $\langle \varepsilon(\omega) \rangle$ spectra, some distinct absorption bands have been found. The band gap (fundamental gap) of the α -NPD films has been calculated at ~ 2.7 eV for the thinner samples, whereas for the thicker samples it increases slightly to 2.8 eV. Also, the electronic transition energies in which the maximum absorption ω_0 takes place have been found at values of $\omega_{01}\approx 3.41$ eV, $\omega_{02}\approx 5.36$ eV, $\omega_{03}\approx 5.72$ eV, and $\omega_{04}\approx 6.71$ eV in accordance with other published results.[10, 11]

The information from the determination of the optical constants of Alq3 and α -NPD films, which have been distinguished in a wide spectral region, provide the tool for the determination of the volume fraction, as well as

the doping level in the case that one material is doped with the other. Also it can contribute to the determination of the individual thicknesses in multilayer films formed using the OVPD[®] technique by alternating Alq₃ and α -NPD layers for flexible organic electronic applications, such as for OLEDs.

- [1] Gordan O. D., Hermann S., Friedrich M., and Zahn D. R. T., *phys. stat. sol. (b)* 242, 2688 (2005).
- [2] Himcinski C., Hartmann S., Janssen A., Meyer N., Friedrich M., Kowalsky W., Zahn D.R.T., and Heuken M., *J. Cryst. Growth* 275, e1035 (2005).
- [3] Djurišić A.B., Kwong C.Y., Lau T., Li E.H., Liu Z., Kwok H.S., Lam L. and Chan W.K., *Appl. Phys. A*76, 219 (2003).
- [4] Choy W.C.H. and Fong H. H., *J. Phys. D: Appl. Phys.* 41, 155109 (2008).
- [5] Cheung C.H., Djurišić A.B., Kwong C.Y., Chan J., Rakić A.D., Tam H.L., Cheah K.W., Liu Z.T., Chan W.K. and Chui P.C., *Thin Solid Films* 489, 235 (2005).
- [6] Masenelli B., Callard S., Gagnaire A. and Joseph J., *Thin Solid Films* 364, 264 (2000).
- [7] Kumar P., Misra A., Bhardwaj R., Kamalasanan M.N., Jain S.C., Chand S. and Tandon R.P., *Displays* 29, 351 (2008).
- [8] Kumar S., Shukla V. K. and Tripathi A., *Thin Solid Films* 477, 240 (2005).
- [9] Kim S.S. Y., Ryu S. Y., Choi J. M., Kang S. J., Park S. P., Im S., Whang C. N. and Choi D. S., *Thin Solid Films* 398-399, 78 (2001).
- [10] Hermann S., Gordan O. D., Friedrich M., and Zahn D. R. T., *phys. stat. sol. (c)* 2, 4037 (2005).
- [11] Himcinski C., Meyer N., Hartmann S., Gersdorff M., Friedrich M., Johannes H.-H., Kowalsky W., Schwambera M., Strauch G., Heuken M. and Zahn D.R.T., *Appl. Phys. A*80, 551 (2005).
- [12] Djurisić A. B., Kwong C. Y., Guo W. L., Lau T. W., Li E. H., Liu Z. T., Kwok H. S., Lam L. S. M., Chan W. K., *Thin Solid Films* 416, 233 (2002).
- [13] Jellison Jr. G.E., Modine F.A., *Appl. Phys. Lett.* 69, 371 (1996).

Theoretical calculations to determine the electro-gyration coefficients in $\bar{3}m$ point group of CaCO_3

A.T. Efremidis, N.C. Deliolanis, C. Manolikas, S. Ves, E.D. Vanidhis*

Department of Physics, Aristotle University of Thessalonik, Greece

* vanidhis@auth.gr

Abstract – Introduction

CaCO_3 crystals belong in the $\bar{3}m$ point group, they are not enantiomorphous and have natural birefringence (n_{01} , n_{03}). They do not exhibit optical activity, electro-optic, and piezoelectric effects, but they exhibit the electro-gyration effect described with two independent coefficients (ζ_{11} , ζ_{41}) [1]. In this report, we describe an analytical light propagation model and an experimental method to evaluate the electrogyration coefficients.

Theoretical analysis

The step-by-step modeling and analysis of light propagation in the $\bar{3}m$ group includes:

1) calculating the general impermeability tensor [3×3 Hermitian], of $\bar{3}m$ group, in the crystallographic coordinate system x_1, x_2, x_3 , after taking into account all the natural and induced effects [1][2].

2) searching for convenient directions of phase propagation (\mathbf{k}) and application of external electric field (\mathbf{E}), where the impermeability tensor's cross section with the wave-front plane, normal to \mathbf{k} [2×2 matrix] is a relatively simple function of coefficient(s). To do so, the x_3 axis is rotated to become parallel to \mathbf{k} . At this plane lie the electric displacement vectors $\mathbf{D}_1, \mathbf{D}_2$ which are orthogonal to \mathbf{k} [3].

3) diagonalizing the 2×2 symmetric (Hermitian, in general) impermeability tensor, by a similarity transformation, the resulting eigenvectors are the Jones eigenstates of polarization of $\mathbf{D}_1, \mathbf{D}_2$. They represent the only two waves that propagate with unchanged polarization in the given direction. The refractive indices n_1 and n_2 for the eigenpolarizations are [$n_1 = 1/\sqrt{\lambda_1}$, $n_2 = 1/\sqrt{\lambda_2}$], where [λ_1, λ_2] are the corresponding eigenvalues [4].

4) “propagating” a known polarization state of light through the crystal and after passing through a linear polarizer, we derive the light intensity as a function of the polarizer angle θ_a and the coefficient(s) [ζ_{11}, ζ_{41}] to be estimated.

Data analysis and results

The unknown electrogyration coefficients can be estimated by fitting the experimentally measured light intensities, for successive values of θ_a (θ_a varying from 0° to 360° by step 1°), with the theoretically calculated intensity using the Levenberg-Marquardt fitting method [5].

From the theoretical calculations of $\bar{3}m$ point group, we find that two simple configurations of crystal cuts (direction of propagation) and directions of externally applied electric field, reveal in 2×2 impermeability tensor the two electro-gyration coefficients ζ_{11} , and ζ_{41} .

In the first configuration, the light propagates along $[110]$ and the electric field is applied to the $[1\bar{1}0]$ direction. After the calculations, the 2×2 impermeability tensor is given by Eq. (1), the eigenvalues [λ_1, λ_2] at that direction by Eq. (2), the eigenvectors by Eq. (3), and the intensity of the light when it propagates consecutively through an input linear polarizer oriented at 45° to x_1 , the crystal, and an analyzer at θ_a angle, by Eq. (4).

$$B_{2\text{cut}[110]} = \begin{pmatrix} \frac{1}{n_{03}^2} & \frac{iE_o\zeta_{11}}{\sqrt{2n_{01}^2n_{03}^2}} \\ -\frac{iE_o\zeta_{11}}{\sqrt{2n_{01}^2n_{03}^2}} & \frac{1}{n_{01}^2} \end{pmatrix} \quad (1)$$

$$\lambda_1 = \frac{n_{01}^2 \cos^2 \Phi + n_{03}^2 \sin^2 \Phi + \sqrt{2}E_o\zeta_{11} \cos \Phi \sin \Phi}{n_{01}^2 n_{03}^2} \quad (2.1)$$

$$\lambda_2 = \frac{n_{01}^2 + n_{03}^2 + (-n_{01}^2 + n_{03}^2) \cos(2\Phi) - \sqrt{2}E_o\zeta_{11} \sin(2\Phi)}{2n_{01}^2 n_{03}^2} \quad (2.2)$$

$$D_1 = \begin{pmatrix} \cos \Phi \\ -i \sin \Phi \end{pmatrix}, \quad D_2 = \begin{pmatrix} -i \sin \Phi \\ \cos \Phi \end{pmatrix} \quad (3)$$

$$I = \frac{1}{2} \left[1 + \cos(\phi_1 - \phi_2) \sin(2\theta_\alpha) + \sin(\phi_1 - \phi_2) \sin(2\Phi) \cos(2\theta_\alpha) \right] \quad (4)$$

$$\text{where } \Phi = \frac{1}{2} \arctan \left(\frac{\sqrt{2} E_o \zeta_{01}}{n_{01}^2 - n_{03}^2} \right), \quad \phi_{1,2} = \frac{2\pi L}{\lambda} n_{1,2},$$

λ is the wavelength, and L is the length of light propagation path through the crystal.

In the second configuration, the light propagates along [011] and the electric field is applied to the [100] direction. The 2×2 impermeability tensor is given by Eq. (5), the eigenvalues $[\lambda_1, \lambda_2]$ at that direction by Eq. (6), the eigenvectors by Eq. (7), and the intensity of the light when it propagates consecutively through an input linear polarizer oriented at 45° to x_1 , the crystal, and an analyzer at θ_a angle, by Eq. (8).

$$B_{2\text{cut}[011]} = \begin{pmatrix} \frac{1}{2} \left(\frac{1}{n_{01}^2} + \frac{1}{n_{03}^2} \right) & -\frac{iE_o (n_{01}^2 + n_{03}^2) (\zeta_{11} - 2\zeta_{41})}{4n_{01}^4 n_{03}^4} \\ \frac{iE_o (n_{01}^2 + n_{03}^2) (\zeta_{11} - 2\zeta_{41})}{4n_{01}^4 n_{03}^2} & \frac{1}{n_{01}^2} \end{pmatrix} \quad (5)$$

$$\lambda_{1,2} = \frac{n_{01}^2 (n_{01}^2 + 3n_{03}^2) \pm (n_{01}^2 - n_{03}^2) \cos(2\Phi) \mp E_o (n_{01}^2 + n_{03}^2) (\zeta_{11} - 2\zeta_{41}) \sin(2\Phi)}{4n_{01}^4 n_{03}^2} \quad (6)$$

$$D_1 = \begin{pmatrix} \cos \Phi \\ -i \sin \Phi \end{pmatrix}, \quad D_2 = \begin{pmatrix} -i \sin \Phi \\ \cos \Phi \end{pmatrix} \quad (7)$$

$$I = \frac{1}{2} \left[1 + \cos(\phi_1 - \phi_2) \sin(2\theta_\alpha) + \sin(\phi_1 - \phi_2) \sin(2\Phi) \cos(2\theta_\alpha) \right] \quad (8)$$

$$\text{where } \Phi = \frac{1}{2} \arctan \left[\frac{E_o (n_{01}^2 + n_{03}^2) \text{abs}(\zeta_{11} - 2\zeta_{41})}{n_{01}^2 (n_{01}^2 - n_{03}^2)} \right], \quad \phi_{1,2} = \frac{2\pi L}{\lambda} n_{1,2},$$

λ is the wavelength, and L is the length of propagation through the crystal.

- [1] Y. I. Sirotni, M. P. Shaskolskaya 'Fundamentals of crystal Physics, (Mir, Moscow, 1982).
- [2] A. Yariv and P. Yeb, 'Optical waves in crystals' (Wiley, New York, 1984).
- [3] J. F. Nye, 'Physical Properties of crystals' (Oxford University Press, Oxford, 1957).
- [4] T. A. Maldonado, T. K. Gaylord 'Accurate method to determine the eigenstates of polarization in gyrotropic media' Applied Optics **28**, 275, (1989).
- [5] A.T. Efremidis, N.C. Deliolanis, C. Manolikas, E.D. Vanidhis 'Dispersion of electro-optic coefficients in Sillenite crystals', Applied Physics B **95**, 467, (2009).

Morphological and Structural Characterization of Polar and Semipolar GaN Quantum Dots in AlN

E. Kalesaki¹, Th. Kehagias¹, J. Kioseoglou¹, A. Lotsari¹, L. Lahourcade², E. Monroy²,
G. P. Dimitrakopoulos¹ and Ph. Komninou^{1*}

¹ Department of Physics, Aristotle University, GR 54124 Thessaloniki, Greece

² CEA-CNRS Group "NanoPhysique et SemiConducteurs," INAC/SP2M/NPSC, CEA-Grenoble, 17 rue des Martyrs, 38054 Grenoble, Cedex 9, France

*komnhnoy@auth.gr

During the last few years group III-nitride heterostructures have attracted considerable interest due to their potential applicability in high efficiency optoelectronic devices. Carrier separation due to polarization-induced electrostatic fields and the quantum-confined Stark effect (QCSE) are the two major obstacles in achieving high efficiency devices. Efforts to overcome these problems are currently focused on growth of ultra-small polar quantum dots (QDs), with an average size that does not exceed 5 nm, or growth along non- and semi-polar orientations. In the case of non-polar growth, the strong anisotropy of the surface properties leads to epitaxial layers with a high density of crystalline defects. The promising results of the alternative approach, i.e. semi-polar growth of III-N heterostructures, can be further improved by combining semipolar orientations with quantum dot nanostructures. The morphology and strain state of the QDs significantly affect their behaviour regarding carrier confinement. Thus a thorough study of the QDs morphological and structural characteristics is essential.

High Resolution Electron Microscopy (HRTEM) and Scanning Transmission Electron Microscopy (STEM) experiments were conducted in order to determine the morphology of ultra-small polar GaN QDs grown on (0001)AlN/(0001)Al₂O₃ and semipolar (11 $\bar{2}2$)- and (10 $\bar{1}1$)- oriented GaN QDs (Fig. 2) grown on (11 $\bar{2}2$)AlN/(1 $\bar{1}00$)Al₂O₃ by plasma-assisted molecular-beam epitaxy (PAMBE), following a modified Stranski-Krastanow growth mode [1]. The corresponding three-dimensional structural models, consistent with the experimental observations, were constructed, and the reduced relative variation of the interplanar spacing along the QD growth directions was determined using geometrical phase analysis (GPA) [2].

Growth of ultra-small polar QDs was achieved by PAMBE under N-rich conditions, at a growth temperature of 750°C. The average height of the dots was 7-8 ML, while the thickness of the wetting layer was approximately 3-4 ML. The thickness of the AlN spacers ranged from approximately 7 nm between the wetting layers to approximately 5 nm between the QDs. Single QDs were then imaged by HRTEM (Fig. 1) in ultra-thin specimens and were found to exhibit morphology consistent with the projection of truncated hexagonal pyramids. The side-facets of the QDs were inclined from 30° up to 45° relative to the basal plane, and hence their possible crystallographic planes are {1 $\bar{1}02$ } and {1 $\bar{1}03$ }. The crystallographically well-defined QD morphology shows that they are appropriate for carrier confinement purposes.

In the case of semipolar QDs, the dominant morphology was that of truncated trigonal or tetragonal pyramids. The side facets of the (11 $\bar{2}2$)-oriented QDs were inclined from 26° to 28° relative to the (11 $\bar{2}2$) plane. In addition, due to the (1 $\bar{1}00$) mirror symmetry, two crystallographically equivalent QD interfaces may be formed on either side of this plane. The side facets of the (10 $\bar{1}1$)-oriented QDs were inclined by 26° to 28° relative to the (10 $\bar{1}1$) plane and the third facet formed a 42° angle with the basal plane. Based on these results we conclude that semipolar QDs are bounded by (11 $\bar{2}n$) and (10 $\bar{1}p$) high index planes. These side facets may assist the reduction of the QCSE and the built-in potential since they are not polar.

In the case of ultra-small polar GaN QDs, GPA measurements of the reduced relative variation of the (0002) interplanar spacing with respect to the AlN spacers showed that it ranged between 3-4% in the QDs region. Concerning the semipolar QDs of Fig. 2 the reduced relative variation was 3.4-4% for the (11 $\bar{2}2$) lattice planes (Fig. 2(b)) and 3.3-3.8% for the (10 $\bar{1}1$) case (Fig. 2(c)). These values are in agreement with the biaxial strain formulation taking into account the accuracy of GPA. Following biaxial strain formulations [3] the strain of the GaN QDs is a function of the angle θ formed between the plane of growth and the c axis. Thus the two observed semipolar growth planes encounter unequal strain components since they form different angles with respect to the c axis (58° for the (11 $\bar{2}2$) and 61.6° for the (10 $\bar{1}1$) planes). However, it is noted that the coexistence of hydrostatic and/or uniaxial components with the biaxial strain in the case of the QDs cannot be excluded.

Density Functional Theory (DFT) calculations of the interfacial energies of GaN pseudomorphically grown on either $(11\bar{2}2)$ or $(10\bar{1}1)$ AlN under biaxial strain were performed with the ABINIT code [4] using the Generalized Gradient Approximation (GGA), and showed that the $(11\bar{2}2)$ interface is energetically more stable (Table 1). The growth kinetics are important in influencing the appearance of the $(10\bar{1}1)$ QDs.

- [1] Lahourcade L., Valdueza-Felip S., Kehagias T., Dimitrakopoulos G. P., Komninou Ph., and Monroy E., Appl. Phys. Lett. 94, 111901 (2009).
 [2] Hytch M.J., Snoeck E., and Kilaas R., Ultramicroscopy 74, 131 (1998).
 [3] Park S. -H., Chuang S. L., Phys. Rev. B59, 4725 (1999).
 [4] <http://www.abinit.org>.

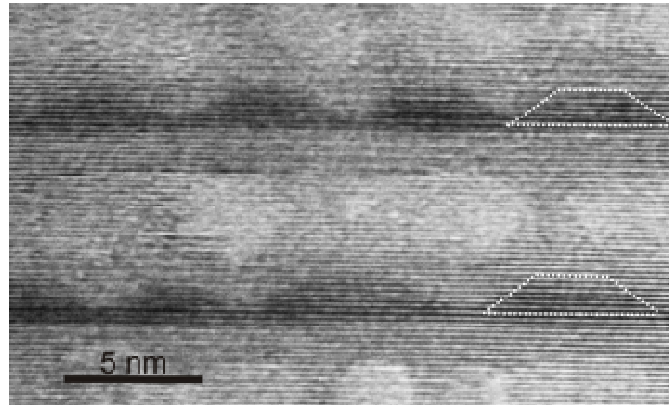


Figure 1. Cross-sectional HRTEM image, viewed along the $[11\bar{2}0]$ zone axis, illustrating two successive layers of ultra-small polar GaN/AlN QDs.

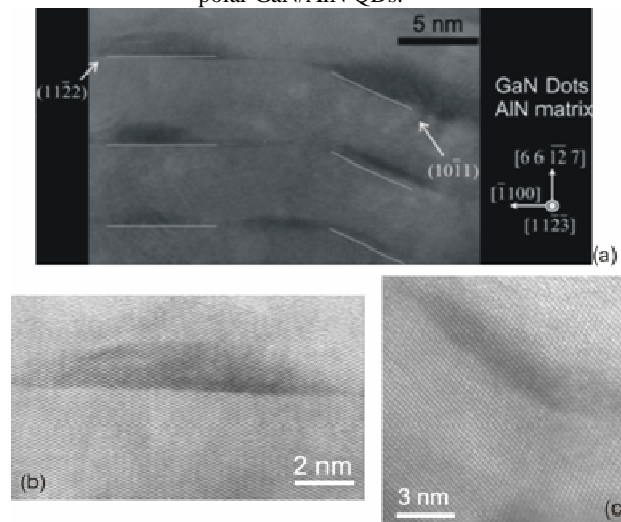


Figure 2. (a) Cross-sectional HRTEM image of GaN QDs grown on the $(11\bar{2}2)$ and $(10\bar{1}1)$ planes viewed along the $[11\bar{2}3]$ zone axis, (b) HRTEM image of a QD grown on the $(11\bar{2}2)$ plane, (c) HRTEM image of a QD grown on the $(10\bar{1}1)$ plane.

Table 1. Difference in formation energy values between the two observed semipolar growth orientations and their energetic difference to the polar growth direction.

	$\Delta E_{11\bar{2}2-10\bar{1}1}$	$\Delta E_{11\bar{2}2-0001}$	$\Delta E_{10\bar{1}1-0001}$
Energy (meV/unit cell)	-7	-18	-12

Acknowledgments

Support under the 7th European Framework Project DOTSENSE (Grant No. STREP 224212) and the MRTN-CT-2004-005583 "PARSEM" project is gratefully acknowledged.

Typical structural defects in 3C-SiC layers grown by various methods on different substrates

M. Marinova, M. Mantzari and E. K. Polychroniadis*

Physics Department, Aristotle University of Thessaloniki 54124, Thessaloniki, Greece

**polychr@auth.gr*

Silicon carbide (SiC) has excellent properties as a wideband gap semiconductor, such as high saturated electron velocity, high breakdown electric field and high thermal conductivity. The interest on this material is always high due to its valuable application, such as high-power, high-frequency, high temperature and radiation resistant electronic devices, as well as substrates for light-emitting GaN films. Among all polytypes, the cubic one (3C-SiC) attracts the scientific, as well as the industrial interest, as it has the smallest bandgap, the highest electron mobility.

However, the use of 3C-SiC for device fabrication is very limited, due to its relatively high (compared to the other polytypes) defect density. For this reason, the interest in the defect-free growth and consequently its microstructural characterization is continuously increasing. Defects that are most frequently observed are inversion domain boundaries (IDBs), coherent and incoherent twins, dislocations, the inclusions of other polytypes and mainly the stacking faults (SFs), which a consequence from the very low SF energy in 3C-SiC (-6.27 mJ/m^2 [1, 2]) as compared to Si for example.

This work presents some recent results on the 3C-SiC structural defects studied by Transmission Electron Microscopy (TEM). The first stages of growth are strongly determined by the type of the substrate, its polarity and orientation as well as the specific method of growth. The 3C-SiC layer reported in the current presentation has been grown by several methods: Sublimation Epitaxy (SE); Physical Vapour Transport (PVT); Continuous Feed Physical Vapour Transport (CF-PVT); Liquid Phase Epitaxy (LPE); Chemical Vapour Deposition (CVD). The 3C-SiC growth could be performed on Si, α -SiC or by homoepitaxy on 3C-SiC. The growth on Si leads to high defects density since the lattice mismatch in Si-SiC system is about 20% lattice.

The most common defects present in the (001) oriented 3C-SiC substrate (coming from its Si substrate) and continuing into the overlayer are the IDBs, Figure 1. These are self-annihilated by turning in {111} orientation. Generally, although the structural quality of the substrate strongly affects the microstructure of the grown layer, immediately above the interface, the final influence of the substrate defects is limited to a few tenths of microns.

For the 3C-SiC grown heteroepitaxially on hexagonal substrate or homoepitaxially on the (111) cubic orientation, the most serious defects are those created along the other {111} orientations. As these three planes are inclined to the growth direction, the generated defects (SFs, twins or hexagonal inclusions) can propagate through the whole thickness of the grown layer. Conclusively, the most persistent defects are the stacking faults, due to their very low energy. They are generated spontaneously during the growth and their density up to now was never observed to be less than the order of 10^{-3} cm^{-1} , which is still far from the structural quality needed for device applications. Here, the meaning of stacking faults is broad including all kinds of disturbances of the exact sequence of the Si-C bilayers leading to a certain polytype. For this reason, the thickness of these "stacking faults" can vary from a single bilayer to a thin lamella. One example of the formation of large polytype inclusion which is most probably due to locally enhanced SF density in 3C-SiC grown by CF-PVT is shown in Figure 2. It seems that even infinitesimal changes in the growth conditions or the lightest strain induced even by doping can produce not only a high density of stacking faults, but also multi-polytypic sequences.

[1] U. Lindefelt, H. Iwata, S. Öberg, and P. R. Briddon Phys. Rev B 67 155204 (2003).

[2] P. Käckell, J. Furthmüller, and Fr. Bechstedt, Phys. Rev B 58 1326 (1998).

Acknowledgments The work is financially supported by MANSiC project (MRTN-CT-2006-035735) financially supported from the EU with FP6 and SOLSiC European project (Contract N° G5RD-CT-2001-00563). The authors are thankful to Dr. G. Ferro from UCBL1 Lyon, Dr. D. Chaussende from INP-CNRS Grenoble and Prof. R. Yakimova from LU, Sweden.

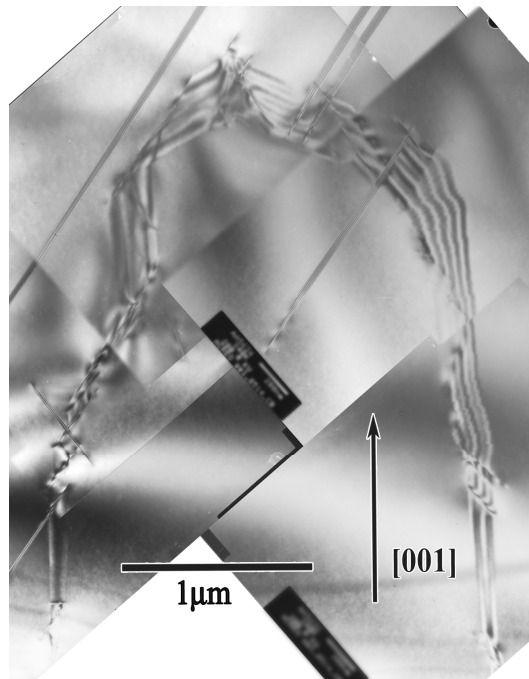


Figure 1. A TEM micrograph showing closing of the IDBs. The IDBs facet parallel to particular crystallographic planes. The physical mechanism that results in the annihilation of IDBs in 3C-SiC, is the change of the crystallographic planes in which IDBs propagate.

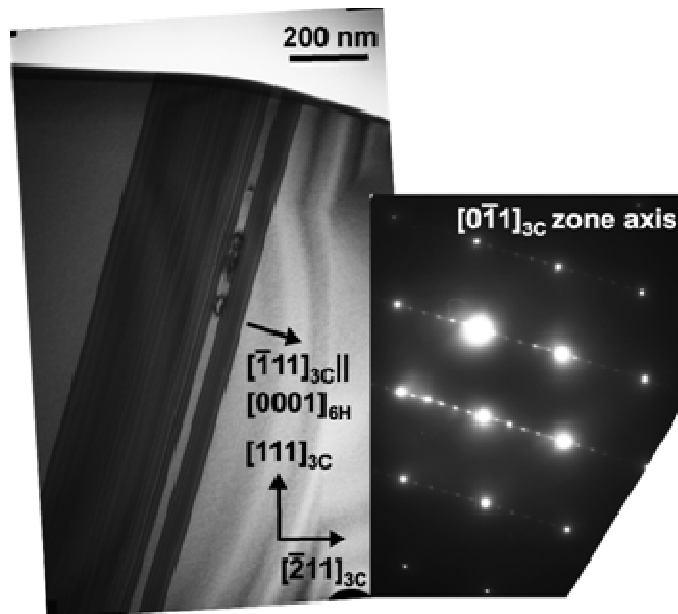


Figure 2. A TEM micrograph showing the formation of large polytype inclusion propagating along the $(\bar{1}11)$ planes. It could be argued that such inclusions are formed due to the strong local increase of SF density. Such inclusions usually propagate until the surface.

Structural and Mechanical Properties of AlN:Ag Nanocomposite Coatings grown by Pulsed Laser Deposition

A. Lotsari^{1*}, G. P. Dimitrakopoulos¹, Th. Kehagias¹, P. Kavouras², P. Patsalas³,
and Ph. Komninou¹

¹Aristotle University of Thessaloniki, Department of Physics, GR-54124 Thessaloniki, Greece

²Technological Educational Institute of Thessaloniki, Department of Applied Sciences, Sindos, Greece

³University of Ioannina, Department of Materials Science and Engineering, GR-45110 Ioannina, Greece

*alotsari@physics.auth.gr

Aluminum nitride (AlN) offers high hardness, high thermal conductivity and refractory character, making it suitable for protective coatings [1]. However, its disadvantages are its brittleness and poor adhesion on various substrates [7]. Adhesion issue can be improved by growing AlN on Al interlayers [7,8]. The incorporation of noble metal nanocrystals into AlN can be employed to enhance its plasticity since besides intrinsic structural and chemical factors, a strong contribution is expected by deformation mechanisms attributed to dislocations and/or grain boundaries. The growth of such AlN-noble metal nanocomposites has not been reported so far. In the present work a new type of AlN-based nanocomposites with Ag inclusions, grown by Pulsed Laser Deposition (PLD), is presented. We study effect of the growth conditions, such as metal content, nanoparticles size and distribution, on the nanostructure of the thin films.

Stable AlN:Ag films with 0-25% nominal Ag concentration were grown at room temperature on *n*-type Si (100) wafers using a 99.999% solid Al target in a flowing N₂ ambient. PLD growth was performed in a turbo-pumped, high vacuum system (base pressure < 1x10⁻⁷ mbar) equipped with a sectored rotating 45mm target and a rotating 50mm sample holder. Improved adhesion of AlN onto Si and avoidance of formation of an amorphous SiN_x interfacial layer was achieved by pre-deposition of a thin (2-3 nm) interlayer of metallic Al followed by exposure to pure nitrogen plasma in order to form an AlN buffer layer. The crystal structure was studied by XRD using a RIGAKU powder diffractometer. Transmission electron microscopy (TEM), both conventional and high resolution (HRTEM) were performed using a 200 kV JEOL 2011 microscope. For this purpose, specimens were prepared in cross-section (XTEM) geometry by mechanical thinning followed by Ar⁺ ion milling. The nanohardness measurements were performed using a Hysitron Tribolab Ubi-1 HT Tribolab modular system with a standard Berkovich indenter tip.

A series of AlN:Ag thin films were studied having thicknesses ranging from 25 up to 130 nm, and containing homogeneously distributed Ag nanoclusters with average sizes ranging from 3 up to 10 nm (Fig. 1(a)). XRD and selected-area electron diffraction showed that AlN was amorphous while Ag was nanocrystalline and exhibited the relaxed *fcc* structure. The size and distribution of the nanoparticles were found to depend on the growth conditions. A reduction of the laser source power was found to induce Ag nanoparticles of increased size (Fig. 1(b)). Furthermore, by increasing the Ag concentration in the PLD target, the nanocrystallite size was also increased (Fig. 2). The internal structure of the nanoparticles was studied with HRTEM. It was found that the larger nanocrystallites often exhibit multiple nanotwins on {111} planes.

The structural properties of the AlN:Ag thin films, were correlated to their mechanical performance through nanohardness measurements. Specimens comprising the same Ag concentration (25%) and having similar thickness (~50 nm) were compared. In specimens with homogenous internal structure comprising nanocrystals of average diameter ~3nm (Fig. 1(a)), the attained nanohardness was found to be 14.90 GPa ± 2.09 GPa and the load-unload curves did not show pop-in events (Fig. 3(a)). A reduced nanohardness of 11.85 GPa ± 0.94 GPa was obtained for the specimen of Fig. 1(b) due to the enhanced ductility offered by the operation of deformation mechanisms in the interfacial zone of Ag nanocrystals with diameter >5nm. The load-unload curves showed pop-in events in the loading segments (Fig. 3(b)) characteristic of crack initiation, probably at the interfacial zone containing the larger crystallites. Both samples are less hard than pure AlN grown under the same conditions and having similar thickness which exhibited an apparent nanohardness of 21±1 GPa.

Thus, by controlling the growth conditions, stable AlN:Ag nanocomposite thin films, with narrow nanoparticle size distribution and desired mechanical properties can be obtained. The apparent hardness of the films is much higher than that anticipated by the rule of mixture showing that the nanostructuring is a critical factor for their mechanical performance.

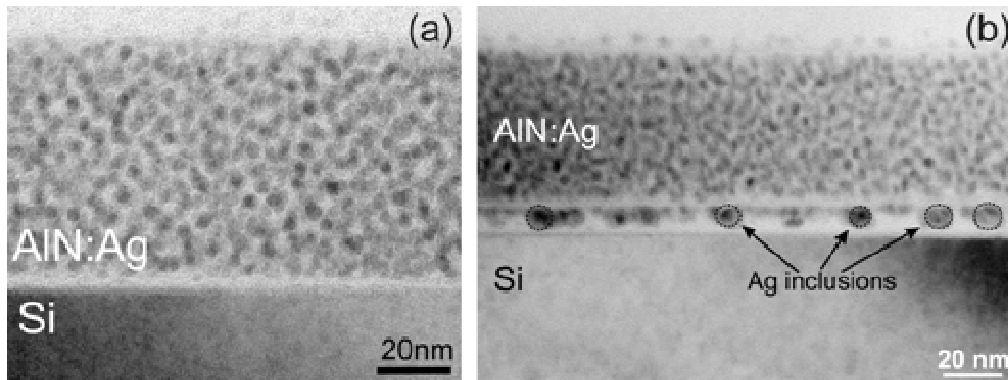


Fig. 1. (a) Cross-sectional CTEM image of a nanocomposite film with 25% Ag, exhibiting a homogeneous distribution of nanoparticles. (b) Cross-sectional CTEM image of a similar specimen comprising an interfacial zone with larger Ag inclusions induced by reducing the power of the laser source.

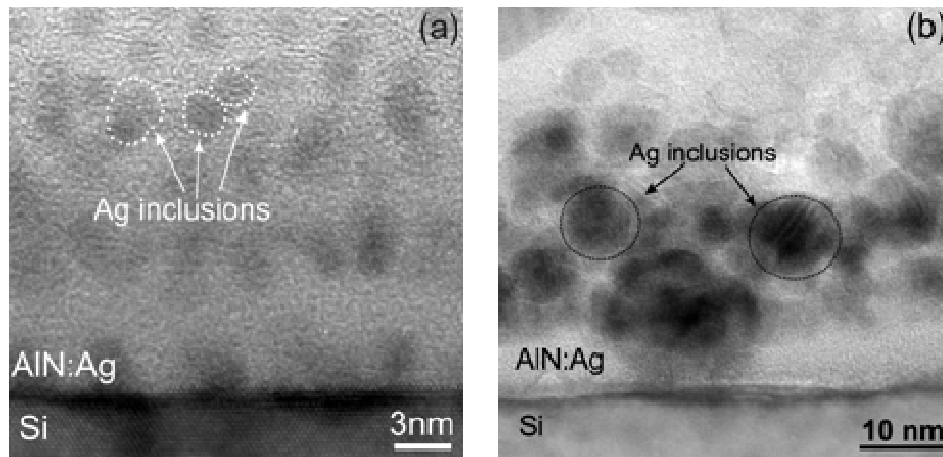


Fig. 2. Cross-sectional HRTEM images along $[011]_{\text{Si}}$ of nanocomposite films corresponding to Ag concentrations of (a) 12.5% Ag, and (b) 25% Ag. The increase of crystallite size is evident.

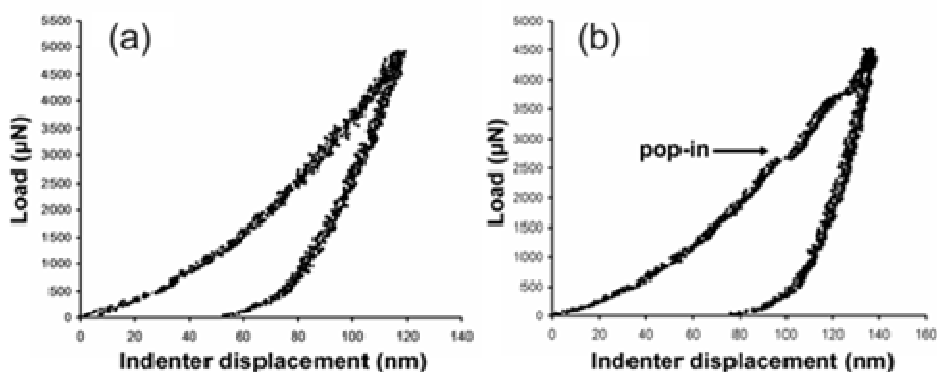


Fig. 3. Load-unload curves corresponding to the specimens of Figures 1(a) and 1(b) ((a) and (b) respectively). Both profiles are characteristic of elasto-plastic deformation, while only in (b) pop-in events are clearly visible.

- [1] S. Bakalova, A. Szekeres, A. Cziraki, C.P. Lungu, S. Grigorescu, G. Socol, E. Axente, I.N. Mihailescu, *Appl. Surf. Sci.* 253, 8215 (2007).
 [2] J.C. Oliveira, A. Cavaleiro, M.T. Vieira, *Surf. Coat. Technol.* 151–152, 466, (2002).
 [3] Z.G. Wu, G.A. Zhang, M.X. Wang, X.Y. Fan, P.X. Yan, T. Xu, *Appl. Surf. Sci.* 253, 2733 (2006).

Acknowledgements Work supported by the European Space Agency under Contract No. 21071/07/NL/PA.

Scattering of Fast Neutrons from Protons in Solids (NbH_{0.80} and LiH): New Quantum Effects in the Attosecond Timescale

C. Aris Chatzidimitriou-Dreismann^{1*}, G. Apostolopoulos², K. Mergia² and S. Messoloras²

¹*Institute of Chemistry, Sekr. C2, Technical University of Berlin, Str. d. 17. Juni 135, D-10623 Berlin, Germany*

²*Institute of Nuclear Technology and Radiation Protection, N.C.S.R. "Demokritos", 15310 Aghia Paraskevi, Athens, Greece*

*dreismann@chem.tu-berlin.de

Nuclei and electrons in condensed matter and/or molecules are usually entangled, due to the prevailing interactions. Usually, the 'environment' of a microscopic scattering system (e.g. a proton) causes an ultrafast decoherence, thus making atomic and/or nuclear entanglement effects not directly accessible to experiments. However, new neutron [1-3] (and recently also electron [2-4]) Compton scattering experiments from protons (H-atoms) in several condensed systems and molecules demonstrated a new striking effect, i.e. an 'anomalous' decrease of scattering intensity from protons, which seem to become partially 'invisible' to the probe particles. Several experiments were done at ambient conditions. Due to the large energy (several tens of eV) and momentum (20-200 Å⁻¹) transfers of these experiments is the collisional time between the probe particle and a struck proton 100–1000 attoseconds long, and the protons represent open quantum systems (OQS). This effect, which has no interpretation within conventional (van Hove) neutron scattering theory [5], is caused by the non-unitary time evolution (due to decoherence accompanying quantum dynamics of OQS) during the ultrashort, but finite, time-window of the neutron-proton scattering process.

Examples of experimental results will be shown. In particular, results from the metallic hydrides NbH_{0.80} and LiH at ambient conditions will be presented. Surprisingly, direct comparison of measured H-momentum distributions (with neutron Compton scattering, NCS) and H-projected phonon states (with inelastic neutron scattering, INS, in the 100-meV-energy range) demonstrate a strong violation of predictions of the standard theory [5a,b], which connects the local effective Born-Oppenheimer potential of the struck proton with the aforementioned measurable quantities.

A theoretical outline 'from first principles' will be presented, related with the Quantum Zeno Effect [6] of fundamental quantum mechanics. The results and their qualitative interpretation show that epithermal neutrons (being available at spallation sources, e.g. SNS/U.S.A. or ISIS/U.K.), and also electron spectrometers with large scattering angles, provide tools for investigation of new physical and chemical phenomena in the sub-femtosecond timescale.

[1] Chatzidimitriou-Dreismann C. A., et al., Phys. Rev. Lett. 79, 2839 (1997).

[2] Chatzidimitriou-Dreismann C. A., et al., Phys. Rev. Lett. 91, 057403 (2003).

[3] Physics Today, p. 9 (Sep. 2003); Discover, p. 16 (Nov. 2003).

[4] Cooper G., Hitchcock A. P., Chatzidimitriou-Dreismann C. A., Phys. Rev. Lett. 100, 043204 (2008).

[5] See e.g.: (a) Watson G. I., J. Phys. Condens. Matter 8, 5955 (1996); (b) Andreani C., et al., Adv. Phys. 54, 377 (2005).

[6] Misra B., Sudarshan E. C. G., J. Math. Phys. 18, 756 (1977).

The influence of the disorder in the Raman spectra of GaSb/AlSb (001) superlattices

D. Berdekas*

Direction of High Schools Education of Larissa, Lykeio of Giannouli, 41500 Larissa, Greece

**dberdek@in.gr*

Abstract. In the present work, we study the influence of interface disorder in the Raman spectra of $(\text{GaSb})_n/(\text{AlSb})_n$ (001) superlattices, for $n=1,2$. The disordered SLs are approximated using primitive cells several times bigger the primitive cells of the perfect SLs. We suppose that disorder appears due either to deviation from the expected sequence of the GaSb and AlSb layers which is imposed by symmetry and/or due to intermixing of Ga and Al in the corresponding cation lattice planes. The dynamical matrix of each SL is constructed from the combination of the dynamical matrices of the bulk crystalline constituents which have been calculated at certain points of the Brillouin zone within the (10) parameter Valence Overlap Shell Model formalism. We also present calculated the Raman spectra, for both perfect and non perfect (disordered) superlattices, using an eight (8) parameter Bond Polarizability Model. Our results show that the intermixing of Ga and Al cations, even to a small extent, produce Raman activity which is not present in the spectra of perfect superlattices.

MO2

P32

Probing the Electronic Structure of Molecular Magnets by Pulse EPR Methods

G. Mitrikas*, Y. Sanakis, C.P. Raptopoulou, G. Papavassiliou

Institute of Materials Science, NCSR 'Demokritos', Agia Paraskevi Attikis, 15310 Athens, Greece

*mitrikas@ims.demokritos.gr

In this work we show how pulse electron paramagnetic resonance (EPR) spectroscopy can give insight into the electronic structure of molecular magnets and probe their potential use as qubits for quantum information processing. The system under study is the trinuclear oxo-centered iron(III) complex, $[\text{Fe}_3(\mu_3\text{-O})(\text{O}_2\text{CPh})_5(\text{salox})(\text{EtOH})(\text{H}_2\text{O})]$ (salox²⁻ is the dianion of salicylaldehyde oxime) (Fig. 1(a)), where the three Fe^{III} ($S = 5/2$) sites are antiferromagnetically coupled to give an $S = 1/2$ ground state [1]. Although this complex belongs to the big family of triferric complexes with $S = 1/2$ ground states, its rare isotropic behaviour due to the lack of non Heisenberg interactions makes it an ideal subject for pulse EPR studies. On the other hand, this compound is the simplest example of spin clusters consisting of an odd number of antiferromagnetically coupled spins which, according to Loss and co-workers [2], could be relevant for quantum computing.

The temperature dependence of the spin-lattice relaxation time T_1 between 4.5 and 11 K shows that the two-level Orbach relaxation process is dominant with the first excited state lying 57 cm^{-1} above the ground state (Fig. 1(b)). The latter result gives further insight into the magnetic properties of the complex since it is directly related to the intra-particle exchange interaction constants. In addition, two-pulse electron spin echo experiments show that the dephasing times are of the order of $2.6 \mu\text{s}$ and exhibit weak temperature dependence [3]. Finally, the coherent manipulation of the electron spins is examined for the first time for molecular magnets by means of transient nutation experiments (Rabi oscillations) which are equivalent to the one-qubit NOT quantum gate (Fig. 1(c)). Our results show that the present trinuclear iron complex is a promising candidate for quantum information processing. Nevertheless, the development of more efficient pulse sequences (quantum gates) is necessary if the general family of these materials are to be used as elements of a quantum computer.

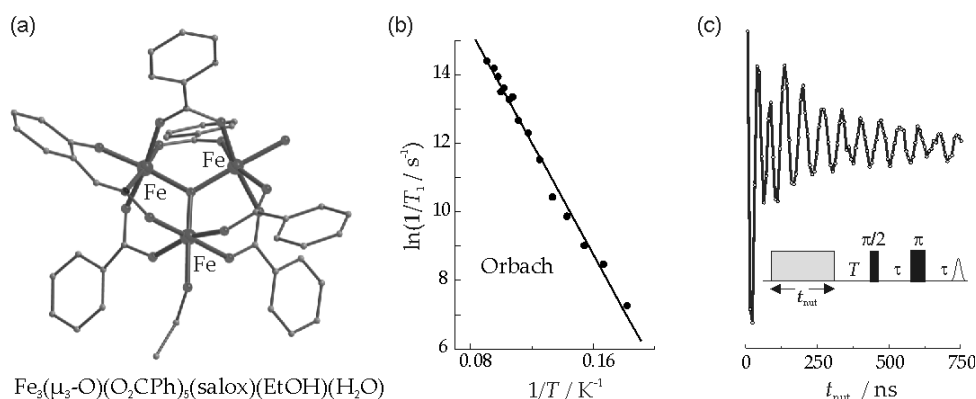


Figure 1: (a) Molecular structure of the $\text{Fe}_3(\mu_3\text{-O})(\text{O}_2\text{CPh})_5(\text{salox})(\text{EtOH})(\text{H}_2\text{O})$ complex. (b) Temperature dependence of the spin-lattice relaxation rate in Orbach representation together with the corresponding linear fit. (c) Echo-detected longitudinal magnetization after a nutation pulse as a function of its length, t_{nut} .

[1] C.P. Raptopoulou, Y. Sanakis, A.K. Boudalis and V. Psycharis, *Polyhedron*, 24, 711 (2005).

[2] F. Meier, J. Levy and D. Loss, *Phys. Rev. B*, 68, 134417 (2003).

[3] G. Mitrikas, Y. Sanakis, C.P. Raptopoulou, G. Kordas, and G. Papavassiliou, *Phys. Chem. Chem. Phys.*, 10, 743 (2008).

Dark Conductivity and Photoconductivity Behavior of Sol-Gel S-Doped TiO₂, Thermally Treated at Different Temperatures

A. Vomvas^{1*}, K. Pomoni¹, N. Todorova² and C. Trapalis²

¹Department of Physics, University of Patras, 26500 Patras, Greece

²Institute of Materials Science, National Centre for Scientific Research "Democritos" 15310, Ag. Paraskevi, Attiki, Greece

*avomvas@physics.upatras.gr

MO2

P35

Abstract

S-doped nanocrystalline titanium dioxide (TiO₂) thin films were prepared by sol-gel route and were thermally treated at five different temperatures. The dark conductivity and the transient photoconductivity of the S-doped TiO₂ sol-gel thin films were studied in vacuum and in air. The photoconductivity reaches very high values and is sensitive on the environment. The larger values in vacuum can be attributed to the reduced amount of adsorbed oxygen at the surface, which acts as electron scavenger.

Introduction

Titanium dioxide (TiO₂) is well known for its photocatalytic and photoelectrochemical properties. There are three crystalline phases existed in TiO₂: anatase, rutile and brookite, but in general, only anatase and rutile have photocatalytic activity [1]. Because of its wide bandgap of 3.0-3.2 eV, only about 4 % of the incoming solar energy on the surface can be utilized. The non-metal doping is one of the many attempts that have been made to improve its optical response under visible light excitation.

The photoconductivity measurement technique is a useful tool for the interpretation of the competition between photogeneration, recombination and trapping. In the present work, the electrical as well as the photoconductive properties of sol-gel S-doped TiO₂, thermally treated at 400, 500, 600, 800 and 1000 °C, have been studied.

Experimental details

The proper quantity of thiourea was dissolved in ethanol in a closed beaker and the solution was stirred for 40 min. Terabutyl orthotitanate (Ti[C₄H₉O]₄) was then added and the solution remained under stirring for 16 h at pH 5. Dip-coating technique was applied for the S-doped TiO₂ film deposition on quartz substrates. The obtained gel films were then thermally treated at different temperatures (400, 500, 600, 800 and 1000 °C) for 1 h.

For the electrical conductivity and photoconductivity measurements coplanar silver electrodes were vacuum deposited on the samples. A vacuum cryostat was used and the temperature was adjusted by a temperature controller. The used light source was a 100 W (white light) Xenon lamp and the full light intensity at the samples surface was adjusted to 500 W/m². The light was switched on and off every 20 min and the photocurrent response was measured by an electrometer and recorded every 10 s. For the elimination of persisting effects of previous light exposure, before any measurement, the samples were annealed at 440 K for 90 min.

Results and discussion

The dependence of the dark conductivity of the S-doped sample, heat-treated at 500 °C and 600 °C, versus inverse temperature, in vacuum, is given in Fig. 1, while the samples heat-treated at 400, 800 and 1000 °C showed no measurable currents. From Fig.1 the dark conductivity appears to be thermally activated with activation energies $E_a=0.55$ eV for the temperature of 500 °C and 0.71 eV for that of 600 °C. These values are lower than the known E_a for pure TiO₂ which varies between 0.75 and 1.18 eV, indicating that S-doping introduces new states in the energy band gap of the material. The corresponding measurements in air were also impossible to be carried out because of the very low currents in the whole temperature range.

The photoconductivity values of all the studied S-doped samples at the end of the first illumination period versus the different temperatures of thermal treatment, at 300 K, in vacuum and in air, are shown in Fig. 2. It seems that the sample heat-treated at 500 °C is the optimum choice, since it presents the higher photoconductivity value.

Fig. 3 illustrates the photoconductivity response at 300 K, in vacuum, of the sol-gel S-doped sample, heat-treated at 500 °C, since the presentation of all together the photoconductivity curves at the different temperatures is not feasible because of the difference in scales. At the end of the first illumination period it reaches the value $1.7 \Omega^{-1}m^{-1}$. It is more than nine orders of magnitude higher than its dark conductivity and it may be attributed to the high density of trapping states in the energy gap of the sample. The rise of the photoconductivity is slow. It follows the known sublinear behavior [2] and no saturation is shown after 20 min of illumination, due to the low scavenger rate in vacuum. The decay behavior after the first illumination period suggests that the thermal release

rate becomes important as time passes. After 20 min in the dark, the transient photoconductivity has not reached yet its value before illumination, since some traps remain still filled. At the subsequent illumination the photogenerated electrons are quickly excited to the conduction band, as fewer trap states have now to be filled, and the photoconductivity reaches higher values causing the observed asymmetry between the first and second rise.

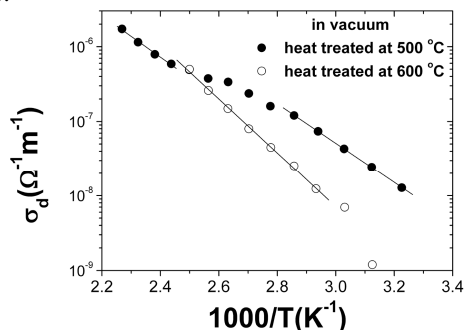


Fig.1. Temperature dependence of the dark conductivity of the S-doped sample heat treated at 500 and 600 °C.

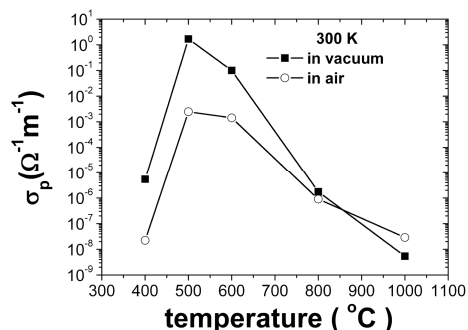


Fig.2. Photoconductivity of all the studied S-doped samples after 20 min of illumination versus thermal treatment temperature, in vacuum and in air, at 300 K

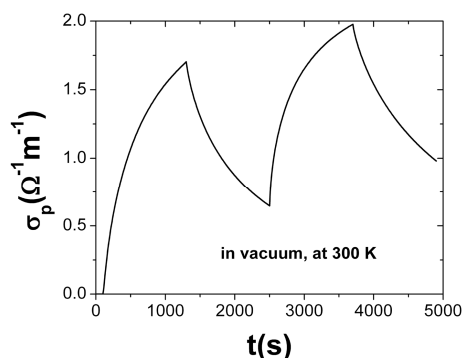


Fig.3. The photoconductivity response at 300 K, in vacuum, of the S-doped nanocrystalline sample, heat-treated at 500 °C.

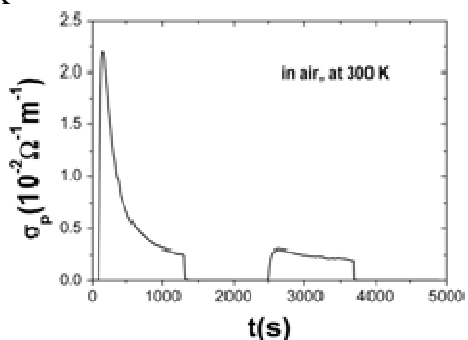


Fig.4. The photoconductivity response at 300 K, in air, of the S-doped nanocrystalline sample, heat-treated at 500 °C.

The photoconductivity of the sol-gel S-doped TiO₂ sample versus time, at 300 K, in air, is shown in Fig. 4. The difference in the behavior between vacuum and air is obvious. The initial photoconductivity rise is fast followed by a quick decrease which slows down as time passes and an abrupt fall is observed when the light is switched off. The influence of the ambient environment is determinative and suggests that recombination dominates in air [3]. The photoconductivity values are more than two orders of magnitude lower than those in vacuum and at the end of the first illumination period the photoconductivity reaches the value $2.5 \times 10^{-3} \Omega^{-1} \text{m}^{-1}$. The surface adsorbed oxygen causes a large amount of electron scavengers which in combination with the created by the S-doping recombination centers result in the photoconductivity decrease.

Conclusions

In this work we present a study of the conductivity behavior of S-doped TiO₂ sol-gel nanocrystalline thin films in dark and in light, in vacuum and in air, heat-treated at 400, 500, 600, 800 and 1000 °C. The E_a values in vacuum for the samples heat-treated at 500 and 600 °C are lower than those of pure TiO₂ because of the additional states that the S-doping introduces. The transient photoconductivity appears to be highly sensitive on environment. The recombination dominates in air, since the adsorbed oxygen molecules act as electron scavengers and new recombination centers are created by S-doping.

References

- [1] Wu Q., Li D., Hou Y., Wu L., Fu X., Wang X. Materials Chemistry and Physics 102, 53 (2007).
- [2] Eppler A.M, Ballard I.M, Nelson J., Physica, E, Low-Dimens. Syst. Nanostruct. 14, 197 (2002).
- [3] Pomoni K., Vomvas A., Trapalis C. Thin Solid Films 479, 160 (2005).

Field and Temperature Dependence of the Small Polaron Hopping Electrical Conductivity in 1D Disordered Systems

M. Dimakogianni*, G. P. Triberis, and M. Tsetseri

University of Athens, Department of Physics, Solid State Section,
Panepistimiopolis, 157 84, Zografos, Athens, Greece

*mdimak@phys.uoa.gr

MO2

P36

In recent years one-dimensional (1D) conductors such as carbon nanotubes, nanowires and conducting molecules have been placed among the most promising materials for nanotechnology. The knowledge of the nature of the carriers and the transport mechanism, responsible for the measured electrical conductivity, will enable researchers to use these materials for innovating applications and the refinement of many others.

Recently, Triberis et. al. [1, 2] investigated small polaron hopping transport in 1D disordered systems, such as DNA, at high temperatures (h), ignoring the effect of correlations. An analytical expression for the temperature dependence of the electrical conductivity, $\ln\sigma^h \sim T^{-2/3}$, was obtained. Most recently Triberis and Dimakogianni [3] showed that the inclusion of correlations (cr) leads to a $\ln\sigma^{h,cr} \sim T^{-1/2}$ law. Their results reproduced satisfactorily the experimental data reported for λ -DNA and for poly(dA)-poly(dT) DNA [4, 5, 6], considering DNA as a one-dimensional disordered molecular wire in which small polarons are the charge carriers. The maximum hopping distances evaluated support the idea of long distance charge migration in DNA.

An analytical expression predicting the electric field and temperature dependence of the DC conductivity taking into account the 1D character of the system, the presence of disorder and the polaronic character of the carriers remains to be theoretically established. This is the purpose of the present work.

The theoretical analysis is based on the Generalized Molecular Crystal Model introduced by Triberis and Friedman [7] and theoretical percolation arguments. The model's Hamiltonian is

$$\langle m|H|n \rangle = \langle m|H_0 + V|n \rangle = E_{i,\{n_k\}} \delta_{j,\{n_k\},\{n'_k\}} + \langle m|V|n \rangle,$$

where H_0 is the zeroth-order (i.e. $J=0$) Hamiltonian, and $\langle m|V|n \rangle$ is the overlap part [7].

The knowledge of the overlap part of the Hamiltonian permits the evaluation of the "microscopic" small polaron velocity operator, the charge current density operator, and thus the "microscopic" electrical conductivity.

Further calculations allow the knowledge of the mobility, the diffusion constant and consequently the "microscopic" jump rate. Based on the knowledge of the average equilibrium transition probability in the presence of an electric field the macroscopic conductivity is evaluated analytically as a function of the temperature and the electric field, applying percolation theoretical arguments.

For the high temperature small polaron hopping regime and low electric fields the conductivity is expressed as

$$\ln \sigma^h(F) \propto \ln \sigma_0^h + h(F) / f^h(T) \quad (1)$$

$$\text{where } \ln \sigma_0^h = -\left(\frac{T_0^h}{T}\right)^{2/3}, \quad f^h(T) = \left[\frac{1}{3}\left(\frac{T_0^h}{T}\right)^{2/3} \frac{1}{g(T)}\right]^{-1}, \quad h(F) = F^2 \quad \text{and} \quad T_0^h = 2.18\alpha^{1/2} N_s^{1/2} / k_B N_0.$$

For the low temperature small polaron hopping regime and low electric fields the conductivity is expressed as

$$\ln \sigma^l(F) \propto \ln \sigma_0^l + h(F) / f^l(T) \quad (2)$$

$$\text{where } \ln \sigma_0^l = -\left(\frac{T_0^l}{T}\right)^{1/2}, \quad f^l(T) = \left[\frac{1}{2}\left(\frac{T_0^l}{T}\right)^{1/2} \frac{1}{g(T)}\right]^{-1}, \quad h(F) = F^2 \quad \text{and} \quad T_0^l = 1.57\alpha / k_B N_0.$$

The analytical expressions for the electrical conductivity, obtained as a function of the electric field and the temperature, show the competitive role of the temperature-vs-electric field. At very low electric fields the hopping conductivity conforms with the ohmic law while increasing the electric field the conductivity presents non-ohmic characteristics. The transition from the ohmic to the non-ohmic behavior starts at smaller values of the electric field at lower temperatures. The rate of the increase of the conductivity is greater at lower temperatures. Our conclusions are in accordance with theoretical results which are referred to variable range hopping and related experiments reported by various workers.

[1] Triberis G. P., Simserides C. and Karavolas V. C., J. Phys. Condens. Matter 17, 2681 (2005).

[2] Triberis G. P. *The Physics of Low-Dimensional Structures, from Quantum Wells to DNA and Artificial Atoms*

(New York: Nova Science, 2007) p 94.

- [3] Triberis G. P. and Dimakogianni M., J. Phys.: Condens. Matter 21, 035114 (2009).
- [4] Tran P., Alavi B. and Gruner G., Phys. Rev. Lett. 85, 564 (2000).
- [5] Yoo K. H., Ha D. H. and Lee J., Phys. Rev. Lett. 87, 198102 (2001).
- [6] Inomata A. *et al.*, J. Phys. Soc. Japan 75, 074803 (2006).
- [7] Triberis G. P. and Friedman L. R., J. Phys. C.: Solid State Phys. 14, 4631 (1981).

Acknowledgments

This work was funded by the program KAPODISTRIAS (ELKE/National and Kapodistrian University of Athens).

Study of LiMgVO₄ Ionic Conductivity Mechanisms

C. Paraskeva², A. Kazakopoulos^{1*}, K. Chrissafis², O. Kalogirou²

¹ Department of Electronics, T.E.I. of Thessaloniki 57 400 Thessaloniki Greece

² Department of Physics, Aristotle University of Thessaloniki 54 124 Thessaloniki Greece

* kazak@el.teithe.gr

MO2

P37

Abstract

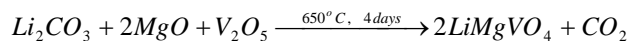
The compound LiMgVO₄ was prepared by solid state reaction at 650 °C for 4 days. Impedance spectroscopy measurements were taken on pellets of the materials at temperatures from 25 to 500 °C with 25 °C steps. The results of the measurements were used to draw equivalent circuits. Each element of these equivalent circuits was assigned to a unique conduction process within the material. In addition to the bulk and grain boundary, a protonic conductivity process was revealed at temperatures up to 175 °C. Arrhenius plots were drawn of each resistance element of the equivalent circuits and the activation energy values of the conduction mechanisms were calculated. The bulk activation energy was found to be 0.62 eV, the grain boundary activation energy was found to be 1.03 eV from 260 to 350 °C and 0.50 eV from 360 to 500 °C.

1. Introduction

LiMgVO₄ is a material widely used in electrochemical devices and in humidity sensors [1-3]. It has interesting properties related to luminescence due to the tetrahedrally coordinated V⁵⁺ atoms. The information related to the cation distribution in the LiMgVO₄ structure is still under debate. LiMgVO₄ has been assigned to the olivine Pbnm(62) space group. The purpose of this paper is to study the conduction mechanisms of LiMgVO₄ at temperatures from 25 to 500 °C, using impedance spectroscopy measurements at frequencies from 42 Hz to 1 MHz, in order to deduct useful information about the Li ion diffusion and mobility in its structure.

2. Experimental

LiMgVO₄ was prepared by high-temperature solid state reaction [4].



The prepared material was chemically characterized by electron microprobe (EDAX). The average size of the grains was calculated using photographs taken by Scanning Electron Microscopy (SEM). The structure was confirmed by X-ray powder diffraction (XRD) using CuKα₁ radiation. Impedance data were collected on cylindrical pellets (~16 mm in diameter with a thickness of 2 mm) obtained by applying pressure of 5 ton/cm² for 30 seconds in a 16 mm die. The electrodes were nickel plates. The impedance data were collected using a HIOKI 3532-50 impedance analyzer over the frequency range from 42 Hz to 1 MHz. Initially, measurements were carried out in order to find the range of the applied voltages where the material displays a linear behavior. The measurements were found to be independent of the applied voltage in the range of 100-250 mV. The final measurements were carried out with an applied constant voltage of 250 mV. The impedance of the samples was measured for 100 frequency values logarithmically distributed in the range from 42 to 10⁶ Hz and at temperatures from 25 to 500 °C in 25 °C steps. Stabilization time before each data acquisition was 1 hour and the temperature deviation during the measurement was less than 1 °C. The temperature was controlled by a Eurotherm 818P temperature controller. TG-DTA measurements were carried out with a SETARAM SETSYS 16/18 TG-DTA equipment, on LiMgVO₄, first immediately after preparation and a week later after exposure to air.

3. Results and discussion

The XRD pattern of the prepared powder displayed no additional lines that could be assigned to the presence of impurities. The material could be completely indexed with the space group Pbnm(62). From electron microprobe (EDAX) it was found that the ratio of the atoms was the same as predicted by the chemical formula. SEM images showed that the average size of LiMgVO₄ grains was ~10 μm. Thermogravimetric measurements (TG-DTA) were carried out on LiMgVO₄ with air carrier gas a) immediately after preparation of the material and b) a week later. TG-DTA measurements showed mass loss at three steps during first heating which was attributed to loss of absorbed water. Repetition of TG-DTA measurements, a week later after exposure to air, displayed again mass loss at three steps. Conductance measurements were taken at frequencies of 42 Hz - 1MHz as the pellet was heated up to 500 °C and then cooled down to room temperature in order to study the

reproducibility of the measurements and hysteresis phenomena. These measurements were carried out while applying a constant voltage of 250 mV to the pellet. The hysteresis observed is due to relaxation phenomena associated with the restoration of electroneutrality as the ions hop through the lattice. The low value of the specific conductivity even at high temperatures indicates that the material has densely packed crystal structure with narrow bottlenecks and without well-defined conduction pathways. It is remarkable that at 500 °C the conductivity is almost independent of frequency. At 500 °C conductivity is almost the same, in the whole frequency range from 42 Hz to 1 MHz. Below 500 °C the real part of the specific conductivity strongly depends on frequency. Above 300 °C and at 50, 100 Hz and 1 KHz the logarithm of the conductivity is almost a linear function of temperature. In the region from 150 to 500 °C and at frequencies 100 KHz and 1 MHz there is no strong dependence from temperature. Using the EQUIVCRT.PAS [5] the results of the impedance measurements were fitted and the equivalent circuits were drawn in the temperature range from 25 to 500 °C at 25 °C steps. Each element of the equivalent circuits was assigned, on grounds of time constant of the parallel (RQ) circuit, to a conduction process. Three conduction conductivity processes were assigned (Fig. 1). The grain interior (bulk) conductivity process, the grain boundary conductivity (gb) process and a third protonic conductivity process that exists up to 175 °C which is related to the humidity adsorption mechanism revealed in the TG-DTA measurements. Arrhenius plots of the elements that correspond to each conduction process were drawn and the activation energies were calculated.

4. Conclusions

The complex impedance study of LiMgVO_4 indicated that the material conductivity increases with temperature, a clear indication of ionic conduction processes. The conductivity increases with frequency but at 500 °C it is the same in the whole frequency range of measurements from 42 Hz to 1MHz. In addition to the bulk and grain boundary conductivity processes a third protonic conductivity process, associated with humidity adsorption mechanism, exists up to 175 °C. The Arrhenius plots of the elements of the equivalent circuits were obtained and the activation energies of the conduction processes were calculated. The bulk activation energy was found to be 0.62 eV, the grain boundary activation energy was found to be 1.03 eV from 260 to 350 °C and 0.50 eV from 360 to 500 °C. The existence of the two grain boundary activation energy values is explained by means of the easy paths theory [6].

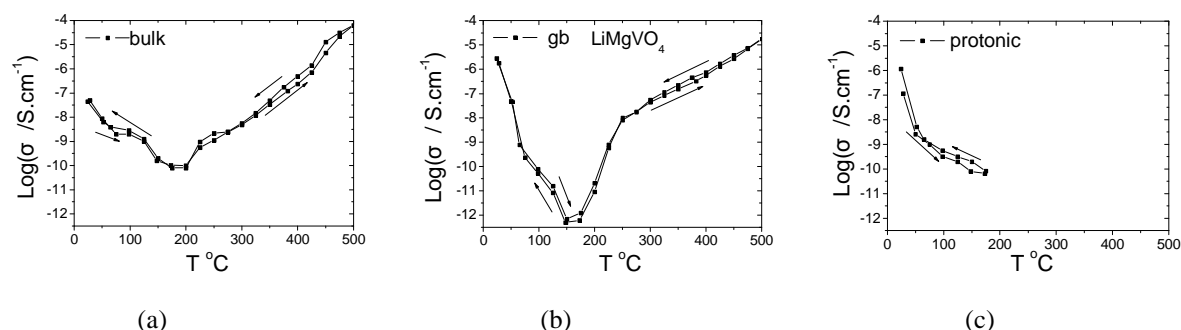


Fig.1 Specific conductivity vs temperature plots for LiMgVO_4 : (a) bulk; (b) grain boundary and (c) protonic conductivity.

5. References

- [1] G. Fu, H. Chen, Z. Chen, J. Zhang and H. Kohler, *Sens. Actuators, B* 2002, B81, 308.
- [2] J. Ying, C. Wan and P. He, *Sens. Actuators, B* 2000, B62, 165.
- [3] M. Wu, H. Sun and P. Li, *Sens. Actuators, B* 1994, 17, 109.
- [4] G.T.K Fey and D.L. Huang, *Electrochimica Acta* 45 1999 295.
- [5] Equivalent Circuit (EQUIVCRT.PAS), Bernard. A. Boukamp, University of Twente.
- [6] E. Barsoukov, J.R. Mackdonald (Eds) *Impedance Spectroscopy*, J. Wiley & Sons, Hoboken, New Jersey, 2005.

Photoluminescence from SiO₂ thin films produced by Reactive Radio Frequency Magnetron Sputtering

S. D. Pappas^{1*}, P. Pouloupoulos², V. Kapaklis³, A. Delimitis⁴, D. Trachylis¹ and C. Politis¹

¹ *Engineering Science Department, School of Engineering, University of Patras, 26504 Patras, Greece*

² *Materials Science Department, University of Patras, 26504 Patras, Greece*

³ *Department of Physics, Uppsala University, Box 530, S-751 21 Uppsala, Sweden*

⁴ *Chemical Process Engineering Research Institute (CPERI), Centre for Research & Technology Hellas (CERTH), Themi 57001, Thessaloniki, Greece*

*pappas@upnet.gr

Nanocrystalline Silicon and its compounds are novel photoluminescent materials for optoelectronic applications, see for example References [1-3]. Here we show the successful growth of thin SiO₂ films by means of reactive radio frequency (r.f.) magnetron sputtering in the following simple way: polycrystalline silicon wafers were used as targets and air, introduced in the ultra high vacuum chamber ($P_{\text{base}} \sim 1 \times 10^{-7}$ mbar) via a fine valve, as the reactive gas. The growth temperature was about 350 K. The films were deposited on single-crystalline Si wafers and polycrystalline alumina substrates. The thickness of SiO₂ films (between 300 and 1.200 nm) was measured precisely with the help of a precalibrated quartz balance system. The samples were annealed in ambient air at about 950 °C. Stoichiometric analysis performed via Scanning Electron Microscopy (SEM-EDX mode) revealed the formation of pure SiO₂ for the samples produced in an oxygen partial pressure larger than about 0.02 Pa. Detailed structural analysis was performed via X-Ray Diffraction. The measurements were performed with the help of a standard powder diffractometer (SEIFFERT) with the Ni-filtered CuK α_1 radiation ($\lambda = 0.15405$ nm). Furthermore, High Resolution Transmission Electron Microscopy combined with Energy-Dispersive X-ray Analysis (EDS) was used to monitor the structure and stoichiometry at the atomic scale.

Photoluminescence spectra at wavelengths between 400-900 nm were recorded via a fully automated homemade micro luminescence setup. The samples were excited with the help of a 378 nm ultraviolet laser source (Radius 375). Intense photoluminescence was exhibited at wavelengths between 400-650 nm. (The samples were producing a green-white light as detected by bare eye inspection, while they were irradiated by an ultraviolet lamp). This is a very important wavelength area for modern optoelectronic applications. Finally, we have measured the influence of the partial pressure of air during growth and of annealing on the photoluminescence signal. The mechanisms which are responsible for the photoluminescence of the films are discussed.

[1] Liqiang J., Yichun Q., Baiqi W., Shudan L., Baojiang J. Libin Y., Wei F., Honggang F., Jiazhong S., Sol. Energy Mater. Sol. Cells 90, 1773 (2006).

[2] Kapaklis V., Politis C., Pouloupoulos P. and Schweiss P., Mater. Sci. & Eng.: B 124-25, 475 (2005).

[3] Kapaklis V., Politis C., Pouloupoulos P. and Schweiss P., Appl. Phys. Lett. 87, 123114 (2005).

Study of an in-Car Refrigerator Using Commercial Bi₂Te₃ Thermoelectric Modules

K.T. Zorbas^{1,2,*}, E. Hatzikraniotis¹, K.M. Paraskevopoulos¹ and Th. Kyratsi²

¹ Department of Physics, Section of Solid State Physics, Aristotle University of Thessaloniki, Greece

² Department of Mechanical and Manufacturing Engineering, University of Cyprus, Nicosia, Cyprus

*kzorbas@physics.auth.gr

Introduction

Thermoelectric coolers [TEC] are all solid-state active heat pumps, which transfer heat from one side of the device to the other side against the temperature gradient (from cold to hot), with consumption of electrical energy. Such a device is also called a Peltier device, Peltier heat pump, solid state refrigerator, or thermoelectric cooler [1]. Recent progress in thermoelectrics and related fields have led to significant reductions in fabrication costs of Peltier modules, heat exchangers and DC power supplies, together with moderate improvements in the module performance [2]. The calculation of the cooling performance of thermoelectric refrigerators can be quite complex (dependent on the type of application), as the way of adaptation of the module, the shape and size of the heat exchangers and the type and size of insulation, affect notably the final result. The choice of the optimal type of TEC depends on the desired temperature difference, the desired cooling rate and the mass and properties of the cooled body.

In this work we have developed a theoretical model for calculating the cooling temperature, power flow and thermal performance of a TEC used as a refrigerator cooling mechanism, taking into account the thermal resistances of the insulation, heat exchangers and contacts of the cooled body. The factors affecting the cooling temperature and the limits of the efficient operation are investigated and the effect of different types of thermal insulation and heat exchangers in the cooling temperature are examined. The results of the theoretical model are compared with experimental results obtained from a prototype thermoelectric refrigerator constructed with the use of a commercially available TEC module.

Theoretical model

For the model calculations (insert in Fig.1) the basic equations for the heat transfer are:

$$\text{The heat rate pumped at the cold side} \quad Q_C = a_{TEC} T_C I - K_{TEC} (T_H - T_C) - \frac{1}{2} I^2 R_{TEC} \quad (1)$$

$$\text{The heat rate released at the hot side} \quad Q_H = a_{TEC} T_H I - K_{TEC} (T_H - T_C) + \frac{1}{2} I^2 R_{TEC} \quad (2)$$

$$\text{The TEC's cold side temperature} \quad T_C = T_a - Q_C W_C \quad (3)$$

$$\text{The TEC's hot side temperature} \quad T_H = T_a + Q_H W_H \quad (4)$$

where, K_{TEC} , a_{TEC} and R_{TEC} and I are the thermal conductance, the total Seebeck coefficient, the total electrical resistance and the current of the TEC, T_H and T_C are the hot and cold temperature on the TEC legs, T_a is the ambient temperature and W_C , W_H are the total thermal resistances of the cold and the hot side respectively. K_{TEC} , a_{TEC} and R_{TEC} are related to material properties and were evaluated as shown elsewhere [3,4].

$$\text{The total thermal resistance of the cold side} \quad W_C = W_{C_cont} + W_{C_SPACER} + W_{C_COOLER} + W_{INSUL} \quad (5)$$

$$\text{The total thermal resistance of the hot side} \quad W_H = W_{H_cont} + W_{H_COOLER} \quad (6)$$

where, W_{C_cont} , W_{H_cont} are the total contact resistances of the cold and the hot side respectively, W_{C_COOLER} and W_{H_COOLER} are the thermal resistances of the cold and hot side heat exchangers (with or without fan) respectively, W_{C_SPACER} is the thermal resistance of the intermediate component and W_{INSUL} is the total thermal resistance of the refrigerator cabinet thermal insulation. The thermal contact resistances depend on the contact pressure, the surfaces roughness and on the thermal grease properties and can be empirically evaluated [5].

The set of equations (Eq.1-4) gives the values of T_H , T_C , Q_C and Q_H , as a function of TEC's current I . This initial calculation of T_H and T_C assumes that the values of α , ρ and κ are for a TEC's average temperature $T_{avg} = (T_H + T_C)/2 = T_a$. The final values of T_H , T_C , Q_C and Q_H result using a proper algorithm [4]. The temperature in the refrigerator cabinet T_{IN} can be evaluated from the Eq. 7, where, P_{FAN} is the power of the internal fan:

$$T_{IN} = T_a - [(Q_C - P_{FAN}) \cdot W_{INSUL}] \quad (7)$$

Results and discussion

The inside volume of the refrigerated cabinet is 8 liters with external dimensions 300×210×250 (mm). Although this volume is small for household refrigeration, it is a suitable size for passenger cars. The cabinet was insulated with polystyrene (type II-IX, density 24-28 kg/m³, average thermal conductivity 0.0305W/mK) at thickness of

25mm. The inner and outer shells were constructed from steel sheet at a thickness of 0.6mm. A rubber seal, between the box and the door was placed.

For the cooling mechanism a commercial 40x40mm Bi₂Te₃ thermoelectric module with N=127 thermocouples (HB, TEC1-12705) was used. At the hot side an aluminum heat sink 150x94x17 (mm) with 18 fins of 13 mm height was used along with a fan 12V DC, 0.14A. In the refrigerated cabinet, a 100x97x24 (mm) aluminum heat sink (in contact with the inner metal sheet of the cabinet) with 8 fins of 20 mm height was used along with a 12V DC, 0.09A fan. For the heat transfer between the cold side of the TEC and the internal heat sink, an intermediate component (spacer) of aluminum was used. All four components were bonded together with two M4 screws, at a pressure between the parts of 4MPa. In order to reduce the thermal contact resistances, all surfaces were lapped at a maximum roughness of about 25μm and a thin layer of graphite thermal grease (Melcor GRF-159) was used.

In Fig.1 the first curve represents the measured internal temperature without an internal fan, while the second and third curves represent the internal temperature with the use of a 3.36 W fan and a 1.08 W fan respectively. It can be seen that the third implementation gives better results. When the refrigerator is switched on, the temperature of the refrigerated cabinet decreases exponentially, from an ambient temperature to a steady state lowest temperature.

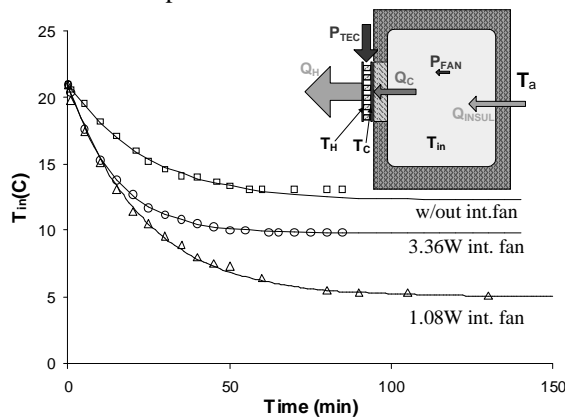


Figure 1: Cooling down temperatures for three different cold side implementations.

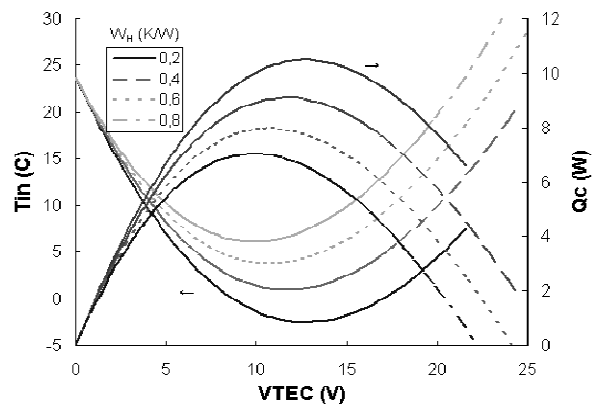


Figure 2: Internal temperature T_{in} and heat rate pumped Q_c for different values of thermal resistance

Fig.2 depicts the calculated values of the cabinet internal temperature T_{IN} and the heat pumped Q_c , using a TEC1-12705 for a refrigerator with internal volume of 8 liters and assuming an ambient temperature of 21°C. As expected, the amount of heat pumped Q_c , and hence the steady state inside temperature T_{IN} , strongly depend on the applied voltage. In our case, the selected TEC could be well combined with the voltage provided by a passenger car (12-14.5V). The achieved value of the heat sink's thermal resistance of both hot and cold side influences very importantly the internal temperature obtained; in fact, as can be seen in Fig. 2, close to the maximum Q_c , the performance of the TEC is affected more by the thermal resistance than from the applied voltage. The use of an internal fan improves notably the temperature equilibration in the inside area, but also adds an extra load.

Conclusion

In this work we have developed a model for the performance evaluation of a TEC used as a cooling device. The model, which takes into account the TEC's design and material characteristics as well as the cooling device and refrigerator's shell thermal resistances, has been successfully applied to a prototype thermoelectric in-car refrigerator. From the results, the minimization of the cold and hot side thermal resistances is the most important factor for the refrigerator's efficient operation. As the amount of the heat pumped Q_c depends strongly on the voltage applied, the proper selection of the TEC type is also important.

- [1] D.M. Rowe. Handbook of Thermoelectrics (CRC Press, 1st ed., 1995).
- [2] Gao Min, D.M. Rowe, Applied Energy 83, 113 (2006).
- [3] K.T. Zorbas, E. Hatzikraniotis, K.M. Paraskevopoulos, Proc. 5th ECT, Odessa, Ukraine Paper #30, (2007).
- [4] K.T. Zorbas, E. Hatzikraniotis, K.M. Paraskevopoulos, Proc. Mater. Res. Soc. Symp. ed. by T.P. Hogan, J. Yang, R. Funahashi, T.M. Tritt, Vol. 1044, U09-15, Warrendale, PA (2008).
- [5] F. Robbe-Valloire and J. Blouet, Int. J. Heat Mass Transfer. 40, 1121 (1997).

Acknowledgements

Authors acknowledge the financial support from Cyprus Research Promotion Foundation (THEMATA project). Pegasos Refrigerators Industry (Cyprus) is also acknowledged for the construction of the prototype cabinet.

Fano resonances in electronic transport through quantum wires

Vassilios Vargiamidis^{1*}, Vassilios Fessatidis², and H. M. Polatoglou¹

¹ *Department of Physics, Aristotle University, GR-54124 Thessaloniki, Greece*

² *Department of Physics, Fordham University, Bronx, New York 10458, USA*

*vargiam@physics.auth.gr

When a discrete level interacts with a continuum of states, a quasibound (resonant) state is created around the discrete level giving rise to asymmetric Fano line shapes. Such asymmetric resonances have been treated theoretically in various condensed matter systems including electronic ballistic transport through quasi-one-dimensional (Q1D) systems (such as quantum wires and rings) with impurities [1-3]. Fano resonances have also been observed experimentally in transport through mesoscopic systems with embedded quantum dots [4, 5].

In electron transport through quantum wires, the Fano function [6] arises as the most general resonance line shape, provided that two transport pathways – a resonant and a nonresonant one, interfere. The interference between the direct (nonresonant) transmission path and the transmission via a quasibound state (created in the impurity) gives rise to a Fano resonance.

For those readers who are not experts in the field, we briefly summarize Fano's theory [6]. Consider a system with a discrete (localized) energy state embedded in a continuum of states, which can be described by the Hamiltonian

$$H = E_c \hat{b}^+ \hat{b} + \sum_k E_k \hat{c}_k^+ \hat{c}_k + \sum_k (V_k \hat{c}_k^+ \hat{b} + V_k^* \hat{b}^+ \hat{c}_k) \quad (1)$$

The above Hamiltonian describes a discrete state with energy E_c , while the operators \hat{b}^+ and \hat{b} create and annihilate electrons respectively in this state. This discrete state may be called the impurity. The operators \hat{c}_k^+ and \hat{c}_k create and annihilate electrons in the continuum of states of energy E_k . The continuum may have a finite bandwidth, which occurs in tight binding models, or it can be a free-particle model. In the last term of Eq. (1), V_k is the coupling strength between the discrete state and the continuum, which is the result of mixing between these two kinds of states. In this term there are two types of processes. In one process, represented by $\hat{c}_k^+ \hat{b}$, the particle hops off the impurity into the continuum while, in the second process, represented by $\hat{b}^+ \hat{c}_k$, the particle in the continuum hops onto the impurity. The nature of the solution of the above model depends critically on whether the energy E_c falls within the continuum band of states E_k , i.e., in the energy range $E_1 < E_c < E_2$. Due to the interactions with the continuous band of states, the energy of the discrete state is modified to a new renormalized energy E'_c . If this modified energy E'_c is still within the continuum band of states, i.e., if $E_1 < E'_c < E_2$, then the solution exhibits a very interesting feature; namely, there would be no more any localized state in the system. This means that a particle in the continuum may hop onto the impurity, spend some time there, and then it may hop off again. Therefore, this is not a well-defined eigenstate, and the impurity state has become a scattering resonance.

We focus now on ballistic conduction through a uniform quantum wire connected with leads to electron reservoirs at different chemical potentials. The most obvious difference between Q1D and three-dimensional scattering is the subband structure that exists in a quantum wire. At a given energy, particles in the asymptotic region of the wire leads can have different momenta, depending on their subband index. In particular, a bound state in one subband (imaginary wave number in the leads) can coexist with an unbound state in another subband. Motivated by the process of multi-channel scattering in 3D, we can also consider the quantum wire as a multi-channel system if we treat the different subbands as "channels". The resonances that we consider are analogous to those arising in multi-channel scattering when a closed and an open channel are coupled, the channels in our case being the propagating and the cut-off subbands.

A particularly suitable approach to treat these resonances is provided by the Feshbach coupled-channel approach [1, 2, 7]. The coupling between channels is provided by an attractive impurity in the wire, which is modeled by a Dirac δ -function potential along the propagation direction while it is Gaussian in the transverse direction. This coupling leads to a Fano line shape in the transmission probability through the quantum wire. Fano resonances have a line shape of the form

$$T(\varepsilon) = |t^{bs}|^2 \frac{(\varepsilon + q)^2}{\varepsilon^2 + 1} \quad (2)$$

where $T(\varepsilon)$ is the transmission probability, $\varepsilon = (E - E_R)/\Gamma$ is the dimensionless energy from resonance, Γ is the resonance width, q is the (Fano) asymmetry parameter, and $|t^{bs}|^2$ is the nonresonant (background) transmission. E_R in Eq. (2) is the shifted quasibound state energy.

We examine here the effect of a transverse electric field on the transmission resonance (i.e., on the shift and width of the resonance). In particular, it has been shown both experimentally [8] and theoretically that shifting the position of the impurity with respect to the “walls” of the wire (or constriction) causes drastic change of the conductance. For instance, if a point attractive impurity falls on the symmetry axis of the wire, the conductance exhibits no resonance structure in the odd subbands, that is, the resonances strongly depend on the impurity position. The shifting of the impurity can be achieved by, for example, applying different gate voltage to the two parts of a split gate [8], which can be thought of as an applied electric field in the transverse direction of the wire. This causes shifting of the confining potential, which is equivalent to a “shifting” of the impurity in the opposite direction. It is important, therefore, to understand how the resonance characteristics are affected by a transverse electric field.

We show in particular that, increasing the field strength from zero causes either the collapse of the Fano profile in the first subband or the collapse of the Fano profile in the second subband, depending on whether the electric field points in the negative or positive direction [3]. When a collapse of a Fano line shape occurs the resonance width shrinks to zero and the quasibound state becomes a true bound state in the continuum. Hence an external electric field may be used as a means for controlling the resonance structure. It is also shown that the usual π phase change when the energy crosses a resonant level is absent (i.e., the phase is constant) when the Fano structure collapses.

- [1] Nöckel J.U. and Stone A. D., Phys. Rev. B 50, 17415 (1994); Kim C. S., Satanin A. M., Joe Y. S. and Cosby R. M., Phys. Rev B 60, 10962 (1999).
- [2] Vargiamidis V. and Polatoglou H. M., Phys. Rev B 72, 195333 (2005); Phys. Rev. B 75, 153308 (2007).
- [3] Vargiamidis V. and Fessatidis V., Phys. Rev. B 79, 205309 (2009).
- [4] Göres J., Goldhaber-Gordon D., Heemeyer S., Kastner M. A., Shtrikman H., Mahalu D., and Meirav U., Phys. Rev. B 62, 2188 (2000).
- [5] Kobayashi K., Aikawa H., Katsumoto S., and Iye Y., Phys. Rev. Lett. 88, 256806 (2002).
- [6] Fano U., Phys. Rev. 124, 1866 (1961).
- [7] Feshbach H., Ann. Phys. (N.Y.) 5, 357 (1958); Ann. Phys. (N.Y.) 19, 287 (1962).
- [8] Timp G. L. and Howard R. E., Proc. IEEE 79, 1188 (1991).
- [9] Sukhorukov E. V., Lubin M. I., Kunze C., and Levinson Y., Phys. Rev. B 49, 17191 (1994); Brandbyge M., Jacobsen K. W., and Nørskov, Phys. Rev. B 55, 2637 (1997).

A Novel Hall Effect Sensor Using Elaborate Offset Cancellation Method

Vlassis N. Petoussis^{1*}, George Stamoulis¹, Panos D. Dimitropoulos²

¹University of Thessaly, Department of Electrical & Computer Engineering.

²Center for Research and Technology Thessaly, or CE.RE.TE.TH

*petousis@inf.uth.gr

Silicon Hall plates show an offset of a few millitesla. A large portion of this offset is caused by mechanical stress in the device. The offset can be reduced with a factor 10^3 to 10^5 when the spinning - current principle is applied. This presentation shows the model and the numerical analysis of a new Hall effect sensor which using a novel offset reduction method. Furthermore we calculate the function which governs the changes in the electric field inside the new Hall effect sensor in presence of magnetic field. This function help us to control in MatLab environment the equipotential lines and to monitor the changes when biasing conditions are change. The combination of his pioneering form and the elaborate sequence of using the dynamic spinning current technique, leads to satisfactory results of produced Hall voltage with small noise in a presence of external magnetic field.

- [1] R.S. Popovic, Hall Effect Devices, Adam Hilger, Bristol, 1991.
- [2] H.H. Wieder, Hall Generators and Magnetoresistors, Pion Limited, London, 1971.
- [3] N.W. Ashcroft, N.D. Mermin, Solid State Physics, Saunders College, Philadelphia, 1976.
- [4] S. Liu, H. Guillou, A.D. Kent, G.W. Stupian, M.S. Leung, Effect of probe geometry on the Hall response in a inhomogeneous magnetic field: a numerical study, J. Appl. Phys. 83 (1998) 6161–6165.
- [5] V.N. Dobrovolsky, A.N. Krolevets, Theory of magnetic-field-sensitive metal-oxide–semiconductor field-effect transistors, J. Appl. Phys. 85 (1999) 1956–1960.
- [6] G. De Mey, Potential calculation in Hall plates, Adv. Electr. Electr. Phys. 61 (1983) 1–62.
- [7] V.N. Dobrovolsky, A.N. Krolevets, Hall current and its use in investigation of semiconductors (review), Sov. Phys. Semicond. 17 (1983) 1–7.
- [8] C. Maier, M. Emmenegger, S. Taschini, H. Baltes, J.G. Korvink, Equivalent circuit model of resistive IC sensors with the box integration method, IEEE Trans. Comput.-Aided Des. Integr. Circuits Syst. 18 (1999) 1000–1013.
- [9] R.S. Popovic, Numerical analysis of MOS magnetic field sensors, Solid State Electron. 28 (1985) 711–716.
- [10] Y. Sugiyama, H. Soga, M. Tacano, H.P. Baltes, Highly sensitive split-contact magnetoresistor with AlAs/GaAs superlattice structures, IEEE Trans. Electr. Dev. 36 (1989) 1639–1643.
- [11] Munter P.J.A, A low offset spinning current Hall plate. Sensors and Actuators, A21-A23 (1990) 743-746
- [12] Sandra Bellekom, Lina Sarro. International Conference on Solid-State Sensors and Actuators, Chicago, June 16-19, 1997 p.233-236.
- [13] Vlassis N. Petoussis , P.Dimitropoulos , George Stamoulis, A Novel Hall Effect Sensor Using Elaborate Offset Cancellation Method, Sensors & Transducers Journal, Vol. 100, Issue 1, January 2009, pp. 85-91.
- [14] *Galvanomagnetic Effects : “Sensors Depending on Hall Effect”*.
Vlassis N. Petoussis, Panos Dimitropoulos. “Journal of Engineering Science and Technology Review” Vol.2. Lecture Note pp.1-7 2009.
- [15] W. Shockley and W. T. Read, “Statistics of the recombinatim of holes and electrons, Phys. Rev, vol. 87, p. 835, 1952.

Acknowledgments I would like to thank my co authors, for the useful advices.

Semiconductor Spintronics

Vlassis N. Petoussis^{1*},

¹*Department of Electronics, Technological Education Institute of Lamia, GR-35100, Lamia, Greece*

**petoussis@inf.uth.gr*

MO2

P42

Modern information technology, i.e. data processing and storage, is based on semiconductors, such as silicon and ferromagnetic materials, such as iron. Information processing and computing takes place in semiconductor transistors and integrated circuits, while information is magnetically stored on high density hard discs. The evolving field of semiconductors 'spintronics' is aimed at combining ferromagnets with semiconductors to develop semiconductor devices, which integrate information processing with information storage [1][2]. Up to now, information processing technology is relying on moving electron charges, ignoring the spin (which is closely connected to magnetism) attached to each electron. In ordinary electronic circuits the spins are oriented randomly and have no effect on the current flow. On the other hand, spintronics devices create spin-polarized currents in which electrons are in spin-aligned state, either spin 'up' or spin 'down', and use the spin to control current flow.

Spin polarized currents (and therefore electron spins) have nevertheless been of importance for information storage in read-out heads for computer hard drives during the last decade [3]. The read-out heads exploit an effect called giant magnetoresistance (GMR) [4][5], which occurs in multilayer heterostructures consisting of alternative thin films of a ferromagnetic metal, for example cobalt, and a non-magnetic metal such as copper. The electrical resistance of such structures can be switched by a magnetic field. When the ferromagnetic material is magnetized, all magnetic moments of the individual atoms or of the conduction electrons align in one direction. Unpolarized electrons from the circuit line acquire the same magnetic moment direction when passing through the first ferromagnetic layer thus creating a spin polarized current. If this spin current passes through the second magnetic layer depends on whether the spin moments or magnetic moments of it's electrons are aligned parallel or antiparallel to the magnetic moments of the ferromagnetic layer. Only for parallel alignment the spins current can pass freely. With no external magnetic field applied, the magnetization of both ferromagnetic layers can alternate depending on the thickness of the inverting non-magnetic spacer metal. Then the flow of a spin polarized current is hindered when passing the second layer. However, if an external magnetic field is applied, which aligns the magnetic moments of all ferromagnetic layers in one direction, the barrier to spin polarized transport is reduced and the resistance drops.

Today's magnetic read-out heads and MRAMs (Magnetic Random Access Memories) are made of ferromagnetic metallic alloys. However micro-electronics companies are solely oriented to semiconductors and not to metals. An important goal is therefore to design and to build all semiconductor spintronic devices using semiconductors which are compatible with existing chip technology. In addition, semiconductor spintronics may even offer more interesting possibilities for information processing since semiconductors have the ability to amplify both optical and electrical signals, which is not possible in metallic devices.

The spin field-effect transistor (spin FET) has been the model device for many years in the field of semiconductor spintronics. It was proposed by S. Datta and B.Das in 1990 [6]. Up to now, no working spin FET prototype has been build. A major obstacle for this realization are difficulties in effectively generating electron spin currents from ferromagnetic metal to semiconductors. In fact, it has been shown by Schmidt *et.al* [7]. This obstacle of spin for spin injection can be bypassed by placing a tunneling or a Schottky barrier between the ferromagnetic metal and the semiconductor [8][9][10]. Recent optical experiments at various laboratories around the world show that the efficient electrical spin injection into semiconductors can be achieved without the need of spin polarized tunneling using novel materials, called diluted magnetic semiconductors as a source spin polarized carriers.

In addition the electrical spin injection, researchers must address and answer several important questions before potential semiconductor spintronic devices such as spin FET can be utilized in a new technology:

- Can diluted magnetic semiconductors or ferromagnetic metals be used in integrated circuits?
- Can we design semiconductors, which exhibit ferromagnetism with a high spin polarization far above room temperature?
- How efficiently can spin polarized currents be injected into semiconductors?
- What is the role of the ferromagnet- semiconductor interfaces for a spin injection?
- On which length scales can spin polarized carriers be transported in semiconductors?
- How can we control the state of individual electron spin by external magnetic or electric field inside the semiconductor?

- What are the fundamental advantages of the spin-based charge-based electronic with respect to speed, power consumption, functionality, and profitability?

This article devoted to address some of the above questions. In particular, it will be focused on the physics of diluted magnetic semiconductors (DMS), which incorporate magnetism by chemical doping of magnetic ions such as manganese (Mn) into non-magnetic group II-VI [11] and group III-V semiconductor compounds. The former class of material is paramagnetic and can be spin polarized by external magnetic field at low temperatures, while the latter even shows ferromagnetism leading to a spontaneous spin polarization of the charge carriers [12][13]. The fundamental electronic and magnetic properties of both classes of DMS material are going to be discussed in the main article.

- [1] S.A. Wolf, D.D. Awschalom, R.A. Burmann, J.M. Daughton, S. von Molnar, M.L. Roukes, A.Y. Chtchelkanova, D.M. Treger, *Science* 294, 1488, (2001).
- [2] D.D. Awschalom and J.M. Kikkawa, *Phys. Today* 52, 33 (1999).
- [3] G. Prinz, *Science* 282, 1660 (1998).
- [4] M.N. Baibich, J.M. Broto, A. Fert, F. Nguyen Van Dau, F. Petroff, P. Eitenne, G. Creuzet, A. Friederich, and J. Chazelas, *Phys. Rev. Lett.* 61, 2472 (1988).
- [5] J. Barlas, A. Fuss, R. Camley, P. Gründberg, and W. Zinn, *Phys. Rev. B.* 42, 8110 (1990).
- [6] S. Datta and B. Das, *Appl. Phys. Lett.* 56, 665 (1990).
- [7] G. Schmidt, D. Ferrand, and L.W. Molenkamp, A.T. Filip, and B.J. van Wess, *Phys. Rev. B* 62, 4790 (2000).
- [8] E.I. Rashba, *Phys. Rev. B* 62, R16227 (2000).
- [9] H.J. Zhu, M. Ramsteiner, H. Kostial, M. Wassermeier, H.P. Schönherr, and K.H. Ploog, *Phys. Rev. Lett.* 87, 016601 (2001).
- [10] A.T. Hanbicki, B.T. Jonker, G. Itskos, Kioseoglou, and A. Petrou, *Appl. Phys. Lett.* 80, 1240 (2002).
- [11] J.K. Furdyna, *J. Appl. Phys.* 64, R29 (1988).
- [12] H. Ohno, *Science* 281, 951 (1999).
- [13] H. Ohno, *J. Mag. Mag. Materials* 200, 110 (1999)

Acknowledgments I would like to thank B. Beschoten, for useful advices.

Correlation Between TL And OSL Signals In $\text{KMgF}_3:\text{Ce}^{3+}$; Bleaching Study Of Individual Glow Peaks

G. I. Dallas^{1,2}, G.S. Polymeris¹, D. Afouxenidis³, N.C. Tsirliganis¹ and G. Kitis^{3,*}

1 Cultural and Educational Technology Institute-R.C. Athena/Archaeometry Laboratory, Xanthi, Greece

2 Democritus University of Thrace/Nuclear Engineering Laboratory, Xanthi, Greece

3 Aristotle University of Thessaloniki/ Nuclear Physics Laboratory, Thessaloniki, Greece

*gkitis@auth.gr

$\text{KMgF}_3:\text{Ce}^{3+}$ is an extremely sensitive TL material which also exhibits intense OSL signal. Despite its complex trap structure, the TL signal of $\text{KMgF}_3:\text{Ce}^{3+}$ can be easily deconvoluted. Therefore, it is a promising candidate among the materials with multiple glow curve structure for a detailed correlation study between TL and OSL signals.

In the present work the TL bleachability of Ce^{3+} doped KMgF_3 crystals after blue optical stimulation, has been investigated. The original sample was initially crushed, and grains with dimensions between 50 and 100 μm were selected and deposited on stainless steel disks of 1 cm^2 area. During the experimental procedure, the residual TL (RTL) glow curve shape of the sample was obtained after a test dose of 370 mGy and continuous wave OSL of various durations (0, 5, 10, 25, 50, 75, 100, 150, 300, 500, 750 and 1000 s).

The RTL glow curve was deconvoluted. The curve appears to consist of six individual and well defined glow peaks (Fig.1). Furthermore, the LM-OSL signal was decomposed (Fig. 2). The RTL signal of each glow peak was integrated and normalized with reference to the TL intensity of the glow curve obtained without OSL stimulation. Then the residual curve of each glow peak following the OSL bleaching was plotted vs stimulation time, decomposed into three components, termed as the fast, the medium and the slow (Fig. 3) and the decay constants were calculated. Finally, the dependence of the decay constant on the TL trap parameters was studied for each component group (fast, medium and slow).

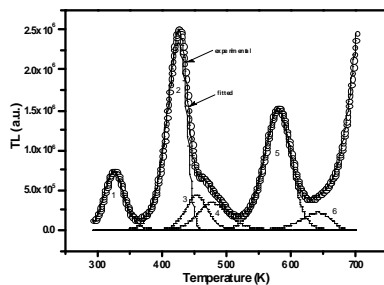


Figure 1: TL glow curve of the sample. Experimental data (open circles), and glow peak obtained from the curve fitting (continuous line).

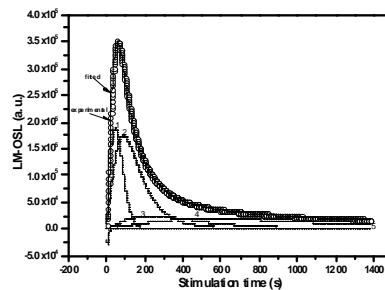


Figure 2: LM-OSL curve analysis. Experimental data (open circles), and glow peak obtained from the curve fitting (continuous line).

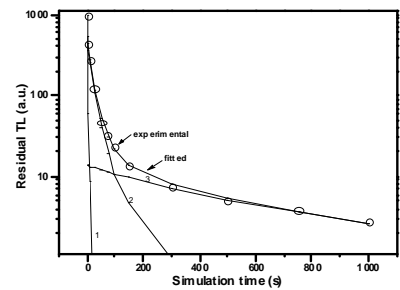


Figure 3: Residual curve by OSL bleaching of TL (for peak 2). Fast (1), medium (2) and slow (3) component.

Thermally Assisted Photo Transfer OSL From Deep Traps In Al₂O₃:C

G. S. Polymeris^{1,*}, S. Raptis^{1,2}, D. Afouxenidis^{1,2}, N. C. Tsirliganis¹, G. Kitis²

¹ *Archaeometry Laboratory, Cultural and Educational Technology Institute (C.E.T.I.), R.C. "ATHENA", Tsimiski 58, 67100 Xanthi, Greece*

² *Aristotle University of Thessaloniki, Nuclear Physics Laboratory, 54124 Thessaloniki, Greece.*

*gpolymer@ceti.gr

Al₂O₃:C is a well-established passive thermoluminescence (TL) and optically stimulated luminescence (OSL) detector for UV and ionizing radiation. Single crystals of the material are known to exhibit a variation to their TL glow curve shape from sample to sample, which is attributed to the degree of occupancy of the deep traps, with the delocalization temperature above 650⁰C, affecting the basic features of the main TL glow peak. The presence of these deep traps was verified by both luminescence and exo-electron emission measurements.

The aim of the present work is to suggest an alternative experimental method in order not only to measure the signal of the deep traps without heating the sample to temperatures greater than 400 °C, but to use the former for dosimetry purposes as well. This method consists of photo transfer OSL measurements performed at elevated temperature, after the sample was previously heated up to 400⁰C in order to empty its main TL dosimetric peak. A similar methodology was proposed earlier by Bulur and Göksu [1] by measuring the phototransferred thermoluminescence (PTTL) instead of OSL.

For the study, only Al₂O₃:C crystals exhibiting narrow TL glow peaks, with FWHM < 40⁰C, were used, after pre-irradiation annealing for 15 min at 1085⁰C. Photo transfer of charges from deep traps takes place during 1ks illumination at the continuous wave (CW-OSL) mode using the blue LEDs housed at the RISØ TL/OSL systems. The thermal assistance of the phenomenon was studied by monitoring the OSL signal at different temperatures ranging between room temperature (25⁰C) and the Tmax of the main dosimetric TL peak, namely 190⁰C, which was selected as the optimum stimulation temperature for the proposed method. For temperatures greater than 100⁰C the phototransfer signal does not resemble the trivial shape of a CW-OSL spectrum, yielding a peak for the early stimulation times. The thermal activation energy of the process was also calculated.

Furthermore, the impact of the heavy dose accrued to the deep traps on the luminescence properties of each single crystal was both qualitatively and quantitatively studied. The dose response of the thermally assisted photo transfer OSL was obtained, being extremely supralinear in the dose region between 5 and 500 Gy, while for larger doses the traps are saturated. Sensitivity as well as peak shape changes imposed by heavy irradiations were monitored for all the crystals under study. Implications on heavy dose dosimetry using aluminum oxide are also briefly discussed.

[1] Bulur, E., Göksu, H. Y., 1999. Radiation Measurements 30, 203 – 206.

Session MO3

ELECTRONIC TRANSPORT

*SEMICONDUCTORS &
DEVICES*

*PHOTONICS &
OPTOELECTRONICS*

PART 1

Monday, 21 September 2009, 14⁰⁰-16³⁰



Advancing III-Nitrides Epitaxy: From Kinetics to New Device Applications

E. Iliopoulos^{1,2,*}

¹ *Physics Department, University of Crete, P.O. Box 2208, 71003 Heraklion-Crete, Greece and*

² *Institute of Electronic Structure and Lasers, F.O.R.T.H., P.O. Box 1385, 71110 Heraclion-Crete, Greece*

**iliopoul@physics.uoc.gr*

Compound III-Nitride semiconductors are the subject of intense scientific research during the last decade, due to their potential importance in a broad range of (opto-)electronic device applications. Already, commercial products, such as blue-green light emitting diodes (LEDs) and near-UV solid state lasers, are available. Further progress in epitaxy, technology development and physical understanding of this important material system is predicted to have a strong impact on a number of technological fields, with most prominent ones being solid-state lighting, photovoltaic technology, high power/high frequency electronics and UV-VIS optoelectronics. The epitaxial growth of III-Nitrides by molecular beam epitaxy had to overcome a number of problems related to (i) unavailability of suitable substrates, (ii) inertness of molecular nitrogen, (iii) limited surface mobility of nitrogen adatoms and (iv) limitations restricting growth temperatures to much lower values than the ones dictated by the extremely high melting points of the III-N binaries. Additional to those, common problems for all epitaxial growth techniques, are the low miscibility of InN with GaN and AlN, as well as, the large differences in lattice constants between them, facts that complicate the design and realization of heterostructures.

The problem of reduced adatoms' surface mobility was successfully addressed, in radiofrequency plasma assisted molecular beam epitaxy (RF-MBE), by the exploitation of self-surfactant effect of the group-III atoms. Today, RF-MBE conditions, where a metallic adlayer on the growth surface is formed, is the "standard model" for the case of $\text{Al}_x\text{Ga}_{1-x}\text{N}$ alloys and lower InN content $\text{In}_x\text{Ga}_{1-x}\text{N}$ heteroepitaxial growth. Under those conditions, growth kinetics are radically different than the ones of other traditional compound semiconductors [1].

However, in the case of RF-MBE growth of InN those "standard" conditions are not applicable, due to the faster decomposition rate of InN, as compared to In adatoms' desorption from the growing surfaces. Detailed studies of growth kinetics [2] not only permitted the RF-MBE growth of InN films with "state of the art" properties, but they also offered further insight into the kinetic mechanisms of III-Nitrides compounds in general. Therefore, new growth approaches can be implemented, in the case of GaN, offering the potential of reduced defect densities' material development.

Epitaxial growth by RF-MBE is an out-of-equilibrium process. Therefore it can be particularly efficient in the development of high InN content $\text{In}_x\text{Ga}_{1-x}\text{N}$ and $\text{In}_x\text{Al}_{1-x}\text{N}$ ternary alloys [3,4], whose realization was hindered, up to now, by phase separation problems. Homogeneous thin films, with single peaked x-ray diffraction patterns, enhanced optical properties and efficient luminescence, grown in the entire composition range is demonstrated, paving the way for optoelectronic applications covering the full UV to NIR range of the electromagnetic spectrum. In addition, the possibility of controlled heteroepitaxy of III-Nitrides ternary alloys, in their full compositional range, opens new possibilities in advanced heterostructure engineering for enhanced device applications.

The lack of inversion symmetry along the [0001] wurtzite axis, which is the usual growth direction of device quality III-Nitrides thin films, results in the presence of very strong piezoelectric fields in heterostructures. For device applications, these fields can pose restrictions, as is the case of quantum well LEDs, or can be exploited to enhance device performance, as is the case of AlGaIn/GaN high-electron mobility transistors (HEMTs). Recently, AlN/GaN HEMTs with record values of two dimensional electron gas, equal to $3.6 \times 10^{13} \text{ cm}^{-2}$ were demonstrated and exploited for the fabrication of high current densities and high transconductance transistor devices.

Finally, the realization of advanced III-Nitride resonant tunneling diodes (RTDs), with high peak to valley current contrast ratios will be presented.

[1] Iliopoulos E. and Moustakas T.D., Appl. Phys. Lett. 81, 295 (2002).

[2] Dimakis E., Iliopoulos E., Tsagaraki K., Georgakilas A., Appl. Phys. Lett. 86, 133104 (2005).

[3] Iliopoulos E., Georgakilas A., Dimakis E., Adikimenakis A., Tsagaraki K., Androulidaki M, Pelekanos N.T., Phys. Stat. Sol. A 203, 102 (2006).

[4] Iliopoulos E., Adikimenakis A., Giesen C., Heuken M., Georgakilas A., Appl. Phys. Lett. 92, 191907 (2008).

The role of gate width in transistor performance: Effects of gate sidewall roughness

V. Constantoudis^{1*}, G.P. Patsis^{1,2} and E. Gogolides¹

¹ Institute of Microelectronics, NCSR "Demokritos", Aghia Paraskevi, Greece

² Department of Electronics, TEI of Athens, Aegaleo, Greece

*vconst@imel.demokritos.gr

Statistical variability of transistor characteristics has become a major concern associated with CMOS transistors scaling and integration. For conventional bulk MOSFETs, the main sources of the statistical variability are the randomness of discrete dopants, the gate sidewall roughness (usually called line edge/width roughness (LER/LWR)) and the granularity of Poly Gate [1]. In this paper, we focus on the impact of LWR on transistor performance (see schematic view in Fig.1a). The aim is to reveal the role of the transistor gate (channel) width on it, which up to now has been overlooked.

The continuing shrinking of the transistor gate length is accompanied by the scaling down of the gate widths. This scaling down has two implications on LER/LWR impact on transistor performance which are usually neglected in the conventional approach to the problem. The first is that the most commonly used LER/LWR metric, 3rms (sigma) value of sidewall edge points, depends on the line length L included in the measurement process, and decreases as L goes down (see solid line in Fig.1b) [2,3]. This dependence becomes more intense when $L < 10\xi$ (with ξ the correlation length) while for low L 3rms $\sim r^\alpha$, where α is the roughness exponent of the line morphology. Transferred to gate terminology, this finding means that for gate widths lower than $\sim 10\xi$, the 3sigma value of Gate Length Roughness (GLR) depends on the gate width, apart from its material and process dependencies. Given that $\xi \sim 10\text{-}30\text{nm}$, the above gate width dependence applies for transistors with gate widths lower than 300nm. The second implication is also related with a LWR metrological finding of last years considering the variation of the CDs of line segments of length L [3]. According to it, the decrease of LWR with L is associated with an increase of the CD variation of line segments so that the sum of their squares remains unaltered. In gate terminology, this finding means that the CD variation among the transistors with the same gate width increases as gate width becomes smaller contrary to the behavior of GLR. This is shown in Fig. 1b with the dashed line.

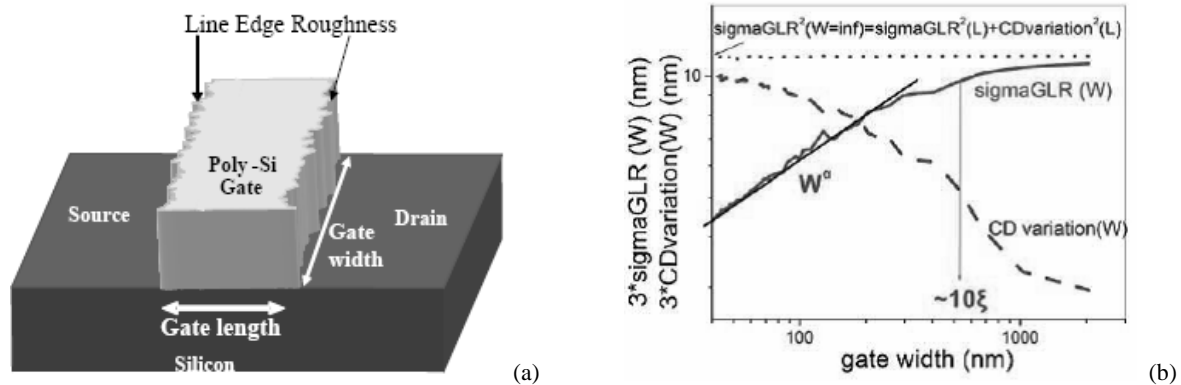


Fig.1. a) Schematic view of a transistor with Line Edge and Line Width Roughness and b) The mean sigma value of GLR (solid line), the CD variation among gates (dashed line) and the sum of their squares (dotted line) versus the gate width W. Notice that as gate width decreases sigma decreases, CD variation increases and the sum of their squares remains fixed to the sigma of GLR with infinite (very large) gate width.

Thus, GLR is not affected alone by the materials of gate stack and the applied processes for transistor formation (lithography and etching steps) but also by a basic design parameter, the gate width. Furthermore, this dependence is controlled by the spatial roughness parameters, the correlation length ξ and the roughness exponent α . In the following, we will examine the effects of ξ, α for fixed W and of W for fixed ξ, α on the statistical variability of transistor performance.

The methodology we employ has been explained elsewhere [4,5]. It is based on modeling both LWR and GLR with fractal self-affine lines characterized by the triplet of roughness parameters (rms value sigma, ξ , α) and also modeling the effects on transistor performance by using the 2D approach proposed by Oldiges [6] in which the transistor is considered a stack of 2D ultra-small transistor with no roughness.

Fig. 3a shows the effects of ξ, α on the mean value of threshold voltage shifts δV_{th} from the nominal (no roughness) value for fixed gate length $CD=45\text{nm}$ and gate width $W=135\text{nm}$. The transistor gates that have milder degradation effects on the device electrical performance (smaller absolute values δV_{th}) are those with low α and ξ values. Also, Fig. 3a shows that correlation length ξ affects more drastically transistor electrical characteristics than the roughness exponent α . Thus, the conclusion here is to seek changes in resist and/or process properties that lead to lower values of all LWR/GLR parameters.

In Fig. 3a we kept the gate width invariant $W=135\text{nm}$. However, the transistors employed in IC may have a spectrum of gate widths W . Fig. 3b quantifies the effects of gate width variations on threshold voltage shift. It shows the curves $F_{gt}(\xi)$ for varying W (90,135 and 180nm), keeping this time fixed the $\sigma(W=\text{inf})=2\text{nm}$, the gate length $L=CD_{\text{nom}}=45\text{nm}$ and the roughness exponent $\alpha=0.5$. The yield F_{gt} is defined as the fraction of transistors F_{gt} with gate voltage thresholds $0.90 V_{gth,ideal} < V_{gth,i} < 1.10 V_{gth,ideal}$. We deduce that the beneficial effect of correlation length reduction remains unaltered for all gate widths W . Furthermore, we find that for fixed CD and GLR parameters [$\sigma(W=\text{inf})$, ξ, α] the yield gets higher values as W increases.

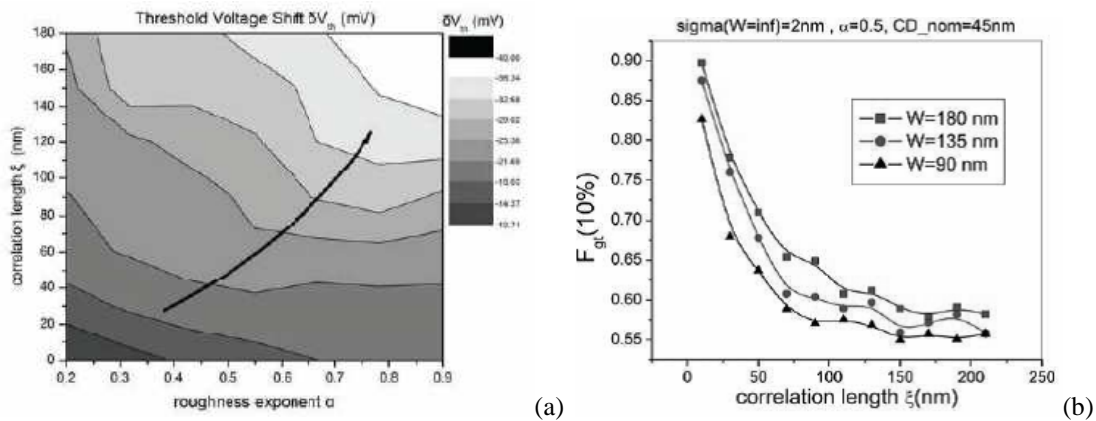


Fig. 2. a) Dependence of the average threshold voltage shift δV_{th} on the spatial GLR parameters α, ξ for fixed $W=135\text{nm}$ and $\sigma=2\text{nm}$. The arrows show the directions for increasing the absolute values of shifts δV_{th} . Modeling predicts that lower α, ξ are more beneficial with respect to GLR effects on threshold voltage deviations. b) Dependence of the transistor yield F_{gt} for various W as a function of ξ keeping fixed $\sigma=2\text{nm}$ and $\alpha=0.5$.

We have also investigated the effects on the average and standard deviation of the off state leakage currents. It has been found that both estimated quantities (average value and standard deviation) decrease as we move to lower α, ξ . Furthermore, it seems that the roughness exponent has more drastic effects on the average value rather than the correlation length. This differentiates the average off current behavior than that of the standard deviation and of threshold voltage shifts and deviations.

[1] Asenov A., Digest of Technical Papers – Symposium on VLSI Technology, art. No. 4339737, 86 (2007).

[2] Constantoudis V., Patsis G.P., Gogolides E. et al., Journal of Vacuum Science and Technology B: Microelectronics and Nanometer Structures 22, 1974 (2004).

[3] Constantoudis V., Gogolides E., Roberts J. and Stowers J., Proceedings of SPIE 5752, 1227 (2005).

[4] Patsis G.P., Constantoudis V., Gogolides E., Proceedings of SPIE 6151 II, 61513J (2006).

[5] Constantoudis V., Patsis G., Gogolides E., Proceedings of SPIE 6518, 65181N (2007).

[6] P. Oldiges, Q. Lint, K. Petrillot, M. Sanchez, M. Jeong, and M. Hargrove, International Conference on Simulation of Semiconductor Processes and Devices, SISPAD, 131 (2000).

Acknowledgments: The European ICT Integrated project “MD³ : Material Development for Double exposure and Double patterning” is kindly acknowledged for financial support.

Electrical Characterization and Design Optimization of Finfets with TiN/HfO₂ Gate Stack

A Tsormpatzoglou^{1,2}, D H Tassis¹, C A Dimitriadis^{1*}, M. Mouis², G Ghibaudo² and N. Collaert³

¹ Department of Physics, Aristotle University of Thessaloniki, 54124 Thessaloniki, Greece

² IMEP, MINATEC, Parvis Louis Néel, 38054 Grenoble Cedex 9, France

³IMEC, Kapeldreef 75, 3001 Leuven, Belgium

*cdimitri@physics.auth.gr

Triple-gate field-effect transistors like FinFETs have been recognized as the best candidates for sub-100 nm scaling of MOSFETs due to their immunity to short channel effects (SCEs) and proximity to standard bulk planar CMOS processing [1-7]. Multi-channel FinFETs have been reported demonstrating their feasibility for digital/analogue circuit applications [6], [8, 9], as well as applications in equipments requiring extremely low power consumption [10-12]. In most of the recent studies, device optimization was studied with simulations using graded doping profile in the source/drain underlap regions [13, 14]. However, as the FinFETs scale down, the fins need to be thinner for better control of the short-channel effects, resulting in difficulties for experimental realization of a specific doping profile in such thin fins [15].

FinFETs with extensions under the spacers between gate and source/drain contacts of constant doping concentration have been demonstrated, which show higher subthreshold leakage current as they are scaled down [16]. This finding suggests that the extensions under the spacers need to be optimized in these devices. In this work, based on experimental and simulation data, we report electrical characteristics of lightly doped n-channel FinFETs with TiN/HfO₂ gate stack and provide the optimized technological parameters of the source/drain extension under the spacers needed to improve the performance of 60 nm gate length FinFETs.

The n-channel triple-gate FinFETs were fabricated at IMEC (Leuven) on SOI wafers with 145 nm buried oxide thickness, following the process described elsewhere [6]. The measured devices were 5-fin FETs with a structure schematically represented in Fig. 1. The channel of the transistors is silicon with background boron doping concentration of about 10^{15} cm^{-3} . As gate insulator, HfO₂ was deposited with equivalent gate oxide thickness 1.7 nm, whereas a 5 nm TiN film was deposited for gate metallization. The length and the doping concentration of the extensions under the spacers between gate and source/drain pads are $L_{\text{ext}} = 50 \text{ nm}$ and $N_{\text{ext}} = 5 \times 10^{19} \text{ cm}^{-3}$, respectively. The doping concentration of the source/drain contacts is about $2 \times 10^{20} \text{ cm}^{-3}$, the fin height is $H_{\text{fin}} = 65 \text{ nm}$, the fin width W_{fin} is varying from 25 to 875 nm and the gate length L_g is varying from 60 to 910 nm. Details of the fabrication processes are described in [17].

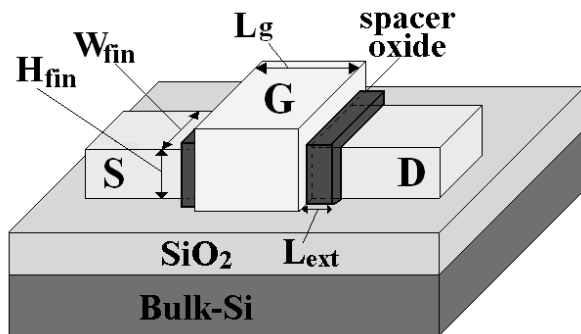


Figure 1. 3-D configuration of the FinFET device.

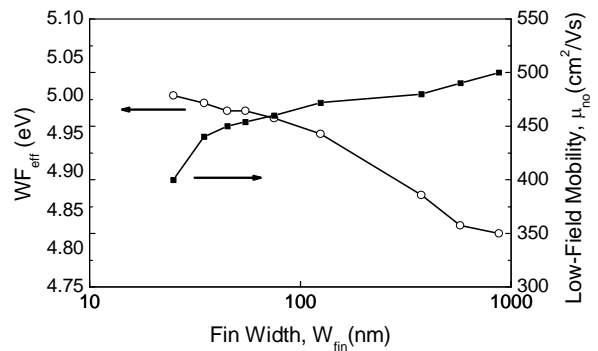


Figure 2. Effective work function WF_{eff} and low field mobility μ_{no} as a function of the fin width.

The experimental transfer characteristics of FinFETs with W_{fin} lying within the range of 875-25 nm and with gate length L_g varying from 910 to 60 nm have been analyzed and reproduced with simulations, using a 3-D commercial software tool (SILVACO-ATLAS). For the simulations, we used as fitting parameters the effective gate work function WF_{eff} for the HfO₂/TiN gate stack and the low field mobility μ_{no} in Shirahata's mobility model. The behavior of WF_{eff} and μ_{no} versus W_{fin} is presented in Fig. 2 (for FinFETs with $L_g=910 \text{ nm}$). It is worth to notice that decrease of the fin width from 875 to 25 nm shifts the effective gate work function from 4.82 to 5.00 eV, i.e. shifts WF_{eff} by $\sim 200 \text{ mV}$. The lower value of the $WF_{\text{eff}} = 4.82 \text{ eV}$ characterizes mainly the

TiN/HfO₂ stack of the top-gate since $W_{\text{fin}} \gg H_{\text{fin}}$, whereas the higher value of $W_{\text{eff}} = 5.00$ eV characterizes the gate stack of the side-gates of the device since $W_{\text{fin}} < H_{\text{fin}}$. This finding can be explained with the results of a recent work obtained from calculations of the TiN/HfO₂ valence band offset, which depends on the interface dipoles; it is shown that the effective work function of the TiN/HfO₂ gate stack depends on the TiN and HfO₂ interface stoichiometry and the species inter-diffusion [18]. In oxygen/nitrogen rich interfaces the effective work function is high (5.1 eV), reducing to 4.7 eV when oxygen is mixed in TiN or oxygen vacancies exist at the TiN/dielectric interface [18]. Therefore, the obtained experimental values of W_{eff} indicate a different stoichiometry of the top and side gates interfaces.

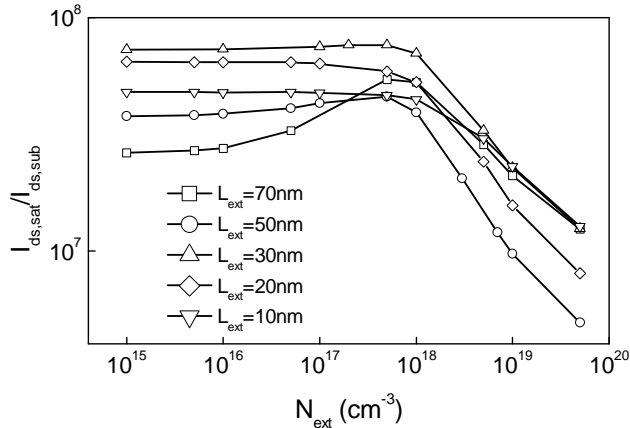


Figure 3. Dependence of the current ratio $I_{d,\text{sat}}/I_{d,\text{sub}}$ on the extension doping concentration N_{ext} and length L_{ext} , for finFETs with $L_g = 60$ nm.

Optimization of the extension regions under the spacers, characterized by the two parameters of extension doping concentration N_{ext} and length L_{ext} was performed for the FinFET with the shorter gate length of $L_g = 60$ nm and fin width $W_{\text{fin}} = 25$ nm (using the aforementioned values of W_{eff} and μ_{no}). In order to develop guidelines for optimal device performance in terms of both N_{ext} s and length L_{ext} , we evaluated their influence on the current ratio $I_{d,\text{sat}}/I_{d,\text{sub}}$. Fig. 3 shows that an extension length smaller than 50 nm and extension doping concentration lower than 5×10^{19} cm⁻³ are required to achieve improved device performance with maximum saturation drain current to subthreshold leakage current ratio ($I_{d,\text{sat}}/I_{d,\text{sub}}$). In fact, optimum current ratio $I_{d,\text{sat}}/I_{d,\text{sub}}$ is obtained (for the 60 nm gate length FinFETs), when $L_{\text{ext}} = 30$ nm and $N_{\text{ext}} \approx 5 \times 10^{17}$ cm⁻³.

- [1] Valamontes E., Nassiopoulou A. G., Glezos N., Surf. Interf. Anal. 16, 203 (1990)
- [2] Iijima S. Invitation to IMC 16. (Tsukuba City, Publisher, 2005).
- [3] Furuya K. and Mori H., Proc. 16th Int. Microsc. Cong., Iijima S., ed., Sapporo, Japan 2, 5 (2006).
- [1] Pei G, Kedzierski J, Oldiges P, Jeong M and Kan E C C, *IEEE Trans. Electron Devices* 49 1411-1419 (2002).
- [2] Park J T and Colinge J P, *IEEE Trans. Electron Devices* 49 2222-2229 (2002).
- [3] Zhang W, Fossum J G, Mathew L and Du Y., *IEEE Trans. Electron Device* 52 2198-2206 (2005).
- [4] Lederer D, Kilchytka V, Rudenko T, Collaert N, Flandre D, Dixit A, De Meyer K and Raskin J P, *Solid-State Electron.* 49 1488-1496 (2005).
- [5] Kranti A and Armstrong GA., *Semicond. Sci. Technol.* 21 409-421 (2006).
- [6] Subramanian V, Mercha A, Parvais B, Loo J, Gustin C, Dehan M, Collaert N, Jurczak M, Groeseneken G, Sansen W and Decoutere S, *Solid-State Electron.* 51, 551-559 (2007)
- [7] Nawaz M, Molzer W, Decker S, Giles L F and Schulz T, *Microelectronics Journal* 38 1238-1251 (2007).
- [8] Choi Y and Hu C, *Solid State Electron.* 46 1595-1601 (2002).
- [9] Pavanello M A, Martino J A, Simoen E, Rooyackers R, Collaert N and Claeys C, *Solid State Electron.* 51 285-291 (2007).
- [10] Wang A and Chandrakasan A, *IEEE J. Solid State Circuits* 40 310-319 (2005).
- [11] Chen J, Clark L T and Cao Y, *IEEE Circuits and Devices* 21 12-20 (2005).
- [12] Joshi R V, Williams R Q, Nowak E, Kim K, Beintner J, TLudwig T, Aller I and Chuang C, *Proceed. of 34th European ESSDERC* 69-72 (2004).
- [13] Kedzierski J, Jeong M, Noward E, Kanarsky T S, Zhang Y, Roy R, Boyd D, Fried D, and Philip Wong H S, *IEEE Trans. Electron Devices* 50 952-958 (2003).
- [14] Trivedi V, Fossum J G and Chowdbury M M, *IEEE Trans. Electron Devices* 52 56-62 (2005).
- [15] Sachid A B, Manoj C R, Sharma D K and Rao V R, *IEEE Electron Dev. Lett.* 29 128-1330 (2008).
- [16] Tsormpatzoglou A, Dimitriadis C A, Mouis M, Ghibaudo G and Collaert N, *Solid-State Electron.* 53 359-363 (2009).
- [17] Collaert N, Demand M, Ferain I, Lisoni J, Singanamalla R, Zimmerman P et al., *Symposium on VLSI Technology Digest of Technical Papers* 108-109 (2005).
- [18] Fonseca L R C and Knizhnik A A, *Physical Review B* 74 195304 (2006).

Acknowledgments This paper is part of the 03ED709 research project, implemented within the framework of the "Reinforcement Programme of Human Research Manpower" (PENED) and co-financed by National and Community Funds (25% from the Greek Ministry of Development-Greek General Secretariat for Research and Technology and 74% from E.U.-European Social Fund).

Electrical and Structural Characteristics of Strained - Si MOS Structures as a Function of Strained-Si Overlayer

N. Kelaidis^{1,*}, V. Ioannou – Sougleridis¹, D. Skarlatos², K. Papagelis³, J. Parthenios⁴, S.N. Georga², C.A. Krontiras², Ph. Komninou⁵, C. Tsamis¹, B. Kellerman⁶ and M. Seacrist⁶

¹Institute of Microelectronics, NCSR “Demokritos”, 153 10 Aghia Paraskevi, Athens, Greece

²Department of Physics, University of Partas, GR-265 04 Partas, Greece

³Department of Materials Science, University of Partas, GR-265 04 Partas, Greece

⁴Foundation of Research and Technology Hellas, Institute of Chemical Engineering and High Temperature Processes, GR-265 04 Patras, Greece

⁵Department of Physics, Aristotle University of Thessaloniki, 541 24 Thessaloniki Greece

⁶MEMC Electronics Materials, Inc, 501 Pearl Drive (City of O’Fallon) St. Peters Missouri 63376, USA

*nkelai@imel.demokritos.gr

Strained-Silicon (s-Si) has already been applied to CMOS technology. The study of the structural and electrical properties of s-Si MOS (Metal-Oxide-Semiconductor) structures with ultrathin gate dielectrics is important, especially as a function of the strained-Si overlayer thickness, where a variety of phenomena remains under investigation [1]-[2]. This is the aim of the present work. For this purpose, ultrathin oxides formed in 100% N₂O ambient are used as gate dielectrics. Si oxynitridation in N₂O ambient leads to the formation of ultrathin oxides at high temperatures [3], thus enabling a parallel study under high thermal budget conditions.

The strained-Si structures examined herein consist of either a 27.5 nm thick s-Si overlayer epitaxially grown on a relaxed constant composition Si_{0.9}Ge_{0.1} substrate (S1) or a higher-strain 13 nm s-Si overlayer on a Si_{0.78}Ge_{0.22} substrate (S2). In order to study the effect of the overlayer thickness, certain structures were chemically etched using a modified RCA solution. Oxynitridation has been performed at temperatures of 800 – 900 °C for various time intervals. Raman spectroscopy and Transmission Electron Microscopy (TEM) have been used in order to study strain preservation and the remaining s-Si overlayer thickness after the etching and oxidation processes. SIMS analysis was performed in order to measure Ge diffusion effect towards the SiO₂/Si interface. Electrical characterisation is performed on Al-gate s-Si MOS capacitors. In the case of thick (>10 nm) s-Si overlayer, C-V characteristics (Figure 1) show a minor frequency dispersion effect, an indication of a very small density of interfacial traps (estimated at 2·10¹⁰ eV⁻¹cm⁻² by the conductance method). In parallel, Raman spectroscopy measurements (Figure 2) indicate strain preservation under the high thermal budget conditions of the oxynitridation process.

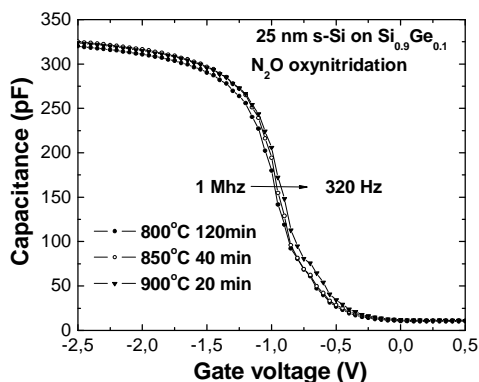


Figure 1: C-V characteristics of a s-Si MOS structure with 4 nm SiO₂ and 25 nm s-Si overlayer on relaxed Si_{0.9}Ge_{0.1}

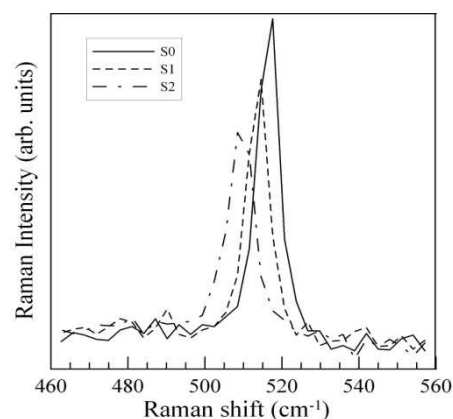


Figure 2: Raman shifts of s-Si/Si_{0.9}Ge_{0.1} (S1) and s-Si/Si_{0.78}Ge_{0.22} (S2) MOS structures with equal oxide thickness (4 nm). The s-Si overlayer is 25 and 11 nm respectively. Oxidation was performed at 900°C for 20 min. Raman spectrum of reference bulk Si (S0) is also included.

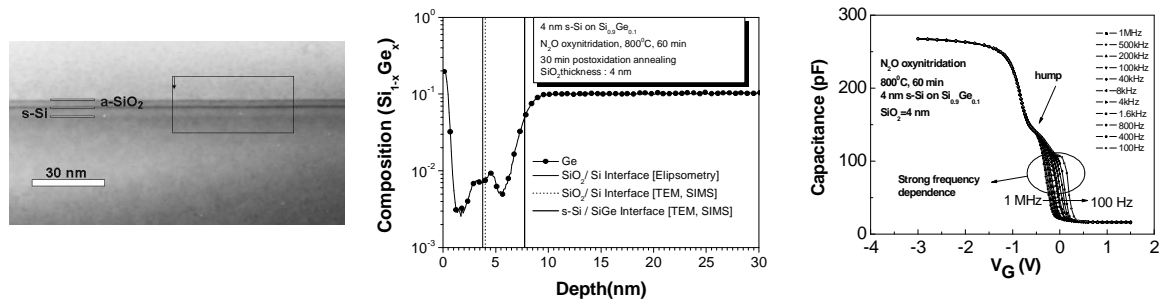


Figure 3: Ge distribution and C-V characteristics of a s-Si MOS structure with 4 nm SiO_2 and 4 nm s-Si overlayer on relaxed $\text{Si}_{0.9}\text{Ge}_{0.1}$

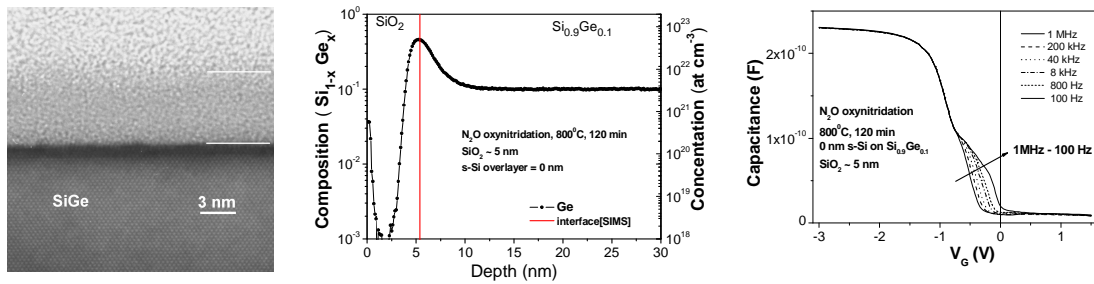


Figure 4: Ge distribution and C-V characteristics of a MOS structure with 5 nm SiO_2 and no s-Si overlayer on relaxed $\text{Si}_{0.9}\text{Ge}_{0.1}$

When the s-Si overlayer is reduced below 5 nm (Figure 3) Ge diffusion from the $\text{Si}_{1-x}\text{Ge}_x$ layer and segregation at the $\text{SiO}_2/\text{s-Si}$ interface takes place. In this case, the C-V measurements show a characteristic hump in the depletion and weak inversion regions and a significant frequency dispersion effect in the region of the hump, an indication of high density of interface traps. For this structure, the density of interface traps is estimated at approx. $1 \times 10^{12} \text{ eV}^{-1} \text{ cm}^{-2}$ using conductance over frequency measurements. Fixed oxide charge density is estimated at $4.3 \times 10^{11} \text{ cm}^{-2}$.

When the s-Si overlayer is eliminated, through over-etching and prolonged oxynitridation processes, a strong Ge pile-up at the $\text{SiO}_2/\text{Si}_{1-x}\text{Ge}_x$ interface takes place (Figure 4). C-V measurements show that the characteristic hump and frequency dispersion effects weaken. For the structure of Figure 4, the density of interface traps is estimated at $5.9 \times 10^{11} \text{ eV}^{-1} \text{ cm}^{-2}$ and fixed oxide charge density is estimated at $1.3 \times 10^{12} \text{ cm}^{-2}$.

Examining the effect of s-Si thickness, we observe an increased interface trap and fixed oxide charge density when the initial s-Si overlayer is decreased. This is generally attributed to the Ge diffusion and pile-up at the s-Si/ SiO_2 interface [1]. In contrast, when eliminating the s-Si overlayer, the interface trap density is significantly reduced, although the Ge pile-up phenomenon is strong. Thus, the higher interface trap density of the samples with less than 5 nm s-Si overlayer compared to those with no s-Si overlayer, originates from defects at or near the s-Si/ $\text{Si}_{1-x}\text{Ge}_x$ interface. Since both interfaces are only a few nanometres apart, they both contribute to the density of interface traps. When the s-Si overlayer is removed through over-etching and prolonged oxynitridation processes, a Ge-rich Silicon area is formed instead of an abrupt and well-defined hetero-interface, resulting in the reduction of frequency dispersion phenomena and in less apparent density of interface traps. Similar results are obtained for S2 substrates.

These results clearly indicate that the two existing interfaces of the strained-Si layer, $\text{SiO}_2/\text{s-Si}$ and s-Si/ $\text{Si}_{1-x}\text{Ge}_x$, contribute in parallel to the measured interface trap density of ultrathin s-Si layers. In addition, the buried strained-Si/ $\text{Si}_{1-x}\text{Ge}_x$ interface constitutes a major source of the high density of interface traps measured.

[1] G.K.Dalapati, S.Chattopadhyay, K.S.K.Kwa, S.H.Olsen, Y.L.Tsang, R.Agaiby, A.G.O'Neil, P.Dobrosz and S.J.Bull, IEEE Trans.El.Dev., 53(5), p.1142,(2006).

[2] L.K. Bera, S.Mathew, N. Balasubramanian, C. Leitz, G. Braithwaite, F. Singaporewala, J. Yap, J. Carlin, T. Langdo, T. Lochtefeld, M. Currie, R. Hammond, J. Fiorenza, H. Badawi, M. Bulsara, Thin Solid Films, 462-463, p. 85- 89, (2004).

[3] E. P. Gusev, H.- C. Lu, E. L. Garfunkel, T. Gustafsson, M. L. Green, IBM J. Res. Develop., 43(3), p.265, (1999).

Polar and semipolar GaN/AlN nanostructures for optoelectronic applications

E. Monroy^{1*}, P. K. Kandaswamy¹, L. Lahourcade¹, A. Wirthmüller¹, M. Tchernycheva², F. H. Julien², Th. Kehagias³, G. P. Dimitrakopoulos³, Ph. Komninou³, P. Ruterana⁴, and M. Eickhoff⁵

¹ CEA-Grenoble, INAC/SP2M/NPSC, 17 rue des Martyrs, 38054 Grenoble, France

² Institut d'Electronique Fondamentale, UMR CNRS 8622, University Paris-Sud XI, 91405 Orsay, France

³ Department of Physics, Aristotle University, GR 54124 Thessaloniki, Greece

⁴ CIMAP, UMR6252, CNRS-ENSICAEN-CEA-UCBN, 6 Boulevard du Maréchal Juin, 14050 Caen, France

⁵ I. Physikalisches Institut, Justus-Liebig-Universitaet Giessen, 35392 Giessen, Germany

*eva.monroy@cea.fr

III-nitride semiconductors are currently the materials of choice for optoelectronic devices in the green to UV spectral region. GaN and AlN are binary compound semiconductors with wurtzite crystallographic structure and direct band gap of 3.4 eV and 6.2 eV, respectively. The huge carrier confinement in GaN/AlN nanostructures, with a conduction band offset ~ 1.8 eV, makes them particularly interesting for the study of quantum phenomena at high temperatures. Furthermore, their thermal and chemical stability open the way to applications in harsh environments or under extreme operation conditions.

Due to the strong carrier confinement, GaN quantum dots (QDs) embedded in an AlN matrix can act as efficient ultraviolet/visible light sources at room temperature and above. The promise of low-threshold lasers, high-temperature generation of entangled photons for quantum cryptography, or coherent manipulation of a quantum bit for quantum information processing has launched the research on GaN/AlN QDs. Moreover, such nanostructures present interesting features for the development of novel opto-chemical transducers [1], taking advantage of the transparency of the substrate, the material stability in harsh atmospheres and the spontaneous sensitivity of the surface Fermi level to the ambient chemistry – which can be additionally enhanced or functionalized. In these devices gas interaction with a catalytic metal or by direct contact to an electrolyte solution results in a chemically-induced external electric field generated by.

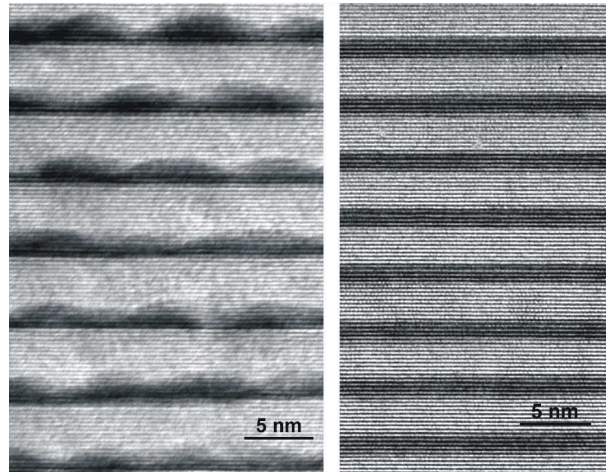


Fig. 1: High-resolution transmission electron microscopy images of (0001)-oriented GaN/AlN QD (left) and QW (right) superlattices.

On the other hand, thanks to their large conduction band offset, GaN/AlN heterostructures in the form of quantum wells (QWs) [2] or QDs [3] are excellent candidates for high-speed unipolar devices operating at optical-fiber telecommunication wavelengths, and relying on the quantum confinement of electrons. A specific advantage of III-nitrides is their extremely short intersubband (ISB) absorption recovery times (~ 200 fs) due to the strong Frölich interaction in these materials, which opens the way for devices operating in the 0.1-1 Tbit/s bit-rate regime. Furthermore, the remote lateral valleys lie very high in energy (>2 eV above the \square valley), which is a key feature to achieve ISB lasing. Additionally, devices would profit from other advantages of nitride technology, such as high power handling capabilities and chemical and thermal robustness. However, due to the rather large electron effective mass of GaN ($m^* = 0.2m_0$), QWs as thin as 1-1.5 nm are required to achieve ISB absorption at 1.3-1.55 μm .

In order to understand the electronic properties of the GaN/AlN system, it is crucial to keep in mind the presence of spontaneous polarization, which arises from the lack of symmetry of the wurtzite crystalline structure. The high piezoelectric constants, combined with a lattice mismatch of 2.5%, result in an additional polarization contribution, apart from setting a strain-engineering challenge for the grower and device designer. Therefore, GaN/AlN heterostructures grown along the c axis present a polarization-induced internal electric field of several MV/cm, which red shifts the luminescence lines and reduces the radiative recombination efficiency. An approach to palliate polarization effects is the use of nonpolar crystallographic orientations, with the c -axis perpendicular to the growth direction (a - or m -planes). However, nitride growth along nonpolar axis is hard to

control because of the strong anisotropy of the surface properties. An alternative to decrease the quantum confined Stark effect is the use of semipolar planes, with the c -axis forming an angle different from 0° or 90° with the growth direction.

Plasma-assisted molecular-beam epitaxy (PAMBE) is the most suitable growth technique for the synthesis of GaN/AlN nanostructures due to the low growth temperature, which hinders GaN-AlN interdiffusion. Furthermore, *in situ* monitoring of the surface morphology by reflection high energy electron diffraction (RHEED) makes it possible to control the growth at the atomic layer scale. As a function of the substrate (either c - or m -sapphire), it is possible to activate the growth of (0001)- or (11-22)-oriented nitride materials. Moreover, PAMBE deposition of GaN on AlN can follow the Frank-Van der Merwe or the Stranski-Krastanow growth mode by the proper tuning of the growth parameters. Therefore, PAMBE growth of polar and semipolar GaN/AlN QWs [2,4] and QDs [3,5] with controlled nanometer dimensions and atomically abrupt interfaces has been demonstrated.

In this talk, we will summarize the latest achievements in terms of PAMBE growth and characterization of polar and (11-22)-oriented semipolar GaN/AlN QW and QD superlattices for the fabrication of opto-chemical transducers as well as unipolar devices such as QW or QD infrared photodetectors (QWIPs or QDIPs). We will discuss the structural and optical properties of these nanostructures, as well as the effect of 1-dimensional or 3-dimensional confinement, the internal electric field and various growth and design parameters on the device performance.

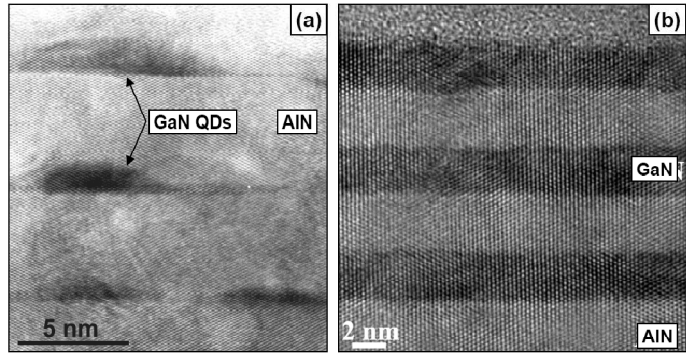


Fig. 2: High-resolution transmission electron microscopy images of (11-22)-oriented semipolar GaN/AlN QD (left) and QW (right) superlattices.

- [1] O. Weidemann, P. K. Kandaswamy, E. Monroy, G. Jegert, M. Stutzmann, and M. Eickhoff, *Appl. Phys. Lett.* 94, 113108 (2009).
- [2] P. K. Kandaswamy, F. Guillot, E. Bellet-Amalric, E. Monroy, L. Nevou, M. Tchernycheva, A. Michon, F. H. Julien, E. Baumann, F. R. Giorgetta, D. Hofstetter, T. Remmele, M. Albrecht, S. Bilner, and Le Si Dang, *J. Appl. Phys.* 104, 093501 (2008).
- [3] F. Guillot, E. Bellet-Amalric, E. Monroy, M. Tchernycheva, L. Nevou, L. Doyennette, F. H. Julien, Le Si Dang, T. Remmele, M. Albrecht, T. Shibata, and M. Tanaka, *J. Appl. Phys.* 100, 044326 (2006).
- [4] L. Lahourcade, P. K. Kandaswamy, J. Renard, P. Ruterana, H. Machhadani, M. Tchernycheva, F. H. Julien, B. Gayral, and E. Monroy, *Appl. Phys. Lett.* 93, 111906 (2008).
- [5] L. Lahourcade, S. Valdueza-Felip, T. Kehagias, G. P. Dimitrakopoulos, P. Komninou, and E. Monroy, *Appl. Phys. Lett.* 94, 111901 (2009).

Acknowledgments: This work is supported by the European Commission within the 7th European Framework Projects DOTSENSE (#224212) and UNITRIDE (#233950), and by the French National Research Agency Projects COSNI (ANR-08-BLAN-0298) and TRANSNIT (ANR-06-BLAN-0130).

Stabilization of a very high-k tetragonal phase in Ge-doped ZrO₂ films grown by direct doping with Germanium

S.F. Galata^{1*}, D. Tsoutsou¹, G. Apostolopoulos², P. Tsipas¹, A. Sotiropoulos¹, G. Mavrou¹, Y. Panayiotatos¹ and A. Dimoulas¹

¹MBE Laboratory, Institute of Materials Science, NCSR DEMOKRITOS, 15310, Athens Greece

²Institute of Nuclear Technology and Radiation Protection, NCSR DEMOKRITOS, 15310, Athens, Greece

*sgalata@ims.demokritos.gr

1. Introduction

High-k oxides are good candidates for the replacement of SiO₂ at CMOS devices since there is a great demand for downscaling. ZrO₂ (zirconia) is a promising dielectric because it has good electrical properties and can withstand transistor processing. Zirconia has the following three low-pressure structural phases, monoclinic P2₁/c, cubic Fm3m and tetragonal P4₂/mmc. From these three phases, the tetragonal phase exhibits the higher k value (k~47) after theoretical calculations [1]. Therefore the idea is to stabilize the higher-k tetragonal phase in ZrO₂ without reducing band offsets, which is beneficial for gate leakage [2].

We have recently reported the stabilization of the tetragonal ZrO₂ phase in ZrO₂/GeO₂/Ge stacks grown by molecular beam epitaxy [3]. This was done during the deposition process where an unintentional finite GeO₂ decomposition takes place followed by the incorporation of Ge into the growing ZrO₂ layer which subsequently stabilizes the tetragonal zirconia phase. In this paper we show that by intentionally incorporating Ge into ZrO₂ films grown on SiON/Si substrates at very low temperatures (225 °C) and low Ge contents of a few at. %, a high-k tetragonal zirconia phase is stabilized. This tetragonal phase remains stable after post deposition N₂ annealing up to 1050 °C.

2. Experimental details

We have deposited thin Ge-doped ZrO₂ films on SiON/pSi substrates by atomic oxygen beam deposition at 225 °C. Ge was evaporated at the same time as Zr during ZrO₂ growth. The Ge atomic fraction x (x=Ge/[Ge+Zr] at. %) was estimated from Rutherford back scattering (RBS) measurements in the range of 3-19.3 at. %. The thickness of Ge-doped ZrO₂ was estimated by x-ray reflectivity (XRR) measurements at ~20 nm. X-ray diffraction (XRD) and grazing incidence XRD (GIXRD) measurements were performed in order to record data for crystallographic phase analysis. Metal-insulator-semiconductor (MIS) capacitor structures were fabricated using shadow mask and Pt deposition. Post deposition annealing at N₂ ambient up to 1050 °C and at forming gas (N₂: 95%, H₂: 5%) ambient up to 450 °C was performed. Finally, electrical measurements such as capacitance-voltage (C-V) were done in order to study the electrical properties of the MIS capacitors.

3. Results and Discussion

Figure 1 shows GIXRD spectra for Ge-doped ZrO₂ films grown at T_g=225 °C on SiON/pSi substrates at Ge concentrations ranging from 0 up to 19.3 at. %. It is clearly shown at the diffraction pattern that from the undoped ZrO₂ (x=0 at. %) which appears to be a mixture of the monoclinic and tetragonal phase, there is a phase transformation into the pure tetragonal phase for the Ge doped ZrO₂ (x=3 up to 6.2 at. %) [4]. The tetragonal phase is the dominant one up to x=6.2 Ge at. %. This is also indicated by the enhancement of the distortion ratio $c/\sqrt{2}a$ (Table 1) and by the shift of the dominant tetragonal (001) reflection to higher diffraction angles (Figs 1(b)-1(d)). For higher Ge doping (x=19.3 at. %) the structure of ZrO₂ becomes amorphous. Fig. 2 depicts the effect of the post deposition annealing temperature to the tetragonal zirconia phase. As shown at the XRD data of a 6.2 Ge at. % doped ZrO₂ film, the tetragonal dominant phase is stable and is retained up to 1050 °C N₂ anneal.

The capacitance-voltage (C-V) characteristics of a 6.2 at. % Ge doped ZrO₂/SiON/pSi MIS capacitor after forming gas anneal is illustrated in Fig. 3 taking into account the R_s correction (R_s=270 Ω) [5]. It is observed that the CV characteristics of the capacitor are close to ideal in terms of hysteresis, frequency dispersion in accumulation and stretch-out. This allows for an estimation of the equivalent oxide thickness (EOT) and k value using MISFIT model [5] taking into account a nominal thickness for SiON IL of 1.5 nm. Fig. 5 presents the variation of k value of a Ge doped ZrO₂ capacitor with respect to the Ge at. % concentration. It is observed that the k value increases as the tetragonal zirconia phase increases having a maximum value of 37.7 for x=6.2 Ge at. %. These data are in agreement with the results presented in Fig. 1. A summary of the structural and electrical characteristics of the as-deposited Ge-doped ZrO₂/SiON/Si stacks is presented in Table 1.

4. Conclusions

We have demonstrated that by incorporating Ge into ZrO_2 films on SiON/Si substrates at low deposition temperature (225°C), the ZrO_2 tetragonal phase stabilizes and remains stable after post deposition N_2 anneal up to 1050°C . This leads to a k value enhancement of the stacks obtaining a maximum k value of 37.7 for a 6.2 at. % Ge doped ZrO_2 film on SiON/Si substrates.

References

- [1] Zhao X and Vanderbilt D., Phys Rev B 65, 075105 (2002).
- [2] Robertson J., J Appl Phys 104, 124111 (2008).
- [3] Tsipas P., Volkos S.N., Sotiropoulos A., Galata S., Mavrou G., Tsoutsou D., Panayiotatos Y., Dimoulas A., Machiori C., Pompeyrine J., Appl Phys Lett 93, 212904 (2008).
- [4] Powder Diffraction File (PDF) Database: Card Nos. 37-1484 monoclinic ZrO_2 and 50-1089 for tetragonal ZrO_2 .
- [5] Apostolopoulos G., Vellianitis G., Dimoulas A. Hooker J.C., and Conard T., Appl Phys Lett 8, 260 (2004).

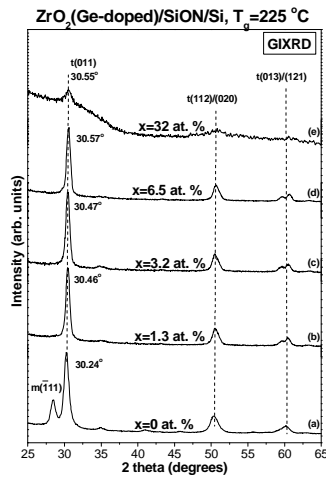


Fig. 1 GIXRD patterns for as-deposited Ge-doped ZrO_2 films deposited on SiON/Si substrate grown at 225°C with respect to Ge content (x). The nominal ZrO_2 thickness is 20 nm. The monoclinic (m) and tetragonal (t) phases are shown in (a) for $x=0$ at. %, whereas the tetragonal (t) is shown in (b)-(d) for $x=3-6.2$ at. %. In (e) ZrO_2 structure becomes amorphous.

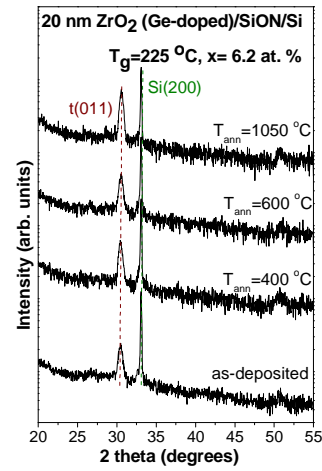


Fig. 2 XRD spectra of a 6.2 at. % Ge doped ZrO_2 film deposited on SiON/Si substrate grown at 225°C with respect to the post deposition annealing temperature.

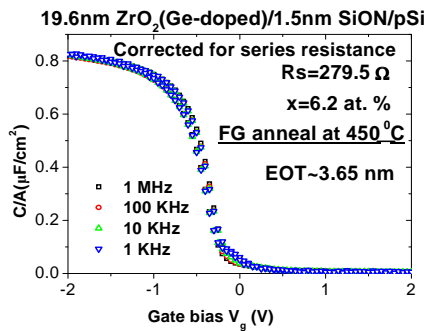


Fig. 3 C-V characteristics of a Ge doped (6.2 at. %) ZrO_2 /SiON/Si stack after FG anneal at 450°C .

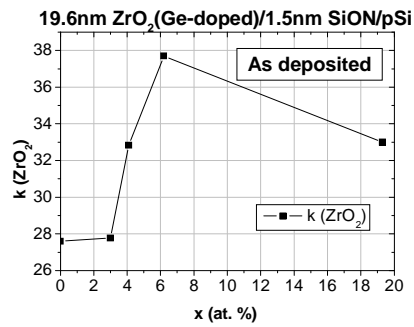


Fig. 4 k value of ZrO_2 as a function of Ge concentration (x) in as-deposited ZrO_2 films.

Table 1 Summary of the crystallographic phases, $c/\sqrt{2}a$ ratio and k values for the samples studied in Fig. 1. ($c/\sqrt{2}a=1$ for the cubic ZrO_2 structure).

Ge content (at. %)	Crystal structure	$c/\sqrt{2}a$ - t- ZrO_2	k
0	t+m ZrO_2	1.01239	27.6
3	t ZrO_2	1.01902	27.8
4.1	t ZrO_2	1.0209	32.8
6.2	t ZrO_2	1.02177	37.7
9.3	amorphous		33

Electrochromic Devices Based On Electrodeposited WO₃ Films With Modified Surface Morphology.

G. Leftheriotis^{1*} and P. Yianoulis¹

¹ Energy and Environment Lab, Physics Department, University of Patras, Rion, 29500, Greece

*glefther@physics.upatras.gr

Tungsten oxide is a well known material with electrochromic properties, suitable for application in switchable electrochromic glazing for solar control in buildings, large area displays and gas sensors [1]. It can be deposited in the form of a thin film with use of various methods, such as vacuum techniques (thermal evaporation, electron beam gun deposition and sputtering) and with chemical methods (sol-gel deposition, spin coating, spray pyrolysis and electrodeposition) [1, 2]. Of these, electrodeposition is a straightforward technique that does not involve the application of complicated and expensive instrumentation (required in the case of vacuum methods) and that can be readily upgraded to coat large areas at high throughput. Furthermore, it permits the exact control of the film thickness and is suitable for the fabrication of composite films that incorporate two (or more) compounds, such as WO₃ – CeO₂, WO₃ – TiO₂, etc [3].

The surface morphology and microstructure of WO₃ films determines their electrochromic performance. Films that possess an 'open' structure, caused by high porosity or by extensive grain boundaries, are more suitable to function as electrochromics since their form facilitates the intercalation of metal ions responsible for coloration [4, 5]. Different methods yield films with different morphologies and structure. With electrodeposited films, a variety of morphologies and microstructures can be obtained by variation of the starting materials, the solution chemistry [6], by alterations in the applied voltage or current [7] and by post deposition thermal treatment [8].

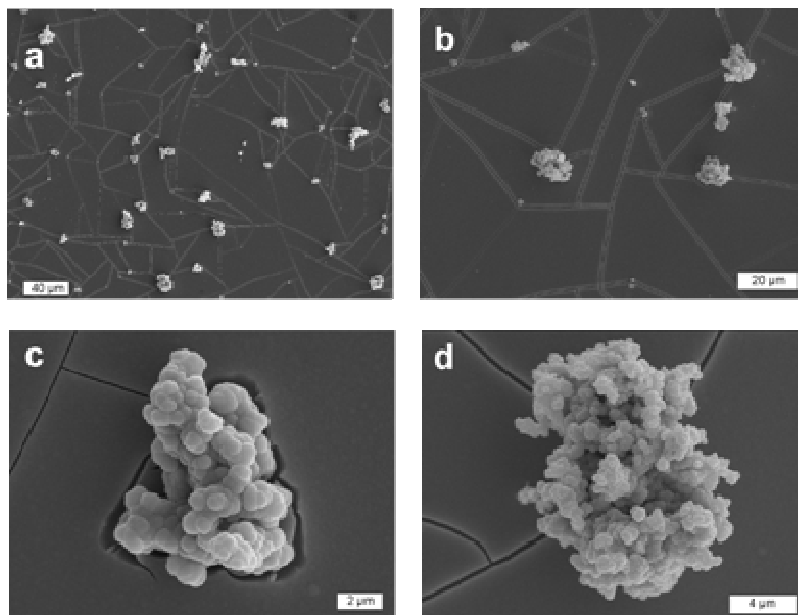


Fig. 1. Scanning Electron Microscopy (SEM) photographs of a WO₃ film electrodeposited 48 hours after the precursor formation

In the present study, we propose a very simple method for the alteration of the surface morphology of electrodeposited WO₃ films. Evidence is presented that the peroxotungstic acid precursor (synthesized in a similar way to that presented in [9]), tends to conglomerate within its solution. If enough time is allowed before film deposition (typically 48 hours), large conglomerates are formed, that possess a grape-like structure. During electrodeposition, these arrive on the substrate surface and are incorporated into the resulting WO₃ film that is being developed, as shown in Fig 1. This phenomenon can be used advantageously in order to modify the resulting WO₃ film morphology: Films with such conglomerates incorporated into their structure have a high effective surface area, improved ion mobility and enhanced electrochromic properties.

The above principle has been applied for the electrodeposition of WO_3 films 48 hours after the precursor formation. They exhibit modified morphology (as shown in Fig.1), with typical thickness of **1.300 nm** and Li ion diffusion coefficient as high as $4.5 \times 10^{-10} \text{ cm}^2/\text{s}$, which is more than an order of magnitude larger than that of typical evaporated tungsten oxide films [1, 10]. These films exhibit promising electrochromic coloration properties: In Fig. 2, cyclic voltammetry (CV) plots of two WO_3 films appear, one deposited immediately after the solution synthesis and another deposited 48 hours later. It becomes evident from a comparison of the two plots that the latter film performs best, as it exhibits a larger negative (coloration) current (up to $-1.3 \text{ mA}/\text{cm}^2$). Furthermore, the area of the cyclic voltammogram which is a measure of the charge intercalated into the film [10, 11], is larger for the latter film.

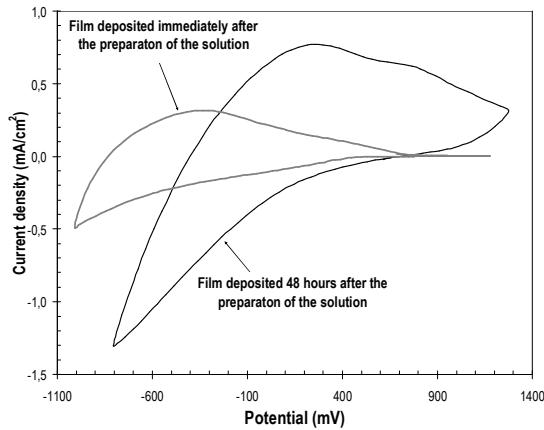


Fig.2: CV plots of electrodeposited WO_3 films

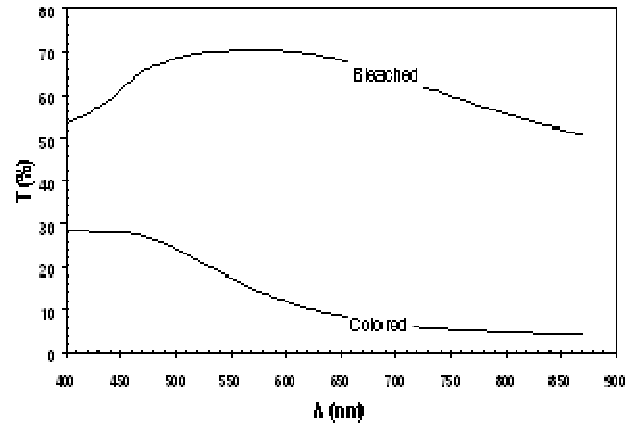


Fig. 3: Transmittance (T) spectra for the coloration of an EC device with an electrodeposited WO_3 film

Electrochromic (EC) devices incorporating the electrodeposited WO_3 films of the form K-glass/ WO_3 /1M LiClO_4 -PC (liquid electrolyte)/K-glass were fabricated in the following manner: Two K-glass sheets (a plain one and one with the tungsten oxide film) were arranged facing each-other, slightly displaced along their longitudinal axis in order to reserve space for the formation of electrical contacts. A cavity was formed between the two glass sheets with use of silicone. The cavity was filled with the liquid electrolyte and sealed with silicone. Electrical receptacles were created on both glass sheets with use of copper adhesive tape. As can be seen in Fig. 3, the increased surface roughness of the WO_3 films does not impede the optical properties of the device. Indeed, in the bleached state the device appears significantly transparent ($T=70\%$ at 550 nm). As it becomes progressively colored, ($T=17\%$ at 550 nm) a satisfactory contrast ratio is achieved. The fabricated devices are stable and can withstand several hundreds of coloration- bleaching cycles with no evident degradation of their performance.

- [1] C.G. Granqvist, Handbook of Inorganic Electrochromic Materials, Elsevier Science, Amsterdam, 1995.
- [2] S. R. Bathe, P. S. Patil, Solar Energy Materials & Solar Cells 91 (2007) 1097–1101.
- [3] Th. Pauporte et. al. Journal of Physics and Chemistry of Solids 64 (2003) 1737–1742.
- [4] B. Yang, H. Li, M. Blackford, V. Luca, Current Applied Physics 6 (2006) 436–439.
- [5] Q. Zhong and K. Colbow, Thin Solid Films, 205 (1991) 85–88.
- [6] J. Livage and D. Ganguli, Solar Energy Materials & Solar Cells 98 (2001) 365–381.
- [7] M. Deepa, A.K. Srivastava, S.N. Sharma, Govind, S.M. Shivaprasad, Applied Surface Science 254 (2008) 2342–2352.
- [8] A.K. Srivastava, M. Deepa, S. Singh, R. Kishore, S.A. Agnihotry, Solid State Ionics 176 (2005) 1161–1168.
- [9] M. Deepa, A.K. Srivastava, T.K. Saxena, S.A. Agnihotry, Applied Surface Science 252 (2005) 1598–1580.
- [10] S. Papaefthimiou, G. Leftheriotis, P. Yianoulis, Solid State Ionics 139 (2001) 135–144.
- [11] G. Leftheriotis, S. Papaefthimiou, P. Yianoulis, A. Siokou, D. Kefalas, Applied Surface Science 218 (2003) 275–280.

Ultrafast Control of Nuclear Spins Using Only Microwave Pulses: Towards Switchable Solid State Gates for Quantum Information Processing

G. Mitrikas*, Y. Sanakis, G. Papavassiliou

Institute of Materials Science, NCSR 'Demokritos', Agia Paraskevi Attikis, 15310 Athens, Greece

*mitrikas@ims.demokritos.gr

Since the idea of quantum information processing (QIP) fascinated the scientific community [1-3], electron and nuclear spins have been regarded as promising candidates for quantum bits (qubits) [4] because they are natural two-state systems and decoherence times for the spin degree of freedom are usually larger than for charge degrees of freedom. Indeed, nuclear magnetic resonance (NMR) in liquid state was the first spectroscopic technique used to demonstrate quantum computation algorithms such as Deutsch, Grover and Shor algorithms [5]. However, when a large number of qubits is required, the bulk NMR method suffers from sensitivity problems because of the small nuclear Zeeman energy compared to the thermal energy kT even at extremely low temperatures ($T \ll 1$ K) [6]. These scalability limitations can be overcome by using electron paramagnetic resonance (EPR) spectroscopy because in this case pure states are experimentally accessible with current technology. In addition, due to their larger relaxation rates, electron spins can result in higher clock rates (GHz) compared to the low nuclear spin transition frequencies (MHz).

A fundamental challenge in the realization of a solid state quantum computer is the construction of fast and reliable two-qubit quantum gates. Of particular interest in this direction are hybrid systems of electron and nuclear spins, where the two qubits are coupled through the hyperfine interaction. However, the significantly different gyromagnetic ratios γ of electron and nuclear spins do not allow for their coherent manipulation at the same time scale. Here we demonstrate the control of the α -proton nuclear spin, $I=1/2$, coupled to the stable radical $\cdot\text{CH}(\text{COOH})_2$, $S=1/2$, in a γ -irradiated malonic acid single crystal, using only microwave (mw) pulses. We show that, depending on the state of the electron spin ($m_S=\pm 1/2$), the nuclear spin can be locked in a desired state or oscillate between $m_I=+1/2$ and $m_I=-1/2$ on the nanosecond time scale. We believe that this procedure is important for QIP technologies because it provides a fast and efficient way of controlling nuclear spin qubits, and also enables the design of spin-based quantum gates by addressing only the electron spin.

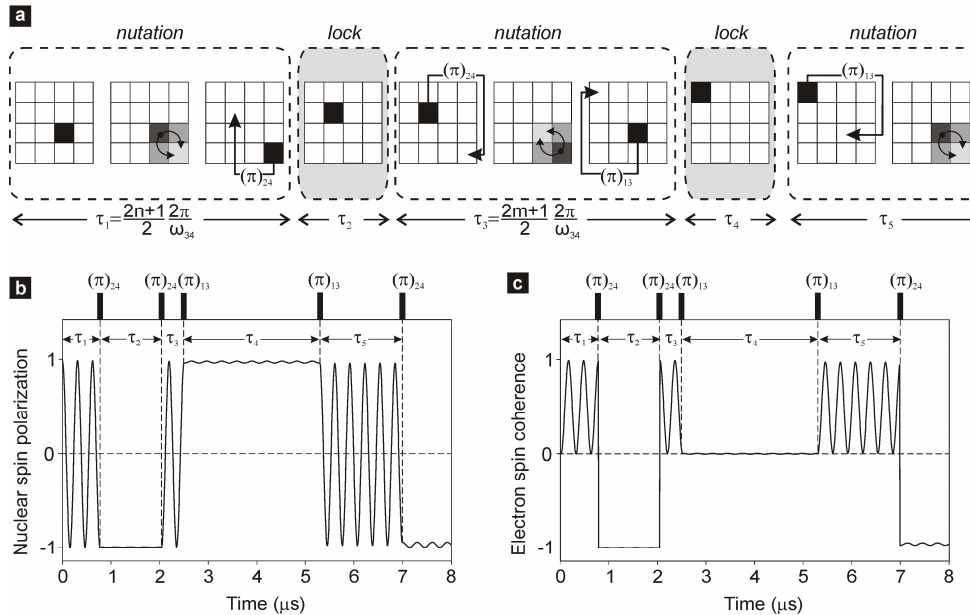


Figure 1: Manipulation of the proton nuclear spin solely by using mw pulses for the case of exact cancellation. (a) Representation of the density matrix in the product basis $|\alpha\alpha\rangle, |\alpha\beta\rangle, |\beta\alpha\rangle, |\beta\beta\rangle$ during nutation or locking time periods. (b) Numerical simulation of the nuclear spin polarization $\langle I_z \rangle$ during the applied pulse sequence that uses semi-selective mw π -pulses (shown at the top). (c) Corresponding numerical simulation of the electron spin coherence $\langle S_x \rangle$ after the detection pulse sequence $(\pi/2)_{2324} - \tau - (\pi)_{2324} - \tau$ with $\tau = 2\pi/\omega_{34} = 310$ ns.

- [1] Deutsch, D., Quantum-Theory, the Church-Turing Principle and the Universal Quantum Computer. Proceedings of the Royal Society of London Series a-Mathematical Physical and Engineering Sciences 400, 97-117 (1985).
- [2] Deutsch, D. and Jozsa, R., Rapid Solution of Problems by Quantum Computation. Proceedings of the Royal Society of London Series a-Mathematical Physical and Engineering Sciences 439, 553-558 (1992).
- [3] Bennett, C. H. and DiVincenzo, D. P., Quantum information and computation. Nature 404, 247-255 (2000).
- [4] Mehring, M., Mende, J., and Scherer, W., in Novel NMR and EPR techniques (2006), pp. 87-113.
- [5] Heidebrecht, A., Mende, J., and Mehring, M., Quantum state engineering with spins. Fortschritte Phys.-Prog. Phys. 54, 788-803 (2006).
- [6] Warren, W. S., The usefulness of NMR quantum computing. Science 277, 1688-1689 (1997).

Session MO4

ELECTRONIC TRANSPORT

SEMICONDUCTORS

& DEVICES

*PHOTONICS &
OPTOELECTRONICS*

PART 2

Monday, 21 September 2009, 17⁰⁰-18⁴⁵



Manipulating Light with Optical Left-Handed Metamaterials

M. Kafesaki^{1,2,*}, R. Penci¹, Th. Koschny^{1,3}, J. Zhou³, E.N. Economou^{1,4}, C.M. Soukoulis^{1,2,3}

¹Foundation for Research and Technology Hellas (FORTH), Institute of Electronic Structure and Laser (IESL), P.O. Box 1385, 71110 Heraklion, Crete, Greece

²University of Crete, Department of Materials Science and Technology, Heraklion Crete, Greece

³Iowa State University – Ames Lab and Physics Department, Ames, Iowa, USA

⁴University of Crete, Department of Physics, Crete, Greece

* kafesaki@iesl.forth.gr

Left-handed metamaterials (LHMs), i.e. artificial composite structures with simultaneously negative electrical permittivity and magnetic permeability, giving rise to negative index of refraction, have attracted great attention in the last decade. This is due to the novel and unique properties of those materials, such like backwards propagation (i.e. opposite phase and energy velocity), negative refraction, reversed Doppler effect and Cerenkov radiation, etc. These novel properties empower the left-handed materials with unique capabilities in the manipulation of electromagnetic waves and give the possibility to create novel electromagnetic components and devices, like sensors, antennas, waveguides, transmission lines etc. Among the main capabilities of LHMs an important one is their superlensing capability, i.e. the ability to give subwavelength resolution imaging. This ability, which was proposed first in 2000, can lead to revolutionary solutions in imaging, lithography and data storage devices.

To be able to exploit the superlensing capability of LHMs in the optical part of the electromagnetic spectrum, many efforts have been devoted recently to push the operation regime of LHMs from microwaves (where the first and most of today's metamaterials have been demonstrated) to the optical regime. Most of those efforts are based on a scaling approach, i.e. they attempt to scale down successful microwaves LHM designs. This is not a straightforward approach though, since the unique properties of today's LHMs are based on a large degree on the perfect conductor properties of the metallic components of those materials; in the optical regime metal does not behave as an almost perfect conductor like in microwaves, and the response of the electrons at the interior of the metallic structures can alter the metamaterial properties, while losses are extremely pronounced and can very easily kill the desired metamaterial response. Moreover, since the experimental demonstration of optimized optical metamaterials requires the fabrication of complicated nanoscale patterns, something difficult with the current fabrication capabilities, the optimization of advanced nanofabrication techniques or the employment of new techniques is an essential step for the achievement of optimized optical metamaterials.

Despite the above mentioned complications, there have been already demonstrated LH metamaterials operating in 100 THz, 200 THz and recently in the lower visible range [1]. These metamaterials though are in their majority monolayer structures, suffering from high losses, and thus they are not very much appropriate for imaging applications.

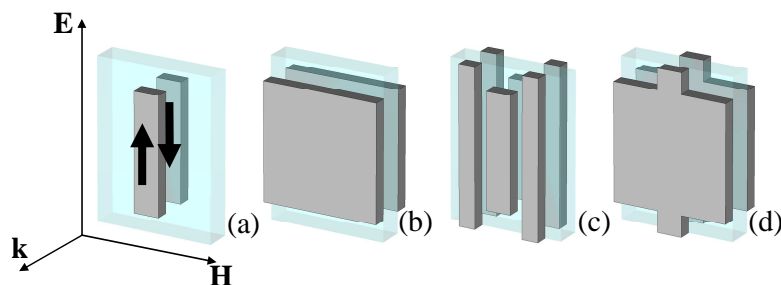


Fig. 1: The unit cell of four designs studied here. (a): Slab-pair system, which provides a resonant permeability response, owned to the resonant antiparallel current mode at the two slabs of the pair (see arrows); (b) wide-slab-pair system; (c) slabs&wires system, which provides both negative permittivity and permeability response; (d) fishnet design.

In this work, with aim to achieve optimized optical LHMs, we study the behaviour of basic metamaterial structures as they are scaled down from mm to nm scale, and we try to understand the wave propagation in those structures. The majority of the structures studied are structures of combining negative permittivity and permeability, such as the ones shown in Fig. 1(c) and 1(d), or structures of only negative permeability (Fig. 1(a) and 1(b)) (the negative permeability component of LHMs is the most difficult to be achieved component in the optical regime, as negative permittivity can be easily obtained using metals). These structures are based on pairs of short slabs, combined or not with continuous wires. The pair of slabs has been

found to exhibit a resonant current mode with antiparallel currents at the two slabs of the pair, providing a resonant magnetic moment and thus resonant permeability with negative permeability values. The continuous wires provide a plasma like response, with a reduced plasma frequency determined by the geometrical characteristics of the wire-lattice. The combination of both leads to negative refractive index behaviour. The specific combination shown in Fig. 1(d), known as fishnet structure, where the slabs are wide along the \mathbf{H} direction and are physically connected with the wires, has been proven the most successful up to now structure for the achievement of optical LHMs.

The advantage of the structures of Fig. 1, apart from their fabrication simplicity, is that they show LH response for incidence normal to the plane of the structure, allowing thus experimental demonstration of this response using only one or very few structure layers.

Detailed study of the structures of Fig. 1, and attempts of their optimization, led to two main conclusions:

- The magnetic resonance frequency of the structures, while in the mm length-scale it scales inversely proportional to the structure size, going to the sub-micron scale it saturates to a constant value (see Fig. 2). This value depends on the geometrical characteristics of the structure and can go up to the plasma frequency of the bulk metal.
- The resonant permeability response of the structures, going to smaller scales, becomes more and more weak, and ultimately ceases to reach negative values [2]. Thus, in nm scale the resonant permeability response of the structures dies out.

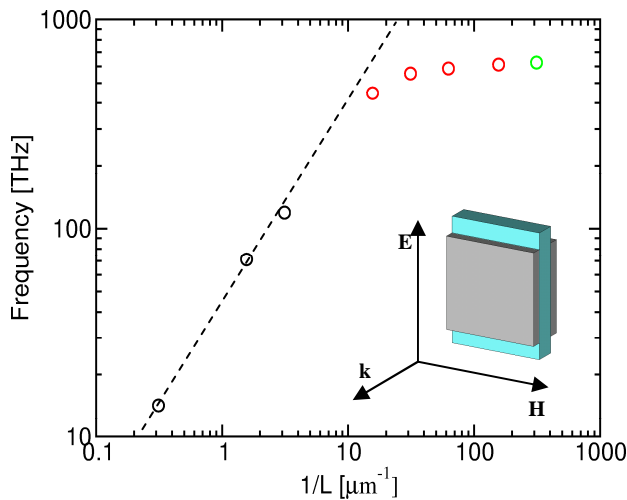


Fig. 2: Scaling and saturation of the magnetic resonance frequency of the wide short-slab pair structure (shown in inset) with the inverse of the unit cell size, L . The black circles indicate that the magnetic resonance form is affected by periodicity, the red circles indicate that the structure is subwavelength in scale, while the green circle indicates that the resonance is too weak to reach negative values for the permeability.

Detailed examination and analysis of the wave propagation in the structures of Fig. 1 showed that both the above mentioned results can be understood taking into account the dispersive properties of the metal, which lead to an inductive contribution in the metal resistance (electrons' inductance). This inductive component scales inversely proportional to the structure length scale (in contrast to the magnetic field inductance which scales proportional to the length scale) and in the submicron scales dominates the wave propagation, weakening any magnetic response of the structures. Detailed calculations, treating our structures as resonant inductor-capacitor circuits, showed that the consideration of the electron's inductance can explain both the saturation of the magnetic resonance frequency and the weakening of the permeability resonance. Moreover, these calculations led to basic design rules for achievement of optimized negative permeability and/or negative refractive index structures in the optical regime [3].

- [1] C. M. Soukoulis, S. Linden, M. Wegener, *Science* 315, 47 (2007); V. M. Shalaev, *Nature Photonics* 1, 41 (2007).
- [2] J. Zhou, Th. Koschny, M. Kafesaki, E. N. Economou, J. B. Pendry and C. M. Soukoulis, *Phys. Rev. Lett.* 95, 223902 (2005).
- [3] M. Kafesaki, R. Penciu, Th. Koschny, J. Zhou, E.N. Economou, C.M. Soukoulis, Designing optical magnetic metamaterials, to be submitted to *Phys. Rev. B*.

Coupled Plasmons and Resonant Effective Permeability of Metal-Dielectric-Metal Nanosandwich Assemblies

C. Tserkezis^{1*}, N. Stefanou¹ and N. Papanikolaou²

¹ *Section of Solid State Physics, University of Athens, Panepistimioupolis, GR-157 84 Athens, Greece*

² *Institute of Microelectronics, NCSR "Demokritos", Ag. Paraskevi, GR-153 10 Athens, Greece*

*ctserk@phys.uoa.gr

Periodic assemblies of in-tandem pairs of metallic nanodisks separated by a dielectric spacer, so-called metal-dielectric-metal nanosandwiches, constitute a novel class of photonic metamaterials with intriguing optical properties. When two metallic nanodisks are brought into strong coupling in a sandwich-like configuration, plasmon hybridization results into a symmetric resonant mode, with the dipole moments of the nanodisks oscillating in phase, and an antisymmetric resonant mode, with the dipole moments oscillating with opposite phase. While the symmetric resonance has an electric dipolar character, the antisymmetric one is associated with a loop-like current in the nanodisk pair and thus a dipole magnetic moment [1]. Two- and three-dimensional structures of such photonic metamolecules may exhibit a negative effective permeability in the region of the antisymmetric resonance, at visible and near-infrared frequencies [2], which is an essential ingredient in the design of negative-index metamaterials. Compared to pairs of rods or of cut-wires, the optical behavior of disk pairs is more isotropic because the latter are invariant under rotation about their axis. It is worth noting that, contrary to the formation of bonding and antibonding electron orbitals in diatomic molecules, in a metal-dielectric-metal nanosandwich, the low-frequency hybrid plasmonic mode is antisymmetric and the high-frequency one is symmetric. This apparently counter-intuitive situation can be understood as follows. Charge oscillations associated with an electric-dipole plasmon mode in a single metallic nanodisk are sustained by restoring forces acting on the collectively displaced conduction-band electrons. In an in-tandem pair of such nanodisks, charge distribution leads to reduction of the appearing restoring forces in the configuration of the antisymmetric mode and enhancement in the case of the symmetric mode. Consequently, the eigenfrequency of the antisymmetric mode is lowered and that of the symmetric mode is raised, as shown schematically in Fig. 1. The situation is reversed if the two nanodisks are on the same plane.

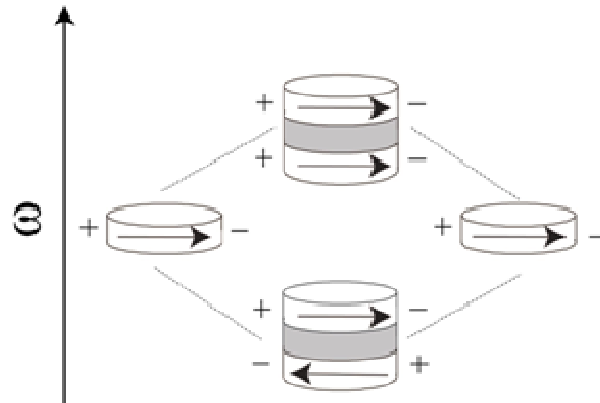


Fig.1. A schematic description of plasmon hybridization in a metal-dielectric-metal nanosandwich.

In the present communication, we report on the effective magnetic permeability of two- and three-dimensional periodic structures of metal-dielectric-metal nanosandwiches by means of full electrodynamic calculations using the extended layer-multiple-scattering method [3]. This method provides a versatile and efficient computational framework for fast and accurate calculations of the optical properties of complex inhomogeneous systems consisting of successive, possibly different, layers of scatterers arranged with the same two-dimensional periodicity. The properties of the individual scatterers enter only through the corresponding T matrix which, for scatterers of arbitrary shape, is calculated numerically by the extended boundary condition method. At a first step, in-plane multiple scattering is evaluated in a spherical-wave basis with the help of proper propagator functions. Subsequently, interlayer scattering is calculated in a plane-wave basis through appropriate transmission and reflection matrices. The scattering S matrix of a multilayer slab, which transforms the incident into the outgoing wave field, is obtained by combining the transmission and reflection matrices of the component layers. For a three-dimensional crystal consisting of an infinite periodic sequence of layers, Bloch theorem leads to an eigenvalue equation that gives the (complex) normal component of the Bloch wave vector, k_z , for given frequency, ω , and in-plane reduced wave vector component, \mathbf{k}_\parallel , which are (real) conserved quantities in the scattering process. The effective electromagnetic parameters of the structure, i.e., the permittivity and permeability functions of an equivalent homogeneous medium, are determined from the scattered field in the far zone by a finite slab of the structure, under plane wave illumination. At normal incidence, inverting the standard Fresnel equations, we obtain closed-form solutions for the effective refractive index, n_{eff} , and impedance, z_{eff} ,

in terms of the complex transmission and reflection coefficients (S -matrix retrieval) [2]. As the thickness of the slab increases, n_{eff} should converge to ck_z/ω (c is the velocity of light in vacuum), which is unambiguously deduced from the complex photonic band structure of the corresponding infinite crystal. The effective permittivity and permeability of the slab are given by $\epsilon_{\text{eff}} = n_{\text{eff}}/z_{\text{eff}}$ and $\mu_{\text{eff}} = n_{\text{eff}}z_{\text{eff}}$. Obviously, ϵ_{eff} and μ_{eff} do not describe the wave field inside the actual structure where, at a given frequency, it has the form of a Bloch wave rather than a simple plane wave. However, the effective parameters must be such that these two waves obey the same dispersion relation and, therefore have the same group (and phase) velocity. This remark is of course meaningful only if there is a single dominant relevant Bloch mode at the given frequency. Moreover, in order for an effective-medium description to be applicable, the wavelength in the embedding medium must be much larger than the in-plane period of the structure. This condition ensures that there is only a single propagating mode of the scattered electromagnetic field corresponding to outgoing waves (refracted and reflected beams). All other components of the wave field (diffracted beams) are evanescent.

We consider layered structures of metal-dielectric-metal nanosandwiches. In each layer, the nanosandwiches are arranged on a hexagonal lattice determined by the primitive vectors $\mathbf{a}_1 = a_0(1,0,0)$ and $\mathbf{a}_2 = a_0(1/2, \sqrt{3}/2, 0)$. We assume that the permittivity of the metallic material is described by the Drude dielectric function, $\epsilon_m = 1 - \omega_p^2 / \omega(\omega + i\gamma)$, where ω_p is the bulk plasma frequency and γ a damping factor that accounts for dissipative losses. The nanosandwiches consist of two metallic nanodisks, of radius $S = 2.5c/\omega_p$ and thickness $h_1 = h_3 = c/\omega_p$, separated by a silica spacer ($\epsilon_{\text{silica}} = 2.13$) of thickness $h_2 = 2c/\omega_p$. Therefore, $h = h_1 + h_2 + h_3 = 4c/\omega_p$ is the total thickness of the nanosandwich. The stacking sequence is defined by $\mathbf{a}_3 = (a_0/2, a_0\sqrt{3}/6, h)$. We take $a_0 = 10c/\omega_p$. In Fig. 2 we display the retrieved μ_{eff} , for slabs one-, two- and eight-layers thick, which clearly converges with increasing slab thickness and exhibits a resonant behavior about the frequency of the antisymmetric plasmon modes. It can be seen that, even assuming that the building units of the structure are non-absorptive with purely real permittivities and permeabilities, the S -matrix retrieval method leads to non-zero imaginary part for μ_{eff} (and also for ϵ_{eff} that we don't show here) in the frequency region of the resonance. However, the retrieval procedure itself ensures that the values of ϵ_{eff} and μ_{eff} are such that the absorption of each effective slab vanishes at any frequency. In some sense, it is not possible that the effective slab complies with the strong restriction to reproduce exactly the transmission and reflection coefficients of the actual metamaterial slab, with real functions $\epsilon_{\text{eff}}(\omega)$ and $\mu_{\text{eff}}(\omega)$ in the resonance region. To make this possible, one has to assume complex functions with negative $\text{Im}\epsilon_{\text{eff}}$ and positive $\text{Im}\mu_{\text{eff}}$, i.e., some fictitious dielectric gain, which counterbalances the fictitious magnetic losses. Obviously, this occurs for given slab thickness, specific characteristics of the incident field, etc. and, therefore, ϵ_{eff} and $\mu_{text{eff}}$ have not the meaning of inherent material parameters [4]. If absorptive losses in the metallic material are taken into account, the resonance structures become smoother and more extended in frequency while the region of negative permeability shrinks and almost disappears, as shown in Fig. 2.

[1] Dmitriev A., Pakizeh T., Käll M., and Sutherland D. S., *Small* 3, 294 (2007).

[2] Tserkezis C., Papanikolaou N., Gantzounis G., and Stefanou N., *Phys. Rev. B* 78, 165114 (2008).

[3] Gantzounis G. and Stefanou N., *Phys. Rev. B* 73, 035115 (2006).

[4] Efros A. L., *Phys. Rev. E* 70, 048602 (2004).

Acknowledgments This work was supported by the research programme ‘‘Kapodistrias’’ of the University of Athens.

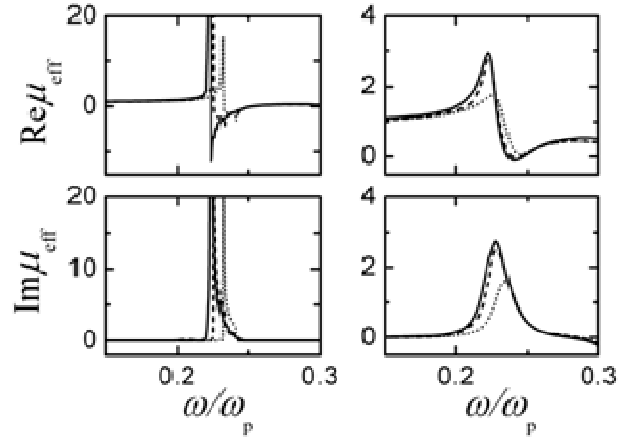


Fig. 2. Effective permeability of one- (dotted lines), two- (dashed lines) and eight- (solid lines) layers thick slabs of the structure under consideration, at normal incidence. Left: Without losses ($\gamma = 0$). Right: With losses ($\gamma = 0.025\omega_p$).

Exciton Polaritons In Resonant Bragg Gratings

F. Biancalana¹, L. Mouchliadis^{2*}, C. Creatore³, S. Osborne⁴ and W. Langbein²

¹ Max Planck Institute for the Science of Light, 91058 Erlangen, Germany

² School of Physics and Astronomy, Cardiff University, Cardiff, United Kingdom

³ Department of Physics "A. Volta", Università degli Studi di Pavia, I-27100 Pavia, Italy

⁴ Tyndall Institute "Lee Maltings", Prospect Row, Cork, Ireland

*mouchliadisl@cf.ac.uk

Photonic crystals are characterized by frequency regions where the propagation of light is suppressed, i.e. photonic bandgaps. When such a structure is resonantly coupled to a semiconductor supporting an exciton resonance, novel intragap modes arise due to the strong light-matter interaction [1].

We investigate the dispersive features of a 3D exciton resonance embedded in a 1D Bragg grating and find that the dispersion relation of the new modes resembles that of a *doublet* of microcavity polaritons [MC1 and MC2 in Fig. 1(a)]. We analyze the interaction between the electromagnetic field in the Bragg grating and the exciton-polarization wave by means of a set of *polaritonic coupled-mode equations*, properly accounting for the large nonlinear optical response of excitons [2].

Calculation of the Bragg polariton group velocity suggests that they can be used for slow-light-enhanced nonlinear propagation, while their extremely small effective mass (of the order of the cavity photon mass) renders them good candidates for the observation of macroscopic coherence phenomena in solid state systems. In analogy with MC polaritons [3], Bragg polaritons (or *Braggoritons*) exhibit an efficient mechanism for strong parametric amplification at two "magic frequencies". This is due to the existence of two inflection points in the UB and LB branches (see Fig. 1(b)). For numerical calculations we use ZnO as the excitonic material and propose a structure of alternating ZnO and ZrO₂ layers (see Fig. 1(c)).

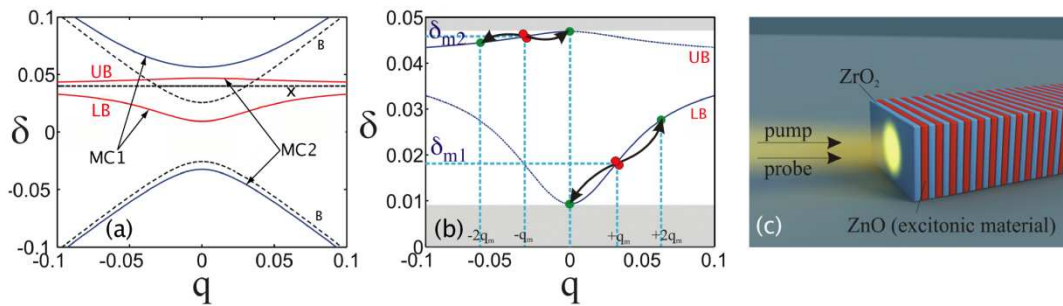


Figure 1: (a) Bragg polariton dispersion for non-zero detuning between the Bragg and exciton frequencies (dimensionless units). Dashed lines indicate the bare exciton and Bragg photon dispersions. (b) Schematics of the parametric scattering process occurring at two magic frequencies δ_{m1} and δ_{m2} . (c) Sketch of the proposed design based on a ZnO/ZrO₂ grating.

[1] A. Yu. Sivachenko, M. E. Raikh and Z. V. Vardeny, Phys. Rev. A **64**, 013809 (2001).

[2] F. Biancalana, L. Mouchliadis, C. Creatore, S. Osborne and W. Langbein, arXiv:0904.0758 (2009).

[3] P. G. Savvidis, J. J. Baumberg, R. M. Stevenson, M. S. Skolnick, D. M. Whittaker, and J. S. Roberts, Phys. Rev. Lett. **84**, 1547 (2000).

Acknowledgments Financial support from MPG, EPSRC and WIMCS is gratefully acknowledged.

Power factor enhancement in Composite Ag-Bi-Ag Planar Thin Film Thermoelectric Structures

Z. Viskadourakis^{* 1,2}, G. I. Athanasopoulos¹, and J. Giapintzakis¹

¹ *Department of Mechanical and Manufacturing Engineering, University of Cyprus,
P.O. Box 20537, Nicosia 1678, Cyprus*

² *Materials Science and Technology Department, University of Crete,
P.O. Box 2208, Heraklion Crete 710 03, Greece*

* zach@iesl.forth.gr

The electrical resistivity and the Seebeck coefficient of Ag-Bi-Ag planar thin film thermoelectric structures are measured, at room temperature, as a function of the length ratio $x=L_{Bi}/L_{tot}$, where L_{Bi} is the length of the Bi layer and L_{tot} is the total length of the structure. The contribution of the interface, formed at the Ag-Bi contact, to the resistivity, the Seebeck coefficient and the thermoelectric power factor of the composite structures is investigated. The experimental results are compared with theoretical predictions obtained by treating the structures as electrical and thermal circuit analogues. An enhancement in the thermoelectric power factor of the structures is observed in the range $0.3 < x < 0.5$. The magnitude of the enhancement is found to depend on the surface area of the Ag-Bi contact.

MO4

O13

Molecular and Polymeric Organic Semiconductors and their Applications in Plastic Optoelectronic and Photonic Devices

Leonidas C. Palilis^{1*}, Maria Vasilopoulou¹, Dimitra G. Georgiadou¹, Nikos A. Stathopoulos²,
Dimitris Davazoglou¹ and Panagiotis Argitis¹

¹ *Institute of Microelectronics, NCSR “Demokritos”, Agia Paraskevi 15310, Greece*

² *Department of Electronics, Technological and Educational Institute of Pireaus, Aegaleo 12244, Greece*

* *lpalil@imel.demokritos.gr*

The use of molecular and conjugated polymer semiconducting materials represents a very attractive alternative technological approach, compared to more conventional semiconductor technologies (such as Si technology), for the fabrication of novel optoelectronic and photonic devices due to their solution processability, facile tunability of their optical and electronic properties, low-cost and large-area fabrication on flexible substrates using various processing techniques, compatible with roll-to-roll printing for large-scale manufacturing. Polymer light-emitting diodes (PLEDs) and photovoltaic cells (PVs) are the two applications closest to commercialization to date. Both devices are fabricated with a light-emitting or a photoactive layer, respectively, sandwiched between two dissimilar electrodes, one of which needs to be transparent to light, on rigid glass or flexible plastic substrates. One of the critical issues for commercialization is the high performance device operation in air that requires balanced and facile charge injection and collection, at the corresponding electrodes, for PLEDs and PVs, respectively. Air stability, typically, requires the use of high workfunction metal cathodes such as Aluminum (Al). Al, however, limits electron injection in PLEDs due to the low electron affinity of most polymers, resulting in lower electroluminescence quantum efficiency and large driving voltage. In PVs, optical interference effects at the highly reflective Al surface may also limit bulk photogeneration, due to the reduced optical-electric field near the electrode, thus reducing the produced photocurrent.

In this talk, I will focus on demonstrating two strategies that we have developed for improving PLED and PV performance with regard to the aforementioned hurdles. In particular, I will report that the combination of polymer semiconductors with either novel inorganic molecular or metal oxides that are robust, transparent in the visible spectral region and easily processable, either by solution or by vapor deposition, can result in enhanced device performance. As two examples, a family of water soluble inorganic molecular oxides (polyoxometalates, POMs) and a series of metal oxides (reduced during evaporation) that can be both deposited as thin interlayers between the active layer and Al will be reported and their influence on device characteristics will be probed by employing spectroscopic, morphological and optical-electrical measurements.

MO4

14

Session TU1

STRUCTURAL, MECHANICAL & OPTICAL PROPERTIES OF CONDENSED MATTER

PART 2

Tuesday, 22 September 2009, 09⁰⁰-11⁰⁰



New Opportunities to Study Defects by Soft X-ray Absorption Spectroscopy

F. Boscherini

Department of Physics, University of Bologna, viale C. Berti Pichat 6/2, I-40127 Bologna, Italy

federico.boscherini@unibo.it

X-ray absorption fine structure (XAFS) can determine the local structure of most atoms in the periodic table. Recently, new opportunities to study dopants and defects in semiconductors have emerged, specifically for those based on low- Z (“light”) elements whose absorption edges lie in the soft X-ray range. This progress stems from improvements in the performance of synchrotron radiation sources and related instrumentation and in the development of computational schemes which are able to reliably simulate XAFS spectra.

In this contribution I will report some recent results that demonstrate how semiconductor physics may greatly benefit from such progress. In fact, doping or alloying of semiconductors with light elements is widely employed to tune their physical properties. XAFS investigations on such systems play an important role in knowledge-based materials design and can be crucial to understand and optimize technological processes.

Hydrogen passivation of N-induced effects in GaAsN dilute alloys (“dilute nitrides”) is an intriguing phenomenon of with important potential applications. Addition of a few % of N to III-V alloys and subsequent H-irradiation is a powerful method for tuning materials properties (especially the band gap). N incorporation leads to a counterintuitive band-gap reduction of the host lattice. H irradiation induces a restoration of the original band-gap, a change which can be reversibly eliminated by annealing; this represents a new method for materials engineering. The actual defect responsible for this phenomenon was unknown and our XAFS investigations provided a determination of its atomic structure [1 – 3]. A combination of experiment and simulation allowed us to show that the H-N complex which forms is composed by two H atoms bound to the same N atom with C_{2v} symmetry; N is in the neutral charge state. Accurate determination of the H and N concentrations with nuclear techniques indicated that a third H atom is weakly bound and can be eliminated by low temperature annealing, leaving the main defect unaffected. The case of “dilute oxide” alloys, formed by adding a few % of O to II – VI alloys has also been studied [4].

ZnO is a wide band gap, naturally n -type semiconductor with great promise for optoelectronic applications; the main obstacle yet to be overcome is p -type doping. Nitrogen, the most promising candidate currently being pursued as a dopant, has been predicted to preferentially incorporate into the ZnO lattice in the form of a N_2 molecule at an O site when a plasma source is used, leading to compensation rather than p -type doping. We have demonstrated this to be incorrect [5] by using N K-edge XAFS and comparing them with first-principles calculations showing that N, in fact, incorporates substitutionally at O sites where it is expected to act as an acceptor. We also detect the formation of molecular nitrogen upon annealing. These results suggest that effective p -type doping of ZnO with N may be possible only for low-temperature growth processes.

The realization of ultra-shallow junctions with a high dopant concentration and sharp doping profiles is of great current interest. A promising method for B doping in Si is solid phase epitaxy regrowth (SPER): implantation of the dopant in a preamorphized substrate and subsequent activation by recrystallization. An open question is the origin of the limited fraction of electrically active B and in particular the process stage in which inactive B atoms appear. By using B K-edge XAFS we have demonstrated [6] that inactive B-B clusters are formed during the very early stages of recrystallization, when the B atoms are still in the amorphous matrix; these clusters are transferred to the crystalline Si matrix.

F incorporation in Si is able to reduce diffusion deterioration of B doping profiles in ultra-shallow junctions. The common interpretation is that this effect is due to an excess of vacancies (V_s) induced by F, but a precise experimental investigation of atomistic structure of F in Si is still lacking. We have very recently studied this issue [7] and have come to the conclusion that F is incorporated in the form of SiF_4 molecules inside nanocavities, also observed by transmission electron microscopy. Cavities, that can be thought as large aggregates of vacancies, are therefore responsible for the peculiar reduction of B diffusion in this system.

- [1] G. Ciatto, F. Boscherini, A. Amore Bonapasta, F. Filippone, A. Polimeni and M. Capizzi, Phys. Rev. B 71 201301R (2005).
- [2] M. Berti, G. Bisognin, D. De Salvador, E. Napolitani, S. Vangelista, A. Polimeni and M. Capizzi, F. Boscherini, G. Ciatto, S. Rubini, F. Martelli, and A. Franciosi, Phys. Rev. B 76, 205323 (2007).
- [3] G. Ciatto, F. Boscherini, A. Amore Bonapasta, F. Filippone, A. Polimeni, M. Capizzi, M. Berti, G. Bisognin, D. De Salvador, L. Floreano, F. Martelli, S. Rubini, and L. Grenouillet, Phys. Rev. B 79, 165205 (2009).
- [4] F. Boscherini, M. Malvestuto, G. Ciatto, F. D’Acapito, G. Bisognin, D. De Salvador, M. Berti, M. Felici, A. Polimeni and Y. Nabetani, J. Phys.: Condens. Matter 19, 446201 (2007).

- [5] P. Fons, H. Tampo, A.V. Kolobov, M. Ohkubo, S. Niki, J. Tominaga, R. Carboni, F. Boscherini and S. Friedrich, *Phys. Rev. Lett.* 96 045504 (2006).
- [6] D. De Salvador, G. Bisognin, M. Di Marino, E. Napolitani, A. Carnera, H. Graoui, M.A. Foad, F. Boscherini, and S. Mirabella, *Appl. Phys. Lett.* 89 241901 (2006).
- [7] D. De Salvador et al, submitted 2009.

Neutron Compton scattering from LiH and LiD

G. Apostolopoulos^{1*}, K. Mergia¹, S. Messoloras¹, N. Gidopoulos²,
J. Mayers² and C.A. Chatzidimitriou-Dreismann³

¹ *Institute of Nuclear Technology - Radiation Protection, NCSR "Demokritos", 15310 Aghia Paraskevi Attikis, Greece*

² *ISIS Facility, Rutherford Appleton Laboratory, Chilton, Didcot, Oxon, OX11 0QX, United Kingdom*

³ *Institute of Chemistry, Technical University of Berlin, Strasse des 17. Juni 135, D-10623 Berlin, Germany*

*gapost@ipta.demokritos.gr

Neutron Compton scattering experiments on various hydrogen containing materials have revealed a striking anomalous deficit in the intensity of the hydrogen recoil peak [1]. The shortfall in intensity ranges from 20% up to 50%, depending on the particular hydrogenous compound, and in most cases shows a dependence on the scattering angle. Initially these experiments were received with great skepticism and questions were raised regarding the correctness of the results and the data analysis. Later detailed control experiments [2] have verified the results and refuted the criticism. Recently, supporting evidence for the effect has been found in electron Compton scattering experiments [3]. Still, this puzzling phenomenon triggers vivid discussions regarding its physical origin, with several different explanations given to date.

In the original publication of Chatzidimitriou-Dreismann et al. on H₂O/D₂O mixtures [4], where such anomalies were reported for the first time, the effect has been attributed to quantum entanglement of the proton with degrees of freedom in its environment. According to these authors, the anomalies in the scattering intensity are due to the extremely short time scale of the collision process (of the order of fs), which is comparable to the lifetime of the entangled proton. Ideas of quantum coherence/decoherence have been pursued further by Karlsson & Lovesey [5] and Karlsson [6], who presented also rough quantitative estimates of the expected scattering intensity reduction. In a different line of reasoning due to Gidopoulos [7] and Reiter & Platzman [8], the rapid movement of the recoiling proton results in electronic excitations via the breakdown of the Born-Oppenheimer approximation. Thus, scattering intensity is transferred from the recoil peak to higher energies and this leads to the apparent reduction of the recoil intensity.

The motivation for the current work was to perform a detailed and careful study of the phenomenon, on well characterized samples, that would allow us to test specific aspects of the existing theories. For this purpose, LiH and LiD were chosen as sample materials, which are the most studied among the light alkali hydrides and deuterides. The wealth of information currently available on the electronic, lattice, optical and defect properties of these materials will greatly facilitate theoretical model calculations and experimental comparisons. Both lithium hydride and deuteride may be currently obtained commercially in high purity due their technological importance as hydrogen storage materials. It is noted that the substitution of hydrogen with deuterium plays an important role in most of the proposed theoretical explanations and thus represents a very useful tool for this study. From the experimental point of view, lithium hydride and deuteride offer a significant advantage: the light lithium atom has sufficiently high recoil energy so that its scattering signal is clearly discernible from stray signals of heavier atoms (e.g. from sample container, cryostat). This reduces significantly the experimental aberrations.

Neutron scattering measurements were performed at the VESUVIO spectrometer of the ISIS pulsed neutron source. The samples were polycrystalline LiH and LiD powders contained in a thin aluminum sample holder. In a NCS experiment (also called deep inelastic neutron scattering experiment), neutrons with energy in the range of 10–150 eV are scattered by the nuclei in the sample. For scattering on hydrogen and deuterium the momentum and energy transfers are large and the protons (deuterons) are recoiled out of their positions in the crystal where they are situated. In the VESUVIO instrument outgoing neutrons are selected within a narrow energy interval, $E_f = 4.91 \pm 0.14$ eV by the use of Au-197 resonance foils. These neutrons have traveled from the pulsed spallation target at ISIS during a time-of-flight (TOF)

$$t = L_0 / v_0 + L_1 / v_1,$$

where v_0 is the velocity of the incoming neutrons and v_1 the velocity of the outgoing ones. The latter is fixed by the resonance foil energy. L_0 and L_1 are the corresponding primary and secondary flight paths, respectively. The TOF at which the recoil peak of a specific nucleus of mass M appears in the spectrum depends on the ratio v_1 / v_0 . From classical kinematics it is easy to show that at a scattering angle θ the following expression holds:

$$\frac{v_1}{v_0} = \frac{\cos \theta + \sqrt{(M/m)^2 - \sin^2 \theta}}{M/m + 1}$$

where m is the mass of the neutron mass. Fig. 1 shows an example of a NCS spectra taken for LiD at one particular scattering angle, $\theta = 135^\circ$. The recoil peaks from the three different masses are seen: Li, D and Al from the sample container.

Currently the available data have been processed according to the standard procedures of the VESUVIO instrument, which are based on the impulse approximation [9]. The area under the recoil peak for mass M is proportional to $N_M \sigma_b$, i.e., the number of atoms times the bound scattering cross-section for the corresponding nucleus. Thus the ratio of the area under the hydrogen or deuterium peak to the area of the Li peak should equal the ratio of the cross-sections $\sigma_{H,D} / \sigma_{Li}$. The nominal values of the cross-section ratios can be easily calculated from cross-section tables and is equal to 59.9 and 5.58 for hydrogen and deuterium, respectively. In the current preliminary phase of data reduction for this very recent experiment, the results obtained for the cross-section ratios are shown in Fig. 2, normalized to their corresponding nominal values. As seen from the figure the normalized values for the cross-section ratios are generally close to unity, indicating that there is no marked intensity anomaly in the LiH/LiD system. This is a striking result in view of previous work on other metal hydrides and deuterides, which all showed an intensity deficit of the proton recoil peak. Further processing of the experimental data is currently under way to assess possible implications of absorption corrections (due to the very large neutron absorption cross-section of Li), multiple scattering and other effects that may affect the cross-section ratio determination.

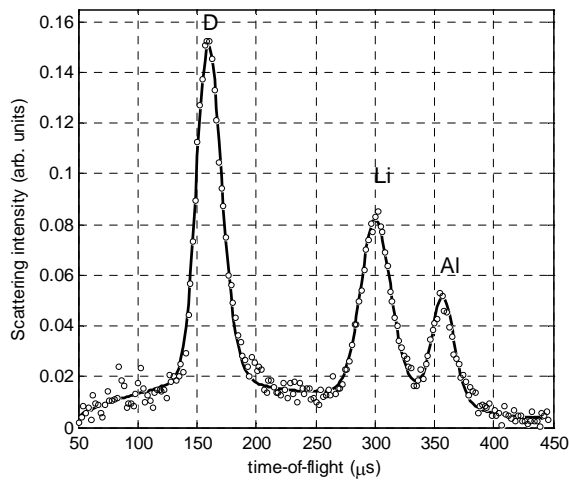


Fig. 1. Typical NCS spectrum. The sample consists of polycrystalline LiD powder in an aluminum container. Circles represent the measured intensity at a scattering angle of 135° as a function of the neutron time-of-flight. The solid line is a fit to the data based on the impulse approximation.

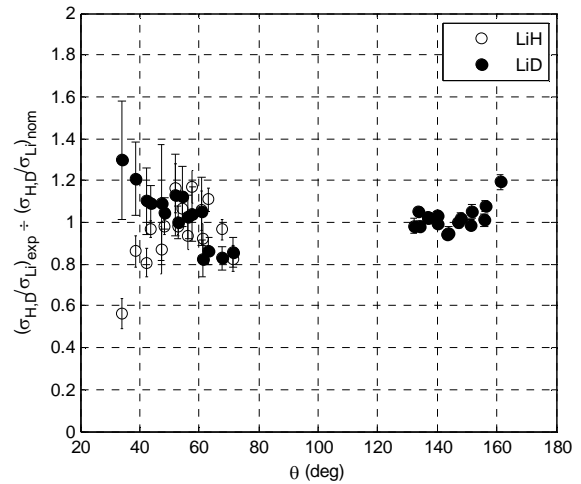


Fig. 2. Experimentally determined ratios $(\sigma_{H,D}/\sigma_{Li})_{\text{exp}}$ normalized to the tabulated ratio $(\sigma_{H,D}/\sigma_{Li})_{\text{nom}}$ as a function of scattering angle.

- [1] for a review see e.g. C. Andreani et al., *Advances in Physics* 54 (2005) 377.
- [2] J. Mayers and T. Abdul-Redah, *Journal of Physics Condensed Matter* 16 (2004) 4811; O. Hartmann et al., *ibid.*, 20 (2008) 104248.
- [3] C.A. Chatzidimitriou-Dreismann et al., *Phys. Rev. Lett.* 91 (2003) 574031; G. Cooper et al., *ibid.* 100 (2008) 43204.
- [4] C.A. Chatzidimitriou-Dreismann et al., *Phys. Rev. Lett.* 79 (1997) 2839.
- [5] E.B. Karlsson and S.W. Lovesey, *Phys. Rev. A* 61 (2000) 62714.
- [6] E.B. Karlsson, *Phys. Rev. Lett.* 90 (2003) 095301; *Physica Scripta* 77 (2008) 065301.
- [7] N.I. Gidopoulos, *Physical Review B* 71 (2005) 054106.
- [8] G.F. Reiter and P.M. Platzman, *Physical Review B* 71 (2005) 054107.
- [9] J. Mayers and T. Abdul-Redah, *J. Phys.: Condens. Matter* 16 (2004) 4811.

Acknowledgments Experiments at ISIS were supported by EU programs NMI3 and FP6.

Identification of New Nano-Scale Phases in $\text{AgPb}_{18}\text{SbSe}_{20}$ Crystals by Electron Crystallography Methods

Ch. B. Lioutas^{1*}, N. Frangis¹, M. G. Kanatzidis²

¹ *Solid State Physics Section, Department of Physics, Aristotle University of Thessaloniki, GR-54124 Thessaloniki, Greece*

² *Department of Chemistry, Northwestern University, 2145 Sheridan Road, Evanston, IL 6020-3113, USA*

**lioutas@physics.auth.gr*

Lead telluride (PbTe) and lead selenide (PbSe) are well-known thermoelectric material used for power generation [1]. Doping of PbTe with Ag and Sb is expected to improve the thermoelectric properties. Interesting members of this family are $\text{AgPb}_{18}\text{SbTe}_{20}$ and $\text{AgPb}_{10}\text{SbTe}_{12}$, which show promising figures of merit and have an interesting nanostructure [2,3]. In the present work the selenium analog $\text{AgPb}_{18}\text{SbSe}_{20}$ is studied by electron microscopy and the new phases found in the nanocrystals are identified.

The electron microscopy study reveals the existence of a very large number of nanocrystals within the matrix material (PbSe). Their size ranges from a few nm up to about 50 nm. The distribution of these nanocrystals in the matrix appears rather homogeneous.

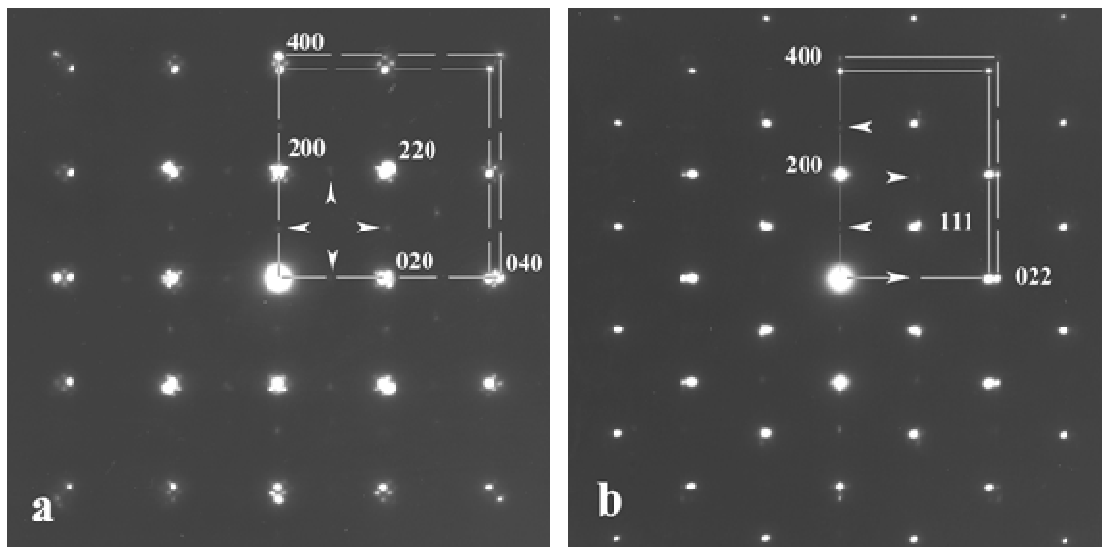


Figure 1: Electron diffraction patterns taken along: a) $[001]$ and b) $[01\bar{1}]$ cubic axes.

Electron diffraction patterns (Fig. 1) contain spots which can be distinguished as coming from three different structures. The strongest ones, corresponding to the smaller frame in Fig.1, are absolutely consistent to a face centered cubic (fcc) NaCl-type of structure. They belong to the matrix PbSe (phase A), which it is known to have a NaCl-type of structure with $a_0 = 0.6134$ nm.

The second group of reflections, corresponding to the larger frame, can also be interpreted as coming from a cubic (phase B). The two lattices are almost perfect parallel one to the other, denoting that the new phase was grown “endotaxially” in the matrix cubic phase. Taking as an internal standard the PbSe matrix reflections the lattice parameter of this cubic phase is deduced as: $a_1 = 0.579 \pm 0.01$ nm. Such a constant is identical with that of the compound AgSbTe_2 , which is known to possess the NaCl structure. However the very weak intensity of the 200 reflections of phase B, in both patterns, is not consistent with a NaCl-type of structure, which is characterized by strong 200 reflections. Calculation of intensities for a zinc-blende type of structure and for AgSbTe_2 yields to very weak 200 reflections and denotes that this is the type of structure for phase B.

In most of the cases of the diffraction patterns, weak spots, indicated by arrows in Fig. 1, appear close to the positions 100 and 011, which are forbidden reflections for the NaCl structure. This indicates the presence of a superstructure (phase C) at least in some of the nanocrystals, with approximately the same lattice parameters as the basic one, but with tetragonal (or even lower, i.e. orthorhombic) symmetry.

TU1

O15

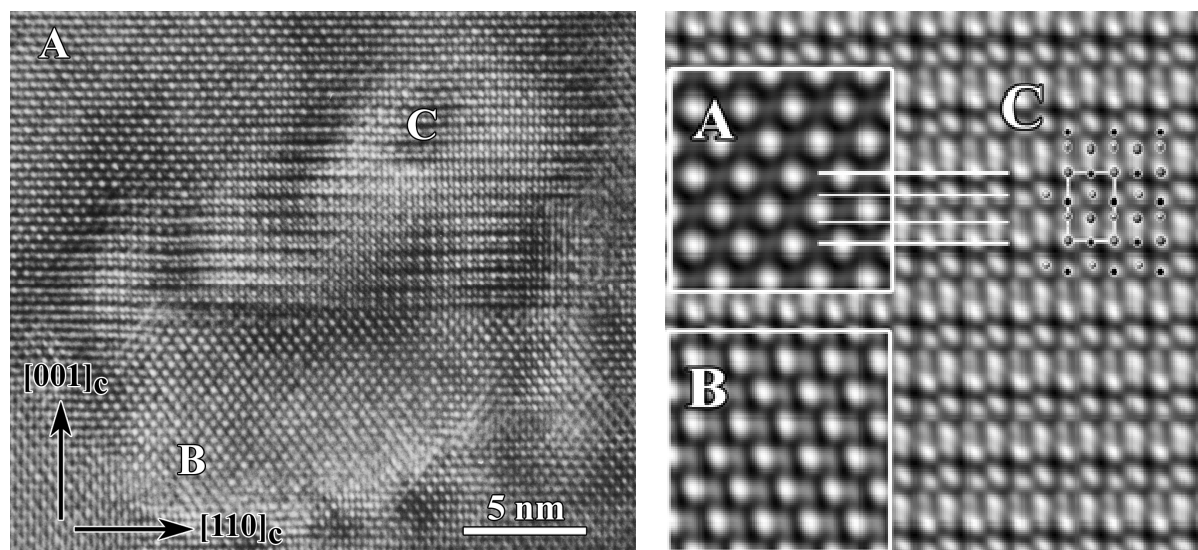


Figure 1: A HREM image from a nanocrystal taken along the $[01\bar{1}]$ cubic axis. In the right panel the averaged images, taking with the use of the appropriate software, for the three phases are shown.

High-resolution electron microscopy (HRTEM) images, as the one in Fig. 2, confirm the above ideas. Usually, both the phases B and C exist in the same nanocrystal, surrounded by the PbSe matrix. Careful measurements from the diffraction patterns and HRTEM images lead to values $c=0.625 \pm 0.01$ nm and $a=0.588 \pm 0.01$ nm, for the tetragonal superstructure, i.e. to a ratio $c/a=1.07 \pm 0.01$. The c tetragonal axis is found to be parallel to one of the $\langle 100 \rangle$ cubic axes and the a , b axes parallel to the other two $\langle 100 \rangle$ cubic axes, i.e. this phase is also grown “endotaxially” in the matrix cubic phase. It can exist in three variants in relation with the cubic basic structure. In each of the variant the tetragonal axis is parallel to one of the three cubic basic axes. So, the presence of the superstructure spots at both the 010 and 001 positions in the diffraction pattern of Fig. 1a is attributed to the presence of two of these variants. The third type of variant has its tetragonal axis parallel to the electron beam and hence does not give any extra spot in the diffraction pattern.

Analysis of the morphological features of HRTEM images from phase C allows concluding that this structure is a deformed cubic structure, with coordination polyhedra similar to those observed in the compounds Ag_2Se and AgSbS_2 . Computer image simulations were performed, involving ordering of Pb, Ag and Sb in the cationic sublattice. The most successful model assumes the distribution of Pb atoms in deformed octahedral sites and those of Ag and Sb in the tetrahedral ones.

In conclusion two new phases were found in $\text{AgPb}_{18}\text{SbSe}_{20}$ nanocrystals, embedded in the PbSe matrix (phase A). A cubic one (phase B), with a zinc-blende structure and a tetragonal superstructure (phase C) which is the result of ordering of Pb, Ag and Sb in the cationic sublattice.

[1] D. M. Rowe ed., CRC Handbook of Thermoelectrics, (CRC Press, Boca Raton, FL, 1995).

[2] Hsu K.F., Loo S., Guo F., Chen W., Dyck J.S., Uher C., Hogan T., Polychroniadis E. K., Kanatzidis M. G., Science, 303, 818 (2004).

[3] Quarez E, Hsu K.F., Pcionek R., Frangis N., Polychroniadis E. K. and Kanatzidis M., J. Amer. Chem. Soc., 127, 9177 (2005).

Ultra-High Time Resolved XAS

A. Erko*, A. Firsov and K. Holldack

*Elektronenspeicherring BESSY II, Helmholtz-Zentrum Berlin für Materialien und Energie GmbH,
Albert Einstein str.15, Berlin, Germany*

*erko@bessy.de

A pump-probe setup for transient x-ray absorption spectroscopy for the study of ultrafast phenomena like the transfer of angular momentum between spins and lattice in ferromagnetic and other materials has been built recently at BESSY. The setup is particularly devoted to X-ray magnetic circular dichroism (XMCD) measurements as the difference of X-ray absorption between left and right circularly polarized X-rays in ferromagnets on a ~100 fs timescale [1].

Short pulses are possible at BESSY II in a single-bunch mode (~ 50 ps) and in the “low-alpha” mode down to 1-3 ps. A temporal resolution of <120 fs was achieved at BESSY with the Femtoslicing Source [2,3]. Here the electron pulse is “sliced” with a femtosecond optical laser where the field of the laser pulse causes an energy modulation in the electron bunch. In the BESSY scheme the energy-modulated electrons are separated from the main pulse in a dipole magnet and subsequently generate fs pulses by passing through a helical undulator.

A major advantage of the Femtoslicing scheme is the perfect synchronization between fs laser and fs X-ray pulses. This is due to the fact that the fs optical pulses from the same laser source are used both for the slicing and the pump processes. The temporal phase between the laser pulse and the energy modulated electrons has to be preserved during propagation from the modulator to the sample. This translates into controlling the optical path length difference between optical and X-ray pulses. The femtoslicing radiator is optimized for polarization dependent spectroscopy in the soft X-ray range and yields 10^6 ph/s/0.1%BW. Behind the plane grating monochromator the fs X-ray flux for 0.1 % bandwidth is reduced to $<10^4$ photons per second which sets tight constraints for the feasibility of certain experiments. This leads to the necessity of highly efficient optics to transfer X-rays to a sample with minimum losses. The optics must perform a focusing of X-rays onto the sample, provide reasonable energy dispersion and has to have a highest possible x-ray transmission. The solution was found using only a single optical element – a reflection zone plate (RZP).

A setup for laser-pump x-ray probe absorption spectroscopy is shown in figure 1. X-ray absorption spectra are recorded by measuring the transmitted X-ray intensity by an avalanche photodiode [4].

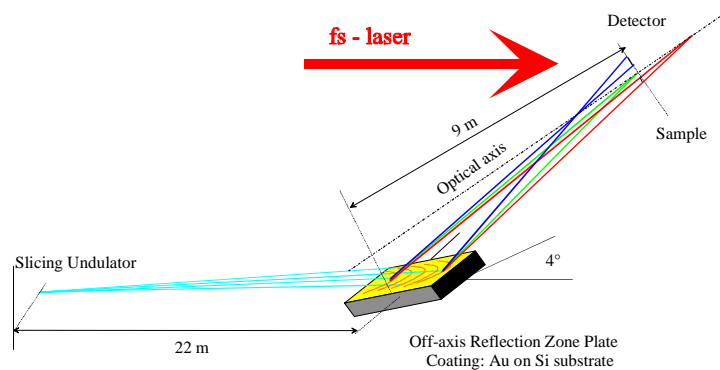


Fig. 1 Optical layout of the experiment.

The undulator source UE56 covers an energy range between 50 eV and 1400 eV and full polarization control. The polarization can be varied between linear (horizontal or vertical) and left and right handed elliptical. A RZP under total external reflection conditions features the important property of not changing the polarization of the beam.

The elliptical zone plates fabricated on a super-flat reflection mirror surface were effectively used for an x-ray monochromatization and beam focusing at photon energies below 1500 eV. This element can be applied in the beamlines with specific beam conditions such as

very high heat load or very low flux. Since the whole setup involves only one reflection it meets the requirement of minimum losses. It is important, that the RZP must be off-axis, to provide the best energy and spatial resolution.

Another demand of slicing users is the preservation of the time resolution from the source. The residual temporal blurring of the short x-ray pulse is in our case a characteristic time of the order of 30 fs. The number of grooves in the diffraction structure along the beam direction should not exceed the value of 5200. This value defines a maximum aperture and maximum energy resolution of the optical element.

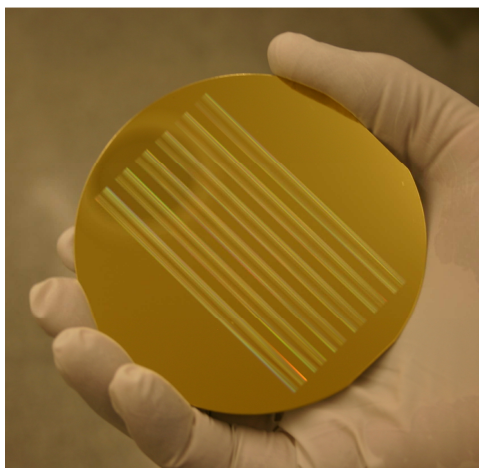


Fig. 2 Reflection zone plates on a Si substrate.

The reflection Fresnel zone plates were produced at the BESSY Centre for Microtechnology in cooperation with Microlithography and Consulting (ML&C) Company in Jena. Six Fresnel lenses designed for the edge energies between 500 eV and 1200 eV were fabricated on the same substrate (figure 2).

The monochromator was tested both with direct undulator beam and white light radiation operating at detuned gap settings. With direct undulator radiation a fluorescence screen was used to visualize an intensity distribution in the focal plane of the reflection zone plate. The result is shown in figure 2 which represents an image obtained on a fluorescence screen with light containing three undulator harmonics: the first at 262 eV; the third at 785 eV and the fifth at 1308 eV. The RZP is optimized for the energy of 765 eV and produces a focused spot at this energy. The other lenses produce a similar distribution in the focal plane but are optimized for five other photon energies.

It must be mentioned that the beamline has only one optical element, therefore the total flux delivered by the beamline is of the order of 20 times higher than the photon flux from a traditional plane grating monochromator (PGM) beamline with a minimum of four reflecting surfaces. In figure 4 a comparison of absorption spectra from the L3 and L2 edges of Co is shown.

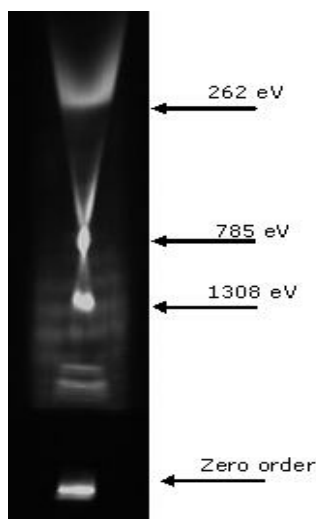


Fig. 3 Footprint of reflected light from the RZP in the focal plane on a P43 phosphor screen.

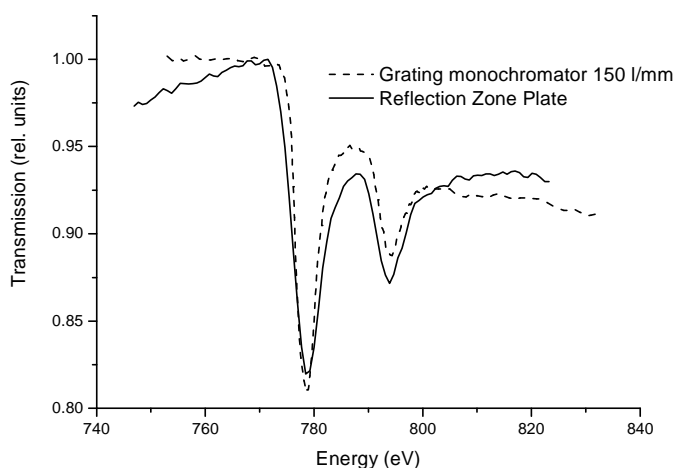


Fig. 4 L-Edge Absorption spectra of a 30 nm thin film of Co taken at different beamlines under identical conditions.

One can see the identical quality of the (single sweep) spectra regarding energy resolution. The difference is that the RZP monochromator the higher flux and easily allows for a parallel registration of the absorption spectra. Specially developed avalanche diodes arrays, consisting of 25 single diodes were tested to record simultaneous spectra from the full dispersion area. An optical fiber is used to improve the spatial resolution of the diode line array down to 50 μm , which corresponds to an energy resolution in experimental geometry of 1.2 eV. The gain in flux of more than order of magnitude has allowed to address a new class of ultrafast user experiments within the past year. Very recent examples will be presented.

References:

- [1] C. Stamm et al., Nature Materials **6**, 740 (2007).
- [2] K. Holldack et al. Phys. Rev. ST Accel. Beams, **8**, 040704 (2005).
- [3] S. Khan et al., Phys. Rev. Lett. **97**, 074801 (2006).
- [4] B. Niemann, Deutsches Patent DE 195 42 679 A1, 16.11. 1995.

Session TU2

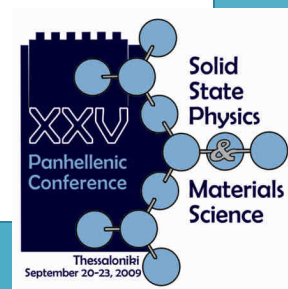
POSTER SESSION

*STRUCTURAL, MECHANICAL &
OPTICAL PROPERTIES – 2*

*MAGNETISM &
SUPERCONDUCTIVITY*

*CULTURAL HERITAGE
MATERIALS &
INTERDISCIPLINARY PHYSICS*

Tuesday, 22 September 2009, 11³⁰-13⁰⁰



In vitro and in vivo efficient magnetic heating with polymer-dressed Fe₂O₃ nanoparticles

D. Tsitrouli¹, I. Rabias¹, E. Karakosta¹, Th. Kehagias³, M. Fardis¹, G. Diamantopoulos¹, D. Stamopoulos¹, and G. Papavassiliou¹

¹ *Institute of Materials Science, National Centre for Scientific Research 'Demokritos', Athens 153 10*

³ *Aristotle University of Thessaloniki, Department of Physics, Thessaloniki 541 24*

dtsit@ims.demokritos.gr

Maghemite nanoparticles, nowadays, are experiencing increasing attention. Finite-size effects along with surface effects and interparticle interactions are mainly the reasons for their unique magnetic and physical properties and therefore for their use in many technological and biological applications¹. One of the most promising applications of maghemite nanoparticles in nanomedicine is hyperthermia i.e the treatment of malignant tumours, based on the capability of nanosized magnetic particles, dispersed in a colloidal fluid, to induce heating when located in an AC magnetic field². The main factors which affect the magnetic heating are the structural and magnetic properties of the magnetic core, the dispersity of nanoparticles as well as the total charge of the fluid produced by the charged coating-molecules. In this work we report on the synthesis and the structural-magnetic characterization of highly charged dextran coated maghemite nanoparticles. The synthetic route followed was the co-precipitation technique according to Massart's method³. HRTEM (High Resolution TEM), SQUID, Mössbauer and zero external field ⁵⁷Fe NMR measurements indicate the existence of defect-free monodomain maghemite nanoparticles with mean diameter \approx 10-12 nm. The in vitro hyperthermia experiment of this highly stable ferrofluid showed a remarkable temperature increase to approximately 98 °C in just 3 minutes and 60 °C in 10 minutes for ferrofluid quantities 0.15 ml and 0.002 ml respectively. This unprecedented result of our investigations shows that this ferrofluid, even in very small quantities, can be used as an efficient hyperthermia agent.

References:

- [1] Berry C, Curtis A "Functionalisation of magneticnanoparticles for applications in Biomedicine" J. Phys. D: Appl. Phys. 36,198–206.
- [2] Jordan A, Wust P, Fahling H, Jonh W, Hinz A and Felix R 1997 "Inductive heating of ferrimagnetic particles and magnetic fluids: physical evaluation of their potential for hyperthermia" *Int. J. Hyerthermia* 9,51–68.
- [3] Massart R "Preparation of aqueous magnetic liquids in alkaline and acidic media" IEEE Trans. Magn. MAG-17,1247.

TU2
P1

Oxygen Permeation Study Through Dense Ceramic Membranes with Perovskite Structure ($Ba_{0,8}Sr_{0,2}M_xB_{1-x}O_{3\pm\delta}$, $M=Co,Al$, $B=Mn,Fe,Ni$)

Pandis P.*, Argirusis Chr., Ftikos Ch.

Laboratory of Inorganic Materials Technology, School of Chemical Engineering, National Technical University of Athens

*ppandis@central.ntua.gr

Ceramic ion conducting membranes are generic group of materials with many potential large-scale applications in solid oxide fuel cells, oxygen generators and partial oxidation reactors. At present the transport and surface exchange kinetic characteristics are emphasized to maximize ionic fluxes. However, as the dense membrane is often fabricated in the form of a thick film on a supported porous structure there is an increasing realization that the available processing routes and thermo mechanical behavior will also strongly influence the selection of materials. Accordingly, increasing attention is now being given to the effect of the imposed chemical potential gradient upon thermo chemical stability and structural integrity.

Mixed conducting membranes that exhibit high oxygen ionic and electronic conductivities gained great interest as clean, efficient and economical means of producing oxygen from air or other oxygen-containing gas mixtures. They will be most competitive at small and intermediate-scale levels in which flexibility of operation is desired and many eventually challenge the present commercial status of cryogenics, pressure-swing adsorption and polymeric membranes [1-3]. In this case these compounds are being studied thanks to their applications as catalysts for the partial oxidation of hydrocarbons, electrodes for solid oxide fuel cells, oxygen pumps, ceramic membranes for oxygen separation but also as dielectric, ferroelectric and piezoelectric materials [4,5].

Among mixed conductive oxides, perovskite related structures (ABO_3) have received much attention for numerous applications [6-10]. Teraoka et al [11], Stevenson et al [12] and Tsai et al [13] studied oxygen permeability of A-site substitution perovskite type oxides focused on the $LaxAl_{1-x}Co_yFe_{1-y}O_{3-\delta}$ system. From their investigations, different results were obtained and such conflict reflects the difficulties in measuring the oxygen fluxes at middle and high temperatures and possible effects of different preparation methods and other parameters on oxygen permeation experiments. Our research aims to investigate the impact on the oxygen permeability in function with the doping on the B-site of the perovskite lattice, the temperature and the oxygen partial pressure, having specimens with specific lengths.

All the oxides were prepared by the amorphous citrate synthesis. The reagents that have been used were nitric oxides and oxides of the metals. The nitric oxides were dissolved in distilled water and the oxides of the metals in nitric acid. All of the mixtures were mixed with citric acid and were heated over a burner until combustion took place and a black-gray powder was formed. The powders were calcinated at 1000°C for 10h and then ball-milled with zirconia spheres in acetone for 24h. In the end, rectangle rods were formed in a GRASEBY SPECAC 25011 press at 90Mpa under air vacuum and sintered at 1300°C for 15h. The heating and cooling rate were controlled at 1K/min.

The X-Ray Diffraction analysis was conducted at room temperature on a Siemens D5000 Diffractometer with the Bragg angle range $10^\circ \leq 2\theta \leq 100^\circ$ using Cu radiation. Further examination and data collection for the lattice parameters were accomplished using the Least Squares Unit Cell Refinement (LSUCR) software (G.A. Novak & A.A. Colville – 1989). The densities of the sintered membranes (rectangle rods) were determined by the Archimedes method. All the densities exceeded 93% of the theoretical one and one phase of structure was observed in all cases.

In oxygen permeation experiments, the flow rates of the inlet gasses were controlled by mass flow controllers. Air was introduced into the upstream of the membrane and helium as the sweep gas for the membrane was fed to the downstream of the membrane. Upstream was maintained at atmospheric pressure whilst downstream was maintained at the half of atmospheric pressure. The effluent stream was lead and analyzed by a gas chromatographer (PERKIN ELMER 8310) with helium as the carrier gas. The oxygen permeation flow was calculated from the flow rates, the oxygen concentration of the effluents and the dimensions of the membrane. If the chromatographer had shown a concentration different than the oxygen's then the measurement was considered void. The calibration of the chromatographer was made with a 99% He and 1% O₂ mixture. The entire system (module) was placed at a horizontal direction.

Oxygen permeation fluxes, at first, had high values but in time decreased and finally level off. Such unsteady-state oxygen permeation flux measurements are reported by several groups [12-15]. This phenomenon occurred at all compounds. It is concluded that the oxygen permeation flux was generally increased with the increase of the oxygen partial pressure, the temperature and with the decrease of oxygen partial pressure with the exception

of some compounds. There is a minimum critical thickness that prevents the determination of oxygen flux at each synthesis. With the above measurements we were able to determine the oxygen vacancy diffusion coefficients (D_V) for each synthesis and temperature. Results showed that the mathematical model used for the regression analysis (figure 1) was suitable for the calculation of activation energies for all the materials.

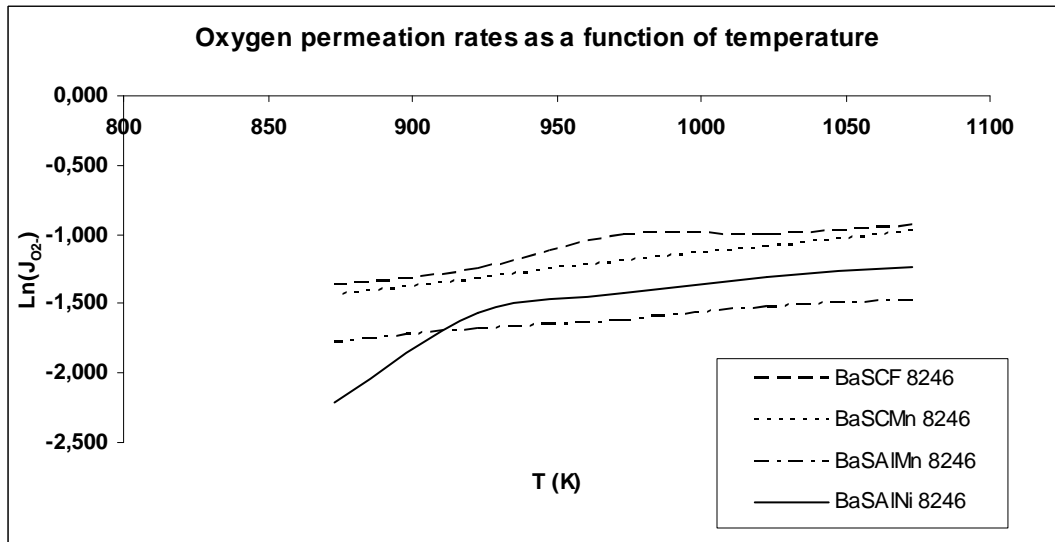


Fig. 1: Experimental estimated permeation rates as a function of the temperature for all materials

- [1] Carolan M. F., Dyer, P. N., LaBar Sr. J. M., Thorogood R. M., Process for Recovering Oxygen from Gaseous Mixture Containing Water or Carbon Dioxide Which Process Employs Ion Transport Membranes. U.S.Patent 5,(1993), 261, 932.
- [2] Carolan M. F., Dyer, P. N., LaBar Sr. J. M.,Thorogood R. M., Process for Recovering Oxygen from Gaseous Mixture Containing Water or Carbon Dioxide Which Process Employs Barium-Containing Ion Transport Membranes. U.S.Patent 5, (1993), 269, 822.
- [3] Liu M., Joshi, A. V. Shen, Y. Krist, K., Mixed Ionic-Electronic Conductors for Oxygen Separation and Electrocatalysis. U.S. Patent 5, (1993), 273, 628.
- [4] Lewandowski, J. T., Beyerlein, R. A., Longo, J. M. and McCauley, R. A., Nonstoichiometric K_2NiF_4 -type phases in the lanthanum-cobalt-oxygen system. J. Am. Ceram. Soc., (1986), 69(9), 699–703.
- [5] Kharton, V. V., Viskup, A. P., Kovalevsky, A.V., Naumovich, E. N.and Marques, F. M. B., Ionic transport in oxygen—hyperstoichiometricphases with K_2NiF_4 -type structure. Solid State Ionics, (2001), 143, 337–353.
- [6] Qiu, L., Lee, T. H., Liu, L.-M., Yang, Y. L., Jacobson, A. J.,Oxygen Permeation Studies of $SrCo_{0.8}Fe_{0.2}O_{3-\delta}$. Solid State Ionics, (1995), 76, 321.
- [7] Gur, T. M., Belzner, A., Huggins, R. A., A New Class of Oxygen Selective Chemically Driven Nonporous Ceramic Membrane. Part I. A-Site Doped Perovskites. J. Membr. Sci. (1992), 75, 151.
- [8] van Hassel, B. A., Kawada, T., Sakai, N.,Yokokana, H., Bouwmeester, H. J. M. Oxygen Permeation Modeling of Perovskites, Solid State Ionics, (1993), 66, 295.
- [9] ten Elshof, J. E., Bouwmeester, H. J. M., Verweij, H.,Oxygen Transport through $La_{1-x}Sr_xFeO_{3-\delta}$ Membrane. I. Permeation in Air/He Gradients. Solid State Ionics, (1995), 81, 97.
- [10] Kharton, V. V., Naumovich, E. N., Nikolaev, A. V., Materials of High-Temperature Electrochemical Oxygen Membranes, J.Membr. Sci., (1996), 111, 149.
- [11] Teraoka, Y., Nobunaga, T., Yamazoe, N.,Effect of Cation Substitution on the Oxygen Semipermeability of Perovskite Oxides, Chem.Lett., (1988), 503.
- [12] Stevenson, J. W., Armstrong, T. R., Carmeim, R. D., Pederson, L. R., Weber, L. R. Electrochemical Properties of Mixed Conducting Perovskites $La_{1-x}M_xCo_{1-y}Fe_yO_{3-\delta}$ (M = Sr, Ba, Ca), J. Electrochem. Soc., (1996),143, 2722.
- [13] Tsai, C. Y., Dixon, A. G., Ma, Y. H., Moser, W. R., Pascucci, M. R. Dense Perovskite, $La_{1-x}A_xFe_{1-y}Co_yO_{3-\delta}$ (A= Ba, Sr, Ca), Membrane Synthesis, Application, and Characterization, J. Am.Ceram. Soc., (1998), 81, 1437.
- [14] Tsai, C.-Y., Dixon, A. G., Moser, W. R., Ma, Y. H., Dense Perovskite Membrane Reactors for the Partial Oxidation of Methane to Syngas. AIChE J., (1997), 43, 2741.
- [15] Kruidhof, H., Bouwmeester, H. J. M., Doom, R. H. E. V.,Burggraaf, A. J., Influence of Order-Disorder Transitions on Oxygen Permeability Through Selected Nonstoichiometric Perovskite-Type Oxides, Solid State Ionicsm, (1993), 63-65, 816.

Surface Characterisation of Nitrogen-Implanted Steel and Corrosion Behaviour in Aggressive Environment.

F. Noli^{1*}, P. Misaelides¹, A Lagoyannis², J.P. Rivière³

¹ Department of Chemistry, Aristotle University, GR-54124 Thessaloniki, Greece

² Tandem Accelerator Laboratory, Nuclear Physics Institute, NCSR Demokritos, GR-15310 Aghia Paraskevi-Attiki, Greece

³ Université de Poitiers, Laboratoire de Métallurgie Physique UMR6630-CNRS, 86960 Chasseneuil, Futuroscope Cedex, France

*noli@chem.auth.gr

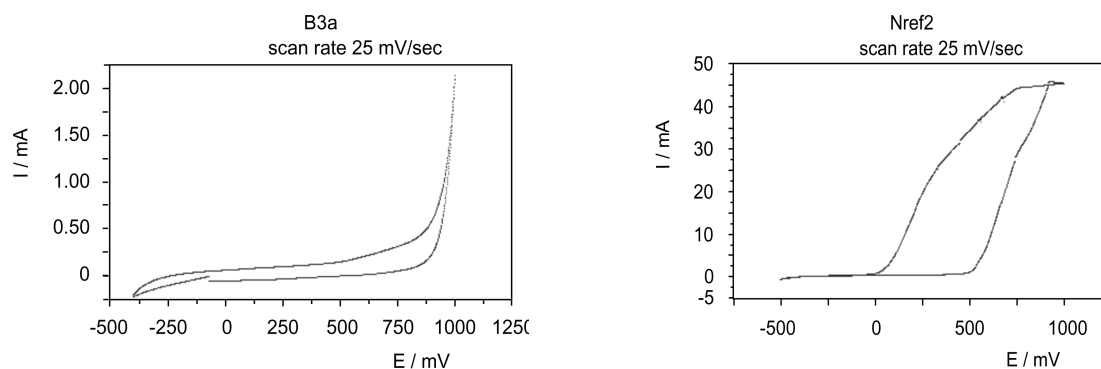
The AISI 304 type stainless steel contains a high chromium content and is a commonly used engineering material mainly because of its corrosion resistance. However, it presents a low surface hardness and a poor wear resistance. For these reasons many surface modification techniques such ion implantation have been developed.

Austenitic stainless steel AISI 304L was implanted with low energy, high current nitrogen ions at moderate temperatures. The nitrogen ions were extracted from a Kauffnan type ion source at a voltage of 1.2 KeV and the ion current was 1 mA/cm². The ion dose considered to be about 4x10¹⁹ ions /cm² corresponds to one hour of treatment. The temperature during the implantation was 400 and 500 °C respectively for the two series of the samples prepared.

The microstructure and surface morphology was examined by X-Ray Diffraction (XRD), Transmission Electron Microscopy (TEM) and Scanning Electron Microscopy (SEM). A metastable fcc interstitial solid solution with a high nitrogen content of about wt. 30% was formed resulting in the increase of the hardness as indicated from the Vickers microhardness measurements.

Investigation of the corrosion behaviour under strong aggressive conditions (hydrochloric acid 2% at 50 °C) was performed using electrochemical techniques (potentiodynamic polarization and cyclic voltammetry). The study of the elemental constitution in the near surface layers and the nitrogen depth profiles were performed by Rutherford Backscattering Spectrometry (RBS) and Nuclear Reaction Analysis (NRA). The samples implanted at 400 °C exhibited remarkable resistance to corrosion as it is shown in figures 1a and 1b corresponding to the N-implanted steel at 400 °C and the untreated material respectively. The corrosion potential (E_{corr}) was reduced and the current density was found to be lower. This could be attributed to the modified surface region and the high nitrogen content. For the samples implanted at 500 °C a slight inhibitive effect was observed.

The results lead to the conclusion that the corrosion behavior of the modified materials seems to be related with the formation of the metastable phases during the nitriding process. The effect of such a low energy, high density nitrogen implantation was explained taking into account the XRD and TEM data combined with the N-depth profiles obtained by RBS and NRA.



Figs. 1a-b: Potentiodynamic polarization curves (rapid scans) of the N-implanted steel sample at 400 °C (1a) and the untreated steel sample (1b).

On the Magnetic Properties of Plastically Deformed Armco Steel

K. Kosmas¹, N. Ntallis², K.G. Efthimiadis², E. Hristoforou^{1*}

¹ *Laboratory of Physical Metallurgy, National Technical University, GR15780 Athens, Greece*

² *Department of Physics, Aristotle University, GR54124 Thessaloniki, Greece*

*eh@metal.ntua.gr

Correlation of structure and magnetic properties in steels is important for non-destructive testing. The microstructure of the materials in terms, of dislocation density and dislocation generated sub-grains, which are responsible for the generation of cracks and defects in the magnetic substance determine the minor magnetic hysteresis loops, from the linear magnetization region till the major loop, in static or quasi-static conditions [1,2]. Thus, provided that the dependence of at least one magnetic property on the dislocation and sub-grain density is monotonic, the non-destructive testing and evaluation of the given magnetic substance can be realized. It is clear that for each type of magnetic substance, i.e. for each type of steel, the above-mentioned correlation of the minor hysteresis loops with the measured dislocation and sub-grain density has to be obtained. This method has two advantages, the first being the measurement of bulk magnetic substances, provided that quasi-static magnetic measurements take place, while the second is the ability of predicting the generation of cracks.

Results on the correlation of structure and magnetic properties in ARMCO steel after mechanical treatment are reported in this paper. Samples have undergone plastic deformation by means of cold rolling and tensile stress in their as-bought state. Minor 0.1Hz magnetic hysteresis loops (B-H), Barkhausen noise (BHN) and magneto-acoustic (MAE) measurements have been performed in the as-bought, plastically deformed samples, concerning the on-line (during applied stress) and the off-line (after unloading stress) case. XRD stress analysis and transmission electron microscopy have been employed to determine the microstructure of the samples. Armco samples have undergone cold rolling with reduction of 12.5%, 22.5%, 35%, 50% and 62.5% and tensile plastic deformation in various deformation percentages up to the breaking point in their as-bought state.

Figure 1 illustrates the on-line stress dependence of the counts and rms value of the single point Barkhausen noise for the Armco steel. It can be seen that the dependence is monotonically increasing, illustrating the dislocation density increase in Armco. A two line response is observed when BHN is plotted against tensile stress (MPa).

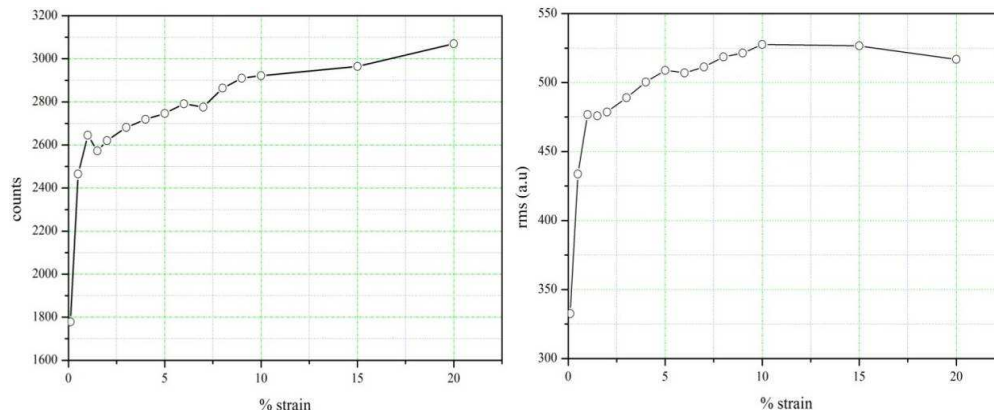


Figure 1. The on-line stress dependence of the counts and rms value of the BHN in Armco steel

The magneto-acoustic emission (MAE) response and minor B-H loops concerning off-line measurements of Armco steel are illustrated in Figure 2. These off-line measurements clearly illustrate the presence of compressive stresses in the off-line measurements, which is in agreement with the two-peak BHN response, illustrated in Figure 3. The XRD stress analysis aided by the Euler cradle method, illustrated compressive residual stresses after removing the applied load, which is in agreement with theory and previous microstructural characterization studies [3]. Figure 4 illustrates two different plastically deformed Armco samples indicating that dislocation based sub-grains are responsible for the stress field introduced in the microstructure. The correlation of the three different magnetic properties with the microstructure and the stress field analysis is based on the micromagnetic theory, particularly concerning the correlation of domain wall motion with respect to dislocations parallel to the domain wall [4]. The complete study of the correlation between magnetic properties and plastic deformation in Armco steel can be found in [5].

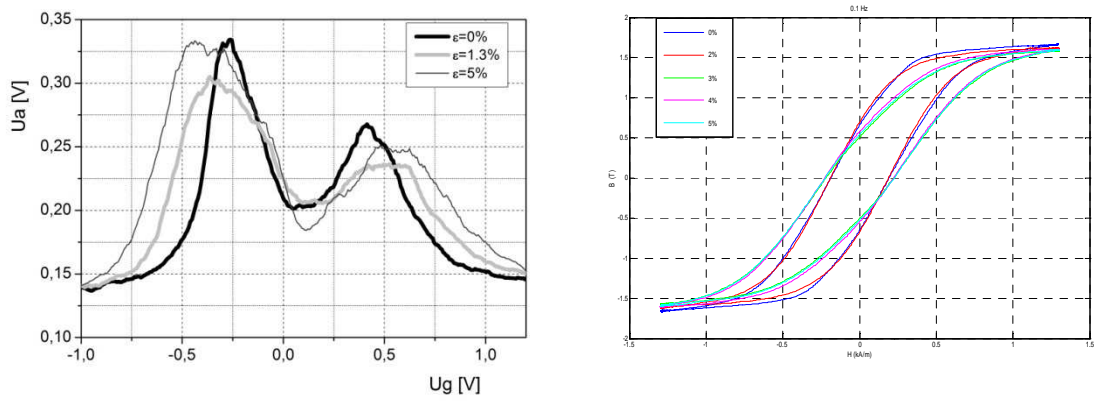


Figure 2. MAE and B-H loop response of different plastic deformation in Armco steel.

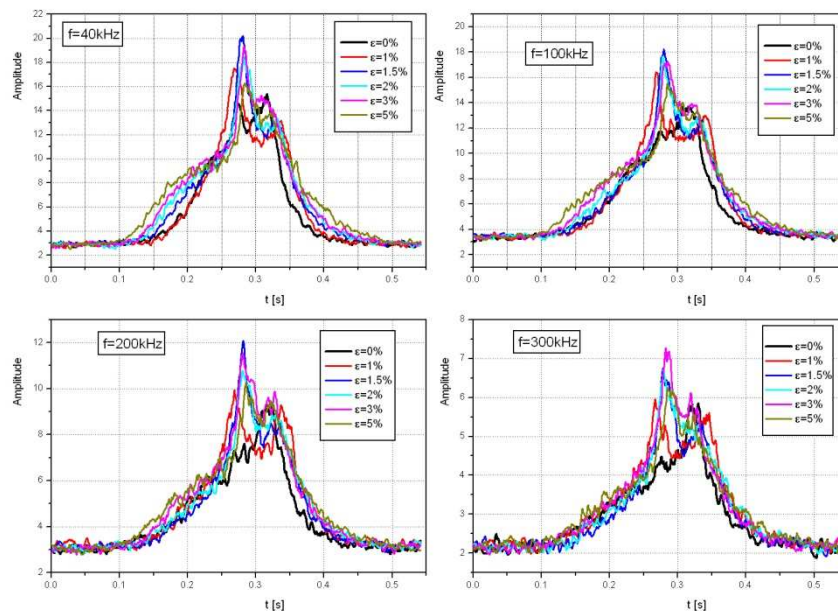


Figure 3. Off-line BHN measurements in plastically deformed Armco steel using different low-pass filters.

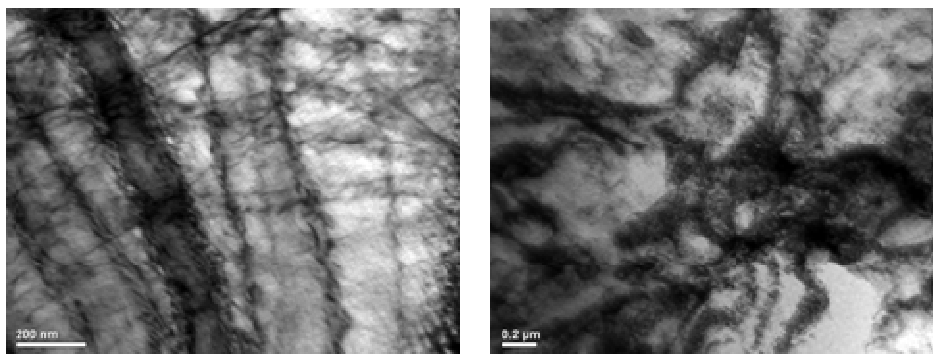


Figure 4. TEM images showing the presence of dislocations in plastically deformed cold rolled (left) and Armco steel (right).

- [1] Chikazumi S., Physics of Magnetism, John Wiley & Sons, 1964.
- [2] Kahn R.W., Physical Metallurgy, North Holland Publishing Co, 1965.
- [3] Gatelier-Rothea C., Chicois J., Fougères R. and Fleischmann P., Acta Mater. 46, 4873 (1998).
- [4] Trauble
- [5] Kosmas K., PhD Thesis, National TU of Athens (2009).

Acknowledgments are due to the ΠENEΔ01 and NTUA ΠΕΒΕ2007 frameworks

Designing Composite Panels For Minimum Cost And Weight

Panos Apostolopoulos^{1, 2*}, Christos Kassapoglou³

¹ School of Physics, Post Graduate Program Physics and Technology of Materials Thessaloniki, Greece

² Maurokordatou 37 Piraeus, Greece

³ Aerospace Engineering Department Delft University of Technology Delft, Netherlands

* apost72@yahoo.gr

Abstract

Stiffened composite panels are being increasingly used in all kinds of applications from bridge decks to ships to aircraft skin panels. Their increased strength and stiffness has led to lower weight designs in many applications. However, taking full advantage of the potential of composites requires fairly advanced design and analysis techniques that accurately account for the wide variety of failure modes that is possible with such materials. In addition, the cost of composite structures only recently has started to become competitive to equivalent metal structures through design optimization and use of robotics. In general, a minimum cost design is significantly different than a minimum weight design. Combining cost and weight in the design process and minimizing with respect to both of them requires detailed understanding of the material strength and stiffness performance as well as accurate modeling of the fabrication processes used. An approach is needed that can model both structural performance and manufacturing process capabilities allowing trade-offs between cost and weight. The present paper describes the beginning of such an approach and shows preliminary results of cost and weight trades.

A composite stiffened panel under compressive load N_x is shown in Figure 1.

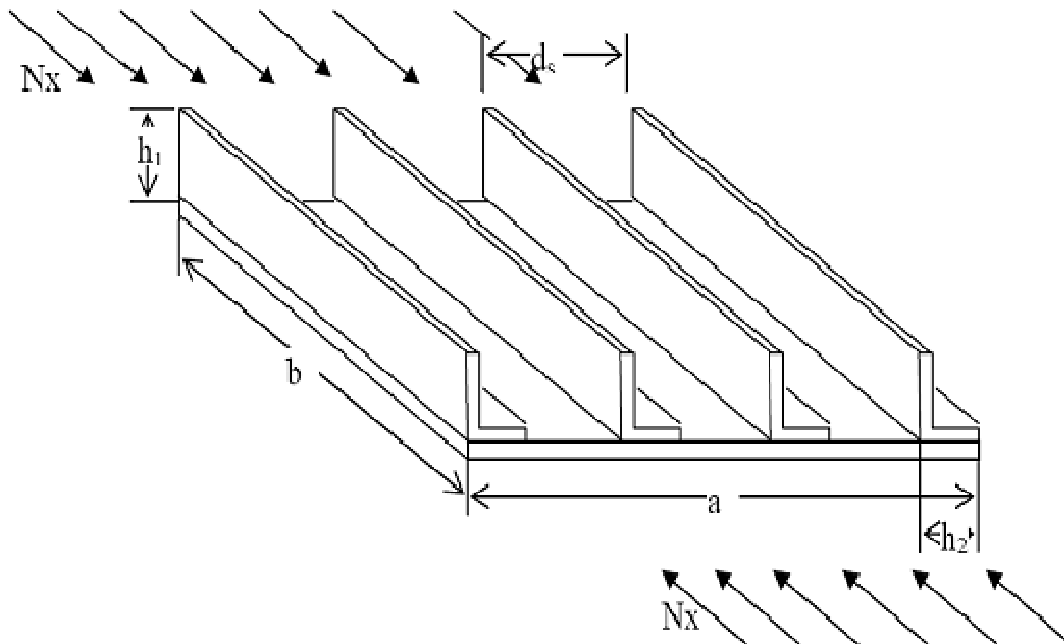


Figure 1. Composite stiffened panel under compression.

The panel consists of “L” or “angle” stiffeners with spacing d_s and the skin. The applied load is distributed between skin and stiffeners and can lead to failure of any of the two stiffener legs or the skin itself. Designing the panel requires selection of the layups of the skin and stiffeners (each stiffener leg and the skin can have different layups) such that no members fails in any of its possible failure modes and, at the same time, the weight and/or the cost of the entire panel are minimized.

The failure modes analyzed are: (a) Column buckling of each stiffener, (b) Crippling of each leg of each stiffener, (c) Material failure of the stiffener, (d) Buckling of the skin between stiffeners, (e) Buckling of the skin between the stiffeners, (f) Buckling of the skin and stiffeners as a whole, and (g) Material failure of the skin. Depending on the geometry and layups selected, the critical failure modes can be different leading to entirely

different designs. For example, stiff closely spaced stiffeners absorb most of the load and first failure occurs by stiffener crippling of the vertical leg of each stiffener. At the other extreme, soft far apart stiffeners, divert most of the load to the skin leading to early buckling failure of the skin between the stiffeners.

In addition to the failure modes just presented, design requirements are imposed to ensure robust performance of the panel as a whole: (a) the stiffeners have a minimum bending stiffness so they act as “panel breakers” ensuring skin buckling between the stiffeners to be the first instability of the structure (b) the layups are symmetric and balanced to avoid unwanted in-plane and out-of-plane coupling, (c) at least 10% of the fibers are in each of the four principal directions (0, 45, -45, and 90) to protect against secondary loading cases.

A layup generator has been created using Visual Basic. This generator creates different layups for the skin and stiffeners obeying the symmetry, balance and 10% rules just mentioned. This generator is included in a larger code that was written that for a selection of layups, solves for stiffener web height (h_1) and flange width (h_2) as a function of stiffener spacing d_s . The equations are non-linear and are solved by iteration. For each acceptable configuration (i.e. configuration that does not fail) the corresponding fabrication cost is calculated. Optimization is performed through a random search combined with local “Pareto optimal” design adjustment (parameters are changed to examine if at least one of the two objectives, cost or weight, improves without worsening the other. Typical results are shown in Figure 2.

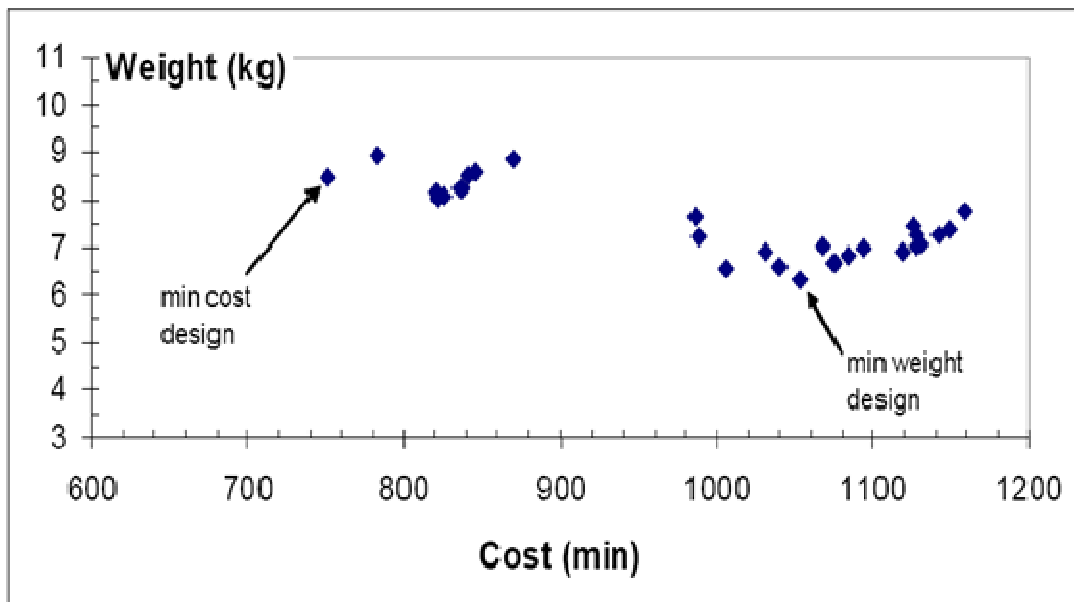


Figure 2. Pareto set of optimum or near optimum designs.

Nanostructural characterization of TiN-Cu films using EXAFS spectroscopy

F. Pinakidou¹, E.C. Paloura^{1*}, G.M. Matenoglou², P. Patsalas²

¹ Aristotle University of Thessaloniki, School of Physics, 54124 Thessaloniki, Greece

² University of Ioannina, Department of Materials Science and Engineering, 45110, Ioannina, Greece

*paloura@auth.gr

Titanium nitride (TiN) exhibits superior mechanical properties compared to other hard materials (e.g. carbides, other transition metal nitrides etc.) and is studied extensively for applications in wear-resistant coatings. Even though TiN has only modest tribological properties (e.g. wear resistance and friction coefficient) when used in combination with a soft-ductile phase (such as a noble metal), [1] it can become superhard or even ultrahard while retaining exceptional mechanical properties and high chemical resistance. [2] Here we present a study of the coordination environment of Cu in a series of TiN-Cu nanocomposite thin films grown by hybrid Pulsed Laser Deposition (PLD). The bonding environment of Cu is investigated using Extended X-ray Absorption Fine Structure (EXAFS) measurements at the Cu-K-edge. The motivation for studying these ternary systems stems from the need to investigate the formation of nanocomposites by incorporating TiN and Cu in comparable concentrations.

The TiN-Cu films were deposited on Si (100) wafers by PLD under flowing N₂ (99.999 %) and were grown from either elemental Ti and Cu (99.95%) targets or from an intermetallic TiCu pellet with Cu:Ti concentration ratio equal to 1. The N₂ partial pressure (P_{N2}) was varied between 0.5x10⁻³ mbar and 150x10⁻³ mbar. Two reference TiCu films were grown from either target under P_{N2}=0. The composition of the studied samples was determined using Auger Electron Spectroscopy (AES). [3]. The growth conditions of the studied TiN-Cu samples are listed in Table 1. The Cu-K-EXAFS measurements were conducted at the KMC2 beamline of the Synchrotron Radiation facility BESSY in Berlin. The Cu-K-EXAFS spectra were recorded in the fluorescence yield (FLY) mode using an energy dispersive (Röntec) fluorescence detector in order to eliminate the background due to the preceding Ti edges.

The Fourier Transforms (FTs) of the raw and fitted k²-weighted $\chi(k)$ Cu-K-EXAFS spectra of the TiN-Cu samples grown from the elemental and the intermetallic targets are shown in Fig 1. The clearly resolved structure in the FTs at distances beyond the 1st nearest neighbor (nn) shell indicates that the samples are characterized by long range order. Therefore the fitting was performed in the three nn shells, i.e. at distances up to 5Å from the absorbing Cu atom. The model for the analysis was that of fcc Cu properly modified. More specifically two different paths, for Cu and Ti respectively, were used for each nn shell. In addition to that it was assumed that x_i% of the atomic sites are occupied by Cu atoms while the Ti atoms replace Cu in the rest (1-x_i) % sites, where i takes the values 1, 2 and 3 that correspond to the 1st, 2nd and 3rd nn shells, respectively.

The Cu-K-EXAFS results reveal that under certain growth conditions Ti replaces Cu in fcc Cu. In addition to that the Cu-Cu and Cu-Ti bondlengths are strongly modulated by the different growth conditions. More specifically, as shown in the upper panel of Fig. 2, in the films grown from elemental targets, as the N₂ pressure increases less Ti atoms substitute Cu in the 1st nn shell of fcc Cu. On the contrary, when growth occurs under the highest P_{N2} (=150x10⁻³ mbar), we do not detect Ti in the 1st nn shell of Cu, i.e. Cu is bonded to 12 Cu atoms, as expected in fcc Cu. Thus, it is revealed that the gradual increase of P_{N2} from 0 to 150x10⁻³ mbar, results to a systematic decrease in the degree of replacement of Cu atomic sites by Ti atoms in fcc Cu (only in the 1st nn shell). Given that the formation of stoichiometric TiN has been previously reported in the studied TiN-Cu films, [3] it can be proposed that when P_{N2} ≥ 0.5 x10⁻³ mbar, Ti bonds to N and only the unreacted (leftover) Ti atoms substitute Cu in fcc Cu. As P_{N2} increases, more Ti atoms are consumed by bonding

Table 1: Growth conditions of the studied TiN-Cu samples.

Sample name	P _{N2} (mbar)	Target
1	0	Ti, Cu plates
2	0.5x10 ⁻³	Ti, Cu plates
3	3.7x10 ⁻³	Ti, Cu plates
4	150 x10 ⁻³	Ti, Cu plates
5	0	TiCu pellet
6	2.3 x10 ⁻³	TiCu pellet

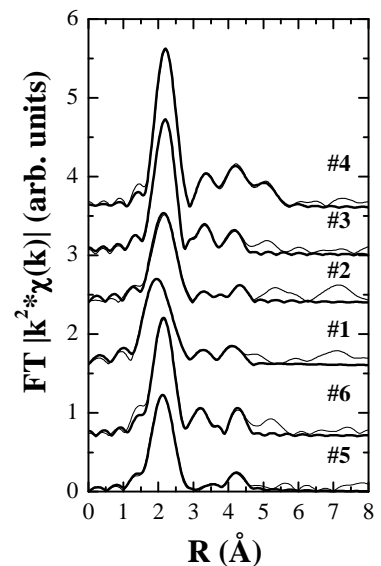


Fig. 1. Fourier Transforms of the k²-weighted $\chi(k)$ EXAFS spectra of the TiN-Cu samples. The raw and fitted data are shown in thin and thick solid lines respectively.

to N_2 , thus inducing an increase in the atomic percentage of Cu in the 1st nn shell of Cu. Since XRD measurements did not identify the formation of the Cu_3N phase [3], it can be proposed that at the highest P_{N_2} limit (150×10^{-3} mbar), only Cu is formed, i.e. all Ti is completely consumed in forming TiN.

In the reference sample grown from the TiCu pellet ($P_{N_2}=0$, sample #5), approximately 55 at% of Cu atoms are substituted by Ti in the 1st nn shell of Cu, i.e. marginally higher than the respective reference sample grown from the elemental targets. Additionally, when the film is grown in N_2 ambient from the TiCu pellet (sample #6), the atomic percentage of Cu is the same as in the reference sample grown in the absence of N_2 , i.e. contrary to the detected increase in the films grown from the elemental targets. The detected modification of the percentage of Cu atoms may be related to the different type of target used: the TiCu pellet promotes the formation of intermetallic TiCu bonds, a finding which is also supported by the shortening of the Cu-Ti bondlength in the 1st nn shell of Cu, and Cu is replaced by smaller atoms.[4] In all studied films, the substitution of Cu atoms by Ti can be explained on the basis of the different enthalpies between the Ti-N and Ti-Cu bonds, i.e. in the former case the bond energy is three times higher than in the case of intermetallic Ti-Cu bonds. Thus, Ti preferentially forms TiN while the unreacted Ti atoms bond to Cu in the fcc Cu phase.

The nitrogen pressure also affects the Cu-Cu and Cu-Ti bondlengths. In particular, as shown in the lower panel of Fig. 2, the Cu-Ti bondlength (R_{Cu-Ti}) increases from 2.46 to 2.58 (± 0.02) when the P_{N_2} increases from 0 to 3.7×10^{-3} mbar. On the contrary, the Cu-Cu bondlength in the 1st nn shell of Cu is equal among all studied TiN-Cu films grown with $P_{N_2} \neq 0$ and lies between 2.52–2.54 Å (± 0.01), i.e. is marginally shorter than the respective in crystalline Cu foil (2.55 Å (± 0.01)). In the highest P_{N_2} limit, Cu bonds only to Cu and the Cu-Cu distances in all nn shells are in excellent agreement with the respective in Cu-foil. On the contrary, when $P_{N_2}=0$, the deformation of the R_{Cu-Cu} bondlength is pronounced.

More specifically, when growth proceeds from the TiCu pellet, R_{Cu-Cu} is equal to the respective in the Cu-foil, while on the contrary R_{Cu-Cu} becomes significantly shorter (2.50 Å (± 0.01)) when elemental targets are used and $P_{N_2}=0$. The shortening of the Cu-Cu bondlength has been previously reported in a series of mechanically prepared CuTi amorphous alloys [5] and in the studied TiN-Cu films can be related to the growth process. In particular, it can be proposed that due to the sequential growth from the Cu and Ti targets, the formation of fcc Cu where Ti can replace Cu is promoted, contrary to the case of the TiCu pellet, where intermetallic TiCu bonds are favored. Thus, it is revealed that the replacement of Cu by Ti atoms in fcc Cu atomic sites does not affect the Cu-Cu bondlengths when $P_{N_2} \neq 0$. On the contrary, the different P_{N_2} results to an elongation of the Cu-Ti bondlength in the 1st nn shell, i.e. the increase in P_{N_2} promotes the formation of a (Cu, Ti) solid solution where the Ti atoms occupy sites predicted from the model of crystalline fcc Cu.

To conclude, the effect of the different growth conditions on the bonding environment of Cu in TiN-Cu nanocomposite films was studied using EXAFS spectroscopy at the Cu-K-edge. The EXAFS results reveal that Ti occupies Cu sites in fcc Cu and the degree of replacement decreases when the P_{N_2} increases from 0 to 3.7×10^{-3} mbar. When $P_{N_2} = 150 \times 10^{-3}$ mbar, only Cu is formed. The Cu-Cu bondlength is equal to the respective in Cu-foil, independent of the growth conditions when $P_{N_2} > 0$. However, when $P_{N_2}=0$, significant changes in both Cu-Cu and Cu-Ti bond lengths are detected. These changes could be attributed to the different growth kinetics when growth proceeds from the elemental and the intermetallic targets. On the contrary, in the 1st nn shell, the Cu-Ti bondlength increases as P_{N_2} increases and the lowest value (2.46 Å) is detected in the sample grown from a TiCu pellet with $P_{N_2}=0$. The formation of a (Cu, Ti) solid solution is attributed to the formation of crystalline TiN: as P_{N_2} increases more Ti is consumed by bonding to N_2 , thus resulting to the decrease in the percentage of Ti atoms that replace Cu in fcc Cu.

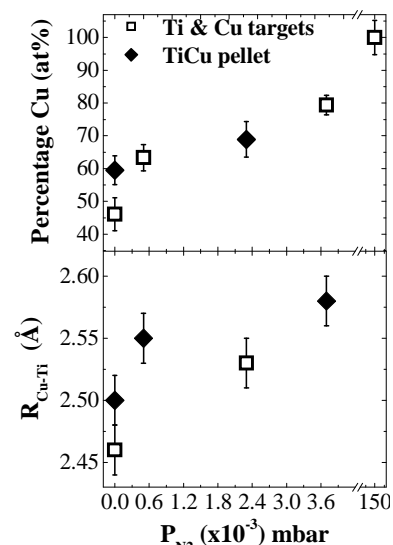


Fig. 2: Modification of the percentage of Cu atoms (at %) in the 1st nearest neighbour (nn) shell of the TiN-Cu films (upper panel) and the increase of the Cu-Ti bondlength (R_{Cu-Ti}) in the 1st nn shell of Cu (lower panel), as a function of the N_2 pressure (P_{N_2}) in the studied TiN-Cu.

[1] Zhang S., Sun D., Fu Y. and Du H., Surf.Coat. Technol. 167, 113 (2003).

[2] Hao S., Delley B., Vepřek S. and Stampfl C., Phys. Rev. Lett. 97, 086102 (2006).

[3] Matenoglou G.M., Evangelakis G.A., Kosmidis C. and Patsalas P., Rev. Adv. Mater. Sci. 15, 38 (2007).

[4] Scheuer U. and Lengeler B., Phys. Rev. B, 44, 9886 (1991).

[5] Nakamura K. and Nagumo M., J. Non-Cryst. Solids 156-158, 575 (1993).

Micro-XRF and micro-EXAFS studies of an Al matrix Fe-Ni composite

F. Pinakidou, M. Katsikini, E.C. Paloura*, G. Vourlias and G. Stergioudis

Aristotle University of Thessaloniki, School of Physics, 54124 Thessaloniki, Greece

*paloura@auth.gr

The mechanical properties of metals can be improved by either alloying or by chemical reactions which lead to the formation of intermetallic products.[1] When the surface of a Fe-Ni alloy is exposed to liquid Al, dissolution occurs followed by growth of intermetallic layers at the alloy-aluminium interface.[2,3] The strength of the matrix can be further improved via a direct reaction synthesis in which reactant powders are directly added into the molten metal.[4] Here we report on the distribution and the local coordination of Fe and Ni in a Fe-Ni rod which was dissolved in liquid Al, using X-ray fluorescence mapping (XRF), micro- (μ -) and conventional extended X-ray absorption fine structure (EXAFS) spectroscopies in the fluorescence yield (FLY) mode. The measurements were conducted at the KMC2 beamline of the Synchrotron Radiation facility BESSY, in Berlin, which is equipped with a double-crystal monochromator and capillary optics that reduce the beam diameter to 5 μ m. The μ -Ni-K- and μ -Fe-K-EXAFS spectra were recorded from spots of the sample's surface with different metal concentration (as identified in the XRF maps) while the conventional (without the capillary) XAFS measurements were recorded from a random spot.

In order to investigate any local inhomogeneities in the distribution of Fe and Ni, two dimensional μ -XRF maps were recorded with excitation energy 9500 eV, i.e. higher than the K_α and K_β edges of Fe and Ni. The μ -XRF maps shown in Fig. 1 reveal that Fe segregates and forms Fe-rich islands which are depleted of Ni, i.e. regions with high (H-) and low (L-) Fe concentration are detected. The opposite behavior is disclosed for the distribution of Ni, i.e. in the Fe-rich (Fe-poor) regions, the Ni distribution exhibits minima (maxima). It is characteristic that in the Fe-rich islands, the Fe K_α fluorescence intensity is 10 times higher than the background intensity and the same significant differences are also detected in the distribution of Ni (in the H-regions the Ni K_α fluorescence intensity is 10 times higher than the respective in the L-regions).

The effect of the varying distribution of both Fe and Ni on their bonding environment is investigated by recording μ -Fe-K and μ -Ni-K-EXAFS spectra from the regions with maximum and minimum Fe and Ni concentration, respectively. The Fourier transforms (FT) of the k^3 -weighted $\chi(k)$ μ -Fe-K-EXAFS spectra (k -range 3.0 - 8.8 \AA^{-1}) recorded from the Fe H- and L- regions are shown in Fig.2(a). The differences in the structure in the FTs of the μ -Fe-K-edge EXAFS spectra, in the distance range 0 to 5 \AA , between the H- and L- regions indicates that the bonding environment of Fe changes as a result of the varying distribution of Fe. The corresponding FTs of the k^3 -weighted $\chi(k)$ μ -Ni-K-EXAFS spectra (k -range 3.5 - 9.0 \AA^{-1}), recorded from the same regions, are shown in Fig. 2(b).

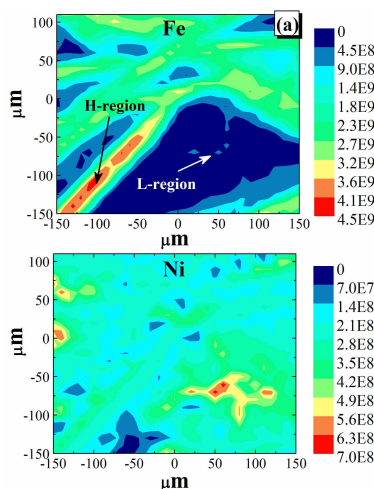


Fig. 1: 350x260 μm^2 μ -XRF map of the distribution of Fe and Ni (upper and lower panels, respectively). The regions with high and low Fe concentration are denoted as H- and L- respectively.

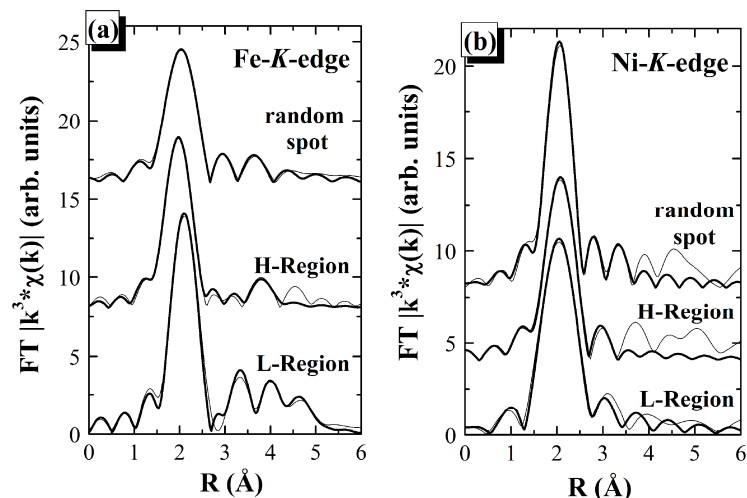


Fig. 2: (a) Fourier Transforms (FTs) of the k^3 -weighted $\chi(k)$ Fe-K- μ -EXAFS spectra recorded from the H- and L-regions and of the Fe-K-EXAFS spectrum recorded from a random spot; (b) FTs of the k^3 -weighted $\chi(k)$ Ni-K- μ -EXAFS spectra recorded from the H- and L-regions and of the Ni-K-EXAFS spectrum recorded from a random spot.

TU2

P7

The μ -EXAFS analysis results, listed in Table 1, reveal that the bonding environment of Fe is different between the L- and H-regions due to the different Fe concentration. In the Fe-rich microcrystallites the Fe atoms belong to FeAl₃ where Fe is bonded to $\cong 10$ Al atoms located at 2.47 Å (± 0.01), i.e. as expected from the crystalline model of FeAl₃. In the 2nd and 3rd nn shells the Fe-Fe and Fe-Al distances are in very good agreement with those in FeAl₃ (4.29 and 4.55 Å, respectively). However these shells are undercoordinated (the coordination numbers in FeAl₃ are 4 Fe and 5 Al atoms, respectively). In the 1st nn shell of the Fe-poor regions, Fe bonds to approximately 12 Al with the Fe-Al distance equal to 2.51 Å (± 0.01), i.e. the formation of FeAl is detected. The 2nd and 3rd nn shells consist only of Fe atoms (Table 1). According to the crystalline model of FeAl, 12 Al, 6 Fe and 12 Fe atoms comprise the three nn shell and the respective Fe-Al, Fe-Fe and Fe-Fe distances are equal to 2.53, 3.58 and 5.06 Å, i.e. the μ -EXAFS results from the L-region are in very good agreement with the interatomic distances according to the crystalline model of FeAl. The analysis of the μ -Ni-K-EXAFS spectra reveal that the even though the Ni/Al atomic ratio is equal to 1, i.e. it is the same in both the H- and L-regions, the Ni and Al atoms form different intermetallic NiAl phases due to the inhomogeneities in the distribution of Ni. In particular, in the Fe rich-regions (that are depleted of Ni), Ni is coordinated with approximately 8 Al atoms and the Ni-Al bondlength is equal to 2.48 Å (± 0.01), i.e. in excellent agreement with the crystalline model of NiAl, where 8 Al atoms are expected at 2.50 Å. However, in the Ni-rich regions (Fe poor-region), Ni belongs to fcc Ni where the Al atoms occupy all atomic sites in the 1st nn shell. The coordination number of Ni is equal to 10.5 \pm 1.1 Al and the corresponding Ni-Al distance is equal to 2.52 Å (± 0.01).

Finally, in order to get a quantitative description of the changes in the bonding environment of Fe and Ni (i.e. percentages of Fe and Ni atoms in different coordination geometries), we resorted to conventional broad-beam EXAFS spectroscopy using mixed structural models. In the Fe-K-EXAFS spectra it was assumed that x% of the Fe atoms belong to FeAl₃ crystallites while the rest (1-x)% form intermetallic FeAl. The Ni-K-EXAFS spectrum was simulated assuming that y% of Ni forms an intermetallic NiAl phase while the rest (1-y)% belong to fcc Ni where Al atoms substitute Ni. The FTs of the $k^3 \cdot \chi(k)$ Fe-K (k range 3.5 – 8.5 Å⁻¹) and Ni-K (k range 3.5 – 9.6 Å⁻¹) EXAFS spectra of the sample are shown in Fig. 2(a) and (b), respectively. The Fe-K-EXAFS analysis reveals that the majority of the Fe atoms (approximately 80 at%) belong to FeAl₃ crystalline islands, embedded to an intermetallic FeAl matrix. In the 1st nn shell, the Fe-Al bondlengths in FeAl₃ and FeAl are equal to 2.48 Å (± 0.01) and 2.51 Å (± 0.02), respectively, i.e. as determined by the μ -Fe-K-EXAFS analysis. On the contrary, the changes in the Fe and Ni concentration in the different sample spots affects only the type of bonding of the Ni atoms. Approximately half of the Ni atoms (50 at%) belong to intermetallic NiAl regions while the rest occupy sites in an fcc Ni matrix where the Al atoms have replaced all Ni atoms in the 1st nn shell. The Ni-Al bondlengths are equal to 2.47 Å (± 0.01) in the NiAl crystallites and to 2.50 Å (± 0.02) in the (Ni,Al) matrix, i.e. in agreement with the μ -Ni-K-EXAFS analysis results.

To conclude, it is demonstrated that the local coordination of Fe and Ni vary due to the inhomogeneous distribution of Fe and Ni. The Ni and Fe atoms bond only to Al and intermetallic FeNi bonds were not detected. In the Fe-rich regions, Fe and Ni belong to FeAl₃ and NiAl, respectively, while in the Fe-poor regions, Fe bonds to Al in an intermetallic FeAl phase while the presence of a (Ni, Al) solid solution is also detected. EXAFS measurements at the Fe-K and Ni-K-edges disclosed that the majority of Fe (~80 at%) belongs to the FeAl₃ microcrystallites embedded into an FeAl matrix. On the contrary, the same percentage of Ni atoms, i.e. approximately 50 at% of the Ni atoms belong to NiAl and to a (Ni, Al) solid solution.

Table 1: Fe-K and Ni-K- μ -EXAFS results of the spectra recorded from the Fe-rich (H-region) and Fe-poor (L-region) regions. N_i is the coordination number, DW_i is the Debye-Waller factor and R_i is the interatomic distance, in the ith nearest neighbour (nn) shell, respectively.

Fe-K edge	H-region	L-region
N ₁	10.2 \pm 0.9 (Al)	11.5 \pm 0.8 (Al)
R ₁ (Å)	2.47 (\pm 0.01)	2.51 (\pm 0.01)
DW ₁ (Å ²)	0.0115	0.0066
N ₂	2.2 \pm 0.6 (Fe)	3.7 \pm 0.9 (Fe)
R ₂ (Å)	4.23 (\pm 0.02)	3.63 (\pm 0.02)
DW ₂ (Å ²)	0.0076	0.0045
N ₃	3.3 \pm 0.9 (Al)	12.2 \pm 3.1 (Fe)
R ₃ (Å)	4.52 (\pm 0.03)	5.07 (\pm 0.03)
DW ₃ (Å ²)	0.0120	0.0059
Ni-K edge	H-region	L-region
N ₁	7.8 \pm 0.9 (Al)	10.5 \pm 1.1 (Al)
R ₁ (Å)	2.48 (\pm 0.01)	2.52 (\pm 0.01)
DW ₁ (Å ²)	0.0045	0.0105
N ₂	-	1.6 \pm 0.5 (Ni)
R ₂ (Å)	-	3.47 (\pm 0.02)
DW ₂ (Å ²)	-	0.015.7

[1] Mathews F.L., Rawlings R.D., Composite Materials: Engineering and Science (Cambridge CRC Press, Woodhead, 1999).

[2] Dybkov V.I., J. Mat. Sci., 21, 3078 (1986).

[3] Dybkov V.I., J. Mat. Sci., 25, 3615 (1990).

[4] Wang X., Brydson R., Jha A, Ellis J., J. Microsc. 196, 137 (1999).

Magnetic Properties of Nd-Fe-B/3:29 and Sm(CoFeCuZr)_{7.5}/3:29 Nanocomposite Permanent Magnets

D. Moussadacos¹, M. Gjoka^{2*}, D. Niarchos², M. Calamiotou¹

¹University of Athens, Dept. of Physics, Panepistimioupoli, Zografou, Athens, Greece

²Institute of Materials Science, N.C.S.R. "Demokritos" Agia Paraskevi 15310 Athens, Greece

*gjoka@ims.demokritos.gr

Abstract

Magnetic properties of nanocomposite magnets prepared from ball-milled powders of Nd-Fe-B nanocrystalline melt-spun ribbons, Pr(Fe,Co,Ti,Cu,Zr)_{9.66} and Sm(Co_{0.74}Fe_{0.1}Cu_{0.12}Zr_{0.04})_{7.5} melt-spun ribbons have been investigated. Annealing of the melt-spun Pr(Fe,Co,Ti,Cu,Zr)_{9.66} and Sm(Co_{0.74}Fe_{0.1}Cu_{0.12}Zr_{0.04})_{7.5} ribbons resulted in the formation of hexagonal TbCu₇ type structure. The saturation magnetization of the Nd₁₅Fe₇₉B₆ was found to be 127 Am² kg⁻¹ at room temperature. The annealed Pr(Fe,Co,Ti,Cu,Zr)_{9.66} ribbons have low coercivity values attributed to the presence of the soft α -Fe(Co) phase (under certain experimental conditions).

1. Introduction

Nanocomposite permanent magnets have attracted extensive attention in the last years due to their enhanced magnetic performances and potential applications [1]. They mainly consist of a fine mixture of a hard magnetic phase and one magnetically soft component with high saturation magnetization (most commonly Fe-based), exchange coupled [2]. The permanent magnet properties of nanocomposites are strongly influenced by a number of factors such as: the preparation method and the composition, the annealing conditions, and the grains size of the two constituting phases [3]. The large values of the remanence are related to the strength of the exchange interactions between the soft and hard magnetic grains, thus the reduction of the grains to sizes below the hard magnetic phase domain walls is essential. If the grains size is below a critical value, which is dependent on the nanocomposite composition, the magnetocrystalline anisotropy of the hard magnetic phase grains is diminishing and results in the drastic decrease of the coercive field.

In the following, it is presented our study on the microstructure and magnetic properties of nanocomposite magnets prepared from mixtures of ball-milled powders of Nd-Fe-B nanocrystalline melt-spun ribbons and respectively Pr₃(Co_{0.79}Fe_{0.019}Cu_{0.1})_{27.5}Ti_{1.5} or Sm(Co_{0.74}Fe_{0.1}Cu_{0.12}Zr_{0.04})_{7.5} intermetallic melt-spun ribbons.

2. Experimental

Alloys of Nd₁₅Fe₇₉B₆ (A₁), Pr₃(Co_{0.79}Fe_{0.019}Cu_{0.1})_{27.5}Ti_{0.5}B₅ (A₂), Pr₃(Co_{0.79}Fe_{0.019}Cu_{0.1})_{27.5}Ti_{1.5} (A₃), and Sm(Co_{0.74}Fe_{0.1}Cu_{0.12}Zr_{0.04})_{7.5} (A₄) have been prepared by arc melting. The alloy ingots were induction-melted in an argon atmosphere and then ejected through the orifice under argon pressure onto a chromium-plated copper wheel rotating at a surface velocity of 40 and 30 ms⁻¹. Amorphous Nd₁₅Fe₇₉B₆ (A₁) and Pr₃(Co_{0.79}Fe_{0.019}Cu_{0.1})_{27.5}Ti_{0.5}B₅ melt-spun ribbons (A₂), were annealed at different temperatures in the range 600-700°C for 10-30 min. to obtain the optimum nanocrystalline microstructure. Pr₃(Co_{0.79}Fe_{0.019}Cu_{0.1})_{27.5}Ti_{1.5} (A₃-3:29 phase), and Sm(Co_{0.74}Fe_{0.1}Cu_{0.12}Zr_{0.04})_{7.5} (A₄) and with intermetallic structures have been annealed at temperatures of 700-900°C for different times. The annealed ribbons have been used as precursors for powders prepared by high-energy ball-milling. Depending on the milling time the size of the micropowders varied between 5 and 100 μ m. The powders have been mixed in different ratios and cold-pressed to prepare nanocomposites as discs having 10 mm in diameter and 1 mm in thickness. Their structural and magnetic properties have been investigated afterwards by means of X-ray diffractometry, scanning electron microscopy, and vibrating sample magnetometry VSM.

3. Results and discussion

X-ray powder diffraction (XRD) results showed that as-spun ribbons of sample A₁ and A₂ present a mixture of phases and the main phase is Nd₂Fe₁₄B type structure. For the sample (samples A₃, A₄) XRD results showed that the main phase is TbCu₇-type, except a small amount of α -Fe(Co). Quantitative Rietveld refinement of the powder pattern for A₄ indicates the presence of the hex-1:7 and Co(Fe) metal phases, in amounts of about 99 % and <1 wt.% respectively. For amorphous a Nd₁₅Fe₇₉B₆ melt-spun ribbons (A₁) the optimum annealing duration is 20 min (Fig 1), the energy product reach the maximum and decreases drastically for 30 min. annealing).

The saturation magnetization, coercivity and ratio M_r/M_s for the optimum conditions of annealing ribbons for the A_4 sample are respectively $43.9 \text{ Am}^2/\text{kg}$, 8.9 kOe and 0.7 . While the A_2 samples presents a relatively higher M_s ($80 \text{ Am}^2/\text{kg}$), smaller coercivity (2.4 kOe) than A_1 and A_4 samples and ratio M_r/M_s equal 0.5 .

Table 1. Magnetic hysteresis parameters for $\text{Nd}_{15}\text{Fe}_{79}\text{B}_6$ ($A1$) melt-spun ribbons as a function of the annealing time.

Time annealing ($^{\circ}\text{C}$)	H_c (kOe)	M_s (Am^2/kg)	M_r/M_s
15	12.7	85	0.64
20	10	80	0.6
25	11	127	0.63

Finally, the A_3 samples as a soft phases have high $M_s=107 \text{ Am}^2/\text{kg}$ and very low coercivity, 80 Oe . Fig. 2 shows a representative magnetization curves of nanocomposite magnets. In the table 2 are shown the magnetic properties for some mixture of milled sample.

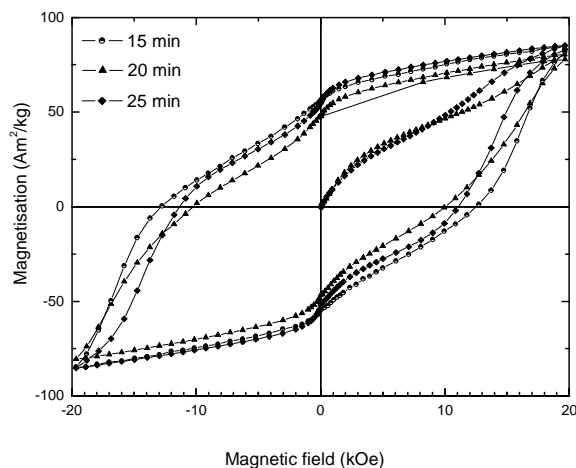


Fig. 3 Magnetization curves of $\text{Nd}_{15}\text{Fe}_{79}\text{B}_6$ ($A1$) melt-spun ribbons annealed at 15, 20 and 25 min.

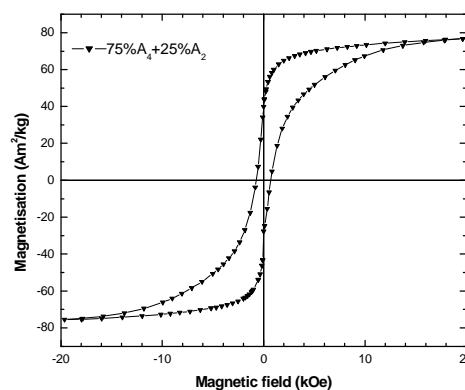


Figure 2. Magnetization curve of a mixture: 75% (weight %) of A_4 +25% (weight %) A_2 .

Table 2. Magnetic properties of nanocomposite magnets.

Sample	Ratio mixture (weight %)	M_s (Am^2/kg)	H_c (kOe)	M_r/M
Mixture 1	A_4 (75%) + A_2 (25%)	77	0.75	0.52
Mixture 2	A_4 (80%) + A_2 (20%)	62	4.3	0.42
Mixture 3	A_1 (80%) + A_4 (20%)	125	1.12	0.36

4. Conclusions

Nanocomposite permanent magnets have been obtained by mixing powders of different hard magnetic phases in different ratios. The powders have been obtained by ball-milling the melt-spun ribbons precursors. The magnetic properties can be tailored by choosing the proper annealing conditions and the optimum ratios of the 2 or more different phases forming the nanocomposites.

- [1] G.C. Hadjipanayis, J. Magn. Magn. Mater. 200 (1999) 373.
- [2] E.F. Kneller and R. Hawig, IEEE Trans. Magn. 27 (1991) 3588.
- [3] B.Z. Cui, C.T. Yu, K. Han, et al., J. Appl. Phys. 97 (2005) 10F308.

Effect of the Steel Composition on the Morphology of Zinc Hot-Dip Galvanized Coatings

N. Pistofidis*, E. Pavlidou, K. Chrissafis, G. Vourlias

Physics Department, Aristotle University of Thessaloniki, Thessaloniki, 54 124 Greece

* npistofi@auth.gr

Zinc hot-dip galvanizing is one of the most effective methods for the corrosion protection of ferrous materials [1]. In this case a zinc coating is deposited on top of the ferrous substrate with its immersion in a bath of liquid zinc, after the necessary pretreatment of the iron surface (degreasing, pickling and fluxing). Under these conditions, liquid zinc diffuses into the iron crystal lattice forming three layers, which could be distinguished based on their relief and correspond to Gamma (Γ), Delta (δ) and Zeta (ζ) phase of the Fe-Zn phase diagram. These layers are covered by a layer of pure zinc (eta- η phase) which is mechanically drifted as the substrate is withdrawn from the liquid zinc. Consequently the deposition of the zinc hot-dipped coatings is not only mechanical, but it is also enhanced through the formation of a metallurgical bond.

In the present work an attempt is made to clarify whether the growth of the above-mentioned phases is affected by the composition of the ferrous substrate. For this reason, specimens of steel U St 37 – 1 (typical carbon steel) and R St 37 – 1 (same composition with U St 37 – 1 but with high silicon) were galvanized in a bath of pure zinc at 450°C (with dipping time equal to 3 min) after the necessary surface pre-treatment (degreasing, pickling and fluxing). Some of the as-coated specimens were left to cool in the air at ambient temperature and were examined with optical and scanning electron microscopy (SEM), after being cut, polished up to 5 μm alumina emulsion and etched in 2% Nital solution. Furthermore Differential Scanning Calorimetry (DSC) was used for the coatings grown on U St 37 – 1.

Some characteristic SEM micrographs are presented in Fig. 1. From these micrographs the differences between the two coatings are obvious. The coating deposited onto U St 37 – 1 steel has the typical morphology of the galvanized coatings as it was previously described. However the coatings grown on R St 37 – 1 steel have different appearance. As the micrograph of Fig. 1 shows, although the delta phase is present, zeta phase covers the rest of the coating, while eta phase is absent. The absence of the eta phase was also verified with DSC (Fig. 2). The DSC plot of an ordinary galvanized coating is characterized by the melting point of pure zinc. By contrast when the eta phase is abstract a smooth line is only recorded, as the melting point of the Fe-Zn phases is much higher with regard to the zinc melting point.

This behaviour is due to the Sandelin effect [2]. This phenomenon is highly undesirable because the as-formed coating is very brittle (Fig. 3) because the Fe-Zn phases are characterized by high hardness (Table 1 [1]). Hence, although it is more susceptible to corrosion with regard to the usual coatings, it is characterized by inferior mechanical properties.

[1] A. R. Marder, Prog. Mat. Sci. 45, 191 (2000).

[2] G. Reumont, P. Perrot, J. Foct, J. Mat. Sci. 33, 4759 (1998).

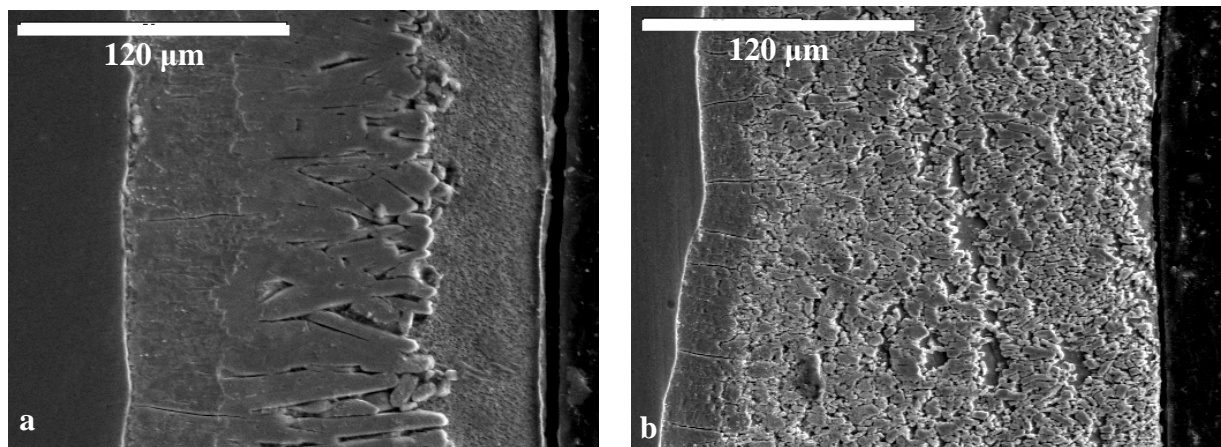


Fig. 1. SEM micrographs of the cross-section of the coatings deposited on U St 37 – 1 (a) and R St 37 – 1 (b) steel.

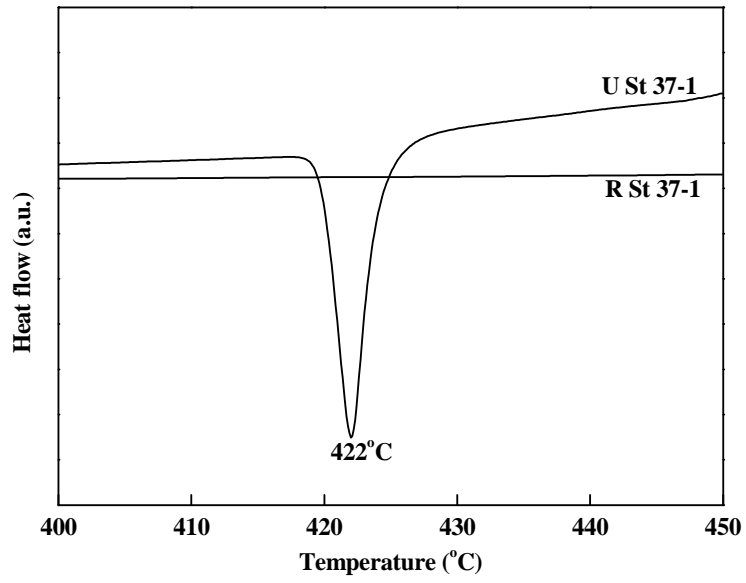


Fig. 2. DSC plot of the coatings deposited on U St 37 – 1 and R St 37 – 1 steel.

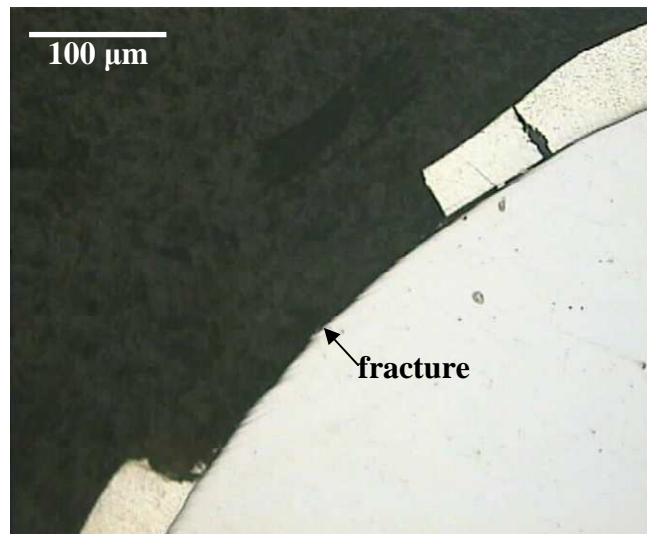


Fig. 3. Optical micrograph of a fracture area of a coating deposited on R St 37 – 1 steel.

Table 1: Hardness of the Fe-Zn phases [1]

Phase	Hardness (VHN)
α -Fe (ferrite)*	104
Γ	326
δ	358
ζ	208
η	52

* Presented only for comparison reasons.

Effect of the Cooling Time on the Morphology of Zinc Hot-Dip Galvanized Coatings

N. Pistofidis*, G. Vourlias

Physics Department, Aristotle University of Thessaloniki, Thessaloniki, 54 124 Greece

* npistofi@auth.gr

Zinc hot-dip galvanizing is one of the most effective methods for the corrosion protection of ferrous materials [1-5]. In this case a zinc coating is deposited on top of the ferrous substrate with its immersion in a bath of liquid zinc, after the necessary pretreatment of the iron surface (degreasing, pickling and fluxing). Under these conditions, liquid zinc diffuses into the iron crystal lattice forming three layers, which could be distinguished based on their relief and correspond to Gamma (Γ), Delta (δ) and Zeta (ζ) phase of the Fe-Zn phase diagram. These layers are covered by a layer of pure zinc (η - η phase) which is mechanically drifted as the substrate is withdrawn from the liquid zinc. Consequently the deposition of the zinc hot-dipped coatings is not only mechanical, but it is also enhanced through the formation of a metallurgical bond.

In the present work an attempt was made to clarify whether the growth of the above-mentioned phases continues when the coated material is withdrawn from liquid zinc. For this reason, specimens of carbon steel SAE 1010 (with low and high silicon) were galvanized in a bath of pure zinc at 450°C (with dipping time equal to 3 min) after the necessary surface pre-treatment (degreasing, pickling and fluxing). Some of the as-coated specimens were left to cool in the air at ambient temperature, while some of them were cooled with immersion in water at 0°C (water and ice). The as-treated specimens were examined with light microscopy, after being cut, polished up to 5 μm alumina emulsion and etched in 2% Nital solution.

Some typical micrographs of specimens cooled in the air and in water and ice are presented in Fig. 1 and 2. The observation of these photographs reveals that in each case the same phases are observed as it was previously explained. Of course the presence of Si affects the relief [6]. However, after fast cooling the thickness of the Fe-Zn phases is very low. Although the total thickness is almost the same, after fast cooling the proportion of the η phase is much higher.

A similar result could be drawn from the diagrams of Fig.3, where the same proportion between the Fe-Zn phases and the η phase is observed.

Thus the growth of the zinc hot-dip galvanized coatings continues also during the cooling of the coated material, after its withdrawn from the liquid zinc.

[1] A. R. Marder, Prog. Mat. Sci. 45, 191 (2000).

[2] P. Maass, P. Peissker, Handbuch Feuerverzinken, Wiley-VCH, Leipzig, 1993.

[3] D. Wetzel, Batch Hot Dip Galvanized Coatings, in ASM Handbook, Vol. 5-Surface Engineering, ASM International, New York, 2000.

[4] G. Vourlias, N. Pistofidis, G. Stergioudis, D. Tsipas, Crys. Res. Tech., 39, 23 (2004).

[5] G. Vourlias, N. Pistofidis, G. Stergioudis, E. Pavlidou, D. Tsipas, Phys. Stat. Sol. A, 201, 1518 (2004).

[6] G. Reumont, P. Perrot, J. Foct, J. Mat. Sci., 33, 4759 (1998).

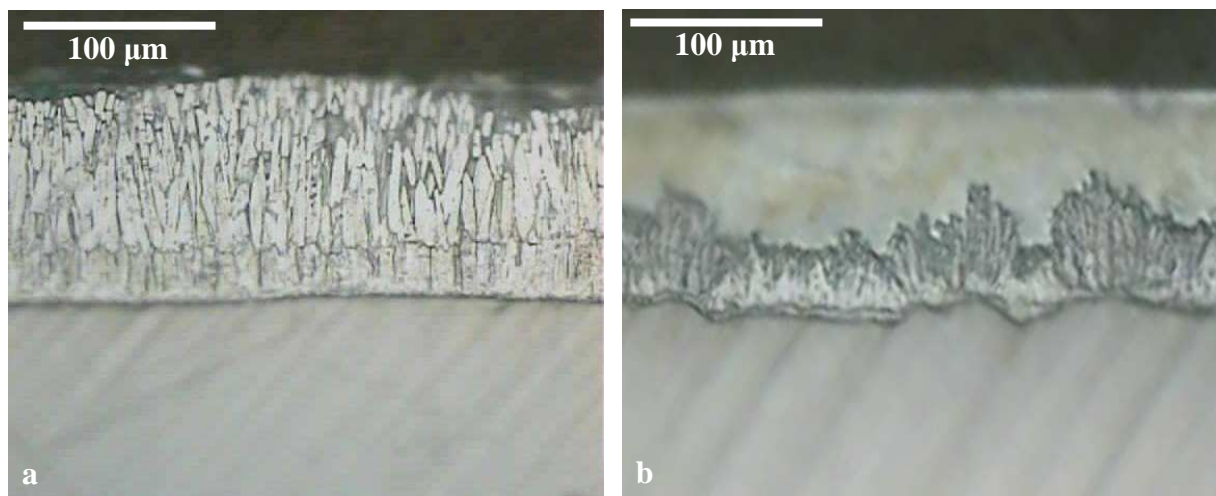


Fig. 1. Optical micrographs of zinc coatings (deposited on low silicon substrates) after air cooling (a) and fast cooling in water and ice (b).

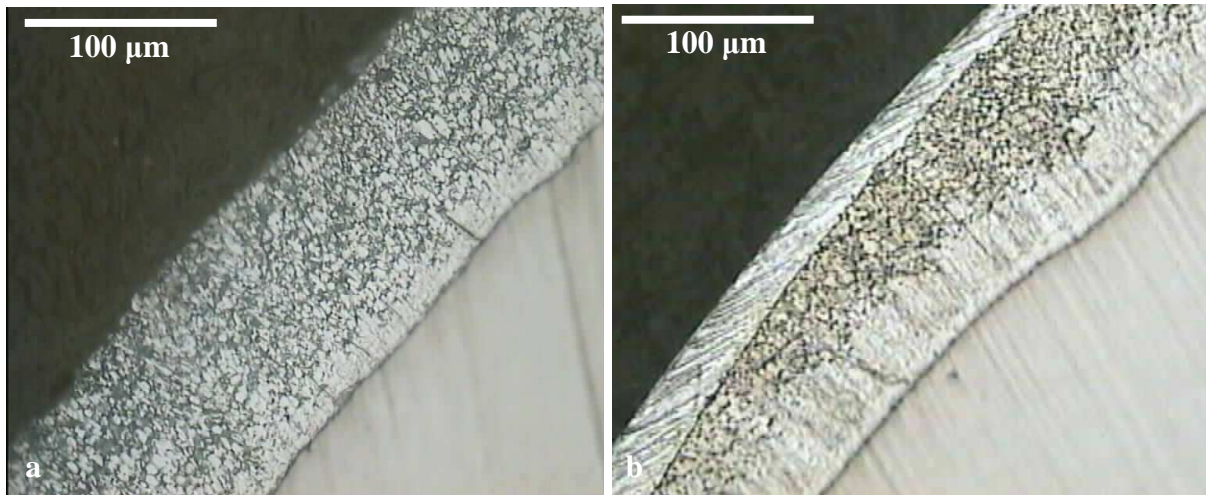


Fig. 2. Optical micrographs of zinc coatings (deposited on high silicon substrates) after air cooling (a) and fast cooling in water and ice (b).

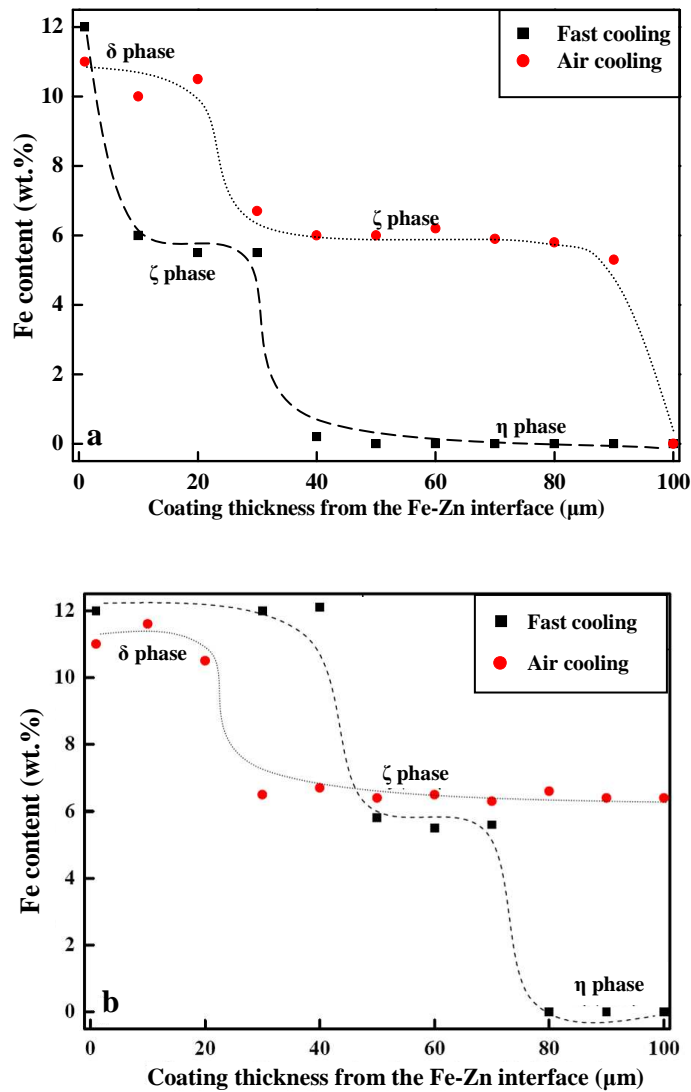


Fig. 2. Plot of the Fe content in a hot-dipped coating with regard to the distance from the Fe-Zn interface (a-low silicon substrate, b-high silicon substrate).

Thermodynamic Evaluation of Zinc Hot-Dip Galvanizing

N. Pistofidis*, G. Vourlias

Physics Department, Aristotle University of Thessaloniki, Thessaloniki, 54 124 Greece

* npistofi@auth.gr

Zinc hot-dip galvanizing is one of the most effective methods for the corrosion protection of ferrous materials [1]. In this case a zinc coating is deposited on top of the ferrous substrate with its immersion in a bath of liquid zinc, after the necessary pretreatment of the iron surface (degreasing, pickling and fluxing). Under these conditions, liquid zinc diffuses into the iron crystal lattice forming three layers, which could be distinguished based on their relief and correspond to Gamma (Γ), Delta (δ) and Zeta (ζ) phase of the Fe-Zn phase diagram. These layers are covered by a layer of pure zinc (eta- η phase) which is mechanically drifted as the substrate is withdrawn from the liquid zinc. Consequently the deposition of the zinc hot-dipped coatings is not only mechanical, but it is also enhanced through the formation of a metallurgical bond.

However the morphology previously described is not unique. Temperature variations of the liquid zinc, along with small changes of its composition, could result in different structures [1]. As these transformations are related to thermodynamic reasons, an estimation of the Gibbs free energy changes during hot-dipping could be useful since it could offer information on the stability of the different phases and on their spontaneous formation.

The Gibbs free energy could be calculated if we consider the different Fe-Zn phases as non ideal mixtures [2]:

$$G^m = \sum_i x_i G_i + RT \sum_i x_i \ln x_i + G^E$$

In this equation, G^m is the Gibbs free energy of the mixture, x_i the mole fraction of element i , G_i the molar Gibbs energy of element i , R the universal gas constant, T the temperature and G^E the excess Gibbs energy. For the calculation of G_i the following equation could be used:

$$G_i = H_i - TS_i$$

where H_i and S_i are respectively the enthalpy and entropy of element i . If standard equations are used for H_i and S_i [2], the final equation is:

$$G_i = G_i^{298} + C_{p_i}(T - 298) - TC_{p_i} \ln\left(\frac{T}{298}\right)$$

where $G_i^{298}=0$ (since both Zn and Fe are pure elements) and C_{p_i} is the specific heat of element i .

The excess Gibbs energy G^E could be expressed in Redlich-Kister polynomial [3]:

$$\frac{G^E}{x_1 x_2} = L_0 + L_1(x_1 - x_2) + L_2(x_1 - x_2)^2$$

where L is a binary interaction parameter, which could be evaluated as a linear function of temperature: $L = A + B \cdot T$. For the Fe-Zn system, the values of A and B are summarized in Table 1 [4-5].

Table 1: Values of the parameters of Redlich – Kister polynomial for the Fe-Zn phases (A in $\text{J}\cdot\text{mol}^{-1}$, B in $\text{J}(\text{K}\cdot\text{mol})^{-1}$).

Phase	L_0		L_1	
	A_0	B_0	A_1	B_1
Γ	-214641.2	180.1403	-283546.1	372.9637
δ	-315871.2	163.0428	-98851.1	0
ζ	0	0	0	0

The Gibbs free energy change during a transformation is calculated by the equation:

$$\Delta G = G^{init} - G^{final}$$

where G^{init} and G^{final} the initial and final Gibbs energy of the system. As a result the final equations for the three phases of the hot-dip coatings are the following:

$$\Delta G^{\Gamma} = 8.314T(x_{Fe} \ln x_{Fe} + x_{Zn} \ln x_{Zn}) + x_{Fe}x_{Zn}[(-214641.2 + 180.1403T) + (-283546.1 + 372.9637T)(x_{Fe} - x_{Zn})]$$

$$\Delta G^{\delta} = 8.314T(x_{Fe} \ln x_{Fe} + x_{Zn} \ln x_{Zn}) + x_{Fe}x_{Zn}[(-315871.2 + 163.0428T) + (-98851.1)(x_{Fe} - x_{Zn})]$$

$$\Delta G^{\zeta} = 8.314T(x_{Fe} \ln x_{Fe} + x_{Zn} \ln x_{Zn})$$

The values of the mole fractions are summarized in Table 2. The mole fractions have been calculated from the iron content of the different Fe-Zn phases as they are formed during hot-dipping [1].

Table 2: Mole fractions of Fe and Zn of the phases formed during zinc hot-dip galvanizing.

Phase	Fe content (wt.%)	minimum		maximum	
		x_{Fe}	x_{Zn}	x_{Fe}	x_{Zn}
Γ	23.5-28.0	0.26	0.74	0.31	0.69
δ	7.0-11.5	0.08	0.92	0.13	0.87
ζ	5.0-6.0	0.06	0.94	0.07	0.93

The final results are presented in Table 3. The temperature values refer to the temperature of the liquid zinc.

Table 3: Gibbs free energy changes ($J \cdot mol^{-1}$) during zinc hot-dip galvanizing.

Phase	450°C		480°C	
	minimum x_{Fe}	maximum x_{Fe}	minimum x_{Fe}	maximum x_{Fe}
Γ	-18400	-20645	-18537	-20553
δ	-10137	-16442	-9846	-15985
ζ	-1364	-1525	-1421	-1588

The data of Table 3 verify that at 450 and 480°C the formation of the Fe-Zn phases is spontaneous. Similar calculations could be repeated at different temperatures (above the melting point of zinc - 419°C [6]) in order to predict whether the formation of a certain phase is feasible. Of course this conclusion is not final because the growth of a certain phase is also highly affected by kinetics.

[1] A. R. Marder, Prog., Mat. Sci. 45, 191 (2000).

[2] J. M. Smith, H. C. Van Ness, Introduction to chemical engineering thermodynamics, 4th ed., McGraw-Hill, New York, 1987.

[3] O. Redlich, A. Kister, Indust. Eng. Chem. 345, 40 (1948).

[4] X. Su, N.-Y. Tang, J. M. Toguri, J. All. Comp. 325, 129 (2001).

[5] J. Nakano, D. V. Malakhov, G. R. Purdy, Calphad 103, 31 (2005).

[6] CRC Handbook of Chemistry and Physics, CRC Press, London, 1999-2000.

Evaluation of Fe-Zn Diffusion Coefficient during Hot-Dip Galvanizing

N. Pistofidis*, G. Vourlias

Physics Department, Aristotle University of Thessaloniki, Thessaloniki, 54 124 Greece

* npistofi@auth.gr

Zinc hot-dip galvanizing is one of the most effective methods for the corrosion protection of ferrous materials [1]. In this case a zinc coating is deposited on top of the ferrous substrate with its immersion in a bath of liquid zinc, after the necessary pretreatment of the iron surface (degreasing, pickling and fluxing). Under these conditions, liquid zinc diffuses into the iron crystal lattice forming three layers, which could be distinguished based on their relief and correspond to Gamma (Γ), Delta (δ) and Zeta (ζ) phase of the Fe-Zn phase diagram. These layers are covered by a layer of pure zinc (eta- η phase) which is mechanically drifted as the substrate is withdrawn from the liquid zinc. Consequently the deposition of the zinc hot-dipped coatings is not only mechanical, but it is also enhanced through the formation of a metallurgical bond.

The formation of the Fe-Zn phases is mainly accomplished with zinc diffusion in the crystal lattice of iron. Secondary growth with homogenous nucleation is also possible, but it is rather limited [1-2]. In the present work an attempt is made to estimate the Fe-Zn diffusion coefficient. For this reason the integrated equation of the second law of Fick was used:

$$C = C_o [1 - \operatorname{erf}(\frac{x}{2\sqrt{Dt}})]$$

where x is the diffusion depth, t the diffusion time, C the Zn content at depth x , C_o the Zn concentration at the Fe/Zn interface (as they are described in Fig. 1) and D the diffusion coefficient.

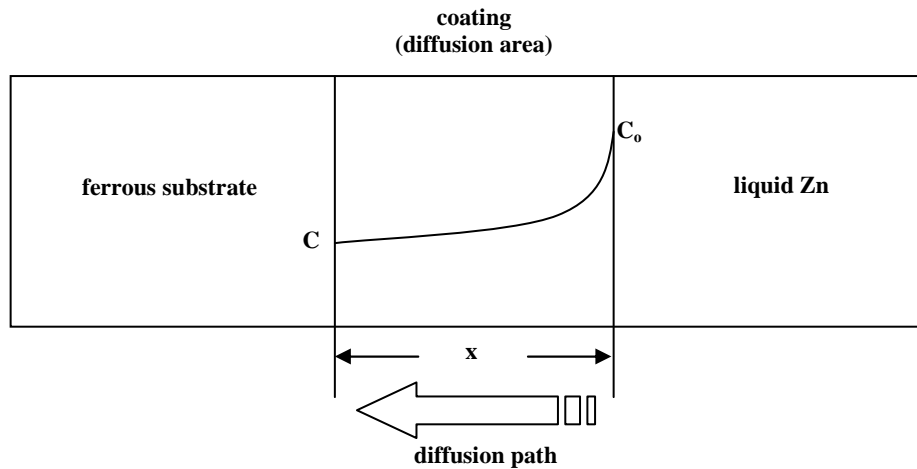


Fig. 1: Diffusion during hot-dip galvanizing. The curve in the coating describes the variation of the zinc content.

For the calculation of the diffusion coefficient D , the diffusion depth x and the zinc content C were measured with SEM/EDS. C was equal to about 78 %mol in every case. Furthermore the following assumptions were made:

- 1) The calculated diffusion coefficient is independent from the zinc content in the ferrous substrate.
- 2) Iron does not diffuse towards zinc.
- 3) The size of the ferrous substrate is big enough so as diffusion through one side is independent from diffusion through the others.
- 4) The liquid zinc does not contain any impurities (hence $C_o = 100$ % mol).
- 5) The thickness of eta (η) phase is not taken into account for the calculations, because it is formed during the withdrawn of the substrate from the liquid zinc.
- 6) Diffusion lasts as long as the substrate remains immersed in the liquid zinc.

The final results are summarized in Table 1. CGS units were used for diffusion coefficient as it is the case in international literature.

Table 1: Zinc diffusion coefficient ($\text{cm}^2\text{sec}^{-1}$) in different ferrous substrates (U St 34 – 1, U St 37 – 1, R St 37 – 1 at 450 and 480°C).

Temperature (°C)	U St 34 – 1	U St 37 – 1	R St 37 – 1
450	$2,13 \cdot 10^{-6}$	$1,88 \cdot 10^{-6}$	$1,22 \cdot 10^{-6}$
480	$2,14 \cdot 10^{-6}$	$2,08 \cdot 10^{-6}$	$1,55 \cdot 10^{-6}$

The comparison of the data of Table 1 with literature data is very interesting. The diffusion coefficient of zinc into α -Fe (ferrite) could be calculated by the following equation (in $\text{cm}^2\text{sec}^{-1}$), where T refers to the temperature [3]:

$$D = 2.6105 * \exp\left(\frac{-54000}{1.9872 * T}\right)$$

For the temperatures of Table 1, the calculated value of D is about $10^{-16} \text{cm}^2\text{sec}^{-1}$ as Table 2 shows.

Table 2: Zinc diffusion coefficient in α -Fe

Temperature (°C)	Diffusion coefficient ($\text{cm}^2\text{sec}^{-1}$)
450	$1.2 \cdot 10^{-16}$
480	$5.5 \cdot 10^{-16}$

However, the following equation is more accurate [4]:

$$D = 32.1 \cdot 10^{-6} * \exp\left(\frac{-25000}{RT}\right)$$

since, for the same temperatures, the calculated diffusion coefficients are about $10^{-7} \text{cm}^2\text{sec}^{-1}$ (Table 3). The difference with the previous equation is due to the fact that in this case the diffusion of zinc through the zeta (ζ) phase is taken into account and not the diffusion of zinc into iron.

Table 3: Zinc diffusion coefficient in the zeta (ζ) phase of the Fe-Zn system

Temperature (°C)	Diffusion coefficient ($\text{cm}^2\text{sec}^{-1}$)
450	$1.43 \cdot 10^{-7}$
480	$1.69 \cdot 10^{-7}$

This observation is very important because it enlightens the growth mechanism of the zinc coatings. As the experimental results are very similar to the results from the last equation, it is obvious that one of the steps is the diffusion of zinc through the zeta phase. Hence this phase is initially formed (probably due to homogeneous nucleation) and the rest of the phases are formed with zinc diffusion through zeta.

[1] A. R. Marder, Prog. Mat. Sci. 45, 191 (2000).

[2] N. Pistofidis, D. Chaliampalias, G. Vourlias, Surf. Eng., DOI 10.1179/174329408X326461.

[3] S. Budurov, P. Kovatchev, Z. Kamenova, Z. Metallkunde 64, 652 (1973).

[4] P. J. Gellings, E. W. de Bree, G. Gierman, Z. Metallkunde 70, 315 (1979).

Comparative examination on structure and oxidation behavior of pack cementation zinc coated and not coated copper alloys substrates

M.Papazoglou¹, D. Chaliampalias^{1*}, E. Pavlidou¹, S. Skolianos², G.Stergioudis¹, G.Vourlias¹

¹Physics Department, Aristotle University of Thessaloniki, Thessaloniki, Greece, 54124

²Department of Mechanical Engineering, Aristotle University of Thessaloniki, Greece

*dimchal@auth.gr

Copper-base alloys have been evaluated and used for a wide range of high-quality indoor and outdoor applications, statue parts, art hardware, high strength and high thermal conductivity applications at elevated temperatures [1]. Furthermore, the mechanical characteristics of copper make this metal suitable for a great variety of metallurgical applications, such as, continuous casting steel moulds, oxygen nozzles in steelmaking converters and slag hole in blast furnaces. However, the usage of these materials at aggressive environments is usually limited because of their severe oxidation. A promising way in order to reinforce the oxidation resistance of similar materials is the deposition of coatings with materials which are less prone in such conditions. Zinc (Zn) has several features that make it well-suited for use as protective coatings to metallic substrates [2]. The usual methods for depositing on copper alloys substrates are hot-dip galvanizing, electrodeposition and thermal spray. A novel technique suitable for this purpose is chemical vapor deposition (CVD) by pack cementation [3]. In this case the substrates are packed and sealed together with the donor material and a chemical halide activator in a ceramic crucible and then are heat treated under argon atmosphere. After the deposition, the as coated samples were subjected at 400°C in air for 24 hours. The aim of this work is to investigate the structure of Zn coatings deposited on copper and leaded brass substrates, with pack cementation process, and to estimate their oxidation resistance. The examination of the samples was performed using a JEOL 840A SEM (20 kV) while the element distribution was investigated using an ISIS 2000 EDS analyzer. Finally the characterization of the phases formed in the coatings was accomplished by PHILIPS PW 1050 diffractometer (CuK α radiation) with Bragg-Brentano geometry.

From the SEM examination of the as deposited samples, it was found that on the copper substrates the coating consists of two compact homogeneous layers with different Zn concentration. Each layer contains different intermetallic phases from the corresponding binary alloy phase diagram. Particularly, the layer located in contact with the copper substrate (internal), corresponds at the β' -phase (CuZn, 45.5-50.7 wt% Zn), while the overlying external layer (external) corresponds to γ -phase (Cu₅Zn₈, 57.7-70.6 wt% Zn) of the Cu-Zn phase diagram. The average thickness of these layers was measured 45 μ m for the internal and 60 μ m for the external layer. The coating on leaded brass substrate is single layered with almost constant zinc concentration. In fact this layer corresponds to the γ -phase (Cu₅Zn₈, 57.7-70.6 wt% Zn) which is also an intermetallic combination of the Cu-Zn phase diagram [4]. The average thickness of this layer was measured 105 μ m. For both substrates the total thickness of the coatings was at the same level. The formation of these layers is a result of the high diffusivity of zinc atoms in copper and brass alloys under the particular deposition temperature. Substitutional diffusion took place due to the comparable atomic radius of the elements and the existence of vacancies in copper and brass crystal lattices. Thus, a strong metallic bond is developed between the coating and the substrates which enhance the adhesion of the two materials. Furthermore, several Pb clusters were tracked dispersed throughout the zinc coating area of the brass substrate. Their radius was measured up to 4 μ m, while their presence is also attributed to the high upward diffusivity of Pb atoms, of the brass substrate, at the particular deposition temperature [5].

From the EDS analysis, performed after the oxidation test, it is concluded that the coatings protect the substrate forming oxide scales on their surface which act as diffusion barriers preventing significantly the diffusion of the oxygen anions. On the surface of the uncoated copper substrate, subjected at the same conditions, a few μ m brittle copper oxide (CuO) was formed which leads to the substrate gradual decomposition at longer exposure periods. The uncoated brass surface was found to be less prone to oxidation from uncoated copper. However, similarly in this case several brittle copper oxides were traced as a result of the substrate oxidation. In the SEM microphotographs the coated substrates appear to maintain their primary chemical composition in most of their areas with the exception of layers on the surface which were found to contain passivating oxides. These remarks were also confirmed by the mass gain oxidation results where it was found that both zinc coated substrates had less weight gain, due to the oxide formation, than bare brass and copper. As a general conclusion it is found that the coated substrates are remarkably sustainable under the same conditions and can be used at similar applications.

[1] Understanding Copper Alloys, J.H. Mendenhall, Ed., Robert E. Krieger, 1977

[2] Marder, A.R, Progress in Materials Science, 2000, 45 (3), pp. 191-271.

- [3] G. Vourlias, N. Pistofidis, D. Chaliampalias, E. Pavlidou, G. Stergioudis, E.K. Polychroniadis, D. Tsipas, Journal of Alloys and Compounds 416 (2006) 125–130
- [4] Alloy Phase Diagrams, in Vol. 3- American Society of Metals, ASM International, 1992, pp.780.
- [5] M. Michailov, M. Vladkov, Surface Science 601 (2007) 3912–3915
- [6] PC Powder Diffraction Files, JCPDS-ICDD, 2000.

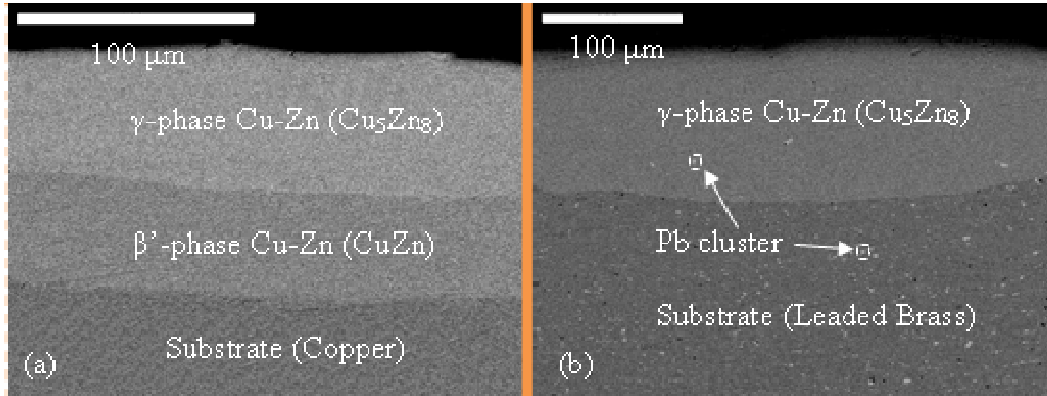


Figure 1 - Cross Section SEM micrographs of (a) Zinc coated copper substrate (b) Zinc coated leaded brass substrate.

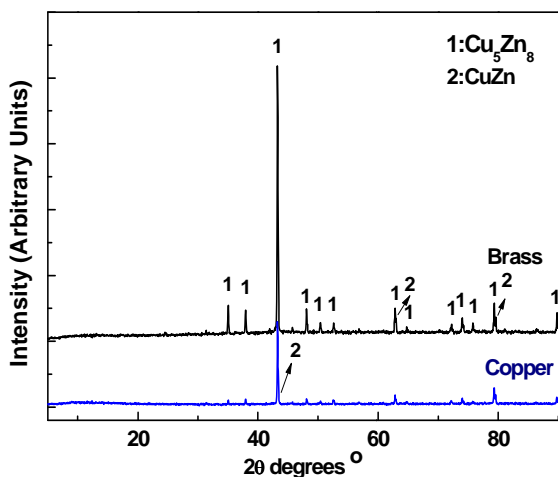


Figure 3 - XRD diagrams reveal the existence of Cu_5Zn_8 and CuZn phases (Pdf# 25-1228, 65-6566, 65-6321) [6].

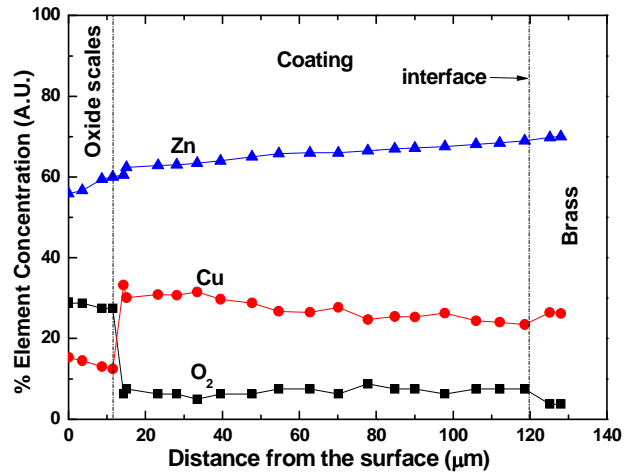


Figure 2 - EDS Line Scanning of oxidised zinc coated leaded brass substrate.

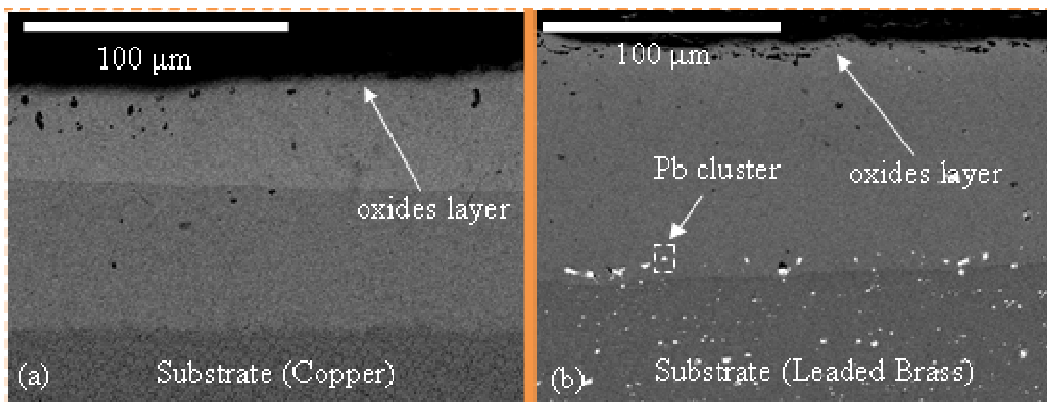


Figure 4 - Cross Section SEM micrographs of (a) Zn - Al (b) Zn - Cr coatings after exposure to elevated temperature oxidation.

Influence of Al and Cr alloying elements on the structure and corrosion resistance of zinc coatings formed by pack cementation process

M. Papazoglou¹, D. Chaliampalias^{1*}, E. Pavlidou¹, S. Skolianos², G. Stergioudis¹, G. Vourlias¹

¹ Physics Department, Aristotle University of Thessaloniki, Thessaloniki, Greece

² Department of Mechanical Engineering, Aristotle University of Thessaloniki, Thessaloniki, Greece

*dimchal@auth.gr

Zinc (Zn) is a well suited metal for use as a protective coating on a variety of ferrous substrates as a result of its durability in several aggressive environments. The performance of zinc results from its ability to react with the atmospheric compounds (O₂, CO₂ and H₂O) and form dense and adherent films on coating surface whose rate of corrosion is considerably below that of ferrous materials (barrier protection). Additionally, Zn is anodic to iron and steel and consequently offers cathodic protection [1]. Aluminum (Al) and Chromium (Cr) are also referred resistant coating elements because of their ability to form adherent films with lower corrosion rate than the usual ferrous materials [2,3]. Their corrosion resistance is attributed to a few atoms thick impermeable oxide layer, which is formed on the surface of the deposition and hinders significantly further diffusion of oxygen into the underlying material. The most widely applied process for zinc deposition is hot-dip galvanizing, where the ferrous substrate is covered by a layer of zinc through its immersion in a bath of molten zinc. However, the high environmental impact of this method imposes the investigation of alternative coating techniques, with lower environmental impact, such as pack cementation [4]. This process is a novel technique and as its application for zinc deposition is relatively rare. In this case, the coating is formed by heating the substrate in a sealed crucible, covered with a mixture of powders containing the donor material, a particular halide activator and an amount of inert filler. In order to estimate the oxidation resistance of the as coated samples, they were subjected at 400°C in air for 24 hours. This work aims to examine the effect of elevated temperature environment on the structure of Zn-Al and Zn-Cr coatings deposited on low alloyed steels with pack cementation. The examination of the samples was performed using a JEOL 840A SEM (20 kV) while the element distribution was investigated using an ISIS 2000 EDS analyzer. Finally the characterization of the phases formed in the coatings was accomplished by PHILIPS PW 1050 diffractometer (CuK α radiation) in Bragg-Brentano geometry.

Comparing with the structure of zinc pack cementation coatings without any other elemental admixture, it was found that the addition of aluminum or chromium in the pack mixture, does not affect significantly the phase composition of zinc coatings, which are mainly composed of Γ -phase (Fe₃Zn₁₀, 23.5-28%wt. Fe) and δ -phase (FeZn₁₀, 7-11.5%wt. Fe) of the Fe-Zn phase diagram [1]. The Γ -phase is traced at the areas close to the substrate (interface), while δ -phase is located at the areas over the Γ -phase. The structure effect of Al or Cr is limited mainly on the surface of the specimens where the formation of an overlying layer in both cases was tracked. In the case of Al addition in the pack mixture, the overlying layer contains high concentrations of Al together with lower amounts of zinc and iron. The thickness of this layer was measured close to 25 μ m while the total coating thickness was measured at 75 μ m. In the case of Cr addition in the pack mixture the overlying layer has very small thickness, comparing with the layer formed in the case of Al addition. Chemically this layer contains high concentrations of Cr and Zn and low amounts of iron. The average thickness of the overlying layer was measured at 15 μ m while the total coating thickness was measured at 150 μ m. Their formation results from the high diffusivity of Al and Cr in zinc under the particular deposition temperature. Substitutional diffusion took place due to the comparable atomic radius of the elements and the vacancies existence in zinc crystal lattice. As a result, metallic bond developed between the supplementary elements and zinc. XRD analysis revealed that, the overlying layer is composed of Fe-Zn-Al and Fe-Zn-Cr intermetallic compounds, as referred to the corresponding ternary alloy phase diagrams. The formation of Zn_xAl₅Fe₂ compound, as referred to Fe-Zn-Al phase diagram, was recorded on the zinc coatings with Al addition. Similarly, the formation of the Fe_xZn₁₇Cr compound, as referred to Fe-Zn-Cr phase diagram, was recorded on the zinc coatings with Cr addition [5].

The oxidation results revealed that zinc coatings containing Al and Cr compounds had less weight gain due to the oxide formation comparing with bare steel and unalloyed Zn coatings. These results are confirmed by the SEM microphotographs were both Zn-Al and Zn-Cr coatings, appear to maintain their primary chemical composition in most of their areas. However, in the case of Al addition the layer on the surface was found to contain several Al, Zn and zinc aluminum iron oxides while in the case of Cr addition in the coating, the as formed layer contain equally Cr, Zn and zinc chromium iron oxides. The formation of these oxides is likely to enhance the oxidation resistance of the samples for longer exposure periods because they increase the passivation ratio of the coupons preventing significantly the oxygen diffusion in the coating and thus, protecting the Zn-Fe phases.

- [1] Marder, A.R, Progress in Materials Science, 2000, 45 (3), pp. 191-271.
- [2] Houngrinou, C., Chevalier, S. Larpin, J.P. Materials Science Forum, 2004, 461-464 (I), pp. 273-280
- [3] Lindsay Jr., J.H., Plating and Surface Finishing, 2004, 91 (8), pp. 16-17.
- [4] G. Vourlias, N. Pistofidis, D. Chaliampalias, E. Pavlidou, G. Stergioudis, E.K. Polychroniadis, D. Tsipas, Journal of Alloys and Compounds 416 (2006) 125–130
- [5] V.Raghaven, Journal of Phase Equilibria and Diffusion Vol. 24 No. 6 2003.
- [6] PC Powder Diffraction Files, JCPDS-ICDD, 2000.

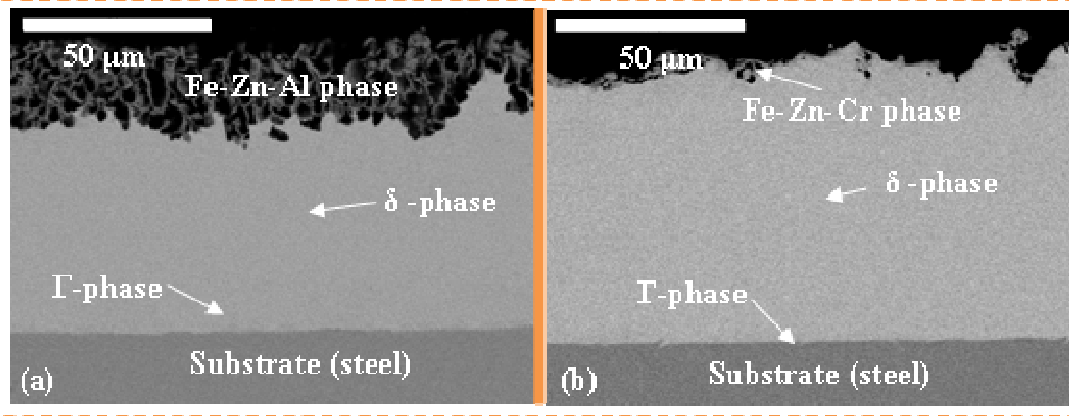


Figure 1-Cross Section SEM micrographs of (a) Zn - Al (b) Zn - Cr coatings

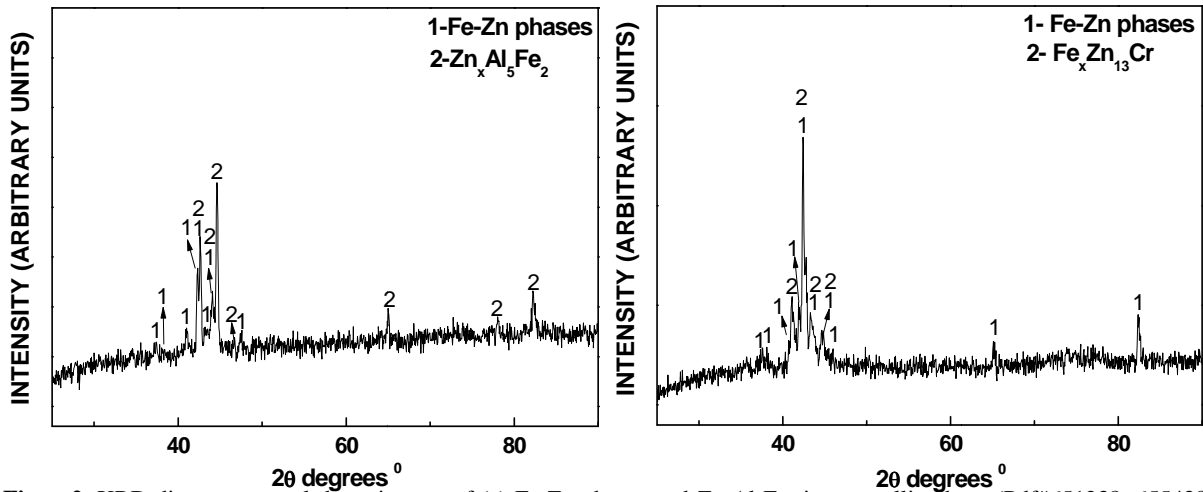


Figure 2. XRD diagrams reveal the existence of (a) Fe-Zn phases and $Zn_xAl_5Fe_2$ intermetallic phase (Pdf#651238, 655438, 657175, 320478, 341314, Pdf#491381). (b) Fe-Zn phases and $Fe_xZn_{13}Cr$ intermetallic phase (Pdf#651238, 655438, 657175, 320478, 341314) [6].

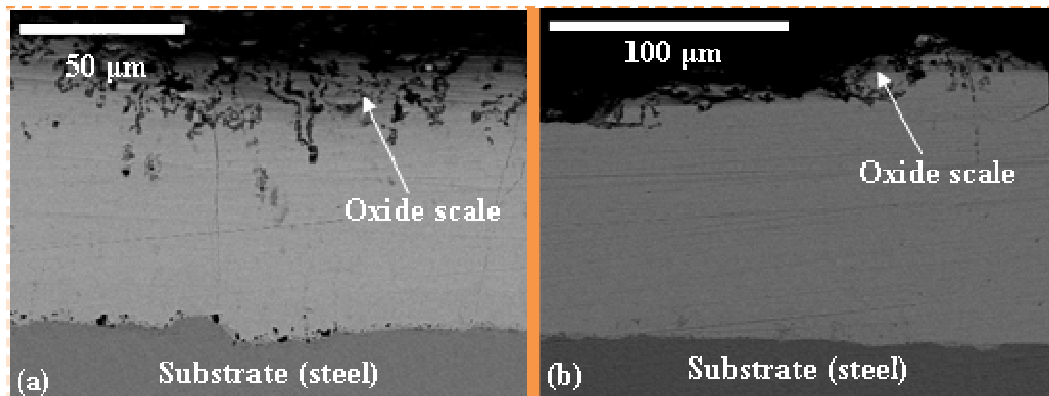


Figure 3. Cross Section SEM micrographs of (a) Zn - Al (b) Zn - Cr coatings after exposure to elevated temperature oxidation.

Coarsening in René 80 Ni-based Superalloy

D. Hadjiapostolidou*, B.A. Shollock

Department of Materials, Imperial College London, Exhibition Road, London SW7 2AZ, UK

*d.hadjiapostolidou05@imperial.ac.uk

Ni-based superalloys owe their remarkable properties to the γ' phase precipitation. The volume fraction, size, shape and distribution of these precipitates strongly affect the properties of these alloys. Coarsening occurs during service, altering the properties of engine components and determining their service life. Most studies focused on the growth kinetics for short times [1-5] compared to the life of engine components. It is important to investigate the coarsening behaviour for long aging times and to understand the mechanisms and growth kinetics in order to have a realistic estimation of the service life. This is especially important in the case of land-based turbines that operate for very long times.

In this study René 80 Ni-based superalloy was used. After the standard heat treatment the microstructure is bimodal and consists of cuboidal primary γ' and spheroidal secondary γ' . Subsequently, 39 aging treatments were performed at temperatures 850°C, 900°C, 950°C, and 1000°C for 8 aging times up to 20000 h and at 1050°C for 7 aging times up to 10000 h. Sections of each sample were polished and electro-etched before being examined using a LEO Gemini 1525 field emission gun scanning electron microscope (FEGSEM). The resulting micrographs were analysed using ImageJ software.

The results for the particle size evolution are shown in Figure 1. For short aging times, 10 – 500h, the average particle size increases for all temperatures. For long aging times, 1000 – 20000h, the average particle size increases for all times for temperatures up to 950°C. For 1000°C the average particle size increases up to 5000 h, but then there is a decrease in the size of the primary γ' because of partial dissolution of the primary precipitates and the precipitation of fine cooling γ' in the interparticle spacings. The same holds for 1050°C after 1000 h. Furthermore, coalescence between particles increased both with time and temperature and therefore the shape of the particles changes from cubic to irregular. The coarsening rate is much faster for short than for long aging times.

The results for the average particle size were used to determine the rate limiting mechanism. If growth is interface controlled, then it obeys the square rate law ($r^2 \sim t$) whereas if growth is diffusion controlled it follows the cube rate law ($r^3 \sim t$) [6]. The average particle size measurements were compared with both laws. For short aging times the square rate law seems to fit the measurements better. For long aging times no mechanism seems clearly dominant. The activation energy for coarsening was calculated to be 127 kJ/mol.

It has been reported for René 80 [6] that at 871°C no more coarsening occurs between 1000 and 1750 h. It is obvious from Figure 2, that coarsening continues after 1000 h, although at a slower rate. Size saturation was observed for higher temperatures and longer times in other alloys (Nimonic 80A, IN939 [7], experimental alloy [8]). These observations might be related to the partial dissolution observed in this study.

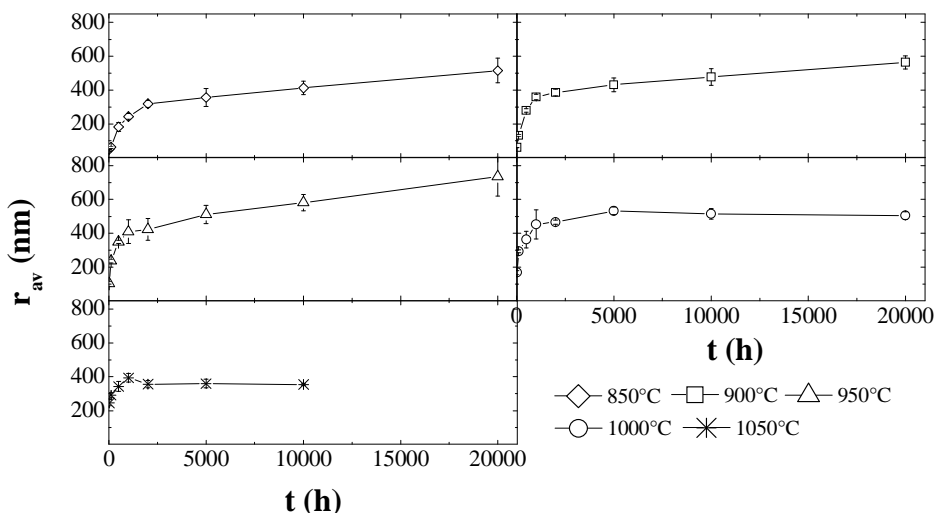


Figure 1: Average precipitate size evolution.

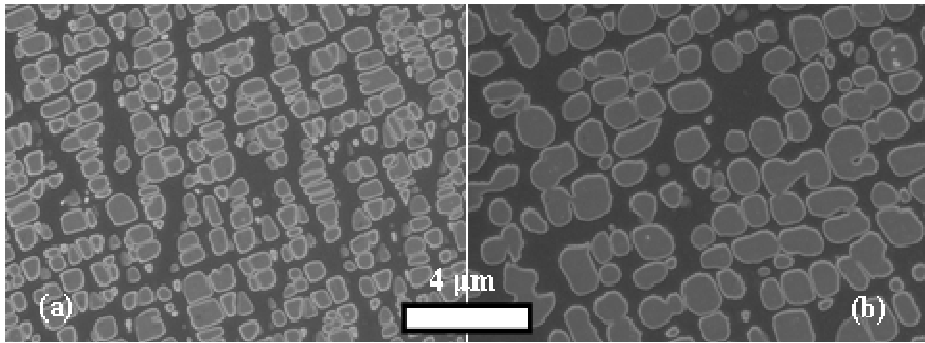


Figure 2: Microstructure after aging at 850°C for (a) 1000 h, (b) 20000 h.

- [1] Ardell, A.J., Acta Metallurgica 16, 511 (1968).
- [2] Ardell, A.J. Metallurgical Transactions 1, 525 (1970).
- [3] Chellman, D.J, Ardell A.J, Acta Metallurgica 22, 577 (1974)
- [4] Kim, H.T., Chun S.S., Yao X.X., Fang Y., Choi, J., Journal of Materials Science 32, 4917 (1997).
- [5] Safari, J., Nategh S., McLean M., Materials Science and Technology 22, 888 (2006).
- [6] McLean D., Metal Science 18, 249 (1984).
- [7] Footner P.K., Richards B.P., Journal of Materials Science 17, 2141 (1982).
- [8] MacKay, R.A, Nathal M.V., Acta Metallurgica Et Materialia 38, 993 (1990).

Acknowledgments: The authors would like to thank EPSRC (EP/C536312/1) for the financial support and RWE npower for providing the material for this study.

Residual Stress Measurements on CuCrZr/W Brazed Alloy Using Neutron Diffraction

K. Mergia^{1*}, M. Kastriotou¹, M. Hofmann², M. Grattarola³ and S. Messoloras¹

¹ Institute of Nuclear Technology and Radiation Protection, N.C.S.R. "Demokritos," Athens, Greece

² FRM-II, TU München, Lichtenbergstr. 1, Garching, Germany

³ ANSALDO Ricerche s.p.a., Corso Perrone 118, 16152 Genova, Italy

*kmergia@ipta.demokritos.gr

The development of joining techniques for the fabrication of components for electronic, nuclear fusion and space applications is an important technological issue. In fusion related applications plasma facing compounds (PFC) consist of two parts: (i) the direct plasma facing material made of carbon or tungsten, and (ii) the heat sink consisting of a copper-rich CuCrZr alloy [1-2]. The protection material can be joined to the heat sink by means of a high temperature brazing process (up to 1040 °C) using silver-free alloys.

The main problem of bonding W or C-material to CuCrZr is the large difference in their coefficient of thermal expansion (CTE). This difference creates very large residual stresses at the interface and may result in damage of the joint simply from cooling it down from the joining temperature. A low yield strength material compliant layer, like pure copper, can be introduced between the protective material and CuCrZr in order to lower the residual stresses by plastic deformation. Another solution is to introduce a high yield strength material interlayer with CTE matching that of the protective material, like molybdenum, in order to transfer the residual stresses from the carbon/metal interface to the strongest metal/metal one.

Neutron diffraction is a unique tool and a well-established non-destructive method for the in-depth determination of residual stresses in materials, since neutrons can penetrate deep in matter [3-4]. The method relies on the precise measurement of the Bragg peaks at different positions within the sample so a three dimensional mapping of the residual stresses can be constructed.

In the present work neutron diffraction measurements have been employed in order to measure the strains and residual stresses in a CuCrZr tube brazed to W tile, in the side of the W tile. Three geometries have been used in order to measure the axial, radial and tangential strains and stresses, at various distances from the weld.

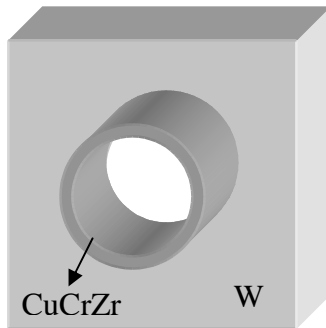


Fig.1. Schematic drawing of the brazed CuCrZr tube to the W tile.

The W tile was brazed to the CuCrZr tube using an active silver free filler at 1040°C. The W tile has dimensions 25×25×12 mm³ and the heat sink tube has an outer diameter of 15 mm. The schematic drawing of the brazed system is depicted in Fig. 1.

The neutron diffraction experiments were carried out at a STRESS-SPEC instrument at FRM-II Research Reactor in Munich, Germany. The wavelength used was 1.67Å from Si(4 0 0) bent monochromator.

The sample was placed on a X, Y, Z translation table which was attached on the top of a rotation table. The W(2 1 1) Bragg peak was monitored on a two dimensional position sensitive ³He detector using three geometries, which correspond to the measurement of axial, radial and tangential strain and stress. The gauge volume used was 1×1×1 mm³.

The Bragg peak position (scattering angle 2θ) was determined by fitting the experimental profile (counts versus angle) to a Gaussian function. The d-spacing of the atomic planes is calculated according to Bragg's law

$$\lambda = 2d \sin \theta \quad (1)$$

The strain, ε , at any measurement point was calculated using the equation

$$\varepsilon = \frac{d^{211} - d_0^{211}}{d_0^{211}} = \frac{\sin \theta_0^{211}}{\sin \theta^{211}} - 1 \quad (2)$$

where d^{211} and d_0^{211} are the interplanar distances between (2 1 1) planes of the stressed material and that of the free-stress material, and $2\theta^{211}$, $2\theta_0^{211}$ the Bragg peaks of the (2 1 1) planes of the stressed material and the free-stress material, respectively. For the determination of d_0^{211} a tungsten tile was used away from the brazed region. The residual stress was calculated from the strain using the generalised Hooke's laws which for the axial stress is given by the Eq. (3).

$$\sigma_{ax} = \frac{E}{(1+\nu)(1-2\nu)} \left[(1-\nu)\varepsilon_{ax} - \nu(\varepsilon_r + \varepsilon_t) \right] \quad (3)$$

where σ_{ax} is the axial, radial and tangential stress and ε_{ax} , ε_r , ε_t the axial, radial and tangential strains, respectively. Similar are the expressions for the tangential and axial stress. E is the Young's modulus, where $E=388.7$ GPa, and $\nu=0.283$ the Poisson's ratio.

Figs. 2a and 2b present schematically the geometry used and the line scans performed for the measurement of the axial strain and stress.

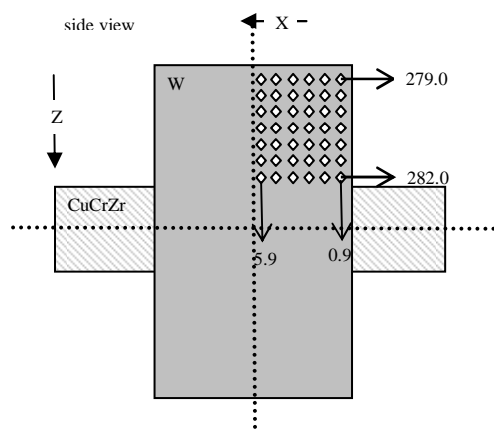


Fig.2a. Schematic drawing of the side view for the measurement of the axial strain depicting the line scans at different positions (indicated by the dots) in X and Z direction.

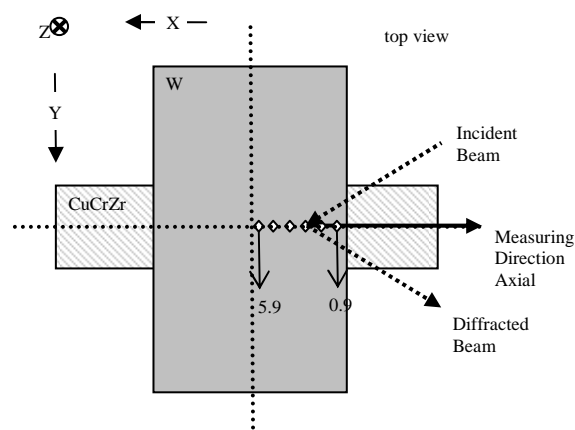


Fig.2b. Schematic drawing of the top view for the measurement of the axial strain depicting the line scans at different positions (indicated by the dots) in X direction.

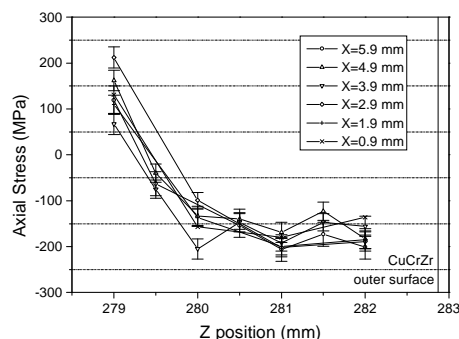


Fig.3. Axial stress along the Z direction for various distances X from the free edge of the W tile.

Figure 3 depicts the axial stress along the Z direction, i.e. vertical to the tube axis, for various distances X from the free edge of the tungsten tile (Fig. 2b). The stresses along the Z direction are compressive for distances up to 3.5 mm from the W/CuCrZr interface whereas they become tensile at about 4 mm from the brazed region and almost of equal value with the compressed ones. No variation along the X direction is observed.

The maximum stresses found are along the tangential direction, they are compressive and reach the value of 400 MPa.

References

- [1] G. Kalinin, W. Gauster, R. Matera, A.A.F. Tavassoli, A. Rowcliffe, S. Fabrietsev, H. Kawamura: J. Nucl. Mater. 233-237, 9 (1996).
- [2] A.A.F. Tavassoli: J. Nucl. Mater. 258-263, 85 (1998).
- [3] M.T. Hutchings and A. Krawitz (eds.) in: Measurement of residual and Applied Stress using Neutron Diffraction, NATO ASI Series E, Vol. 216 (1992).
- [4] L. Pintschovius, in: Analysis of Residual Stress by Diffraction using Neutrons and Synchrotron Radiation, edited by M.E. Fitzpatrick and A. Lodini. (London, Taylor & Francis, 2003).

Acknowledgments

This work has been carried out within the framework of the Integrated European Project "ExtreMat" (contract NMP-CT-2004-500253) with financial support by the European Community. The paper only reflects the views of the authors and the European Community is not liable for any use of the information contained therein. Also, the support of the European Commission under the 6th Framework Programme through the Key Action: Strengthening the European Research Area, Research Infrastructures. (Contract no: RII3-CT-2003-505925).

Brazing of Nimonic Superalloy to Carbon-based Ceramic Composites

N. Moutis^{1,*}, C. Jimenez², T. Speliotis³, X. Aspiroz², S. Messoloras¹ and K. Mergia¹

¹ Institute of Nuclear Technology and Radiation Protection, NCSR "Demokritos" 15343 Aghia Paraskevi, Greece

² Fundación INASMET, Parque Tecnológico, E-20009 San Sebastian, Spain

³ Institute of Materials Science, NCSR "Demokritos" 15343 Aghia Paraskevi, Greece

* nmoutis@ipta.demokritos.gr

Joining of carbon or silicon carbide-based composites to metals is exceedingly interesting, both scientifically, as complicated surface interactions can be studied, and technologically for high temperature applications in fusion and aerospace [1]. In this work we present the results of a generic approach for joining ceramics to metals. This approach was initially applied for joining graphite to a Nimonic superalloy and it was further explored on joining C_f/C and C_f/SiC ceramic composites. The basic idea of this approach is to develop a layered structure on the ceramic by metallizing its surface in such a way as to accommodate the different linear coefficients of thermal expansion (CTE) between ceramic and the metal.

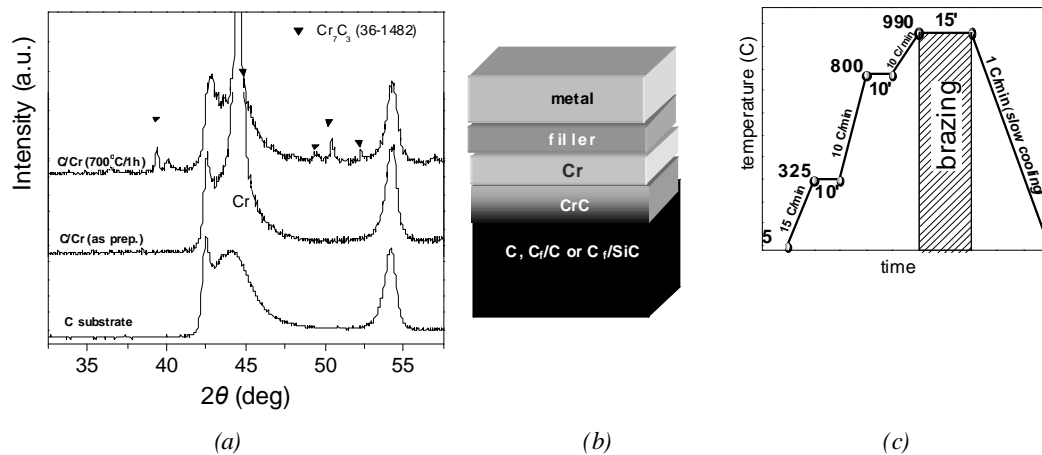


Fig. 1: (a) X-ray diffraction patterns of graphite substrate, C/Cr as prepared and annealed at 700°C/1h, where chromium carbide is indicated, (b) schematic of the metal-ceramic joint and (c) thermal cycle brazing.

Commercial (Goodfellow) carbon graphite and industrial (EADS) ceramic composites were used as substrates for the deposition of 2 μm thick layer of chromium by magnetron sputtering technique. Subsequently, the samples were annealed at 700°C under vacuum of 10^{-6} mbar for 1 hour to form chromium carbides and thus enhance the wetting of the filler. An intermediate layer of the chromium carbide Cr_7C_3 was formed between the surface of the composite and the remaining Cr, as it is evidenced by the X-ray diffraction pattern (Fig.1a). The layered ceramic/carbide/chromium structure was brazed to a Nimonic superalloy under a high temperature thermal cycle, aided by the use of a TiCuAg active brazing metal (Ag-26.7Cu-4.6Ti wt.%) in paste form (Fig.1b). Nimonic is a wrought nickel-cobalt based alloy (Ni-20Co-18Cr wt.%) which combines high strength and creep resistance for high temperature service ($\sim 1000^\circ\text{C}$). The brazing was performed in a high vacuum furnace under a slow thermal cycle up to 990°C (Fig.1c) a temperature at which the active brazing alloy (filler) is in a melted state. The joint structures were examined by scanning electron microscopy (SEM) and were also subjected to mechanical tests to evaluate the shear strength of the joint.

The joint of the Cr/CrC/C(substrate) ceramic with the nimonic showed a rough and crack-free interface. There is a rearrangement of metallic elements concentrations close to filler/Cr interface and diffusion of the supplied metals (Ti, Cu, Ag and Cr) from the interface to the carbon bulk, filling up all the graphite pores within a depth up to 50 μm . The filling of the graphite pores is in a layered form, Cr diffuses through carbon and coats the inner wall of the carbon pore, followed by Ti and Ag-Cu. This arrangement is of increasing CTEs. Thus, a tailored-made porosity of the ceramic part might encourage a crack-free relief of thermal stresses of such metal-ceramic joints.

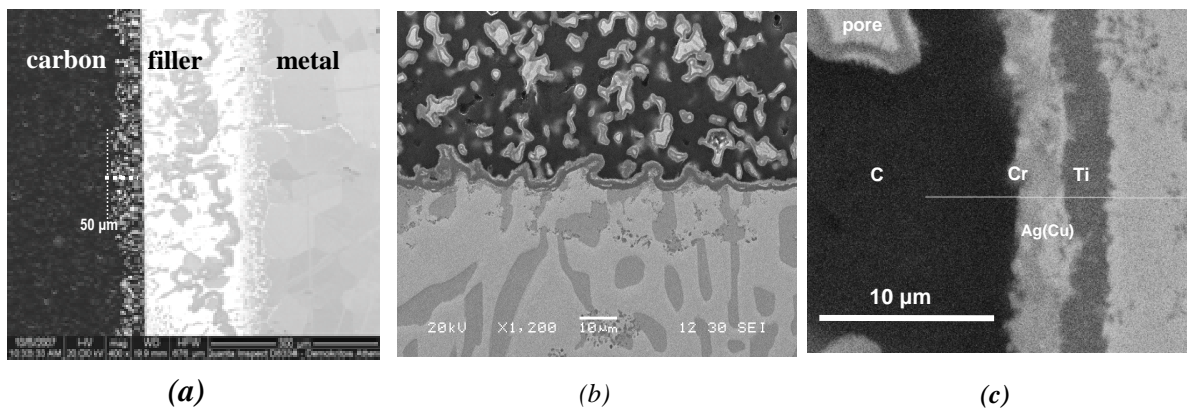


Fig. 2. (a) Scanning electron microscopy of the cross-section of metallized graphite/Nimonic joint, (b) graphite/filler metal interface and (c) closer view of the graphite/filler metal interface indicating the metallic layered structure.

The successful joining procedure applied to the simple carbon system [2], was extended to the more complex ceramic composites C_f/C and C_f/SiC which are of technological interest for aerospace applications. The brazing to Nimonic superalloy using a TiCuAg filler metal was equally successful as it is shown by the cross-section SEM analysis (Fig.3a). The joint samples were subjected to mechanical shear tests at room temperature (Fig.3b). In all cases the fracture has been produced through the ceramic part independent of the treatment performed, as is evidenced in Fig. 3(c). Cracks were propagated parallel to the ceramic/metal interface. An analysis of the effect of the Cr layer on the surfaces showed that Cr diffuses into the filler metal, while Ti reacts with carbon, and the Cr is as a skin in a sandwich construction where the core is the titanium.

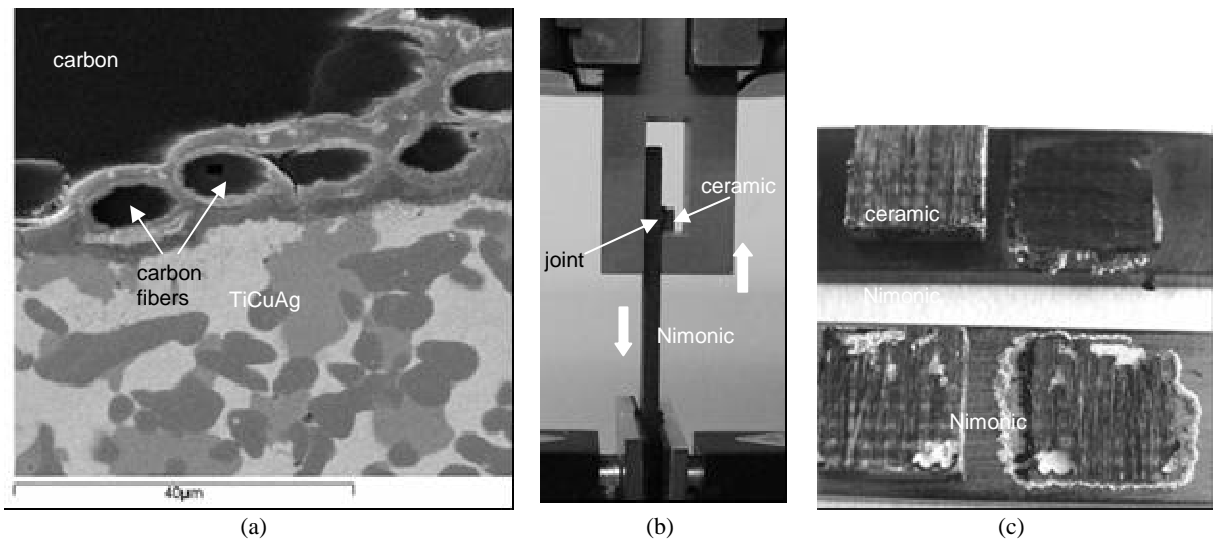


Fig. 3. (a) Cross-section SEM image at joint of $C_f/C/Cr$ (annealed at 700C for 1h) with Nimonic via TiCuAg metal, (b) the setup for measuring the shear strength of the joint and (c) the fracture surfaces after the mechanical testing.

Ceramic-metal composites are important structures in aerospace applications in which it is required these two dissimilar materials to serve under extreme variation of temperature. In order the joint structures to withstand these conditions a matching of the CTEs is required. In this work a concept of modifying the surface of the ceramic part has been realized. A chromium layer was deposited at the ceramic, followed by heat treatment to develop a chromium carbide intermediate layer. Then this layered structure was joint using a commonly applied brazing technique to a Nimonic superalloy. Evaluation of the ceramic-metal joint by SEM and mechanical tests showed that a successful joint was produced which could be utilized in aerospace applications. .

References

[1] R. Taylor, Comprehensive Composite Materials,4 (Boston, Elsevier Science Ltd, 2000).
 [2] N. V. Moutis, C. Jimenez, T. Speliotis, X. Azpiroz and K. Mergia, Adv. Mat. Res. 59, 209 (2009).

Effect of Indium Implantation on the Bonding Environment of GaN

Y. Keremi, M. Katsikini*, F. Pinakidou, E. C. Paloura

¹Department of Physics, Aristotle University of Thessaloniki, 54124, Thessaloniki, Greece

*katsiki@auth.gr

InGaN/GaN heterostructures find applications in the fabrication of high efficiency light emitting diodes as well as in high - frequency, high - power microelectronic devices [1]. Ion implantation is a promising method for the growth of nanomaterials, like InGaN/GaN heterostructures and InGaN quantum dots, which enhance the emission characteristics of InGaN - based laser diodes [2]. Although ion implantation has the advantage of precise dose and profile control, it causes lattice damage which can be recovered via annealing. Here, we apply extended X - ray absorption fine structure (EXAFS) spectroscopy at the Ga - K edge, in order to determine the implantation induced changes in the nanostructure of GaN. EXAFS spectroscopy is well suited for the study of disordered materials since the main mechanism involved is the backscattering of the outgoing photoelectron wave from the neighboring atoms, which does not depend on the periodicity of the lattice.

The 450nm-thick GaN layer was grown on Al₂O₃ by Plasma Enhanced Molecular Beam Epitaxy using AlN buffer layer [3]. The sample was diced and the individual pieces were implanted at 77 K with 700 keV In ions with fluences that range from 1×10^{14} to 1×10^{16} cm⁻². The Ga - K edge EXAFS spectra were recorded at the KMC-II beamline of the synchrotron radiation storage-ring BESSY of the Helmholtz Center Berlin for Materials und Energy GmbH. The beamline is equipped with a double SiGe graded crystal monochromator. The fluorescence photons were detected using a Si photodiode and in order to avoid polarization effects, the angle of incidence was equal to the magic angle (55° to the sample surface) [4]. The spectra were normalized with the intensity of the incident beam.

EXAFS refers to the fine structure of the X-ray absorption coefficient, $\mu(E)$, due to the interference of the outgoing and the backscattered to its neighboring atoms photoelectron wave. Prior to analysis the $\mu(E)$ spectra were subjected to subtraction of the atomic background $\mu_0(E)$ and transformation from the energy space to the photoelectron wavenumber, k , space. The resulting $\chi(k)$ spectra were fitted using the FEFFIT program with the photoelectron scattering theoretical paths that were constructed with the FEFF8 code [4]. The model used for the construction of the theoretical scattering paths provides the necessary electron mean free path and the backscattering amplitude and phase as well as the starting values for the fitting of the coordination numbers and the nearest neighbor (nn) distances. The fitting was performed in the four nn shells up to a distance of 4.5 Å. The $\chi(k)$ spectra and the corresponding Fourier transforms (FT) are shown in Fig. 1 (a) and (b), respectively. The FT's correspond to the radial distribution function around the absorbing atom and thus the first and the second peaks correspond to 1st and 2nd nn shells that consist of 4 N and 12 Ga atoms, respectively.

The EXAFS analysis reveals that the nn distances are not affected by the ion implantation. In contrast, the effect of the ion fluence on the coordination numbers is strong, as it is evident in Fig. 2. More specifically, implantation causes significant decrease of the coordination numbers especially

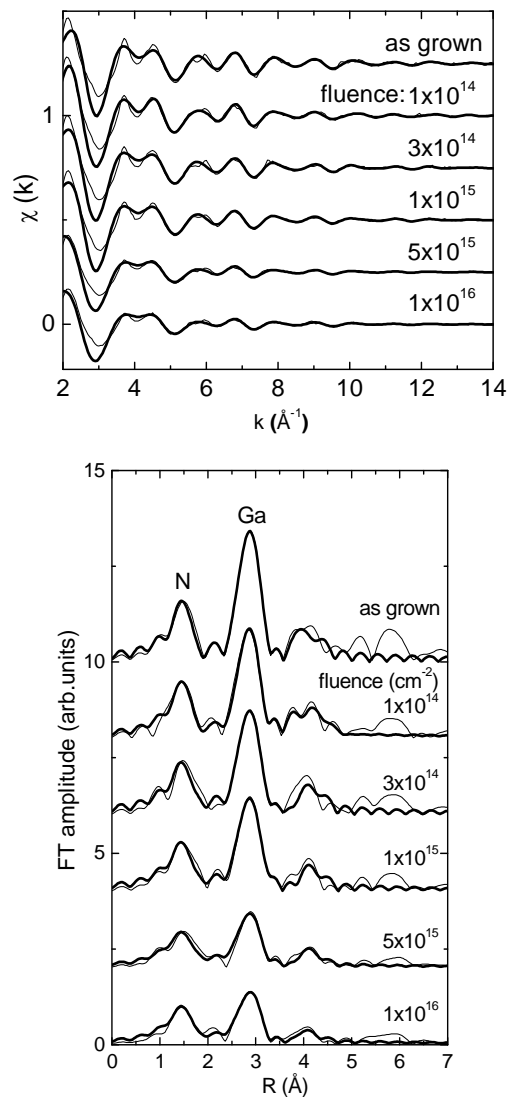


Fig. 1: (a) $\chi(k)$ spectra of the as grown and the implanted samples; (b) Fourier Transforms of the corresponding $k^2 \chi(k)$ spectra. The experimental data and the fitting are shown in thin and thick solid lines, respectively.

in the 2nd and 3rd shell. This reduction is attributed to the increased number of atoms that are displaced from their equilibrium positions due to collisions with the implanted ions. The coordination number for the 1st nn shell is less affected by the ion implantation, revealing that the tetrahedral coordination of the Ga atoms remains unaffected.

The effect of implantation on the structural order is also reflected in the Debye-Waller factors (DWF), defined as the mean square relative displacement due to thermal and static disorder, of the atoms that comprise a specific neighboring shell. The values of the DWF determined from the fitting, are listed in Table 1. Implantation affects mainly the DWF of the 1st nn shell, due to the increased static disorder. The DWF of the 2nd nn shell is almost unaffected by the implantation fluence most probably due to the decrease of the number of atoms that comprise the shell as the fluence increases. However, in high fluences, like $1 \times 10^{16} \text{ cm}^{-2}$ where the sample becomes completely amorphous, the DWF of the first two nn shells are significantly lower compared to the sample implanted with $5 \times 10^{15} \text{ ions/cm}^2$. To coordination number of the second nn shell and the DWF of the first shell partially recover after annealing at 900°C [6].

In conclusion, implanted GaN with 700keV indium ions with fluences 1×10^{14} , 3×10^{14} , 1×10^{15} , 5×10^{15} and $1 \times 10^{16} \text{ cm}^{-2}$ is studied using Ga-K edge EXAFS spectroscopy. The nn distances are not affected by the increase of the implantation fluence. Furthermore, the tetrahedral coordination of the Ga atoms is conserved although the DWF increases significantly with the fluence. The effect of ion implantation in the coordination number of the second nn shell is detrimental and a reduction of almost 50% is observed after implantation at the high fluence.

Table 1: Debye-Waller factors for the two nearest neighbor shells.

fluence (cm^{-2})	$\sigma_1^2 (\text{\AA}^2)$	$\sigma_2^2 (\text{\AA}^2)$
as grown	0.0016	0.0046
1×10^{14}	0.0028	0.0066
3×10^{14}	0.0054	0.0061
1×10^{15}	0.0061	0.0067
5×10^{15}	0.0082	0.0051
1×10^{16}	0.0042	0.0067

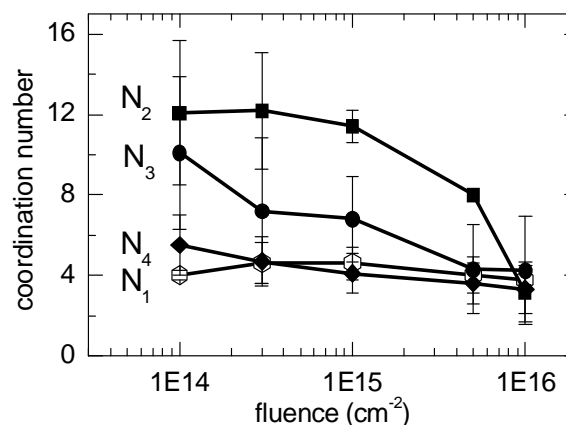


Fig. 2: Dependence of the coordination numbers for the four nearest neighbor shells on the implantation fluence.

REFERENCES

- [1] Group III-nitride Semiconductor Compounds: Physics and Applications, edited by B. Gil, (Oxford, Clarendon, 1998).
- [2] A. B. Denison, L. J. Hope-Weeks, R.W. Meulenberg, L. J. Terminello, in Introduction to Nanoscale Science and Technology, edited by Massimiliano Di Ventra (Kluwer Academic Publishers, Boston, 2004) p.194.
- [3] T. D. Moustakas, T. Lei, B. J. Molnar, Physica B 185, 36 (1993).
- [4] M. Katsikini, E.C. Paloura, T.D. Moustakas, J. Appl. Phys. 83 (1998) 1437.
- [5] A. L. Ankudinov, B. Ravel, J. J. Rehr, S. D. Conradson, Phys. Rev. B 58, 7565 (1998).
- [6] M. Katsikini, F. Pinakidou, E.C. Paloura, F. Boscherini, E. Wendler, and W. Wesch, Mater. Sci. Engin. B 152, 132 (2008).

Pressure-induced Phase Separation in the Y123 Superconductor

E. Siranidi^{1*}, D. Lampakis¹, E. Liarokapis¹, I. Margiolaki², K. Conder³, A. Gantis⁴ and M. Calamiotou⁴

¹Department of Physics, National Technical University - GR-15780 Athens, Greece

²ESRF-BP 220, F-38043 Grenoble Cedex 9, France

³Paul Scherrer Institute, Villigen, Switzerland

⁴Solid State Physics Department, School of Physics, University of Athens - GR-15784 Athens, Greece

*esiran@central.ntua.gr

Systematic Raman studies on various high- T_c cuprates have revealed that the application of hydrostatic pressure can induce non-linear lattice distortion, lattice instabilities, and phase separation effects [1–3], which seems to correlate with the non-monotonic pressure dependence of the corresponding transition temperature. In the case of Y123 a clear deviation from linear dependence on pressure has been observed for the A_g -symmetry Raman active mode of the in-phase vibrations of the plane oxygen atoms, which appeared as a double peak above ~ 2 GPa [1]. This has been attributed to a small lattice distortion, which occurs at a critical pressure [1]. Concerning the pressure dependence of the transition temperature on the same compound, Koch et al. [4] have observed that T_c increases up to 3 GPa, remains constant between 3 and 6 GPa, and above 6 GPa it shifts to lower temperatures. On the other hand, structural studies for the Y123 compound under hydrostatic pressure are scattered in the literature leading to contradictory and confusing results. In order to delineate the effect of pressure on Y123, we present here the results of a high-pressure structural study of $YBa_2Cu_3O_y$ using synchrotron angle-dispersive powder diffraction.

The high-quality $YBa_2Cu_3^{18}O_y$ powder sample has been prepared with the classical solid-state reaction technique and carefully oxygenated to optimal doping. The amount of oxygen and the isotopic substitution has been checked by the shift of the energy of the Raman active oxygen modes. The peak position and width of those modes indicate that the compound was fully oxygenated and homogeneous with roughly 90% of ^{18}O . The high-pressure synchrotron angle-dispersive powder diffraction patterns have been collected at beamline BM01A of ESRF using a diamond anvil cell and a 4:1 methanol-ethanol mixture as pressure medium. The fluorescence line of ruby crystals was used for in situ pressure measurement. 2D powder diffraction images have been recorded with a MAR345 image plate, covering the pressure region up to 12.7 GPa with pressure steps of 0.5 GPa. The 2D raw images have been first converted to 1D intensity-*vs.*- 2θ patterns, using FIT-2D [5], and after analyzed with the Rietveld method.

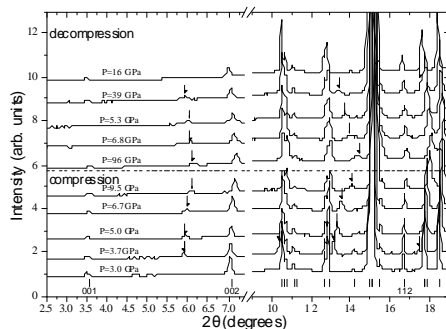


Fig.1. Evolution of diffraction patterns upon compression and decompression [6].

The intensity of the new lines appearing for $p \geq 3.7$ GPa varies with the azimuthal angle. This can be clearly seen for line A, which has a characteristic fiber-type azimuthal distribution in intensity. In addition line C exhibits a small variation in d-spacing along azimuthal angle, unlikely the diffraction lines of the Y123 phase, indicating that there are some shear strains experienced in the new phase. For the higher pressures, $p > 8$ GPa, the distortion of the d-spacing values with azimuthal angle (shear stains) seems to be relieved while texture intensity variation became clearly visible. Moreover, assessment of the observed line broadening by the Williamson-Hall plots has revealed that it is of microstrain/disorder type [6]. These observations are considered as another indication that the new peaks correspond to a new disordered phase that develops coherently with a preferred orientation and we have therefore excluded them from the refinement.

For the main Y123 phase in the pressure range ($3.7 \text{ GPa} < p < 10 \text{ GPa}$) mainly the c-axis undergoes a clear

Fig.1 shows selected diffraction patterns with increasing and decreasing pressure [6]. At 3.7 GPa four new weak Bragg peaks appear. The peak intensity of the new lines decreases and their full width at half maximum (FWHM) increases with pressure. The increase of the line widths is much more pronounced than the corresponding of the Y123 phase. Besides, the new peaks disappear completely for low pressures ($p < 3.9$ GPa). Any efforts to index the pattern including these new lines so as to obtain a reasonable superstructure or another symmetry solution did not work. Therefore we have considered the appearance of the new lines as resulting from a pressure-induced new metastable phase. This new phase exhibits strong disorder and texture effects as can be seen by the 2D diffraction images (fig.2).

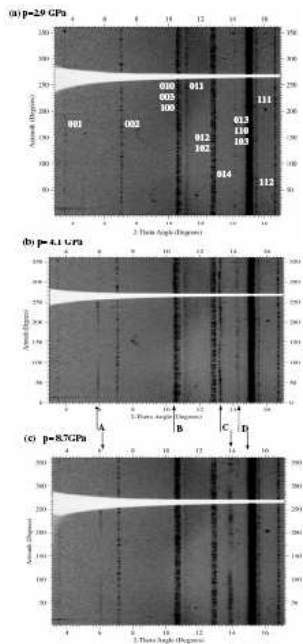


Fig.2. 2D diffraction patterns in Cartesian coordinates azimuthal angle vs. 2θ , at some characteristic pressures $p=2.9\text{GPa}$ (a), $p=4.1\text{GPa}$ (b), $p=8.7\text{GPa}$ (c) [6].

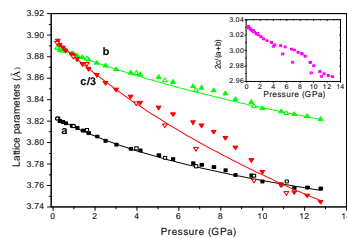


Fig.3. Dependence of lattice parameters on pressure. Inset: the pressure dependence of the ratio $2c/(a+b)$ [6].

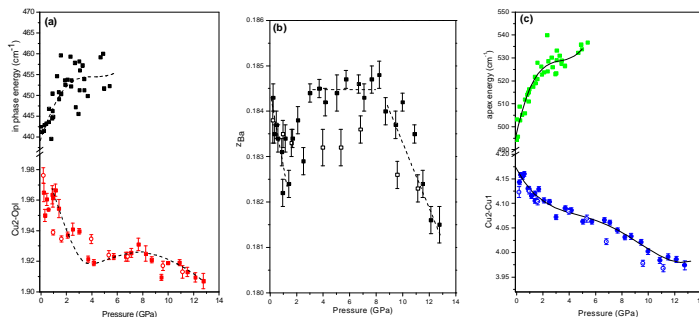


Fig.4. Pressure dependence of the (a) average Cu2-Opl bond length and frequency of the in-phase oxygen Raman active mode, (b) fractional coordinate z of Ba atom along the c -axis, and (c) Cu2-Cu1 distance together with the apex oxygen mode frequency [6].

deviation from the expected equation of state (fig.3, full symbols) [6]. Upon the pressure release (fig.3, open symbols) the data follow the anticipated dependence showing a strong hysteresis. The c -axis modifications upon pressure are a result of the interatomic bond length changes resulting from pressure induced charge redistribution and/or internal strains in the structure. The in-plane Cu2-Opl bonds, the Cu2-Cu1 distance and the fractional coordinate of Ba atom along the c axis of the Y123 phase, obtained from the Rietveld refinement, show modifications at characteristic pressures (fig.4). At the same pressure the new weak lines appear in the diffraction pattern attributed to a pressure induced new phase. The high-pressure Raman results have indicated modifications in the in-phase oxygen mode, which appears as a double peak at about 2GPa [1], i.e. at the pressure where the bond distance Cu2-Opl and the position of the Ba atom show a non-linear dependence on pressure. The splitting of the mode is reflected in the wide spread of the Raman data in fig. 4(a), which is a result of the phase separation. In the optimal to overdoped oxygen concentration of the same compound, the in-phase oxygen mode was found to soften due to a modification in the buckling of the CuO2 planes, which affects also the c -axis. Those lattice distortions have an effect also on the superconducting properties showing two transition temperatures that reflect the coexistence of phases. The effect of pressure seems to be the same with the optimal to overdoping; non-linear dependence of the Cu2-Opl bond length and the in-phase mode, an anomaly of the c -axis, and changes in the T_c . It should be noted that a non-linear dependence on pressure was detected also for the apical oxygen frequency [1], which correlates (as expected) with the pressure modifications of the Cu2-Cu1 bond lengths.

If we try to make a connection of the lattice anomaly with the high-pressure Raman results, the pressure dependence of T_c , and the possible indexing of the new peaks with a phase of double a -, b -axis and slightly larger c -axis, we can speculate that the trigger of the phase separation and the lattice instability lies among the CuO2 and BaO planes. This must be related with the redistribution of the carriers among the planes, which obviously affects the T_c and the lattice constants. In such a case, similar pressure effects should be present in the other cuprates as well.

- [1] Lampakis D., Liarokapis E., Karpinski J., Panagopoulos C. and Nishizaki T., J. Supercond., 17 (2004) 121.
- [2] Liarokapis E., Lampakis D., Palles D., Karpinski J. and Panagopoulos C., J. Phys. Chem. Solids, 67 (2006) 2065.
- [3] Lampakis D., Liarokapis E., Kazakov S. M. and Karpinski J., Phys. Rev. B, 72 (2005) 014539.
- [4] Koch U., Lotter N., Wittig J., Assmus W., Gegenheimer B. and Winzer K., Solid State Commun., 67 (1988) 959.
- [5] Hammersley A. P., Svensson S. O., Hanfland M., Fitch A. N. and Hausermann D., High Press. Res., 14 (1996) 235.
- [6] M. Calamiotou, A. Gantis, D. Lampakis, E. Siranidi, E. Liarokapis, I. Margiolaki, K. Conder, EPL 85 (2009) 26004.

Acknowledgments

We thank the Swiss-Norwegian committee for beam time allocation at the SNBL BM01A, at ESRF. Work partially supported by the E.C. STREP project No. 517039 "COMEPHS" and by the Special Research Account (Kapodistrias) of the University of Athens.

Influence of Antiferromagnetic Interactions and of Alloy Disorder on the Ferromagnetic Properties of p -type (Cd,Mn)Te Quantum Wells

C. Simserides^{1*}, A. Lipińska², A. Majhofer³, K. N. Trohidou¹ and T. Dietl^{2,4}

¹ Institute of Materials Science, NCSR Demokritos, Athens, Greece

² Institute of Physics, Polish Academy of Science, Warszawa, Poland

³ Institute of Experimental Physics, University of Warsaw, Warszawa, Poland

⁴ Institute of Theoretical Physics, University of Warsaw, Warszawa, Poland

* simserides@ims.demokritos.gr

Modulation-doped p -type (Cd,Mg,Zn)Te/(Cd,Mn)Te/(Cd,Mg,Zn)Te quantum wells (QWs) are a unique medium allowing to probe carrier-induced Ising-like ferromagnetism in the two-dimensional case [1]. The (Cd,Mg,Zn)Te barriers are doped with non-magnetic acceptors (e.g. N), while the CdTe quantum well is doped with magnetic impurities (e.g. Mn). A surprising result in this system is the absence of hysteresis loops below the Curie temperature, T_C . To obtain information on the mechanisms controlling spin dynamics, going beyond mean field theories, we have extended our previous Monte Carlo simulations combining the Metropolis algorithm with the determination of hole eigenfunctions at each Monte Carlo sweep [2].

Our numerical calculations show that the short-range antiferromagnetic superexchange interactions between the Mn spins, which compete with the hole-mediated long-range ferromagnetic coupling, play an important role in the magnetization relaxation of the system. Moreover, we reveal that the effect of antiferromagnetic interactions becomes much reduced if the thickness of the layer containing the Mn spins is narrower than the extend of the hole wave function [3]. This implies that magnetic hysteresis should be recovered in QWs, if the thickness of the Mn-doped layer is smaller than the region visited by the holes.

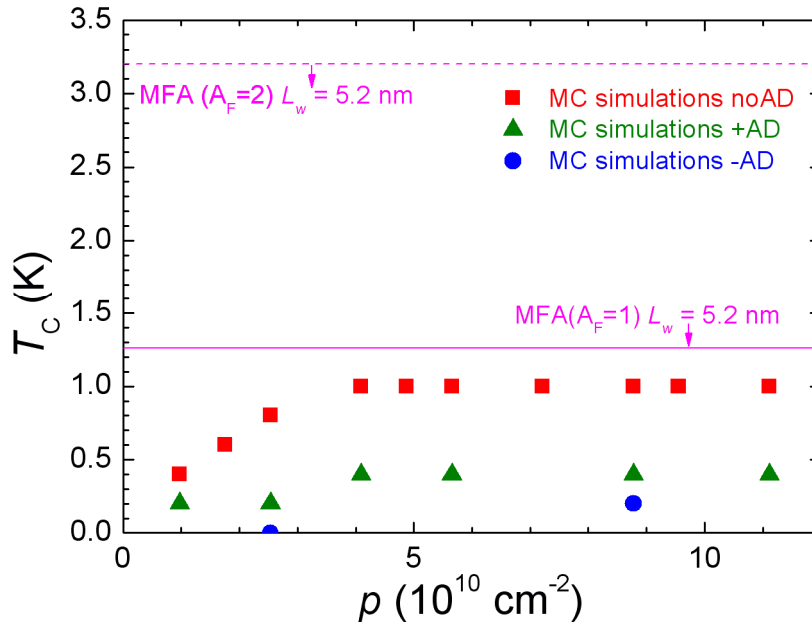


Figure 1. The critical temperature T_C as a function of the sheet hole concentration, p . The full symbols denote results of our Monte Carlo simulations for a quantum well of width 5.2 nm. The molecular fraction of Mn is 4%. These are single-particle calculations without alloy disorder ($\delta V = 0$, squares) as well as for repulsive alloy disorder potential ($\delta V > 0$, triangles) and attractive alloy disorder potential ($\delta V < 0$, circles). Mean-field results are shown with a continuous line. The dashed line presents mean-field results taking into account carrier correlations with the Landau parameter $A_F = 2$.

Furthermore, we analyze theoretically the role of spin-independent alloy disorder (cf. Fig.1) and we find that it reduces T_C , particularly in the range of low hole concentrations [3]. We have performed simulations for repulsive as well as for attractive alloy potential, δV . Interestingly, the repulsive alloy potential $\delta V > 0$ (cf. Fig. 2a-b), the case of (Cd,Mn)Te, leads to reduced magnitudes of T_C comparing to the values determined for $\delta V = 0$. We interpret this finding by noting that in the presence of a repulsive alloy potential, the amplitude of the wave function at the Mn ions is decreased compared to the case $\delta V = 0$. This reduces the p - d coupling and shifts the appearance of the carrier-mediated ferromagnetic order to lower temperatures. The attractive alloy potential (cf. Fig. 2c-d) washes the ferromagnetism virtually entirely out because holes get localized for the chosen magnitude of δV . Hence, our results substantiate the view that delocalized or weakly localized carriers are indispensable to set a long-range order between diluted spins. Obviously, smaller amplitude of the attractive alloy potential or greater hole concentrations will lead to carrier delocalization and the re-entrance of a ferromagnetic order.

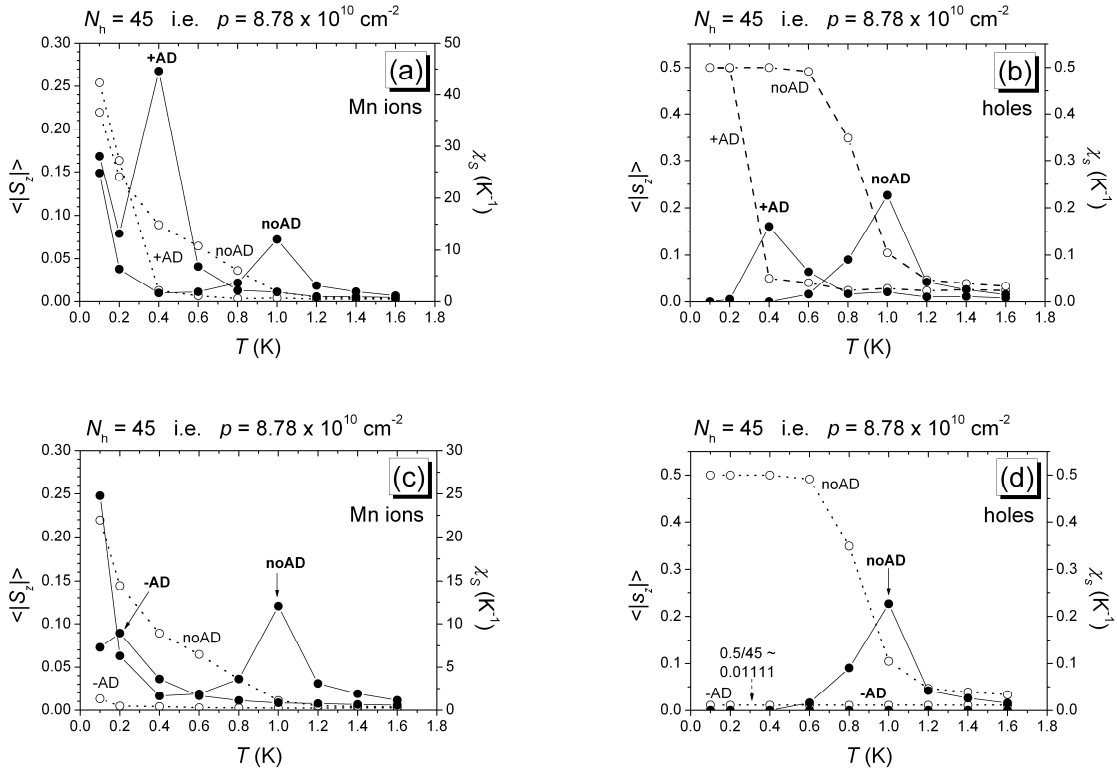


Figure 2. The z -component of the absolute spin projections $\langle |S_z| \rangle$ and $\langle |s_z| \rangle$ (open symbols – dotted lines; left scale) and the spin susceptibilities χ_S and χ_s (full symbols - solid lines; right scale) for the Mn ions (a,c) and for the holes (b,d), in the absence of alloy disorder (noAD, $\delta V = 0$), for repulsive alloy disorder potential (+AD, $\delta V > 0$) as well as for attractive alloy disorder potential (-AD, $\delta V < 0$). A maximum in the temperature dependence of the spin susceptibilities is identified as the Curie temperature below which the holes induce a long range ferromagnetic order. Here the number of holes in the simulation slab $N_h = 45$, which corresponds to hole sheet concentration $p = 8.78 \times 10^{10} \text{ cm}^{-2}$.

[1] Boukari H., Kossacki P., Bertolini M., Ferrand D., Cibert J., Tatarenko S., Wasiela A., Gaj J. A., and Dietl T., Phys. Rev. Lett. 88, 207204 (2002).

[2] Kechrakos D., Papanikolaou N., Trohidou K. N., and Dietl T., Phys. Rev. Lett. 94, 127201 (2005).

[3] Lipińska A., Simserides C., Trohidou K. N., Goryca M., Kossacki P., Majhofer A., and Dietl T., Phys. Rev. B in press, also at arXiv:0903.0406v1 [cond-mat.mtrl-sci].

Numerical Study of the Exchange Bias Effect in nanoparticles with ferromagnetic core / ferrimagnetic shell morphology

M. Vasilakaki^{1*} and K. N. Trohidou¹

¹ NCSR 'DEMOKRITOS', Institute of Materials Science, Athens, Greece

**marianna05@ims.demokritos.gr*

The exchange bias effect, known as the asymmetry in the horizontal axis of the hysteresis loop of nanoparticles with core/shell morphology, has been studied extensively in nanoparticles with FM core/AFM shell [1], where the effect has been initially observed [2]. Recently, the exchange bias effect has also been studied in nanoparticle systems where nanoparticles with a ferromagnetic core are surrounded by a disordered ferrimagnetic shell, freezing in a spin glass like state at low temperatures. The existence of an intrinsic multistate energy structure in the shell makes these systems to present some peculiar features in their magnetic behavior [3].

We have used the Monte Carlo (MC) simulation technique to investigate the effect of the ferrimagnetic-disordered shell on the hysteresis behavior of composite magnetic nanoparticles with ferromagnetic core and ferrimagnetic disordered shell morphology [4]. They are spherical nanoparticles of radius R expressed in lattice spacings on a simple cubic lattice. We have assumed nearest-neighbor Heisenberg exchange interactions between the spins in the nanoparticle and at each crystal site they experience a uniaxial anisotropy.

We have examined the cooling field dependence of the exchange bias (H_{ex}), the coercive field (H_c) (Fig. 1) and the remanent magnetization (M_r) and we find that an increase in the cooling field results initially in an increase in H_{ex} , H_c and M_r . We attribute this behavior to the initial alignment of a certain amount of ferrimagnetic spins at the interface along the field direction. After some H_{cool} value further increase in H_{cool} causes a reduction in H_{ex} and H_c , but M_r remains constant. For higher H_{cool} values the Zeeman coupling between the field and the ferrimagnetic spins dominates the magnetic interactions inside the system causing the decrease of both H_{ex} and H_c . Our results are in good agreement with the experimental ones of Fe/FeO nanoparticles systems [3,5].

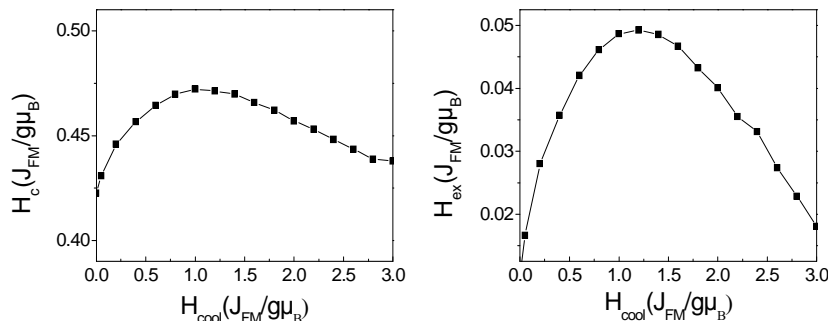


Fig. 1 Cooling field dependence of the coercive field and the exchange bias field for a composite nanoparticle with ferromagnetic core and ferrimagnetic shell morphology.

To study the role of the shell size, we keep the core size constant and we increase the shell thickness. Our simulations show that an increase in the shell thickness for a given core size enhances the exchange bias field and reduces the remanent magnetization. We find also that the vertical shift increases with the shell thickness confirming the fact that it originates from the uncompensated spins in the shell as in the case of composite nanoparticles with ferromagnetic core and antiferromagnetic shell.

We have also studied the temperature dependence of the coercive and the exchange bias field for different shell thickness (Fig. 2). We find that the H_{ex} decreases rapidly with increasing temperature, because the interfacial interaction is masked by the thermal fluctuations. We observe that the decrease of the H_{ex} is exponential as it is observed experimentally in Ref.[5]. The H_c also exhibits an exponential decay with temperature for bigger shell thickness.

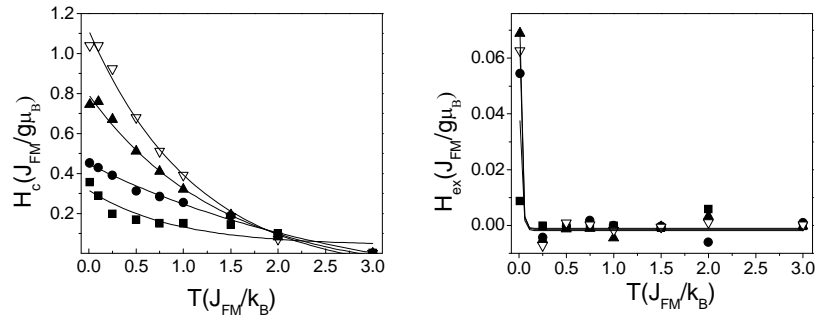


Fig. 2 Temperature dependence of coercive and exchange bias field for nanoparticles with core radius five lattice spacings and shell thicknesses of 4 (■), 7 (●), 9 (▲) and 15 (▽) lattice spacings, respectively.

Finally we consider the core size dependence of the exchange bias field and the coercive field. In Fig. 3 the hysteresis loops are shifted and the nanoparticle with the smaller core radius have the bigger coercive and exchange bias field, in agreement with the experimental findings of references [6,7]. This is due to the fact that the biggest contribution from the interface is obtained in the nanoparticle with the smallest core radius. This behavior is reversed as the temperature increases. The coercive field is decreasing faster with temperature in the case of the smaller core nanoparticles than in the bigger ones. There is a crossing temperature above which the nanoparticles with the bigger core radius have higher coercivity. This is the temperature at which the shell becomes totally disordered. Above this temperature the coercivity follows the temperature dependence of the core. The smaller in size core becomes faster superparamagnetic. Our results are in good agreement with experimental findings [7].

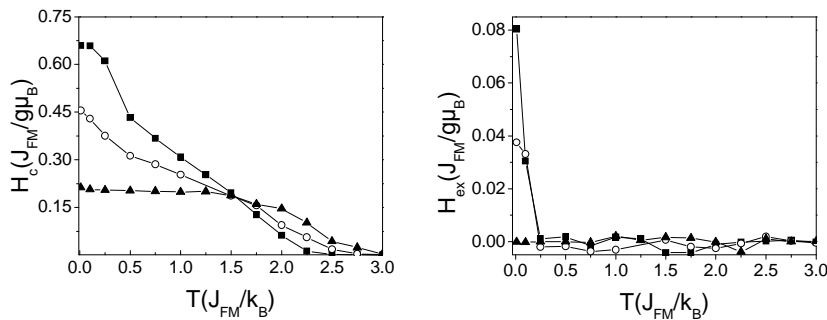


Fig. 3 Coercive and exchange bias field as a function of temperature for nanoparticles with shell thickness of seven lattice spacings and core sizes of three (■), five (○), and ten (▲) lattice spacings, respectively.

- [1] Noguees J., Sort V., Langlais V., Skymryev V., Surinach S., Munoz J. S., and Baro M. D., Phys. Rep. 422, 65 (2005).
- [2] Meiklejohn W. H., Bean C. P., Phys. Rev. 105, 904 (1957).
- [3] Del Bianco L., Fiorani D., Testa A. M., Bonetti E., Signorini L., Phys. Rev. B 70, 052401 (2004).
- [4] Vasilakaki M. and Trohidou K. N., Phys. Rev. B 79, 144402 (2009).
- [5] Baker C., Hasanain S. K., Ismat Shah S., J. Appl. Phys. 96, 6657 (2004).
- [6] Trohidou K. N., Soukoulis C. M., Kostikas A., Hadjipanayis G., J. Magn. Magn. Mater. 104, 1587 (1992).
- [7] Gangopadhyay S., Hadjipanayis G. C., Dale B., Sorensen M., Klabunde K. J., Papaefthymiou V., Kostikas A., Phys. Rev. B 45, 9778 (1992).

Acknowledgments The work was supported by EU STREP Project No. NMPCT-2004-013545 Nanospin (Self-Organized Complex-Spin Magnetic Nano-Structures).

Structural Investigation of Optimal Doped Manganites at High Temperature NMR

Panopoulos Nikolaos*, Koumoulis Dimitrios and Papavassiliou George

Institute of Materials Science, NCSR Demokritos, 152 10 Aghia Paraskevi, Attiki, Greece

*panon@ims.demokritos.gr

Optimal doped manganites constitute proper materials to survey critical phenomena such as the ferromagnetic to paramagnetic phase transition and the enhanced CMR effect. Extensive studies verify the strong dependence on temperature, namely the unit cell distortion and the structural transition that is observed.

^{139}La NMR lineshape inquiries revealed luminous evidence of both the quadrupolar and structural character of polycrystalline $\text{La}_{0.67}\text{Ca}_{0.33}\text{MnO}_3$, $\text{La}_{0.7}\text{Sr}_{0.3}\text{MnO}_3$. Measurements were performed 9.4 T external magnetic field, in the temperature range 80 K to 900K.

Inhomogeneous lineshape broadening dominates the spectra in both compounds, although LSMO exhibits a gradual increase of the central line width in contrast to the Ca-dopant abrupt line behavior. Regarding LCMO, the central transition is depicted by the narrow feature of the lineshape which emerges at $T=320$ K. An increase in temperature promotes the formation of rhombohedral phase (R-3c), while the decrease of the satellite frequency distribution initiates the departure from the octahedral crystal structure (Pnma) at $T=700$ K. This structural phase transformation is shown to be independent of the applied magnetic field [1].

LSMO remains in the same rhombohedral space group, implying a slighter influence of heating and Jahn-Teller effect in symmetry (Fig. 1).

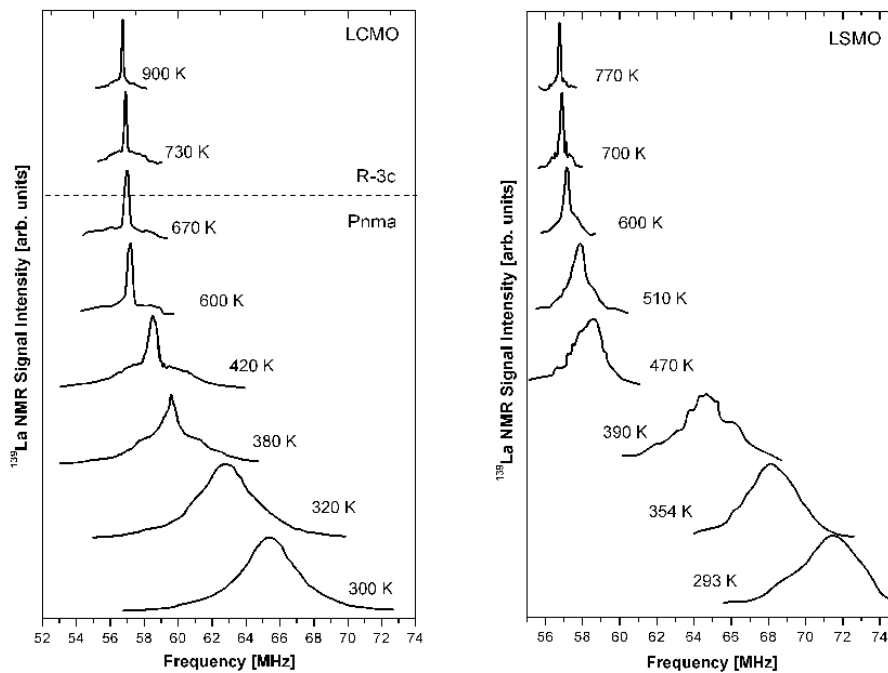


Fig. 1: ^{139}La NMR spectra for optimally doped LCMO ($x=0.33$) and LSMO ($x=0.3$) in 9.4 Tesla external magnetic field.

Critical temperature T_c was determined by the inflection point of the ν_0 vs. T curves in high magnetic field, giving 290 K and 400 K for Ca and Sr-dopant respectively (Fig.2).

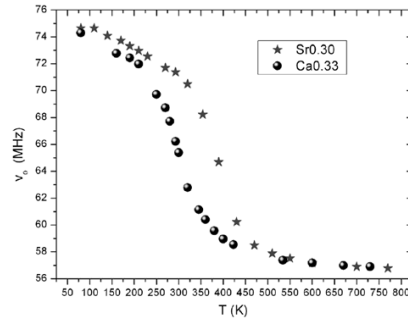


Fig. 2: The ^{139}La NMR frequency as a function of temperature for LCMO (circle) and LSMO (star).

Further investigation, in zero external magnetic field, conveys that extra parameters have to be invoked, such as Jahn-Teller distortion, polarons and strains, in addition to the quadrupolar identity of the specimens [2]. Such an assumption results in accurate simulating attempts based on an Ising Hamiltonian with random bond, random field and strain field parameters [3]:

$$H = -\frac{1}{2} \sum_{i,j} \left[J_{ij}^{(0)} + \sum_{\nu} J_{ij}^{\nu} \varepsilon_{\nu} \right] S_i^Z S_j^Z - \sum_i f_i S_i^Z + \frac{1}{2} N \sum_{\nu} \tilde{C}_{\nu} \varepsilon_{\nu}^2$$

$\tilde{C} = \nu_0 C_{\nu}$, C_{ν} irreducible elastic constant, ν_0 unit cell volume, N number of unit cell in the crystal.

- [1] Souza J. A., Terashita H., Granado E., Jardim R. F., Oliveira N. F., Muccillo R., Phys. Rev. B 78, 054411 (2008).
 [2] Argyriou D. N., Lynn J. W., Ren Y., Chen Y., Mukowskii Y. M., Shulyatev D. A., Phys. Rev. B 76, 014437 (2007).
 [3] Papantopoulos G., Papavassiliou G., Milia F., Schmidt V. H., Drumheller J. E., Pinto N. J., Blinc R. Zalar B. Phys. Rev. Lett. 73, 276-279 (1994).

¹³⁹La NMR study reveals peculiar spin ordering and antiferromagnetism in the overdoped region of La_{1-x}Ca_xMnO₃ phase diagram.

D. Koumoulis^{1,2*}, N. Panopoulos¹, M. Fardis¹, C. Charitidis² and G. Papavassiliou¹

¹ NCSR "Demokritos" Institute of Materials Science, 153 10 Ag. Paraskevi, Athens, Greece

² School of Chemical Engineering, National Technical University of Athens, 157 80 Athens, Greece

*dimkoumoulis@ims.demokritos.gr

Overdoped perovskite-type manganites have attracted a great deal of attention in the last few years as multi-component systems. The richness of the physics in overdoped manganites is characterized by a complex phase diagram, which comprises various magnetic structures and regions of phase coexistence. It is argued that in this doping region ($x > 0.5$) the physics governed by tremendously couplings and modulations of charges and spins. Heavily doped La_{1-x}Ca_xMnO₃ with $x > 0.5$ have shown interesting physical properties, such as a charge ordered CE-type antiferromagnetic state (CO/AFM), an orbital ordered antiferromagnetic state (OO/AF), and phase separation. The conditions of existence and the magnetic properties of antiferromagnetic states have not been considered experimentally so far. Nevertheless, a plenty of theoretical prefigurations have been anticipated for antiferromagnetism in the heavily doped region ($x > 0.5$). The antiferromagnetic state in the heavily doped region of La_{1-x}Ca_xMnO₃ varies with calcium concentration from CE-type ($0.5 < x < 0.56$) to C-type ($0.6 < x < 0.7$). The interplay of spin, charge, lattice and orbital degrees of freedom maintaining a major overissue in understanding the physics of exotic ordered phases. Recently, neutron diffraction, electron microscopy and X-ray scattering studies have shown for doping concentration, $x = 0.5$, 0.66 and 0.75 superstructures with singularly periodicities of $2a$, $3a$ and $4a$, respectively. Essentially, neutron patterns revealed that La_{1-x}Ca_xMnO₃ in the vicinity of $x = 0.66$ exhibits an incommensurate magnetic structure. Recent magnetization and neutron diffraction studies present the mixed phase (AFM/FM) of the La_{0.37}Ca_{0.545}MnO₃ sample and the purely antiferromagnetic character of the La_{0.31}Ca_{0.63}MnO₃ [1,2,3]. In this work, in order to understand the nature of antiferromagnetism and the relevance between charge and spin ordering, we utilized ¹³⁹La NMR spectroscopy.

Nuclear Magnetic Resonance (NMR) has been a powerful local probe for a static and dynamic investigation of magnetic states due to the distribution of local magnetic fields in the sample via hyperfine interactions. In ¹³⁹La NMR the lanthanum nucleus ($I = 7/2$) directly exhibits the magnetic state (FM or AF) of the nearest manganese ions neighbors. The local field derived by the nuclear spin originating from 3d manganese ions magnetic moments has the form,

$$H_L = I \sum \hat{A} S + c \sum_i \hat{I} g S \frac{(3 \cos^2 \theta_i - 1)}{r_i^3} \quad (\text{Eq.1})$$

The first term relates the hyperfine interaction between the lanthanum spin and the manganese t_{2g} electron spin, and the second term the dipole-dipole interaction of lanthanum nuclei with all the manganese neighbors [2]. In particularly, we performed ¹³⁹La NMR measurements as a function of temperature in La_{0.37}Ca_{0.545}MnO₃ and La_{0.31}Ca_{0.63}MnO₃ in order to get insight into the nature of the low temperature antiferromagnetic ground state. Spin echo spectra were obtained by measuring the integrated echo intensity versus frequency. In addition a two pulse sequence with the width of the pulses adjusted to a maximum spin echo for a given spectrum and utilizing a wide band spectrometer with a carefully tuned and perdurably probe at low temperatures. The samples claimed high rf power levels, due to the low rf enhancement factor for non ferromagnetic materials. Spin echo NMR experiments were carried out at temperatures over the range 5 - 340 Kelvin in an applied field 4.7 Tesla, for which the unshifted ¹³⁹La Larmor frequency is 28,2658 MHz.

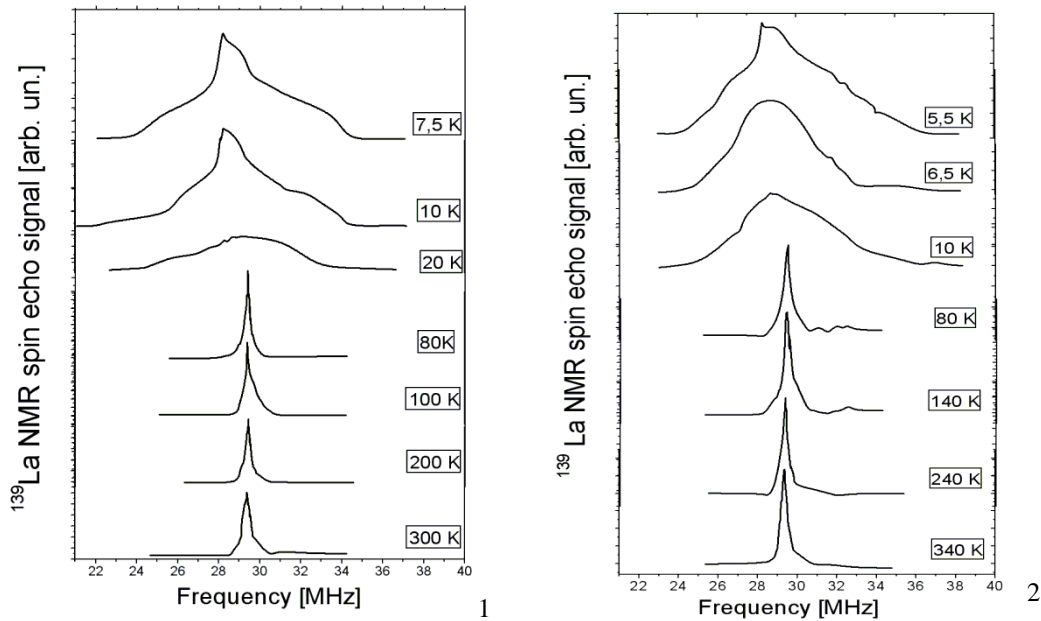


Figure 1, 2 . Temperature dependence of spin echo spectra for $\text{La}_{0.455}\text{Ca}_{0.545}\text{MnO}_3$ and $\text{La}_{0.37}\text{Ca}_{0.63}\text{MnO}_3$. The ^{139}La NMR signal intensity, I , corrected by the Boltzmann factor, as a function of temperature.

The antiferromagnetic signal is not observable in zero field, but in an external field the antiferromagnetic resonance occurs near to Larmor frequency due to the polarized nearest manganese neighbors respect to the applied field. Figures 1, 2 shows at low temperatures the NMR line shapes are extremely broad and asymmetric which indicate that each ^{139}La site present a different electronic environment. The local field of ^{139}La nucleus prescribes by the e_g electron density. The mechanism of the low temperature magnetic broadening differs from that associated with the highest temperatures (80 – 340 K). The mechanism at microscale remains unclear, but may be due to static incommensurate magnetic order like the stripe type charge – ordered antiferromagnetism or static lattice inhomogeneities (Jahn – Teller effect) [3,4,5]. At high temperatures, when the itinerant e_g electrons delocalize from the antiferromagnetic ordering, the motion narrowed NMR signal rises accordingly.

In addition to the information extracted from the NMR lineshapes about the static magnetic interactions, we performed spin – spin relaxation measurements (T_2) versus temperature which provide remarkable information about the dynamic part of these magnetic couplings. Figure 3, shows for both of doped samples that at low temperature T_2 relaxation mechanism exhibit major increment. The increase of T_2 at the lower temperature (~70 K) indicates an onset of magnetic order in heavily doped samples. Consequently, the behaviour of the relaxation times combined with the extremely spectra broadening at low temperatures provide the existence of a peculiar (i.e. stripe ordered, checkerboard) ordering in the antiferromagnetic ground state.

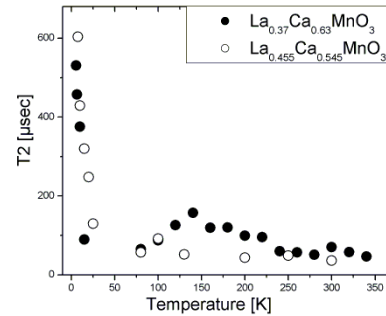


Figure 3. The temperature dependence of Spin-Spin relaxation time for both samples. The dramatic increase of T_2 at low temperature is particularly noteworthy.

- [1] M. Coey, Nature Vol. 430 (2004).
- [2] G. Papavassiliou, M. Fardis, F. Milia, A. Simopoulos, G. Kallias, M. Pissas, Phys. Rev. B. 55, 22 (1997).
- [3] M. Pissas and G. Kallias, Phys. Rev. B. 68, 134414 (2003).
- [4] P. M. Singer, A. Hunt, A. Cederstrom and T. Imai, Phys. Rev. B 60, 22 (1999).
- [5] C. Chen and S-W. Cheong, Phys. Rev. Letters 76, 21 (1996).

Matrix effects in carbon nanotube polymer composites

V. Likodimos^{1*}, S. Glenis¹, N. Guskos¹, G. Zolnierkiewicz², C. L. Lin³

¹ Solid State Physics Section, Department of Physics, University of Athens, Panepistimiopolis, Athens, Greece

² Institute of Physics, Szczecin University of Technology, 70-310 Szczecin, Poland

³ Department of Physics, Temple University, Philadelphia, PA 191 22, USA

*likodimo@chem.demokritos.gr

Harnessing the unparalleled mechanical, electrical and thermal properties of carbon nanotubes (CNs) has been the impetus of intensive research toward a variety of potential applications including nanopores, molecular reinforcements in composites, displays, sensors, energy-storage media and electronic devices [1]. Based on their exceptional mechanical properties (elastic modulus of the order of 1 TPa and tensile strengths of 100 GPa, far in excess of conventional fibrous materials used in engineering polymer composites), CNs hold great promise as structural reinforcements for polymer nanocomposites, simultaneously endowing the polymer with their thermal and electrical conductivity [2]. Interface engineering and reduction of CN agglomeration are key issues for the production of carbon nanotube reinforced polymers characterized by sufficient interfacial stress transfer between nanotubes and the polymer matrix without compromising the inherent CN properties [1,2].

Electron spin resonance (ESR) in combination with static magnetization measurements have been profitably exploited to probe the variation of the electronic properties of multi-wall carbon nanotubes (MWNTs) caused by the confined CN geometry and the acceptor action of structural defects in pristine materials [3] and chemical doping that leads to Fermi level shifts and quasi-bound localized states [4]. Recently, we have shown that the magnetic response of γ -Fe₂O₃ nanoparticles embedded in poly(ether-ester) copolymer matrices correlates with the copolymer relaxation, suggestive of matrix effects emerging from the magneto-elastic coupling of the oxide nanoparticles with the polymer [5,6]. In this work, we have studied the presence of matrix effects in MWNT-reinforced polymer composites by means of ESR and static magnetization measurements.

Nanocomposites were prepared using the *in situ* polycondensation reaction process, where the MWNTs are introduced as filler at 0.1 wt % in the poly-trimethylene terephthalate (PTT) polymer during its synthesis [7]. Static magnetization measurements as a function of the magnetic field and temperature reveal a drastic variation of the MWNTs magnetic response in the PTT matrix, compared to that of the free MWNTs (Fig. 1). Both the isothermal magnetization curves (left panel-Fig. 1) and the temperature dependence of the static magnetization (right panel-Fig. 1) for the PTT/0.1 wt % MWNT specimens, where the diamagnetic contribution of the PTT matrix is subtracted, reveal a reduction of the strong diamagnetic orbital susceptibility of pristine MWNTs that has been described within the quasi-2D graphite band model with a relatively low amount of hole doping [3]. While the PTT/0.1 wt % MWNT composite retains the diamagnetic behavior of the MWNT filler, a distinct paramagnetic-like contribution dominates its temperature dependence. Analysis of the latter behavior yields a Curie-Weiss constant of $C=2.2(1)\times 10^{-6}$ emu K/g that is similar to that of pristine MWNTs [3], despite their dilution in the PTT polymer matrix, indicating a significant increase of localized spins at the interface of the functionalized MWNTs with the polymer matrix.

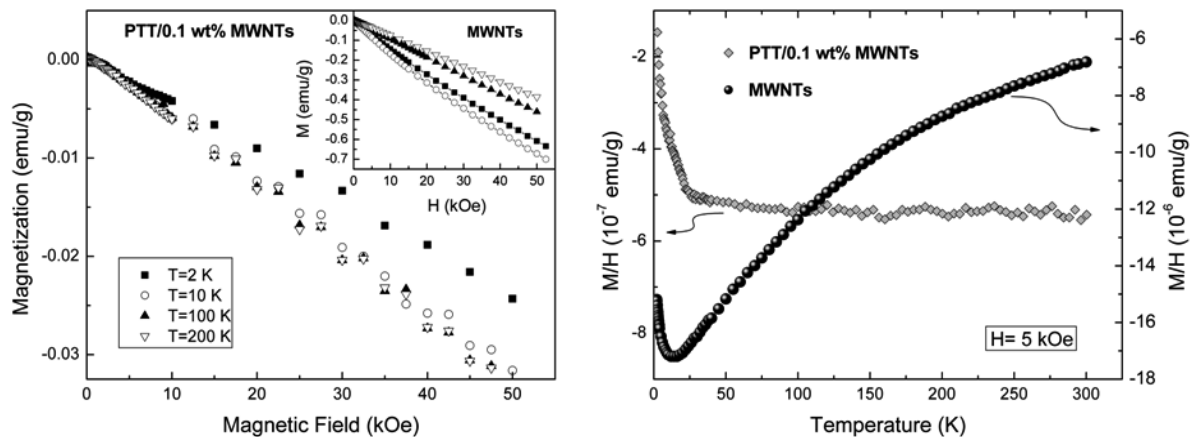


Figure 1. Static magnetization PTT/0.1 wt % MWNTs as a function of the magnetic field (left panel) and temperature (right panel), in comparison with the magnetic response of the pristine MWNT filler.

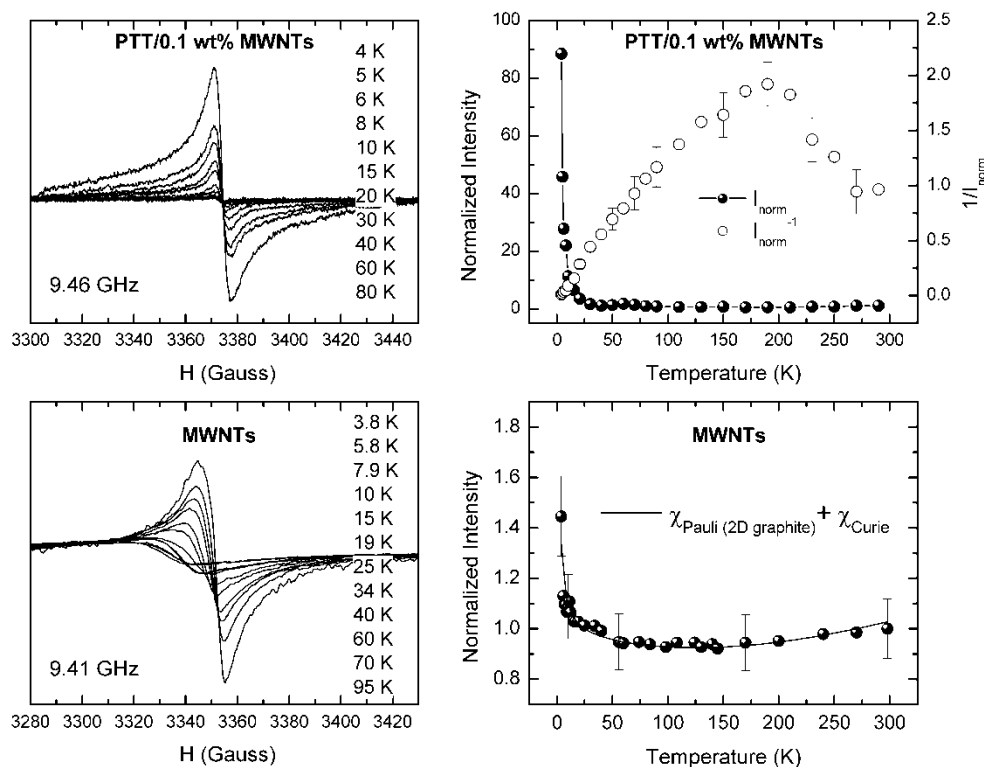


Figure 2. Temperature dependence of the ESR spectra and the corresponding normalized ESR intensity of PTT/0.1 wt % MWNTs in comparison with the pristine MWNT filler.

This behavior is directly evidenced by the ESR measurements for the PTT/0.1 wt % MWNTs composite, where a single resonance line is observed as a function of temperature (Fig. 2). This ESR line is centered at $g=2.003$ with a narrow peak-to-peak linewidth of ~ 5 G, both varying weakly with temperature. This is in marked contrast with the strongly temperature dependent ESR spectra of pristine MWNTs, dominated by the anisotropic resonance spectrum of conduction electrons [3,4]. This behavior is directly reflected in the temperature dependence of the ESR intensity, which is proportional to the underlying spin susceptibilities for the PTT/0.1 wt % MWNTs composite, compared to the pristine MWNT filler. While the ESR line for the composite system follows a Curie-Weiss-like behavior, characteristic of localized spins, the ESR intensity of MWNTs is dominated by the weakly temperature dependent Pauli susceptibility of conduction electrons, described by the quasi-2D graphite band model adapted for the CN geometry and a rather small Curie-like contribution [3]. In addition, a clear anomaly is resolved in the temperature variation of the inverse ESR intensity at high temperatures ($T > 200$ K). This behavior correlates with the dynamic relaxation of the PTT polymer [6], reflecting a matrix effect that arises from the interfacial coupling of MWNTs with the surrounding polymer, alike the functional nanocomposites of magnetic nanoparticles embedded in elastomeric copolymer matrices [5].

In summary, ESR and static magnetization measurements on MWNT reinforced PTT polymers in comparison with the pristine CN materials have been exploited to probe the presence of matrix effects and the interfacial coupling of carbon nanotubes with the polymer matrix. Both techniques provide direct evidence for the modification of the electronic properties of the carbon nanotube filler through the variation of its diamagnetic response and the appearance of enhanced concentration of localized spins together with the influence of polymer relaxation on spin dynamics.

- [1] Endo M., Strano M. S., Ajayan P. M., Topics Appl. Physics 111, 13 (2008).
- [2] Ajayan P. M., Tour J. M., Nature 447, 1066 (2007).
- [3] Likodimos V., Glenis S., Guskos N., Lin C. L., Phys. Rev. B 68, 045417 (2003).
- [4] Likodimos V., Glenis S., Lin C. L., Phys. Rev. B 72, 045436 (2005).
- [5] Guskos N., Glenis S., Likodimos V., Typek J., Maryniak M., Roslaniec Z., Kwiatkowska M., Baran M., Szymczak R., Petridis D., J. Appl. Phys. 99, 084307 (2006).
- [6] Guskos N., Likodimos V., Glenis S., Maryniak M., Baran M., Szymczak R., Roslaniec Z., Kwiatkowska M., Petridis D., J. Nanosci. Nanotech. 8, 2127 (2008).
- [7] Broza G., Kwiatkowska M., Roslaniec Z., Schulte K., Polymer 46, 5860 (2005).

Magnetic properties of single-wall carbon nanotubes

V. Likodimos^{1*}, S. Glenis¹, N. Guskos¹, C. L. Lin²

¹ Solid State Physics Section, Department of Physics, University of Athens, Panepistimiopolis, Athens, Greece

² Department of Physics, Temple University, Philadelphia, PA 191 22, USA

*likodimo@chem.demokritos.gr

Single-wall carbon nanotubes (SWNTs) represent a close realization of one-dimensional (1D) conductors with strong electron-electron interactions providing access to the low-energy properties of strongly correlated mesoscopic systems, the most notable aspect being the Luttinger-liquid state driven by the Coulomb repulsion of 1D electrons [1,2]. Recently, nuclear magnetic resonance experiments on ¹³C enriched double-wall CNs revealed the formation of a gap in the spin excitation spectrum below 20 K [3], pointing out the rich variety of electronic instabilities that may arise in the 1D CN structure. Despite the high perfection of the CN structure, the presence of low amounts of disorder due to defects and imperfections can essentially modify electronic transport in CN-based devices [4]. In addition, theoretical studies have shown that structural defects such as vacancies and adatoms may acquire spin polarization depending on the CN radius and chirality [5], while the formation of localized edge states in heterostructured C/BN nanotubes has been also predicted to promote magnetism [6]. In this work, we present a comparative study of the magnetic properties of CNs by means of electron spin resonance (ESR) and static magnetization measurements unveiling the opening of a spin gap for SWNTs, which is discussed in terms of an electronic instability or the presence of defect-mediated spin magnetism.

Figure 1 summarizes the dc magnetic response of different CN structures, namely multi-wall CNs (MWNTs), boron (B)-doped MWNTs and SWNTs. The static magnetization of MWNTs, Fig 1(a), is largely determined by the strong orbital diamagnetism of quasi 2D-graphite, which accounts well for the high field diamagnetic susceptibility of MWNTs, when appropriately adapted to the confined CN geometry [7]. Boron doping of MWNTs results in the reduction of the orbital diamagnetic susceptibility [Fig 1(b)] and the enhancement of the Pauli spin susceptibility, both explained by the acceptor action of substitutional boron atoms that, within a rigid band model, leads to a Fermi level shift towards the valence band by ~0.2 eV [8].

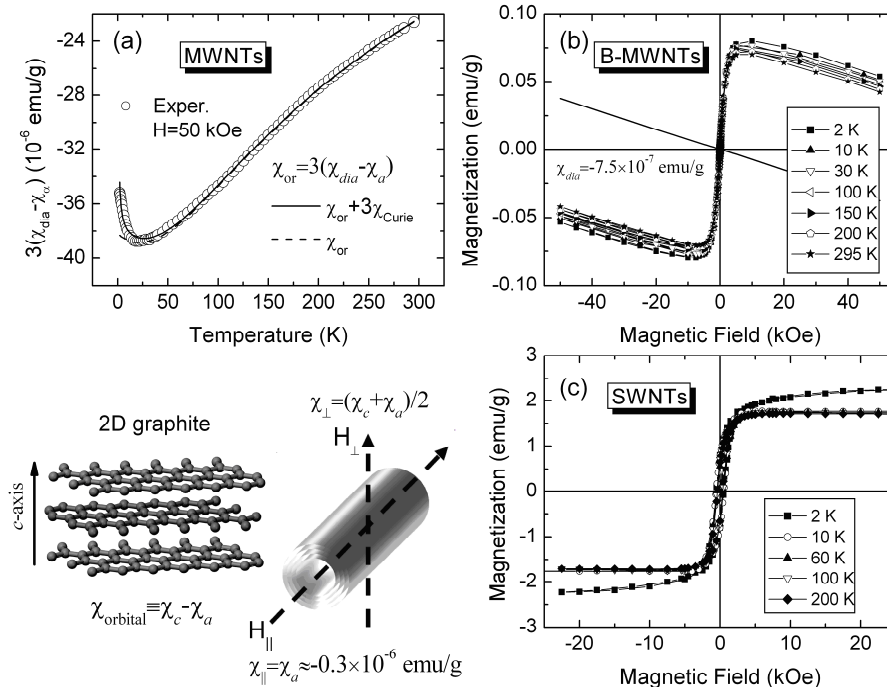


Figure 1. Static magnetization response of carbon nanotubes. (a) Orbital susceptibility $\chi_{or}(T)$ for MWNTs at $H=50$ kOe and scheme for the quasi-2D graphite model in the CN geometry. Solid and dashed lines represent the bset fit lines to the model of quasi-2D-graphite with an effective Curie term $\chi_{Curie}=C/T$. (b) Magnetization loops of B-doped MWNTs at different temperatures. The solid line corresponds to the diamagnetic susceptibility of $\chi_{dia}=-7.5 \times 10^{-7}$ emu/g. (c) Magnetization loops of SWNTs at different temperatures.

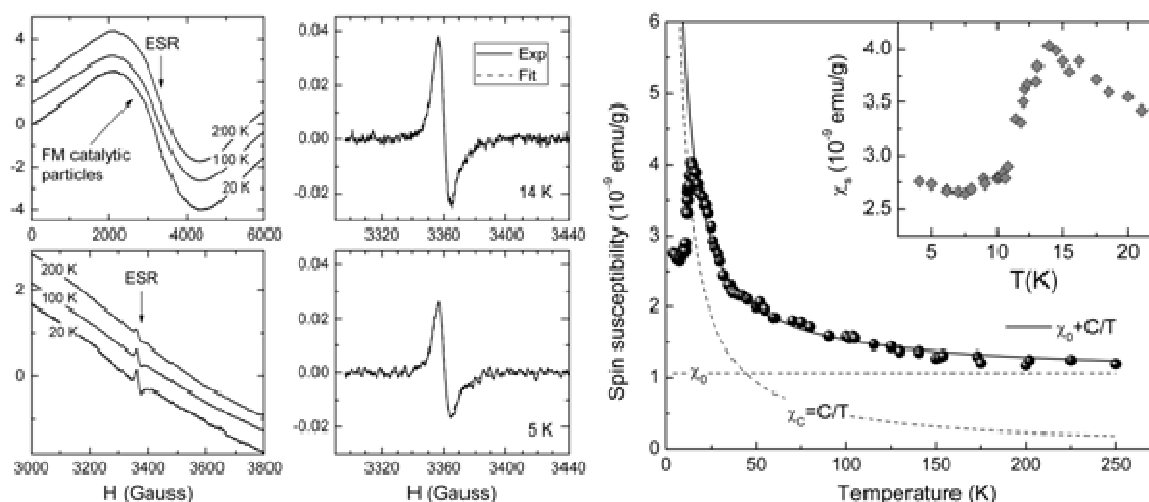


Figure 2. (left) ESR spectra of SWNTs at different magnetic field scans. Arrows in the larger field scans indicate the narrow ESR line superimposed on the FMR of the catalyst particles. Thin dashed lines in the small scan spectra show the best fit metallic line shapes at 5 and 14 K after subtraction of the ferromagnetic background. (right) Temperature dependence of the spin susceptibility χ_s for SWNTs. The inset shows in detail the low-temperature variation of $\chi_s(T)$.

Most importantly, the static magnetization of B-MWNTs reveals a clear ferromagnetic signal up to room temperature [Fig 1(b)], coexisting with the orbital and spin magnetism of the conduction electrons, which provides first evidence for the presence of itinerant ferromagnetism in heterostructured C/BN nanotubes. On the other hand, the intrinsic magnetic response of SWNTs grown by the catalytic laser oven vaporization technique is practically hindered by the strong ferromagnetic background of residual (Ni, Co) catalyst particles [Fig 1(c)]. Likewise, the ESR spectra of SWNTs are dominated by the broad ferromagnetic resonance (FMR) of the catalyst particles, which varies weakly with temperature [Fig 2(left)]. However, a narrow ESR line superimposed on the broad FMR signal, is successively resolved upon zooming in the $g=2.0$ region. After subtraction of the FMR background, the narrow ESR signal exhibits an asymmetric line shape, characteristic of conducting samples, when the sample thickness is comparable to the skin depth. The corresponding spin susceptibility $\chi_s(T)$ is nearly constant down to 150 K, followed by a moderate increase at lower temperatures [Fig 2(right)]. This temperature variation complies with the strong exchange coupling of conduction electrons and localized spins that leads to a single resonance line. The spin susceptibility becomes $\chi_s = \chi_0 + \chi_C$ stemming from the superposition of a temperature-independent (Pauli) term χ_0 , dominant at high temperatures, and a Curie contribution $\chi_C = C/T$ arising from localized spins, responsible for the upturn of $\chi_s(T)$ at lower temperatures. However, the spin susceptibility decreases rapidly below 14 K, decaying exponentially down to about 7 K, below which a slight upturn of $\chi_s(T)$ is observed [Fig 2(right)]. This steep drop of $\chi_s(T)$ complies with the thermally activated spin susceptibility of 1D systems with a spin gap of the order of the $\chi_s(T)$ maximum temperature, a typical feature of spin density or charge density wave instabilities that lead to an insulating antiferromagnetic ground state. An electronic instability of the SWNT's ground state causing the opening of a gap in the spin excitation spectrum may be accordingly suggested, in accordance with theoretical predictions for the effects of electron-electron interactions in SWNTs. Alternatively, a defect-driven mechanism may be invoked, where the exchange interactions between localized spins should be mediated by the conduction electrons, in contrast to ordinary localized spin magnetism. This would be in agreement with recent theoretical work predicting that localized states induced by vacancies in graphene may spread over many lattice sites in the presence of a finite impurity concentration [9]. The latter could provide an additional mechanism for the coupling of localized and itinerant spins in some defective SWNTs causing the low temperature anomaly in $\chi_s(T)$.

- [1] Bockrath M., Cobden D. H., Lu J., Rinzler A. G., Smalley R. E., Balents L., McEuen P. L., Nature 397, 598 (1999).
- [2] Ishii H. *et al.*, Nature 426, 540 (2003).
- [3] Singer P. M., Wzietek P., Alloul H., Simon F., Kuzmany H., Phys. Rev. Lett. 95, 236403 (2005).
- [4] Bockrath M., Liang W., Bozovic D., Hafner J. H., Lieber C. M., Tinkham M., Park H., Science 291, 283 (2001).
- [5] Lehtinen P. O., Foster A. S., Ayuela A., Vehviläinen T. T., Nieminen R. M., Phys. Rev. B 69, 155422 (2004).
- [6] Choi J., Kim Y.-H., Chang K. J., Tománek D., Phys. Rev. B 67, 125421 (2003).
- [7] Likodimos V., Glenis S., Guskos N., Lin C. L., Phys. Rev. B 68, 045417 (2003).
- [8] Likodimos V., Glenis S., Lin C. L., Phys. Rev. B 72, 045436 (2005).
- [9] Pereira V. M., Guinea F., Lopes dos Santos J.M.B., Peres N.M.R., Castro Neto A. H., Phys. Rev. Lett. 96, 036801 (2006).

Study of a Magnetic NDT Method with Finite Elements Analysis

N. Ntallis¹, K. Kosmas², E. Hristoforou² and K.G. Efthimiadis^{1*}

¹ *Department of Physics, Aristotle University, GR54124 Thessaloniki, Greece*

² *Laboratory of Physical Metallurgy, National Technical University, GR15780 Athens, Greece*

*kge@auth.gr

Nondestructive testing (NDT) has been defined as engulfing those test methods that examine an object, material or system, without impairing its future usefulness. Because NDT does not require the disabling or sacrifice of the system of interest, it is a highly valuable technique that saves both money and time in product evaluation, troubleshooting, and research. Nondestructive tests in great variety are in worldwide use to detect variations in structure, minute changes in surface finish, the presence of cracks or other physical discontinuities; to measure the thickness of materials and coatings and to determine other characteristics of industrial products. They are divided into various methods, each based on a particular scientific principle. These methods may be further subdivided into various techniques. The various methods and techniques, due to their particular nature, may lend themselves especially well to certain applications and be of little or no value at all in other applications. Therefore, the choice of the right method and technique plays an important role.

One of the categories, and the one in this study presented, concerns the magnetic methods [1, 2]. These are mostly applied to ferromagnetic materials. Despite the existence of standard techniques for the measurement of cracks and defects of a size in the order of several μm (X-ray radiography, ultrasonic and thermal tests), at the moment there is no standard or industrially-adopted experimental method to predict the initiation of cracks or to measure cracks in the order of nm and sub-nm. Taking into account that spatial distribution and arrangement of dislocations (or stress field gradient or stress tensor in grains) is responsible for the residual stress non uniformity and therefore for the initiation of a defect, as well as the fact that the magnetization process is dependent on the said spatial distribution and the arrangement of dislocations (or stress field gradient or stress tensor) of the tested specimen, one can measure the change of minor B-H loops in a given steel, and the correlation between magnetic properties and plastic deformation may be possible.

The magnetic domain wall mobility during the quasi-static magnetization process on a given ferromagnetic substance depends mainly on the behavior of the magnetic pinning centers [3]. The pinning centers inside the magnetic domain are either point, or line, or plane, or volume discontinuities, caused by enclosures, or dislocations of any type, or impurities [4]. Each one of these pinning centers represents an energy barrier, which must be over-passed by the domain wall in order to allow for the magnetization process. The higher the energy barrier is, the higher the additionally applied magnetic field for the domain wall to over-pass the barrier (or pinning center). The measurement of the additional required magnetic field to allow for the continuation of the magnetization process is the probe of the existence and amplitude of the energy barrier. Thus, the amount of field (energy) required to over-pass the said barrier determines the size of the pinning center and therefore the level of the local stress tensor.



Figure 1. A typical arrangement for B-H loop determination

First the sample (dog bone shape) is being under controlled strain and stress mechanisms so the created structure faults can be approximately estimated. Magnetic hysteresis loops are measured by employing magnetic yokes in various arrangements, offering a magnetization field in a quasi-static frequency range (~ 0.1 Hz) as uniform as possible. The detecting coils surround the samples under test, while excitation coils may be around

the under-test sample or around the magnetic yoke (fig. 1). Thus the input is the applied magnetic field and the output the voltage on the detecting coil.

The purpose of this study is principally the evaluation of the method, to check if it works properly. Another purpose is the optimization of the method, examining a number of parameters (such as the yoke types) that lead to more reliable results.

In order to optimize the method, the computer simulation was considered essential. The theoretical study was made with Finite Element Analysis (F.E.A.) using the Comsol Multiphysics. The first goal is the more efficient design of the excitation coil for the simulation procedure. It was thus drawn as one squared turn with length and width the ones of the real coil. A current equal to NI is flowing through it, where N is the number of turns and I the current passing through the real coil. Then the magnetic field created by the coil is simulated in a frequency of 0.1 Hz so to check out the spatial distribution of the field.

Then, the sample under test and the yoke are added (fig. 2), and the problem is solved checking out the changes of the magnetic induction, with the frequency as a parameter varying from 0.1 to 100 Hz. Solutions with different shaped yokes, having the same magnetic permeability, either on the one side or symmetrically on both sides of the sample under test are also obtained. What needs to be seen is how well driven the field is and what the response of the now closed magnetic circuit is (fig. 3). The detecting coil is not drawn at all because an amplifier is connected to it for the real measurement, so theoretically it has infinite resistance. For the simulation work this is like measuring the emf induced in the surrounding air.

Through the calculation of the magnetic energy stored and the Joule heating losses, the self-inductance coefficient and the resistance of the coil are estimated. Moreover, an estimation of the eddy currents created is made. Furthermore, calculating the magnetic flux passing through the sample and the yokes, the impedance of the complete magnetic circuit is estimated.

The last step is to examine the magnetic hysteresis contribution. This is done by solving additionally the differential equation

$$\frac{d\vec{M}}{dt} + \frac{\vec{M}}{\tau} = \frac{\vec{M}_o}{\tau} B_J(\alpha |\vec{B}|),$$

where τ is the relaxation time of the material, $B_J(x)$ is the Brillouin function and α a parameter depending on the magnetic properties of the material.

The problem is solved for at least 2 periods of the signal, thus at least 20 seconds and 100 examination points per period, so as to ensure that any kind of transition phenomena have stopped. So we are able to export the initial magnetization curve and also one or more of H-M loops. Having two H-M loops, the first one and one of the following, we are able to see the complete magnetic behavior of the sample as a function of the applied magnetic field. There won't be any saturation state, from a magnetic point of view, because the yokes used do not reach the necessary magnetic induction.

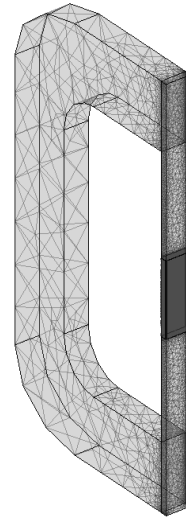


Figure 2. Geometry used in the simulation

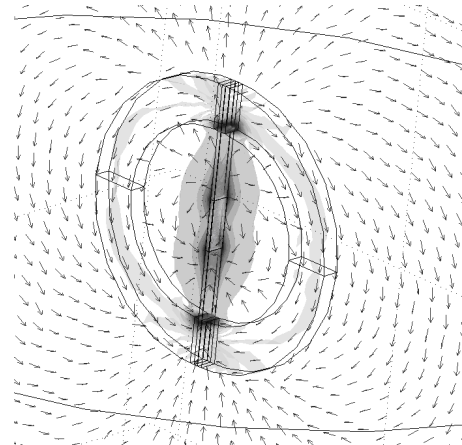


Figure 3. Magnetic flux density in the case of two symmetrical half-circled yokes

- [1] D.C. Jiles, NDT International, 21 (1988) 311.
- [2] D.C. Jiles, NDT International, 23 (1990) 83.
- [3] S. Chikazumi, Physics of Magnetism, John Wiley & Sons, 1964.
- [4] R.W. Kahn, Physical Metallurgy, North Holland Publishing Co, 1965.

Optimization of Time Response in Electromechanical Systems with Iron Core

P. Arampatzis-Ziamos and K.G. Efthimiadis*

Department of Physics, Aristotle University, GR 54124 Thessaloniki, Greece

*kge@auth.gr

All the automated industries worldwide coordinate the operation of individual parts of production lines with the use of electromechanical systems (Magnetic brakes, clutches etc.). The modern systems use cores from specifically manufactured magnetic materials, in order that they respond to modern requirements. Nevertheless, industries 10 years old or even modern use electromechanical systems with iron cores. The iron is selected as a very good soft ferromagnetic material, and of low cost. However, iron, as good conductor does not present good time response, because of the eddy currents induced.

The time delay of iron does not create problems at low frequencies of operation, it limits however the maximum frequency of operation. With the continuously increasing requirements of industry for increase of production, the system should function in higher frequencies, thus the system should either be replaced or improved.

In the present work a device is presented that can improve the time response of an iron core up to 80%, thus increasing the frequency of operation of a production line, without any replacement required.

The basic idea of the set is the following:

The industrial electromagnets are driven with tetragonal pulses, from 0V (operation OFF) to 24V (operation ON). The time delay (rise time) in a usual electromechanical system with iron core is roughly 40 μ s. If the drive pulse is modified suitably, so that at the start it reaches 110V and is maintained for a specific time, then the core is magnetically overdriven and reaches the desirable magnetization in shorter time.

The following block diagram of the experimental set (fig.1) presents how this result is achieved.

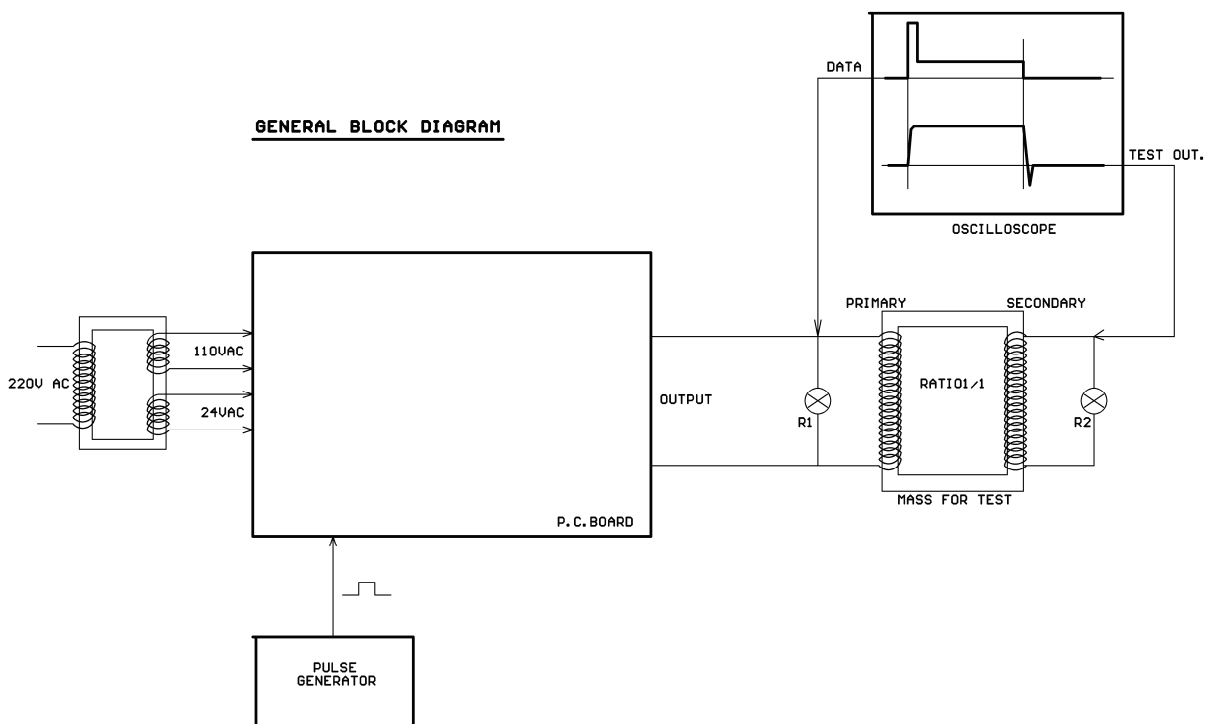


Figure 1. Block diagram of experimental set.

The drive circuit of the electromechanical system (Fig.2) is modified to compose 2 tetragonal pulses, (a) one with 24V amplitude and time duration that is determined by the frequency of operation (drive pulse) and (b) a second one with 110 V amplitude and time duration of 4 μ s (overdrive pulse).

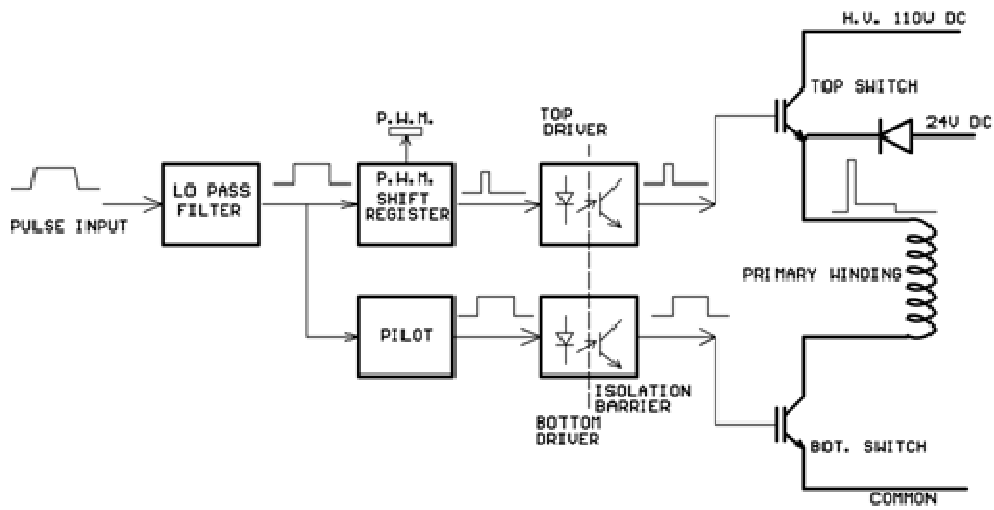


Figure 2. Drive circuit (P.C. Board on fig. 1).

Figures 3 and 4, which are photographs from oscilloscope, show the change of time response of the iron core with and without the overdrive. In both figures the upper signal is the input pulse in the primary winding of the electromechanical system and the lower signal is the output pulse from the secondary winding presenting the time response of the system.

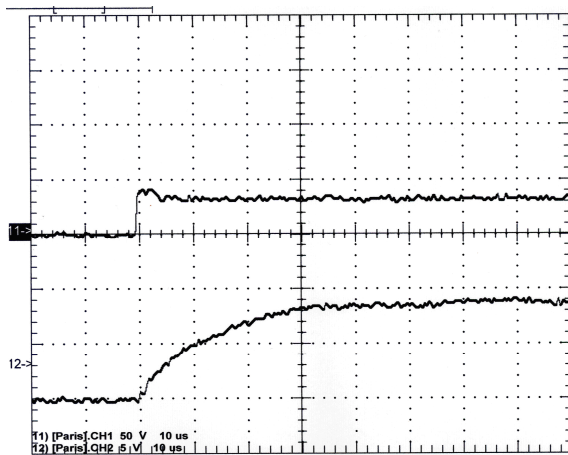


Figure 3. Without overdrive pulse.

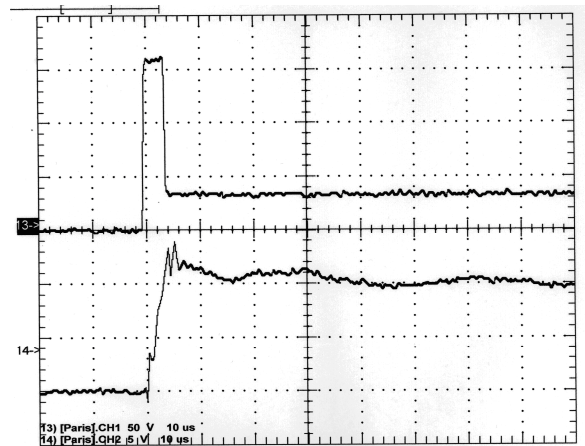


Figure 4. With overdrive pulse.

Acknowledgments The authors gratefully acknowledge the substantial assistance offered by Mr. J. Arampatzis during long discussions.

Experimental Errors in Magnetic Viscosity Measurements and Activation Volume Calculations

C. Serletis¹, M. Gjoka², G. Litsardakis³ and K.G. Efthimiadis^{1*}

¹ Department of Physics, Aristotle University, GR 54124 Thessaloniki, Greece

² Institute for Materials Science, NCSR "Demokritos", GR 15310 Ag. Paraskevi, Greece

³ Department of Electrical & Computer Engineering, Aristotle University, GR 54124 Thessaloniki, Greece

*kge@auth.gr

Magnetic viscosity is a time-dependent phenomenon, consistently observed in hard magnetic materials. It regards the time-variation of the magnetization of a substance under constant temperature and applied magnetic field, and it is due to a non-reversible variation of the magnetization, due to thermal disturbances. The first extended study of the magnetic viscosity was made in 1949, by Street & Wooley [1], where it was reported and also qualitatively explained that, after a constant field is applied and a certain time for relaxation is allowed for, the magnetization of a hard ferromagnetic material keeps varying with time, according to $\Delta M = S \ln(t)$, where S is the coefficient of magnetic viscosity. The latter takes on positive values when the material is magnetized, and negative ones when it is demagnetized. Since its discovery in the late '30s, magnetic viscosity is considered as a parameter used to characterize the magnetic microstructure of a material.

The irreversible magnetic susceptibility (χ_{irr}) is that part of the total magnetic susceptibility, that is due to irreversible changes of magnetization when the applied magnetic field is altered. All the above mentioned irreversible changes are attributed to the energy barriers in the magnetization of a material, formed by magnetocrystalline anisotropy and bipolar interactions. Magnetic viscosity is used in conjunction with irreversible susceptibility in the calculation of the activation volume ($v_a = kT\chi_{irr}/\mu_0 M_s S$) of magnetization reversal, another parameter used to characterize the magnetic microstructure of a material [2].

Both the magnetic viscosity and the non-reversible susceptibility are hard to be measured with confidence and repeatability. Consequently, the computation of the activation volume is too often carried out with a large margin of uncertainty. One must follow a definite experimental method, without deviations and small changes that lead to great experimental errors. The experimental method usually regards the demagnetization of the material, and starts with an initially saturated magnetic specimen. The initial saturation condition, that depends both on the intensity of the applied field and the previous magnetic history of the sample, must be strictly the same, in order to achieve a repeatability of the measurements. The specimen is next demagnetized, under a field of opposite direction. The rate of the variation of the applied field from saturation to the value where the measurements are to take place plays also an important role, as regards the repeatability of the measurements. Usually, the stabilization of the field is accompanied initially by small variations that fade out shortly. These variations of the field intensity must be very small, because they cause great experimental errors. Finally, small variations of the temperature during the time the measurements are executed can destroy the experimental results.

The measurement of the magnetic viscosity is usually carried out after 1000 s from the stabilization of the applied field have elapsed, in order for the transient phenomena irrelevant to it to be terminated. On the contrary, it is customary to measure the irreversible susceptibility during the first 100 s (fig. 1). This measurement is performed during the demagnetization of the material, by recording its magnetization as a function of the applied field. The slope of this function includes both reversible and irreversible phenomena, and corresponds to the total magnetic susceptibility (χ_{tot}). At a specific value of the intensity of the applied field, the rate of variation of the field is brought to zero and reversed, as instantaneously as possible. The initial slope of the magnetization during

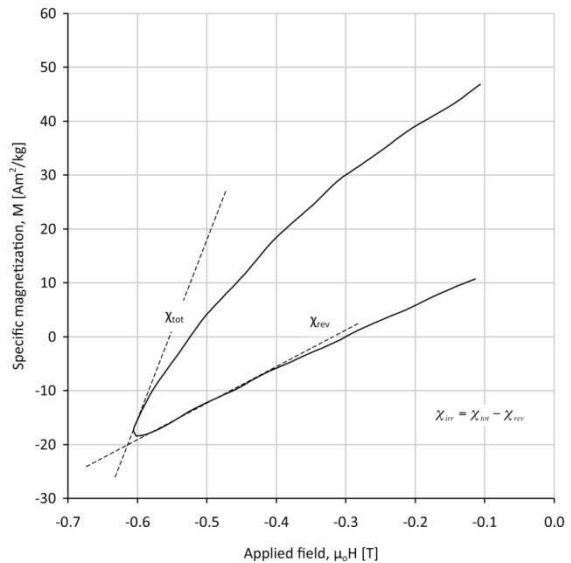


Figure 1. Measurement of irreversible susceptibility during the first 100s.

the reverse variation of the applied field corresponds to the reversible susceptibility (χ_{rev}). The irreversible susceptibility is calculated by the difference $\chi_{irr} = \chi_{tot} - \chi_{rev}$.

This method of estimating χ_{irr} carries along both accidental and systematic errors, due to the transient phenomena that take place during the zeroing and the reversal of the field. Furthermore, it leads to an erroneous calculation of the activation volume, because the measurements of S and of χ_{irr} in different times correspond to irreversible changes of magnetization for different distributions of energy barriers.

This work is an effort to estimate the above mentioned experimental errors. The materials used are an M-type ferrite $Sr_{0.8}La_{0.2}Fe_{11.8}Co_{0.2}O_{19}$, prepared by the chemical co-precipitation method and $Sm[Co,Cu,Fe,Zr]_{8.5}$ ribbons, prepared by melt spinning and without any thermal treatment. The ferrite was chosen because it exhibits Stoner-Wohlfarth behavior, whereas the ribbons present a nucleation type magnetic behaviour. All the measurements are taken at room temperature, because at higher temperatures thermal effects become very strong and it becomes more difficult to estimate other parameters.

Taking into account all the factors, we conducted several viscosity measurements using the same set of experimental parameters, and the results show that repeatability in measurements can be achieved. Another experiment was conducted to evaluate the χ_{irr} at the same time the magnetic viscosity was measured. In this experiment, a minor loop (no more than 150G) was recorded after 1000s of constant applied field (fig. 2). The results indicate that activation volume calculations differ significantly if irreversible susceptibility is measured at the same time viscosity is measured.

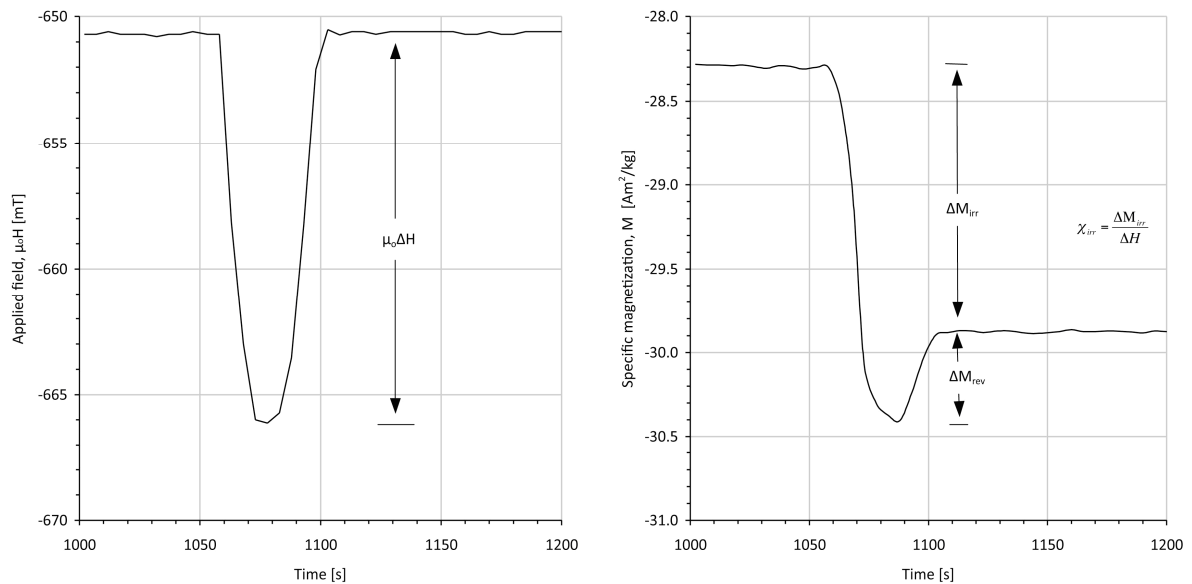


Figure 2. Measurement of irreversible susceptibility after 1000s of constant applied field.

[1] R. Street, J.C. Wooley, Proc. Phys. Soc. 62 (1949) 562.

[2] D.C. Crew, S.H. Farrant, P.G. McCormick, R. Street, J. Magn. Magn. Mater. 163 (1996) 299.

Electromagnetic properties and absorption of new La substituted Sr W-type hexaferrite in the 2-18 GHz frequency range

C. A. Stergiou, T. V. Yioultsis and G. Litsardakis*

Department of Electrical and Computer Engineering, Aristotle University, Thessaloniki, GR-54124, Greece

**Lits@eng.auth.gr*

Ferrite composites play a key role in applications related to electromagnetic wave attenuation and interference suppression. As electronic systems are moving up to higher working frequencies, spinel ferrites seem to fall short due to intrinsic restrictions imposed by the low anisotropy and the occurrence of their ferromagnetic resonance in the GHz region (Snoek's limit). On the contrary, soft hexagonal ferrites with planar magnetocrystalline anisotropy (Z-, Y-type), exhibiting relatively high resonance frequency, are employed in this field. Co substituted W-type hexagonal ferrites are particular members of ferroxplana family as Co can modify anisotropy from c-axis to c-plane, while keeping high values of permeability and magnetic losses. Additionally, despite the interesting effect of rare-earth elements (RE) and especially La substitutions on static magnetic properties of hexagonal ferrites, there is a lack of reports on electromagnetic properties of La-doped hexagonal ferrites. Therefore the aim of the present work is to study the electromagnetic behavior of new hexagonal ferrites with composition $\text{Sr}_{1-x}\text{La}_x\text{Co}_2\text{Fe}_{16}\text{O}_{27}$ ($x=0, 0.05, 0.10$) in the 2-18 GHz frequency range.

These compounds were composed by the chemical coprecipitation method with precursors of nitrate salts. Aqueous solutions of reagent grade salts $\text{Sr}(\text{NO}_3)_2$, $\text{Fe}(\text{NO}_3)_3 \cdot 9\text{H}_2\text{O}$, $\text{Co}(\text{NO}_3)_2 \cdot 6\text{H}_2\text{O}$ και $\text{La}(\text{NO}_3)_3 \cdot 6\text{H}_2\text{O}$ were added to NaOH solution, maintaining a $\text{OH}^-/\text{NO}_3^- = 2$ molar ratio [1]. After 2 hours of vigorous stirring at 130°C the coprecipitated solutions were filtered, repeatedly washed with distilled water and dried at 90°C for 16 hours. In order to facilitate sintering, dried mixtures were pressed to form discs that were annealed at $1200\text{--}1250^\circ\text{C}$. Finally, bulk ferrite samples were manually ground for further characterization as powders. Also, toroid composite samples containing 80wt% of hexaferrite particles dispersed in polyethylene matrix were prepared for microwave properties measurements with a coaxial line method.

In order to prepare single-phase compounds we had to deviate from the stoichiometric amounts of cations, yet considering the typical formation reaction of W-type hexaferrites between spinel (S: CoFe_2O_4) and M-type hexaferrite (M: $\text{Sr}_{1-y}\text{La}_y\text{Fe}_{12}\text{O}_{19}$) [2]. By analyzing the X-ray diffraction patterns (Seifert XRD 3003 TT, FeKa) of samples with modified chemical formula, it was discovered that the excess of Sr in M-hexaferrite molecule ($\text{Sr}:\text{Fe} = 1:10$) as well as spinel deficiency ($\text{M}:\text{S} = 1.7\text{--}1.9$) lead to pure hexaferrite samples, through this specific preparation method. It is also inferred that La-doping necessitates more intensive annealing, in terms of temperature and time, probably due to additional lattice distortion caused by the RE ion. Chemical formulas of the three single phase compounds along with their optimal preparation conditions are shown in Table 1. All samples were identified as W-type hexaferrites (JCPDS No.: 78-0135 και S.G.: $\text{P6}_3/\text{mmc}$).

Table 1. Composition and annealing conditions of samples

Sample	Chemical formula	Annealing
SC	$\text{Sr}_{1.2}\text{Co}_{1.9}\text{Fe}_{15.8}\text{O}_{27+\delta}$	$1200^\circ\text{C} \times 15\text{h}$
SL1	$\text{Sr}_{1.15}\text{La}_{0.05}\text{Co}_{1.7}\text{Fe}_{16}\text{O}_{27+\delta}$	$1250^\circ\text{C} \times 15\text{h}$
SL2	$\text{Sr}_{1.10}\text{La}_{0.10}\text{Co}_{1.7}\text{Fe}_{16}\text{O}_{27+\delta}$	$1250^\circ\text{C} \times 24\text{h}$

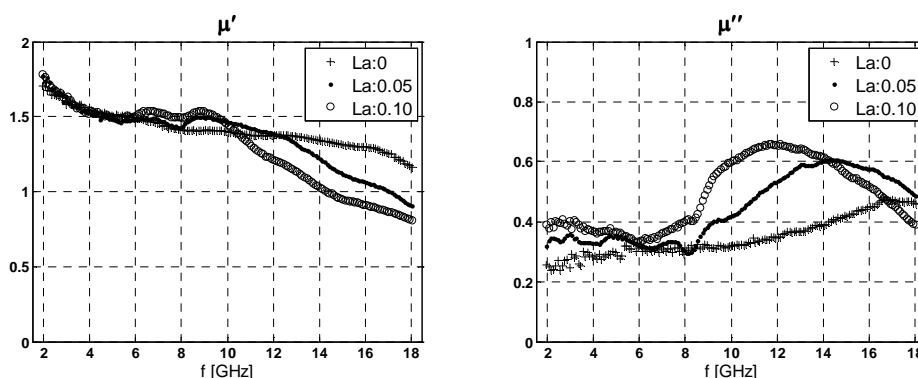
The microstructure of the samples was observed by means of JEOL JSM 840A scanning electron microscope. Besides the dissimilarities of the bulk ferrites, ground powder samples were found to consist of resembling particles, with regard to average size and shape. The majority of grains synthesized were about $0.8\text{--}10\ \mu\text{m}$, thus powders comprise mainly multidomain particles. So it is noticed that static magnetic and electromagnetic properties should be interpreted on the basis of common morphological characteristics.

Hysteresis loop measurements were carried out at room temperature on nonaligned powder samples using a vibrating-sample magnetometer and yielded magnetization M_s and coercivity H_c values, shown in Table 2. Decrease of coercivity with La doping is attributed to the increase of Fe^{+2} ions, formed according to the reaction $\text{Sr}^{+2} + \text{Fe}^{+3} \rightarrow \text{La}^{+3} + \text{Fe}^{+2}$, while Fe^{+2} ions lead to increase of anisotropy coefficient k_1 ($k_1 < 0$) and reduction of anisotropy field H_θ (out of plane anisotropy). Furthermore, steady decrease of H_c with La substitution implies planar anisotropy for all compounds. Initial increase of magnetization is in agreement with the enhancement of super-exchange $\text{Fe}^{+3}\text{--O--Fe}^{+3}$ found for small La doping [3], actually improving magnetic order. Stabilized value of M_s for $y = 0.1$ is ascribed to contradictory impact of increasing concentration of Fe^{+2} ions.

Table 2. Remanence and coercivity values of samples

Sample	Chemical formula	H_C [kA/m]	M_r [Am ² /kg]
SC	$Sr_{1,2}Co_{1,9}Fe_{15,8}O_{27+\delta}$	4,2	74,31
SL1	$Sr_{1,15}La_{0,05}Co_{1,7}Fe_{16}O_{27+\delta}$	2,9	75,59
SL2	$Sr_{1,10}La_{0,10}Co_{1,7}Fe_{16}O_{27+\delta}$	2,5	75,41

Complex permeability $\mu^*(f)$ measurements (Fig. 1) revealed the decrease of ferromagnetic resonance frequency of composite materials with La from 16.65 to 11.75 GHz, which stems from corresponding reduction of out of plane anisotropy H_ϕ . Increase of both real μ' and imaginary permeability μ'' in the proximity of the resonance, also noticed in Fig. 1, results from increased saturation magnetization and mainly reduced in plane anisotropy field H_ϕ . Complex permittivity $\varepsilon^*(f)$ of composites shows practically no dispersion effects in the measured spectrum, but evidently increases with La amount. This trend is justifiable, as the addition of La increases dielectric polarization as well as the chance of electron hopping through the mechanism $Fe^{+3} \leftrightarrow Fe^{+2}$, yielding higher dielectric constant and losses [4].

Figure 1. Measured real (μ') and imaginary (μ'') permeability values in the 2-18 GHz frequency range

Zero-reflecting conditions for single layer configuration were calculated by means of the Transmission-Line method, using the measured electromagnetic properties of the new hexagonal ferrites. Thus, maximum reflection loss of 45 dB was calculated for an 1.5 mm thick SL1 composite layer at 18 GHz and 64 dB for an SL2 layer of thickness 1.65 mm at 16.5 GHz. Similar levels of reflection losses with the reference compound SC can be attained with a layer thicker than 8.5 mm. Calculated reflection losses and measured electromagnetic properties demonstrate the potential use of new La substituted Sr W-type hexaferrites in the design and manufacture of single- or multi-layer electromagnetic wave absorbing structures.

- [1] Litsardakis G., Manolakis I., Serletis C., and Efthimiadis K. G., J. Magn. Magn. Mater. 316, 170 (2007).
 [2] Lotgering F. K., J. Inorg. Nucl. Chem., 1960, 16, 100-108, (1960).
 [3] Kui J., Lu H. and Du Y., J. Magn. Magn. Mater. 31-34, 801-802, (1983).
 [4] Li H., Zou H., Yuan L., Xu J., Gan S., Meng J. and Hong G., J. Rare Earths, 25, 590-595, (2007).

Acknowledgements

The authors acknowledge K.G.Efthimiadis and C.Serletis for magnetization measurements and E.Pavlidou for SEM observations.

This paper is part of the 03ED742 research project, implemented within the framework of the “Reinforcement Programme of Human Research Manpower” (PENED) and co-financed by National and Community Funds (25% from the Greek Ministry of Development-General Secretariat of Research and Technology and 75% from E.U.-European Social Fund).

Study of the mechanism through which microstructural characteristics affect the impedance of NiCuZn ferrites

D. Sakellari^{1*}, A.Kazakopoulos², K.G. Efthimiadis¹, V. Tsakaloudi³, V. Zaspalis³ and E. K. Polychroniadis¹

¹ Department of Physics, Aristotle University of Thessaloniki-Greece

²Department of Electronics, Technological Educational Institute of Thessaloniki, Greece

³Laboratory of Inorganic Materials, Center for Research and Technology-Hellas, Thessaloniki-Greece

*dsakel@physics.auth.gr

NiCuZn ferrites are a very important category of magnetic materials with a variety of applications [1,2]. At high frequencies losses are mainly influenced by the eddy current losses. Since eddy current are inversely proportional to the resistivity, the study of electrical properties of such materials is of great importance. Meanwhile, it is well known that microstructure affects the electrical conductivity. The aim of this work is to understand the mechanism through which it also affects the resistivity.

Samples with the stoichiometry $(\text{Ni}_{0.22}\text{Cu}_{0.15}\text{Zn}_{0.63})\text{Fe}_{1.93}\text{O}_4$ were synthesized by the mixed oxide process which involves: wet mixing, drying, pre firing, milling, drying, granulation, pressing and finally sintering. The sintering temperatures varied from 925°C until 1100°C, over a period of 3h. Microstructural study was carried out using Conventional and High Resolution Transmission Electron Microscopy (TEM, JEOL 100CX and HREM JEOL 2010) equipped with an EDS detector. Pore volume was measured by nitrogen sorption, t-plot method using Autosorb-1, Quantachrome. Impedance spectroscopy, in the range of 42Hz-1MHz for 25, 100, 200 and 300°C, was performed for the electrical characterization of ferrites.

All samples were polycrystalline with spinel structure. Grain size and porosity of samples were influenced by the sintering temperatures conditions. As we can see from Fig. 1, grain sizes of samples were significantly high for samples sintered at 1100°C, where the diameter reaches 100 μm. Meanwhile, the porosity of samples decreases with the sintering temperature (Fig. 1). It must be mentioned that porosity as it is measured by BET can not be distinguished between interporosity and intraporosity. But in combination with the microscopic investigations we have a complete view of the sample's porosity. Having this in mind, the results show that for 1100°C the porosity is due to intraporosity, while for lower temperature interporosity is evident.

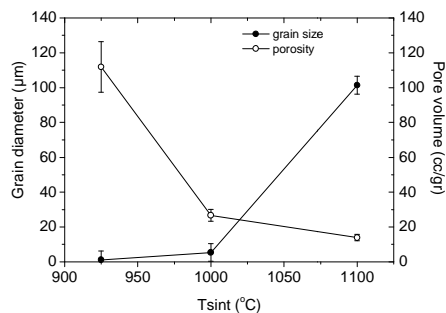


Figure 1: Grain size and porosity for various sintering temperatures

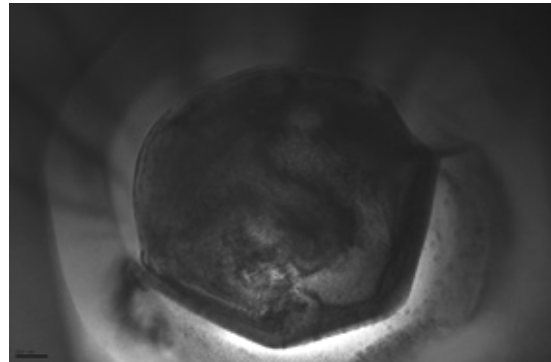


Figure 2: Cu₂O inclusion inside a pore of ferrite

TEM study revealed dislocations and subgrain boundaries on the interior of the grains. Both of them are investigated for samples up to 1000°C. For higher temperatures, stress relaxation takes place, as those defects seem to disappear. A Cu-rich phase in the form of a thin lamellae was investigated for samples sintered at 1100°C. The formation of these phases is related to the reduction of Cu at these temperatures. The mechanism through which Cu undergoes reduction is already published in our previous work [3]. A characteristic image is presented in Fig. 2, where Cu₂O phase was observed and cross checked by EDS analysis. At high sintering temperatures EDS also revealed that Cu segregation happens at grain boundaries.

Impedance spectroscopy of samples was performed for 25, 100, 200 and 300°C. The experimental results were fitted using the software EQUIVCRT.PAS[4]. The results provide an equivalent circuit, which models the electrical conductivity of ferrites. An indicative example for both the experimental and the fitted data, along with the resultant equivalent model for a sample sintered at 1100°C, is shown in Fig. 3. For all samples the equivalent

circuit consists of two sets of parallel R and Q elements in series. Each one of them is attributed to the impedance of grain and its boundaries. Table 1 presents the specific impedance of grain and grain boundaries along with the total impedance of samples for the frequency of 1kHz.

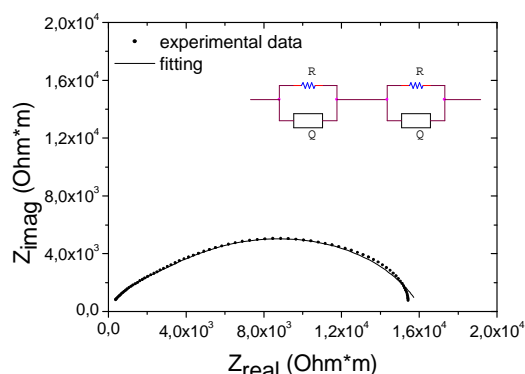


Figure 3: Nyquist plots for 100°C from sample sintered at 1100°C

It is obvious that the total impedance drops. As it is very well known, conductivity in ferrites is due to electron hopping between ions that exist at different valence states, like Fe [5]. In fact, the more the pairs of multivalent ions, the higher the conductivity. At these temperatures Cu exists in two valence states [3]. This means that in addition to Fe, Cu might participate to the conductivity of ferrite. Additionally, for higher temperatures, the grains become bigger which has an even stronger effect in the reduction of impedance. Meanwhile, from the models results the conductivity of both grains and grain boundaries were calculated and the respective Arrhenius plots were created.

According to the Arrhenius equation:

$$\sigma = A \exp(E_a/KT) \quad (1)$$

where A is the preexponential factor, E_a is the activation energy, k is Boltzmann constant and T is the temperature. From Eq. (1) and in combination with the graphs, the activation energy of conductivity was calculated (Table 1). The activation energy is the barrier that electrons must overcome to hop, simply put, it expresses the hopping probability. The activation energy of the interior of the grain is almost unchanged for samples of sintering temperatures of 925°C and 1000°C, while for higher temperatures it drops. This is related to stress relaxation and the disappearance of related defects, such as dislocations and subgrain boundaries. As explained above, at such temperatures Cu exists in two valence states and that in addition to Fe, Cu might also participate to the conductivity of the grains. Contrary to activation energy of grains, the activation energy of grain boundaries seems to follow the systematic reduction of porosity.

Table 1: Results from the fitting of electrical measurements

Sintering temperature (°C)	Z ($\times 10^3$ Ohm*m) at 100°C and 1kHz		Z ($\times 10^3$ Ohm*m) 1MHz, 100°C	Activation energy (eV)	
	Z _g	Z _{gb}		E _{act} (grain)	E _{act} (g.b.)
925	677	479	1024	0.61	0.60
1000	340	289	551	0.59	0.66
1100	2	13	15	0.47	0.49

In this work ($\text{Ni}_{0.22}\text{Cu}_{0.15}\text{Zn}_{0.63}\text{Fe}_{1.93}\text{O}_4$) were investigated in order to understand the mechanism through which microstructure affects the impedance. For samples of higher temperatures the impedance is highly dependent on the grain size and also on the Cu contribution to total conductivity. Meanwhile, analysis shows that the impedance of grains is mainly affected by the stress relaxation that takes place in the interior of the grains and also to Cu contribution. It seems though that it is not affected by the intraporosity. On the other hand, the impedance of grain boundaries is mainly due to the reduction of porosity of the boundaries.

[1] A.R.Bueno, M.L.Gregori, M.C.S.Nobrega, Mater. Chem. Phys. 105 (2007) 229-233.

[2] Hua Su, Huaiwu Zhang et al, Mater. Sci. Eng. B 129 (2006) 172-175.

[3] D. Sakellari, V. Tsakaloudi, V. Zaspalis, E.K. Polychroniadis, J. Am. Ceram. Soc., 91 [2] 366-371 (2008).

[4] EQUIVCRT.PAS: Equivalent Circuit, Bernard, A. Boukamp, University of Twente.

[5] N.Sivakumar, A. Narayanasamy et al, J. Phys. D: Appl. Phys. 39 (2006) 4688-4694.

This work was partially supported by the General Secretariat for Research and Technology-PENED 2003. This research project is co-financed by E.U.-European Social Fund (75%) and the Greek Ministry of Development-GSRT (25%). The authors would like to thank O.Kalogirou for the use of the software EQUIVCRT.PAS and E.Pavlidou for SEM observations.

Magnetic Thin Films Deposited on PDMS Nanotemplates

A. Markou¹, K.G. Beltsios¹, I. Panagiotopoulos^{1,*}, M.-E. Vlachopoulou², A. Tserepi²,
V. Alexandrakis³, T. Bakas⁴, T. Dimopoulos⁵

¹ Department of Materials Science and Engineering, University of Ioannina, Ioannina 45110, Greece

² Institute of Microelectronics-NCSR Demokritos, Aghia Paraskevi 15310, Greece

³ Institute of Materials Science-NCSR Demokritos, Aghia Paraskevi 15310, Greece

⁴ Physics Department, University of Ioannina, 45110 Ioannina Greece

⁵ Austrian Research Centers GmbH – ARC, Donau-City-Strasse 1
1220 Vienna, Austria

*ipanagio@cc.uoi.gr

The magnetic properties of nanostructured magnetic materials have attracted considerable interest due to their application in magnetic recording and spintronics [1]. An alternative to the use of “top-down” lithographic processes that are expensive and unfavourable to scaling up to large areas, “bottom-up” techniques as chemical synthesis of nanoparticles and deposition on nanostructured templates have been successfully used [2-4]. It was shown that by deposition of Co/Pd multilayers on nanospheres, regular arrays of magnetically isolated Co/Pd nanoparticles in the form of “nanocaps” can be obtained [3,4], with potential application as perpendicular recording media. This is based on the fact that when depositing on a non-flat surface the curvature of the surface plays an important role for the deposited film thickness. The effect is more pronounced in the case of magnetic multilayers due to the sensitive dependence of the magnetic properties on the individual layer thickness. On the other hand the deposition of metallic films on elastomeric polymers has been suggested as route for the appearance of complex, ordered structures induced by the buckling of thin metal films owing to thermal contraction of an underlying substrate [5]. Here we report on the modification of magnetic properties by deposition on PDMS films and nanostructured templates of two different systems: Co films (with in-plane anisotropy) and Co/Pt multilayers (with perpendicular anisotropy). It is found that apart from the etched nanosize features, maze-like submicron features develop after the sputter deposition as a result of film buckling due to thermal contraction of the underlying PDMS layer.

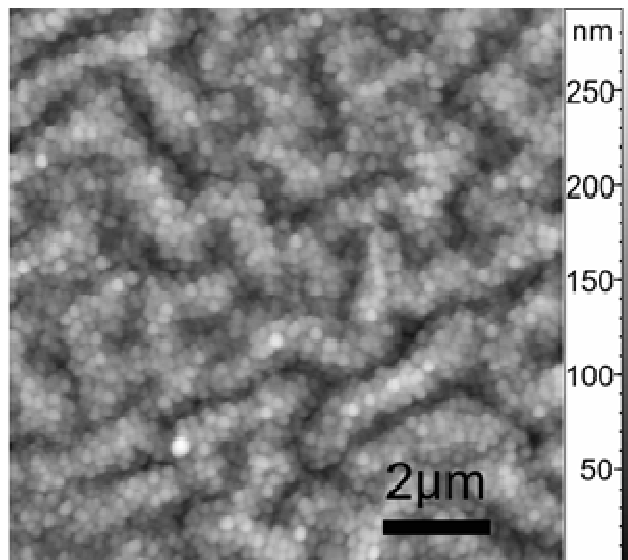


Fig.1 AFM image of a 30nm thick single layer Co film deposited on nanostructured PDMS.

In Fig.1 a typical AFM image of a 30nm thick single layer Co film deposited on nanostructured PDMS is shown. The nanoscale (200 nm) features due to the nanostructuring of the PDMS are superimposed on larger maze-like patterns 800 nm in width and several microns in length attributed to the buckling of metallic films owing to thermal contraction of the underlying PDMS layer. The considerable height variations (300 nm) of the buckling patterns do not allow direct detection of any possible nanoscale variation of the deposited metallic film thickness. However it must be noted that the metallic films grown on nanostructured PDMS are electrically

insulating unlike their counterparts grown on untreated PDMS or directly on Si wafers. This shows that the continuity of the metallic layers is disrupted by the nanostructure and not by the buckling features. In order to estimate the extent up to which the contraction induced rippling itself affects the magnetic properties as opposed to the effect of the nanotemplate, films were also grown on untreated PDMS.

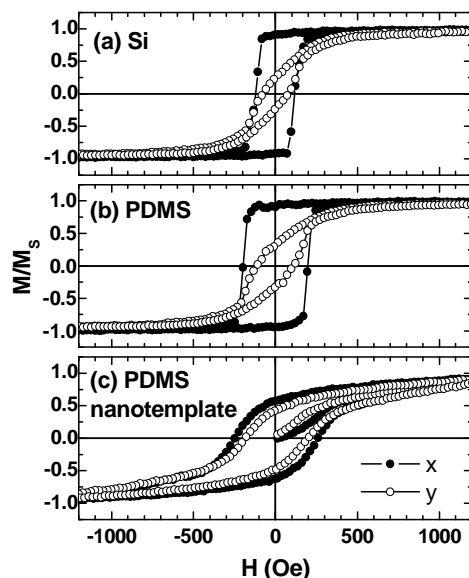


Fig.2 Comparison of the hysteresis loops of a 28nm Co films measured along different directions on the substrate plane. The films were deposited, under the same conditions, on (a) Si wafer (reference sample); (b) PDMS layer; (c) PDMS nanostructure (1 min etching).

The buckling of magnetic film owing to thermal contraction of the PDMS substrate creates features in the range of few μm that can be used to improve the magnetic properties of the films with in-the-film-plane anisotropy but cannot isolate the magnetic grains. These buckling patterns can be aligned along a specific direction on the substrate by oblique deposition, enhancing the in-plane anisotropy of the magnetic properties. Buckling patterns of shorter period also develop when depositing on nanostructured PDMS. However in this case the magnetic properties are mainly influenced by the nanotemplate features which lead to magnetically isolated entities and an increase of coercivity. The hysteresis loops of films deposited under oblique geometry show a substantial in-plane anisotropy between the x and y directions (Fig.2). The in-plane anisotropy is much more pronounced for the samples deposited on Si or untreated PDMS (where it is apparent in the whole loop shape) than for the samples on nanostructured templates (where it is evident only by the initial curve shapes and coercive values). It is known that shadowing effects can induce directional grain growth during physical vapour deposition processes [6]. It seems that in our case, this induces in turn some directionality in the buckling PDMS patterns.

In Co/Pt multilayers with perpendicular anisotropy the magnetic properties are not modified by deposition on PDMS layers at least within the thickness ranges checked. This could be related to the fact that the main anisotropy term contribution that defines their magnetic behaviour is the perpendicular one. Unpatterned substrates do not influence film growth and its structural properties. By deposition on PDMS nanotemplates the magnetic properties deteriorate. This is related to a loss of the perpendicular anisotropy, which may be attributed to the acuteness of the PDMS columnar features. Strong correlation of the magnetic state of the magnetic entities within the range of the buckling patterns is observed.

[1] For instance S.D. Bader; *Rev. Mod. Phys* 78, 1 (2006).

[2] S. Landis, B. Rodmacq, and B. Dieny; *Phys. Rev. B* 62, 12271 (2000).

[3] M Albrecht, Guohan Hu, Ildico L. Guhr, Till C. Ulbrich, Hohannes Boneberg, Paul Leiderer and Günter Schatz, *Nature Materials* 4, 203 (2005).

[4] T. C. Ulbrich, D. Makarov, G. Hu, I. L. Guhr, D. Suess, T. Schrefl, and M. Albrecht; *Phys. Rev. Lett.* 96, 077202 (2006).

[5] Ned Bowden, Scott Brittain, Anthony G. Evans, John W. Hutchinson, George M. Whitesides, *Nature* 393, 146 (1998).

[6] Herma van Kranenburg and Cock Lodder *Materials Science and Engineering RII* (1994) 295-354.

Controllable synthesis and characterization of hcp and fcc nickel nanoparticles.

A. Kotoulas^{1*}, C. Dendrinou-Samara², K. Simeonidis¹, S. Mourdikoudis¹, M. Angelakeris¹, M. Gjoka³, J. Georgiadis⁴ and O. Kalogirou¹.

¹ Department of Physics, Aristotle University of Thessaloniki, 54124 Thessaloniki, Greece

² Department of Chemistry, Aristotle University of Thessaloniki, 54124 Thessaloniki, Greece

³ Institute of Materials Science, NCSR "Demokritos", 153 10 Ag. Paraskevi, Attiki

⁴ Department of Geology, Aristotle University of Thessaloniki, 54124 Thessaloniki, Greece

*ankotoul@physics.auth.gr

ABSTRACT

Nickel nanoparticles were prepared via thermal decomposition of nickel acetate tetrahydrate in the presence of oleylamine, which acted as solvent, reducing agent and surfactant. Additionally, trioctylphosphine oxide (TOPO) and 1-adamantane carboxylic acid (ACA) were used as capping ligands. By changing the reaction temperature from 225 °C to 290 °C fcc or hcp nickel nanoparticles have been obtained, respectively. In the present work we have prepared six hcp samples (S1-S6) and two fcc (S7, S8). In order to estimate the role of the surfactants at the hcp samples, we kept constant all the reaction conditions, while the ratio of the surfactants (ACA, TOPO) ranged in various proportions. The fcc samples S7 and S8 were synthesized with the same proportions such as S2 and S6, respectively, but at different reaction temperature (225 °C). Electron microscopy and XRD techniques were used to determine the size and the crystal structure of the nanoparticles, while the magnetic properties were evaluated by VSM and SQUID magnetometry. Thermogravimetric analysis (TG) and FTIR spectroscopy were used to examine qualitatively and quantitatively the role of the surfactant molecules in the self-assembly procedures. Finally, their response to hyperthermia was preliminary examined.

INTRODUCTION

Nickel nanocrystals have been extensively studied because of their potential applications in magnetic sensors, memory devices, conducting materials, catalysis and biomedicine [1]. The hcp nanoparticles, in addition to the fcc ones, are not widely investigated, consequently their magnetic properties are not well defined. In this work magnetic characterization and size dependence on the proportion of the surfactants TOPO and ACA are clarified.

SYNTHESIS

Eight different samples were prepared (S1-S8). Six of them were hcp (S1-S6) and two fcc (S7, S8). In a typical procedure (S2) 0,558 g Ni(ac)₂·4H₂O (2,2 mmol), 0,309 g TOPO (0,8 mmol) and 0,180 g ACA (1 mmol) were inserted in a spherical flask under inert argon atmosphere and magnetic stirring (700 rpm) in the presence of 30 ml oleylamine. The mixture was degassed for 20 min before heated to 130 °C and maintained at this temperature for 20 min in order to evacuate the water molecules from the decomposition of the precursor. Then it was further heated at 290 °C (S1-S6) or at 225 °C (S7, S8) at a rate of 3 °C/min, remained at this point for 1h and allowed to cool at room temperature. The solid sediment obtained by centrifugation was washed several times with a mixture of acetone and hexane in order to remove the byproducts and oleylamine. The final product was dispersed and stored into hexane. The ratio of the surfactants ranged in various proportions TOPO/ACA=0,4 up to 3,2 for the samples S1-S4 and for the samples S5, S6 ACA/TOPO=1,6 and 3,2 respectively. Samples S7, S8 were similarly synthesized as S2, S6 but at 225 °C.

STRUCTURE AND MORPHOLOGY

In figure 1 the images that have been taken by a conventional TEM device are shown. By changing the proportions of the ligands, nanoparticles with different sizes were synthesized. Raising the proportion of ACA against TOPO, smaller nanoparticles were received and the aggregation increased. Hence, the mean diameter of the nanoparticles at S2 sample was ~77,6 nm, while being ~56,8 at S6.

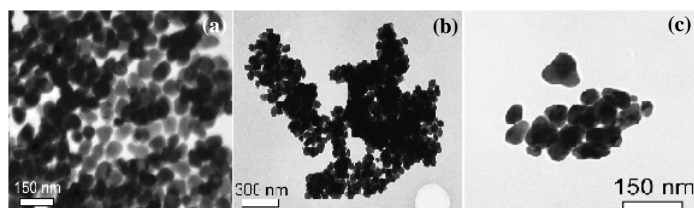


Fig. 1: TEM images for samples S2, S6 and S8 (a, b and c respectively)

In the absence of the system TOPO/ACA the nanoparticles were dramatically smaller

[2]. In addition, the fcc nanoparticles were more agglomerated than the hcp ones, due to their enhanced magnetic interactions. Their size were ~ 147 nm and $\sim 58,8$ nm for S7, S8, respectively. The samples S6 and S8, at which the ratio TOPO/ACA was 1/3,2, have nearly equal sizes. At all samples the nanoparticles have a polygonal, smooth-angled shape. Figure 2 indicates the X-ray diffraction patterns of the samples. As it was expected, samples S1-S6 have hcp structure, while S7, S8 have fcc. The crystal structure of the nanoparticles hinges on the reaction temperature exclusively and no dependence appears from the ratio of the ligands or oleylamine. These results are in absolute consonance with the literature, whereby fcc nanoparticles are forming below 240 °C whereas hcp over 260 °C [2-3].

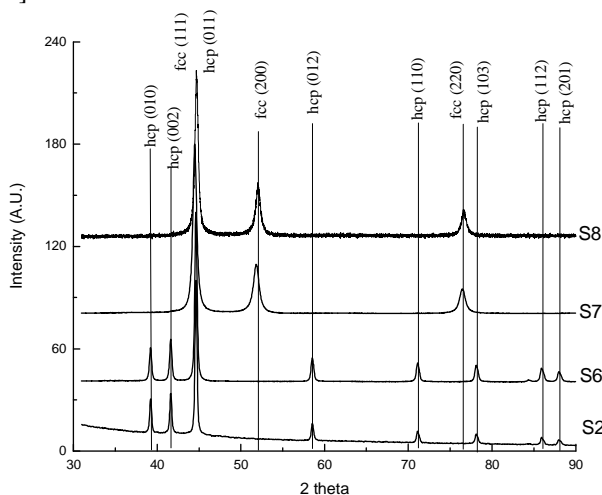


Fig. 2: X-ray powder diffraction patterns for S2, S6, S7, S8.

MAGNETIC CHARACTERIZATION

For the magnetic characterization of the hcp nanoparticles SQUID technique was applied. In figure 3 the magnetic loops for S2, S6 are given, where almost the same magnetic behavior is observed. As shown at both samples, particularly at S2, weak ferromagnetism is perceived. The values of coercivity at 5 K are 66,5 and 710 Oe, respectively. Additionally at an external field of 5T, S2 reaches maximum magnetization of $2,7 \text{ Am}^2/\text{kg}$ and S6 $4,4 \text{ Am}^2/\text{kg}$. The blocking temperature for S2 is 6 K and for S6 in the range between 13 and 17 K.

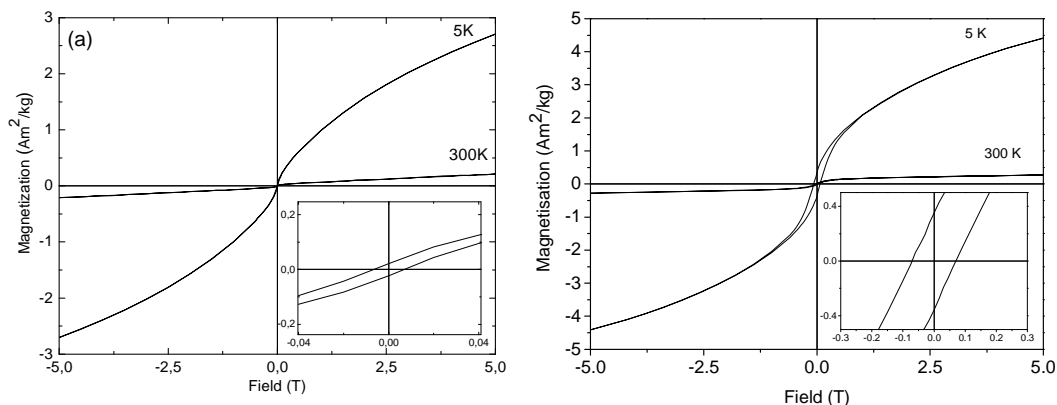


Fig. 3: Magnetization vs field for S2 and S6 (a, b respectively) samples at 5K and at 300K.

CONCLUSIONS

Ni nanoparticles with controlled crystal structure were synthesized by thermal decomposition of nickel acetate tetrahydrate, at which the proportions of the surfactants ranged. Herein we found that their size and their magnetic properties are influenced by this ratio.

REFERENCES

- [1] D. Guo, C. Wu, H. Hu, X. Wang, X. Li and B. Chen. Biomed. Mater. 4 (2009) 025013.
- [2] S. Mourdikoudis, K. Simeonidis, A. Vilalta-Clemente, F. Tuna, I. Tsiaoussis, M. Angelakeris, C. Dendrinou-Samara and O. Kalogirou, J. Magn. Mater. 321 (2009) 2723.
- [3] Y. Chen, D.-L. Peng, D. Lin and X. Luo. Nanotechnology 18 (2007) 505703.

The beneficiary role of intentional alloying in noble metal-Cobalt multilayered systems

I. Giannarakis^{1*}, A. Frangouli¹, K. Simeonidis¹, P. Pouloupoulos², M. Angelakeris¹
and N.K. Flevaris¹

¹*Department of Physics, Aristotle University of Thessaloniki, 54124, Thessaloniki, Greece*

²*Materials Science Department, University of Patras, Patras 26504, Greece*

*igiannar@physics.auth.gr

ABSTRACT

The combination of Co with Pd or Pt either in alloy or multilayer form yields significant tunable features mainly in the macroscopic magnetic behavior i.e. enhanced magnetization and perpendicular magnetic anisotropy. In an effort to thoroughly study and further exploit Co-based multilayers, we investigate the structural and magnetic properties of Co/Pt (or Pd) multilayers where one of the constituent materials is substituted by CoPt (or CoPd) alloy. The role of intentional alloying within the multilayer period, though it preserves high degree of crystallinity, it promotes stronger perpendicular magnetic anisotropy and enhanced magnetization features, that are highly plausible by the requests for magnetic recording applications.

INTRODUCTION

Co-based magnetic multilayers have been extensively investigated since perpendicular magnetic anisotropy (PMA) was found in Pd/Co and Pt/Co multilayers [1-2]. On the other hand CoPd and CoPt alloys have also attracted considerable interest during the last two decades due to their noticeable magnetic and magneto-optic properties [3]. A comparative study between PtCo alloys and Pt/Co multilayers has shown that the alloys exhibit higher values of magneto-optic Kerr rotation for Co concentration between 40-60 at.%, while the multilayers exhibit greater PMA especially for small values of thickness of the Co layers [3]. Our previous works on Co-based multilayers have revealed magnetic properties suitable for related technological applications [4-6]. In an effort to improve the magnetic and magneto-optic features of such multilayered systems alternative strategies are employed including the alloying of the Co layers with Pd or Pt that is presented in this work. Consequently, this leads to the formation of a hybrid structure in between alloys and the conventional two-element multilayers with tailor-made properties suitable for ultra-high density magnetic and magneto-optic recording media.

EXPERIMENTAL SECTION

The noble metal-Cobalt multilayered systems were grown by e-beam evaporation on glass substrates. The structural properties of the samples were studied via θ -2 θ x-ray diffraction (XRD) using the CuK α radiation. The magnetic characterization was performed at temperatures from 77 to 300K via vibrating sample magnetometry (VSM) with maximum magnetic field 1.1T.

A series of conventional Pt_m/Co_n samples as well as Pt_m/[Co_xPt_{1-x}]_n, [Co_xPt_{1-x}]_m/Co_n, [Co_xPd_{1-x}]_m/Co_n and Pd_m/[Co_xPd_{1-x}]_n samples were grown on glass substrates by e-beam evaporation of pure (99.99%) Pt or Pd and Co targets under ultra high vacuum (UHV) conditions. The numbers m, n denote atomic planes per multilayer period and range between 1 and 10, while x is the at.% concentration of Co in the alloyed layers. A 12-20 nm Pt (or Pd) buffer layer was predeposited in order to ensure and improve crystallinity and <111> texturing. The deposition of the multilayer was always ending with a thin Pt or Pd or Co overlayer in order to protect the internal layers against oxidation and corrosion. The atomic concentration of Co in the alloyed layers (CoPt, CoPd) was determined with energy dispersive X-ray spectroscopy (EDX) experiments and it was found to be from 33 to 70 at.%, depending on the sample.

RESULTS AND DISCUSSION

The structural and modulation characteristics were studied by θ -2 θ XRD. The individual layer thicknesses (m and n) together with the multilayer period Λ and the number of bilayers N are known to significantly affect the structural features of multilayers and eventually, the number, the intensity and the width of the peaks appearing in the XRD pattern. In Fig.1, a comparative graph of the influence of intentional alloying in cases where layer thickness is kept below 5 atomic layers is shown. In all cases a strong <111> texture is observed due to Pt underlayer while the existence of both small-angle and high-angle diffraction satellite reflections indicates high degree of crystallinity and multilayer stacking. One may also see diffraction peaks of Pt(111) and Pt(002) (or Pd(111)) arising from the overlayer and the buffer layer. The multilayer period Λ and the individual thicknesses m and n were experimentally verified by the positions of small and high-angle XRD peaks. Eventually, the

structural features of multilayers with intentionally alloyed layers resemble the conventional multilayers comprising of two pure elements.

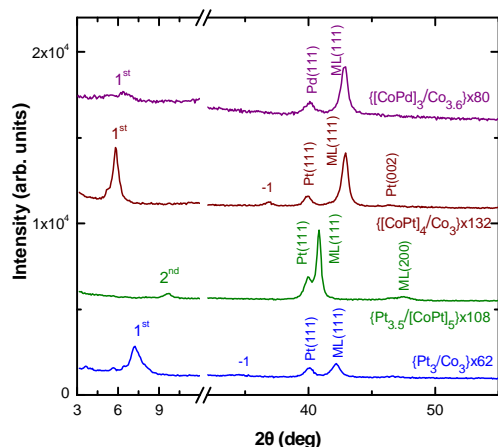


Figure 1:

Experimental θ -2 θ XRD patterns for different types of Co-based multilayers with intentionally alloyed layers

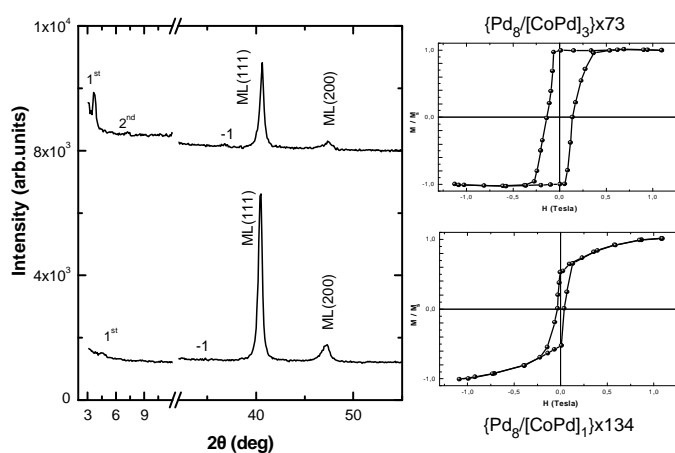


Figure 2:

Experimental θ -2 θ XRD patterns for Pd-[CoPd] multilayers (on the left) and corresponding out-of-plane VSM room-temperature hysteresis loops (on the right).

In Fig.2 the XRD patterns of two Pd-CoPd multilayers with different CoPd layer are depicted (on the left). Despite the small layer thickness of CoPd (<3 atomic layers) in both cases multilayer peaks appear indicating the high quality of stacking. However, in the second sample comprising of only ~ 1 atomic layer of magnetic material (CoPd), as expected for such thin layers, multilayer periodicity degrades due to potential interdiffusion effects. A corresponding decline is also observed in magnetic hysteresis loops recorded under perpendicular to film plane magnetic field and room temperature shown on the right side of the graph for the same samples. We may see the unambiguous development of perpendicular magnetic anisotropy which becomes stronger in the case of the higher quality multilayer sample with squareness ratio close to unity. Similar observations at smaller extent may be seen for the second sample that also exhibits PMA but with milder features (smaller M_{rem} , H_c and M_{rem}/M_s). Therefore, the introduction of alloyed layers within a multilayer significantly tunes the PMA and results to systems with scalable magnetic features.

CONCLUSIONS

The structural characteristics in hybrid structures combining intentional alloying with multilayer stacking were correlated with macroscopic magnetic behavior. The substitution of individual elemental layers with corresponding alloyed ones seems to be beneficiary if properly combined with relatively small layer thicknesses in order to allow interface effects to dominate over magnetic behavior. Thus, the intentional alloying of the magnetic layers gives an additional degree of freedom for tailoring and optimizing crucial properties of films for technological applications.

REFERENCES

- [1] P.F. Carcia, A.D. Meinhaldt, A. Suna, Appl. Phys. Lett. 47, 178 (1985).
- [2] W. B. Zeper, J. A. M. Greidanus, P. F. Carcia, and C. R. Fincher, J. Appl. Phys. 65, 4971 (1989).
- [3] D. Weller, W. Reim, K. Sporn and H. Brandle, J. Magn. Magn. Mater. 93, 183 (1991).
- [4] P. Pouloupoulos, M. Angelakeris, Th. Kehagias, D. Niarchos, N.K. Flevaris, Thin Solid Films 371, 225 (2000).
- [5] P. Pouloupoulos, M. Angelakeris, E. Th. Papaioannou, N. K.Flevaris, D. Niarchos, M. Nyvlt, V. Prosser, S. Visnovsky, Ch. Mueller, P. Fumagalli, F. Wilhelm, and A. Rogalev, J. Appl. Phys. 94, 7662 (2003).
- [6] M. Angelakeris, E.Th. Papaioannou, P. Pouloupoulos, A. Vlachos, F. Wilhelm, A. Rogalev and N. K. Flevaris, Phys.Stat. Sol (a) 205 2302- 2306 (2008).

Evaluation of iron oxide nanoparticles prepared by high-energy ball milling in drinking water treatment

Th. Gkinis¹, S. Tresintsi², P. Moschou², K. Simeonidis^{1*}, M. Mitrakas², Th. Kehagias¹
O. Kalogirou¹ and M. Angelakeris¹

¹ Department of Physics, Aristotle University of Thessaloniki

² Chemical Engineering Department, Aristotle University of Thessaloniki

* ksime@physics.auth.gr

ABSTRACT

Iron oxide nanoparticles were produced by grinding a magnetite (Fe_3O_4) powder, using a wet ball-milling procedure into heptane. Different particle sizes and distributions were achieved depending on the rotational speed and milling duration. In order to stabilize smaller particle sizes (<50 nm) and obtain shape homogeneity, fatty acids and amines were also introduced as surfactants. The resulting nanoparticles combine good magnetic properties with relatively high surface area. Therefore, they were examined as possible candidates for the sorption of As in drinking water and their removal by magnetic separation.

INTRODUCTION

Due to small particle size and large surface area, nanomaterials have considerable potential for use in environmental engineering. However, the demand for large-scale production is not yet fulfilled by the proposed chemical “bottom-up” methods for the synthesis of magnetic nanoparticles. High-energy ball-milling is a simple, inexpensive and efficient method for size reduction of nanocrystalline powders [1]. The primary advantages are the applicability of this method to the production at tonnage proportions, the high purity and the affordable control of the geometrical features of obtained nanomaterials. In addition, the employment of high-energy ball milling in the presence of an organic carrier liquid and surfactants may overcome limitations in size reduction and result in the stabilization of nanoparticles smaller than 30 nm. The role of surfactants is also important in chemical protection and lubrication of particles surfaces that reduces plastic deformation, local heating and contamination.

The natural occurrence of As, a well-known carcinogen, in groundwater is of great concern due to the toxicity of As and the effects of chronic exposure. To address this problem, many methods are currently in use for removing As from drinking water including anion exchange, reverse osmosis, chemical precipitation, and adsorption. Magnetite nanoparticles are potential sorbents for arsenic removal as its interaction with iron oxides is strong and irreversible, even on nanoscale particles [2]. Their large magnetization values allow also their selective, fast and efficient (compared to centrifugation or filtration) removal with the use of magnetic fields [3]. In this work we studied the influence of various milling parameters in the obtained size, composition and aggregation degree of iron oxide nanoparticles, and in a second step the evaluation of their As adsorption ability at aqueous solutions (pH=6-8) as a function of their magnetically driven recovery.

PREPARATION

Magnetite (Fe_3O_4) powder (size distribution under 40 μm) was milled in a high energy planetary ball-mill (Fritsch Pulverisette 6 with hardened steel vials and balls) at rotational speeds 200-400 rpm to produce iron oxide nanoparticles. The milling was performed in a protective argon atmosphere with the ball-to-powder weight ratio of 10:1 for milling times varying from 0.5 to 150 hours. Heptane (50-150 % of powder weight) was introduced in the grinding bowl as a solvent together, in some of the samples, with a mixture of oleic acid and/or oleylamine (12 % of powder weight) as surfactants (wet milling). In the slurry mixture obtained after milling, a size selection process including washing with ethanol and centrifugation cycles was performed.

STRUCTURE AND MAGNETISM

The size variation in different milling times was estimated by means of transmission electron microscopy (TEM) observations. The chemical composition was identified by the corresponding electron diffraction patterns and the shift of the magnetic properties measured by using vibrating sample magnetometry (VSM). Figure 1 illustrates the gradual reduction of the mean particle size depending on the milling energy and the use of surfactants. Conventional milling without surfactants has a limit in the minimum achieved size around 400 nm. In this case, the samples consist of large polycrystalline agglomerates as welding seems to be the dominant effect after crushing. Higher milling speeds result in a faster approach of the size limit. On the opposite, the role of surfactants is critical in the isolation and stabilization of smaller sizes reaching 20 nm at 300 rpm.

TU2
P34

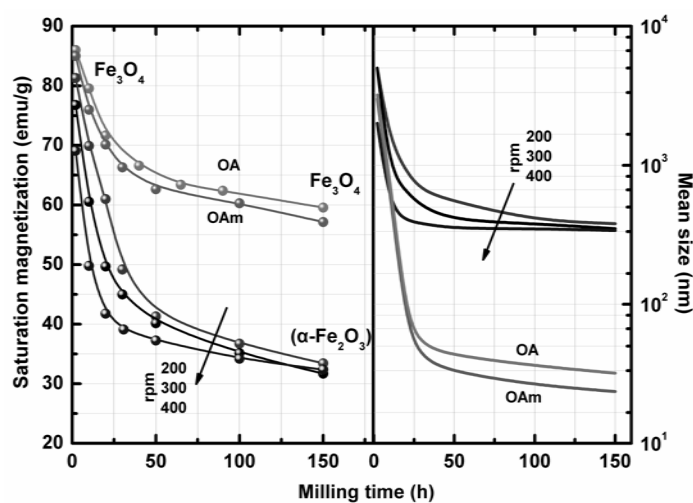


Fig 1. Saturation magnetization and particle size as a function of milling time.

Oleic acid (OA) and oleylamine (OAm) are absorbed on the surface of the majority of nanoparticles preventing re-welding and allowing the dispersion of the nanoparticles in organic solvents. It is remarkable that although wet milling leads to much smaller particle size, magnetization values are barely reduced, due to nanoscale effects, as the organic coating improves protection from chemical contamination during this intense mechanical process.

However, long periods of ball milling without surfactants cause a significant magnetization loss mainly due to structural amorphization and the phase transformation taking place on particles surface indicated by a color change to brown. The identification of α - Fe_2O_3 in the final product is relevant to this assumption.

ARSENIC ADSORPTION

As the resulting iron oxide particles are getting smaller their specific surface increases dramatically and may serve as good sorbents for arsenic. The absorption capacity q , for Fe_3O_4 particles around 600 nm without surfactants was studied at a pH range 6-8 for As(III) containing water (Table 1). Experiments were performed in batches of shaking flasks with 80 mg of absorbent/L and a contact time of 24 h. The initial and residual arsenite concentration was measured by graphite-furnace atomic absorption. For comparison, the corresponding absorption for the raw Fe_3O_4 powder and the effect of the absorbing material concentration are also shown. It is clear that absorption capacity is directly proportional to the increment of specific surface (~15 times higher in 600 nm sample). Moreover, the pH of the treated water seems to be a very critical parameter since it determines the surface charge and enables structural transformations. In this case, the rise of pH up to 8, causes the partial appearance of amorphous iron hydroxides with a large number of active sites, leading to the maximization of absorption capacity. Finally, by doubling the added Fe_3O_4 powder, residual As concentration could be limited to 5 $\mu\text{g/L}$ (pH=8) though absorption capacity is lower. Further experiments will clarify the removal ability of surfactant coated nanoparticles that exhibit many times higher specific surfaces.

Table 1. As(III) removal and magnetic separation efficiency.

Particle size (nm)	pH	Absorbent (mg/L)	Residual As ($\mu\text{g/L}$)	q (mg As/g)	% absorbent separation
>5000	7	80	98	0.03	100
600	6	80	71	0.36	99
600	7	80	55	0.56	95
600	8	80	15	1.06	75
600	8	160	5	0.59	73

Initial As(III) concentration was 100 $\mu\text{g/L}$

Once As was sorbed onto particles surfaces, magnetic separations by the application of a 0.2 T field provided a way to remove the solid materials from solution. The separation degree depends on the percentage of non-magnetic oxides and superparamagnetic Fe_3O_4 nanoparticles in each sample. Therefore, the formation of hydroxides explains the reduction of particles removal at high pH values. It looks that for an efficient magnetic separation, operation conditions should be optimized towards structural stability than the maximum As removal.

REFERENCES

- [1] A.I. Gusev and A.S. Kurlov, Nanotechnology 19, 265302 (2008).
- [2] S.R. Kanel, B. Manning, L. Charlet, H. Choi, Environ. Sci. Technol. 39, 1291 (2005).
- [3] C.T. Yavuz, J.T. Mayo, W.W. Yu, A. Prakash, J.C. Falkner, S. Yean, L. Cong, H.J. Shipley, A. Kan, M. Tomson, D. Natelson, V.L. Colvin, Science 314, 964 (2006).

Synthesis and Magnetic Properties of $\text{LaCoO}_{3-\delta}$ and $\text{La}_{0.8}\text{Sr}_{0.2}\text{CoO}_{3-\delta}$

Gaki A.^{1*}, Karavangelis Ch.¹, Kakali G.¹, Wiglusz R. J.², Strek W.²

¹National Technical University of Athens, School of Chemical Engineering, Greece

²Polish Academy of Sciences, Institute of Low Temperature and Structure Research, Department of Excited States Spectroscopy, Poland

*gakianna@central.ntua.gr

Lanthanum Cobaltites doped with alkali earth elements (Ca, Sr, Ba) exhibit unique properties and are considered as promising materials for numerous applications such as catalysts for various oxidation-reduction reactions, oxygen permeable membranes or electrodes for different electrochemical devices such as solid oxide fuel cells [1]. Moreover, strontium doped lanthanum cobaltites have received much attention in recent years due to their unique magnetic and transport properties and possible technical applications [2, 3]. In the present work $\text{LaCoO}_{3-\delta}$ and $\text{La}_{0.8}\text{Sr}_{0.2}\text{CoO}_{3-\delta}$ powders are prepared by a wet chemical polymeric precursor route, and their magnetic properties at low temperatures are discussed.

$\text{LaCoO}_{3-\delta}$ and $\text{La}_{0.8}\text{Sr}_{0.2}\text{CoO}_{3-\delta}$ powders were prepared by a Pechini type polymeric precursor route, which involves the chelation of metal cations with citric acid, the polyesterification of the metal chelates with ethylene glycol forming a polyester resin which is dried and calcined to form the oxides. [4, 5] Microwave heating was applied for the completion of the polyesterification reaction and drying of the resins. Synthesis details are given elsewhere [6, 7].

The XRD patterns of the powders calcined at 1000 °C for 3 h are presented in Fig. 1.

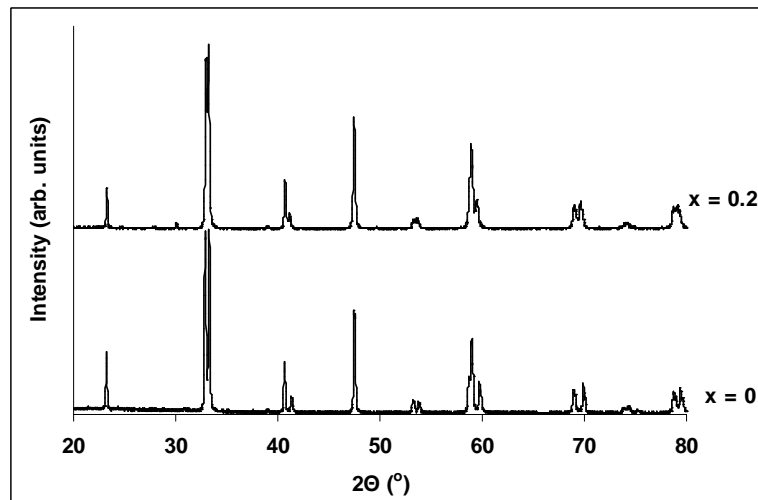


Figure 1: XRD patterns of $\text{La}_{1-x}\text{Sr}_x\text{CoO}_{3-d}$

The powders crystallize in the perovskite structure without the presence of any secondary phases in the patterns, indicating the high purity of the final products. Both patterns are indexed in rhombohedral symmetry with space group $R\bar{3}C$ (167). The splitting of the diffraction peaks is reduced by strontium doping, indicating that the rhombohedral distortion is reduced.

$\text{LaCoO}_{3-\delta}$ is often referred to as paramagnetic [2, 8-9]. However, many research have reported a ferromagnetic transition in LaCoO_3 below 100 K. [10-13]. The temperature dependence of magnetization and inverse susceptibility under a magnetic field of 1kOe are given in Figures 2-3 a, b respectively, and the field dependent magnetization at 1.7 K in Figures 2-3 c.; however at temperature below 80K an increase of the magnetization with cooling is observed. There is an FM transition with $T_c \approx 80$ K suggesting the ferromagnetic state of the sample at low temperatures.

The inverse susceptibility curve above 100 K follows the Curie-Weiss law. However as it can be seen the curve is not linear suggesting the appearance of ferromagnetic interactions even at higher temperatures. The ferromagnetic state of $\text{LaCoO}_{3-\delta}$ at low temperatures is also indicated by the remanent magnetization observed in Figure 2c. The $M(H)$ curve does not exhibit saturation even at a magnetic field of 50 kOe indicating the absence of true long-term ferromagnetic order in $\text{LaCoO}_{3-\delta}$.

For the doped sample, the magnetization increases below 210 K, where the transition to ferromagnetic state occurs. The range of this transition is rather wide, indicating an increased inhomogeneity of the magnetic phases throughout the material. At higher temperatures the sample is paramagnetic and the inverse susceptibility curve

follows the Curie-Weiss law with a $T_c=208$ K. The $M(H)$ curve shows no saturation along with a remanent magnetization, as in the case of the undoped sample, and the magnetic state can be described as spin-glass.

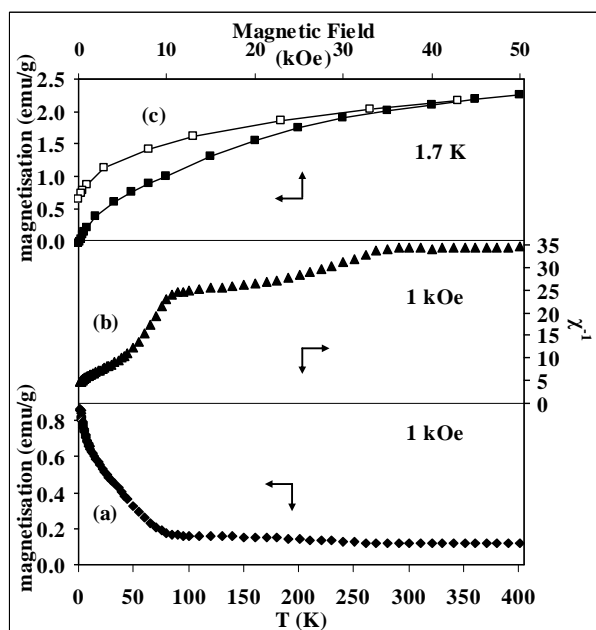


Figure 2: Temperature dependence of magnetization (a), inverse susceptibility (b) and field dependence of magnetization (c) of $\text{LaCoO}_{3-\delta}$

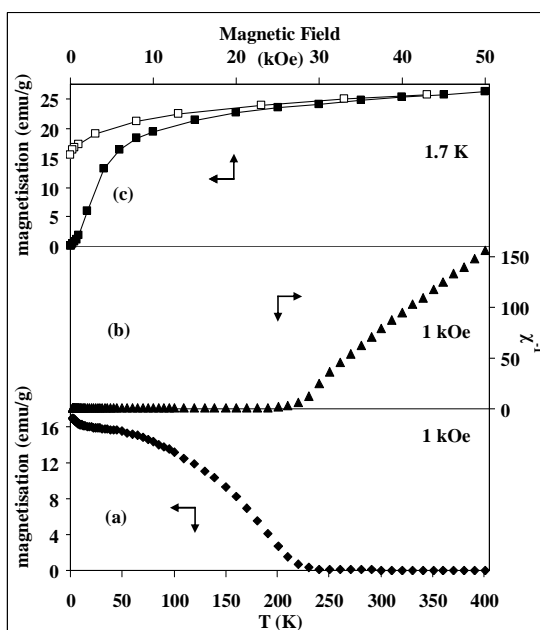


Figure 3: Temperature dependence of magnetization (a), inverse susceptibility (b) and field dependence of magnetization (c) of $\text{La}_{0.8}\text{Sr}_{0.2}\text{CoO}_{3-\delta}$

The substitution of La with 0.2 Sr promotes the formation of Co^{4+} and significantly increases the magnetization due to the increase of the positive $\text{Co}^{3+}-\text{Co}^{4+}$ interaction and the stabilization of the Co^{3+} in a higher spin state [3].

References

- [1] A. N. Petrov, V. A. Cherepanov, A. Yu. Zuev, *J Solid State Electrochem.* 10, 517 (2006).
- [2] M. Itoh, I. Natori, S. Kubota and K. Matoya, *J. Phys. Soc. Japan* 63, 1486 (1994).
- [3] M.A. Señaris-Rodríguez and J.B. Goodenough, *J. Solid State Chem.* 118, 323 (1995).
- [4] M.P. Pechini, U.S. Patent No. 3 330, 697 (1967).
- [5] M. Kakihana, *J. Sol-Gel Sci. Technol.* 6, 7 (1996).
- [6] A. Gaki, O. Anagnostaki, D. Kioupis, T. Perraki, D. Gakis, G. Kakali, *J. Alloys Compd.* 451, 305 (2008).
- [7] A. Gaki, Ch. Karavangelis, G. Kakali, R. J. Wiglusz, L. Kępiński, W. Strek, *Proceedings of the Fifth International Materials Symposium (MATERIAIS 2009)*, Lisbon, Portugal, 499 (2009).
- [8] C.N.R. Rao, O. Parkash, D. Bahadur, P. Ganguly and S. Nagabhushana, *J. Solid State Chem.* 22, 353 (1977).
- [9] A.N. Petrov, O.F. Kononchuk, A.V. Andreev, V.A. Cherepanov, P. Kofstad, *Solid State Ionics* 80, 189 (1995).
- [10] Menyuk, K. Dwight, and P. M. Raccah, *J. Phys. Chem. Solids* 28, 549 (1967).
- [11] J. Androulakis, N. Katsarakis, and J. Giapintzakis, *Phys. Rev. B* 64, 174401 (2001).
- [12] J.-Q. Yan, J. S. Zhou, and J. B. Goodenough, *Phys. Rev. B* 70, 014402 (2004).
- [13] S. Zhou, L. Shi, J. Zhao, L. He, H. Yang, S. Zhang, *Phys. Rev. B* 76, 172407 (2007).

Acknowledgments

This work is part of the PhD thesis of one of the authors, Miss A. Gaki, funded by the Hellenic State Scholarships Foundation.

The authors acknowledge the financial support of this research under program Grant No: PEBE 2008/65/1700. The project is funded by the National Technical University of Athens.

Magnetic Anisotropy of Ho-Fe-Co-Cr intermetallic compounds

N. Sheloudko¹, C. Sarafidis^{2*}, M. Gjoka³, K.G. Efthimiadis² and O. Kalogirou²

¹Faculty of Physics, "St. Kl. Ohridski" University of Sofia, 1164-Sofia, Bulgaria

²Dept. of Physics, Aristotle University of Thessaloniki, 54 124 Thessaloniki, Greece

³NCSR "Demokritos", Institute for Materials Science, 153 10 Ag. Paraskevi, Athens, Greece

*hsara@physics.auth.gr

Nd₃(Fe,Ti)₂₉-type compounds crystallize in the monoclinic system with the A2/m space group [1]. In that structure the rare earth ion occupies two and the Fe atoms eleven crystallographic sites. It has been shown that for the formation of the 3:29 phase with more than 40% Co, a large amount of stabilizing atom is needed. This large amount of Co affects the magnetocrystalline anisotropy, from planar to uniaxial, in high Co content 3:29 compounds with R = Gd or Sm [2,3].

In a previous work [4], we have tried to stabilize similar 3:29 compounds with R = Ho, Tb and Co for Fe substitution up to 80% by using large amounts of Cr for stabilizing the structure. In the case of Ho a disordered variant of the hexagonal 2:17 phase (Th₂Ni₁₇-type, S.G. P63/mmc) has been formed. Both this phase and the 3:29 compounds have the same rare earth to transition metal ratio, 1:9.7, and the formation of either phase depends on composition and synthesis conditions [5]. In this work we report a more detailed study of the magnetic properties and the magnetocrystalline anisotropy of these compounds.

Preparation and basic characterization of the alloys under study have been reported elsewhere [4]. Rietveld analysis has shown that the samples were practically single phase. In the present work the temperature dependence of the magnetization was measured by means of a SQUID magnetometer (5 – 300 K) in low fields (field-cooled (FC) and zero-field-cooled (ZFC) pots). Magnetically aligned samples were prepared for the study of the magnetocrystalline anisotropy. A mixture of fine powder (less than 37 μm) of the compound and epoxy resin was put into a glass tube of cylindrical shape. Then the tube was rotated in a magnetic field of 1 T until the epoxy resin solidified. For the SQUID measurements the hard magnetization direction (HMD) of the easy-plane compound is along the tube axis. For VSM measurements HMD is perpendicular to the tube axis. Magnetization curves were recorded with the external field applied either parallel or perpendicular to HMD at RT, 100 and 5 K by means of a VSM and a SQUID with field strength up to 2 and 5 T, respectively. The saturation magnetization, M_S, was derived by M – 1/H plots extrapolated to infinite field.

From the FC and ZFC temperature dependence of magnetization it was derived that the compound with 80% Co content presents a compensation point at about 55 K. At that temperature, 3d-sublattice moment is equal to the Ho-sublattice moment and due to the ferrimagnetic coupling the two sublattice moments cancel each other. The rare earth moment decreases faster with temperature than the 3d moment. Hence, above 55 K the 3d-sublattice moment dominates the rare earth one, but below it is the opposite.

As reported in [4], the HMD of the compounds is along the c axis and the easy magnetization directions (EMD) are in the plane normal to it, i.e. the (a,b) plane. In Fig. 1, a typical example of magnetization curves is shown.

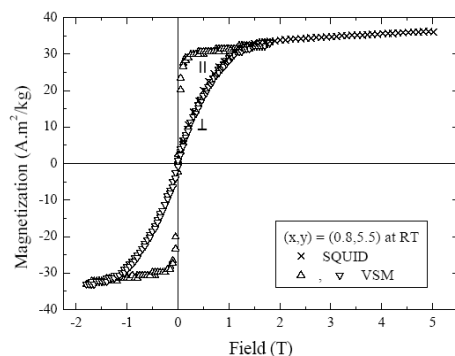


Fig. 1: Magnetization curves parallel and perpendicular to HMD for 80% Co sample (RT).

The results are summarized in Table 1.

The symmetry of the rotation-aligned samples is that of a uniaxial system having a hard axis and easy plane, with anisotropy in the basal plane. For a planar anisotropy system with its EMD normal to the field and its

Determination of the anisotropy field and anisotropy constants was based on the reversible recoil curves in hard magnetization direction. In this case magnetization takes place only by reversible rotation processes. The curves at RT practically show no remanence. The remanence measured for field applied parallel to the RT hard magnetization direction can be taken as a measure of the degree of grain alignment. A perfectly aligned sample would be expected to show zero remanence in hard direction of magnetization. From the RT demagnetization curves in the hard direction, we may consider that the c-axes of the different crystallites in the powders are aligned within 0.8° for both samples. For the determination of the anisotropy field we have plotted the magnetization in the perpendicular direction as a function of 1/H², expecting a change of the slope at the anisotropy field. The result for (x,y) = (0.6,4.5) sample at RT is shown in Fig. 7 as an example.

TU2

P36

magnetization making an angle θ with the field, the anisotropy constants K_1 and K_2 can be obtained by the Klein equation, where H is the applied field, M_{\perp} is the magnetization measured in HMD, M_s the spontaneous magnetization, K_1 and K_2 the phenomenological anisotropy constants.

$\text{Ho}_3(\text{Fe}_{1-x}\text{Co}_x)_{29-y}\text{Cr}_y$	T (K)	M_s (Am ² /kg)	K_1 (J/K)	K_2 (J/K)	$\mu_0 H_A$ (T)	
					from (-2K/M _s)	from $\Delta M(H)$
$x = 0,6$ $y = 4,5$	300	58,2	-54	12	1,8	1,6
	100	27,4	-92	42	6,8	7,0
	005	20,0	-101	19	10,1	8,6
$x = 0,8$ $y = 5,5$	300	38,8	-32	10	1,7	1,6
	100	13,5	-34	17	5,8	5,3
	005	16,9	-109	24	12,9	12,9

$$\frac{\mu_0 H}{M_{\perp}} = -\frac{2K_1 + 4K_2}{M_s^2} + \frac{4K_2}{M_s^4} M_{\perp}^2$$

Table 1: The saturation magnetization, M_s , anisotropy constants, K_1 and K_2 , and anisotropy field, $\mu_0 H_A$, for $(x,y) = (0,6,4,5)$ and $(0,8,5,5)$ samples.

A plot of $\mu_0 H/M_{\perp}$ against M_{\perp}^2 can give $(-2K_1+4K_2)/M_s$ from the intercept and $4K_2/M_s$ from the slope (Sucksmith-Thompson method [6]). The RT Sucksmith-Thompson plots for the compounds under study are presented in Fig. 2. From the values of K_1 and K_2 the anisotropy field was calculated as $\mu_0 H_A = -2K_1/M_s$. The obtained values for K_1 and K_2 satisfy the relations for easy-plane anisotropy: $K_1 < 0$, $K_2 > 0$ and $(K_1 + 2K_2) < 0$ for both compounds, at 300, 100 and 5 K.

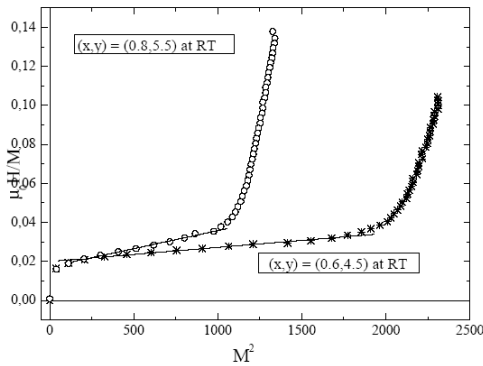


Fig. 2: Sucksmith - Thompson plot for $(x,y) = (0,6,4,5)$ and $(0,8,5,5)$ samples at RT.

The anisotropy of the T-sublattice, studied on Y_2T_{17} compounds, has an easy plane character for both Y_2Fe_{17} and Y_2Co_{17} , however it changes to uniaxial in $\text{Y}_2(\text{Fe}_{1-x}\text{Co}_x)_{17}$ series, when $0,55 < x < 0,95$, at RT and at low temperatures [7], because of preferential occupation of Fe and Co in the T-sites, especially of Fe atoms at dumb-bell sites. Since the compounds under study have hexagonal $\text{Th}_2\text{Ni}_{17}$ -type structure with a concentration of Fe and Co atoms close to that of the $\text{Y}_2(\text{Fe}_x\text{Co}_{1-x})_{17}$ series mentioned above, the anisotropy of the transition sublattice could be uniaxial. However, our results show that the anisotropy of the compounds under investigation is planar both at low temperatures and at RT. At RT, where the R-sublattice anisotropy energy decreases, the total anisotropy of the compounds is determined by the T-sublattice. Consequently, the anisotropy of the T-(Fe,Co,Cr) sublattice in the compounds under investigation should be planar. That means there are also Co and/or Cr atoms at dumb bell sites instead of only Fe atoms there. Such an observation is in agreement with our conclusions in Ref. [4] that there would be Cr and/or Co atoms in dumb-bell sites by means of crystallographic arguments. Moreover, it should be taken into account that our compounds crystallize in the disordered 2:17 structure with non-stoichiometric rare earth to transition metal ratio. In this structure the dumb-bells of Fe atoms replace some R ions at the 2b position [8].

- [1] O. Kalogirou, V. Psycharis, L. Saettas, D. Niarchos, J. Magn. Magn. Mater. 146 (1995) 335.
- [2] J.L. Wang, et al. J. Appl. Phys. 93 (2003) 6924.
- [3] W. Wang, J. Wang, W. Li, B. Liu, G. Wu, H. Jin, F. Yang, J. Alloys Compd. 358 (2003) 12.
- [4] K.G. Efthimiadis, C. Sarafidis, M. Gjoka and O. Kalogirou, J. Magn. Magn. Mater. 316(2) (2007) e458.
- [5] D. Hadjiapostolidou, M. Gjoka, C. Sarafidis, E. Pavlidou, T. Bakas, O. Kalogirou, J. Alloys Compd. 367 (2004) 255.
- [6] W. Sucksmith and J.E. Thompson, Proc. Roy. Soc. (London) 225 (1954) 362.
- [7] R.S. Perkins and S. Strässler, Phys. Rev. B 15 (1977) 477.
- [8] O. Moze, R. Caciuffo, B. Gillon, G. Calestani, F.E. Kayzel and J.J.M. Franse, Phys. Rev. B 50 (1994) 9293.

Acknowledgments

This work was supported by the 089-c bilateral Greek-Bulgarian project of the General Secretary for Research and Technology, Greece and by grant BG – 15/2005.

Structural, morphological and magnetic features in exchange-biased Co nanoparticles

K. Simeonidis^{1,*}, F. Frangeskou¹, C. Martinez-Boubeta², I. Tsiaoussis¹, S. Mourdikoudis¹,
C. Dendrinou-Samara³, M. Angelakeris¹ and O. Kalogirou¹

¹ Department of Physics, Aristotle University of Thessaloniki, 54 124 Thessaloniki, Greece

² Institut de Ciència de Materials de Barcelona (ICMAB-CSIC), Campus UAB, Bellaterra 08193, Spain

³ Department of Chemistry, Aristotle University of Thessaloniki, 54 124 Thessaloniki, Greece

*ksime@physics.auth.gr

ABSTRACT

Spherical Co particles with an average diameter under 20 nm were synthesized via the thermal decomposition method of proper precursors. Contrary to iron case, it is possible to maintain stable cobalt nanoparticles under atmospheric environment for a long period after synthesis keeping the precise control of the composition and the structure of the nanoparticles, thus tuning oxidation mechanisms during or after the synthetic procedure. Small sized nanoparticles (e.g. < 8 nm) facilitate relatively easy diffusion of oxygen through their volume and are readily and completely oxidized to CoO or Co₃O₄. For bigger particle diameters (>10 nm), the core of the nanoparticles is protected against oxygen diffusion and oxidation is finally limited at a surrounding shell. The magnetic measurements support such core/shell morphology by the appearance of the exchange bias effect which occurs at ferromagnetic/antiferromagnetic interfaces.

INTRODUCTION

Cobalt-based nanostructures reside between the most promising materials for technological applications like information storage, magnetic fluids and catalysts [1,2]. The low crystal anisotropy of cobalt also promotes their study as a model system for the effects of size, shape, crystal structure, and surface anisotropy on their macroscopic magnetic response. Additionally, the Co/CoO interface, a proximity between a ferromagnetic (FM) and an antiferromagnetic (AFM) material leads to interesting effects that result from the structural modification and competition of different types of magnetic ordering at the interface between them. In particular, the exchange coupling at a FM/AFM interface may induce unidirectional anisotropy in the FM below the Neel temperature of the AFM (CoO), causing a shift in the hysteresis loop, a phenomenon known as exchange bias (EB). In recent years, the study of EB in nanoparticles and nanostructures has gained renewed interest since it has been shown that control of the core/shell interactions or exchange coupling between the particle surface and the embedding matrix can increase the superparamagnetic limit for their use as magnetic recording media [3].

In a previous work, we have studied the synthetic parameters that influence the size, structure, composition and arrangement of cobalt nanoparticles [4]. The aim of this work was to examine the effect of different parameters in the self-arrangement, the yield, the structural and magnetic properties of cobalt nanoparticles. The role of the cobalt precursor, the surfactants, the working temperature and the presence of oxidants were mainly emphasized. Currently, we focus on small spherical nanoparticles exhibiting the EB effect and examine its size dependence.

EXPERIMENTAL DETAILS

In a typical synthetic procedure a cobalt precursor (Co₂(CO)₈) is added in a high boiling point ether containing one or two long-chain organic surfactants (oleic acid, oleylamine, trioctylphosphine oxide) and mixed under inert or open air conditions at room temperature. The temperature is set between 180 – 300 °C for 60 – 180 min to assist the progress of the reactions. The final product is cooled to room temperature, centrifuged and washed with ethanol to remove any non-reacted compounds and excessive solvent.

Different cobalt or cobalt oxide nanoparticle systems were produced, depending on the details of the thermal decomposition procedure. Parameters like the working temperature, the physical and chemical properties of the precursor and the surfactants specify the mechanism of particles growth and thus the final size and shape. X-ray Diffraction (XRD), Transmission Electron Microscopy (TEM) and thermogravimetric analysis (TGA) on particle powders were used to identify the cobalt phases and the organic content. Magnetic loops were recorded together with field cooled-zero field cooled (FC-ZFC) magnetization cycles in the temperature range 5-300 K.

STRUCTURE AND MAGNETISM

According to the structural study, it seems that atmospheric oxygen may naturally oxidize Co nanoparticles at different extent depending on their lateral dimensions and the exposure period. By the TEM observation (bottom inset in Fig. 1), for a representative sample, it appears that nanoparticle size in this case is 13 nm±10%, while oxidation, contrary to other cases [4], is not dominating within nanoparticle volume as the corresponding electron diffraction pattern (top inset in Fig. 1) shows. In this case, oxidation occurs only at a limited extent since fcc-Co rings appear in ED image together with CoO ones. Similar observations were done for the 10 nm sample.

TU2

P37

The coexistence of both phases yields a possibility of an EB system as revealed by the horizontal shift of hysteresis loop at low temperatures shown in Fig.1.

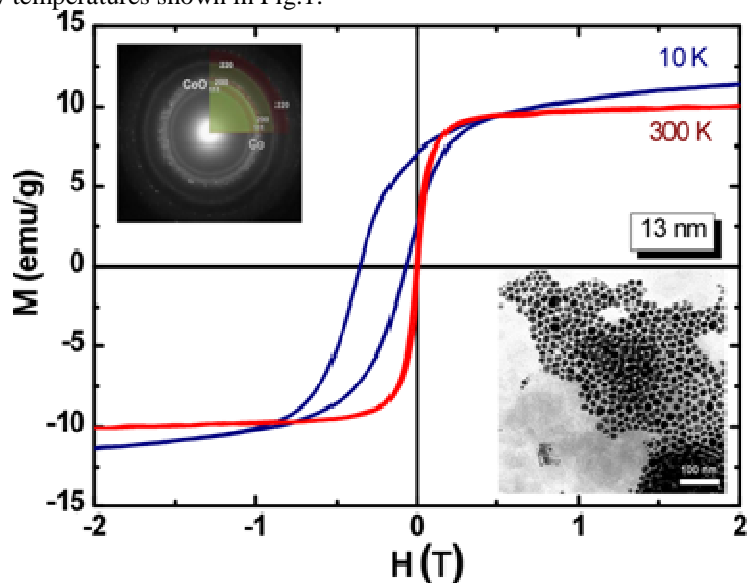


Fig 1. Hysteresis loops recorded at 10 and 300 K showing the EB effect, together with planar TEM illustration of nanoparticles arrays (bottom inset) and corresponding ED image (top inset) indicating the existence of two phases.

Eventually, oxygen diffusion length is limited under a radius of few nm (~ 5 nm) and nanoparticles smaller than this threshold are fully oxidized and exhibit antiferromagnetic features. Nanoparticles bigger than this size sustain a core/shell morphology with a size-dependent attenuating exchange-bias effect, varying by the degree of oxidation.

The size dependence of the exchange-bias effect is shown in Fig. 2 where its temperature dependence for the 10 nm and 13 nm nanoparticles is shown. As expected, H_{ex} enhances with decreasing temperature similarly to the coercive field, while for temperatures higher than 200 K diminishes.

A significant value for H_{ex} (1.6 kOe and 2.1 kOe) is measured for both systems, though the slightly bigger particles (13 nm) appear to exhibit a stronger effect most probably due to bigger Co core and eventual different interface morphology and/or structural modifications and competition of different magnetic orderings at the interface between them.

Similar effects were also observed for nanoparticles up to 18 nm. For bigger nanoparticles, the effect is attenuating since the shell thickness is small enough compared to core size to modulate exchange coupling between them.

Consequently, size dependence of oxidation depth in Co nanoparticles, results in different Co-phases within nanoparticle volume and EB effects are tuned and enhanced accordingly.

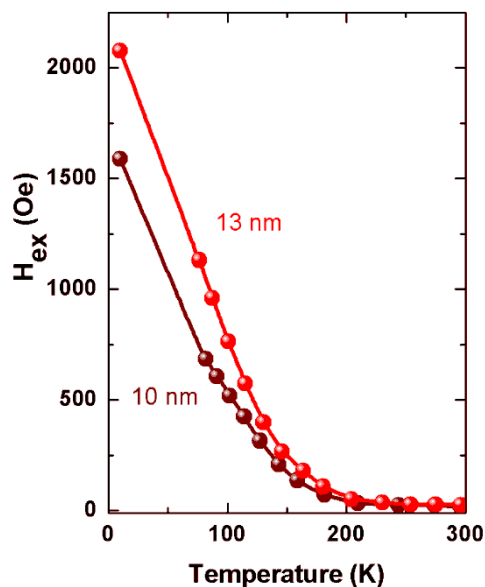


Fig 2. Temperature dependence of exchange-bias field for cobalt nanoparticles

ACKNOWLEDGEMENTS

This work was supported by the Greek Secretariat for Research and Technology – Contract No: 03EΔ667

REFERENCES

1. V.F. Puentes, K. Krishnan, A.P. Alivisatos, *Science*, 291 (2001) 2115.
2. V. Skumryev, S. Stoyanov, Y. Zhang, G. Hadjipanayis, D. Givord, J. Nogues, *Nature*, 423 (2003) 850.
3. J. Nogués, J. Sort, V. Langlais, V. Skumryev, S. Suriñach, J.S. Muñoz, M.D. Baró, *Phys. Rep.* 422 (2005) 65.
4. S. Mourdikoudis, K. Simeonidis, I. Tsiaoussis, C. Dendrinou-Samara, M. Angelakeris, O. Kalogirou, *J Nanopart. Res.* DOI 10.1007/s11051-008-9567-9.

A Quantum Circuit for Quantum Key Expansion from 6 to 24 Qubits

P. Vlachos^{*}, I. G. Karafyllidis

Democritus University of Thrace, Department of Electrical and Computer Engineering, 67100 Xanthi

**pvlahos@ee.duth.gr*

Quantum key generation and distribution protocols are the first real life application of quantum computing. The BB84 quantum key distribution protocol in which polarized photons are used as qubits is already in use and is commercially available. The cost and robustness of this protocol depends on the number of qubits included in each key. In this work we describe a quantum key expansion protocol in which a quantum key generated and transmitted using BB84 can be expanded to more qubits by the receiver which will use the larger expanded key to decipher the data. We develop a quantum key expansion scheme using quantum cellular automata. We model this scheme as a quantum circuit and use a quantum computer simulator to for the simulation of its operation. Using this scheme a 6-qubit key transmitted from the sender to the receiver, using one of the quantum key distribution protocols, can be expanded to a 24-qubit key without any further communication between the two parts.

- [1] M. Nielsen, I.L. Chuang, Quantum Computation and Quantum Information (Cambridge University Press, 2000).
- [2] J. Ng, D. Abbot, Microelectronics Journal 33 (2000) pp. 171-177.
- [3] F. Shafee, Microelectronics Journal 37 (2006) pp. 1321-1324.
- [4] D. Deutch, Proceedings of the Royal Society of London A400(1985) pp. 97-117.
- [5] L.K. Grover, Physical Review Letters 79 (1997) pp 325-328.
- [6] P. W. Shor, SIAM Journal of Computing 26 (1997) pp. 1484-1509.
- [7] C. H. Bennett , G. Brassard, Proceedings of the International Conference on Computer Systems and Signal Processing, Bangalore, India, IEEE New York (1984) pp. 174-189.
- [8] Marco Tomassini , Mathieu Perrenoud , Elsevier Applied Soft Computing 1 (2001) pp. 151-160.
- [9] I. G. Karafyllidis, Physical Review A 70(2004) pp. 0044301 pp. 1-4.
- [10] I. G. Karafyllidis, , IEEE Transactions on Circuits and Systems I 52(2005) pp. 1590 - 1596.
- [11] S.C. Benjamin , S. Bose, Physical Review A 70(2004) 032314 pp.1-7.
- [12] C.A. Perez-Delgado , Donny Cheung, Physical Review A 76 (2007) 032320 pp.1-15.
- [13] D.J. Shepherd, T. Franz , R.F. Werner, Physical Review Letters 97 (2006) 020502 pp. 1 - 4.
- [14] J J. Twamley, Physical Review A 67(2003), 052318 pp.1-12.
- [15] I. G. Karafyllidis, Physics Letters A 320(2003) pp. 35-38.
- [16] G. A. Barbosa, E. Corndorf, P. Kumar , H. P. Yuen, Physical Review Letters 90(2003) 227901 pp.1-4.
- [17] J M. J. Mihaljevic, Physical Review A 75 (2007) 052334 pp.1-15.
- [18] E. Bihlam, M. Boyer, P.O. Boykin, T. Mor , V. Roychowdhury, Journal of Cryptology 19 (2006) pp.381-489.
- [19] T. Nishioka, T. Hasegawa, H. Ishizuka, K. Imafuku , H. Imai, Physics Letters A 327 (2004) pp. 28-32.

TU2

P38

Thermal degradation kinetics of in-situ prepared PET nanocomposites containing fumed silica nanoparticles (SiO₂)

G.Antoniadis¹, K.M. Paraskevopoulos¹, D.N Bikiaris², K. Chrissafis^{1*}

¹Department of Physics, Aristotle University of Thessaloniki, 54124 Thessaloniki, Greece.

²Department of Chemistry, Aristotle University of Thessaloniki, 54124 Thessaloniki, Greece.

*hrisafis@physics.auth.gr

Abstract

Poly(ethylene terephthalate) nanocomposites were prepared by *in situ* polymerization using different amounts of fumed silica nanoparticles (SiO₂). From the thermogravimetric curves it could be concluded that PET and the samples with different nanoparticles presented good thermostability, since no remarkable mass loss occurred up to 320 °C (<0.5%). The activation energy (E) of degradation of the studied polyesters was estimated using the Ozawa, Flynn and Wall (OFW) method. Neat PET had an $E=223.5$ kJ/mol and almost identical is the activation energy in PET/SiO₂ nanocomposites (222.1 kJ/mol).

Introduction

In last years there is an increased interest for the precise determination of the reaction model and the activation energy of PET. Thermogravimetric Analysis (TGA) is one of the widely used techniques for the study of the thermal decomposition of polymers. In absence of prior information about real kinetic mechanism, the reaction model can be chosen from a set of well-known reaction models to fit experimental data, usually performed in model-fitting techniques. Recently there is also an increased interest for the preparation of PET nanocomposites due to their enhanced mechanical, thermal and gas barrier properties useful for many applications [2]. However only some papers are presented related to the study of thermal stability properties of PET nanocomposites. Zheng et al [3] studied PET with different silica content of 1, 3, 5 wt% using non-isothermal measurements under N₂ gas.

In the present study PET nanocomposites containing different amounts of SiO₂ were prepared and studied by *in situ* polymerization. The objective of this study is to evaluate the effect of these nanoparticles and their percentage participation on thermal degradation of PET nanocomposites.

Results and Discussion

Thermal degradation of PET with different stoichiometries of SiO₂ was studied by following its mass during heating. Samples were heated from ambient temperature to 600 °C in a 50 ml/min flow of N₂. Heating rates of 5, 10, 15 and 20 °C/min were used and continuous records of sample temperature, sample weight, its first derivative and heat flow were taken. In Figure 1 are presented the mass (TG%) curves of all studied samples, at a heating rate of 10 °C/min. From the thermogravimetric curves it can be seen that PET and the samples with different nanoparticles present good thermostability. No remarkable mass loss occurred until 320 °C (<0.5%). In order to be analysed more deeply the degradation mechanism of PET with SiO₂, it is important kinetic parameters (activation energy E and pre-exponential factor A) and conversion function $f(\alpha)$ to be evaluated. The relationship between kinetic parameters and conversion (α) can be found by using the mass curves recorded in TG dynamic thermograms. The thermogravimetric curves of PET-2% SiO₂ heated in N₂ at different heating rates are shown in Figure 2 from temperature above the melting point till 550 °C. Activation energy E can be calculated by various methods. One of them is the isoconversional method of Ozawa, Flynn and Wall (OFW) [4]. According to this method plotting $\ln(\beta)$ against $1/T$ should give straight lines, the slope of which is directly proportional to the activation energy ($-E/R$). If the determined activation energy is the same for the various values of α , the existence of a single-step reaction can be concluded with certainty. In Figure 3 can be seen the dependence of the activation energy (E) versus conversion α for PET, and PET-2% SiO₂, comparatively.

In order to determine the conversion function $f(\alpha)$ we used a method referred to as the “model fitting method”. This method that does not assume the knowledge of E and $f(\alpha)$ in advance, was applied simultaneously on the experimental data taken at the heating rates $\beta=5, 10, 15$ and 20 °C/min. In Figure 4 can be seen the results of this fitting for PET-2% SiO₂. The form of the conversion function, obtained by fitting is the mechanism of nth-order auto-catalysis that is described by equation $f(\alpha)=(1-\alpha)^n(1+K_{cat}X)$ for all the studied samples. The calculated parameters are shown in Table 1 for two of the samples. The correlation coefficient was above of 0.9999. The

values of the activation energy are between the limits of the calculated values from the OFW method. As it can be seen the fitting to the experimental data is very good for all the complete range of α .

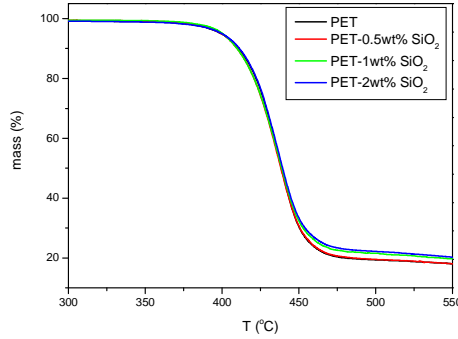


Figure 1. Mass (%) versus temperature versus temperature with a heating rate $\beta= 10^\circ\text{C}/\text{min}$.

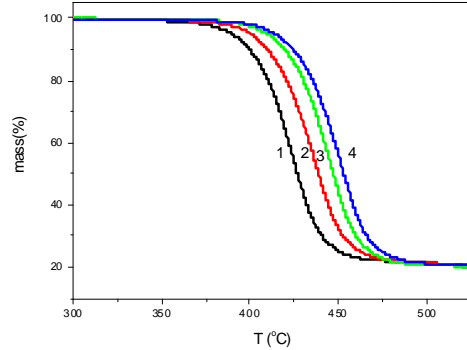


Figure 2. Mass (%) curves at different heating rates β for PET-2% SiO₂. 1: 5°C/min, 2: 10°C/min, 3: 15°C/min, 4: 20°C/min

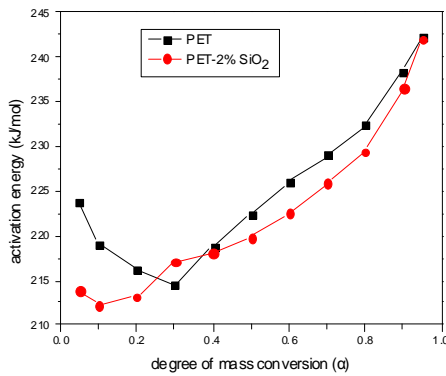


Figure 3. Dependence of the Activation Energy (E) on the degree of the conversion (α) of the mass loss, as calculated with OFW method for the different samples.

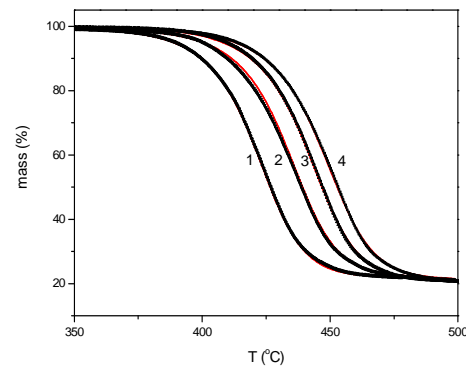


Figure 4. Fitting and experimental mass (%) curves for all the different heating rates for PET-2% SiO₂. 1: 5°C/min, 2: 10°C/min, 3: 15°C/min, 4: 20°C/min

Table 1. Calculated values of activation energy, pre-exponential factor and exponent n for two studied samples.

Samples	$\log A$	E (kJ/mol)	n	$\log K_{cat}$
PET	14.05	223.5	1.51	0.73
PET-2% SiO ₂	13.95	222.1	1.62	0.73

References

[1] K.Chrissafis, J. Therm. Anal. Calorim., 95 (2009) 273.
 [2] X.Yao, X.Tian, D.Xie, X.Zhang, K. Zheng, J. Xu, G. Zhang and P. Cui, Polymer, 50 (2009) 1251-1256.
 [3] J. Zheng, P. Cui, X. Tian and K. Zheng, J. Appl. Polym. Sci., 104 (2007) 9.
 [4] Ozawa T. J Thermal Anal., 2 (1970) 301.

Thermal degradation kinetics of in-situ prepared PET nanocomposites containing organically modified montmorillonite (MMT) nanoparticles

G.Antoniadis¹, K.M. Paraskevopoulos¹, D.N. Bikiaris², K. Chrissafis^{1*}

¹Department of Physics, Aristotle University of Thessaloniki, 54124 Thessaloniki, Greece

²Department of Chemistry, Aristotle University of Thessaloniki, 54124 Thessaloniki, Greece

*hrisafis@physics.auth.gr

Abstract

A series of PET nanocomposites were prepared by in-situ polymerization using different amounts of organically modified montmorillonite (MMT). PET and PET nanocomposites presented good thermostability, since no remarkable mass loss occurred up to 320 °C (<0.5%). Neat PET presents an activation energy of $E=223.5$ kJ/mol, while PET/MMT nanocomposites presented higher values (228.3 kJ/mol) indicating that MMT had a stabilizing effect upon the decomposition of the matrix. The form of the conversion function for all the studied samples obtained by fitting was the mechanism of n^{th} -order auto-catalysis.

Introduction

TGA is one of the widely used techniques to study the thermal decomposition of polymers [1]. In absence of prior information about real kinetic mechanism, the reaction model can be chosen from a set of well-known models to fit experimental data usually performed in model-fitting techniques. In recent years there is an increased interest for the precise determination of the reaction model and the activation energy of PET. Recently, there is, also, an increased interest for the preparation of PET nanocomposites due to their enhanced mechanical, thermal and gas barrier properties suitable for many applications [2]. Wang et al [3] studied the thermal stability and degradation of PET/MMT nanocomposites with TGA under N_2 atmosphere. They showed that the onset temperature of degradation and the temperature at maximum mass loss rate are increased significantly by adding MMT. When MMT content is in low range (<5%), in the observed thermal stability behaviour of PET/MMT are contributing both MMT content and its dispersion quality. The objective of this study is to evaluate the effect of these nanoparticles as well as their amount on thermal degradation of PET nanocomposites.

Results and Discussion

When montmorillonite is to be used as additive, it is modified with organic additives, mainly with ammonium salts [4] in order to achieve finer dispersion into polymer matrix. However, these additives are not stable and cannot be used in the case of PET, which has a melting point higher than 250°C. For this reason in the present study a new modifier was prepared which is thermally stable. Thermal degradation of PET with different stoichiometries of MMT-P nanoparticles was studied by following its mass during heating. In Figure 1 are presented the mass (TG%) curves of all studied samples, at a heating rate of 10 °C/min. As can be seen from its thermogravimetric curve the decomposition of MMT-P takes place at 3 different stages. At first stage, a small mass loss (less than 5 wt%) is gradually occurring till 300°C, at which mainly the absorbed water of montmorillonite is lost. The highest rate of the second decomposition is taking place at temperature 325°C, which is far away from the temperature that PET is synthesized, and the third decomposition is taking place at temperature 470°C. This is a proof that a thermally stable organic modifier is prepared. From the thermogravimetric curves it can be seen that PET and the samples with different nanoparticles present a good thermostability. No remarkable mass loss occurred until 330 °C (<0.4%). In order to be analysed more deeply the degradation mechanism of PET with MMT, it is important that kinetic parameters (activation energy E and pre-exponential factor A) and conversion function $f(\alpha)$ to be evaluated. The relationship between kinetic parameters and conversion (α) can be found by using the mass curves recorded in TG dynamic thermograms. The thermogravimetric curves of PET-2% MMT heated in N_2 at different heating rates are shown in Figure 2, from temperature above the melting point till 550 °C. In Figure 3 can be followed the dependence of the activation energy (E) versus conversion α for PET and PET-2% MMT, calculated by Ozawa-Flynn-Wall (OFW) method [5]. To determine the conversion function $f(\alpha)$ we used the “model fitting method” and for the fitting different kinetic models were used. In Figure 4 can be seen the results of this fitting for PET-2% MMT. The calculated parameters are shown in Table 1 for two of the samples.

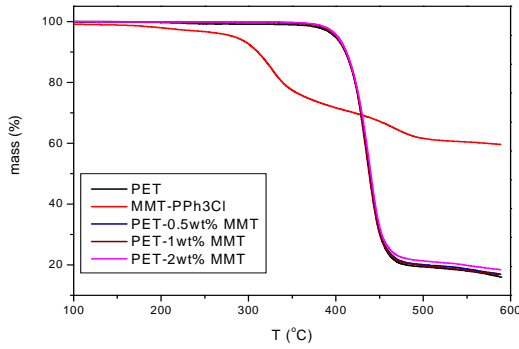


Figure 1. Mass (%) versus temperature with a heating rate $\beta=10^\circ\text{C}/\text{min}$ for PET-MMT.

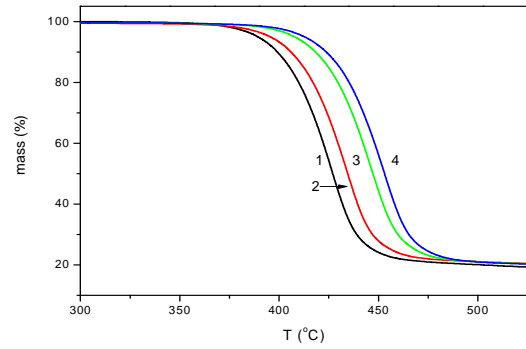


Figure 2. Mass (%) curves at different heating rates β for PET-2% MMT. 1: $5^\circ\text{C}/\text{min}$, 2: $10^\circ\text{C}/\text{min}$, 3: $15^\circ\text{C}/\text{min}$, 4: $20^\circ\text{C}/\text{min}$.

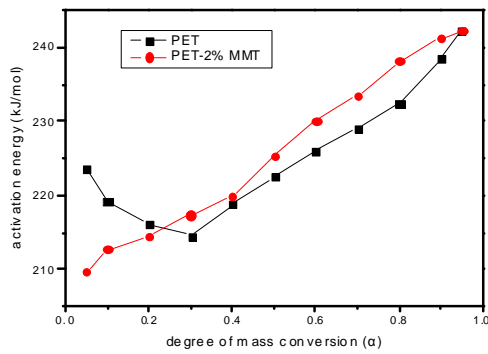


Figure 3. Dependence of the Activation Energy (E) on the degree of the mass conversion (α), as calculated with OFW method for two of the samples.

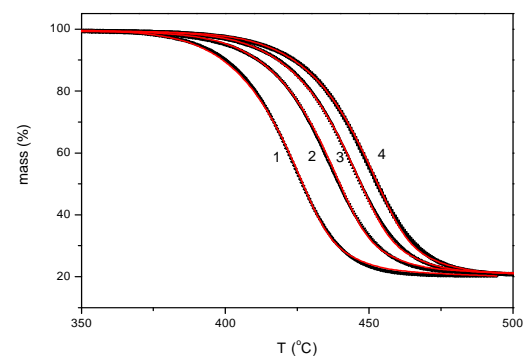


Figure 4. Fitting and experimental mass (%) curves for all the different heating rates for PET-2% MMT. 1: $5^\circ\text{C}/\text{min}$, 2: $10^\circ\text{C}/\text{min}$, 3: $15^\circ\text{C}/\text{min}$, 4: $20^\circ\text{C}/\text{min}$.

Table 1. Calculated values of activation energy, pre-exponential factor and exponent n for two studied samples

Samples	$\log A$	E (kJ/mol)	n	$\log K_{\text{cat}}$
PET	14.05	223.5	1.51	0.73
PET-2% MMT	14.46	228.3	1.49	0.57

References

[1] K.Chrissafis, J. Therm. Anal. Calorim., 95 (2009) 273.
 [2] X. Yao, X. Tian, D. Xie, X. Zhang, K. Zheng, J. Xu, G. Zhang and P. Cui, Polymer, 50 (2009) 1251-1256.
 [3] Y. Wang, J. Gao, Y. Ma and U.S. Agarwal, Composites, B 37 (2006) 399.
 [4] K. Chrissafis, G. Antoniadis, K.M. Paraskevopoulos, A. Vassiliou, D.N. Bikiaris. Comp. Sci. Techn. 67 (2007) 2165.
 [5] Ozawa T. J Thermal Anal., 2 (1970) 301.

Scientific collaboration in Europe, and the Overlapping Tree Network

A. Garas* and P. Argyrakis

Physics Department, Aristotle University of Thessaloniki, 54124, Thessaloniki Greece

*agara@physics.auth.gr

We use tools of network theory to provide a novel approach in analyzing data, which takes us beyond usual statistical analysis. This approach provides clearer pictures of patterns in the data, uncovering properties not easily identifiable by classical means. We apply these tools to the collaboration network of European Institutes, by constructing networks considering each participant in the Framework Programmes (FPs) as a node, and by representing the collaborations between partners as links between the nodes. Furthermore, we consider as link weight w_{ij} of the connection between nodes i and j the total number of projects between these two partners. The network follows a power-law degree distribution for both FPs, and for all the different funding schemes (instruments), as it is demonstrated in Fig. 1. This means that the bulk of the participants has few connections, while there exist some (few indeed) very well connected hubs.

Identification of patterns in the collaborative flow in Europe is of great importance for policy making as it could provide insights to the way funding is distributed. Here we show that during the course of the last two FPs, there is an enhancement of collaboration between institutions over time, even though the number of signed contracts, and the total number of unique partners has been decreased. Taking a step further, we are able to use a measure of the central role that a country plays in the network, by using the degree that each country has in the Maximal Spanning Tree (MST) of the collaboration network. The important role of the hubs of the network for all the different funding schemes is highlighted [1].

We also present a novel technique to filter information from complex networks, by extracting a subgraph with the strongest links [2]. We name this technique Overlapping Tree Network (OTN). The OTN even if it is based on the MST, it gives much richer filtered outcomes, while it can as well be applied to a variety of systems.

Using the OTN method we are able to identify a nucleus, a strongly interconnected community, of the most frequent hubs of the network. The other countries play satellite role around this nucleus. Therefore we are able to relate the significance of a country to the collaboration network, not with the absolute number of its institutions as it is often thought, but with the number of international collaborations that are established by its institutions.

This is valuable information for policy makers and government, since it is common that most administration officers fail to understand the importance of international and are focused more on the number of research centers that a country has, and the number of their personnel.

[1] Garas A. and Argyrakis P., EPL 84, 68005 (2008).

[2] Garas A. and Argyrakis P., EPL 86, 28005 (2009).

Acknowledgments

This work is part of the 03ED840 research project, implemented within the framework of the "Reinforcement Programme of Human Research Manpower" (PENED) and co-financed by National and Community Funds (25% from the Greek Ministry of Development-General Secretariat of Research and Technology and 75% from E.U.-European Social Fund).

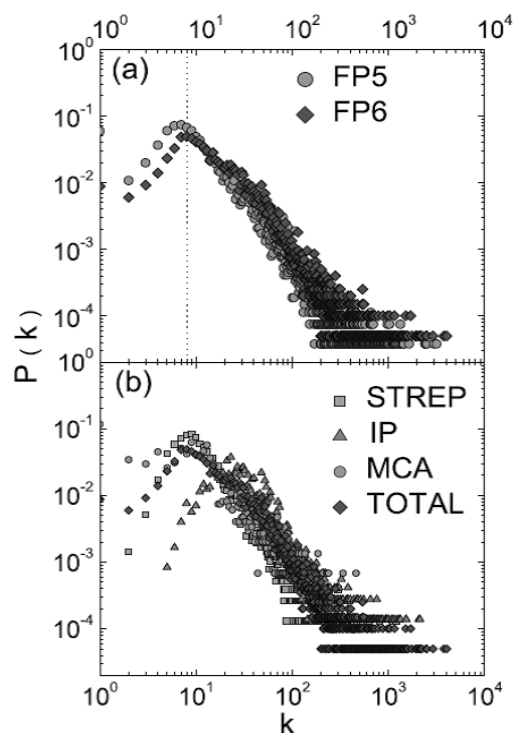


Fig. 1. (a) Probability distribution of the degrees for the FP5 and FP6 collaboration networks. (b) Probability distribution of the degrees of the collaboration networks for different instruments of FP6.

Trapping in complex networks

A. Kittas^{1*}, S. Carmi^{2,3}, S. Havlin² and P. Argyrakis¹

¹ Department of Physics, University of Thessaloniki - 54124 Thessaloniki, Greece, EU

² Minerva Center & Department of Physics, Bar-Ilan University - 52900 Ramat Gan, Israel

³ Center for Polymer Studies, Boston University - Boston, MA 02215 USA

*akittas@auth.gr

The properties of the random walk greatly vary depending on the dimension and the structure of the medium in which it is confined [1–4], where a particularly interesting medium for the study of the random walk are complex networks [5–9]. Networks describe systems from various fields, such as communication (e.g. the Internet), the social sciences, transportation, biology, and others. Many of these networks are scale free (SF) [10–13]. This class of networks is defined by a broad degree distribution, such as a power law $P(k) \sim k^{-\alpha}$, where α is a parameter which controls the broadness of the distribution.

Trapping is a random-walk problem in which traps are placed in random locations, absorbing all walkers that visit them. This problem was shown to yield different results over different geometries, dimensions and time regimes [2,3,14–17]. The main property of interest during such a process is the survival probability $\rho(t)$, which denotes the probability that a particle survives after t steps. The problem was studied in regular lattices and in fractal spaces [2,14–17] and recently, in small-world networks [6].

Trapping in networks is an analogue to the propagation of information in a network. This information is in the form of “packets” e.g. like the data packets used in communication networks in routers, which receive and transmit packets over a communication network. A trap acts as a node which is malfunctioning and where the information is lost i.e. like a router which can receive but not transmit data due to a malfunction or an e-mail server unable to forward incoming mails. Furthermore, the model may be relevant in social systems, where some information may initially spread randomly, but in later stages it might be held by certain individuals.

We study the survival probability $\rho(t)$ of random walkers on random regular networks (networks in which all nodes have equal degree), Erdos-Renyi (ER) networks and SF networks. In the trapping reaction in low dimensions, the occurrence of $A-T$ reactions creates a depletion zone around the trap, which is a form of self-segregation of reactants [18]. A number of studies have been devoted to the problem of the depletion zone [18–20]. The growth of the zone in the trapping reaction in low dimensions leads to anomalous kinetics for a variety of dynamic quantities. $\rho(t)$ is a measure of the amount of particles available on the network at a specific time, however it provides no information of how the particles are distributed on the network and in relation to the location of the trap. We study the depletion zone dynamics various network types, connectivity patterns and trap locations, namely the particle density in respect to the distance r from the trap $\rho(r)$.

We perform simulations only on the largest cluster of the network. Starting from a fixed density of particles initially placed in random nodes, particles hop with equal probability to one of their nearest neighbors. Certain nodes are randomly chosen to serve as traps. These are perfect traps; if a particle falls on them it is trapped and removed from the network. In the case of multiple traps, $n = cN$ traps are placed in the network, where c is the trap concentration.

We derive analytical expressions for $\rho(t)$ for a wide range of trap degrees and concentrations and highlight the role of the network structure, obtaining new scaling relations for the survival probability and average trapping time which are absent in lattices. We find, using theory and simulations that in ER networks, while for short times $\rho(t)$ exhibits an exponential decay behavior in the form of: $\rho(t) \sim \exp(-Act)$, for longer times it exhibits a more complex behavior, with explicit dependence on both the number of traps n and the size of the network N (eq. 1). In SF networks we reveal the significant impact of the trap’s location: $\rho(t)$ is drastically different when a trap is placed on a random node (eq. 2) compared to the case of the trap being on the node with the maximum connectivity (eq. 3, fig. 1).

The depletion zone near the trap, which is characteristic of lattices is absent in complex networks although the particle density $\rho(t)$ maybe be an exponential decay function of time in both cases. We find that in contrast to lattices, the particles in regular and ER networks are homogeneously distributed, with a deviation for small values of $\langle k \rangle$ in ER networks, the trap having no effect in forming a density gradient in its immediate vicinity. In SF networks we reveal the important role of high degree nodes and show that there is significant difference if multiple occupancy is allowed on the nodes of the network. The high random walk centrality of the hubs have pronounced effect in the distribution of the particles in the network. It is also evident that connectivity of the network plays a significant role in the distribution of the particles in SF networks, recovering the depletion zone formation for high γ values (fig 2).

$$\rho(t) \approx \exp \left[-n \langle k \rangle \left(1 - \exp \left[\frac{At}{N \langle k \rangle} \right] \right) \right] \quad (1) \quad \rho(t) = \exp \left(-\frac{Amt}{N \langle k \rangle} \right) \quad (2) \quad \rho(t) = \exp \left(-\frac{Amt}{N^{\frac{\gamma-2}{\gamma-1}} \langle k \rangle} \right) \quad (3)$$

(ER, n traps, random k) SF, 1 trap, random k ,
 $m \geq 3$, $t \gg N \langle k \rangle$ SF, 1 trap on the hub,
 $m \geq 3$, $t \gg N \langle k \rangle$

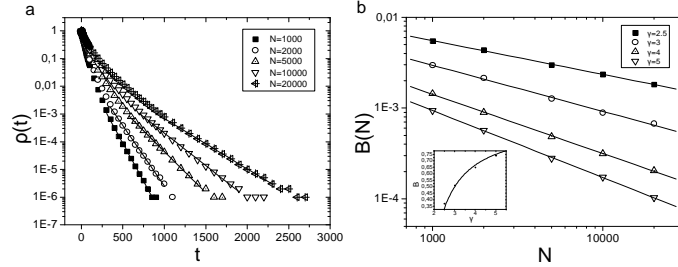


Figure 1 - Trapping in SF networks after failure of the most connected node. **(a)** Particle density $\rho(t)$ vs t for SF networks with $\gamma=2.5$ and $m=3$, for different system sizes. One trap is placed on the node with the maximum degree. Solid lines represent fitting to an exponential decay $\rho \sim e^{-Bt}$ in the long-time regime. **(b)** The exponent B vs N , for $\gamma=2.5$ plotted in (a) as well as for $\gamma=3,4,5$. In this case $B \sim N^\beta$ with $\beta \sim \gamma-2/\gamma-1$ (inset), in agreement with Eq. (3)

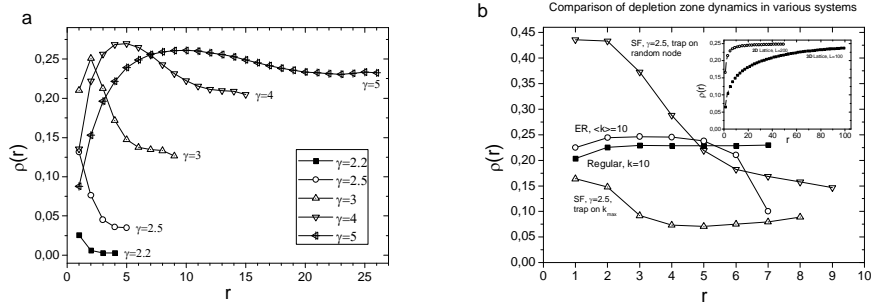


Figure 2 – **(a)** Particle density $\rho(r)$ vs distance r for $t=200$ MCS. SF networks of $N=10^5$ and $m=2$, with the trap placed on k_{max} . Comparison of networks with different values of γ . **(b)** Comparison of depletion zone dynamics in various systems. 2D lattice, 3D lattice, regular random network with $N=10^5$ and $k=10$, ER network with $N=10^5$ and $\langle k \rangle=10$, SF network with $N=10^5$ and $\gamma=2.5$ with the trap placed i) on a random node or ii) on the node with maximum degree.

References

- [1] ben-Avraham D. and Havlin S., Diffusion and Reactions in Fractals and Disordered Systems (Cambridge University Press, New York) 2000.
- [2] Weiss G. H., Aspects and Applications of the Random Walk (North-Holland, Amsterdam) 1994.
- [3] Redner S., A Guide to First-Passage Processes (Cambridge University Press) 2001.
- [4] Havlin S. and ben-Avraham D., Adv. Phys., 36 (1987) 695.
- [5] Gallos L., Phys. Rev. E, 70 (2004) 046116.
- [6] Jasch F. and Blumen A., Phys. Rev. E., 64 (2001) 066104.
- [7] Gallos L. and Argyrakis P., Phys. Rev. Lett., 92 (2004) 138301.
- [8] Noh J. D. and Rieger H., Phys. Rev. Lett., 92 (2004) 118701.
- [9] Noh J. D. and Kim S.-W., J. Korean Phys. Soc., 48 (2006) S202.
- [10] Barabasi A.-L. and Albert R., Science, 286 (1999) 509.
- [11] Albert R. and Barabasi A.-L., Rev. Mod. Phys., 74 (2002) 47.
- [12] Dorogovtsev S. N. and Mendes J. F. F., Evolution of Networks: From Biological Nets to the Internet and WWW (Oxford University Press, Oxford) 2003.
- [13] Pastor-Satorras R. and Vespignani A., Structure and Evolution of the Internet: A Statistical Physics Approach (Cambridge University Press, Cambridge) 2004.
- [14] den Hollander F. and Weiss G. H., in Contemporary Problems in Statistical Physics, (SIAM, Philadelphia) 1994.
- [15] Bunde A., Havlin S., Klafter J., Graff G. and Shechter A., Phys. Rev. Lett., 78 (1997) 3338.
- [16] Havlin S., Larralde H., Kopelman R. and Weiss G. H., Physica A, 169 (1990) 337.
- [17] Donsker N. D. and Varadhan S. R. S., Commun. Pure Appl. Math., 32 (1979) 721.
- [18] Weiss G. H. and Havlin S., J. Stat. Phys., 37 (1984) 17.
- [19] S. Park, S. Peng, S. Parus, H. Teitelbaum, R. Kopelman, Phys. Chem. A. 106, 7586 (2002).
- [20] G. H. Weiss, R. Kopelman, and S. Havlin, Phys. Rev. A 39, 466 (1989)

Optical Emission Spectroscopy in a Glow Discharge Plasma During the Restoration of Iron Corroded Objects

E. Filippaki^{1*}, I. Kotzamanidi,¹ C. L. Xaplanteris^{1,2}

¹ Plasma Physics Lab., IMS, NCSR "Demokritos", 15310, Ag. Paraskevi Attiki

² Hellenic Military Academy, Vari, Attiki

*lfilip@ims.demokritos.gr

Restoration and conservation of archaeological metal objects by using plasma chemistry methods have been extensively used for the last two decades in Plasma Physics laboratory of N.C.S.R. "Demokritos" [1]. The method is based on the reduction of the corrosion products on the metal excavated objects by reactive reducing species such as hydrogen atoms in an H₂ glow discharge plasma of low pressure and temperature. In the glow discharge plasma, electrons accelerated by an external electrical field, have enough energy –among many other interactions- to dissociate hydrogen molecules (H₂) from atoms (H) at low pressure and temperature. The reduced layer of objects become brittle and can be removed easily by the conservators. In addition the phases containing chloride ions can be destabilized and the chlorides can be removed to the gaseous phase of the discharge.

In this paper, optical emission spectroscopy, was used as the diagnostic method for the study of the hydrogen glow discharge plasma or its mixtures with other gases such as nitrogen or methane. The goal of this method is to investigate atoms, molecules or radicals in the glow discharge plasma, the presence of which will help to the clarification of the possible reactions that take place, both on the gaseous phase of the discharge and on the surface of the metal objects. The impact of the macroscopic parameters of the discharge, as well as, the hydrogen dissociation with other gases, during the treatment, were also studied. A comparison between spectrums with and without objects was carried out, for the investigation of gas excitation, which was due to the chemical processes that took place on the metal surface of the treated objects.

Experimental

A radio frequency (RF) glow discharge plasma apparatus was used, similar to the Veprek's prototype apparatus. The reactor is a Pyrex-glass bell jar of 40cm inner diameter and 1.34cm length. It is evacuated down to 10⁻²Torr and the H₂ gas is introduced through a needle valve and a flowmeter in the reactor. The temperature is monitored. The power from an RF generator (27.12MHz, 2.8KWatt) is coupled through two copper electrodes 30 x 32 cm², placed externally along the reactor. The objects are placed in Pyrex grids along the axis of the discharge. The objects have been treated in different conditions:

100 % H₂ plasma under 1kWatt power, 280°C temperature and 1 Torr pressure

50% H₂, 25% CH₄, 25% N₂ under 0.7kWatt power, 300°C temperature and 1 Torr pressure

40% H₂, 10-60%N₂ under 0.7kWatt power, 300°C temperature and 1.3 Torr pressure

An optical emission spectrometer (SpectraPro 500) sensitive to the radiation of atomic species was used to monitor the process. It was focused in the middle of the reactor from outside, through a quartz glass port in the Pyrex tube.

Results

It was shown that hydrogen dissociation with methane has lead to a reducing emission of atomic or molecular hydrogen. Methane molecules consume power and as a result a degradation of electron's energy is taking place which finally concludes to the elimination of hydrogen excitation rate. Finally, the reducing action of hydrogen discharge on the surface of metal artifacts is eliminated. As far as the hydrogen dissociation with nitrogen is concerned, more complicated results are concluded. So, whereas this mixture of gases offers the advantage of energy reduction, it also reduces the intensity of Balmer lines for a mixture of 30%N₂. For a mixture of 40-90% N₂, Balmer lines intensity is either slightly increased or even it is kept steady. In addition, since no emission line from sputtered or volatile elements was identified, it is concluded that optical emission spectroscopy cannot give any information about the chemical reactions taking place on the surface of the objects.

[1] Kotzamanidi I., A. Anastasiadis, L. Filippaki, S. E. Filippakis, P. Vassiliou, Em. Sarris (2002), Anticorrosion Methods & Materials, Vol. 49 (4), pp. 256-263.

Effect of the Hydrogen-Reductive Plasma on Underwater Oxidized Objects. Chaotic Plasma Configuration

S. Ahmed Saleh¹, E. Filippaki^{2*}, C. L. Xaplanteris^{2,3} and Y. Bassiakos²

¹ *Department of Materials Science and Engineering, National Technical University of Athens, Iroon Polytechniou 9, 15780, Athens, Greece*

² *Plasma Physics Lab., IMS, NCSR "Demokritos", 15310, Ag. Paraskevi Attiki*

³ *Hellenic Military Academy, Vari, Attiki*

* *lfilip@ims.demokritos.gr*

The issue of the plasma influence while it is in contact with a solid surface, was set along with the pursuit of the thermonuclear fusion. The question was how the high thermal plasma leans to the reactor's wall without melting the metal. An extended literature has been gathered on this subject [1]. On the other hand, there is a great interest for the cold plasma-solid interaction, which is caused of mechanical, physical and chemical reasons. Firstly, Daniels and coworkers used the low temperature plasma to reduce the tarnish of silver on daguerreotypes [2]. In the early 80's, Veprek and coworkers, led the method to become one of massive plasma treatment by creating a suitable plasma production device (Veprek's prototype reactor) [3, 4].

Those procedures were very soon adopted by the Plasma Laboratory of N.C.S.R. "Demokritos" with the purpose of cleaning and restoring archaeological artifacts. During the last ten years intensive studies have been undertaken in our Laboratory [5-8]. The first experiments were occupied with the reduction of hydrogen plasma on iron oxidized objects. An extensive search on a large number of historical objects with variable oxidation rate, has been carried out. A combination of gases and plasma parameters (pressure, plasma density, ions and electrons temperature) were used to take various values. Serious knowledge which was obtained, is that plasma, as a multi-parametric state makes every case unique.

In last years, we have studied the plasma-surface interaction theoretically [7], by taking into consideration a number of experimental conditions. In this way, we described the plasma sheath parameters (ion- electron velocity, ion- electron density, sheath potential). Thus, we enforced an external d.c. potential on the treatment object, in order to affect the plasma sheath potential and consequently, the reduction rate. Expanding our conception, we passed a d.c. current between objects and plasma, and led into some important results on the cleaning and restoring rate. Part of our results have been summarized and presented in the last international Conference "Chaos 2009" in the form of treatment tables, useful to the conservators of archaeological artifacts [9].

Experimental.

Historical objects from underwater sites of Paros island were treated for several hours using 100% H₂ plasma reduction method in different temperatures 120°C, 200°C and 300°C. Before and after each stage of treatment a chemical characterization of the objects was performed by means of scanning electron microscopy (S.E.M.) and energy dispersive spectrometry (E.D.S.) in order to identify chloride concentration and the rate of desalination of the objects depending on the temperature and on the time of treatment. XRD method was also used to detect and identify the crystal structure of the chemical compounds produced either as a result of the corrosion reactions that took place in the environment (before any plasma treatment), or as a result of the chemical reduction that took place on the surface of the objects into the hydrogen plasma environment.

Results

By evaluating the results from scanning electron microscope and X-ray diffraction, we conclude that the higher temperatures lead to a more efficient desalination of the objects in a shorter period of plasma treatment. The temperature of plasma treatment is of special interest since the objects must be protected from a probable change in the metallographic characteristics of the metal. Since, the first recrystallization temperature of iron is about 400°C, where the elongated grains of wrought iron will be transformed into spherical grains resulting to the loss of precious metallurgical information [10], the temperature of 300°C is considered safe for the preservation of the integrity of the object. In addition, the careful selection of the treatment temperature is essential because each object may be of different corrosion stage. The objects that have no metal core, it is better to be treated in lower temperatures in order to avoid any damage of their initial shape.

References

[1] J. Wesson, Tokamaks, 2 edn. (Clarendon Press, Oxford, 1997).

- [2] Daniels V., Plasma Reduction of Silver Tarnish on Daguerreotypes, *Stud. In Conserv.*, 26, 1981.
- [3] Veprek, S., Patscheider, J. and Elmer, J., Restoration and Conservation of ancient artifacts: A new area of application of plasma chemistry, *Plasma Chem. Plasma process*, Vol. 5(2), 1985.
- [4] Veprek, S., Eckmann, Ch. ,and Elmer, J. Th., Recent progress in the restoration of archaeological metallic artifacts by means of low-pressure plasma treatment *Plasma Chem. Plasma process*. Vol. 8 (4), 1988.
- [5] Kotzamanidi I., Sarris Em., Vassiliou P., Kollia C., Kaniias G.D., Varoufakis G.J. Filippakis S.E., "Corrosion behavior of oxidized steel treated in reducing plasma environment-Chloride ions removal", *British Corrosion Journal*, 34(4), 285-291, (1999).
- [6] Kotzamanidi, I. Vassiliou, P. Sarris, Em. Anastasiadis, A., Filippaki, E., Filippakis, S.: Anti-corrosion methods and materials, Vol 49, No 4, 2002.
- [7] Xaplanteris, C., Filippaki, E. Plasma –surfaces interaction and improvement of plasma conservation system by application of a d.c. electrical potential. *Topics on Chaotic Systems, Selected Parers from CHAOS 2008 International Conference* pp 406-415.
- [8] Xaplanteris, C., Filippaki, E. Mechanical and chemical results in the plasma-surface contact. An extended study of sheath parameters. (in preparation).
- [9] Xaplanteris, C., Filippaki, E. Chaotic behavior of plasma surface interaction. A table of plasma treatment parameters useful to the restoration of metallic archaeological objects. *Selected papers from CHAOS 2009 International Conference*, (submitted).
- [10] T. Stambolov. *The corrosion and conservation of metallic antiquities and works of art*. Amsterdam, 1985.

Efficacy of hydrophobic polymeric coatings and superhydrophobic nanoparticle based composite films for the protection of stone

S. K. Papadopoulou^{1*}, A. Kyriotis¹, I. Karapanagiotis², I. Zuburtikudis³ and C. Panayiotou¹

¹*Aristotle University of Thessaloniki, Thessaloniki Greece*

²*“Ormylia” Art Diagnosis Centre, Ormylia, Greece*

³*TEI of Western Macedonia, Kozani, Greece*

*stelloupa@gmail.com

The protection of stone against water is of crucial importance towards the conservation of outdoor monuments. It is well known that water causes chemical, physical and optical deterioration of stone. Water repellents are usually polymeric materials providing moderate protection of the stone surface. Hydrophobicity, in the case of polymers, is a result of chemical factors, such as their low surface energy [1]. On the other hand, composite materials based on polymers demonstrate superhydrophobic properties. Superhydrophobicity, in this case, can be attributed to both chemical and physical factors. The physical factor responsible for the enhancement of hydrophobicity, is the creation of surface roughness [2].

The primary goal of the present work was to study the effects of the fluorine content in the polymer chain on the surface and protective properties of three fluorinated methacrylic polymers. It is well known that these polymers demonstrate meritorious film properties due to the stable C-F bonds, leading to chemical, thermal and photochemical stability [3]. The aforementioned properties are strongly depended on the characteristics of perfluoroalkyl group side chains. Each polymer was applied and tested on marble specimens. The application of polymeric solutions on stone was made by spraying.

The homopolymers under study were poly(2,2,2-trifluoroethyl methacrylate) (PTFEMA), poly(1,1,1,3,3,3-hexafluoroisopropyl methacrylate) (PHFIMA) and poly(2,2,3,3,3-pentafluoropropyl methacrylate). The polymers were synthesized by free radical polymerization, using AIBN as initiator in tetrahydrofuran. Fourier Transform Infrared Spectroscopy (FTIR), Size Exclusion Chromatography (SEC), Differential Scanning Calorimetry (DSC) and Thermo-Gravimetric Analysis (TGA) were employed in the characterization of all the polymer samples. Marble of Thassos was the substrate used in our study. The protective efficacy of the materials on marble was evaluated by means of capillary water absorption, static contact angle, colour variation and water vapour permeability measurements before and after treatment.

The results revealed that all the polymers were hydrophobic, demonstrating contact angles with water not higher than 120°. In fact, the higher the fluorine content in the molecule is, the lower their surface energy appears. As far as the protective properties of the polymers are concerned, all coatings lived up to the protection standards set.

The second goal of this study was to create superhydrophobic surfaces based on the three fluorinated methacrylic polymers. As mentioned above, an approach to boost hydrophobicity, is the creation of surface roughness. That can be achieved by the use of nanoparticles [2]. A composite film consisted of polymers and nanoparticles exhibits superhydrophobic properties due to the migration of the particles on the surface and good adhering behavior attributed to the polymeric coating. In this work, silica (SiO₂) nanoparticles with a 7 nm mean diameter were mixed with the polymer solutions and were sprayed on marble. The resulting enhanced hydrophobicity was evaluated by studying three different nanoparticle concentrations in polymer solutions. The detailed measurements concerning the protective characteristics of the composite films are under progress.

The primary goals of this work were fulfilled, firstly, by turning a marble's hydrophilic surface into hydrophobic through the use of low surface polymers and secondly, by going beyond hydrophobicity through the creation of superhydrophobic nanoparticle based polymeric coatings.

[1] Poli T., Toniolo L., Chiantore O., Appl. Phys. A 79, 347 (2004).

[2] Manoudis, P.N., Karapanagiotis, I., Tsakalof, A., Zuburtikudis, I., Panayiotou, C., Langmuir, 24, 11225 (2008).

[3] Signori F., Lazzari M., Castelvetro V., O. Chiantore, Macromolecules 39, 1749 (2006).

Acknowledgments

This work was supported by the Greek Ministry of Development – GSRT (25%) and the European Union – European Social Fund (75%) through the research grant PENED 2003 with MIS 03EΔ 91

Magnetically induced hyperthermia: Size, Phase and Concentration-dependent heating power of magnetic nanoparticles

E. Anagnostopoulou, B. Voutou, K. Simeonidis, S. Mourdikoudis, Th. Samaras, O. Kalogirou and M. Angelakeris*

Department of Physics, Aristotle University of Thessaloniki, 54124, Thessaloniki, Greece

**agelaker@auth.gr*

ABSTRACT

Various systems of Fe, Ni and Co based magnetic nanoparticles are examined as potential magnetic hyperthermia carriers. Magnetic nanoparticle colloidal solutions are synthesized with wet-chemistry approaches optimized to get monodisperse nanoparticles with controllable shape and narrow size distributions. The detailed profile of each specimen comprises of structural information according to X-ray diffraction and electron microscopy techniques, while magnetic features are recorded by vibrating sample magnetometry for powder samples. Eventually, the heating power of each nanoparticles system is readily examined by subjecting it under AC magnetic field of different intensities. The heating effect is found to depend on the size, shape and permeability of the nanoparticles as well as on the frequency and magnitude of the applied field. Finally, besides Fe-based nanoparticles that are widely used for such applications, Ni and Co nanoparticles also exhibit tunable features that may be further exploited for specific hyperthermia protocols.

INTRODUCTION

One of the most important applications of nanoparticles is magnetically induced hyperthermia aiming to fight off the cancer cells. The basic characteristic/weakness of tumors is the fact that in the temperature range of 41-45 °C they can be easily destroyed while healthy surrounding tissues only suffer a fever shock. The basic idea of hyperthermia is the insertion of magnetic nanoparticles into the tumor and the application of an alternating magnetic field which causes a local heat of the tissue. Since tumor cells are more fragile in thermal variation, they either become damaged or are more susceptible to radiation treatment and chemotherapy.

The heat arises from magnetic processes of the particles, in the case of ferromagnetic particles mainly by hysteresis loss, while for superparamagnetic particles relaxation losses are dominant. On the other hand, nanoparticles to be used in such a procedure have to accomplish some ifs and musts such as: a) small size comparing to biological entities to be easily manipulated inside the human body, b) biocompatibility and non-toxicity to avoid immunology system attack and c) strong heating power to use minimal frequency and external field amplitude to avoid further patient's discomfort. Eventually, desirable is a fast increase up to the final temperature together with a maximum heating response in order to reduce the quantity of injected material, therapy cost, duration and potential side effects.

SAMPLES AND PROPERTIES

In this work, iron-oxide, metallic Ni and core-shell Co/CoO organic-soluble nanoparticles with tunable sizes between 10 and 50 nm are studied. All colloids were synthesized by the thermal decomposition of proper precursors in liquid environment and inert conditions [1-3].

The structural properties of nanoparticles were initially studied and analyzed by X-ray Powder Diffraction (XRD). The average crystalline size was estimated in each case by Scherrer's equation while crystal structure in each case was identified. Additional experiments included Transmission Electron Microscopy (TEM) observations and selected area diffraction (SAED) patterns. From the structural point of view, we notice that the majority of iron's particles consist of very well crystallized magnetite while a small maghemite content may also appear in specific cases [1]. As for nickel, the XRD resulted in the formation of either fcc-structured particles or hcp-structured ones depending on thermal conditions during synthetic procedure [3]. Co nanoparticles are found to be either core/shell when size is bigger than 8 nm comprising of a metallic Co core with a Co-oxide shell or Co-oxide particles for smaller size particles and oxidizing agent's presence during synthesis [2].

The magnetic measurements were obtained by a vibrating sample magnetometer on powder samples under 1 T at temperatures from 77 K to 300 K. In all cases, the macroscopic magnetic behavior may be comprehended assuming two different contributions, one superparamagnetic and one ferromagnetic dominating at different temperature regimes and occurring mainly due to size distribution of nanoentities within colloid.

HYPERTHERMIA EXPERIMENTS

For the magnetic hyperthermia measurements colloidal dispersions (1 ml) of nanoparticles in hexane were used. These colloids were exposed to an alternating magnetic field of 785 kHz of different intensity (145, 235

TU2

P46

and 340 Oe) for 600 s. The resulting change in temperature of the liquid was measured and recorded as a function of time using an optic fiber thermometer with a sampling period of 0.4 s. To accurately determine magnetic nanoparticles contribution in heating power, a hexane reference sample (1 ml) was also measured at identical conditions and its response was subtracted from experimental data.

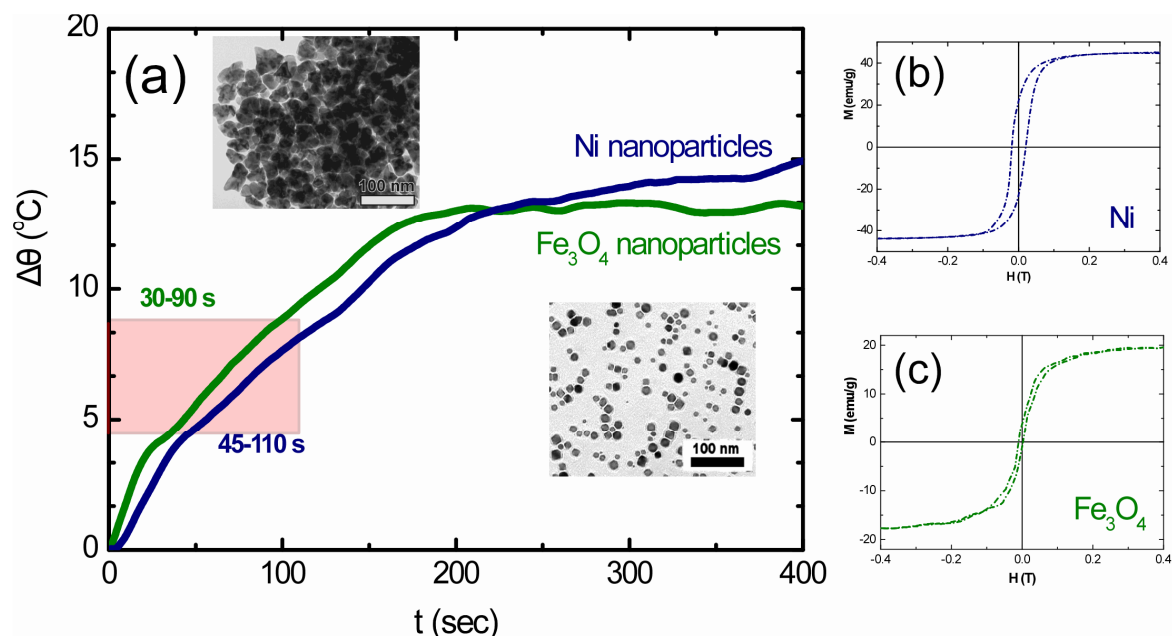


Figure 1: Heating power and TEM images for Ni-fcc (top image) and Fe_3O_4 (bottom image) nanoparticles (a). The desirable temperature increase and duration are also indicated. Corresponding magnetic hysteresis recorded at 300 K (b, c).

In Fig. 1a the temperature difference for two representative samples Fe_3O_4 and Ni is shown. The attainable temperature rise depends on the strength of the magnetic field, on the magnetic content within the colloid and consequently on their interaction. The heating rate is high during the first 200 s and then reaches a saturation plateau till the end of the measurement cycle. The fact that the Ni system, appears to attain a higher saturation plateau may be correlated with size-dependent features and eventual macroscopic magnetic behavior. As shown in Fig. 1a, the TEM illustrations of both samples give an average size for Ni nanoparticles ($28 \text{ nm} \pm 10\%$) while for Fe_3O_4 ($14 \text{ nm} \pm 10\%$) leading to higher saturation magnetization and coercivity as corresponding hysteresis loops indicate (Fig. 1b, c).

CONCLUSIONS

Finally, the requested temperature increase ($4.3\text{-}8.1 \text{ }^\circ\text{C}$ leading to final temperatures $41\text{-}45^\circ\text{C}$) is achieved relatively fast in both cases (Fe_3O_4 : 30-90 s and Ni: 45-110 s), as shown by the shaded area. This rapid increase is a very promising prerequisite for magnetic hyperthermia protocols. Since the heating effect is determined by the size and macroscopic magnetic features as well as on the frequency and magnitude of the applied field, it seems that tunable heating rate features may be further exploited for alternative hyperthermia protocols based on systems different than iron oxide nanoparticles.

REFERENCES

- K. Simeonidis, S. Mourdikoudis, M. Moulla, I. Tsiaoussis, C. Martinez-Boubeta, M. Angelakeris, C. Dendrinou-Samara and O. Kalogirou: J. Magn. Magn. Mater. 316, Issue 2, e1-e4 (2007).
- S. Mourdikoudis, K. Simeonidis, I. Tsiaoussis, C. Dendrinou-Samara, M. Angelakeris, O. Kalogirou, J Nanopart. Res. DOI 10.1007/s11051-008-9567-9.
- S. Mourdikoudis, K. Simeonidis, A. Vilalta-Clemente, F. Tuna, I. Tsiaoussis, M. Angelakeris, C. Dendrinou-Samara and O. Kalogirou, J. Magn. Magn. Mater. 321 pp. 2723-2728 (2009).

Technique and Painting Materials Characterization of St Athanasius Church in Moschopolis, Albania (18th Century)

E. Pavlidou^{1*}, N. Civici², T. Zorba¹, N. Vouroutzis¹, K.M. Paraskevopoulos¹

¹ Department of Physics, Aristotle University, GR-54124 Thessaloniki, Greece

² Institute of Cultural Monuments, Tirana, Albania

*elpavlid@auth.gr

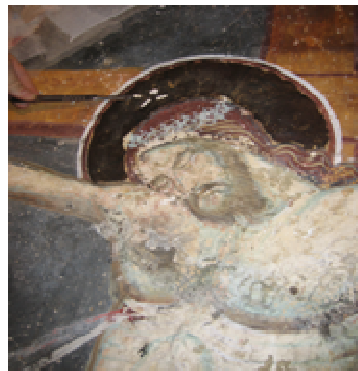
In this work is presented a study of the painting materials and the techniques used in 18th century wall paintings that originated in the orthodox church of St Athanasius, in the city of Moschopolis, Albania. The church was painted in 1745 by Konstantinos and Athanasios Zografis, and during recent years, conservation activities have been performed in the church. A total number of eight series of samples, that include plasters and pigments of different colours, were collected from important points of the wall paintings. Additionally, as some parts of the wall-paintings were over-painted, the analysis was extended to the compositional characterization of these areas. The identification of the used materials was performed using complementary analytical methods such as Optical Microscopy, Fourier Transform Infrared Spectroscopy (FTIR) and Scanning Electron Microscopy (SEM-EDS).

Common pigments used in this area at 15-16th centuries, such as cinnabar, green earth, manganese oxide, carbon black and calcite were identified. The presence of calcite in almost all the pigments is indicative for the use of the fresco technique at the studied areas. The detection of gypsum and calcium oxalate indicates environmental degradation and biodegradation

Experimental details: At first, a general overview of the used pigments was obtained by in-situ measurements performed at several areas with different colours using a field portable X-ray fluorescence (EDXRF) system. This allowed us to select carefully some important points at which representative samples were collected for further and more detailed examinations using Optical Microscopy, Fourier Transform Infrared Spectroscopy (FTIR), Scanning Electron Microscopy -Energy Dispersive Spectroscopy (SEM-EDS) and Total Reflective X-Ray Fluorescence TXRF. A total number of 8 characteristic groups of samples that include plasters and pigments of different colours, with dimensions from about 4 to 10 mm², were collected from different areas of the wall paintings, with special attention in collecting samples from points that were slightly destroyed (Figure 1).



S1



S2

Figure 1. Painted areas from where the samples S1 and S2 were extracted.

Results and discussion: Plasters: From the combination of EDS analysis and FTIR measurements of the plasters it is confirmed the presence of calcite [1] with the additional presence of traces of silicate material (probably sand). In some places gypsum and calcium oxalate were detected by FTIR spectra, indication of an environmental degradation along with a biodegradation [2, 3]. **Samples S1:** The analysis with TXRF and EDS gives Mn and Ca as essential elements, along with traces of S, Al and Si. From the FTIR spectrum calcite and gypsum [1] with small participation of quartz (1000-1100cm⁻¹), could be identified. The above results could lead to the conclusion that MnO₂ was used as black pigment. The presence of MnO₂ could not be identified by FTIR because it presents its characteristic broad peak below 550cm⁻¹, which is the lower limit for the MCT detector. **Samples S2 and S3:** For the samples S2 and S3, which are extracted from the halo of Jesus Christ and Holy Spirit, it can be seen that the gold painted area is covered inartistically, with black. A detailed observation, with an optical microscope, reveals the presence of three layers; a white-yellow layer above the plaster, a gold layer and finally a black layer on the surface. The EDS analysis of the white-yellow layer detected C as major element and traces of Ca, S and Si, while the FTIR spectra (Figure 2) beyond CaCO₃ and few CaSO₄, detect –from the

peaks at ~ 1730 and at $3100\text{-}2800\text{cm}^{-1}$ - the presence of an organic material. The gold layer consists of pure Au as it is confirmed from EDS measurements. Finally, for the black layer, the elemental analysis suggests the existence of C mainly, with small quantities of S, Ca and Pb. From the FTIR spectra it was possible to have only indications of calcium oxalate and Pb white. From the above results we can estimate the use of CaCO_3 as white pigment at the lower layer and the use of organic material probably animal glue as adhesive medium for the gold leaf. As for the overpainted layer, we can consider that carbon black is used, along with Pb-white, part of which is turned to PbS due to the atmospheric conditions [4]. The absence of any organic material in the FTIR spectra, along with the bad adhesion of this layer, impose questions about the composition and the reasoning of this layer.

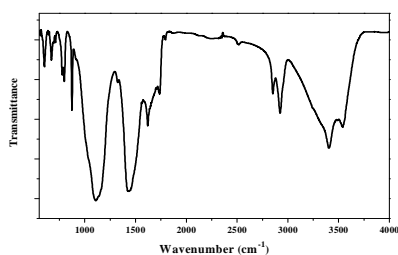


Figure 2. FTIR spectrum obtained from the white-yellow layer of the sample S2.

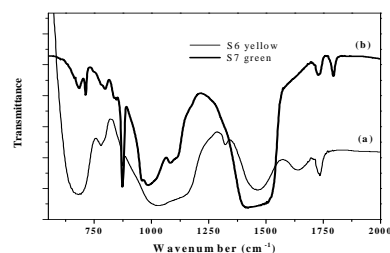


Figure 3. FTIR spectra obtained from (a) the yellow layer of the sample S6 and (b) the green layer of the sample S7.

Samples S4: This group of samples presented a light red surface and a very decayed plaster beneath. From the EDS measurements it is evident that the red pigment is cinnabar (HgS) due to the detection of Hg in great amount, while the presence of Ca and S is identified by FTIR as calcite and gypsum. **Samples S5:** The FTIR spectra obtained from the red, grey and white grains of this sample present mainly the characteristic peaks of calcite along with gypsum and calcium oxalate without any other characteristic peaks attributed to red or black color. On the other hand the EDS and TXRF (Figure 3) analysis detected Hg, Ca, S and Pb. The combination of the two methods leads us to consider that the used red pigment is cinnabar, while the black is carbon black. Moreover, the presence of Pb is an indication of the use of lead white although that, in the FTIR spectrum, it isn't so clearly evident -due to the very strong peaks of the calcite. **Samples S6:** The EDS analysis of the yellow layer showed mainly the presence of Pb (40%), Sb (26%) and Ca (8%). This suggests the presence of lead antimonite as yellow pigment. The FTIR spectra (Figure 5) confirm the use of lead antimonite from the strong peak at about 700cm^{-1} [5]. In the same spectrum we identify also calcite and an organic material, probably egg, from the peaks at $3010\text{-}2900$, 1734cm^{-1} [6]. That suggests the use of tempera technique for this painted area. Finally, for the black layer only carbon black is extracted from EDS measurement. **Samples S7:** The detection of Si, Mg and Al by EDS and TXRF (Figure 3) analysis suggests the use of green earth as green pigment. Additionally the FTIR spectra confirm the presence of green earth and in particular as celadonite along with an organic medium probably egg [6]. **Sample S8:** The area from where the sample S8 is extracted is blue partially covered with black, the optical microscope, showed aggregates of small blue crystals with a black cover at the external surface. The elemental analysis detected Si, Mg, Co, As, Ca and the FTIR spectrum presents a broad band at $1200\text{-}1000\text{cm}^{-1}$ attributed to glass silicate matrix [8]. With the combination of these results we may safely conclude that the blue pigment is smalt, but it is unexplainable the absence of calcite or an organic binder, although many FTIR spectra from different points were obtained. Regarding the identification of blackish area we suppose that carbon black is related with the soot of the cantles, oil lamps or any other kind of illumination by organic combustible burning.

Conclusions: In this area of Balkans the majority of pigments are common, as green earth, cinnabar and carbon black, while the use of manganese oxide as black pigment and lead antimonate is observed for the first time in the present case. The fresco technique is used for the most of the samples we studied, but there are also painted areas, yellow and green, where the tempera technique is used. The deterioration, evidenced by gypsum and calcium oxalate, is limited in comparison to other older churches.

REFERENCES

- Brian Smith, *Infrared Spectra Interpretation, A Systematic Approach* p.165-174 (CRC, 1999)
- R. Van Grieken, F. Delalieux, and K. Gysels, *Pure & Appl. Chem.* 70, 2327 (1998)
- L. Dei, M. Mauro, and G. Bittossi, *Thermochimica Acta* 317, 133 (1998)
- Ashok Roy, *Artists Pigments: A Handbook of Their History and Characteristics*, vol.2, p.67-77 (Oxford Un, 1993)
- R. Feller, *Artists Pigments: A Handbook of Their History and Characteristics*, vol.1, p.242-243 (Oxford Un, 1993)
- M. Fabbri, M. Picollo, S. Porcinai, and M. Bacci, *Applied Spectroscopy* 55, 428 (2001)

Study of the Painting Materials from 4th Century B.C. Vergina Tomb

E. Pavlidou^{1*}, A. Kyriakou², E. Mirtsou³, M. Anastasiou¹, T. Zorba¹, K. M. Paraskevopoulos¹

¹Physics Department Aristotle University of Thessaloniki, 54124 Thessaloniki, Greece

²Faculty of History & Archaeology, Aristotle University of Thessaloniki, 54124 Thessaloniki, Greece

³Archaeological Museum of Thessaloniki, 54646 Thessaloniki, Greece

*elpavlid@auth.gr

In Northern Greece, not far from the city of Veroia, lies Vergina, a modern village, in the fields where the first capital of the Macedonians, Aegae is being excavated since 1938. Although the capital was transferred to Pella in the beginning of the fourth century B.C, Aegae was still the royal necropolis of the Macedonians. The most impressive finds come from the unlooted tombs of the Great Tumulus, where the grave of Philip II, father of Alexander the Great, was discovered.

Two cist-graves enclosed with stone slabs bear painted decoration inside: a myrtle branch and white garland and red ribbons hanging from blue nails depicted with perspective in one grave, and a simple red zone in the other. In these two graves were deposited the bones of the dead after cremation in addition to weapons, gilded wreaths, pieces of jewelry, remains of decorated wooden furniture and ceramic vases broken in small pieces. The vases, a local, rather unique production, bear polychrome floral and geometric decoration with blue and red colors on a white fond.

Experimental details: A scientific investigation on a representative number of microsamples was carried out. Two types of the samples have been studied: fragments from the wall paintings of the tombs with dimensions about 1-2 mm with white, red and blue color on the surface and broken pieces from ceramics vases with small painted areas colored, also, with white, red and blue (Figure 1). The characterization of the used pigments was performed through the combined use of Fourier Transform Infrared Spectroscopy (FTIR) and Scanning Electron Microscopy (SEM-EDS).



Figure 1. Representative photo from wall-painting

FTIR spectra were obtained using a Perkin-Elmer FTIR spectrometer, model Spectrum1000 connected with an i-series FTIR microscope, equipped with a nitrogen-cooled MCT detector. The IR transmittance spectra, were received from different areas of the specimens using a working aperture 40-100 μm . Compositional properties of the samples were obtained with Energy Dispersive X-ray analysis in a Jeol 840A Scanning Electron Microscope (SEM-EDS).

Results and Discussion: FTIR analysis revealed characteristic CaCO_3 peaks at 1407, 872 and 712 cm^{-1} for all colored surface samples from the wall-paintings, attributed to asymmetric stretch, out-of-plane bend and in-plane bend modes respectively of the CO_3 group of CaCO_3 . The presence of Ca was confirmed by EDS analysis, and was ubiquitous throughout the samples. These analyses indicate that the wall paintings are made with fresco technique where figures are painted onto a lime wet layer.

Blue pigments: The EDS and FTIR spectra collected from the blue colored surface of the wall-paintings are presented in Figures 2. Peak frequencies at 1280 and 1000 cm^{-1} are attributed to Si-O-Si stretching vibrations while subsequent peaks can be attributed to calcite vibrational modes, already, mentioned. The special technical feature of the mixture of pigment with the plaster of the wall, is a strong indication of the use of wet fresco as the painting technique. Comparison of FTIR spectra with spectral library and literature [3, 4] suggest the presence of Egyptian blue ($\text{CaCuSi}_4\text{O}_{10}$). The elemental analysis obtained by EDS, confirm the presence of Egyptian blue by the detection of Ca, Cu, and Si. This pigment is a particularly suitable pigment for use with all kinds of supports and techniques [5]. In Figure 2, a representative FTIR spectrum from the blue grains obtained from the painted area of the ceramic vases, is also presented. As it can be seen the spectrum is almost identical with that from wall-paintings and only the peaks of calcite are absent. In accordance with the EDS results the blue pigment is

identified as Egyptian blue, as well. Egyptian blue is the first synthetic pigment manufactured by fusing sand and other materials together with copper compounds used as coloring agents. The invention of the manufacturing process goes back to the first dynasties of ancient Egypt about 3100 B.C. Egyptian blue –brought in Greece by trade- was an important blue pigment in Greek area, used from the first half of the third millennium B.C. until the Roman period.

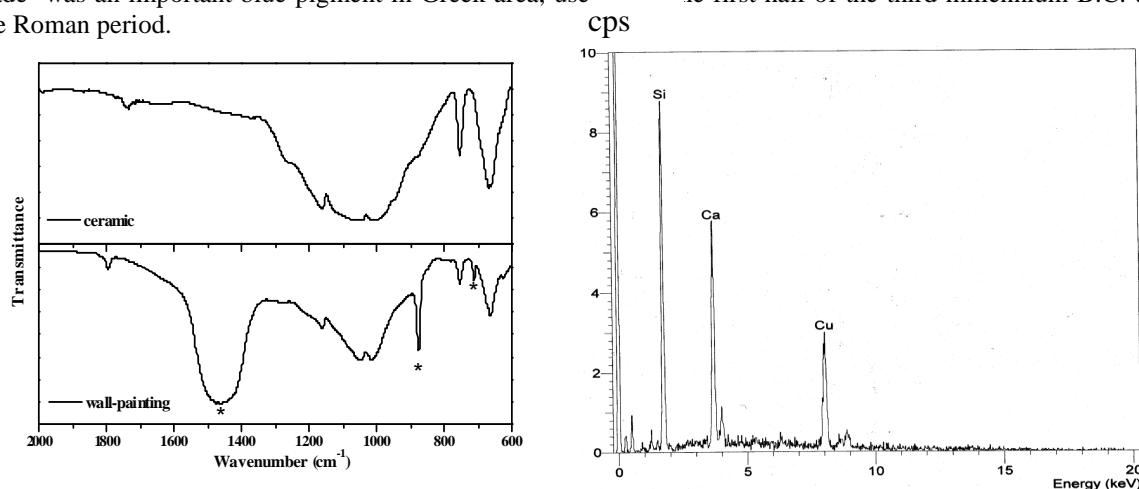


Figure 2. (a) FTIR spectra obtained from the blue specimens of wall-painting and ceramic vase, (b) EDS spectra obtained from the blue specimen of wall painting (* peaks of calcite)

White pigments: The main elements that are detected from EDS measurements for both white colored surfaces, in wall-painting and ceramic vases, are Ca, Si, Mg and Al, with Ca in comparatively much lower quantities in ceramics. Additionally, the presence of Mg in great amounts suggests the use of a magnesium silicate material [6] -such as talc- as well, but this is difficult to be confirmed from FTIR measurements due to overlapping peaks.

Red pigments: Elemental analysis on the red coloured surfaces identified Fe along with Al and Si, indicating the existence of iron oxide as the possible material producing the red colour. The coexistence of the alumino-silicate materials with the iron oxide, leads to the conclusion that the pigment is red ochre.

Conclusions: The tombs that are dated in the mid-fourth century B.C., a period during which Macedon under the reign of Philip II takes up a leading role in the history of Greece, were paint decorated. All the finds and details of the funeral procedure indicate that the occupants of the tombs were high-ranking army officials belonging to the upper class of the Macedonian society in this thrilling period. From our results, it can be concluded for the tombs decorated with wall paintings, that the technique used was the fresco technique, probably wet. The pigments that were used for the creation of the wall paintings are common in that period in the Greek area, and it must be noticed the use of the imported Egyptian blue pigment that continued to be the source of blue coloring material during that period. The ceramic vases were also decorated with the same type of pigments, with a small difference for the white colored surfaces in which probably talc is used, as well. It is remarkable the limited number of the pigments used, expressing a simplicity, despite the high social status of the deceased. The work, that is under continuation, is a part of a bigger project studying the wall paintings in Balkan peninsula from the prehistoric period till post Byzantine, in order to find similarities in the materials and the techniques used.

REFERENCES

1. E. Pavlidou, M. Arapi, T. Zorba, M. Anastasiou, N. Civici, F. Stamati, K.M. Paraskevopoulos, "Onoufrios, the famous XVI's century iconographer, creator of the "Berati School": Studying the technique and materials used in wall paintings of inscribed churches" *Appl. Phys. A*, 83, 709 (2006).
2. W.S. Taft, "Fresco to Oils" *MRS Bulletin*, 21, 18 (1996).
3. S. Bruni, F. Cariati, F. Casadio, L. Toniolo, "Spectrochemical characterization by micro-FTIR spectroscopy of blue pigments in different polychrome works of art" *Vibrational Spectroscopy* 20, 15 (1999).
4. M.C. Edreira, M.J. Feliu, C. Fernández-Lorenzo, J. Martín, "Spectroscopic study of Egyptian blue mixed with other pigments" *Helvetica Chimica Acta* 86, 29 (2003).
5. D. Ulrich, "Egyptian Blue and green frit characterization, history and occurrence, synthesis" *PACT* 17, 323 (1987).
6. W. Noll, R. Holm, and L. Born, "Painting of ancient ceramics" *Angewandte Chemie International Edition* 14, 602 (1975).

Preparation, characterization and in-vitro toxicity test of nanoparticle-based system for magnetic hyperthermia of cancer tissues

A. Chalkidou^{1,2}, K. Simeonidis¹, Th. Samaras¹, C. Martinez-Boubeta³, M. Angelakeris^{1*}, K. Papazisis², C. Dendrinou-Samara⁴ and O. Kalogirou¹

¹ Department of Physics, Aristotle University of Thessaloniki, 54 124 Thessaloniki, Greece

² Molecular Oncology Laboratory, Theagenio Cancer Hospital, Al. Simeonidis Str 2, 54 007 Thessaloniki, Greece

³ Institut de Ciència de Materials de Barcelona (ICMAB-CSIC), Campus UAB, Bellaterra 08193, Spain

⁴ Department of Chemistry, Aristotle University of Thessaloniki, 54 124 Thessaloniki, Greece

*agelaker@auth.gr

ABSTRACT

In this work we study the heating efficiency of Fe/MgO magnetic core/biocompatible cell nanoparticles as a possible candidate for magnetic hyperthermia applications. The solutions consisted of magnetic nanoparticles with Fe core and MgO shell with a mean diameter of 75 nm dispersed in deionized water. X-ray powder diffraction and electron microscopy techniques were employed to structurally characterize the samples while static magnetometry experiments, at the temperature range 77-300 K were performed to study the magnetic features. Different breast cancer cell lines were used and showed a very good cytotoxicity profile with a significant uptake together with relatively high specific absorption and fast thermal response, features that guarantee adequate thermal efficiency and minimum duration of treatment.

INTRODUCTION

One of the most challenging, until now not satisfactorily solved problems of modern medicine, is cancer. Though the standard therapies based on surgery, chemotherapy, irradiation, or combinations of them steadily improve, there are many attempts with a multitude of alternative therapy concepts among which different types of hyperthermia have already entered into clinical practice [1].

In magnetically mediated hyperthermia, one deposits magnetic material in the tumor which is heated by means of an external alternating magnetic field. The temperature increase, with respect to standard temperature of the human body, is considered to be therapeutically useful over a relatively broad temperature range where different mechanisms of cell damaging occur with increasing temperature. Magnetic nanoparticles being subjected to a magnetic AC field may show remarkable heating effects related to energy losses during the magnetization reversal process of the particles. It is advantageous to achieve the temperature enhancement needed for a special application with as low as possible amount of magnetic nanoparticles (MNPs). Therefore, the specific absorption rate (SAR) of the MNPs which is measured in watts per gram of magnetic material to be applied must be high enough. This is particularly important for applications where target concentration is very low, for instance in antibody targeting of tumors. There is a variety of known magnetic materials which, however, for biomedical applications is strongly restricted by the demand of biocompatibility.

Besides the opportunity of a localized heat generation, the application of magnetic nanoparticles offers the possibility of a self-limitation of the temperature enhancement by using a magnetic material with suitable Curie temperature. Two therapy modalities are commonly differentiated: treatments at temperatures of 42–45 °C for up to few hours - actually denoted as hyperthermia - need a combination with other assisting toxic agents (mostly irradiation or chemotherapy) for reliable damage of tumor cells. In contrast, thermoablation aims for the thermal killing of all tumor cells by applying temperatures in excess of at least 50 °C in the tumor region for exposure times of at least few minutes [2].

In any case, to reach the therapy temperature with minimum particle concentration in tissue the specific heating power of the magnetic nanoparticles in magnetic AC fields should be as high as possible. Magnetic losses to be utilized for heating arise due to different processes of magnetization reversal in systems of magnetic nanoparticles which depend in different manners on the applied magnetic AC field amplitude and frequency. Moreover, there is a strong dependence of magnetic particle properties on structural ones like mean size, width of size distribution, particle shape and crystallinity. An alternate route towards larger SAR values is expected to be the enhancement of the magnetic moment per particle, e.g. by using Fe particles instead of iron oxides provided that the problem of chemical stability and biocompatibility is satisfactorily solved as in our case by the MgO shell.

NANOPARTICLE PROPERTIES

The general view of the obtained samples is nearly spherical nanoparticles with a primary diameter of about 75 nm and 16% standard deviation. High-resolution transmission electron microscopy and dark-field imaging clearly showed a MgO layer surrounding a crystalline body-centered-cubic Fe core. Powder X-ray diffraction patterns indexed to MgO and Fe crystalline phases with no evidence for the presence of iron oxides. Magnetization measurements indicate that blocking temperature is well above 300 K with saturation magnetization (M_s) values (210 emu/g at 300 K) very close to that of bulk bcc iron (223 emu/g). The heating efficiency of the nanoparticle solutions was measured by subjecting them in AC magnetic field of 765 kHz for different concentrations of the original sample from 2 mM to 21 mM and within the field amplitude of 100 to 370 Oe. In all cases, SAR was estimated to be higher than 400 W/g Fe together with the fast thermal response (15 °C/ 10 min), features that satisfy the request of high-enough thermal efficiency and minimum treatment duration.

IN-VITRO PROCEDURES

Three different (MDA, SkBr3 and MCF7) breast cancer cell lines were used in order to assess cytotoxicity, measure the intracellular uptake and evaluate the heating effect of Fe/MgO nanoparticles within the cancer cells. The samples showed a very good cytotoxicity profile while a significant uptake for the different cell lines varying between 42 and 126 pg Fe/cell. All hyperthermia experiments were performed in samples of equal volume (1 ml) and equal nanoparticle concentration (when applicable) i.e. 2 mM. For each cancer cell line, four measurements were performed. Initially, the heating response of a water solution of magnetic nanoparticles was examined. Secondly, the PBS sample which comprised of cell feeding material together with nanoparticles was measured. The experimental sequence was continuing by recording the heating curve of the cancer cell solution without MNPs (control sample) and finally, the solution of nanoparticles in the control sample. The subtraction of these two last measurements (denoted hereafter MDA or MCF7) is the signal resulting from nanoparticles within the cancer cells.

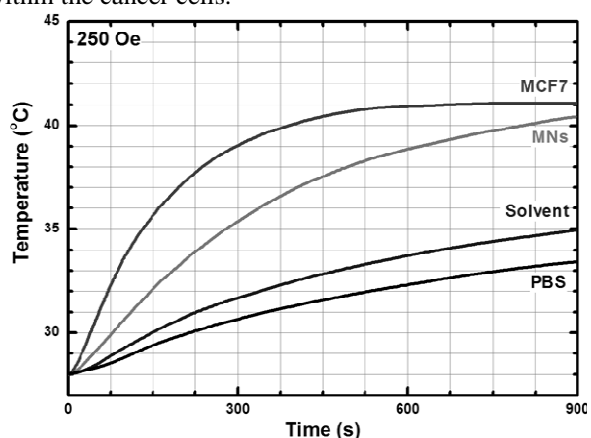


Fig 1. Experimental hyperthermia measurement circle for cancel cell line MCF7 under AC magnetic field (250 Oe and 765 kHz).

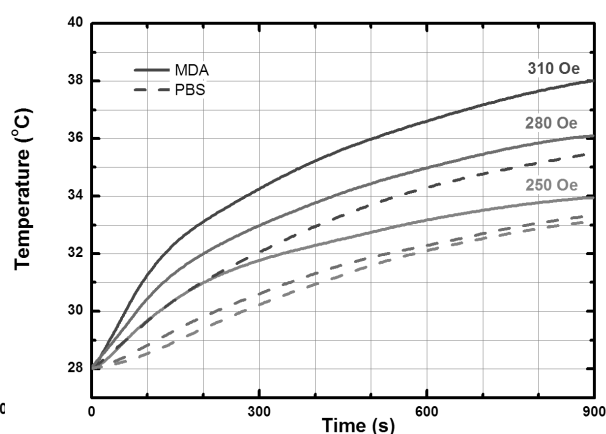


Fig 2. Experimental hyperthermia measurement circle for cancel cell line MDA for three different intensity magnetic fields. Dashed curves denote similar experiments at PBS sample.

In Fig. 1 a representative case is shown (Sample MCF7). Top curve is the subtraction of actual measurement minus the control sample signal. The temperature variation within the cancer cells (from 28 to 41°C) is high enough to destroy by locally heating the tumor. The signal of MCF7 is comparable with the magnetic nanoparticles signal (curve MNs) though a little higher, most probably due to locally increased concentration. The solvent curve refers to deionized water and is given for comparison reasons with the PBS signal which also mainly consists of water and is suited well below the overall signal. In Fig.2 the field dependence is shown for another cancer cell line (MDA). In this case the effect is smaller but scalable with the magnetic field and a temperature rise of ~9 °C was achieved for the highest magnetic field of 310 Oe.

Eventually, our results show, that the alternative use of Fe nanoparticles in magnetically mediated hyperthermia is very promising and may be tuned to further improve heating efficiency.

ACKNOWLEDGEMENTS

This work was supported by the Greek Secretariat of Research and Technology – Contract No: 03EΔ667

REFERENCES

- [1]. Q A Pankhurst, J Connolly, S K Jones and J Dobson, *J. Phys.: Condens. Matter* 18, S2919 (2006).
- [2]. R. Hergt, S. Dutz, R. Müller and M. Zeisberger, *J. Phys. D: Appl. Phys.* 36, R167 (2003).

Studying Technique and Pigments of wall paintings in the Byzantine Church of “40 Holy Martyrs” in Veliko- Turnovo in Bulgaria

E. Sakellariou¹, T. Zorba¹, E. Pavlidou¹, S. Angelova² and K.M. Paraskevopoulos^{1*}

¹ *Physics Dept. Aristotle University of Thessaloniki, 54124 Thessaloniki, Greece*

² *Dept. of Archeology, Univ. of Sofia, Sofia, Bulgaria*

*kpar@auth.gr

In Veliko –Turnovo, in Bulgaria, that was the capital of Bulgaria during the Second Bulgarian Empire, the most famous medieval monument is the church of “St. 40 Martyrs” that is located in Assenova mahala, at the foot of Tsarevets, one of the three hills, where the town lies. The great Tsar Ivan Assen II built the church in 1230 AD after the victory against Epyrus despot Theodor Comninos. It houses the tombs of the prominent Bulgarian sovereign Tsar Kaloyan and of St. Sava of Serbia, and exhibits original columns and frescos.

It consists of two buildings - a six-column basilica and another, smaller building on its western wall, which was built later. During the presence of the Ottoman Turks, maybe until the first half of the 18th century, the church remained Christian. When it was converted to a mosque, all the christian symbols in it were destroyed.

The archeological researches on site were initiated in 1969. As it is clear the 40 Martyrs church, is a historical monument of culture with great significance. The church had murals, from the earlier period, but in the following years and especially during the Ottoman period, the church has suffered many and different destructions. Nevertheless, the pieces of murals that are rescued till nowadays, provide important information for the technique and the pigments that were used on its wall paintings 0.

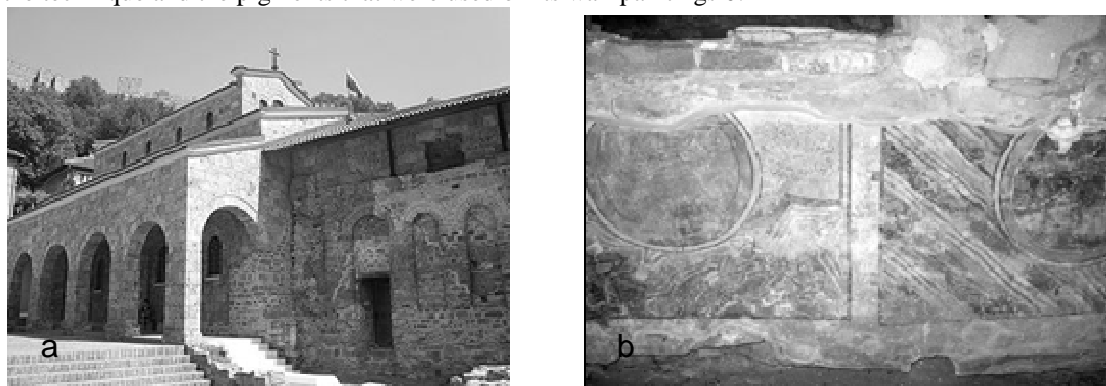


Fig. 1: a) The church of Forty Holy Martyrs, b) Murals from the interior of temple

In the present work, twelve series of samples from the wall paintings were studied in order to characterize the materials and the technique used for church iconography. The study was based on the micro-analytical techniques of the Fourier Transform Infrared micro-spectroscopy (μ s-FTIR), the Optical Microscopy and the Scanning Electron Microscopy (SEM) coupled to an Energy Dispersive X-ray Spectrometer (EDS).

In the FTIR spectra of all pigments the characteristic peaks of calcite were detected, confirming the use of fresco technique for the creation of murals 0. The identification of egg yolk in only one sample (Fig. 2) indicates the additional use of secco technique in some points, probably for some corrections from the painter 0. The combination of FTIR spectroscopy and SEM-EDS analysis, reveal the existence of lapis-lazuli 0 for the blue color, green earth (celadonite) 0 for the green color (Fig.2), cinnabar 0 and hematite for the red color, limonite for the yellow color, calcite 0 for the white color (Fig.2) and carbon black for the black color. The presence of red ochre along with Mn (Table 1), in one of the samples that were examined, revealed the use of umber for the brown color. Additionally, the red colored areas consisted of two layers, the lower one containing hematite and the upper cinnabar, as red pigment.

TU2
P50

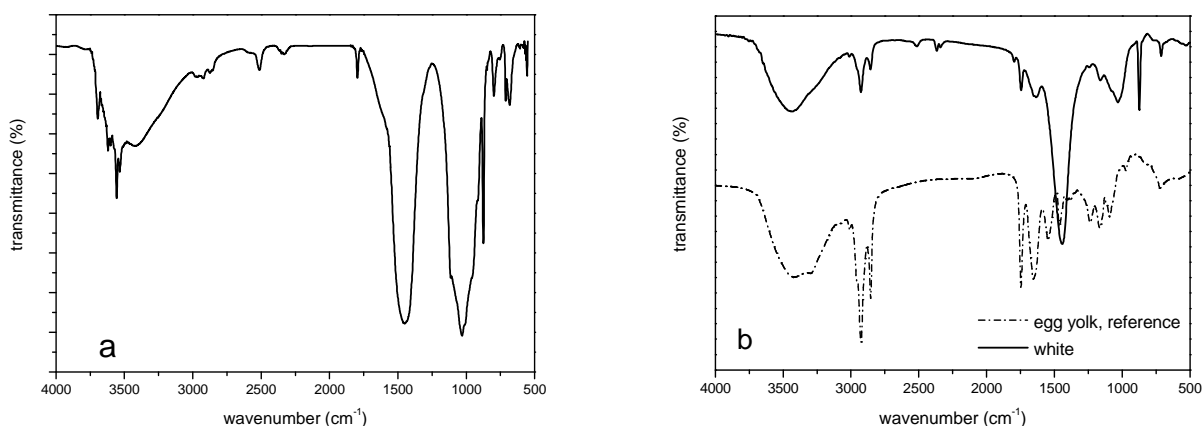


Fig. 2: FTIR spectra for a) green and b) white pigment

Finally, the surface of some samples was covered by a transparent and tensile material. This material was characterized by μ s-FTIR spectroscopy as an organic substance, probably a natural resin that was used to protect the murals in the early ages 0.

Table 1: EDS analysis of pigmented samples

Colour	Green VT10, VT7	Blue VT4	Red VT1 VT3		Yellow VT4, VT10 VT12		Brown VT12	White VT5	Black VT7
% Ca	30-50	3-17	8-80	4.8-29	2.1-83	4-84	0.8-48	5-27	31-57.3
% Al	4.5-13	10-15	3.5-11	3-22	1.6-13	1-4	9-32	0.3-3	3-16.2
% Si	12-31.6	6-19	4.3-19	0.7-35	3.8-51	3-17	31-53	0.9-11	2.6-49
% Fe	11-57	-	5-50	4-70	11-50	3-90	4-36	-	-
% Mg	1.6-4	-	-	-	-	-	-	-	-
% K	3.7-10.5	-	-	-	-	-	-	-	-
% Na	-	0.8-13	-	-	-	-	-	-	-
% Cl	-	0.8-4	-	-	-	-	-	-	-
% S	-	0.7-6	0.7-14	2-12	-	-	-	-	-
% Mn	-	-	-	-	-	-	0-3.6	-	-
% Hg	-	-	72-81	13-80	-	-	-	-	-

REFERENCES

- [1] http://www.historymuseum.org/upload/fek_editor/40%20mazenizi1.htm.
- [2] D. Siapkas, T. Zorba and K.M. Paraskevopoulos, Proceedings of the 4th General Conference of the Balkan Physical Union, Bul. Journ. of Physics 27, Suppl. 2, 105 (2000).
- [3] T. Zorba, E. Pavlidou, M. Stonojlovic, D. Bikiaris, K.M. Paraskevopoulos, V. Nikolic, P.M. Nikolic, Appl. Phys. A 83, 719 (2006).
- [4] Ashok Roy, Artist's Pigments : "A handbook of their history and characteristics", vol. 2, Oxford University Press, Cambridge, (1986) .
- [5] Robert L. Feller , Artist's Pigments : "A handbook of their history and characteristics", vol. 1, Cambridge University Press, Cambridge, (1985).
- [6] D. Bikiaris, S. Daniilia, S. Sotiropoulou, O. Katsimbiri, E. Pavlidou, A.P. Moutsatsou, Y. Chrysoulakis, Spectrochimica Acta Part A 56, 3 (1999)
- [7] F. Mizzoni, S. Nunziante Ce.saro, Spectrochimica Acta Part A 68, 377 (2007) .

Order Against Frustration in a Spin-2 Triangular Lattice System α -NaMnO₂

A. Lappas^{1,*}, C. Stock², O. Adamopoulos^{1,3}, L.C. Chapon², M. Giot^{1,2}, J.W. Taylor¹, M.A. Green^{4,5}, C.M. Brown⁴, and P.G. Radaelli²

¹ Institute of Electronic Structure and Laser, Foundation for Research and Technology-Hellas, Vassilika Voutou, 71110 Heraklion, Greece

² ISIS Facility, Rutherford Appleton Laboratory, Didcot, Oxon, OX11 0QX, United Kingdom

³ Department of Chemistry, University of Crete, Voutes, 71003 Heraklion, Greece

⁴ NIST Center for Neutron Research, 100 Bureau Drive, Gaithersburg, Maryland 20899-6102, USA

⁵ Department of Materials Science and Engineering, University of Maryland, College Park, Maryland 20742-2115, USA

*lappas@iesl.forth.gr

In geometrically frustrated magnets, each spin cannot satisfy all pair wise interactions and therefore remains disordered to temperatures below the Curie-Weiss temperature where magnetic order is expected [1]. The ground state degeneracy imposed by lattice topology may lead to unconventional magnetic properties, including spin-liquid and nematic phases [2]. Recently, AMO₂ (A= H, Li, Na; M= 3d transition metal) compounds have attracted significant interest not only as intermediate electrodes in rechargeable Li batteries [3], but also as model low-dimensional magnetic systems. Experimental and theoretical investigations have been motivated because of the frustrated, triangular arrangement of the transition metal ions in the lattice.

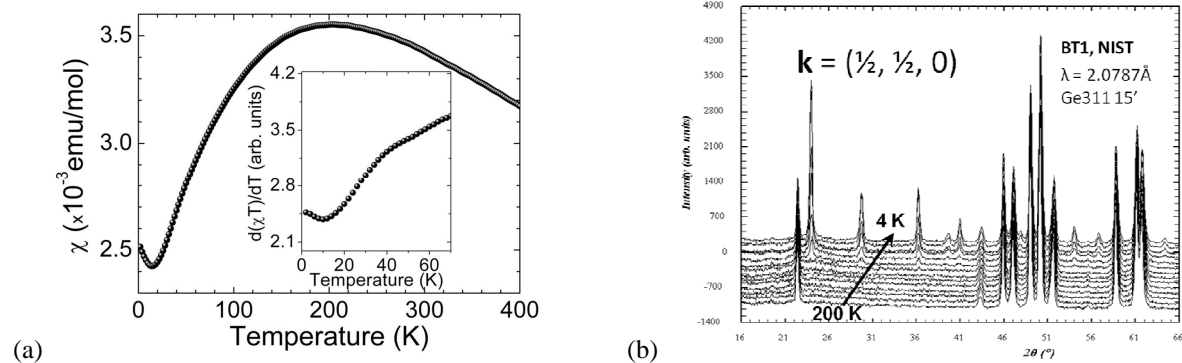


Figure 1. Temperature evolution of the α -NaMnO₂ (a) dc magnetic susceptibility (zero-field cooled, H= 1 Tesla) and (b) its neutron powder diffraction patterns; a number of magnetic Bragg peaks develop at T < 45 K, with a propagation vector \mathbf{k} .

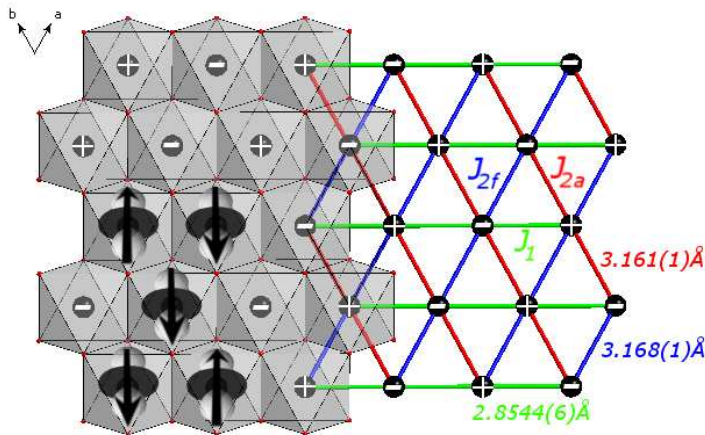


Figure 2. Schematic representation of the magnetic order in the ab plane of the α -NaMnO₂. The + and - signs indicate the direction of the magnetic moments along the $d_{3z^2-r^2}$ orbital shown. Due to a magneto-elastic phase transition at 45 K the nearest-neighbour Mn-Mn bonds and the corresponding exchange integrals become inequivalent and the frustration is relieved.

Our work discusses the unexpected magnetic behavior (Fig. 1a) of the monoclinic α -NaMnO₂ compound (space group C2/m; a= 5.670 Å, b= 2.855 Å, c= 5.804 Å, β = 113.23°, at 300 K). Neutron powder diffraction experiments (BT1, NIST-USA) have revealed the interplay between a Néel state (T_N = 45 K) and strong two-dimensional (2D) diffuse scattering, indicative of short-range spin correlations (Fig. 1b). The Jahn-Teller distorted Mn³⁺ ($3d^4$, $S = 2$) cations form antiferromagnetic (AFM) chains parallel to the b axis, while the moment direction is fixed along the $d_{3z^2-r^2}$ orbital order (Fig. 2). The lattice topology could

then support different intrachain (J_1) and interchain (J_2) exchange pathways. We find that long-range magnetic order occurs simultaneously with a triclinic to monoclinic structural distortion. As a result the degeneracy of the (frustrated) ground state is lifted through the magneto-elastic phase transition [4], which renders all Mn-Mn bonds in the triangles inequivalent (Fig. 2).

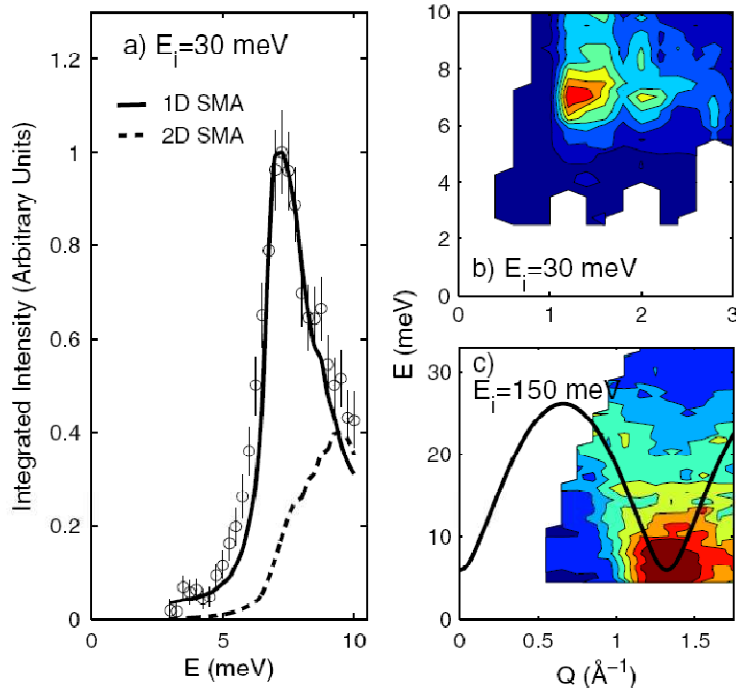


Figure 3. (a) The magnetic density of states integrated over the range of $1.0 < Q < 2.5$ ($T = 5$ K). The solid and dashed lines are calculations based on the 1D and 2D SMA models, respectively. (b) The low-energy spectrum on MARI, with $E_i = 30$ meV; the white spaces are due to gaps in the detectors. (c) The excitation spectrum measured with $E_i = 150$ meV illustrates the dispersion and the location of the top of the magnetic band. The solid line is the single crystal dispersion, taking $Q //$ to the Mn chains.

topology. α - NaMnO_2 therefore represents a model system where the geometric frustration is resolved through the lowering of the dimensionality of the spin interactions.

- [1] M. F. Collins and O. A. Petrenko, *Can. J. Phys.* 75, 605 (1997).
- [2] P.W. Anderson, *Mater. Res. Bull.* 8, 153 (1973).
- [3] M. Winter, J.O. Besenhard, M.E. Spahr, and P. Novak, *Adv. Mater.* 10, 725 (1998).
- [4] M. Giot, L.C. Chapon, J. Androulakis, M.A. Green, P.G. Radaelli, and A. Lappas, *Phys. Rev. Lett.* 99, 247211 (2007).
- [5] P.C. Hohenberg and W.F. Brinkman, *Phys. Rev. B* 10, 128 (1974).
- [6] M.B. Stone et al., *Phys. Rev. B* 64, 144405 (2001); T. Hong et al., *Phys. Rev. B* 74, 094434 (2006).

Acknowledgements. We acknowledge partial financial support from the European Commission (“Construction of New Infrastructures”, contract no. 011723).

Further surprises arise when this $S = 2$ anisotropic triangular lattice is studied by neutron inelastic scattering (MARI, ISIS-UK). We find that the AFM order is established with the opening of a spin gap ($\Delta = 7.5$ meV). The spectral weight of the magnetic dynamics has been analyzed by the single-mode approximation (SMA) [5]. The momentum integrated magnetic intensity (Fig. 3) is a measure of the magnetic density of states and is sensitive to the dimensionality of the system [6]. The peak in the integrated weight is surprising as it implies that the spin correlations are not 2D. Excellent agreement with the experiment is achieved when a dominant exchange interaction $|J|/k_B = 73$ K, along the monoclinic b axis and a sizable easy-axis magnetic anisotropy ($|D|/k_B = 3$ K) are considered. Despite earlier suggestions for 2D spin interactions, the dynamics illustrate strongly coupled antiferromagnetic $S = 2$ chains and cancellation of the interchain exchange due to the lattice

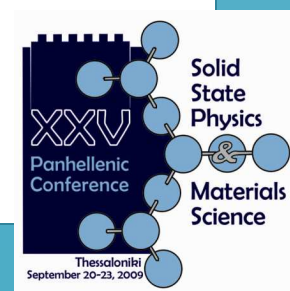
Session TU3

MAGNETISM & SUPERCONDUCTIVITY

PART 1

in memory of A. Simopoulos & A. Kostikas

Tuesday, 22 September 2009, 14⁰⁰-16³⁰



Magnetism at the nanoscale

Michael Farle

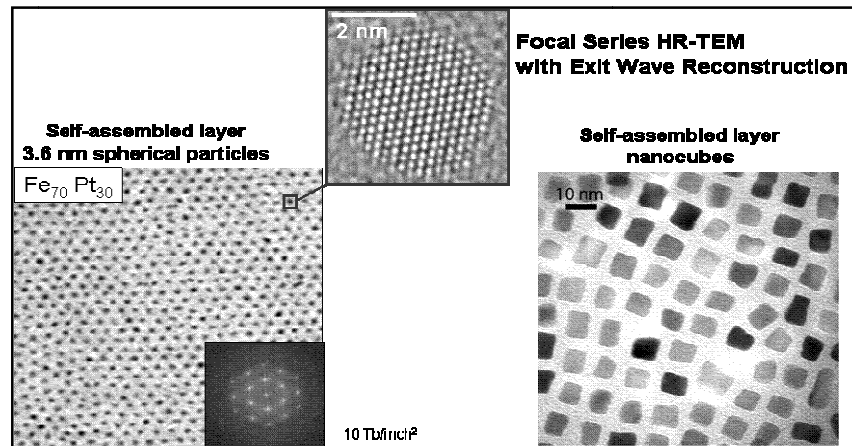
*Department of Physics and Center for Nanointegration Duisburg-Essen, University of Duisburg-Essen,
Lotharstr. 1, 47057 Duisburg, Germany*

**farle@uni-due.de*

Magnetism in structures with dimensions on the few - nanometer scale have been the center of many investigations ranging from topics in spin-torque and spin-injection dynamics and interactions in biomedical applications to the creation of new types of hard, soft or multi-functionalized materials. Such nanostructured “building blocks” offer new exciting possibilities to create new artificial materials like multifunctional hollow magnetic microspheres or luminescent magnetic particles [1,2], some of which will be presented in this talk.

In biological and medical technologies magnetic hybrid or functionalized particles find applications in site-targeted therapy, diagnosis, cell separation and water purification. While most of this work does not require a detailed understanding of the intrinsic magnetism of the nanoparticle, future nanotechnological devices based on one single nanoparticle require the knowledge of local crystal as well as electronic and magnetic structure and surface composition. Based on these microscopic results the collective magnetic response of nanostructured self-assembled hybrid structures can be understood.

Using monodisperse magnetic nanoparticles synthesized by gasphase condensation or organo-metallic synthesis in well controlled sizes ranging from 2 – 15 nm as examples the theoretical predictions for the individual particle’s response (like the magnitude of the magnetic moment and its orbital and spin contributions) as well as the macroscopic response of a collection of interacting nanoparticles will be discussed in relation to experimental observations. Examples on how the magnetic and crystalline interior and surface structure can be calculated and experimentally analysed with sub-Angstrom resolution and with element specificity will be presented: For example, the element-specific magnetism of individual atoms and the interface properties inside a nano-particle can be studied by combining superparamagnetic resonance and different x-ray absorption spectroscopies. For CoO@Co shell@core hybrid particles it has been shown that apparent „giant“ magnetic properties like 300 % enhanced orbital moments in 10 nm Co particles find a simple explanation in conventional solid state physics and crystal field theory [3]. Structural and compositional changes in bimetallic $\text{Fe}_x\text{Pt}_{1-x}$ nanoparticles are discussed to highlight the strong correlation between surface properties (ligand covered versus non-oxidized colloidal particles), crystalline structure and magnetism [5]. It is pointed out that non-uniform layer-wise relaxation of the crystal structure or the concentration gradients must be considered in the interpretation of magnetic data and can also be observed in 6 nm FePt nanoparticle by sub-Ångstrom resolved transmission electron microscopy [6]. Finally, challenges for magnetic and electronic structure analysis will be pointed out.



- [1] M. Spasova, et al, J. Mater. Chem. 15 (2005) 2095.
- [2] V. Salgueiriño-Maceira et al., Adv. Funct. Mat. 16 (2006) 509.
- [3] U. Wiedwald et al., ChemPhysChem 6 (2005) 2522.
- [4] C. Antoniak et al, Europhysics Letters 70 (2005) 250, and Phys. Rev. Lett. 97 (2006) 117201.
- [5] M. E. Gruner, G. Rollmann, P. Entel, and M. Farle, Phys. Rev. Lett. 100 (2008) 087203.
- [6] Rongming Wang, et al. Phys. Rev. Lett. 100 (2008) 017205.

Acknowledgments Supported by Deutsche Forschungsgemeinschaft SFB 445, the National Center of Electron Microscopy, LBL, Berkeley and EU network “Syntorbmag”. The research efforts of my colleagues in the research training network “Syntorbmag”, of my students and postdoctoral collaborators are thankfully acknowledged.

TU3
Ple4

New Sensors Based on the Magnetostrictive Delay Line Technique

Evangelos Hristoforou

Laboratory of Physical Metallurgy, School of Mining and Metallurgy Engineering, National TU of Athens, Zografou Campus, Athens 15780, Greece

*eh@metal.ntua.gr

This presentation refers to the recent advances concerning sensors based on the magnetostrictive delay line (MDL) technique. Three sensors are presented, namely a flexible length position sensor, a tensile stress or plastic deformation sensor and a blood coagulation sensor.

Position sensors to be used in pneumatic pistons suffer from low sensitivity, high cost and flexibility in length [2]. Targeting the development of such position sensors [2] we have developed our latest version of position sensor, which is illustrated in Figure 1. Two parallel conductors including the MDL, transmit pulsed current thus inducing pulsed eddy currents on conductive disks, firmly set parallel and on top of the conductor – MDL arrangement. The pulsed eddy currents generate elastic pulses at each MDL-conductive disk intersection. Hence, a train of voltage pulses is induced at the search coil output. The amplitude of the individual pulsed voltage outputs depends on the biasing field at the above mentioned MDL-conductive disk intersection, thus allowing for measurement of the distribution of the magnetic biasing field at each intersection. A contactless moving permanent magnet parallel to the conductors-MDL arrangement causes change in the biasing field at the neighboring intersections of conducting disks and MDL. The sensing element can be produced in the form of long tapes thus allowing for the development of flexible or variable length position sensors dependent on the given request. A laser interferometer has been used as the comparison instrument for the calibration of the MDL position sensor. Both magnetic tape and MDL sensor have been used to measure the static displacement of different permanent magnets. All tested magnets were Nd-Fe-B cylinders in various sizes and various distances from the MDL. The typical sensitivity and uncertainty of the position sensor have been determined to be better than $1 \mu\text{m/m}$ and $5 \mu\text{m/m}$ respectively, using a 24 bit dc ADC. Permanent magnets (probably in the form of disks) may be fixed above the conductive disks to allow monotonic decrease of the generated elastic pulse amplitude with respect to moving magnet displacement. The conductive disks may also be soft magnets to combine both requirements of low resistivity for eddy current generation and high coercive field for polarising the MDL.

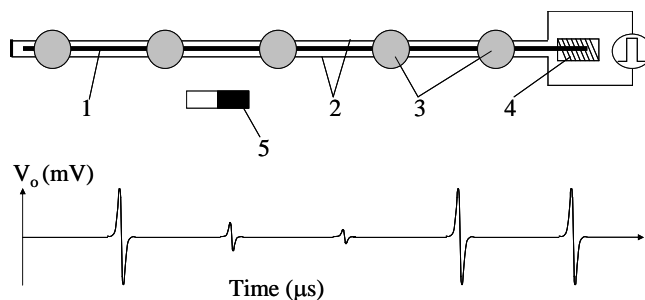


Figure 1. The schematic of the sensor (1) MDL, (2) pulsed current conductors parallel to the MDL, (3) conducting disks, (4) search coil, (5) moving permanent magnet. The sequence of voltage output pulses illustrates the response of the search coil for a possible position of the permanent magnet between two conductive disks.

The second sensor refers to non destructive testing of the magnetic permeability of ferromagnetic surfaces. The method is based on the arrangement shown in Figure 2. A balanced set-up of pulsed current excitation conductors is symmetrical around the MDL that is therefore free from any stresses, even if the pulsed current I_e is transmitted (in the same direction) in the two conductors [3]. In the absence of any other magnetic bodies in the neighborhood of the MDL, there is no magnetic flux in the delay line and consequently no pulsed voltage output is detected. Contrary, the presence of a ferromagnetic specimen at any side of the MDL and conductors balanced structure will destroy the symmetry due to partial flux closure through that specimen. This will cause an elastic excitation of the MDL and result in a pulsed voltage output of the search coil. The detected peak voltage V_o depends on the permeability of ferromagnetic specimen, distance from the pulsed-current conductors, as well as on the lift-off distance between MDL and the specimen being thus under the test. For a minimum distance between MDL and pulsed current conductors equal to 0.1 mm and a minimum lift-off distance between MDL and ferromagnetic specimen equal to 0.2 mm, the obtained maximum MDL output V_o was around 50 mV, corresponding to a reference high-permeability ribbon. Maintaining these distances at the amplitude allows

estimating of the magnetic permeability at a small area of the magnetic specimen at the MDL-conductors location. Experiments were performed using Armco and electric steels after a mechanical treatment. The plastic deformation of the samples was evaluated by an “Instron” stress machine and the permeability was determined by a home-made hysteresis-meter. The MDL measurements showed monotonic dependence of the MDL output V_o on the plastic deformation or on the material permeability (Figure 3). Thus, the designed sensor can be used for scanning that may result in measuring the distribution of plastic deformation at the tested specimen surface, which is often an indication of the plastic deformation of the whole material.

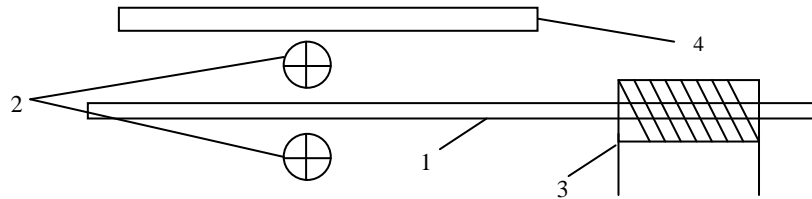


Figure 2. The testing device. (1) Magnetostrictive delay line (MDL); (2) Pulsed current conductors; (3) Receiving coil; (4) Specimen under the test.

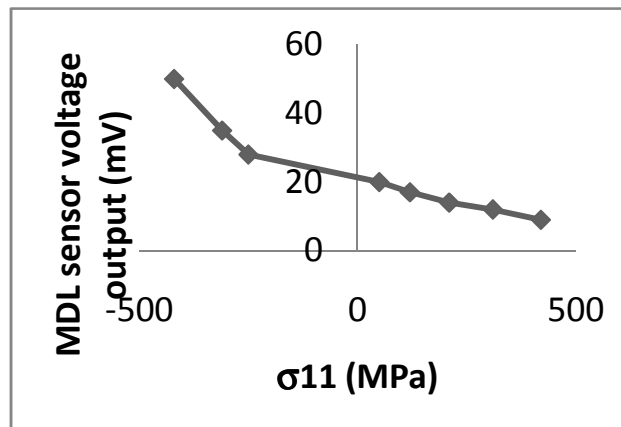


Figure 3. Dependence of the MDL output on the σ_{11} stress tensor component.

The coagulation-sensing element is an MDL, having the shape of an acoustic waveguide with rectangular cross section area can be made of FeSiB amorphous ribbons, offering high magneto-mechanical coupling factor and the smallest possible hysteresis. An excitation and a search coil are set around the MDL at the two ends of it. The output MDL signal is strongly affected by the pressure or coagulated liquid on top of the MDL. A typical dependence of the MDL pulsed-voltage output on the time of a blood drop set on top of the MDL between the two coils is illustrated in Figure 4.

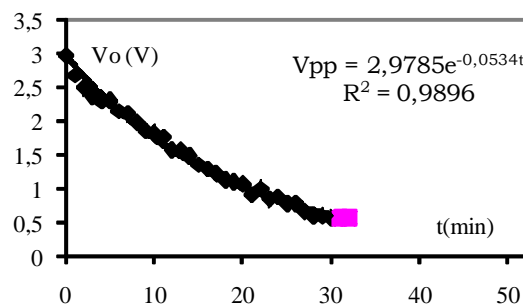


Figure 4. MDL output dependence on the time of a blood drop on the MDL surface.

[1] Reininger T, Welker F. and von Zeppelin M., *Sensors and Actuators A: Physical*, 129, 270 (2006).
 [2] Hristoforou E., Dimitropoulos P.D. and Petrou J., *Sensors and Actuators A: Physical*, 132, 112 (2006).
 [3] Hristoforou E., Kosmas, K., *Int. J of Appl. Electromagnetics*, 25, 287 (2007).

Magnetic and Magneto-Optic Properties of Transition Metal Films with Sub-Wavelength Antidot Arrays

E. Th. Papaioannou^{1,*}, V. Kapaklis¹, P. Patoka², M. Giersig², P. Fumagalli³ and G. Ctistis⁴

¹*Department of Physics and Materials Science, Uppsala University, 75121 Uppsala, Sweden*

²*Helmholtz-Zentrum Berlin für Materialien und Energie GmbH, 14109 Berlin, Germany*

³*Institut für Experimentalphysik, Freie Universität Berlin, 14195 Berlin, Germany*

⁴*Center for Nanophotonics, FOM Institute for Atomic and Molecular Physics (AMOLF), Kruislaan 407, 1098 SJ Amsterdam, The Netherlands*

**vangelis@fysik.uu.se*

Magnetic thin films perforated with holes arranged in regular patterns (antidot arrays) present new and fascinating properties at reduced dimensions. In particular, patterning holes into ferromagnetic thin films is an effective way to engineer their magnetic properties. Simultaneously, patterning holes into metal thin films is an effective way to achieve extraordinary optical properties like the enhanced transmission through sub-wavelength hole arrays of metallic films (Ag, Cr, Au). In this work, we present a combined study of the interaction of light with periodically arranged nanostructures composed of magneto-optic active material (Fe, Co, and Ni) in the presence of a magnetic field. Our results could lead to exciting developments in the field of magneto-photonics.

Nanohole arrays in Co, Fe, Ni thin films have been prepared using self-assembly nanosphere lithography [1]. The arrays exhibited long range ordering with hexagonal symmetry (Fig. 1). Different meshes were used with holes diameters (d) ranging between 220 and 330 nm while the inter-hole distance has been kept constant at 470 nm. The film thickness was 100 nm.

According to the hysteresis loops the magnetization for all three magnetic materials lies mainly in plane. Nevertheless, the introduction of nanoholes in the films drives the appearance of out-of-plane magnetization components, which are getting stronger by increasing the hole diameter. For the case of Co (Fig. 2) the saturation field in the polar configuration decreases strongly and reaches 0.8 T for the sample with 330 nm holes, while perpendicular remanent magnetizations appear. The trend of magnetic hardening as the hole size increases is present for all of the magnetic films. The observed hysteretic behavior of the samples is straightforward connected with the magnetic domain imaging.

The magnetic domain structures have been studied by analyzing magnetic force microscopy images at remanent and at saturation states. Different domain structures have been observed depending on the geometrical characteristics of the films. Dark and bright regions, can be distinguished in the magnetic image without correlation to the topography. Such a case is presented in Fig. 3 for a Fe nanohole film with hole diameter 248 nm. A comparison with micromagnetic simulations is presented. The interplay between in and out of plane components to reduce the magnetostatic energy is discussed. The results reveal the capability to modify the magnetization dynamics of the films through the control of the hole pattern.

Magneto-optic measurements show a spectacular magneto-optic response for all the magnetic films at wavelengths where surface plasmon-polaritons are supported by the structure as deduced in optical measurements. The measured spectra show a higher polarization than a control Fe (Co, Ni) film (Fig. 4) and are a result of an enhancement effect closely related to surface plasmons excitations.

In conclusion, the results of the magnetometry reveal the dominant role of the presence of the holes in the reversal behavior over the intrinsic anisotropy of the magnetic films and demonstrate the ability to control the coercivities, remanences, anisotropies and switching characteristics of the films. The tuning of the magneto-optic behavior renders the structures important for technological applications in magneto-optic data storage media, and in the new field of magnetic photonic crystals since it leaves a further degree of freedom to manipulate light-matter interaction and thus control the propagation of light.

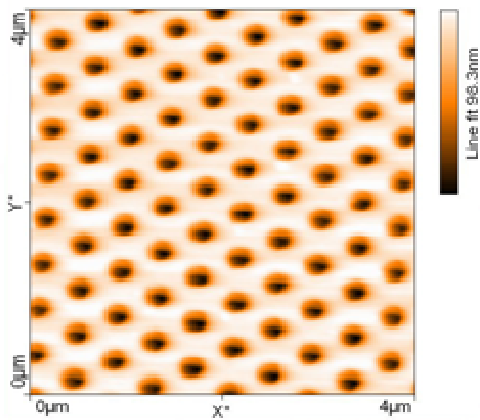


Fig. 1: AFM image of the Co hole array with $d = 220$ nm. A large defect-free area is present.

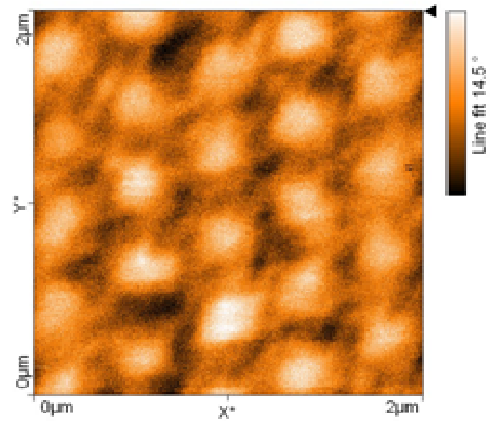


Fig. 3: Magnetic Force Microscopy (MFM) image of a Fe nanohole film with 248 nm holes in diameter.

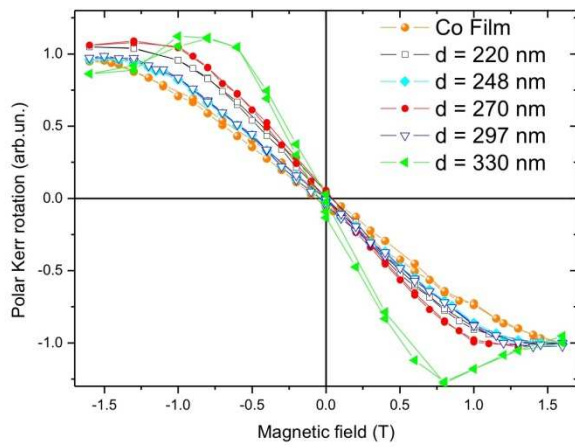


Fig. 2: Polar hysteresis loops for patterned Co films with different hole diameters.

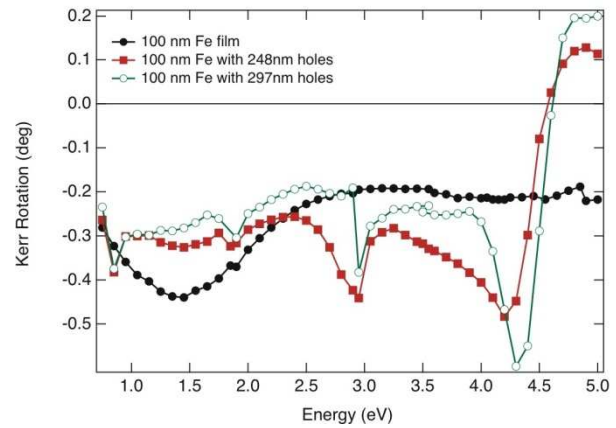


Fig. 4: Magneto-optic Kerr measurements for two different Fe hole diameters and for a continuous Fe film.

[1] G. Ctistis, E. Papaioannou, P. Patoka, J. Gutek, P. Fumagalli, and M. Giersig, "Optical and Magnetic Properties of Hexagonal Arrays of Subwavelength Holes in Optically Thin Cobalt Films", *Nano Lett.* **9** (1), 1 (2009).

Exchange Spring Effects in FePt/Fe(Co)/⁵⁷Fe multilayers

O. Crisan^{1*}, A.D. Crisan¹, V. Raghavendra Reddy², V. Kuncser¹ and Ajay Gupta²

¹ National Institute for Materials Physics, Bucharest, Romania

² UGC-DAE Consortium for Scientific Research, Indore, India

*ocrisan@yahoo.com

FePt system is of large interest due to its high magnetocrystalline anisotropy and perspectives as new magnetic recording media. The ordered L10 FePt superlattice phase is hard magnetic. In structures where this phase co-exists with soft magnetic phases, an exchange coupling magnet, based on the exchange spring effect may be obtained. We have prepared by ion beam sputtering multilayers made of FePt(L1₀)/Fe(Co)/⁵⁷Fe/Fe, with the purpose to investigate the exchange coupling between the hard FePt and the soft Fe(Co) layers. This kind of systems exhibits the exchange spring effect. An external magnetic field applied non-collinearly with respect to the easy axis, induces a twist of the magnetic moments that depends on the magnitude of the field. The reversible nature of this mechanism renders this system to be a magnetic exchange spring. In particular, the thin probe layer of ⁵⁷Fe is deposited with the aim of probing, by Mossbauer spectrometry, the gradual reversal of soft magnetic moments that describes the exchange spring effect. Detailed magnetic measurements obtained with VSM at various temperatures are correlated with structural and Mossbauer data in order to probe this effect. Remanence enhancement as in the case of exchange coupled nanocomposite magnets is obtained in these multilayers.

Acknowledgments The authors acknowledge the financial support in the frame of the Romania-India scientific bilateral cooperation project no. R06/2007. Also, the financial support from the PN II project 71-060 / 2007 and 12-129 / 2008 of the Romanian Ministry of Research is gratefully acknowledged.

New Magnetic Ferrite Materials for Innovative RFID Concepts

V. Tsakaloudi*, E. Eleftheriou, V.T. Zaspalis

Laboratory of Inorganic Materials, Chemical Process Engineering Research Institute,
PO Box 60361, 57001 Thessaloniki

* vikaki@cperi.certh.gr

RFID Applications (acronym for Radio-Frequency IDentification) consist the most up-to-date identification technique using high frequency radiation on a “tag-antenna” communication setup. With significant advantages compared to the conventional barcode utilities that include greater reading distances without a requirement for a direct line of sight, very high read rates (>40 tags/sec), reusability and most importantly, a read-write capability and communication, RFID systems are already introduced in most supply chain automations, asset tracking, access control, equipment/personnel tracking, animal/pet tracking and various medical applications [1].

The communication efficiency between the tag and the antenna can be significantly improved when the tag (usually a copper coil pattern) is supported on a background of a ferromagnetic material. Due to the development of a magnetic field around the copper coil, which is parallel to the surface of the identified item, an elimination of signal distortion is accomplished and signal enhancement is achieved.

In the present work a new ceramic magnetic material was developed in order to improve the RFID data transfer for the 900 MHz operation frequency, in terms of reading distance and a possible miniaturization of the ferrite antenna. A hexagonal Y-type ferrite material was specially designed to meet the magnetic requirements of high initial permeability, low magnetic losses at the operation frequency and a resonance frequency above 2 GHz. An increase of the reading distance by a factor of 2 was detected on the prototype RFID setup with the ferrite backing the tag in near-field measurements.

Experimental

The Y-type hexagonal ferrites of the molecular formula $Ba_2(Co_x Cu_y Zn_z)Fe_{12}O_{22}$, where $x + y + z = 2$ were prepared by the solid state reaction method. The raw materials were wet mixed and the mixed powder was pre-fired at 1050-1150°C in air for several hours. The obtained Y-type hexagonal phase was checked by X-Ray Diffraction and the powder was subsequently milled for 3 hours. A PVA binder was added to the dried powder by roll granulation and ferrite toroids and cylinders were uniaxially pressed to form compacts of a green density of 3.30 g/cm³. Sintering cycles between 1100-1400°C were applied and the electromagnetic properties of the sintered specimens were measured up to 3 GHz, using a spectrum analyzer and an impedance analyzer. Thin disc-shaped slices with a thickness of 0.5-1 mm were cut from the sintered cylindrical specimens by a microtome.

Application testing

The experimental setup used for the evaluation of the ferrite slices in terms of reading distance enhancement is schematically described in Fig. I. A loop antenna (1) is connected through a special module (2) (Skyetek M9) and an interface (3) to the USB port of the computer (4) carrying the appropriate software (Skyetek, Skyware 4). The tag (5) (type IN26, RSI ID technologies) is placed on a sliding surface opposite to the antenna. As long as the tag is identified by the antenna, a signal appears on the computer screen. Upon increasing the distance between the tag and the antenna at a certain moment the tag is no longer readable. This is defined as the maximum reading distance (MRD). Once MRD is registered for the tag alone, the experiment is repeated with the tag supported on a thin (0.5-1mm) slice of ferrite material (6). The new MRD is also registered and any difference with the reference is recorded.

Results-Discussion

In Fig.II the initial permeability (μ_i , measured at 20 kHz), the quality factor (Q_{900} , measured at 900 MHz) and the MRD enhancement are shown for samples S1-S6. The MRD enhancement is defined as given in Eq. I:

$$MRD = \frac{(MRD_{with\ ferrite} - MRD_{without\ ferrite})}{MRD_{without\ ferrite}} \times 100 \quad (1)$$

It is found that as the Co content is increased (S1-S6), the initial permeability decreases, while the quality factor increases. This is due to the highly anisotropic character of Co, which leads to a shift of the resonance frequency to higher levels [2]. As a consequence, the quality factor increases, as it depends strongly on the onset of the ferromagnetic resonance and the imaginary part of the permeability. This behavior of the permeability is a well known phenomenon described by Snoek's law [3] and its modifications for polycrystalline systems [4,5] and also holds for other ferrite materials, like those of the cubic spinel structure. The mentioned trends also follow the gradual decrease of the Zn content, in accordance to previous studies [6]. Comparing samples S4-S5-S6, a

gradual permeability drop is detected, caused by insufficient densification due to the absence of Cu, which is known to act as a sintering aid in ferrite systems [7].

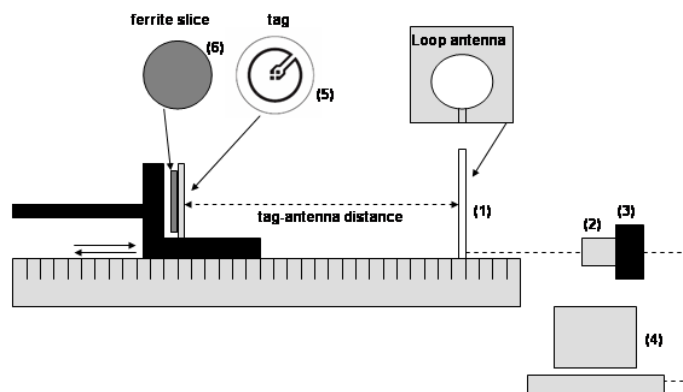


Fig.I. Experimental setup for the RFID measurements

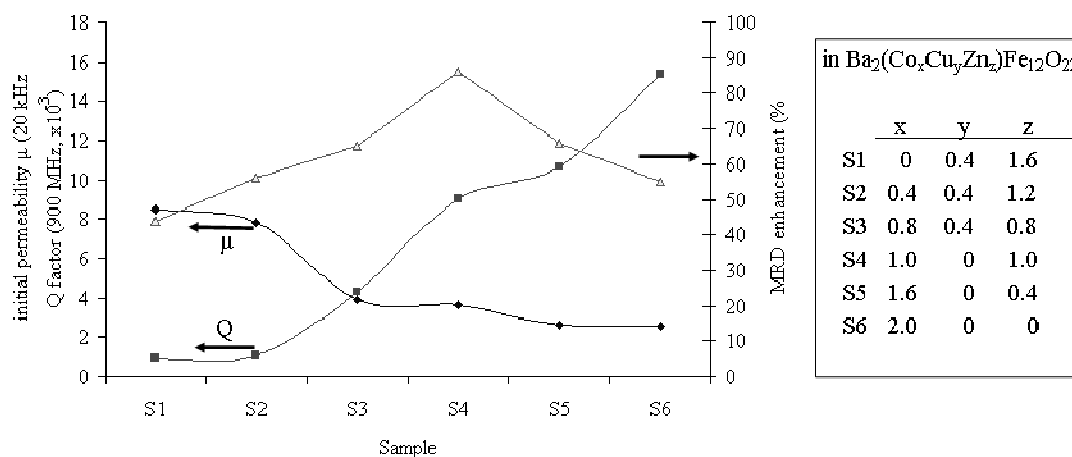


Fig.II. Initial magnetic permeability, quality factor and MRD enhancement for samples S1-S6

It is found that there is an optimal set of conditions required to achieve the greatest MRD enhancement, which indicates that a certain density is required to give an adequate average permeability-high quality factor set. A maximum MRD enhancement of 86% is achieved with sample S4. Under the chosen experimental conditions (e.g. antenna, tag type etc.) the typical net reading distance (without the ferrite support) of 10mm increases to 18.5 ± 0.3 mm when the tag is supported on the S4 ferrite slice.

Finally, the strong dependence of the quality factor on the morphological characteristics of the polycrystalline microstructure, such as potent insufficient densification, secondary recrystallization phenomena and second phase inclusions is also evident on the evaluation of the MRD modifications under the same ferrite chemistry.

Conclusions

It can be concluded that for an effective increase of the reading distance in 900 MHz RFID applications, hexagonal Y-type ferrite slice supports can be effectively used with a minimum permeability of approximately 3 and a high quality factor at the operation frequency.

Future investigation towards the direction of component design aspects, which also play a crucial role in the final system performance and on the manufacturing cost, is in progress.

- [1] Hunt V.D., Puglia A., Puglia M, "RFID—A Guide to Radio Frequency Identification", Wiley-Interscience (2007).
- [2] Tsakaloudi V., Eleftheriou E., Stoukides M., Zaspalis V., J. Magn. Magn. Mat. 318 (2007).
- [3] Smit J., Wijn H.P.J., "Ferrites", Wiley-New York (1959).
- [4] Visser E. Johnson M.T., J. Magn. Magn. Mat. 101 (1992).
- [5] Goldman A., "Handbook of Modern Ferromagnetic Materials" Kluwer-Boston (1999).
- [6] Haijun Z., Xi Y., Liangying Z., J. Eur. Cer. Soc. 22 (2002).
- [7] Nam J. H., Jung H.H., Shin J.Y., Oh J.H., IEEE Trans. Magn. 31 (1995).

Defect-Induced Defect-mediated magnetism in Diluted Magnetic Semiconductors

Antonios N. Andriotis^{1*}, R. Michael Sheetz² and Madhu Menon^{2,3}

¹ *Institute of Electronic Structure and Laser, FORTH, P.O. Box 1527, 71110 Heraklio, Crete, Greece*

² *Center for Computational Sciences, University of Kentucky, Lexington, KY 40506-0045*

³ *Department of Physics and Astronomy, University of Kentucky, Lexington, KY 40506-0055*

*andriot@iesl.forth.gr

While it has been established that dopants (structural defects and/or impurities) can create unpaired electrons in otherwise non-magnetic materials, their ferromagnetic coupling (essential for developing ferromagnetism) requires additional mechanisms. In the present work it is shown that the dopant induced unpaired electrons may be coupled ferromagnetically upon the synergetic action of two suitably chosen *codopants*. The essence of the *codoping* is that one of the *codopants* induces or provides the unpaired electrons, while the other codopant mediates their ferromagnetic coupling even for defect/impurity concentrations smaller than those dictated by the percolation threshold. These findings allow us to propose a more general recipe for developing this type of defect-induced defect-mediated (DIDM) ferromagnetism in new materials of great technological interest. The recipe is quite general, although its realization is system specific. In each case, the required basic step is to find two *complementary and synergetic codopants* which are able to act as a donor-acceptor pair. DIDM magnetism appears to be applicable for a wide variety of materials, and can be especially very effective in diluted magnetic semiconductor materials.

TU3

O20

Session TU4

MAGNETISM & SUPERCONDUCTIVITY

PART 2

in memory of A. Simopoulos & A. Kostikas

Tuesday, 22 September 2009, 17⁰⁰-18⁰⁰



MAGNETIC FORCE MICROSCOPY ON THIN FILMS AND NANOSTRUCTURES

P. Pouloupoulos^{1*}, S.D. Pappas², V. Kapaklis^{2,3}, V. Karoutsos¹, Ch. Dounos¹, V. Pissas²,
S. Grammatikopoulos², G. Diamantogiannis² and D. Trachylis²

¹ *Materials Science Department, University of Patras, 26504 Patras, Greece*

² *Engineering Science Department, School of Engineering, University of Patras, 26504 Patras, Greece*

³ *Department of Physics and Materials Science, Uppsala University, Box 530, S-751 21 Uppsala, Sweden*

*poulop@upatras.gr

Magnetic Force Microscopy (MFM) is a variant of the Atomic Force Microscopy (AFM) imaging technique. It records the magnetostatic forces or force gradients between a ferromagnetic sample and a small magnetized ferromagnetic tip. The main advantages of this technique as compared to other magnetic domain imaging techniques are the high resolution (better than about 20 nm) and its insensitivity to protective non-magnetic overlayers [1].

In this work we will apply the MFM technique to study magnetic domain patterns on magnetic thin films and nanostructures. The surface morphology and magnetic domain structure in our films has been observed by using a Multimode Microscope with a Nanoscope IIIa controller and a 120 μm x 120 μm magnet-free scanner (Model AS-130VMF) developed by Digital Instruments. We used a Co/Cr coated Si probe tip magnetized parallel to its long axis. The images were recorded by using the amplitude detection mode. Prior to measurements, most of the films were perpendicularly magnetized with the help of a small permanent magnet capable of producing a stray field of about 4 kOe. For specific measurements the samples were magnetized along various axes up to their saturation field, which may reach even the value of 20 kOe, with the help of a water-cooled electromagnet.

Pioneer works in ultrathin magnetic films have shown perpendicular magnetic domains in the demagnetized state. The source of this perpendicular anisotropy is the interface anisotropy developed at the interface. Similar domains could be observed in tetragonally distorted ultrathin films due to the magnetoelastic anisotropy. On the other hand, single-crystalline hexagonal close packed (*hcp*) Co films when grown epitaxially with the *c*-axis oriented perpendicular to the film plane may show perpendicular stripe magnetic domains even up to a thickness of about 500 nm. In that case the source of perpendicular anisotropy was the magnetocrystalline anisotropy of bulk Co, which favors the *c*-axis [2].

In this work, we have grown by radio frequency magnetron sputtering polycrystalline Co and alloyed CoPd films in the thickness range of 15 - 4500 nm. We have used various substrates, such as Corning glass, silicon wafers and Al-foil. Some of these films have been deposited on microstructured Silicon substrates [3]. The substrate temperature was about 350 K. The films have been found by x-ray diffraction experiments to present various structures and textures depending on the preparation conditions, mainly the Ar-pressure and deposition rate. Stripe- and labyrinth-like domain configurations are observed in Co films textured along the *c*-axis, and in Co films with a mixture of *hcp* and *fcc* grains, respectively. Co films which show mainly *fcc* or amorphous structure do not form perpendicular domains [4]. On the other hand, CoPd films with a strong *fcc*{111} texture exhibit perpendicular magnetic domains. The results are discussed with respect to magnetization loops recorded via a home-made newly established and fully automatic polar magneto-optic Kerr effect (MOKE) magnetometer and are compared to similar ones recorded on Co/Au and Co/Pt multilayers [5,6]. The possible formation of canted magnetic states is also considered [7]. The magnetic prehistory of the samples in terms of magnetization and demagnetization along certain axes is shown to produce stripes, labyrinths or bubble-domain structures. The results are analyzed with respect to the magnetic free energy of the films.

[1] A. Hubert and R. Schaefer, *Magnetic Domains: The Analysis of Magnetic Microstructures*, Springer, Berlin (2000).

[2] M. Hehn, S. Padovani, K. Ounadjela and J.P. Bucher, *Phys. Rev. B* 54, 3428 (1996).

[3] P. Pouloupoulos, V. Kapaklis, S.D. Pappas, D. Trachylis and C. Politis, *J. Nanosci. Nanotechnol.* (in press).

[4] V. Karoutsos, P. Pouloupoulos, V. Kapaklis, S.D. Pappas, D. Trachylis and C. Politis, *J. Nanosci. Nanotechnol.* (in press).

[5] E. Th. Papaioannou, V. Karoutsos, M. Angelakeris, O. Valassiades, P. Fumagalli, N.K. Flevaris and P. Pouloupoulos, *J. Nanosci. Nanotechnol.* 8, 4323 (2008).

[6] V. Karoutsos, P. Pouloupoulos, M. Angelakeris, E. Th. Papaioannou, P. Fumagalli and N. K. Flevaris, *Solid State Phenomena* 152-153, 241 (2009).

[7] R. Froemter, H. Stillrich, C. Menk and H.P. Oepen, *Phys. Rev. Lett.* 100, 207202 (2008).

Acknowledgments Work was partially supported by the GSRT, project PENED2003 03EA_667 ‘Self-assembled networks of magnetic nanoparticles for applications of permanent magnets, sensors and magnetic recording media’.

Hot Electron Transport and High Resolution Magnetic Imaging on Co/Cu/Co and Co/Cu/NiFe Spin Valves

A. Kaidatzis^{1*}, S. Rohart¹, A. Thiaville¹ and J. Miltat¹

¹ *Laboratoire de Physique des Solides, CNRS, Université Paris Sud, UMR 8502, 91405 Orsay cedex, France*

**andreas.kaidatzis@gmail.com*

The research of magnetic systems with reduced dimensions implies the capability of imaging magnetic structures down to the nanometer scale. The scanning tunnelling microscope (STM) is a powerful tool for high resolution imaging [1]. For magnetic imaging, we develop a variant of the STM named the ballistic electron emission microscope (BEEM) [2]. Beyond imaging, this microscope offers perspectives for local hot electron transport studies in magnetic structures. This allows a better understanding of the physics of components like the spin valve transistor [3], or the magnetic tunnel transistor [4], operating on the basis of hot electron transport.

BEEM is a three terminal modification of the STM (see Fig. 1). A BEEM sample is constituted by a thin metallic layer or multilayer (10 to 20 nm thick), deposited on a semiconductor. The STM tip is used as a local, adjustable energy electron source (injector). When injecting electrons at a given energy above the sample Fermi level, a fraction of them crosses the metallic layers without being scattered (ballistically) and conserve their initial energy (hot electrons), while the others are thermalized to the Fermi level. Thanks to the Schottky barrier present at the metal/semiconductor interface that acts as an energy filter, only the hot electrons enter into the substrate. Two sample contacts are utilized: one on the metallic layer (base), and the other on the semiconductor (collector). The yield of the hot electrons entering into the semiconductor is measured using the collector terminal, while the thermalized electrons are evacuated by the base terminal. Thus, it is possible to measure locally the hot electron transmission of the multilayer with a nanometre scale resolution.

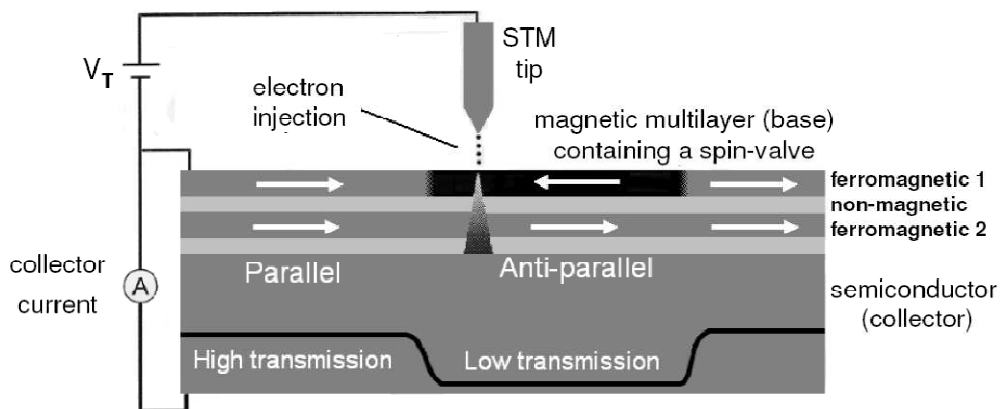


Figure 1: Configuration of a BEEM experiment for high resolution magnetic imaging. The STM tip (injector), the magnetic multilayer (base), and the semiconductor substrate (collector) are apparent. For parallel magnetic configuration of the spin valve the multilayer hot electron transmission is high, while it is low for anti-parallel configuration.

When the metallic multilayer contains a “spin valve”, two ferromagnetic layers separated by a non-magnetic layer, the transmission depends on the relative magnetization orientation of the two layers (see Fig. 1). This is a consequence of the mean-free path difference between the hot majority and minority electrons in a ferromagnetic metal. An important magnetic contrast, up to several hundred percent at room temperature, can be thus observed. For performing magnetic imaging, the one of the ferromagnetic layers is magnetically saturated, acting as an “analyzer” of the hot electrons “polarized” when crossing the magnetic structures of the other ferromagnetic layer.

Multilayers were deposited in an ultrahigh vacuum (UHV) chamber (base pressure $<10^{-9}$ mbar) using an e-gun evaporator. The hydrogenated Si(111) surface was used as a substrate. Initially a Au layer of some nanometers was deposited to form a homogeneous Schottky interface. Afterwards, a Cu/F1/Cu/F2/Cu multilayer was deposited, with F1 and F2 being 2 nm thick ferromagnetic layers (Co or NiFe). All the experiments were performed at room temperature using a UHV-STM. Samples containing single ferromagnetic layers have been

also fabricated and measured, in order to serve as a reference for analyzing the hot electron transport in the spin valves.

First, the hot electron transport properties of the single Co and NiFe layers will be presented. The transmission study as a function of the layer thickness yields the hot electron mean free path in each metal. By comparing the results obtained on the single ferromagnetic layer samples with those of the spin valve samples, it is possible to separate the hot electron mean free path as a function of their spin, in the range 1 to 2 eV above the Fermi level [5]. It is demonstrated that the mean free path is 2 to 3 times longer for the majority electrons. Consequently, in the spin valve samples, a transmission contrast of 50 to 200% between the parallel and anti-parallel state is observed, well above the giant magnetoresistance value measured for the same samples (approximately 1%).

Magnetic images obtained from the spin valve samples, will be also discussed [5]. The magnetization reversal of the Co and NiFe layers by nucleation and growth is observed as a function of the externally applied magnetic field. The observation of 360° domain walls in the Co layers (see Fig. 2) will be discussed in detail. The microscope resolution allows discussing their shape and size. It is demonstrated that the domain wall has an asymmetric profile when a magnetic field is applied in a non-collinear direction with respect to the domain wall direction. These results are compared to micromagnetic calculations, and it is shown that the microscope magnetic resolution is better than 50 nm.

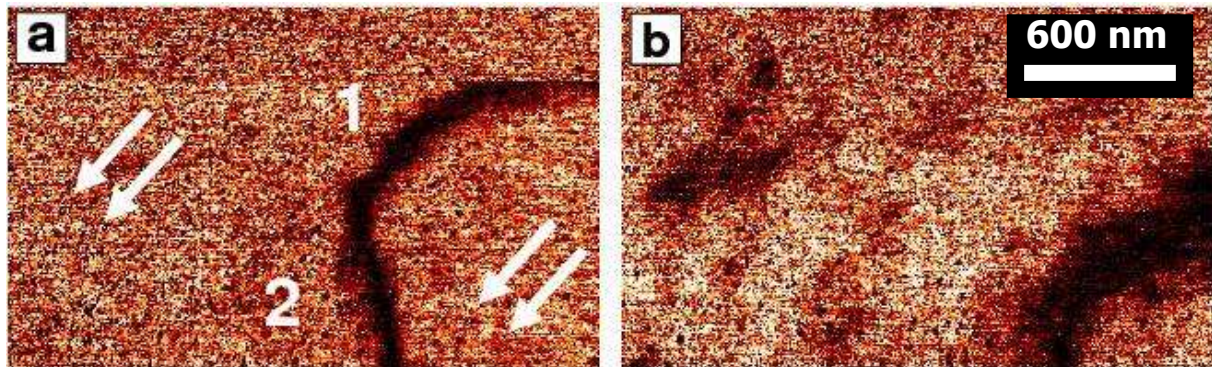


Figure 2: BEEM imaging of a Co/Cu/Co. The scanning area is $2.4 \times 1.5 \mu\text{m}^2$. (a) Imaging in a 100 Oe externally applied magnetic field. The white arrows indicate the direction of the magnetization in the two magnetic layers, which is saturated by the applied field. The observed dark structure corresponds to a 360° domain wall in one of the two Co layers. Part 1 corresponds to a domain wall collinear to the direction of the applied magnetic field and presents a symmetric profile; part 2 corresponds to a non-collinear to the applied field domain wall and presents an asymmetric profile. (b) Imaging in a 20 Oe externally applied magnetic field (same field direction and scanning area as before) obtained after image (a). The domain wall has been displaced and it is less narrow than in the previous image.

In conclusion, the capacity of our microscope to perform spin-dependent hot electron transport studies in magnetic multilayers and to obtain high resolution magnetic domain images has been demonstrated. This microscope allows for precise studies of magnetic configurations in multilayers and nanostructures.

- [1] Binnig G., Rohrer H., IBM J. Res. Develop. 30, 279 (1986).
- [2] Rippard W.H. and Buhrman R.A., Phys. Rev. Lett 84, 971 (2000).
- [3] Monsma D.J. et al., Science 281, 407 (1998).
- [4] van Dijken S. et al., Appl. Phys. Lett. 83, 951 (2003).
- [5] Kaidatzis A. et al., Phys. Rev. B 78, 174426 (2008).

Acknowledgments The authors gratefully acknowledge the help of J. Ferré for magneto-optical characterization, M. Aprili for e-beam evaporation and the loan of his deposition setup, and A. Gloter for band-structure calculations. Financial support was provided by C’Nano Île de France (STCalib project). A.K. received funding from the EC Marie Curie host training site Emergent CondMatPhys (Grant No. MEST-CT-2004- 514307).

Exchange Bias Effects in Co nanoparticles dispersed in a Mn matrix

K. N. Trohidou^{1*}, M. Vasilakaki¹, J. A. Blackman², D. Fiorani³, A. M. Testa³, N. Domingo^{3,4} and C. Binns⁵

¹ NCSR 'DEMOKRITOS', Institute of Materials Science, Athens, Greece

² Department of Physics, Reading University, RG6 2AF, Reading, UK

³ ISM-CNR, Institute of Structure of Matter, Area della Ricerca di Roma, Via Salaria km29.500, C.P. 10-00016 Monterotondo Scalo, Roma, Italy

⁴ Department of Fisica Fonamental, Universitat de Barcelona, Diagonal 647, 08028 Barcelona, Spain

⁵ Department of Physics and Astronomy, University of Leicester, Leicester LE1 7RH, UK

*trohidou@ims.demokritos.gr

Recently it has been recognized that gas-phase clusters can be deposited on to surfaces to produce high-performance magnetic films [1]. If this is done in conjunction with an atomic vapour from a conventional MBE-type source the nanoparticles become embedded in a matrix of choice. This method has been labelled the Low Energy Cluster Beam deposition (LECBD) technique [2]. We study Co nanoparticles of 1.8 nm diameter dispersed in a magnetically disordered spin glass-like Mn matrix produced by the LE CBD technique. In these systems there is significant alloying between the ferromagnetic cluster material (Co) and the antiferromagnetic matrix (Mn), which introduces new possibilities and different interface exchange coupling effects [3].

We model the behaviour of the Co@Mn assemblies and we compare it with the experimental findings. We consider N identical magnetic particles (grains), with spherical shape and diameter D placed at random on the nodes of a hexagonal lattice. In order to take into account the core/shell structure of these nanoparticles and the contribution of the interface in the magnetic behaviour of the assembly, we consider that each nanoparticle consists of four regions. A ferromagnetic Co core with uniaxial anisotropy, a ferromagnetic Co rich Co/Mn alloy interface with uniaxial anisotropy, an antiferromagnetic Mn rich Co/Mn alloy interface and an antiferromagnetic Mn spin glass like shell with random anisotropy. The Co cores interact via long-range dipolar forces.

Results for the hysteresis loop are given at the Fig. 1 for Co volume fraction 5% after applying a cooling field $H=0.4(\text{J/g}\mu_B)$. At the same figure we have plotted for comparison the hysteresis loop for the Co nanoparticles in an Ag matrix at the same volume fraction. In this case for the description of the randomly placed Co nanoparticles in the Ag matrix we have used the single spin Stoner Wohlfath type model, which we have described elsewhere [4].

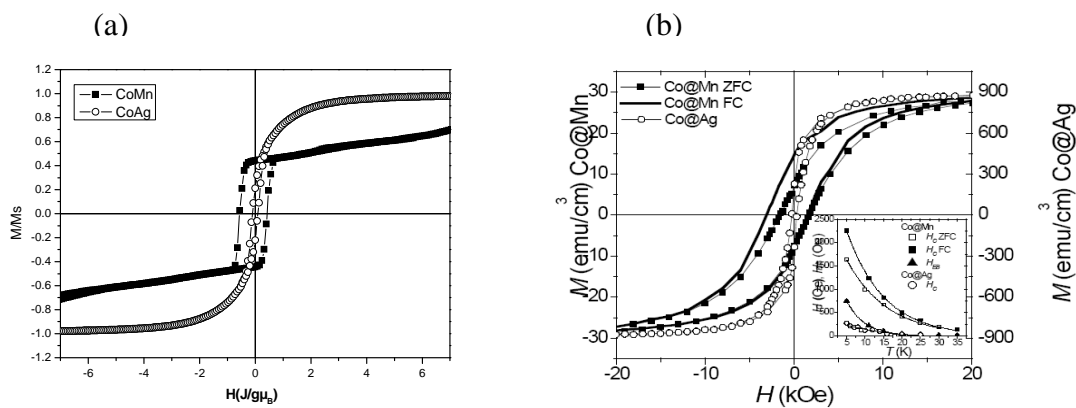


Fig. 3 Hysteresis loops of (a) Monte Carlo simulations and (b) of experiment at 5 K [3] for Co/Mn and Co/Ag nanoparticle assemblies.

We observe that the hysteresis loop is shifted for the Co@Mn nanoparticle assemblies in contrast to the hysteresis loop for Co@Ag assemblies which is symmetric. The Co@Mn nanoparticle assemblies have much higher coercive field ($H_c = 0.495 \text{ J/g}\mu_B$) from the Co@Ag nanoparticle assemblies ($H_c = 0.096 \text{ J/g}\mu_B$) and an exchange bias field $H_{ex} = 0.08 \text{ J/g}\mu_B$. Fig.1(a) describes the data of Fig.1(b) reasonably well confirming the description of the Co nanoparticles in the Mn matrix by taking into account the Co-Mn alloying that is responsible for the low Co moments.

In Fig. 2 we have plotted the ZFC curve for Co@Mn and Co@Ag nanoparticle assemblies. We observe that the T_{max} is much higher in the case of the Co@Mn assemblies in agreement with experimental findings that give a T_{max} of Co@Mn almost three times bigger than T_{max} for Co@Ag.

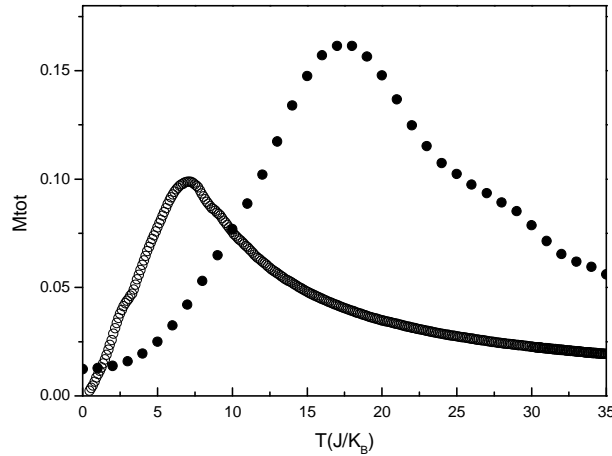


Fig. 4 ZFC curves for Co@Mn (full circles) and Co@Ag (open circles) nanoparticle assemblies.

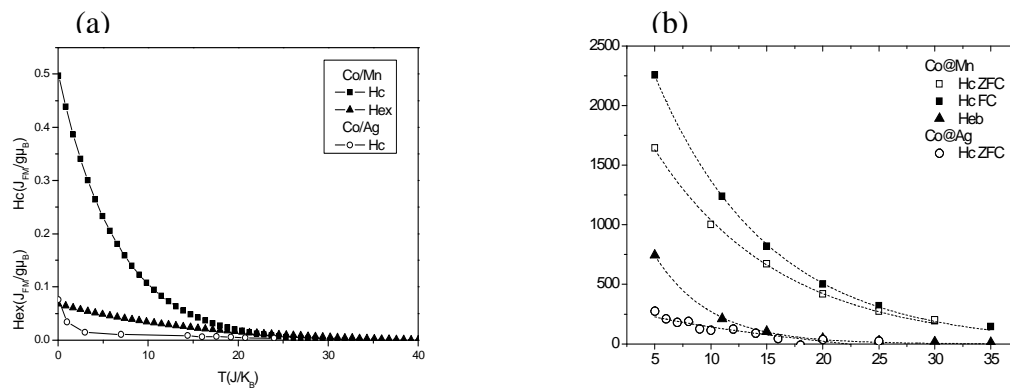


Fig. 5 Temperature dependence of the coercive and the exchange bias field of (a) Monte Carlo simulations and (b) experimental results for Co@Mn and Co@Ag nanoparticles assemblies (the solid lines are the exponential decay fitting) and of Hc for the Co@Ag nanoparticle assemblies (the solid line is the power law $H_c(1-a^t)$ fitting).

We observe that indeed the Hex and Hc exhibit an exponential decay with the temperature in agreement with the experimental findings. In the case of Co@Ag nanoparticle assemblies the solid line gives a power law fitting $H_c(1-a^t)$, with the exponent t differing from the $-1/2$ power of the Kneller and Luborsky [5] thermal decay of Hc.

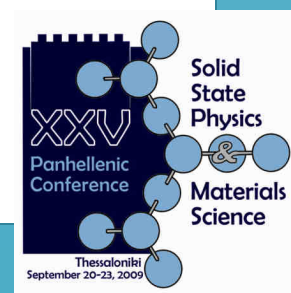
- [1] Binns C., Trohidou K. N., Bannsmann J., Baker S. H., Blackman J. A., Bucher J. P., Kechrakos D., Kleibert A., Louch S., Meiwes-Broer K. H., Pastor G. M., Perez A. and Xie Y., J. Phys. D: Appl. Phys. 38, R357 (2005).
- [2] Perez A., Melinon P., Dupuis V., Jensen P., Prevel B., Tuailon J., Bardotti L., Martet C., Treilleux M., Broyer M., Pellarin J., Vaillat J. L., Palpant B. and Lerme J., J. Phys. D: Appl. Phys. 30, 709 (1997)
- [3] Domingo N., Testa A. M., Fiorani D., Binns C., Baker S., Tejada J., J. Magn. Magn. Matt. 316, 155(2007)
- [4] Binns C., Maher J., Pankhurst Q.A., Kechrakos D. and Trohidou K.N., Phys. Rev. B 66, 184413 (2002)
- [5] Kneller E. F. and Luborsky F. E., J. Appl. Phys. 34, 656 (1963).

Acknowledgments The work was supported by EU STREP Project No. NMPCT-2004-013545 Nanospin (Self-Organized Complex-Spin Magnetic Nano-Structures).

Session TU5

CULTURAL HERITAGE MATERIALS & INTERDISCIPLINARY PHYSICS

Tuesday, 22 September 2009, 18⁰⁰-19³⁰



The use of iron oxide nanoparticles in hyperthermia

Theodoros Samaras^{1*}

¹*Department of Physics, Aristotle University of Thessaloniki*

**theosama@auth.gr*

Introduction

Hyperthermia is a cancer treatment modality used as an adjunct to established therapies, like radiotherapy and chemotherapy. There are several techniques to induce hyperthermia, including the infusion of hot water for peritoneal and systemic hyperthermia, capacitive heating and inductive heating, radiofrequency and microwave radiation and ultrasound. Hyperthermia should be distinguished from thermal ablation. The latter works with a temperature rise greater than 50°C and by direct cell killing inside the tumor, whereas the former, also known as mild temperature hyperthermia or MTH, works in the temperature range of 39°C to 42°C by inducing more subtle effects.

Among the biophysical mechanisms, which render MTH effective, the most important ones are (1) the induction of a heat shock response and immune system stimulation, and (2) the increased blood flow in the tumor. The tumor core is frequently resistive to conventional treatments, like radiotherapy (since it is hypoxic) and chemotherapy (due to low drug supply). However, the increased blood perfusion induced by hyperthermia can enhance the damage of tumor cells at its center. Although hyperthermia has proven its efficacy with numerous phase III clinical trials [1-2], it has not gained the wide acceptance one would expect.

The major technical problem, which has delayed its promulgation, is the difficulty in heating the tumor region to the intended temperature while sparing the normal tissue. It appears that this problem can be solved by introducing the concept of intracellular hyperthermia; it is possible to deliver submicron magnetic particles inside the tumor cells and let them generate heat under an alternating magnetic field (AMF).

Nanoparticle properties

Among the nanoparticles that can be used for this purpose iron oxides, namely magnetite (Fe_3O_4) and maghemite ($\gamma\text{-Fe}_2\text{O}_3$) are the most frequently used ones, due to their low toxicity and their known pathways of metabolism. However, there are other properties, such as biocompatibility, injectability and high absorption in the tumor cells, which the nanoparticles must possess in order to be used in hyperthermia. The size of nanoparticles determines to a large extent their suitability for the method in vivo.

There are two main issues that need to be tackled if the nanoparticles are to be injected in the main blood stream, i.e. glomerular filtration and opsonization. Kidneys will rapidly clear away from the blood particulate matter with a molecular weight less than about 40kDa (10nm) [3]. On the other hand, blood protein binding to the particles (opsonization) will make them a target of macrophage cells, which will remove them from the blood stream through phagocytosis and lead to their accumulation in organs like the liver, spleen, bone marrow and lymph nodes. Even when nanoparticles are wrapped within polymers, like dextran, starch or polyethylene glycol, a large percentage of them will eventually end up in these organs.

Delivery to the target

The most obvious way to avoid the above mentioned disadvantages of systemic nanoparticles administration is to inject them directly into the tumor. However, this is not always possible due to tumor location. Moreover, the dense extracellular matrices present in tumors do not allow in many cases the injection of enough nanoparticles to achieve the desired thermal result. It is, therefore, important to examine the delivery mechanisms of nanoparticles to the tumor target. If they stay in the blood stream long enough, there is a slow accumulation of them in the tumor for two reasons, namely extravasation, due to vascular leakiness, and faulty lymph drainage. The latter is responsible for the high interstitial pressure, which is another difficulty with direct injection. As a consequence, extravasated nanoparticles remain in the perivascular area and do not penetrate deeply into the tumor.

Another technique to deliver magnetic nanoparticles to the tumor site is termed ferromagnetic embolization hyperthermia [4]. Using this approach, the nanoparticles are injected to the feeding artery that supplies the tumor with blood. An excellent site of implementation for this technique is the liver, where tumors, contrary to the normal liver parenchyma, mainly derive their blood supply from the hepatic arterial system [5]. To facilitate cell adsorption of magnetic nanoparticles some researchers have proposed the use of magnetic cationic liposomes (MCL) [6]. The particles are wrapped in a phospholipid bilayer (liposome) with a positive surface charge, which

increases adsorption to tumor cells. Finally, the fabrication of antibody-conjugated nanoparticles is the best practice for the preferential accumulation inside the tumor [7].

Heat generation mechanism

If they are used in their pure form, i.e. not coated with a material to impede opsonization, the nanoparticles tend to agglomerate, building structures of a larger size, a fact which negatively influences their biomedical and magnetic properties. Ferromagnetic resonance (FMR) of iron's unpaired electron is a physical mechanism, which can produce heat. It takes place in the frequency range of 1MHz to 1000 MHz. Hysteretic heating can also occur in the frequency range of 50kHz to about 1MHz.

However, in the clinical practice and the experiments conducted so far, heating appears to be generated predominantly by the Néel and Brownian relaxations, since the sizes of the used nanoparticles is rather small (less than 30nm). Rosenweig [8] has proposed that the theoretical heat dissipation is proportional to the frequency and the squared strength of the externally applied AMF. Therefore, one would expect that high values of heat generation rates, expressed in terms of specific absorption rate (SAR), in the tissues could be achieved by increasing the magnetic field amplitude and frequency. However, this procedure is limited by the initiation of eddy currents in the patient's body. Eddy currents increase with the cross-sectional area of the body volume subjected to the AMF. This is perhaps why during the clinical application of the technique patients tolerated better the therapy in the head region, than in the pelvic and the upper thoracic regions, where they complained for discomfort (pain) [9]. Typical values of the AMF strength used at 100kHz are 8.5kA/m for tumors in the head (glioblastoma) and 3-5kA/m for pelvic tumors. The SAR for an 8kA/m field in a glioblastoma can reach a value larger than 700W/kg.

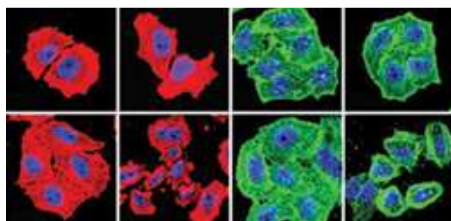


Fig.1. Cells exposed to nanoparticles (second row) and a magnetic field (second and fourth columns) display disrupted cytoskeletons [10]



Fig.2. Iron-bearing nanoparticles injected directly into a brain tumor, heated using a focused magnetic field, weaken and even kill cancer cells [11]

Limitations of treatment

As mentioned above the main limitation of the treatment is the generation of eddy currents. Another exclusion criterion is the presence of metallic or active implants at a small distance from the treatment area (e.g. artificial hip joints for pelvic treatments, teeth's amalgam fillings or gold crowns for head and neck tumors, or cardiac pacemakers and implanted defibrillators).

References

- [1] van der Zee J., van Rhoon G.C., Int. J. Hyperthermia 22, 229 (2006).
- [2] Moyer H.R., Delman K.A., Int. J. Hyperthermia 24, 251 (2008).
- [3] Oliver 3rd J.D., Deen W.M., Bull. Math. Biol. 56, 369 (1994).
- [4] Moroz P., Jones S.K., Winter J., Gray B.N., J. Surg. Oncol. 78, 22 (2001).
- [5] Archer S.G., Gray B.N., Br. J. Surg. 76, 545 (1989).
- [6] Shinkai M., Yanase M., Honda H., Wakabayashi T., Yoshida J., Kobayashi T., Jpn. J. Cancer Res. 87, 1179 (1996).
- [7] Shinkai M., Le B., Honda H., Yoshikawa K., Shimizu K., Saga S., Wakabayashi T., Yoshida J., Kobayashi T., Jpn. J. Cancer Res. 92, 1138 (2001).
- [8] Rosensweig R.E., J. Magn. Magn. Mater. 252, 370 (2002).
- [9] Thiesen B., Jordan A., Int. J. Hyperthermia 24, 467 (2008).
- [10] Drake Ph., Cho H.-J., Shih P.-S., Kao C.-H., Lee K.-F., Kuo C.-H., Lin X.-Z. and Lin Y.J., J. Mater. Chem., 17, 4914 (2007).
- [11] w1.siemens.com/.../molecular_therapy.htm .

Study of the Effect of a Uniform Electric Field on the Bond Lengths and the Electronic Distribution of Diatomic and Polyatomic Molecules

P. Papanikolaou, P. Karafiloglou*

Faculty of Chemistry, Department of General and Inorganic Chemistry, Aristotle University of Thessaloniki, POB 135, 54124 Thessaloniki, Greece

* *karafilo@chem.auth.gr*

The study of molecular systems under the experience of an electric field, both theoretically and experimentally consists an important issue in chemistry, physics and biology. Initially, such studies were impelled from the will to gain a deeper insight into the dynamics of chemical reactions through the control of the orientation of the participating molecules. In that framework, recent studies of Shaik et al[1],[2] have revealed that an electric field can affect the energetics of different reaction paths and so to drive a reaction towards the desired products. The authors characteristically mention that an electric field can play the role of a catalyst for a reaction by lowering the activation barriers and in that way control the product formation. Concerning the interest of physics and biology in electric field studies, we report recent investigations on the impact of an electric field on the electronic structure of molecular crystals[3] and the structure of water clusters[4]. For the latter case, it is revealed that an electric field can affect the formation of water assemblies and change their structure from that of a ring to an open water-wire scheme with tremendous biological importance.

Analogous theoretical and experimental efforts from the point of solid state chemistry and physics have opened the way for the design of new materials with potential applications on molecular electronic devices and machines fabrication. Troisi, Ratner, Ho and Donhouser report that the electric field produced by two electrodes can turn the conformation of a molecule which resides between them and by consequence change its molecular conductivity [5]. The understanding of such phenomena holds an important position in the design of molecular junctions and diodes and the rationalization of electron transport processes through them. In the same framework also, it is reported that electric fields can govern the controlled rotation of molecular motors[6].

Furthermore, electric fields are directly related with lasers. Lasers are reported to maintain a substantial role in the attainment of specific molecular excited states [7] with further interesting in the design of quantum computers, an idea which looks becoming reality in the years to come.

Different research groups[8],[9] also bear that strong local electric fields are often present in chemical systems containing ionic and polar entities and as such, it is of great importance to be able to predict their effects on the electronic structure and the geometry of molecular species.

In the present work we examine theoretically the influence of the strength and the direction of a uniform electric field on the bond lengths and the electronic distribution of the molecules HF, HCl, CH₄, SiH₄, H – C ≡ C – H, CH₃Cl, SiH₃Cl, H – C ≡ C – CH₃ and H – C ≡ C – SiH₃. For that reason, we pursue on the geometry optimization of the above molecules (RHF/6-31G*/MP2/6-31G*) in the presence of different strengths and for two different directions of the applied electric field. These optimizations are performed using the GAMESS(US)[10] suit of codes which allows the calculation of molecular wavefunctions under the experience of an electric field.

The electronic distribution of the molecules is expressed by both electrostatic charges of the atoms consisting the molecules and the resonance structures of a chemical bond as they are described in the Valence Bond Theory of Pauling[11]. The weights of the resonance structures of the bonds under study are calculated from the respective molecular orbital (MO) wavefunctions by applying the Polyelectron Population Analysis (PEPA)[12] technique in the basis of the nonorthogonal hybridized natural orbitals (PNHOs)[13]. For the diatomic molecules HF and HCl as well as H – C ≡ C – H, the field is applied along the molecular axis for both directions while for the rest of the molecules the field is applied on the C₃ symmetry axis, again for both directions. From the correlation of the results it is revealed that for a typical simple bond, the application of a Favorable electric field, as it is determined from the main ionic structure of the bond, leads to an increase in the difference of the weights of the two ionic structures of the bond in comparison with the existing difference in the absence of the field and to an increase of the bond length as well. The application of an Unfavorable electric field, in contrast, seems to decrease both the difference between the weights of the two ionic structures and the length of the bond, with a potent existence of a minimum for the later. The only exception in the above generality consists the C_{sp3} – H bond which follows the aforementioned concerning the influence of the field on the weights of the ionic structures but presents a decrease in the bond length until 0.02 a.u. (1 a.u. = 5.1423e11 V/m) strength of a Favorable electric field while an Unfavorable electric field provokes a continuous increase on it. For the triple bonds, it is revealed that the C ≡ C bond of propyne seems to follow the behavior of the simple bonds for both its

ionic structures and bond length. The corresponding bonds of acetylene and silyloacetylene are characterized by a continuous increase in both their length and weight-difference of the ionic structures of their π -components under the influence of an electric field. This is predictable for the centrosymmetric bond $C \equiv C$ of acetylene but not for the triple bond of silyloacetylene.

We also pursue in the investigation of the effects of an applied electric field on the hyperconjugation phenomenon, as it emerges in the molecules studied here. As our scope is to examine if and in which extent, the different delocalization effects appearing into the selected molecules can be controlled by an electric field, we estimate, using the NBO program[14], the delocalization energies $E^{(2)}$ and the weights of well selected localized electronic distributions which describe the electron transport from one region of the molecule to another, as they are determined by the corresponding NBOs of the main Lewis structure, under the experience of different strengths and two directions of an electric field. Precisely, the description of the electron delocalization in the frame of resonance theory includes the calculation of the weights of localized wavefunctions – electronic distributions which are represented by localized Slater determinants. Such wavefunctions may be achieved from the usual MO-wavefunctions through Moffitt's theorem[15] and can comprise any type of orbitals which can be written as a linear combination of the basis functions. In our case, we use the NBOs[13b] of the main Lewis structure and the estimation of the weights of this kind of determinants rests on the PEPA methodology which uses both Moffitt's theorem and the second quantization formalism to introduce conditions for electron holes. The results reveal that both the strength and the direction of the applied field can be used in the control of the electronic delocalization from one region of a molecule to another. Important is also the fact that while for the silyloacetylene molecule in the absence of a field, there is not any type of delocalization involving the Si – H bonds and the π -system of the triple bond, the application of a field can activate that hyperconjugation phenomenon in both directions.

Finally, in the framework of the new branch of Molecular Electronics and based on our conclusions concerning the impact of a field on the hyperconjugation phenomenon, we propose two molecular systems which, under the influence of an electric field can act as molecular logic gates.

- [1] Sason Shaik, Sam P. de Visser and Devesh Kumar, *J. Am. Chem. Soc.* 2004, 126, 11746 – 11479.
- [2] Hajime Hirao, Hui Chen, Maria Angels Carvajal, Yong Wang and Sason Shaik, *J. Am. Chem. Soc.* 2008, 130, 3319 – 3327.
- [3] Jaroslav Tóbič, Andrea Dal Corso, Sandro Scandolo, Erio Tosatti, *Surface Science* 566 – 568 (2004) 644 - 649 .
- [4] Young Cheol Choi, Chaeho Pak and Kwang S. Kim, *J. Chem. Phys.* 124 094308 (2006).
- [5] Alessandro Troisi and Mark A. Ratner, *J. Am. Chem. Soc.* 2002, 124, 14528 – 14529 and references cited therein .
- [6] a) Gwénaél Rapenne, *Org. Biomol. Chem.*, 2005, 3, 1165 – 1169; b) Alexandre Carella, Gwénaél Rapenne and Jean-Pierre Launay, *New J. Chem.*, 2005, 29, 288 – 290.
- [7] Sitansh Sharma, Purshotam Sharma and Harjinder Singh, *J. Chem. Sci.* 119, 2007, 433 – 440 and references cited therein
- [8] Kersti Hermansson and Harald Tepper, *Mol. Phys.* 1996, 89, 1291 – 1299.
- [9] a) Hiroshi Nakatsuji, Toshiaki Hayakawa and Teiji Yonezawa, *J. Am. Chem. Soc.* 1981, 103, 7426 – 7432; b) Yasushi Honda, Hiroshi Nakatsuji, *Chemical Physics Letters* 293 (1998) 230 – 238.
- [10] Michael W. Schmidt, Kim K. Baldridge, Jerry A. Boatz, Steven T. Elbert, Mark S. Gordon, Jan H. Jensen, Shiro Koseki, Nikita Matsunaga, Kiet A. Nguyen, Shyjun Su, Theresa L. Windus, Michel Dupuis and John A. Montgomery, Jr., *J. Comput. Chem.* 14, 1347 – 1363, 1993.
- [11] a) Philippe Hiberty, Sason Shaik, *J. Comput. Chem.* 28, 137 – 151, 2007; b) Gjergji Sini, Philippe Maitre, Philippe Hiberty and Sason Shaik, *J. Mol. Struct. (THEOCHEM)*, 229, 163 – 188 (1991) .
- [12] Ramón M. Parrondo, Padeleimon Karafiloglou, Enrique Sánchez Marcos, *Int. J. Quantum Chem.* 52, 1127–1144 (1994).
- [13] a) J. P. Foster and F. Weinhold, *J. Am. Chem. Soc.* 1980, 102, 7211 – 7218; b) Alan E. Reed, Larry A. Curtiss, Frank Weinhold, *Chem. Rev.* 1988, 88, 899 – 926.
- [14] NBO 5.0. E. D. Glendening, J. K. Badenhoop, A. E. Reed, J. E. Carpenter, J. A. Bohmann, C. M. Morales and F. Weinhold, *Theoretical Chemistry, Institute, University of Wisconsin, Madison* (2001).
- [15] a) Moffitt, W. *Proc R Soc* 1953, A218, 486; b) Karafiloglou P., Ohanessian, G. *J Chem Ed* 1991, 68, 583.

Wall painting materials and technique: The case of the famous iconographer Onoufrios

E. Pavlidou¹, M. Arapi², N. Civici³, T. Zorba¹, F. Stamati⁴, K.M. Paraskevopoulos¹

¹ *Department of Physics, Aristotle University, GR-54124 Thessaloniki, Greece*

² *Institute of Cultural Monuments, Tirana, Albania*

³ *Institute of Nuclear Physics, Tirana, Albania*

⁴ *Institute of Popular Culture, Tirana, Albania.*

elpavlid@auth.gr

In the 16th century, regarding the iconography in the former Byzantine area, besides the School of Crete, and besides Francos Catelanos and his school, a third artistic personality who created his own school too, Onoufrios, appeared in the central Albania and expanded his activity as a painter till northern Greece, the nearby areas, Ohrid etc. Inscriptions documenting the works of Onoufrios are found in some of the churches that he decorated with wall paintings: “St. Apostles” (1547) Kastoria Greece, “St. Nicolas” Shelcan Albania, “St. Paraskevi” (1554), Valsh Albania, while are attributed to him the church of “St. Theodores” in Berati, Albania (before 1547) and others. He is one of the best icon painters of the whole Balkan region and the best painter that had ever worked in Albanian territory. Onoufrios managed to combine the local painting tradition with the best tradition of the eastern (Paleologian) and western (Italian) schools, resulting in a realistic and natural drawing. He is the creator of the “Berati School” that expanded in other parts of the peninsula. Ground and paint layers were examined using micro-FTIR, Optical Microscopy, TXRF and SEM-EDS, to characterize materials and methods used by the artist to create these works. Our findings in each church are discussed and compared each other in order to understand how and with what material and resources the painter worked, and how he developed his technique.

Experimental details: A total number of 24 kind of samples that include plasters and pigments of different colours were collected from the three churches. In each of the sampling points, small pieces of pigment and plaster (about 5 mm²) were removed with a scalpel and placed in small plastic vials with hinged caps to avoid contamination, these being the samples for FTIR, SEM-EDS and optical microscopy, while a small amount of material was also rubbed off the same spot of painted area by means of a dry cotton bud (a Q-tip) that was next placed in a clean plastic bag, these being the samples for TXRF. Due to the destructive nature of sampling, the samples were carefully chosen from areas that had no aesthetic or iconographic value for future reconstruction. A common characteristic of the wall paintings in the studied churches is related with their state of the preservation. Apart from the damages, the remaining fragments of the wall paintings seem to suffer –more or less- a colour change. Looking attentively it can be observed topically white areas as a thin layer. This phenomenon, related probably with the environmental pollution, is observed also in other churches and is discussed in the continuation.

Results and discussion: Plaster: In the FTIR spectra of all plasters, a common characteristic is the strong presence of calcium carbonate with a small participation of gypsum and silicon compounds. The existence of calcite is identified from the bands at 1445, 866 and 712cm⁻¹, while the bands at 602, 668, 1146, 3406 and 3550cm⁻¹ are attributed to the bending and stretching modes of the SO₄ group of gypsum. The SEM-EDS analysis of plaster samples from all churches show that calcium is the element with the highest concentration associated with smaller amounts of magnesium, silicon and partially gypsum [1,2]. Therefore the FTIR and EDS results are in good agreement. Similar results were obtained from TXRF measurements of the plaster samples.

Deterioration: The surface of the wall paintings was covered topically by white areas having a crystalline texture. The analysis of the effected areas identified the presence of gypsum in all churches and calcium oxalate, except “St.Nikolaos”. These results indicate the presence of two types of deterioration: (i) The alteration of calcite (CaCO₃) –which is in high amount in wall paintings- to gypsum (CaSO₄ .2H₂O) due probably to acid air pollution (sulphur oxides), (ii) Biodeterioration by lichens which cause -except of mechanical damages- and chemical damages by excretion of oxalic acid. [3,4]

Blue pigments: The presence of copper in great amounts from the TXRF and EDS results of the blue specimen gives us a strong indication that the pigment is azurite (fig. 1). The comparison of the obtained FTIR spectrum of the sample, with the spectrum of azurite from the spectral library, confirms that the used blue pigment is azurite.

Green pigments: Green Earth could be recognized from the comparison of the results of EDS and FTIR methods. The presence of Fe, Si and Mg from EDS analysis of green samples, leads to the conclusion that the pigment can be attributed to Green Earth. From a detailed examination of FTIR spectra, the four narrow bands

OH stretching in the $3610\text{-}3530\text{cm}^{-1}$ region and the area $1100\text{-}900\text{cm}^{-1}$ of Si-O stretching lead us to characterize the green earth as celadonite.

Red pigments: Elemental analysis on the red coloured layers from St. Nikolaos and St. Paraskevi churches identified Fe along with Al and Si, indicating the existence of iron oxide as the possible material producing the red colour. Moreover the coexistence of the alumino-silicate materials guide to the consideration that the pigment is red ochre. This result is supported with the FTIR spectra of the above samples that are almost identical with the spectrum of the red ochre from the spectral library. The red samples from St. Theodori church present a difference referring to the use not only red ochre but also cinnabar, especially for the light red areas. The identification of cinnabar is based in the presence of Hg and S as major elements in the EDS results. Hg was also detected by TXRF.

Table 1: The used pigments from the painter Onoufrios

	Saint Theodori	Saint Nikolaos	Saint Paraskevi
Green	Green earth	-	Green earth
Blue	Azurite	-	-
Yellow	Yellow ochre	Yellow ochre	Yellow ochre
Red	Red ochre +/- Cinnabar	Red ochre	Red ochre
Brown	Red ochre	-	Red ochre
White	Calcite	Calcite	Calcite
Black	Carbon black	Carbon black	Carbon black
Grey	-	-	Calcite + Carbon black

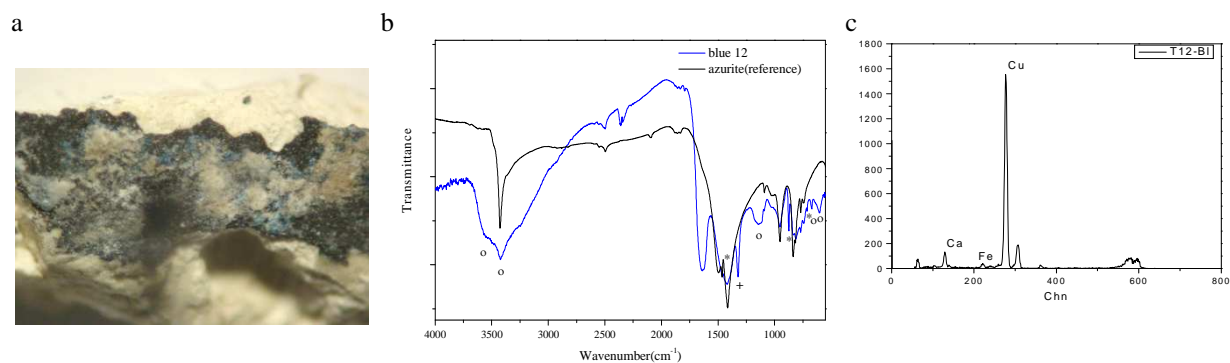


Fig 1: Sample T12-B1 (a) optical photograph, (b) FTIR transmittance spectra (o for gypsum, + for calcium oxalate and * for calcite), (c) TXRF

Conclusions:

The chosen analytical methods permitted the identification of plasters and pigments of the three monuments. The plaster of all the wall paintings, made with the fresco technique, was generally characterized by the strong presence of calcite with a small participation of gypsum and silicon compounds. Plaster samples from the churches of “St.Theodori” and “St.Nikolaos”, taken from the wall-paintings of anonymous painters, showed more or less no participation of gypsum, leading thus to the conclusion that gypsum is a characteristic of Onoufrios’ wall painting technique. As far as concerned Onoufrios’ technique, he was using for the wall paintings the fresco technique while the inclusion of gypsum in the plaster is a characteristic of his way of painting. As it is testified from the Table 1, Onoufrios used the same type of pigments for the same colour shades in all three churches (azurite, green earth, red ochre, cinnabar, yellow ochre, carbon black, calcite) with the exception of cinnabar, for the rendering of red colour, detected only at the church of “St.Theodori”.

Deterioration of the wall paintings was analyzed and the presence of gypsum in all churches and calcium oxalate, except “St.Nikolaos”, was detected .

REFERENCES

- [1] G. Biscontin, M. Pellizon Birelli, E. Zendri: *J. Cultural Heritage* 3, 31 (2002).
- [2] D. Alfano, C. Scarabino, D. Inverso, A. Proto: *Annali di Chimica* 95 (2005).
- [3] R. Van Grieken, F. Delalieux, K. Gysels: *Pure & Appl. Chem.*, 70 No12, 2327 (1998).
- [4] G. Horta, I. Ribeiro, L. Afonso: *The ‘Calvary’ of S. Francisco’s church in Leiria: Workshop practice in a Portuguese late gothic wall painting*, *Contributions to the Dublin Congress of Painting Techniques History, Materials and Studio Practice*, International Institute for Conservation of Historic and Artistic Works, Edited by A. Roy and P. Smith, p 65 (1998).

Random Walk in Complex Systems with the Particle Diffusion Model - PDM

M. Maragakis^{1*}, S. Carmi², P. Argyrakis¹ and S. Havlin²

¹ *Department of Physics, University of Thessaloniki, 54124 Thessaloniki, Greece*

² *Minerva Center & Department of Physics, Bar-Ilan University, Ramat Gan 52900, Israel*

*mmara@kelifos.physics.auth.gr

Communication networks in real systems in several cases have limited resources. The bandwidth between the nodes (computers, cell phones or other wireless devices) allows for the transmittance of data with specific rates. The data transmitted can, and in most cases have, different importance for the user. Some data are more useful than other. An example can be a peer to peer network, like skype, where video and audio data are transmitted along with text. The text can be considered as more important than both audio and video, with audio being more important than video. In a limited bandwidth situation (network overload or broken main connection) we may be required to at least have the ability to write. This means that priority must be given to the transmission of text.

We use a model for the motion of two types of particles, A and B , with priority, which can represent any type of information [1]. We investigate several protocols for the diffusion of particles, based on either a random choice of site or that of a randomly chosen particle out of both species. We define them respectively as “site” and “particle” protocols. In all cases, when both species coexist in the same space, the movement of A takes precedence over that of B . Assigning an opposite priority would simply produce symmetric results. We apply strict priority of A over B , meaning that B will not move until all coexisting A have left the same site. To find the probability of a B leaving the site we must therefore find the probability of a site being empty of A , f_0 .

We initiate our study from lattices and then move on to more complex systems like networks (random graphs, scale-free, fractal and real world networks). Analytic and simulation results confirm that the site protocol depends inversely on the density of A , ρ_A , while the particle protocol exhibits an inverse exponential behavior. This means that when the particle protocol is applied in lattices, the system tends to go into an equilibrium state much faster than with the site protocol and the mobility of B is lower. Results show that both species execute normal diffusion, although the B move slower than the A . We calculate the normalized diffusion coefficient Φ of these systems and find the dependence on density (Figure 1).

In networks, for the particle protocol, it is found that the number of sites empty of the high priority population depends exponentially on the degree, k , (Figure 2). As previously in lattices the motion of either species is also strongly related to the density of A . It is interesting though to mention that this dependence on either parameter is the same in various kinds of networks with totally different topologies like random graphs and scale-free. The movement of B decreases exponentially with the degree, while for A it increases. This is due to two reasons: a) the higher the degree, the more likely that a B will lose its movement, thus giving it to an A and b) the higher the degree, more A will move through this node and particles from that node will be chosen more frequently. Therefore, the installment of priorities leads to a faster movement of A and the concentration of B at the hubs, where their motion is hindered. This can be easily seen in the waiting time distribution for B particles of a specific degree (Figure 3). It is obvious that for low node degree the waiting time of B is short, while for high degree nodes it is significantly increased. Simulation results from the average waiting time, $\langle t \rangle$, versus the degree (Figure 4) present a similar picture. Also verified is the existence of finite size (networks of finite size) and time (finite number of Monte Carlo Steps) effects, as we had expected. Additionally, the average number of particles per node is exponential to the degree. For regular real world networks the coverage of small degree networks is very low and they are essentially empty of both species most of the time. The high degree nodes are rich in particles and the low degree are poor.

In conclusion, we have presented a novel way of information transmission through random walk with priorities in complex systems. This priority diffusion model can have important technological applications in communication networks as well as possibly other social, ecological or even roadway traffic systems. In lattices and regular networks the two species move as two non interacting ones with different mobility. In scale free (and real world) networks the low priority species is mired in the central hubs while the high priority ones move faster. This effect can be utilized to selectively halt all diffusion of certain types of information in a network and dedicate all available bandwidth in the high priority information.

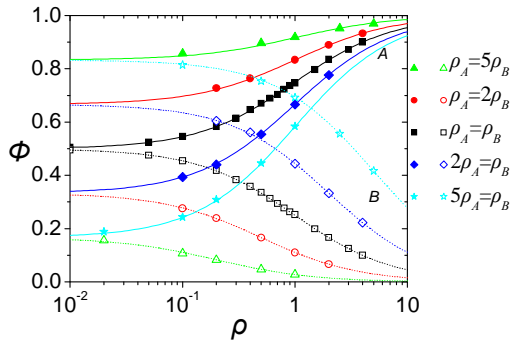


Figure 1. Diffusion coefficient over the density for various ratios of densities. Lines are the corresponding theory. Full lines and symbols represent *A* and hollow symbols and dash lines *B* particles.

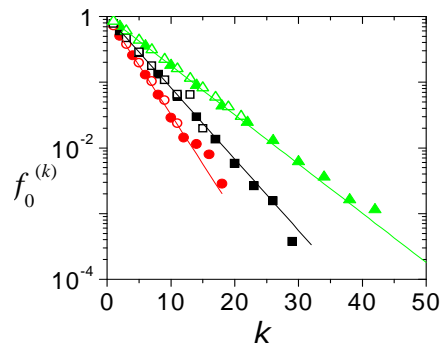


Figure 2. The number of empty sites per node degree. Full symbols are results from scale-free networks, hollow from ER. The lines are the corresponding theory.

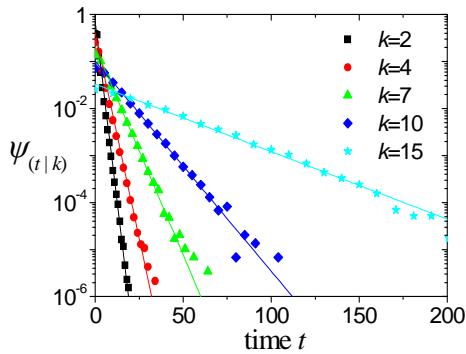


Figure 3. The distribution of waiting times of *B* particles for various node degrees. The higher the degree the higher the probability of a *B* particle to stay more time in that node. Lines are theoretical results, symbols are simulations. For higher order degrees the results become independent of time (not shown due to poor statistics).

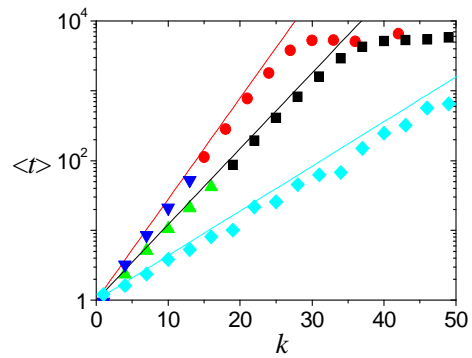


Figure 4. Average waiting time of *B* particles over the node degree. For high values of $\langle t \rangle$ there are finite time effects. Blue and green triangles are ER results, black and red are for scale free. The cyan are results from a real computer network (AS level internet) where PDM is applied. Lines are corresponding theory.

[1] M. Maragakis, S. Carmi, D. ben Avraham, S. Havlin, and P. Argyrakis, Phys. Rev. E Rapid Communication, 77, 020103 (2008).

Acknowledgments

This work is part of the 03ED840 research project, implemented within the framework of the "Reinforcement Programme of Human Research Manpower" (PENED) and co-financed by National and Community Funds (25% from the Greek Ministry of Development-General Secretariat of Research and Technology and 75% from E.U.-European Social Fund).

Towards Luminescence Dating Of Turquoise Gemstone Using TL And OSL Methods

B. Subedi^{1, 2, 3*}, D. Afouxenidis^{1, 2, 3}, G. S. Polymeris¹, N. C. Tsirliganis¹, K.M. Paraskevopoulos³, and G. Kitis¹

1 Archaeometry Laboratory, Cultural and Educational Technology Institute (C.E.T.I.), R.C. "ATHENA", Tsimiski 58, 67100 Xanthi, Greece.

2 Nuclear Physics Laboratory, Aristotle University of Thessaloniki, 54124 Thessaloniki, Greece.

3 Physics Department, Solid State Physics Section, Aristotle University of Thessaloniki, 54124 Thessaloniki, Greece.

* *bsubedi@physics.auth.gr*

Turquoise was among the first gem stones used in jewelry and possessing cultural value since 6000 BC (at least). In the past it was used as a stone of natural protection for the occupational groups who were exposed to especially high degree of risk such as pilots, air crews but now it is mainly use in jewelry and in modern gemstone therapy for those suffering from depression. The aim of this research is to identify and characterize this valuable stone scientifically by using both thermally stimulated luminescence (TL) and optically stimulated luminescence (OSL) techniques and investigate its potential use towards luminescence dating purposes.

Experimental investigation includes study of natural TL and OSL signal, as well as the sensitivity of both signals in successive dose - measurement cycles. Thermal activation curves were also studied {annealed sample 1273K (900C⁰)} which showed presence of at least three traps. The main dosimetric peaks have a peak temperature at the maximum at 339K (66C⁰) and 514 K (241C⁰). However, among these peaks, only the latter becomes of great interest for dating proposes. Both activation energy and frequency factor of this trap were determined and the mean trap life time was estimated to be in the order of 23.6ka.

The OSL resulting from the same trap was also studied by performing a series of thermal annealing experiment. A series of doses were delivered, ranging from 2.5Gy up to 40Gy for both signals and showed linearity in the dose response. Small sensitization was observed at 493K (220C⁰) and deactivation takes place in the range of temperature 773K (500C⁰). The results of the present work are very promising and clearly support the possibility of extrapolating to characterize provenance of turquoise according to geological location, authenticity testing and dating of the ancient turquoise artifacts and to reveal its efficient dosimetric application.

Session WE1

INHOMOGENEOUS & DISORDERED MATERIALS

POLYMERS & BIOMATERIALS

Wednesday, 23 September 2009, 09⁰⁰-11⁰⁰



Complementary methods for the study of biomaterials

I. Margiolaki*¹, J. P. Wright¹, Y. Watier¹, I. Collings¹, A. N. Fitch¹,
N. Papageorgiou² and B. Canard²

¹ *European Synchrotron Radiation Facility (ESRF), Grenoble, France*

² *Architecture et Fonction des Macromolécules Biologiques (AFMB), UMR 6098 CNRS, Marseille, France*

*margiolaki@esrf.fr

Studying biological macromolecules in the absence of good quality single crystals is a challenging field attracting considerable scientific interest. Modern developments of X-ray powder diffraction have allowed the structural investigation of a range of proteins establishing the method as a useful complementary tool to traditional approaches [1]. Protein powder specimens consist of a large number of randomly oriented diffracting micro-crystals which are usually formed rapidly by batch crystallization under a variety of conditions. An overview of the most recent developments in this field will be presented including: (a) application of the molecular replacement technique and structure refinements of selected proteins (b) methods for successful cryocooling (c) experimental phasing and extraction of molecular envelopes (Figure) (d) high throughput automated data collection allowing systematic investigations such as screening and phase diagram mapping and (e) application of the method on biologically interesting proteins such as non-structural viral replication proteins coming from emerging viruses [3].

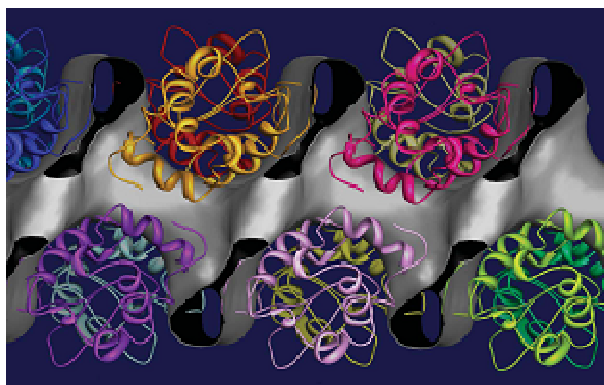


Figure Solvent channels in hen egg white lysozyme crystals. The molecular envelope derived via the single isomorphous replacement method using a gadolinium derivative is represented as grey surface. The figure shows the linear solvent channel which traverses the crystal parallel to the c axis (horizontal display direction). The protein crystal structure, represented as a main-chain ribbon model, is superimposed on this map. [1]

References

- [1] Margiolaki, I. & Wright, J. P., *Acta Cryst.* (2008). A64, 169-180.
- [2] I. Margiolaki et al., *J. Am. Chem. Soc.* (2007). 129, 11865-11871.
- [3] H. Malet et al., *J. Virol.* (In Press).

Acknowledgments We thank the ESRF for provision of beamtime.

Synthesis of Novel Transition Metal Dithiolenes. Synthesis, Experimental and Theoretical Investigation.

G. Soras*^{1,2}, N. Psaroudakis², M. J. Manos³, A. J. Tasiopoulos³, D.G. Liakos⁴, G. A. Mousdis¹, and D. Palles¹

¹Theoretical & Physical Chemistry Institute, National Hellenic Research Foundation, 48 Vass. Constantinou Aven., 116 35 Athens, Greece

²University of Athens Chemistry Department, University Campus, Athens, GR 157-71, Greece

³Department of Chemistry, University of Cyprus, 1678 Nicosia, Cyprus

⁴Institute for Physical and Theoretical Chemistry, Bonn University, Wegelerstrasse 12, 53115 Bonn, Germany

*gsoras@eie.gr

Transition-metal complexes with 1,2-dithiolene ligands have received much attention because of their capacity to give molecular metals and superconductors [1] and more recently because of their potential applications as thirdorder non-linear optical materials [2]. The importance in the chemistry of such square-planar $M(\text{dithiolene})_2$ complexes is due to their ability to overlap with each other including strong electronic interactions between the units, which is a condition to obtain electronic properties, such as conductivity or even unusual magnetic behavior [3]. These $M(\text{dithiolene})_2$ complexes have a similar structure to the tetrathiafulvalene (TTF) and that is the reason for further investigation in these areas [4]. Among them the metal complexes of 5, 6-dihydro-1, 4-dithiin-2, 3-dithiol (ddd) [5] are the most important due to similarities with the BEDT-TTF. BEDT-TTF [6] was permitted the synthesis of radical cation salts with a quasi two-dimensional character gave more than 750 superconductors [7] and raised their critical temperature at 14.2 K [8].

The lecture will focus in the synthesis and study of a new Transition metal 1, 2-dithiolene, similar to (ddd) (FIGURE 1). The experimental measurements will also be compared with the results from theoretical investigations by employing computational approaches, involving density functional theory and semiempirical methods [9].

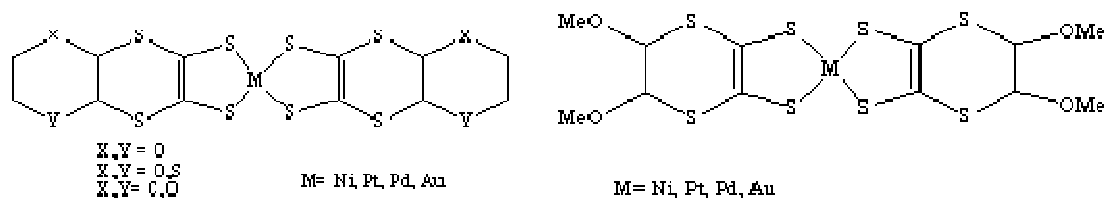


Fig.1. Transition metal dithiolenes.

- [1] A.E. Underhill, J. Mat. Chem. 2 (1992) 1.
 [2] C.S. Winter et al., Appl. Phys. Lett. 58 (1991).
 [3] a) A.T. Coomber et al., Nature 380 (1996) 144 ; b) K. Awaka et al., Inorg. Chem. 33 (1994) 5598.
 [4] R. Kato, *Chemical Reviews*, 2004, **104**, 5319.
 [5] C. T. Vance, R. D. Bereman, J. Bordner, W. E. Hartfield, J. M. Helms, Inorg. Chem., 1985, 24, 2905.
 [6] R. P. Shibaeva and E. B. Yagubskii, *Chemical Reviews*, 2004, **104**, 5347.
 [7] J. M. Williams, J. R. Ferraro, R. J. Thorn, K. D. Carlson, U. Geiser, H. H. Wang, A. M. Kini and M. -H. Whangbo, *Organic Superconductors (Including Fullerenes): Synthesis, Structure, Properties and Theory*; Prentice Hall: Englewood Cliffs, NJ, 1992. T. Ishiguro, K. Yamaji and G. Saito, *Organic Superconductors*; Springer-Verlag: New York, 1998.
 [8] Taniguchi, H.; Miyashita, M.; Uchiyama, K.; Satoh, K.; Mori, N.; Okamoto, H.; Miyagawa, K.; Kanoda, K.; Hedo, M.; Uwatoko, Y. J. Phys. Soc. Jpn. 2003, 72, 468.
 [9] M. J. Frisch, et al.; Gaussian 03, Revision C.02 Gaussian, Inc., Wallingford CT, 2004.

Acknowledgments

This work was financially supported by the Greek General Secretariat for Research and Technology / Ministry of Development through a PENED 2003 grant.

In situ Monitoring of Cement Gel Growth Dynamics. The Use of a Miniaturized Permanent Halbach Magnet for Precise ^1H NMR Studies

**E. Karakosta^{1*}, G. Diamantopoulos¹, M. S. Katsiotis¹, M. Fardis¹, D. Panagiotaras²,
and G. Papavassiliou¹**

¹*Institute of Materials Science, NCSR Demokritos, 153 10 Aghia Paraskevi, Attiki, Greece*

²*Department of Mechanical Engineering, Technological Educational Institute of Patras, 26334, Patras, Greece*

**elkarako@ims.demokritos.gr*

The most critical parameter that affects important cement paste properties, such as strength, shrinkage, creep, and permeability, is its pore structure [1]. Pores in hydrated cement form an extremely complicated network, with a very broad size distribution, ranging from nanometers to millimeters [2], which changes with the chemical composition, relative humidity, temperature, and applied load. Here, without recourse to drying methods, we monitor the evolution of the pore structure during the progressive hydration and setting of three white cement pastes with different hydration kinetics. By combining ^1H NMR spin-lattice relaxation T_1 and diffusion measurements performed in a portable 0.29 Tesla Halbach magnet, it is possible to distinguish among gel and capillary pores, and study the growth dynamics of cement gel (T_1 measurements), and the associated shrinkage of the capillary pore system (diffusion measurements). In this way, aspects of the hydration kinetics are unveiled, which are difficult to observe with other techniques.

[1] Greener J., Peemoeller H., Choi C., Holly R., Reardon E. J., Hansson C. M., Pintar M. M., J. Am. Ceram. Soc., 83, 623 (2000).

[2] Jennings H. M., Bullard J. W., Thomas J. J., Andrade J. E., Chen J. J., Scherer G. W., Journal of Advanced Concrete Technology, 6, 5 (2008).

WE1

O28

Transmission Electron Microscopy of Proteins and Single Particle 3D Reconstruction

N. Papageorgiou^{1*}, B. Coutard¹, V. Lantez¹, E. Gautron², B. Canard¹

¹ *Architecture et Fonction des Macromolécules Biologiques, UMR 6098 CNRS, Université de la Méditerranée and Université de Provence, Case 925, 163 Avenue de Luminy, 13288 Marseille cedex 9, France*

² *Institut des Matériaux Jean Rouxel, IMN UMR 6502, Université de Nantes, 2 rue de la Houssinière BP 32229, 44322 Nantes cedex 3, France*

* *Nicolas.Papageorgiou@afmb.univ-mrs.fr*

During the first half of the XXth century a great number of new ideas and experimental achievements established the corner stones of our actual fundamental and technological approaches concerning both materials science as well as molecular biology. All these achievements in both physics and biology were possible by the improving of our experimental techniques such as ultra high-vacuum techniques, synchrotron radiation facilities, plasma techniques, LASER, several light and electron spectroscopies as well as near and far field microscopies. For the last three decades solid-state physics has explored new materials with novel mechanic and optoelectronic properties based on organic molecules as carbon fullerenes, nanotubes, phthalocyanines and polymers. These studies have convinced us that carbon-based materials are indeed very promising and have begun to familiarize physicists with the idea that biological material as DNA/RNA or proteins, essentially composed by carbon and nitrogen, are worth to be studied in detail.

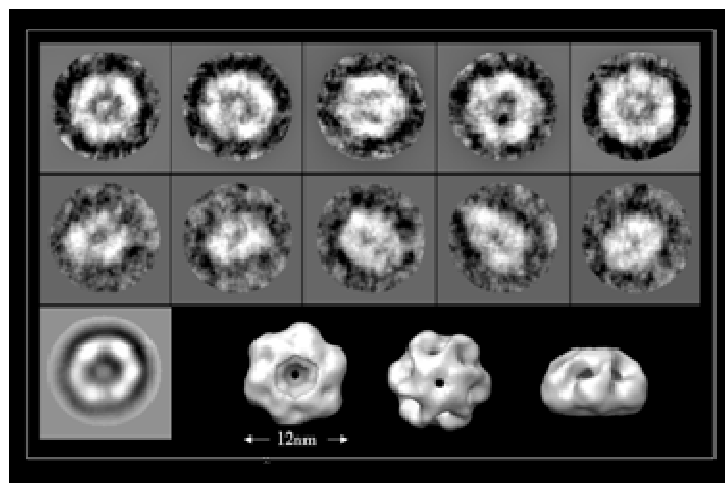
Proteins are large linear polymers composed by smaller molecules called peptides. The exact series of peptides in a protein sequence is coded by RNA/DNA strands. Each protein is folded in a unique way. This folding is responsible for its structural or catalytic properties. There are two kinds of proteins. The ones used as building blocks of living organisms (structural proteins) and those used during the cell-cycle for replication or metabolism (non structural proteins). For example, replication proteins “read” the genetic code in order to make “copies”, which in turn are translated to proteins on cellular ribosomes. This kind of proteins is characterized by extremely selective and efficient substrate adsorption and catalytic sites for hydrolysis, protein-membrane binding, RNA/DNA binding or proton/metal atom transfer.

Concerning applications in the domain of materials science, the study of structural proteins could be useful in order to elaborate novel materials which mimic the organization of living building blocks as fibers, porous materials, various kinds of membranes etc. On the other hand, there are many things to learn from non structural proteins concerning catalysis, “clever” self-assembling, or nanostructures with novel functions and properties as molecular devices, nanorobots etc.

From the physicist’s point of view, the first thing to know about a protein is its 3D structure. A great amount of proteins have been crystallized until now and their 3D structure has been solved by X-ray diffraction techniques from crystals or recently from micro-crystal powders [1]. However, in many cases crystallization is not possible or very difficult to achieve, especially in the case of protein complexes or very large proteins. In that case other techniques as small angle X-ray scattering (SAXS), dynamic light scattering (DLS), electron and nuclear magnetic resonance (EMR, NMR), transmission electron microscopy (TEM) and atomic force microscopy (AFM) may be used in order to extract structural information. One application of major importance concerning structural knowledge is in the field of “drug design”. For example knowing the topology and chemistry of a protein’s active site permits the design of small molecules, which after adsorption onto the active site inhibits the protein function. One of the best examples is the HIV protease inhibition achieved this way and used in patients in the case of AIDS therapies.

Here we present a structural study of the viral non-structural protein 2C by means of TEM [2]. The protein 2C under study is the putative helicase of the echovirus 30, a virus which belongs to the *Picornaviridae* family. Picorna viruses are RNA viruses responsible for a large spectrum of human diseases such as hepatitis A, poliomyelitis, various kinds of meningitis and the common cold. Protein 2C is one of the most conserved non structural viral proteins within the *Picornaviridae* family which means that a possible drug targeting its action and designed for hepatitis A could also be used against the common cold. The 2C protein is believed to be endowed with helicase activity based on signature sequences containing conserved motifs, found in NTP-binding proteins as well as in helicase super family 3 (SF3) [3, 4]. The protein shows ATPase activity but no helicase activity has ever been demonstrated neither any structural data are available for any 2C protein. Apart from its putative helicase activity, 2C protein also functions as a membrane-anchoring protein as well as an agent for virus self-assembling and structural rearrangements of intracellular membranes. A stable and soluble construct of the 2C protein was selected and studied here by means of negative staining TEM, SAXS, AFM and DLS. Only the TEM and AFM

measurements showed that the protein adopts a hexameric shape reminiscent to that of SF3 helicases. Indeed, our measurements show that the main fraction of the purified protein tends to aggregate leaving behind a small fraction of monomers and an even smaller fraction of hexamers impossible to observe with SAXS or DLS. Typical TEM micrographs of the hexamer particle are shown in the figure together with a 3D reconstruction of the hexamer particle calculated out of 1500 collected particles. Surprisingly, the hexameric structure observed here by TEM is in line with results obtained from other SF3 helicases of DNA viruses whose crystal structure is known and which form hexameric oligomers.



We will discuss the above results and especially insist in some technical aspects concerning protein preparation (genetic cloning) and handling of protein samples, the problem of protein adsorption on carbon coated microscope grids, the preparation of the samples by negative staining techniques, the effects of the electron beam on the samples and experimental conditions to respect, the acquisition of TEM images on photographic plates their subsequent digitalization and numerical treatment and finally the procedure that permits to reconstruct the 3D structure of a single particle out of a large number of TEM images.

Finally we will discuss some interesting properties of the helicase molecules. Helicases unwind double DNA or RNA strands and also are used by the replication complex as motors (molecular motors) [5]. The 2C protein is also believed to transport other viral proteins and participate in the self-assembling of progeny virus before their take off from the infected cells.

- [1] Margiolaki I. and Wright J.P., *Acta Cryst.* (2008). A64, 169–180.
- [2] Papageorgiou N. et al. to be published, *Journal of General Virology*.
- [3] Walker, J. E. et al. (1982). *Embo J* 1(8): 945-51.
- [4] Gorbalenya, A. E. and Koonin, E. V. (1993) *Current Opinion in Structural Biology* 3, 419-429.
- [5] Tuteja, N. and R. Tuteja (2004b). *Eur J Biochem* 271(10): 1849-63.

Effect of Inorganic Additive on the Chain Crystallization in Polymer / Layered Silicate Nanohybrids

K. Chrissopoulou^{1*}, E. Pavlopoulou^{1,2}, H. Papananou^{1,3}, S. Fotiadou^{1,3}, G. Portale⁴, W. Bras⁴
and S. H. Anastasiadis^{1,3,5}

¹ Institute of Electronic Structure and Laser, Foundation for Research and Technology-Hellas P. O. Box 1527, 711 10 Heraklion, Crete, Greece

² Department of Materials Science and Technology, University of Crete, Heraklion, Crete, Greece

³ Department of Chemical Engineering, Aristotle University of Thessaloniki, 54124 Thessaloniki, Greece

⁴ DUBBLE CRG, European Synchrotron Radiation Facility, Grenoble, France

⁵ Department of Chemistry, University of Crete, Heraklion, Crete, Greece

*kiki@iesl.forth.gr

Polymer / layered silicate nanocomposites constitute an interesting class of materials which allow the investigation of basic scientific problems and at the same time are utilized in many technological applications. Mixing polymers with layered silicates leads to three different micro- or nanostructures depending on the interactions between the chains and the inorganic surfaces: the phase separated, where the two materials are immiscible, the intercalated that the polymer chains reside in the interlayer galleries of the silicates forming 0.8-2.5nm films and the exfoliated, in which the structure of the inorganic material is destroyed and the platelets are dispersed in the polymeric matrix. [1,2] A reason that these materials have attracted the scientific interest is related with their unique properties that render them candidates for numerous technological applications. In the case of crystalline polymers, the improvement in the properties can be attributed further than the reinforcing contribution of the inorganic additives and the formation of different nanostructures, to the alteration of the crystalline behaviour and characteristics of the polymer chains due to the presence of the inorganic material.

In this work we investigate the structure, morphology and crystallization behavior of a hydrophilic, semi-crystalline polymer, poly(ethylene oxide), PEO, ($M_n=100000$, $T_g=-67^\circ\text{C}$, $T_m=65^\circ\text{C}$) when mixed with natural montmorillonite (Na^+ -MMT) in a range of compositions that covers the whole regime from pure polymer to pure clay. The structure of the hybrids was investigated by X-ray diffraction, Polarizing Optical Microscopy (POM), Differential Scanning Calorimetry (DSC) and Small Angle X-ray Scattering (SAXS).

Figure 1 shows the X-ray diffraction patterns for the pure components and the nanohybrids. [3] The pure Na^+ MMT shows a main (001) diffraction peak at $2q=8.8^\circ$, which corresponds to an interlayer spacing of 1.0 nm. As the PEO concentration increases, the Na^+ MMT diffraction peak disappears and two other peaks emerge at 6.8° and 4.8° that correspond to interlayer distances of 1.30 and 1.85 nm and whose relative intensities depend on the PEO content. At concentrations up to 20 wt%, the PEO chains within the galleries form either a single- or a double-layer structure of disordered liquid-like chains. Further increase of the PEO concentration reveals only double-layers of intercalated PEO chains. Moreover, for PEO content below 70 wt% no peaks are observed that can be assigned to the crystalline structure of PEO. It is only for PEO concentrations higher than 70 wt% that two peaks at 18.9° and 23.2° emerge, which agree with the diffraction peaks of bulk PEO due to its monoclinic crystal structure (with a unit cell parameter of 1.93 nm along the helix axis). This indicates crystallization of the excess polymer outside the completely full galleries.

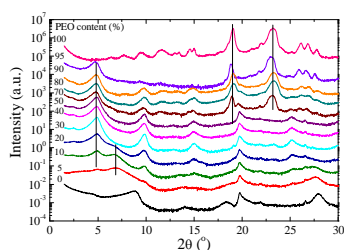


Figure 1: X-ray diffraction spectra of PEO/ Na^+ MMT nanocomposites.

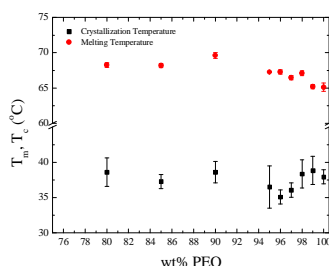


Figure 2: Composition dependence of the melting and crystallization temperatures.

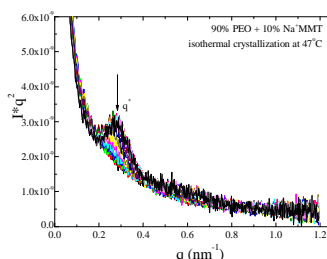


Figure 3: Wavevector dependence of the scattered SAXS intensity for the 90wt%PEO+10wt% Na^+ MMT hybrid

Indeed DSC measurements on hybrids with low polymer content [4] reveal that the PEO chains remain amorphous and it is only for composites with 70wt% PEO and more that the characteristic melting and crystallization transitions appear in agreement with the XRD data. In the latter cases, a small effect of the

inorganic additive on the melting and crystallization temperatures is observed (Figure 2). Furthermore, the polymer crystallinity resulting from both the XRD and the DSC analysis show a small increase for low inorganic content. Moreover, these results are verified by independent FT-IR and Raman Spectroscopy measurements in which the sharp peaks that correspond to the crystalline PEO are observed only in nanohybrids with high polymer content. [4]

In the case of hybrids with high polymer content, where the chains are able to crystallize, the kinetics of crystallization along with the crystalline characteristics were recorded utilizing time resolved Small Angle X-ray Scattering (SAXS) measurements carried out at the Dutch-Belgian Beamline (DUBBLE) at the European Synchrotron Radiation Facility (ESRF) in Grenoble, France, in the scattering vector range $0.06 < q < 1.2 \text{ nm}^{-1}$. The samples were annealed above the melting temperature, T_m , and then quenched at different isothermal crystallization temperatures, T_{IC} . Sequential SAXS patterns were acquired, following the isothermal crystallization at the respective temperatures. Figure 3 shows the scattering patterns (after utilization of the Lorentz correction) of the nanocomposite with 90% PEO + 10% Na^+ -MMT collected during isothermal crystallization at 47°C . The initial scattering curves correspond to those of the melt state of the amorphous polymer. After a while, a peak appears at approximately $q=0.27\text{nm}^{-1}$, corresponding to a lamellar period of 23nm. The intensity of the peak increases until the end of the crystallization process, and then remains constant. The patterns of all the nanocomposites at various T_{IC} were similar, however differences were observed in the intensity and the evolution time of the crystallinity peak. [5]

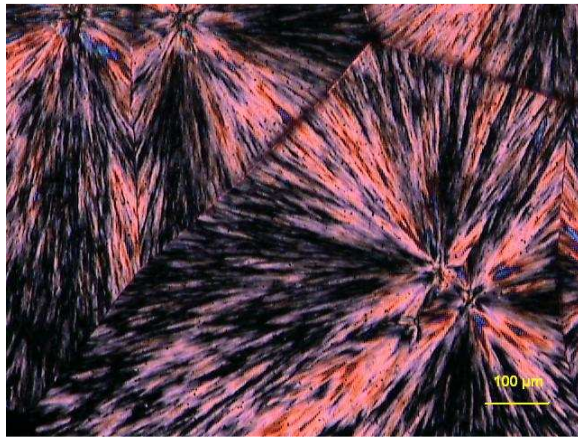


Figure 4: POM image of PEO obtained during isothermal crystallization at 53°C .

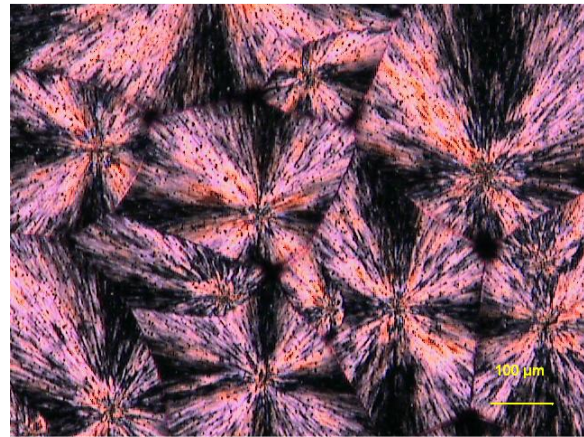


Figure 5: POM image of 99wt%PEO + 1wt% Na^+ MMT obtained during isothermal crystallization at 53°C .

Polarized Optical Microscopy images were recorded for pure PEO and nanohybrids with low amount of additive (Figures 4 and 5) as well. [5] The samples were placed in a heating stage, melted at 120°C for 5min and then cooled down either to room temperature or to selected crystallization temperatures. The images reveal that even the presence of very small amount of the inorganic material results in an important decrease of the spherulite size accompanied with an increase in the spherulite number. In all cases, increase of the spherulite size was observed with the increase of the crystallization temperature as well. It is noted that for each system, the ideal melting temperature was estimated and its dependence on the inorganic content was examined.

Furthermore, results from both SAXS and DSC kinetic experiments indicate that the crystallization mechanism is altered due to the silicate from that of homogeneous nucleation for the pure polymer to heterogeneous and epitaxial nucleation with the increase of the inorganic material.

- [1] Giannelis E. P., Krishnamoorti R., Manias E., *Adv. Polym. Sci.* 138, 107 (1999).
- [2] Alexandre M., Dubois P., *Materials Science and Engineering* 28, 1 (2000).
- [3] Elmahdy M. M., Chrissopoulou K., Afratis A., Floudas G., Anastasiadis S. H., *Macromolecules* 39, 5170 (2006).
- [5] Fotiadou, S., Chrissopoulou, K., Andrikopoulos, K., Anastasiadis, S. H. *In preparation* (2009).
- [6] Chrissopoulou, K., Papananou, H., Pavlopoulou, E., Portale, G., Bras, W., Anastasiadis, S. H. *In preparation* (2009).

Acknowledgments: Part of this research was sponsored by the Greek General Secretariat for Research and Technology (Programmes ΠΕΝΕΔ 03ΕΔ581 and ΠΑΒΕΤ 05ΡΑΒ96), by the European Union (Programmes STREP NMP3-CT-2005-506621), NATO Scientific Affairs Division (Science for Stability Programme) and INTERREG IIIA Greece-Cyprus 2000-2006.

Tight Binding Parameters for Charge Transport in DNA

G. Kalosakas^{1*}, L. G. D. Hawke¹, and C. Simserides²

¹ *Materials Science Department, University of Patras, GR-26504 Rio, Greece*

² *Institute of Materials Science, NCSR Demokritos, GR-15310 Athens, Greece*

*georgek@upatras.gr

We examine the tight-binding parameters pertinent to charge transfer along DNA. The \square molecular structure of the four DNA bases, adenine (A), thymine (T), cytosine (C), and guanine (G), is investigated within the linear combination of atomic orbitals approach, using a recently introduced parametrization [1,2]. The HOMO and LUMO wavefunctions and energies of DNA bases are then used for calculating the corresponding wavefunctions of the two B-DNA base-pairs, adenine-thymine (A-T) and guanine-cytosine (G-C). These results are used for estimating charge transfer parameters between neighboring bases and also between successive base-pairs, considering all possible combinations between them [3]. The calculated microscopic quantities can be used in mesoscopic theoretical models of electron or hole transfer along the DNA double helix, as they provide the parameters for a tight-binding phenomenological description based on the \square molecular overlap [3,4]. The obtained results for the HOMO and LUMO base energies are in good agreement with experimental values.

A tight-binding description of a single carrier (electron or hole) is obtained assuming that a hole travels through HOMOs and an electron through LUMOs. Such a description may be either at the base-pair level or at a single-base level. In the former case charge transfer is considered to occur between successive base-pairs of the DNA. The HOMO/LUMO (H/L) base-pair wavefunctions are given through

$$\Psi_{H/L}^{bp}(r) = \sum_{i=1}^N C_i^{H/L} p_z^i(r), \quad (1)$$

where the sum is extended over the N atoms (contributing p_z electrons) of the whole base-pair ($N=18$ for A-T base-pairs and $N=19$ for G-C). The time-dependent wavefunction of the whole DNA molecule is written as

$$\Psi_{H/L}^{DNA}(r,t) = \sum_{\lambda} A_{\lambda}(t) \Psi_{H/L}^{bp(\lambda)}(r), \quad (2)$$

with the sum extended over all base-pairs of the DNA segment under consideration. The time evolution of the coefficients $A_{\lambda}(t)$ is obtained through time-dependent Schrödinger equation $i\hbar \frac{d\Psi_{H/L}^{DNA}}{dt} = H^{DNA} \Psi_{H/L}^{DNA}$. Following standard assumptions one obtains the following system of equations [3]:

$$i\hbar \frac{dA_{\lambda}}{dt} = E_{H/L}^{bp(\lambda)} A_{\lambda} + t_{H/L}^{bp(\lambda;\lambda-1)} A_{\lambda-1} + t_{H/L}^{bp(\lambda;\lambda+1)} A_{\lambda+1}, \quad (3)$$

where $E_{H/L}^{bp(\lambda)}$ is the HOMO/LUMO energy of the corresponding base-pair, while the hopping parameters $t_{H/L}^{bp}$ are obtained through

$$t_{H/L}^{bp(\lambda;\lambda')} = \sum_{i=1}^{N_{\lambda}} \sum_{j=1}^{N_{\lambda'}} C_{i(\lambda)}^{H/L*} C_{j(\lambda')}^{H/L} V_{ij}. \quad (4)$$

The matrix elements V_{ij} are given by the Slater-Koster expression [5]

$$V_{ij} = V_{pp\sigma} \sin^2 \phi + V_{pp\pi} \cos^2 \phi, \quad (5)$$

where ϕ is the angle formed by the line connecting atoms i and j and the base-pair plane. The intermolecular matrix elements $V_{pp\sigma}$ and $V_{pp\pi}$ are provided by approximate exponentially decaying expressions [6,7].

The tight-binding description at the single-base level considers charge transfer between neighboring bases. Here the starting point is the molecular single-electron HOMO or LUMO wavefunction for the bases

$$\Psi_{H/L}^b(r) = \sum_{i=1}^N c_i p_z^i(r), \quad (6)$$

where the sum is now extended over the N atoms of the base, that contribute P_z electrons ($N=11$ for G, $N=10$ for A, and $N=8$ for C and T). In this case the time-dependent wavefunction of DNA is

$$\Psi_{H/L}^{DNA}(r,t) = \sum_{\lambda} [A_{\lambda}(t) \Psi_{H/L}^{b(\lambda,1)}(r) + B_{\lambda}(t) \Psi_{H/L}^{b(\lambda,2)}(r)], \quad (7)$$

where λ denotes base-pairs and the sum is again over all successive base-pairs of DNA. $\Psi_{H/L}^{b(\lambda,1)}$, $\Psi_{H/L}^{b(\lambda,2)}$ are HOMO/LUMO wavefunctions of bases located at the one and the other DNA strands, respectively. The corresponding tight-binding equations for the time dependent coefficients in Eq. (7) read

$$\begin{aligned} i\hbar \frac{dA_{\lambda}}{dt} &= E_{H/L}^{b(\lambda,1)} A_{\lambda} + t_{H/L}^{b(\lambda,1;\lambda,2)} B_{\lambda} + t_{H/L}^{b(\lambda,1;\lambda-1,1)} A_{\lambda-1} + t_{H/L}^{b(\lambda,1;\lambda+1,1)} A_{\lambda+1} + t_{H/L}^{b(\lambda,1;\lambda-1,2)} B_{\lambda-1} + t_{H/L}^{b(\lambda,1;\lambda+1,2)} B_{\lambda+1} \\ i\hbar \frac{dB_{\lambda}}{dt} &= E_{H/L}^{b(\lambda,2)} B_{\lambda} + t_{H/L}^{b(\lambda,2;\lambda,1)} A_{\lambda} + t_{H/L}^{b(\lambda,2;\lambda-1,2)} B_{\lambda-1} + t_{H/L}^{b(\lambda,2;\lambda+1,2)} B_{\lambda+1} + t_{H/L}^{b(\lambda,2;\lambda-1,1)} A_{\lambda-1} + t_{H/L}^{b(\lambda,2;\lambda+1,1)} A_{\lambda+1} \end{aligned} \quad (8)$$

Here $E_{H/L}^b$ are base HOMO/LUMO energies and the hopping parameters t_H^b or t_L^b are inter-base transfer integrals of the following form

$$t_{H/L} = \sum_{i=1}^{N_1} \sum_{j=1}^{N_2} c_{i(1)}^{H/L*} c_{j(2)}^{H/L} V_{ij}, \quad (9)$$

with V_{ij} given from Eq. (5).

We have calculated all the tight-binding parameters appearing in Eqs. (3) or (8), for both electrons and holes, and for all possible combinations of neighboring base-pairs or bases, respectively [3]. As an example, Table 1 below shows the hopping parameters $t_{H/L}^{bp}$ of Eq. (3), for all combinations between successive base-pairs.

Base-pair sequence	t_H^{bp} (meV)	t_L^{bp} (meV)
AA, TT	-8	-29
AT	20	0.5
AG, CT	-5	3
AC, GT	2	32
TA	47	2
TG, CA	-4	17
TC, GA	-79	-1
GG, CC	-62	20
GC	1	-10
CG	-44	-8

Table 1. Transfer parameters between successive base-pairs XY (first column) given in the direction 5'-3'. The notation XY denotes successive base-pairs X-X_{complementary} and Y-Y_{complementary}, where the one DNA strand contains the XY bases in the direction 5'-XY-3', while the complementary strand is 3'-X_{complementary}Y_{complementary}-5'. Hole hopping parameters t_H^{bp} are shown in second column and electron hopping parameters t_L^{bp} in third column.

- [1] Hawke L.G.D., Kalosakas G., Simserides C., *Mol. Phys.* (2009) in press. (arXiv:0808.3984v2)
[2] Hawke L.G.D., Simserides C., Kalosakas G., *Mater. Sci. Eng. B* (2009) in press. doi:10.1016/j.mseb.2009.02.012.
[3] Hawke L.G.D., Kalosakas G., Simserides C., 'Tight binding parameters for charge transfer along DNA', *preprint* (2009).
[4] Endres R.G., Cox D.L., Singh R.R.P., *Rev. Mod. Phys.* 76, 195 (2004).
[5] Slater J.C., Koster G.F., *Phys. Rev.* 94, 1498 (1954).
[6] Menon M., Allen R.E., *Phys. Rev. B* 38, 6196 (1988).
[7] Lathiotakis N., Andriotis A.N., *Solid State Comm.* 87, 871 (1993).

Session WE2

POSTER SESSION

*INHOMOGENEOUS
& DISORDERED MATERIALS*

*POLYMERS
& BIOMATERIALS*

*NANOSCALE &
SURFACE SCIENCE*

Wednesday, 23 September 2009, 11³⁰-13⁰⁰



Evaluation of Surface Characteristics of Prealloyed Cr-Mo-steel Powder

D. Chasoglou*, L. Nyborg and E. Hryha

Chalmers University of Technology, Gothenburg, Sweden

*dimitris.chasoglou@chalmers.se

The Powder Metallurgy (PM) process for making sintered steel products concerns the fabrication of metal powder, pressing of a powder blend into a green body (that resembles the final component) and sintering at elevated temperature. This usually results in a product with very good dimensional stability with appropriate mechanical properties at competitive cost for middle to large volume serial production. Unfortunately, until recently, the presence of a small amount of inherent porosity in the produced components that arise from the PM process has hindered their usage in high load applications [1]. Today, the PM industry is oriented towards improving the products mechanical properties by minimizing porosity, optimizing the final microstructure and controlling the sintering atmosphere. To do this it is paramount to control the microstructure development by careful alloying with e.g. chromium during the powder fabrication process. However, gains in mechanical properties can only be achieved when chromium's high affinity to oxygen during the heating stage of the sintering has been successfully dealt with [2,3].

The present study is an effort to establish a methodology for the characterization of the powder surface in terms of composition, distribution, size and morphology of surface products. To facilitate characterization, surface sensitive analytical techniques like Auger electron spectroscopy (AES), X-ray photoelectron spectroscopy (XPS) along with ion (Ar) etching and secondary ion mass spectroscopy (SIMS) were applied for evaluating the composition and chemical state of the powder surface. Furthermore for acquiring micrographs of the powder surfaces and also perform chemical analysis high-resolution scanning electron microscopy coupled with energy-dispersive X-ray spectroscopy was used.

The considered model material was water atomized steel powder pre-alloyed with 3wt.% Cr and 0.5wt.% Mo (other elements like Si and Mn were kept below 0.1wt.%) that has undergone subsequent annealing. In previous studies it has been shown that the surface of the powder particles consists of a Fe-oxide layer with a thickness ranging 6-7nm in which particulate features can be encountered [2,3,4,5].

XPS Survey spectra were used in order to evaluate the surface composition of the powder particles, Fig.1. As expected there are characteristic peaks of oxygen (O1s), manganese (Mn2p), chromium (Cr2p) and iron (Fe2p) in the spectra. Carbon (C1s) can also be found but mainly on the very surface and it originates from adsorbed species. As soon as the sample is ion etched by Ar ions, the layer of organic substances is removed and the amount of carbon deeper in the material is in the range of below 1 at.%. This amount could indicate the presence of carbides or even unetched areas in the sample but the change in chemical composition and the absence of data for carbides for this system gives no possibility to draw safe conclusions.

The thickness of the surface iron oxide layer was estimated using the relative intensity of the iron peaks ($I_{\text{met}}/I_{\text{met}260}$). In the case of a uniform oxide layer and assuming that the electron mean free path in Fe-oxide is $\lambda_{\text{ox}} \sim 15 \text{ \AA}$ and the oxide layer thickness is between 50-100 nm, then the metal intensity ratio representative for the oxide/metal interface is calculated to be about 65% [2,3]. Having this in mind the oxide layer thickness was estimated to be 6 nm. This value verifies previous studies which indicate oxide layer thickness 6-7 nm [2,3].

From high energy resolution narrow scans over the binding energy ranges of the elements under investigation it was possible to acquire information about their chemical state. Peaks from Fe and Cr especially after ion etching reveal contribution from both metallic and oxide states while those of Mn and Si reveal the presence only of oxide state. In more detail the Fe peak consists of Fe^{3+} , Fe^{2+} and Fe^{met} . Fe^{3+} is the dominant cation but the change in composition due to the ion etching must be taken into account. Cr peak shows contribution from Cr^{3+} and Cr^{met} . In both of the elements mentioned above the contribution of the metallic peak increases with increasing etch depth. This corresponds to the removal of the oxide layer with the ion etching.

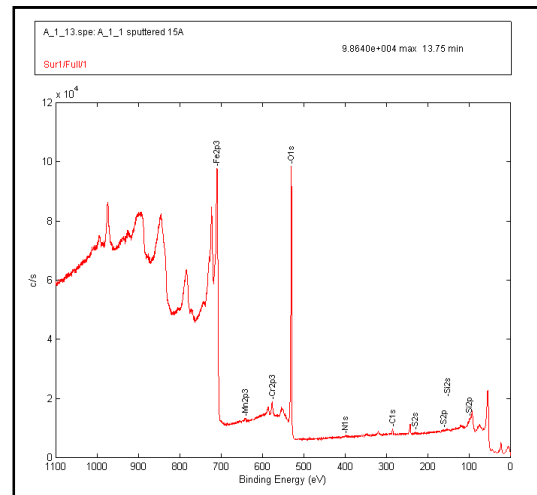


Fig.1: XPS general surface spectrum

WE2

P1

By correcting the oxide peak areas with the use of standard relative intensity factors the relative cation concentration of the surface oxide could be estimated from the representative high energy resolution narrow scans [3,6]. As expected the Fe-cation concentration decreases with increasing etch depth whereas for Cr- and Mn-cation concentration there is an increase, especially after 8 nm when most of the Fe-oxide is removed the increase becomes more pronounced. The cation concentration of Cr and Mn reaches almost 70% of the total cation concentration at larger etch depths. This increase in total along with the high amount of oxygen shows that the particulate compounds formed by Cr and Mn are actually stable oxides. Having in mind also the amount of each of these elements in the material, an enrichment factor can be calculated for the oxides present. For the case of Cr it is ~20 and for Mn it is ~150.

From high resolution SEM micrographs it was observed that the single particulate features found on the powder surface have a size of approximately up to 0.5 μ m as seen in Fig.2. The observed features were also found to form agglomerates of several microns in size.

Each particulate and agglomerate was examined separately using EDX. This analysis is in good agreement with the XPS results apart from the appearance of Si as seen in Table.1. The particulates were thus mostly complex Fe-Cr-Mn-Si-oxides.

	O	Si	Cr	Mn	Fe	Total
Sp.1	44.5	0.7	10.9	5	38.9	100
Sp.2	18.8	5.7	2.5		72.9	100
Sp.3			3.7		96.3	100

disadvantage of the EDX analysis is that the acquired information originate from a large interaction volume. Therefore the measurements in Table.1 can be used only for qualitative interpretation. In order to acquire more detailed information about the composition of the particulate features AES was used. Due to its much higher resolution (30nm) it was possible to analyze each of these features individually (Fig.3).

Dynamic SIMS was also used for depth profiling that would supplement the observations performed with the rest of the techniques. For the purposes of the analysis the sample was ion (Bi) etched and the resulting profile verified the existence of an Fe-oxide layer on the powder particles surfaces and simultaneously the existence of strong oxide forming elements such as Cr and Mn.

This work has been focused in using different surface sensitive analytical techniques for the investigation of the surface characteristics of metal powder particles. By using data from previous studies it was possible to verify the existence of a heterogeneous oxide layer on the surface of the powder particles [2,3,4,5]. This layer was consisting of a Fe-oxide layer with thickness about 6nm and particulate features consisting of complex Fe-Cr-Mn-Si oxides. These oxides have spherical shape and size up to 0.5 μ m. They can also form larger agglomerates sizing up to a few μ m. Further investigation needs to be carried out in order to identify the type and structure of oxides which will enable further understanding of their origin and way of formation.

- [1] R.M German: Powder Metallurgy Science, 2nd Edition, Metal Powder Industries Federation (1994).
- [2] H. Karlsson, L. Nyborg, S. Berg & Y. Yu, Proc. of EuroPM 2001, Nice, France, Oct 22-24, 2001, EPMA, 22-28 (2001).
- [3] H. Karlsson, L. Nyborg & S. Berg, Powder Metallurgy, 2005, vol. 48, no.1, pp. 51-58 (2005).
- [4] I. Olefjord & I. Nyborg, Powder Metallurgy, 1985, vol. 28, no. 4, pp. 234-243 (1985).
- [5] D. Briggs & M.P. Seah, Practical Surface Analysis, John Wiley & Sons, NY (1983).

Acknowledgments

This project is a part of a frame work between Höganäs AB and Chalmers University of Technology. Höganäs AB is gratefully acknowledged for the financial, technical and scientific support of the project.

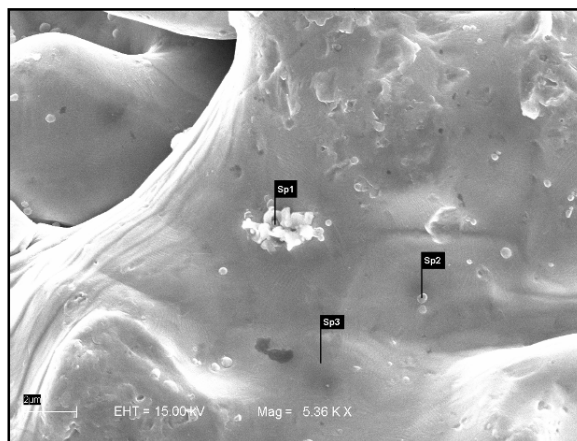


Fig.2: HR-SEM micrograph of the powder surface

A

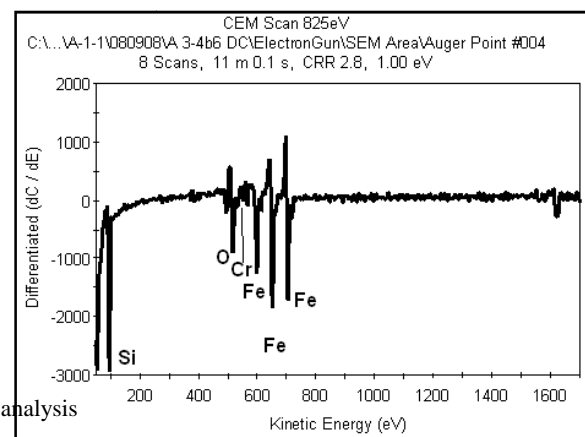


Fig.3: AES point analysis

Study of thin YSZ coatings deposited by e-beam evaporation

Z. Sompoulos and P. Yianoulis*

Renewable Energy Laboratory, Physics Department, University of Patras

*yianpan@physics.upatras.gr

Introduction

The Solid Oxide Fuel Cell (SOFC) technology permits efficient generation of electrical power from a wide range of fuels and it can have many applications [1-4]. During the past two decades the SOFC has received much attention and development [5-8], aiming at the development of an efficient, cost effective and stable ultimate system.

Efforts to develop SOFCs operating at intermediate temperatures aim at extending the lifetime of the devices and reducing the material costs for commercial applications. Accordingly, researchers worldwide work on developing a technically viable processing tool than can yield a thin and impervious electrolyte film, so that the operating temperature of the SOFC can be reduced to a low level, such that several years of stable system operation can be secured.

The electron-beam evaporation (e-beam) technique has been used to deposit YSZ (ZrO_2 stabilized by 8 wt. % Y_2O_3) thin films on a variety of porous and non porous substrates. Thin films have been grown on glass, on conducting films on glass, on mono-crystalline silicon wafers and on highly porous NiO-YSZ substrates. Films ranging from 0.7 to 2 μm in thickness have been manufactured. The influence of substrate structure and deposition rate has been investigated. The film thickness has been measured in situ via a quartz crystal monitor and ex situ by a stylus profilometer. Moreover, the morphology of the films has been studied by scanning electron microscopy and atomic force microscopy. Samples have been also investigated in terms of chemical composition via x-ray photoelectron spectroscopy.

YSZ films (1 – 2 μm thick) were deposited on different substrates in order to study the influence of substrate material and structure on the film growth process. The growth rate of the film during the deposition process has marked influence on the crystallite size and morphology of the deposited film. For the anode supported SOFCs, an important factor in the determination of the maximum thickness of sufficiently dense electrolyte film is the pore structure of the anode substrate. The NiO-YSZ substrates that have been used had pores less than 1 μm in size (Fig. 1a and 1b). The samples were thoroughly cleaned in ultrasonic bath and heated at about 350 to 400°C before the YSZ film deposition.

The deposited films were dense and very transparent and thus only the color of the substrate was visible through the transparent electrolyte layer. While observing the film structure in depth (Fig. 1a and 1b) we note that the cross section of the film has the typical columnar structure of grains normal to the substrate plane that has also been observed by other investigators [9].

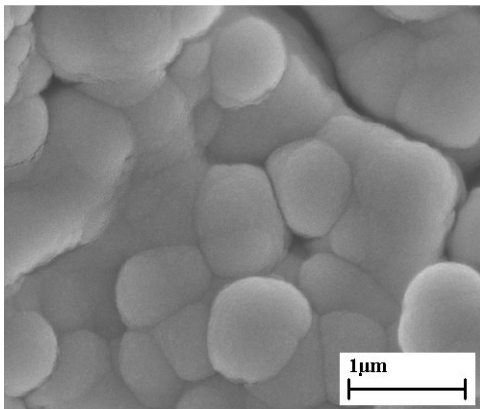


Fig. 1a: Top view of YSZ on NiO/YSZ

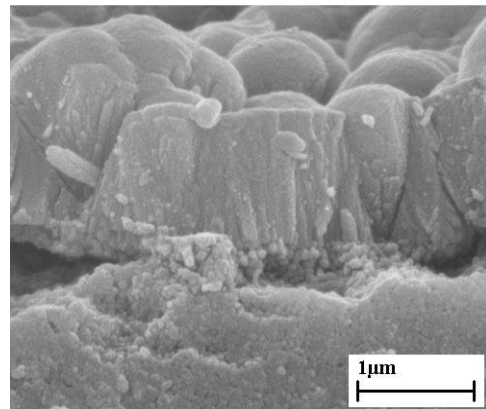


Fig. 1b: Cross section of YSZ on NiO/YSZ

As it is mentioned elsewhere [10], the best ionic conductivity is registered when the crystalline orientation of the YSZ electrolyte is cubic (111). This is the prevailing orientation in the deposited films, as shown in Fig. 2. The sharpness of the (111) peak is another indicator of the film homogeneity. It could be that during the e-beam deposition process the vapor stream consists of small clusters, depending on powder type. These clusters could

form the initial growing stages influencing the entire film's structure, as the crystal structure of the deposited material is repeated on the deposited film. The general structure and crystal orientation of the film did not seem to depend on the substrate material and structure.

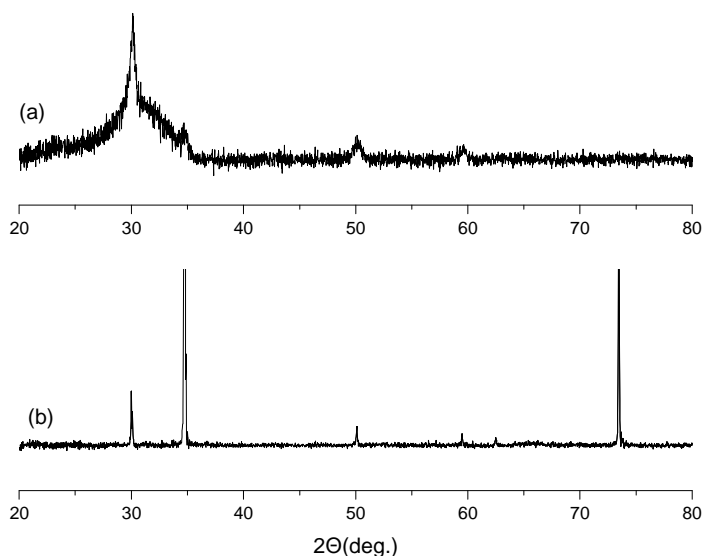


Fig. 2: XRD graph of deposited YSZ film (a) and YSZ powder (b)

Electron beam gun vacuum deposition is suitable for preparing thin YSZ films on various substrates. This technique provides high deposition rates and sufficient control of the film morphology. Depending on the deposition parameters, the films have a packing density ranging from 0.6 to 0.9 and a crystallinity size of 40 – 70 nm. The deposition process is difficult to control demanding experience with the facility that has been used; however, the adhesion of the film on the substrate and the homogeneity it presented was satisfactory.

- [1] L. Carrette, K. A. Friedrich, U. Stimming, *Chem. Phys. Chem.* 1 (4) (2000) 163.
- [2] B.M. Barnett, W.P. Teagan, *Journal of Power Sources* 37 (1-2) (1992) 15.
- [3] D. Hart, *Journal of Power Sources* 86 (1), (2000) 23.
- [4] A. Bauern, D. Hart, *Journal of Power Sources*, 86 (1), (2000) 482.
- [5] N.Q. Minh, *J. Am. Ceram. Soc.* 76 (1993) 563.
- [6] S. de Souza, S.J. Visco, L.C. De Jonge, *Solid State Ionics* 98 (1997) 57.
- [7] O. Yamamoto, *Electrochimica Acta* 45 (2000) 2423.
- [8] N.P. Brandon, S. Skinner, B.C.H. Steele, *Annu. Rev. Mater. Res.* 33 (2003) 183.
- [9] K. Wada, M. Yoshiya, N. Yamaguchi, H. Matsubara, *Surf. & Coat. Technology*, 200 (2006) 2725.
- [10] P.C. Johnson, *Phys. Thin Films*, 14 (1989) 129.

Acknowledgments This paper is part of the 03ED375 research project, implemented within the framework of the “Reinforcement Programme of Human Research Manpower” (PENED) and co-financed by National and Community Funds (20% from the Greek Ministry of Development-General Secretariat of Research and Technology and 80% from E.U.-European Social Fund).

Atomistic Simulations of Carbon Nanofoams

C. Mathioudakis¹, G. E. Vantarakis^{1,2}, and P. C. Kelires^{2,3,*}

¹*Department of Materials Science and Technology, University of Crete, P.O. Box 2208, 71003 Heraklion, Crete, Greece*

²*Department of Mechanical and Materials Science Engineering, Cyprus University of Technology, P.O. Box 50329, 3603 Limassol, Cyprus*

³*Department of Physics, University of Crete, P.O. Box 2208, 71003 Heraklion, Crete, Greece*

**pantelis.kelires@cut.ac.cy*

Carbon nanofoam is a new form of carbon, which has some unique physical properties, such as ultra low density (less than 1 g/cm³), open structure and large surface area. This material attracted attention after reports proposing that it exhibits intrinsic magnetism. The origin of this unexpected phenomenon is not clear, but it is believed to be instigated by unpaired spins at the kinks and junctions between the structural elements comprising the nanofoam. Candidate carbon nanostructures to serve as building blocks are various types of schwarzite structures. These are composed of graphite-like sheets possessing sevenfold rings, beside the normal sixfold rings, and having negative (hyperbolic) Gaussian curvature. They are analogous to the C₆₀ fullerene structure, which contains fivefold rings and has a positive curvature. Schwarzites have low density, nearly half that of graphite.

Here, we report our first results from atomistic simulations of carbon nanofoams. We primarily aim at elucidating the structure of the material at the nanoscale and beyond and also obtain its optoelectronic properties. We use Monte Carlo simulations with empirical potentials to generate initial structures, which are subsequently fully relaxed with tight-binding molecular dynamics simulations. We shall discuss the properties of two differently prepared three-dimensional nanofoam structures. The first type is generated by constructing nanocrystalline structures, in which the grains are schwarzites separated by grain boundaries. The second type is generated by condensing a vapor of schwarzite molecules under applied external pressure. In both cases, emphasis is given on the interlinking of the units and the stability of the overall structure as a function of its density.

Theory of Defects in Si Nanocrystals Embedded in a-SiO₂

G. C. Hadjisavvas* and P. C. Kelires

*Department of Mechanical & Materials Science Engineering,
Cyprus University of Technology, P.O. Box 50329, 3036 Limassol, Cyprus
and*

Physics Department, University of Crete, P.O. Box 2208, 710 03, Heraclion, Crete, Greece

*g.chatjisavvas@cut.ac.cy

Silicon nanocrystals (NCs) embedded in amorphous dielectric matrices (a-SiO₂) have attracted considerable attention both for their fundamental properties and potential applications in photonics and nanoelectronics. These nanocomposite systems exhibit strong optical activity (suitable for optical devices), and can also be efficiently charged (suitable for charge storage elements in non-volatile memory devices). It is universally accepted that these properties strongly depend on the nature of the interface between the NCs and the embedding medium, but exactly this parameter is the least well understood issue of the whole problem.

We present here Monte Carlo simulations and first-principles calculations aiming at resolving this issue. In our approach, the generation of realistic a-SiO₂ structures embedding the Si-NC is achieved via a modified Wooten-Winer-Weaire method, while the geometry optimization and calculation of the electronic structure and optical properties have been performed using ab-initio calculations.

Our preliminary results show that two-member-ring patterns (2M-R), not considered previously, are formed at the interface. The formation energy of 2M-R is calculated and compared with the formation energies of other interface defects (Pb centers, Si=O double bonds, Si-O-Si bridge bonds, etc.), revealing their configuration stability. We are at present analyzing the optoelectronic properties of these defects (density of states, absorption coefficient, dielectric function, etc.) in order to reveal possible origins of light emission from embedded Si nanocrystals.

Nanostructured thin films for dye sensitized solar cells

G. Syrokostas* and M. Giannouli

University of Patras, Renewable Energy Laboratory, Dept. of Physics, 26500 Patras, Greece

*gesirrokos@upatras.gr

The use of nanostructured films has played a very important role for the development of dye sensitized solar cells. Nanostructured films offer a huge internal area for dye adsorption and a porous structure that enhances the diffusion of the electrolyte ions and of the dye molecules during sensitization. Previous attempts for the sensitization of single-crystal semiconductors for dye sensitized solar cells gave poor results [1].

Nanostructured TiO₂ thin films were prepared by spreading a colloidal paste of nanoparticles on conducting glass substrates. The paste was prepared by mixing a small quantity of powder with water, acetylacetone and Triton X-100 in a porcelain mortar [2]. The paste was then spread on the conducting glass surface via the doctor blade method using a glass slide. Acetylacetone acts as a dispersing agent, since it prevents coagulation of nanoparticles. Instead of acetylacetone, hydrochloric acid was also used for the same purpose. Triton X-100 was added to facilitate the spreading of the paste on the substrate. Film thickness was about 10 μm, as measured with a stylus profilometer (XP-1) and it is mainly determined by paste concentration. The surface structure of the films and a rough estimation about the size of the nanoparticles were determined from images, taken using a scanning electron microscope (SEM). The TiO₂ films obtained through this method were used for the development of dye sensitized solar cells, with the aim of investigating the effect of the film's properties on the efficiency of the solar cells.

Different powders were used for the TiO₂ paste. First, a powder with micrometer sized TiO₂ particles was used, and then a powder with nanometer sized particles. Films prepared with the first powder were opaque, due to superior internal scattering of light on the large aggregates, and had poor adherence to the substrate. On the other hand, films prepared by the powder with nanometer sized particles were more transparent, in spite of their larger thickness, and had better adherence to the substrate. In the following SEM images we can see two different films prepared by the two different powders. The difference of the size of the TiO₂ particles is very characteristic. A few large aggregates can be observed for the film prepared by nanometer sized particles. Cells prepared with films from the second powder exhibited higher efficiencies, as verified by I – V characteristic curves.

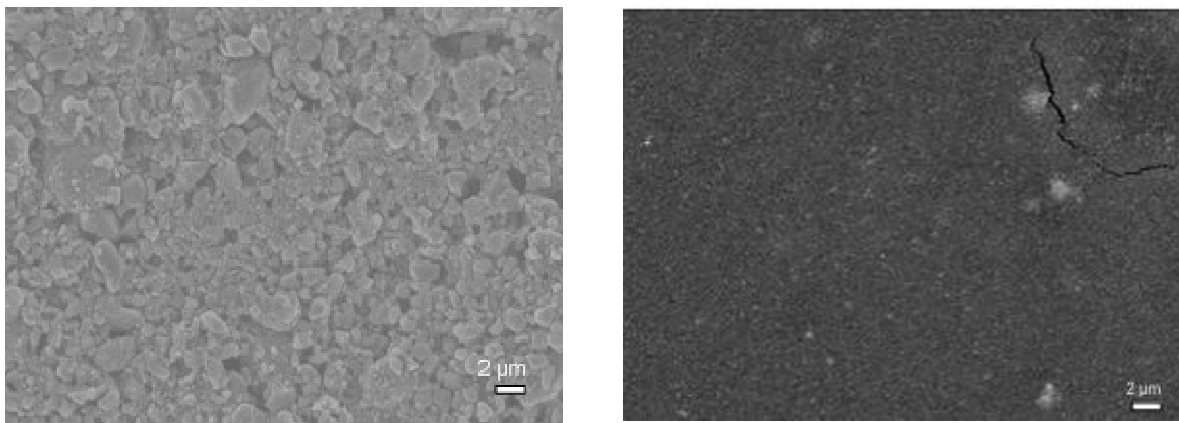


Fig. 1: SEM images from a film prepared by a powder containing micrometer sized TiO₂ particles (left) and nanometer sized TiO₂ particles (right).

In order to break down the aggregates into smaller pieces, mechanical stirring of the paste and an ultrasonic bath for the paste in water were tested. A small magnet was used for stirring the colloidal solution. The results were more apparent when a hydrochloric acid solution was used for the preparation of the paste, instead of acetylacetone. The average size of the nanoparticles, as verified by SEM images, was reduced; as the dispersion of large aggregates was more efficient. High shear forces developed during grinding of the paste are responsible for this effect. Two different concentrations were tested for the hydrochloric acid solution (1M and 1.5M). In the following SEM images we can see two different films; one prepared using acetylacetone and one using

hydrochloric acid (1M) solution. Cells with films prepared with hydrochloric acid exhibited higher efficiency and better stability when the films were sensitized in basic dye solutions.

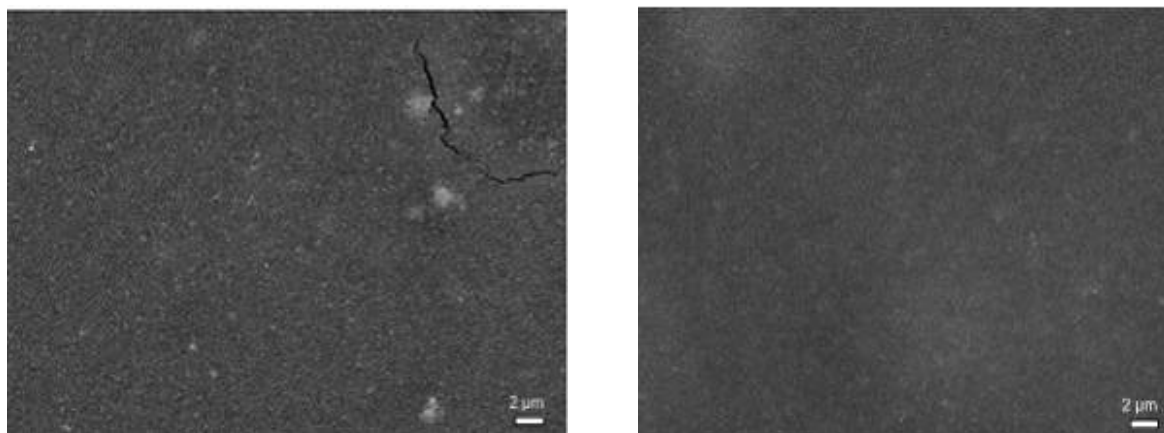


Fig. 2: SEM images from a film prepared by a powder with acetylacetone (left) and by a powder containing hydrochloric acid (right).

The size of the nanoparticles affects various films' properties such as porosity, surface roughness, transparency and conductivity. The electrical contact between neighboring nanoparticles is lower when large aggregates are present in the film, since the interconnection area between neighboring nanoparticles is reduced. Therefore, the resistance for charge transfer is greater. On the other hand, film's porosity is enhanced when large aggregates are present in the film, reducing the internal area for dye adsorption and enhancing electron recombination [3].

Films were also prepared by mixing the powder with micrometer sized particles and the powder with nanometer sized particles, in order to find out if the presence of some large aggregates affects the efficiency of the solar cells. These large aggregates can scatter the light striking photo-inactive parts of the solar cell more efficiently. Photons are then more likely to be absorbed by dye molecules due to internal scattering [4].

These films were used in order to develop dye sensitized solar cells. I – V characteristic curves were obtained both under illumination and in the dark. A typical I – V curve from a cell with a film prepared using hydrochloric acid is shown below.

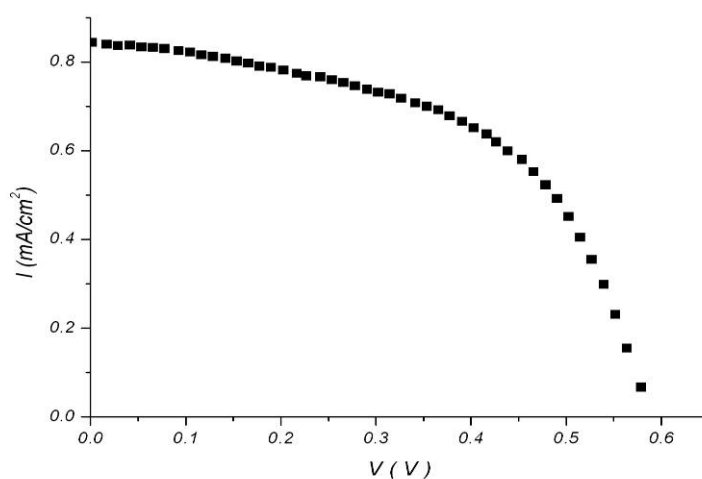


Fig. 3: I – V characteristic curve.

[1] D. F. Watson and G. J. Meyer, *Annu. Rev. Phys. Chem.* 56, 119 (2005).

[2] M. K. Nazeeruddin, A. Kay, I. Rodicio, R. Humphry-Baker, E. Miiller, P. Liska, N. Vlachopoulos, and M. Gratzel, *J. Am. Chem. Soc.* 115, 6382 (1993).

[3] G. Syrokostas, M. Giannouli and P. Yianoulis, *Renewable Energy* 34 (7), 1759 (2009).

[4] G. R. A. Kumara1, S. Kaneko, A. Konno, M. Okuya, K. Murakami, B. Onwona-agyeman and K. Tennakone, *Prog. Photovolt: Res. Appl.* 14, 643 (2006).

Electrolytic Hydrogen production using ternary and quaternary Nickel based coatings

Spanos Ioannis*, Yianoulis Panayiotis

University of Patras, Renewable Energy Laboratory, Department of Physics, 26500 Patras Greece

**ioaspanos@upatras.gr*

Electrolytic hydrogen production has gained considerable ground in recent years due to the discovery of new, efficient [1-2] and low cost alloy compounds compared to the very expensive and very efficient Platinum (Pt).

In this work we analyze the electrolytic hydrogen production and the fabrication of electrodeposited ternary Nickel-based thin film alloys. The addition of the Fe, Co, Mo transition metals in Nickel-based and Co-based alloys is of great interest in terms of research, because of their great electrocatalytic properties and high hydrogen production. These alloys even surpass Platinum (Pt), which is the most efficient metal used as a hydrogen production catalyst.

The use of sulfate [3-5] and chloride [6-7] baths to electrodeposit Iron-group metals onto different substrates is widely used due to the excellent electrocatalytic properties of the as-prepared cathodes. The electrodeposition of thin film alloys offers porous, inexpensive and resistive to corrosion, in both basic and acidic environment, compounds. The alloys we fabricated were, NiCoZn, NiFeZn, NiCoFeZn and NiMoZn. Our main goal was to study the electrodeposition process conditions and the manner in which they affect the morphology and the properties of the thin film alloys.

Nickel and Cobalt based coatings, electrodeposited on stainless steel and copper substrates were investigated as hydrogen evolution electrocatalysts, in 2M KOH aqueous electrolytes at room temperature. We studied the mechanism of Hydrogen Evolution Reaction (HER) and the dependence of the electrocatalytic activity of the cathode catalysts, on the pH of the coating solution and the current density of the electrodeposition process. Hydrogen evolution overpotential measurements were carried out on an AMEL MODEL-2053 galvanostat, using a typical 3-electrode electrochemical cell with an Ag/AgCl reference electrode. NiMoZn, NiCoZn, NiFeZn and NiCoFeZn cathode electrodeposits with low overpotentials at a current density of 50mA/cm² were fabricated, showing a Volmer-Tafel HER mechanism (Fig. 1 & 2).

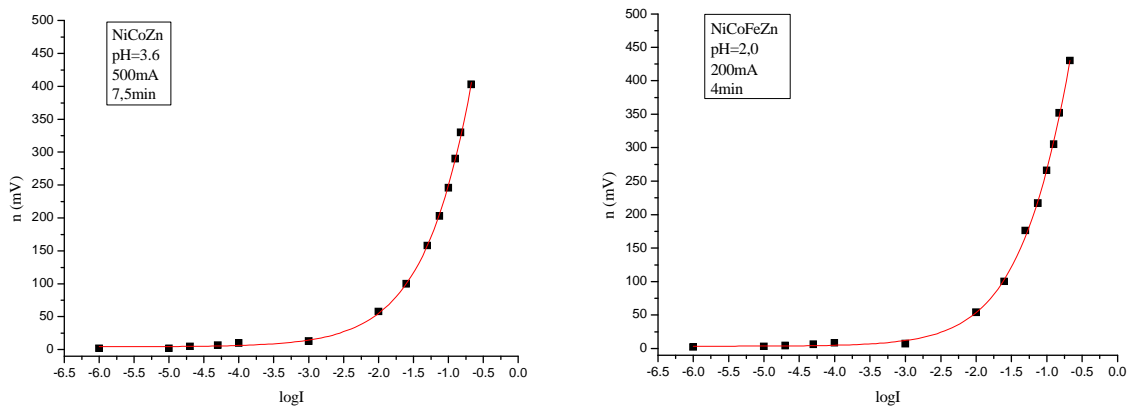


Fig. 1 & 2 Tafel plots (n vs logI) for NiCoZn and NiCoFeZn electrodeposits indicating the Volmer-Tafel HER mechanism

The electrocatalytic properties of the Nickel and Cobalt based cathodes were determined by the values of the exchange current density, hydrogen overpotential, Tafel slopes and by SEM micrographs (Fig. 3-6).

WE2

P6

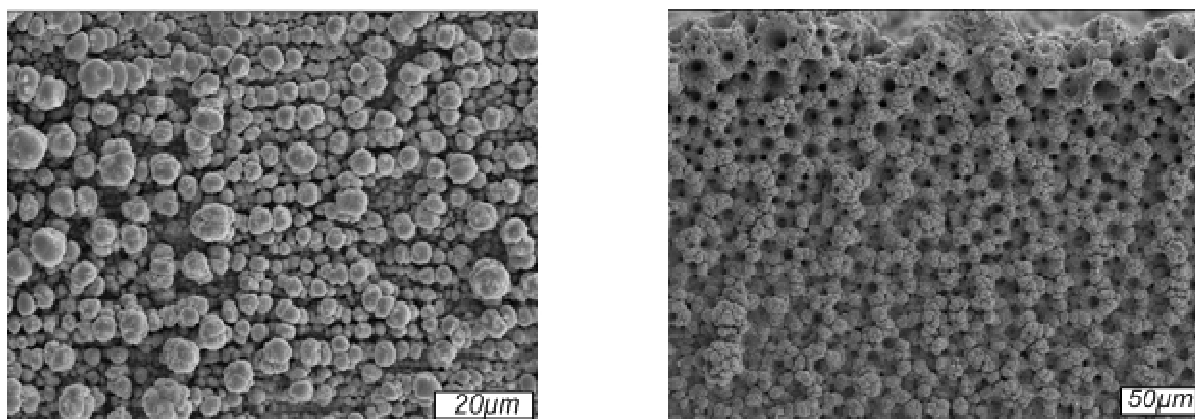


Fig. 3 & 4 SEM micrographs of NiCoFeZn and NiCoZn electrodeposits respectively, indicating the larger surface area of the NiCoFeZn cathode which consists of smaller particles.

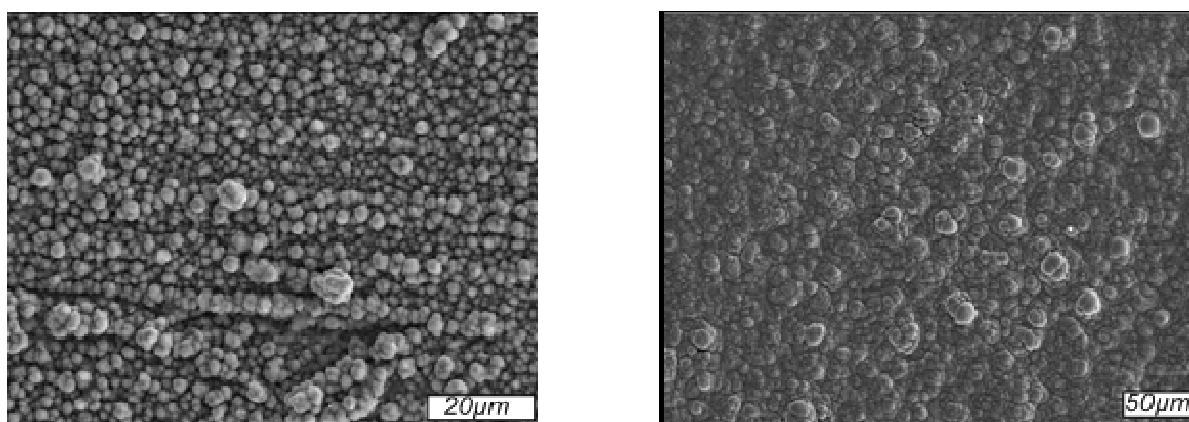


Fig. 5 & 6 SEM micrographs of NiMoZn and NiFeZn electrodeposits.

Finally on a typical H-type (Hoffman) electrolysis cell with a stainless steel anode, we conducted measurements of hydrogen production and electrolysis efficiency (Eq. 1), where n refers to the moles of the H_2 gas produced, H is Gibbs free energy of H_2 , V and I are the measured voltage and current and t is the duration of the electrolysis procedure.

$$n = \frac{W_{H_2}}{W_{el}} = \frac{nH}{\sum VIt} \quad (1)$$

The NiMoZn and NiCoFeZn alloys showed the best electrocatalytic behavior, thus leading to the conclusion that NiCoFeZn alloys are very promising materials for hydrogen production.

- [1] LUO Beiping, REN Buye, XU You and ZHENG Yajie, *Rare Metals* 26, 3, (2007).
- [2] F.C. Crnkovic, S.A.S.Machado, L.A. Avaca, *International Journal of Hydrogen Energy* 29 (2004) p. 249 – 254.
- [3] Keith Y. Sasaki and Jan B. Talbot., *Journal of The Electrochemical Society*, 147 (1) 189-197 (2000).
- [4] F. J. Fabri Miranda, O. E. Barcia, O. R. Mattos and R. Wiert, *J. Electrochem. Soc.*, Vol. 144, No. 10, 1997.
- [5] Jing-Yin Fei, G.D. Wilcox, *Electrochimica Acta* 50 (2005) 2693–2698.
- [6] Z.F. Lodhi, J.M.C. Mol, W.J. Hamer, H.A. Terry, J.H.W. De Wit, *Electrochimica Acta* 52 (2007) 5444–5452.
- [7] Z.F. Lodhi, J.M.C. Mol, A. Hovestad, H. Terry, J.H.W. de Wit, *Surface & Coatings Technology* 202 (2007) 84–90.

Interacting Si Nanocrystals in a-SiO₂: a Monte Carlo study

K. T. Kleovoulou¹ and P. C. Kelires^{1,2} *

¹ *Physics Department, University of Crete, P.O. Box 2208, 710 03, Heraklion, Crete, Greece*

² *Department of Mechanical & Materials Science Engineering,
Cyprus University of Technology, P.O. Box 50329, 3036 Limassol, Cyprus*

**pantelis.kelires@cut.ac.cy*

Silicon nanocrystals (NCs) embedded in amorphous dielectric matrices (a-SiO₂) have attracted considerable attention both for their fundamental properties and potential applications in Si-based optoelectronic and quantum computing devices. It is particularly a very interesting subject to realize ordered Si-NC assemblies (quantum dot photonic crystals or two-dimensional superlattices). For such an aim, it is necessary to control both the size of Si NCs and their inter-particle distances and positioning/ordering. Despite its importance, a lot of issues concerning the inter-particle interaction of Si-NCs still remain unclear.

We present here results of Monte Carlo simulations which shed light onto these issues. In our approach, the generation of the embedding a-SiO₂ structure is achieved via a modified Wooten-Winer-Weaire method. Starting from crystalline beta-cristobalite, the network is amorphized through bond-breaking and switching moves. The Si NC is positioned at the center of the cell. The energies are calculated using the Keating-like potential. Bond-conversion moves of the type Si-Si to Si-O-Si, and vice versa, allows us to study interdiffusion in the system. A 3.0 nm Si NC is chosen for our simulations. Through the periodic boundary conditions the inter-particle distance of the NCs vary from 0.5 to 4.0 nm.

The energetics, stability and mechanical properties of embedded Si NCs in a-SiO₂ and their variations versus the inter-particle distances are examined. From preliminary results, we find a decrease of the formation energy of Si NCs as their separation increases. We are currently examining whether there is a minimum in this variation. The formation energies have small positive values indicating that the NCs are slightly metastable. Penetration of oxygen into the NC, limited to few Angstroms, is observed. From an oxidation-number analysis, it comes out that the width of the interface is about seven Angstroms. We are at present analyzing the stresses in the area between the NCs in order to get more insight into this effect.

Application of Time-Series Analysis Methods for the Study of Nonlinear Dynamical Phenomena during Nanosurface Characterization in AFM Metrology

Georgakaki D.^{1*}, Mitsas Ch.², Polatoglou H.M.¹

¹Physics Department, Solid State Physics Section, AUTH., 54124

²Laboratory of Mechanical Measurements, E.I.M., Thessaloniki, 57022

* georgakd@auth.gr

ABSTRACT

High precision measurements are of great importance in AFM nanometrology. During the AFM scanning process, the interaction forces between the nanotip and the specimen must be carefully examined and analyzed. In this paper a numerical model is developed and studied, in order to describe the nonlinear dynamical response of an AFM system. The results from the theoretical analysis will be used in future work for the evaluation of deterministic uncertainty in real-time AFM measurements that is being introduced because of these phenomena. The confirmation of chaos existence and the prediction of the regions where chaotic motion is possible, remains crucial for the AFM image quality.

INTRODUCTION

Atomic Force Microscopy is the most widely used form of Scanning Probe Microscopy. Basic AFM modes measure the topography of a sample as well as its electrical, mechanical, and chemical properties [1]. In a typical AFM system there exist three different open-loop operational modes, according to small changes in cantilever tip-sample surface separation: i) contact mode, ii) tapping or intermittent mode and iii) non-contact mode.

The tapping mode of operation combines characteristics of both the contact and non-contact modes by oscillating the cantilever tip at or near its natural resonance frequency while allowing it to impact the target sample for a minimal amount of time [2,3]. This mode is the most potent non-destructive high-resolution technique for topographic imaging, ideal for the characterization of soft and fragile materials. It reduces adhesive and friction forces that are apparent in contact operational mode and it provides repeatability and variety in measurements as it collects data from both attractive and repulsive force regions [4].

Though widely practiced, the dynamic AFM modes exhibit the potential for unwanted dynamic phenomena such as phase jumps, period doublings or even chaotic behavior in the cantilever tip displacement [5], thus rendering erroneous topographical information and causing instabilities that reduce the quality of the image. As a result, recent research on AFM systems has focused on detailed numerical analysis such that this chaotic behavior region can be well defined and ideally avoided [3].

In this paper, time-series analysis methods (TSA) are applied to analyze signals generated by a numerical single-degree-of-freedom lumped-model of a tapping-mode AFM. The signal characteristics will provide useful insight of the nonlinear system response, important for the dynamic AFM metrology.

THE NUMERICAL MODEL & ITS SIMULATION

The numerical AFM model [3,5,6] is a nonlinear spring of stiffness k with an effective tip mass m_e and a dumping coefficient c . The cantilever resonates with an excitation frequency ω_c . The position of the root of the cantilever is represented by $d(t)$ and the motion of the tip by $x(t)$. $P(x(t))$ represents the force acting on the tip resulting from the tip-sample interaction (van der Waals force). The differential equation that describes the AFM system is given below in equation (1):

$$m_e \cdot x''(t) + c \cdot (x'(t) - d'(t)) + k \cdot (x(t) - d(t)) = P(x(t)) \quad (1)$$

where $c = \frac{k}{Q \cdot \omega_c}$ (2), with Q being the quality factor, $d(t) = A \cdot \sin(\omega \cdot t)$ (3), with A being the driving amplitude and finally,

$$P(x(t)) = \frac{R \cdot A_h}{6 \cdot (z - x(t))^2} - \frac{\sigma^6 \cdot R \cdot A_h}{180 \cdot (z - x(t))^8} \quad (2)$$

which represents the single-mode approximation utilizing Lennard-Jones potential, with R being the tip radius, A_h the Hamaker constant, σ the molecular diameter and z the distance between the fixed frame and the sample surface.

The mathematical model that simulates the AFM system was created in Mathematica, and two different time-series of data were studied: a series that exhibits periodic behavior and a series with traces of chaotic behavior. The fixed parameters used in the mathematical model regarding the properties of the cantilever are taken from [3,5,7] and the ones that can be changed are the driving amplitude and the distance z .

METHODS

(i) Phase Portraits

By plotting the tip displacement versus tip velocity [8], we can get a first approach of the periodic and chaotic regimes of the dynamical AFM system. The different phase diagrams (Fig 1a-1b) correspond to different driving amplitude values and different z values.

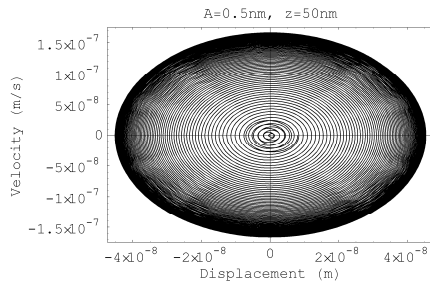


Fig. 1a: Periodic Regime, non-contact mode

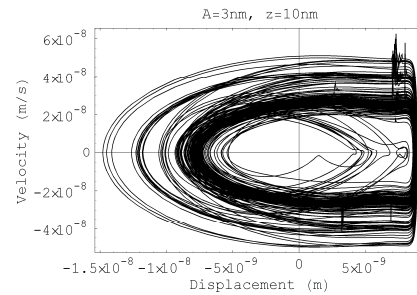


Fig. 1b: Chaotic Regime, transition from non-contact to tapping mode

(ii) Autocorrelation function (ACF)

The Autocorrelation function diagrams reveal possible correlations between time consecutive tip deflection measurements. In our case, the data exhibit short-range correlations in both cases, and the ACF function bounces around zero without decreasing (as for example in an AR(1) procedure with $\phi < 0$ [9]). This behavior strongly indicates the presence of nonlinear phenomena in the AFM system.

(iii) Power Spectral Density (PSD)

The PSD diagrams reveal the oscillation modes of the system and the presence of noise in the frequency spectrum indicates the transition from a periodic to a chaotic regime, as can be observed in fig 2a-2b.

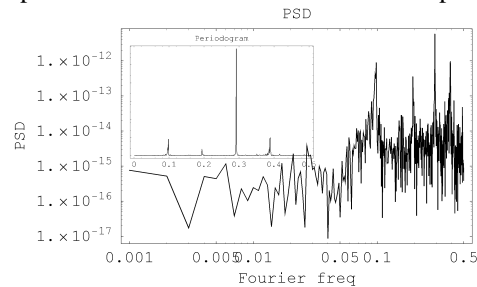


Fig 2a: Noisy frequency spectrum, various oscillation modes

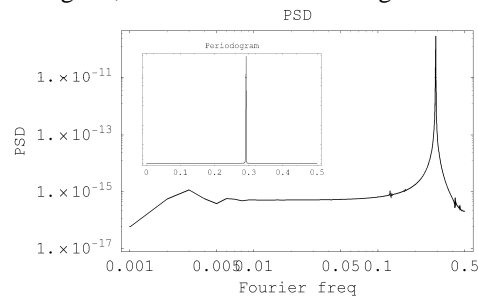


Fig 2b: Flat frequency spectrum, one oscillation mode

All computational methods were developed in Mathematica and Matlab environment. Further details for the TSA methods can be found in [9].

Conclusions

The TSA techniques described above reveal valuable information regarding the correlation of tip-deflection measurements, which unavoidably lead to a new approach in the calculation of dynamical uncertainty of AFM measurements [10]. The presence of chaos influences the image quality so the amplitude of vibration in which chaos is appeared needs to be carefully investigated. Both issues will be solved in future work.

References

- [1] Bharat Bhushan, Springer handbook of nanotechnology, Springer-Verlag Berlin Heidelberg (2004).
- [2] Pishkenari H.N. et al, Mechatronics 16 (2006) 655–664 .
- [3] Jalili N., Laxminarayana K., Mechatronics 14 (2004) 907–945.
- [4] Dankowicz H., Phil. Trans. R. Soc. A (2006) 364, 3505-3520.
- [5] Liu M., Chelidze D., International Journal of Nonlinear Mechanics 43 (2008) 521-526.
- [6] Burnham N.A. et al, Nanotechnology 8 (1997) 67–75.
- [7] Raman A. et al, Proc. R. Soc. Lond. A 2003 459, 1925-1948.
- [8] Hu S., Raman A., PRL 96, 036107 (2006).
- [9] Falk M, A first course in time-series analysis – examples with SAS, Chair of Statistics, University of Wurzburg (2006).
- [10] Zhang N.F., Metrologia 43 (2006) S276-S281.

Structural Characterization of Ti / TiB₂ Multi-nano-layer Films by Means of Electron Microscopy Techniques.

Ch. B. Lioutas, N.Z. Vouroutzis, N. Frangis, N. Kalfagiannis, S. Logothetidis

Solid State Physics Section, Department of Physics, Aristotle University of Thessaloniki,
GR-54124 Thessaloniki, Greece

*lioutas@physics.auth.gr

Multilayered composites consisting of alternating metal and ceramic layers offer extraordinary strength, hardness, heat resistance and unexpected new properties. In the present work Ti/TiB₂ multilayer coatings were fabricated on c-Si substrates, employing the Magnetron Sputtering technique. The periodic structure was achieved through the rotation of the sample holder between a Ti and a TiB₂ target. In all cases a negative bias of -60 V were applied on the substrate. Electron Diffraction, Conventional and High Resolution Transmission Electron Microscopy (HRTEM) were used to measure the films thicknesses and study their nano-structural features.

Results from X-Rays and TEM studies are summarized in Table 1 for Ti / TiB₂ multilayer films.

TABLE - 1

Specimen	T224	T225	T226	T227
Rotation speed (rpm)	2	4	6	9
Density Ti (g/cm ³)	4.2	4.16	3.57	3.5
Density TiB ₂ (g/cm ³)	4.12	3.92	3.55	3.49
Layers interdistance (nm) X-Rays	9.34	5.556	3.49	2.33
Layers interdistance (nm) TEM	8.93	4.93	3.01	2.16

Electron diffraction patterns showed that films deposited with rotation speed higher than 6rpm exhibit an amorphous structure (Fig. 1a), although the two composites form distinguishable layers (Fig. 2). For lower speeds, thicker layers are grown. The electron diffraction patterns indicate the presence of nanocrystals giving characteristic fibrous texture (Fig. 1b).

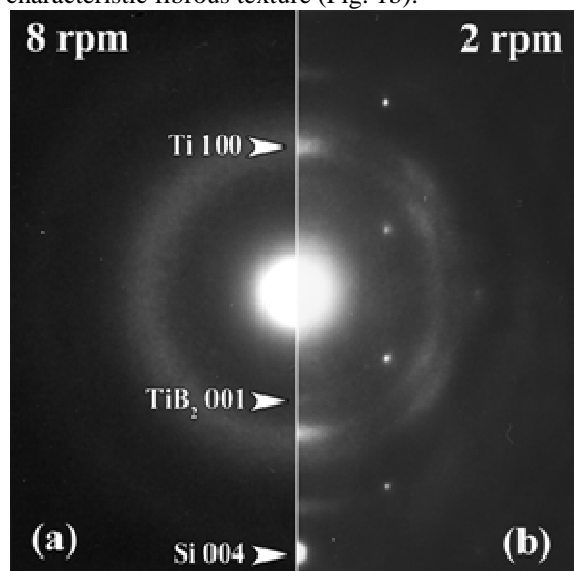


Fig. 1 Electron diffraction patterns from the films deposited with rotation speeds 8 and 2 rpms (a and b respectively). The diffuse intensity ring (a) reveals the amorphous nature of the material in high speed deposited film. For the low speed (b) it is clear that small crystalline areas are grown. The locations of the maxima of the diffracted intensity suggest the presence of preferential growth. The Ti [10.0] hexagonal axis is nearly parallel to the [001] cubic direction of the Si substrate.

Dark Field images as well as HRTEM micrographs (Fig. 3), reveal the growth of very thin crystallites less than 2nm in width, mainly in the Ti layers. In all cases the Ti [10.0] hexagonal direction is nearly parallel to the [001] direction of the Si substrate (Fig. 1b).

The nanomechanical properties, hardness and elastic modulus, of the multilayer films were studied using depth-sensing nanoindentation. The elastic modulus values were found to remain almost constant, while slight dependence of the hardness to the bilayer thickness was detected

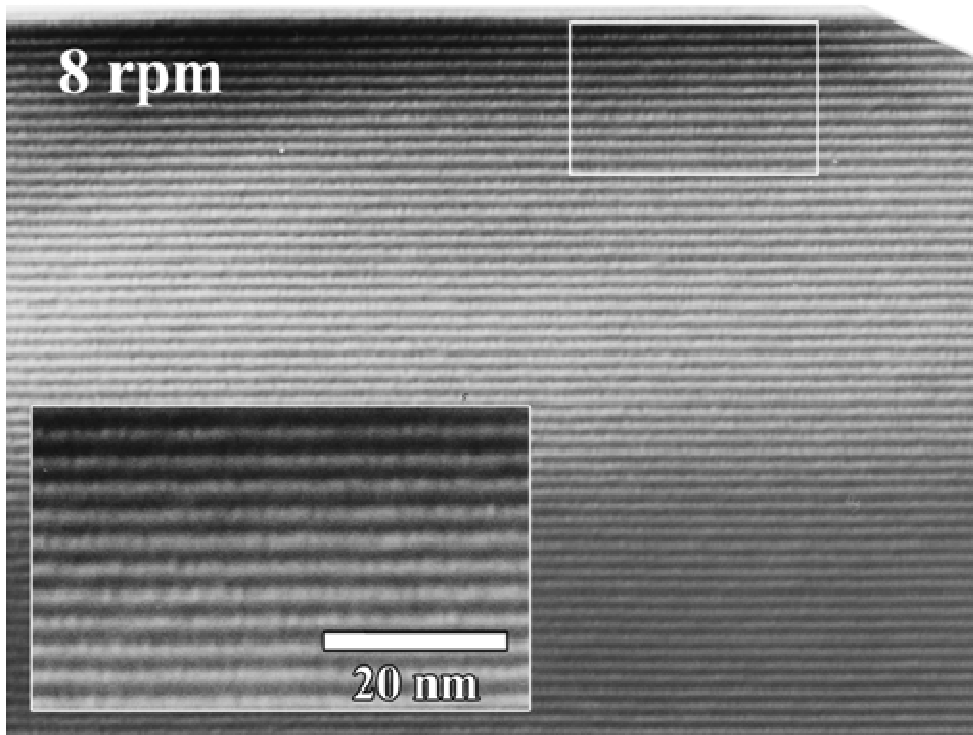


Fig. 2 Conventional high magnification Bright Field TEM image from a film deposited with high speed rotation of the substrate. The ED pattern obtained from the film shows characteristic amorphous intensity distribution. However the image shows that the two composites (Ti and TiB_2) are grown in distinct layers.

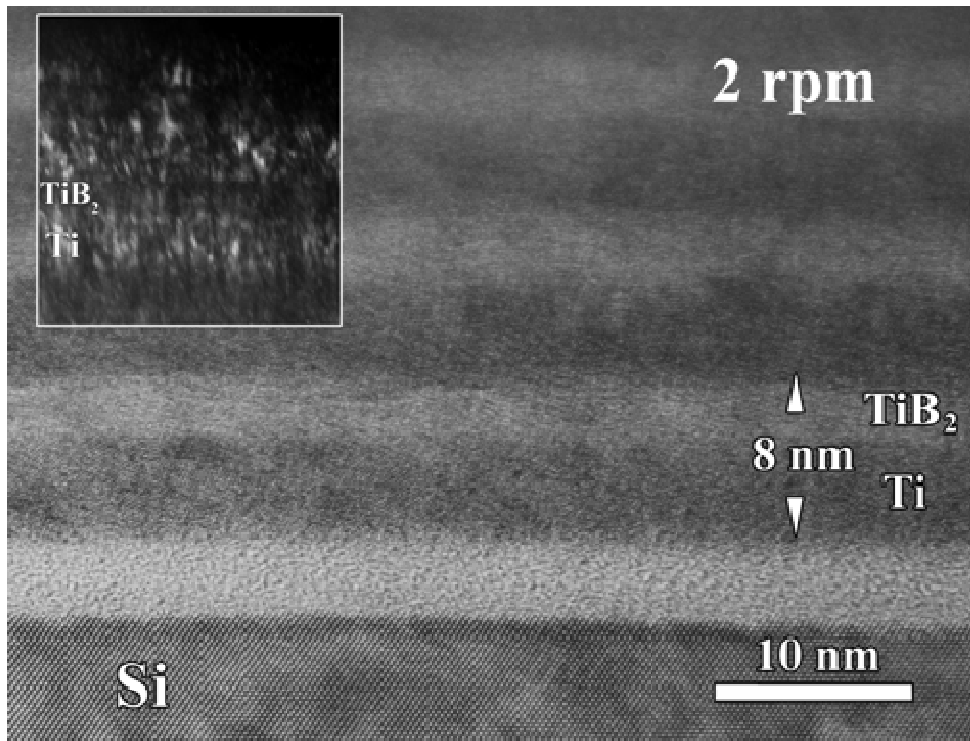


Fig. 3 High Resolution TEM image from a film deposited with low speed. It is obvious the growth of nanocrystals in both composites layers. The Dark Field High magnification image, shown as inset, demonstrates a fibrous development mainly in Ti layers. The fibre axis is nearly parallel to the growth direction.

Oxidization behaviour of amorphous SiC Coatings

D. Lafatzis and K. Mergia

*Institute of Nuclear Technology and Radiation Protection, National Centre for Scientific Research
"Demokritos", 15310 Agia Paraskevi Attikis, Greece*

*dlafatzis@ipta.demokritos.gr

For the aerospace applications of composite materials, such as Cf/SiC and SiCf/SiC, oxidation resistant SiC coatings have to be developed. This work aims at understanding the oxidation of SiC in air at high temperatures and long times and the degree on which the formed SiO₂ film acts as a protection to further oxidation.

SiC layers having a nominal thickness of 309 nm have been fabricated on (100) crystalline silicon substrates polished at both sides, using rf sputtering. The same sample was oxidized at a specific temperature and for different times in a furnace open to the ambient air. The oxidation temperatures were 600, 800, 1000, 1200°C and the oxidation times varied up to 418, 37.5, 9 and 1.92 h, respectively.

The as deposited samples have been characterized by X-Ray Reflectivity (XRR) and Fourier Transform Infrared (FTIR) spectroscopy. Grazing incidence X-ray diffraction measurements (GIXRD) measurements showed a small degree of crystallization of the as deposited SiC layers. XRR measurements of the as deposited SiC samples show Bragg peaks up to 6th order which correspond to a periodic bilayer structure of the SiC film having a thickness of 46 Å. The bilayer consists of SiC sublayers with densities 2.87 and 2.74 g/cm³.

The oxidized samples were also characterized with XRR, FTIR and when it was necessary with GIXRD. Both sides of the oxidized samples were measured with XRR in order to correlate XRR and FTIR data. To accomplish that, Si samples were also oxidized under the same experimental conditions and characterized with the same techniques in order to quantify the FTIR results from the SiO₂ layer formed on SiC. It was also confirmed that the SiO₂ layer formed on SiC surface has the same structure as that formed on Si surface.

Comparison of the FTIR and XRR data, leads to a linear correlation between the integrated FTIR absorbance area from the Si-O stretching vibration mode, associated with the formation of SiO₂ on SiC, and the SiO₂ thickness determined from the XRR data. This correlation is very useful as it can be used for SiO₂ thickness determination in case it is difficult to have accurate information about SiO₂ thickness with other techniques such as XRR. Oxidation of SiC results in the appearance of fringes in the reflectivity curves from which by least square fittings the characteristics of the formed SiO₂ layer are determined. As the SiO₂ layer grows the distance between the fringes (Fig. 1) becomes smaller.

In figure 2, the thickness of SiO₂, as determined from XRR data, versus oxidation time is presented. Theoretical models for the evolution of SiO₂ on SiC with oxidation time are under evaluation. GIXRD and FTIR measurements have shown no signs of SiC crystallization even for the longest oxidation time at 1200°C. On the other hand, the same measurements testify the complete crystallization for the formed SiO₂ layer at 1200°C after oxidation for 1.25 h, and the onset of crystallization at 800°C/37.5h and 1000°C/9h.

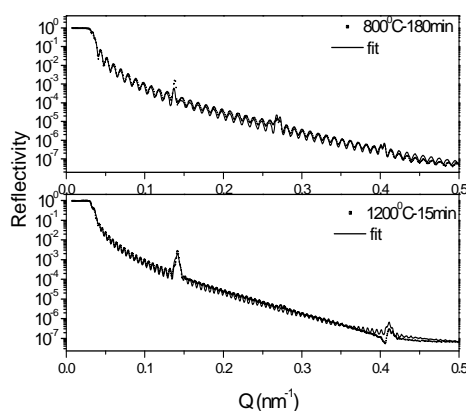


Fig.1. X-ray reflectivity from the oxidized SiC coatings at 800°C for 180 min and at 1200°C for 15 min. Solid lines: least squares fit to the data.

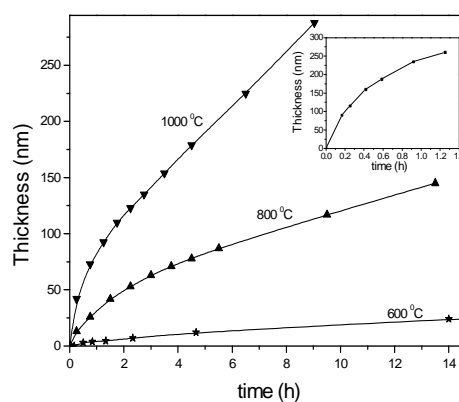


Fig.2. Thickness of SiO₂ versus oxidation time at 600, 800, 1000°C. The insert presents SiO₂ thickness at 1200°C versus oxidation time. The solid lines are guide to the eye.

CuZr Nanoclusters by ab-initio calculationsG. Bokas^{1*}, Ch.E. Lekka², G. A. Evangelakis¹¹ University of Ioannina, Department of Physics, Ioannina 45100, Greece² University of Ioannina, Department of Materials Science and Engineering, Ioannina 45110, Greece

*george.bokas@gmail.com, chlekka@cc.uoi.gr, gevagel@cc.uoi.gr

The CuZr bulk metallic glass is experimentally known to consist of small sized clusters basically of icosahedral-like structure (ICOs) that are embedded in the amorphous matrix [1-5] and most probably influence its mechanical response inducing ductility [2,3,5]. Nevertheless, studies concerning the fundamental mechanisms behind or even the properties of the small CuZr clusters themselves are limited. Starting from the simple case of free standing nanoclusters we calculated the electronic and structural properties of icosahedral (ICO) $\text{Cu}_x\text{Zr}_{13-x}$ ($x=0-13$) and rhombic dodecahedra (RD) $\text{Cu}_y\text{Zr}_{15-y}$ ($y=0-15$) clusters across the compositional range. We found that the pure Cu ICOs are energetically favored against the RD clusters, which in turn, are energetically preferred in the case of pure Zr clusters. Interestingly, in the cases of mixed clusters, the ICOs with $x=1-7$ are Cu centered, while the rest ($x=8-12$) are Zr centered. It is worth to be noted that for the ICO clusters with almost equal concentration ($x=6,7$) the energy difference between the Cu and Zr centered is very small. In addition, from the electronic density of states (EDOS) we found that all clusters exhibit metallic character, with the energetically favored clusters manifesting enhanced EDOS's at the Fermi level. These results are also reflected in the HOMO electronic wavefunctions; especially for the Cu centered ICO clusters we found strong orbital hybridization between the central atom and two to four shell atoms. The present results could be used as the first step for the understanding of the role of the CuZr clusters in the electronic and structural properties of the bulk metallic glass.



Figure. Icosahedral and rhombic dodecahedra CuZr nanoclusters

- [1] D.B. Miracle, *Nat. Mater.* 3 (2004), p. 697.
 [2] Ch.E. Lekka, A. Ibenskas, A.R. Yavari and G.A. Evangelakis, *Appl. Phys. Lett.* 91 (2007).
 [3] M. Wakeda, Y. Shibutani, S. Ogata and J. Park, *Intermetallics* 15 (2007), p. 139.
 [4] A.E. Lagogianni, G.A. Almyras, Ch.E. Lekka, D.G. Papageorgiou, G.A. Evangelakis, *J. Alloys and Comp.* in press.
 [5] H.W. Sheng, W.K. Luo, F.M. Alamgir, J.M. Bai and E. Ma, *Nature* 439 (2006), p. 419.
 [6] Ch.E. Lekka, A. Ibenskas, A.R. Yavari and G.A. Evangelakis, *Appl. Phys. Lett.* 91 (2007).

Structural and electronic properties of octahedral Titanium Oxide on Graphene by ab-initio calculations

M.Gialampouki and Ch.E.Lekka*

Department of Materials Science and Engineering, University of Ioannina 45110, Ioannina, Greece

**chlekka@cc.uoi.gr*

The fabrication of nanoscaled TiO_2 is of considerable interest due to its potential technological applications in catalysis, biosensing and gas sensing. To address this need CNT have been used as templates, while the benzyl alcohol was experimentally found to be an excellent tool for controlling the size of the deposited TiO_2 particles upon crystallization and phase transformation [1,2]. Graphene is a new carbon-based material that consists of a single atomic layer of graphite and the production of TiO_2 coating on this material would be of major importance for future nano-technological applications [3,4].

In this work we present Density Functional Theory calculations results referring to the structural and electronic properties of the octahedral Titanium oxide deposited on graphene. In addition, we investigated the role of the benzyl alcohol as surfactant in uniformly coating pristine graphene with TiO_2 . In particular, we studied the early stages of the adsorption mechanisms and the nature of bonding between the TiO_6 -Graphene with and without the presence of benzyl alcohol, as well as the influence of the latter on the system's electronic distributions.

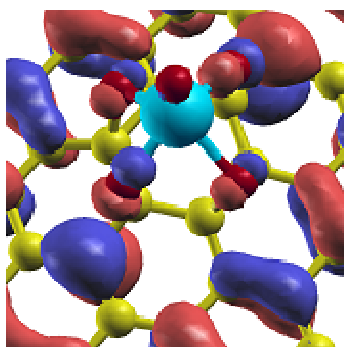


Figure 1. Octahedral titanium oxide deposited on graphene.

- [1] D. Eder, Ian.A.Kinloch, A.H.Windle, Chem.Commun.1448-1450 (2006).
- [2] X,B,Yan, B.K.Tay, Y.Yang, J.Phys.Chem.B 110, 25844 (2006).
- [3] S. Malola, H. Häkkinen, and P. Koskinen, Appl. Phys. Lett. 94, 043106 (2009).
- [4] J. Scott Bunch, Arend M. van der Zande, Scott S. Verbridge, Ian W. Frank, David M. Tanenbaum, Jeevak M. Parpia, Harold G. Craighead, Paul L. McEuen, Science 315, 490 (2007).

Acknowledgments This work was supported by the Research Committee of the University of Ioannina (No 80018) should be placed at the end of the document.

Magnetic nanoclusters synthesized by a new gas-stabilised aggregation technique

O. Crisan^{1*}, K. von Haefen², A.M. Ellis³ and C. Binns²

¹ *National Institute for Materials Physics, Bucharest, Romania*

² *Condensed Matter Physics CMP, University of Leicester, LE1 7RH, Leicester, UK*

³ *Department of Chemistry, University of Leicester, LE1 7RH, Leicester, UK*

*ocrisan@yahoo.com

Nanoscale organized materials for different purposes, such as nano-electronics, biomedicine, or magnetic applications are extensively studied. Novel nanoscale architectures are now engineered by using molecule-by-molecule or atom-by-atom assemblies, into building blocks for nanoscale devices, with a variety of properties, within the so-called “bottom-up” approach. A novel method for production of free clusters as building blocks for nanoscale devices is presented. These clusters may be subsequently functionalized in-situ by adding atoms/molecules of different nature, on the surface of readily formed clusters. The method uses a cold beam of rare gas (Ar) molecules and clusters, passing through a region of low-pressure atomic vapour, in an ultra-high-vacuum multiple chamber facility. The atoms are collected and condensed by the rare gas beam in the pick-up zone, and a large variety of very small cold clusters, metals, oxides, molecules, etc. are thus formed. We prove that the cluster size is extremely well controlled by the vapour pressure of the picked-up species. The method is versatile, since it allows multiple pick-up processes within the same rare gas cluster for producing, for example metal/oxide core-shell nanoparticles that are furthermore functionalized by attaching to the surface of the cluster, various molecules such as pentacene, for applications in nanoelectronics and aptamers, nucleotides, antibodies, for applications in biomedicine. Initial formation of Fe gas-stabilised clusters, Fe/Fe oxide core-shell nanoparticles, their structure and morphology, are presented and discussed.

Acknowledgments The authors acknowledge the financial support in the frame of the EPSRC grant, EU projects Nanospin and Nanocase as well as the financial support from the PN II project 71-060 / 2007 and 12-129 / 2008 of the Romanian Ministry of Research.

WE2

P13

Effect of the Adhesive Forces and Time-Dependent Response of Polydimethylsiloxane Elastomer on the Nanomechanical Properties Determination by Nanoindentation

C.A.Charitidis*, E.P.Koumoulos

School of Chemical Engineering, National Technical University of Athens, 9 Heroon Polytechniou St., Zographos, Athens, Greece GR-157 80

*charitidis@chemeng.ntua.gr

Polydimethylsiloxane (PDMS) is a silicone elastomer with properties that make it attractive for the development of MEMS and microfluidics components for biomedical applications. It is chemically inert, thermally stable, permeable to gases, simple to handle and manipulate, exhibits isotropic and homogeneous properties as well as lower cost than silicon, and can conform to submicron features to develop microstructures. There is significant interest in examining the compatibility of PDMS with both MEMS technology and biomedical applications. Therefore, further investigation of the structural and surface properties of PDMS in nanoscale is needed in order to accelerate its wider adoption for the development of BioMEMS devices and applications [1].

In this study nanoindentation technique is used to characterize the nanomechanical properties, namely the hardness (H) and elastic moduli (E) of PDMS specimens (8 parts per hundred (phr) concentration of montmorillonite nanoclays in the PDMS matrix) at different loading rates and to study the interactions between the Berkovich tip and the PDMS nanocomposite surface before, during and after contact. The influence of polymer's viscosity and the effect of loading rate on hardness and elastic modulus values of PDMS are taken into account. All indentation tests were performed with Hysitron TriboLab® Nanomechanical Test Instrument equipped with a Berkovich tip. Feedback Control was used for its ability to operate under closed loop load or displacement control (this capability provides the means of performing traditional tests utilized for viscoelastic property measurements of biomaterials and polymers, such as creep and stress relaxation tests). The load-depth results revealed an almost reversible feature, which indicated elastic deformation. Significant initial penetration depths, created during the finding surface process, were found [2]. The effect of loading rate on hardness and elastic modulus values was studied for loading rates 0.1, 0.8, 1.2, 1.5, 8, 20 and 40 $\mu\text{N}/\text{sec}$.

Considerable uncertainties arise when applying the nanoindentation technique to very soft materials with elastic modulus below 5 MPa or adhesive PDMS samples [3, 4]. For soft PDMS surfaces, the initial contact load can create an initial penetration depth in the order of nanometer, so that the contact area tends to be underestimated, which leads to an overestimation of hardness and modulus values. Gupta et al. [5] investigated the effects of adhesion on the elastic modulus determined from nanoindentation results for soft PDMS elastomers with different nanoclays concentrations. The load-depth curves for all PDMS concentrations showed a nearly linear characteristic for a large range of applied load [2]. This unique linear characteristic may be attributed to the distinct contact conditions caused by the strong adhesion between the tip and the sample.

The load vs. displacement plot (Fig. 1) into the PDMS surface illustrates the insensitivity of this signal to surface contact on soft materials. Nearly 850 nm of displacement was required before 12 μN of force was registered (Fig. 1). The dynamic load signal (dynamic contact stiffness) can be used to provide much greater sensitivity to surface contact and surface stiffness in comparison with a change in a quasi-static force or stiffness measurement. The dynamic load signal as the tip approaches the surface, snaps into contact because of surface forces, and measures the increase in the surface stiffness with displacement [6].

The findings of the study suggest that consideration of the adhesion energy at the tip-PDMS surface interface is a significantly important parameter and needs to be taken into account for consistent elastic modulus determination of soft materials by nanoindentation. Instrument calibration, strain effects and material heterogeneity are several examples of complications that arise when small volumes of PDMS are tested. The slightly more divergent results for PDMS samples with different percentage of nanoclays might be indicative of these types of effects. Thus, the current calculation methods, though seemingly adequate for these polymeric materials, will not be able to capture the dynamic response of materials for which viscous or rubbery flow conditions exist (i.e., where energy loss is a more significant factor).

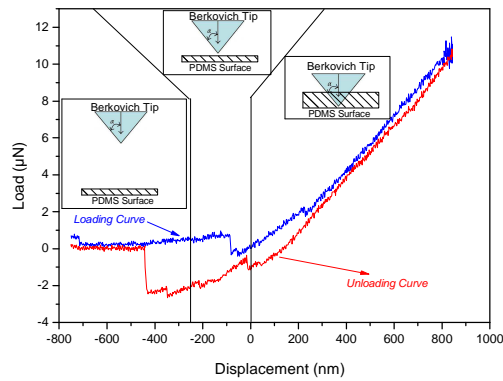


Figure 1. Load (dynamic contact stiffness) vs Displacement as the tip approaches the surface, snaps into contact because of surface forces in the surface of PDMS [7].

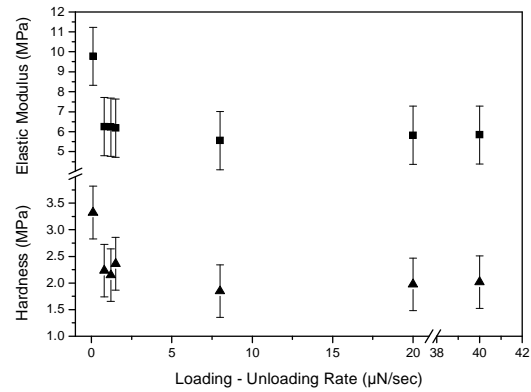


Figure 2. H & E values for different loading rates.

The effect of loading rate on hardness and elastic modulus values was studied for loading rates 0.1, 0.8, 1.2, 1.5, 8, 20 and 40 $\mu\text{N}/\text{sec}$ in PDMS (8phr) with a maximum load of 500 μN . It was found that hardness and elastic modulus values are high (3.3 and 9.8 GPa, respectively) for a loading rate of 0.1 $\mu\text{N}/\text{sec}$, decreasing with the increase of loading rate and reaching stable values (~ 2 and 5.8 GPa respectively). The unloading rate was the same with that of loading in each case. The H and E values estimated by Oliver-Pharr model [8] are presented in Table 1. H & E values were estimated taking into account the first 30% of the unloading part of the load-unload curve (Fig.2).

Table 1. H and E values estimated by Oliver-Pharr model [8].

Loading – Unloading Rate ($\mu\text{N}/\text{sec}$)	Hardness (MPa)	Elastic modulus (MPa)
0.1	3.327	9.770
0.8	2.234	6.258
1.2	2.146	6.226
1.5	2.360	6.176
8.0	1.848	5.552
20.0	1.974	5.820
40.0	2.016	5.836

The hardness and elastic modulus for loading rates 0.1, 0.8, 1.2 and 1.5 $\mu\text{N}/\text{sec}$ have been found higher than those for loading rates 8, 20 and 40 $\mu\text{N}/\text{sec}$. The minimum values of hardness and elastic modulus (1.85 and 5.55 MPa, respectively) were found for loading rates 8, 20 and 40 $\mu\text{N}/\text{sec}$. Since the same force profile was applied during a longer time interval at low loading-unloading rates than that at loading-unloading rates, a larger amount of kinetic energy was applied to the PDMS at low loading rate than that at high loading rate, resulting to differences in nanomechanical properties because of the time-dependant viscoelastic behavior of PDMS. For quantitatively accurate and reproducible results, nanoindentation of soft and adhesive materials requires further validation and suitable modification. These challenges present numerous opportunities for the continued development of indentation instrumentation and techniques and a redesign of the experimental protocol is needed.

References

- [1] A. Mata, A. J. Fleischman and S. Roy, 7(4) 281–293 (2005).
- [2] E. Koumoulos, ‘Nanomechanical properties of polymer-based systems. Case studies: I. Silicone elastomers and II. SiO_x thin films on PET’, Master Thesis in School of Chemical Engineering, National Technical University of Athens (March 2009); E. Koumoulos, C.A. Charitidis, S. Vasilakos, P.A. Tarantili ‘Nanoindentation of Nanocomposites Polydimethylsiloxane Elastomers’, 7th Conference of Chemical Engineering, Patra (June 2009).
- [3] D. Tranchida, S. Piccarolo, J. Loos, and A. Alexeev, Appl. Phys. Lett. 89, 171905 (2006).
- [4] J. C. Lotters, W. Olthuis, P. H. Veltink, and P. Bergveld, J. Micromech. Microeng. 7, 145 (1997).
- [5] S. Gupta, F. Carrillo, C. Li, L. Pruitt, and C. Puttlitz, Mater. Lett. 61, 448 (2007).
- [6] C.C. White, M.R. Vanlandingham, P.L. Drzal, N.K. Chang and S.H. Chang, J. Polymer Science: Part B: Polymer Physics, 43, 1812–1824 (2005).
- [7] Pethica, J. B., Oliver, W. C. Phys Scr T, 19, 61–66 (1987).
- [8] W.C. Oliver, G.M. Pharr, J. Mater. Res. 7 1564 (1992).

Nanoindentation Studies and High Stress Sensitivity of Fatigue Life of Rolled AZ31 Magnesium Alloy

C.A. Charitidis^{1*}, A. Skarmoutsou¹, A.N. Chamos², Sp.G. Pantelakis²

¹*School of Chemical Engineering, National Technical University of Athens, 15780 Athens, Greece.*

²*Laboratory of Technology and Strength of Materials, Department of Mechanical and Aeronautical Engineering, University of Patras, 26500 Patras, Greece.*

* charitidis@chemeng.ntua.gr

Weight reduction is of major concern for the aeronautical industry, in order to increase operational capacity and reduce environmental impact via reduction of fuel consumption. Extensive investigations for the utilization of low weight materials are an obvious consequence of the above need. Amongst the materials considered as presently candidates for tomorrow aircraft structures, magnesium alloys could represent a break through provided some essential drawbacks such as high corrosion susceptibility and poor damage tolerance behaviour as compared to other structural alloys, like aluminum and titanium, could be faced. Currently, several works are in progress to develop wrought magnesium alloys for aerospace applications, e.g. [1].

One of the challenges in studying the local mechanical properties in a small volume of material having microstructural gradients is that the traditional methods, e.g. tensile test and microhardness test, used to evaluate the mechanical behaviour of bulk materials are not applicable. Nanoindentation testing provides a convenient measurement of the mechanical properties of very small volumes of material. It is revealed that some materials exhibit indentation size effect (ISE), which shows an increase in hardness with decreasing applied load [2,3]. Apparently, the existence of ISE may hamper the accurate measurement of hardness value. Based on the elastic deformation theory, elastic modulus (E) and hardness (H) values can be extracted from the experimental data of indenter load and depth of penetration, i.e. Oliver-Pharr method [4-6].

For very small indentation loads (100 μN –1 mN), which determine mechanical properties, “pop-in phenomena” were observed for a variety of materials. A material is said to pop-in if a sudden increase is seen in the displacement without any appreciable increase in the load. This happens during the loading phase of the nanoindentation experiment [7- 10]. Gerberich et al. [11] have proposed that dislocations are generated prior to pop-in and the pop-in indicates failure of a passive oxide film on the surface. Mann and Pethica [12] have proposed that the pop-in is indicative of nucleation of dislocation.

The indentation analysis was performed using a Hysitron TriboLab® Nanomechanical Test Instrument. The instrument allows the application of loads from 1 to 10.000 μN and the recording of penetration depths as a function of applied loads with a high load resolution (1 nN) and a high displacement resolution (0.04 nm). A Berkovich diamond indenter was used, since pile up effects are less pronounced in this case. In all depth- sensing tests a total of 10 indents were averaged to determine the mean hardness [H] and Young’s modulus [E] values for statistical purposes, with a spacing of 50 μm .

Indentation tests were performed to sample AZ31 at loads 80, 200, 2500, 5000 and 8000 μN , in order to decide on the applied load to proceed with the fatigue specimens. Pop-ins were observed at loads 2500 μN and 5000 μN in sample AZ31. Nanoindentation tests were performed at the fatigue specimen, which was applied to cyclic fatigue for $N=0, 5 \times 10^3, 10^4$ cycles, at maximum stress of $\sigma_{\text{max}}= 160$ MPa. Load-displacement curves of the tests revealed a plastic behaviour. In Table 1 H & E values of cyclic fatigue specimens are presented.

From the measurements it becomes evident that there is no significant change of surface hardness after 5×10^3 cycles (~17% Nf). This is a first indication that the material can hardly accumulate damage in terms of cyclic plasticity at the initial stage of the fatigue damage accumulation process. It is worth noting that in [13] a crack of 61 μm was detected after 5×10^3 cycles under the same loading conditions. The observed hardness increase after 10^4 cycles (~34% Nf) should not be misinterpreted as stage of cyclic plasticity of the material during the fatigue damage accumulation process. The stage of cyclic plasticity in polycrystalline materials, and hence the cyclic hardening or softening, begins from the very first fatigue cycles.

Table 1: H & E values of cyclic fatigue specimens.

Cyclic Fatigue	N=0 cycles	N=5x10 ³ cycles	N=10 ⁴ cycles
H (GPa)	1.38	1.4	3.5
E (GPa)	58	55	105

The threshold stress intensity at which the fracture progresses spontaneously is called the critical stress-intensity factor, K_{Ic} , or the fracture toughness of the material. The unit of K_{Ic} is $\text{MPa m}^{1/2}$. Toughness is a

measure of the ability of the material to absorb energy up to failure. Materials with higher strength have lower toughness. Fracture always starts at a point of stress concentration. If the stress-intensity factor exceeds K_{Ic} , fracture will occur, even though ultimate strength is not exceeded. The indentation cracking method is especially useful for measurement of fracture toughness of thin films or small volumes. Based on fracture mechanics analysis, Lawn et al. [14] developed a mathematical relationship between fracture toughness and indentation crack length, c , given as [14,15]:

$$K_{Ic} = B \left(\frac{E}{H} \right)^{1/2} \frac{P}{c^{3/2}} \quad (\text{Eq. 1})$$

where E is the Young's modulus, H is hardness, P is the applied load, B is an empirical constant related to tip geometry and c is the radial crack length. B for a Berkovich tip is ~ 0.016 [16-18]. Fracture toughness measured by Eq.1 for AZ31 is $\sim 1 \text{ MPa m}^{1/2}$ [15,19], but there is approximately 10–20% uncertainties in this calculated value (depends on the statistics model and definition of crack length uncertainty used) and it is most likely attributed to the unequal crack length in the three sided Berkovich tip [15,20]. Note that Eq.1 does not count the effect of residual stress. Once the tensile residual stress is counted, the estimated fracture toughness should be slightly increased.

In the present work, an investigation on the nanofatigue and high stress sensitivity of the fatigue life of the AZ31 rolled magnesium alloy under constant amplitude fatigue loading has been carried out. Different damage parameters were involved to quantify fatigue damage accumulation at the various scales of material volume corresponding to the changing fatigue damage mechanisms which prevail at the various stages of the fatigue life [21]. The experimental work included mainly nano-indentation measurements to evaluate hardness evolution at the nano-scale due to cyclic plasticity, results of micro-crack monitoring by using the replication technique, fracture toughness values and fractographic analysis to obtain the fracture characteristics of the fatigue specimens after failure. The hexagonal close-packed structure of the alloy and the resulting difficulty for the activation of five independent slip systems required for homogeneous plastic deformation were considered to determine the high stress sensitivity of the fatigue life observed for the rolled AZ31 alloy under the investigated loading conditions.

Acknowledgements

The authors are grateful to the European Commission for financial support under the contract Anon. AERONautical application of wrought MAGnesium (AEROMAG). EC/FP6 Growth/Aeronautics, 2005-2008.

- [1] Anon. Integrated Design and product development for eco-Efficient production of low-weight Aeroplane equipment (IDEA). EC/FP6 – IP/Aeronautics, 2005- 2008.
- [2] Doerner M.F. and Nix W.D., *J. Mater. Res.* 1, 601 (1986).
- [3] Rodriguez R. and Gutierrez I., *Mater. Sci. Eng. A* 361, 377 (2003).
- [4] Oliver W.C. and Pharr G.M., *J. Mater. Res.* 7, 1564 (1992).
- [5] Field J.S. and Swain M.V., *J. Mater. Res.* 8, 297 (1993).
- [6] Sneddon I.N., *Proc. Cambridge Philos. Soc.* 44, 492 (1948).
- [7] Asif S.A.S. and Pethica J.B., *Phil. Mag.* A 76, 1105 (1997).
- [8] Woïrgard J., Tromas C., Girard J.C., Audurier V., *J. Eur. Ceram. Soc.* 18, 2297 (1998).
- [9] Kucheyev S.O., Bradby J.E., Williams J.S., Jagadish C., Swain M.V., *Appl. Phys. Lett.* 80, 956 (2002).
- [10] Gaillard Y., Tromas C. and Woïrgard J., *Phil. Mag. Lett.* 83, 553 (2000).
- [11] Gerberich W.W., Nelson J.C., Lilleodden E.T., Anderson P., Wyrobek J.T., *Acta Mater.* 44, 3585 (1996).
- [12] Mann A.B. and Pethica J.B., *J. Langmuir* 12, 4583 (1996).
- [13] Pantelakis Sp.G., Chamos A.N., Spiliadis V., In *Proc. of the 1st ICEAF Conf.* p.115- 124.
- [14] Lawn B.R., Evans A.G., Marshall D.B., *J. Amer. Ceram. Soc.* 63, 574 (1980).
- [15] Anstis G. R., Chantikul P., Lawn B. R., Marshall D. B., *J. Am. Ceram. Soc.* 64, 533 (1981).
- [16] Ostojic P., McPherson R., *Inter J. Fract* 33,297 (1987).
- [17] Jackson A P., Vincent J. F. V., Turner R. M., *Proc. the Royal Soc. of Lon. Series B, Biolog. Scie.* 234, 41540 (1988).
- [18] Anstis G. R., Chantikul P., Lawn B. R., Marshall D. B., *J. Amer. Ceram. Soc.* 64, 533 (1981).
- [19] Ohring, M., *The Materials Science of Thin Films.* Academic Press, New York . (1992).
- [20] Yan H.-Y., Ou K.-S., Chen K.-S., *Strain*, 44, 259 (2008).
- [21] Chamos A.N., Charitidis C.A., Skarmoutsou A., Pantelakis Sp.G., Accepted to *Fatigue and Fracture of Engineering Materials and Structures* (2009).

Shape and Properties of Gold Nanoparticles

G. D. Barmparis and I. N. Remediakis*

*Department of Materials Science and Technology, University of Crete,
71003 Heraklion, Crete, Greece*

* remed@materials.uoc.gr

Although gold is known to be a noble metal, gold nanoparticles show extreme chemical activity and are widely used in catalysts. Such catalysts are used today for CO oxidation at room temperatures. The performance of these catalysts depends critically on the shape of its nanoparticles.

In the present work, we predict the shape and the properties of gold nanoparticles in different environments based on first-principles simulations. We calculate the surface tension of Au for all low-index Au(hkl) surfaces ($h, k, l < 4$), both clean and covered with different adsorbates. We then use the calculated surface energies together with Wulff's theorem to predict the equilibrium shapes of gold nanoparticles. We employ an atomistic version of the Wulff plot to predict the nanoparticle shape as a function of its volume.

We are in particular interested at particles sizes of the order of a few tens of nanometers, where the shape of nanoparticles changes with particle size. As the size changes by adding an integer number of atoms, new faces can emerge or disappear, a fact that effects the catalytic properties of the nanoparticle.

Finally, we discuss the effect of the environment of the nanoparticle, by explicitly considering adsorption of representative molecules and radicals on its various surfaces. We aim to model nanoparticles formed in soft matter matrices, and functional nanoparticles used in heterogeneous catalysis. We investigate the properties of the Au-adsorbate system depending on the particular adsorbate and the exposed metal face, and discuss trends in the adsorption energy.

Electron Microscopy Studies of the Structural Transformation of $\text{VOHPO}_4 \cdot 1/2\text{H}_2\text{O}$ Precursors to $(\text{VO})_2\text{P}_2\text{O}_7$ Catalysts

A. Delimitis^{1*}, O. Orfanou¹ and C.J. Kiely²

¹ Chemical Process Engineering Research Institute (CPERI), CERTH, GR-57001 Thessaloniki, Thessaloniki, Greece

² Center for Advanced Materials and Nanotechnology, Lehigh University, Bethlehem, PA 18015-3195, USA

*andel@cperi.certh.gr

Vanadium Phosphorus Oxide (VPO) catalysts are used industrially for the mild oxidation of n-butane to maleic anhydride [1]. Topotactic transformations between crystallographically different VPO phases are a characteristic feature of this catalyst system. Previous structural studies on VPO [2],[3] have shown that, upon activation, the $\text{VOHPO}_4 \cdot 1/2\text{H}_2\text{O}$ (hemihydrate) precursor undergoes a topotactic structural transformation to $(\text{VO})_2\text{P}_2\text{O}_7$ (pyrophosphate). However, since the transformation involves a complex sequence of dehydration, bond restructuring, partial oxidation and reduction processes [2], it is of significant importance to study this transformation in greater detail, as its exact nature will affect the resulting catalyst material in terms of morphology and catalytic properties. Controlling the transformation process would be crucial for the production of improved quality VPO, mainly because the pyrophosphate phase is generally accepted as the major component in the most active and selective catalysts [1]. In order to elucidate the structural transformation sequences, we have used a combination of transmission electron microscopy (TEM-HRTEM) and image simulation techniques to study the complex changes occurring at the onset of the conversion of hemihydrate.

The VPO precursor was prepared by an organic synthesis, using iso-butanol as the reducing agent and activated by heating at 750°C under an N_2 flow for 0.5 h, in order to eliminate any possible oxidation effects of V^{4+} ions to V^{5+} . The samples were examined in a JEOL 2011 high resolution transmission electron microscope (HRTEM) operating at 200 kV with a point resolution of 0.23 nm and a spherical aberration coefficient of $C_s = 1$ mm. Image simulation studies were carried out by constructing a 6 nm bi-crystal of hemihydrate (66.6%) and pyrophosphate (33.4%) and HRTEM simulated images were subsequently calculated using EMS, employing the multislice approximation, in both plan-view and cross-section orientations.

The $\text{VOHPO}_4 \cdot 1/2\text{H}_2\text{O}$ precursor consisted of platelets with the typical for VPO rhomboidal shape [4] and dimensions of up to 3 μm . The overall rhomboidal morphology was retained in the sample heated for 0.5 h in N_2 , illustrating the topotactic nature of transformation. An HRTEM image and selected area diffraction (SAD) pattern obtained from one such platelet are presented in Fig. 1(a) and (b), respectively. Fig. 1(b) indicates, to a first approximation, the [100] projection of pyrophosphate, along with extra reflections, marked with white arrows, which suggest the co-existence of epitaxial crystalline hemihydrate. These spots correspond to the (220) and $(2\bar{2}0)$ planes, *i.e.* the [001] projection of $\text{VOHPO}_4 \cdot 1/2\text{H}_2\text{O}$. The co-existence of both VPO phases in the same area is clearly revealed in the simulated patterns of Fig. 2(c), where both the pyrophosphate [100] and the hemihydrate [001] projections are superimposed. Their epitaxial orientation relationship can be defined as:

$$\begin{aligned} (001)_{\text{hemi}} // (100)_{\text{pyro}} \\ [010]_{\text{hemi}} // [010]_{\text{pyro}} \end{aligned}$$

in accordance with previous findings [2],[3]. Similar diffraction experiments showed that these partially transformed platelets comprised approximately 10 vol% of the sample, with the rest being pyrophosphate, hence they confirmed the rapid transformation of $\text{VOHPO}_4 \cdot 1/2\text{H}_2\text{O}$ into $(\text{VO})_2\text{P}_2\text{O}_7$ during the initial activation stages.

Analysis of the lattice fringe separation and their intersection angles in Fig. 1(a) -equal to 0.312 nm and 82°, respectively- suggest that the fringes correspond to the (024) and $(0\bar{2}4)$ pyrophosphate planes, *i.e.* the image is dominated by the $(\text{VO})_2\text{P}_2\text{O}_7$ [100] projection. Furthermore, the HRTEM image shows characteristic coarser Moiré-type fringes, which originate from the superposition of the two VPO phases. The fringes appear to lie roughly parallel to each other, which is indicative of their common origin. The Moiré fringes are of mixed type; hence, their periodicity, $d_{\text{Moiré}}$, and the angle, $\theta_{\text{Moiré}}$, between the Moirés and the (024) pyrophosphate planes are equal to [5] $d_{\text{Moiré}}=3.6$ nm and $\theta_{\text{Moiré}}=42.2^\circ$, respectively. Estimation of their experimentally observed separation and Moiré fringe angle with the (024) $(\text{VO})_2\text{P}_2\text{O}_7$ planes give values of about 3.5 nm and 42°, respectively, both measured over wide areas in VPO platelets. The agreement between the theoretical and experimentally determined values clearly demonstrates that the origin of the Moiré fringes is the intimate co-existence of $\text{VOHPO}_4 \cdot 1/2\text{H}_2\text{O}$ and $(\text{VO})_2\text{P}_2\text{O}_7$ structures within the same platelet. These findings suggest that both the precursor and catalyst lattices are in intimate contact during the transformation, with the pyrophosphate phase gradually developing on, and eventually consuming, the hemihydrate phase. Furthermore, the Moiré fringe formation indicates a full relaxation of both lattices, with no significant retention of interfacial misfit strains.

Due to the added complexity of the co-existence of the $\text{VOHPO}_4 \cdot 1/2\text{H}_2\text{O}$ and $(\text{VO})_2\text{P}_2\text{O}_7$ structures in the same platelet, image simulation techniques were applied to interpret the HRTEM findings. The results are shown in Fig. 2(a) and (b), both for cross-section and plan view configurations. The similarities between the simulated image in (b) and the experimental one in (c) are illustrated. Both images show two Moiré bands that have a separation of about 3.8 nm, each with a width of roughly 2 nm. Furthermore, under certain defocus values, the projected image inside the dark Moiré bands has an almost “amorphous-like” contrast, interspersed with single-crystal-like contrast. The general similarities of the simulated image in Fig. 2(b), with the experimental result in (c) are obvious and lend support to the co-existence of single crystalline $\text{VOHPO}_4 \cdot 1/2\text{H}_2\text{O}$ and $(\text{VO})_2\text{P}_2\text{O}_7$ in the same projected region of a partially transformed VPO platelet.

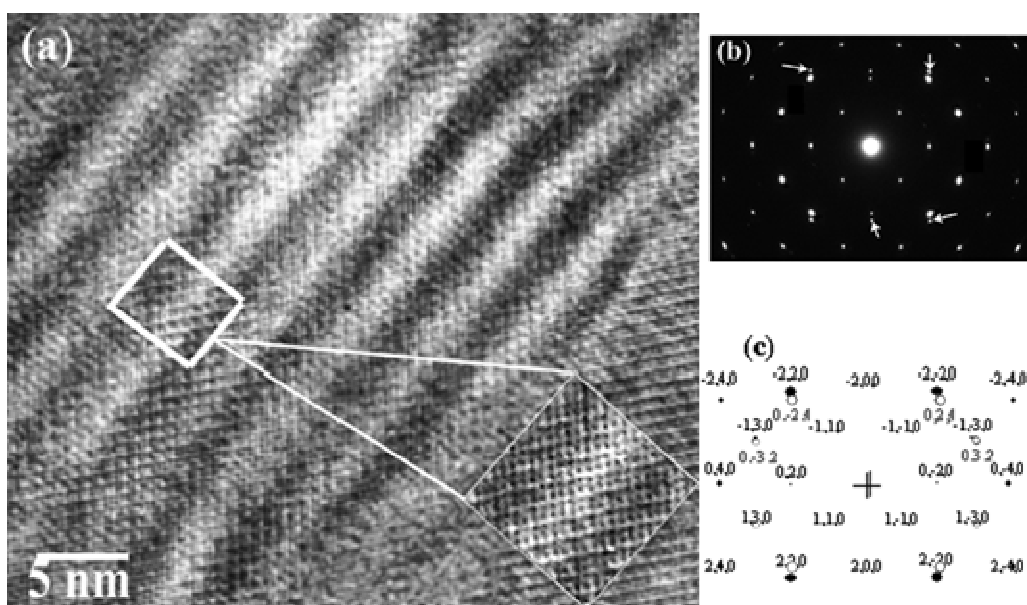


Fig. 1: (a) HRTEM image of a VPO platelet from the sample heated in N_2 , (b) the SAD pattern from the same area. The white arrows depict the reflections attributed to the hemihydrate phase co-existing with pyrophosphate. (c) Simulated SAD pattern of overlapping hemihydrate and pyrophosphate, corresponding to the experimental case shown in (b). All hemihydrate reflections are indexed, whereas only the main pyrophosphate reflections are shown with open circles.

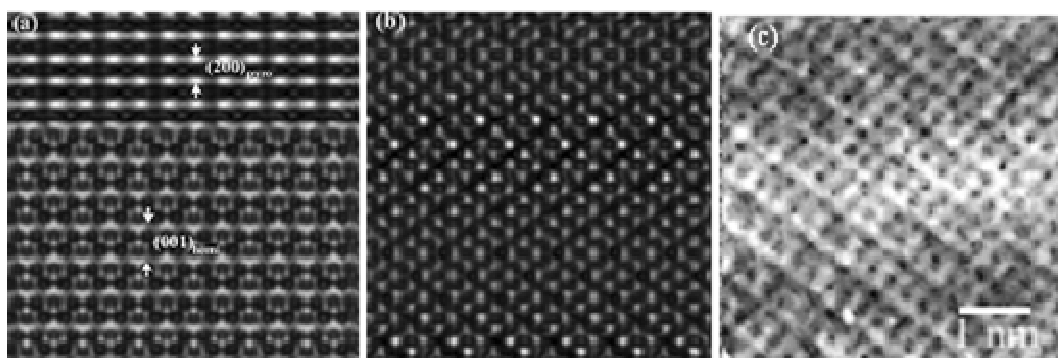


Fig. 2: Simulated images from the hemihydrate/pyrophosphate bi-crystal: (a) cross-section view (defocus -50 nm), (b) plan view (defocus -70 nm). The inset experimental image from Fig. 1(a) is also reproduced in (c), for direct comparison reasons.

- [1] Centi G., Catal. Today 16, 5 (1993).
- [2] Kiely C.J., Burrows A., Hutchings G.J., Bere K.E., Volta J.C., Tuel A., Abon M., J. Chem. Soc. Faraday Discuss. 105, 103 (1996).
- [3] Duvauchelle N., Kesteman E., Oudet F., Bordes E., J Sol. St. Chem. 137, 311 (1998).
- [4] Sartoni L., Delimitis A., Bartley J.K., Burrows A., Roussel H., Herrmann J.M., Volta J.C., Kiely C.J., Hutchings G.J., J. Mater. Chem. 16(44), 4348 (2006).
- [5] Hirsch P.B., Howie A., Nicholson R.B., Pashley D.W. and Whelan M.J., Electron Microscopy of Thin Crystals, (London, Butterworths, 1965).

Acknowledgments: The authors wish to thank G.J. Hutchings, J.C. Volta and J.J. Calvino, for the provision of the VPO samples and fruitful discussions.

Temperature Dependence of Photoluminescence in Individual Self-Assembled Quantum Dots

A. Zora^{1*}, C. Simserides², G. P. Triberis¹

¹ University of Athens, Physics Department, Panepistimiopolis, Zografos, GR-15784, Athens, Greece

² Institute of Materials Science, NCSR Demokritos, GR- 15310, Athens, Greece

*azora@phys.uoa.gr

We have developed a quantum-mechanical theory for the interaction of light and electron-hole excitations in semiconductor quantum dots (QDs) [1]. Taking into account the free-carriers, the free-photons, the electron-hole interaction, and the interaction of carriers with light Hamiltonians and applying the Heisenberg equation of motion to the photon number expectation values, to the carrier distribution functions and to the correlation term between the photon generation (destruction) and electron-hole pair destruction (generation), we have obtained a set of three luminescence equations. Under incoherent conditions where the optical polarization has decayed via dephasing [2], and under quasi-equilibrium conditions, we have obtained a closed-set of two luminescence equations. Solving analytically the above luminescence equations, in the non-linear (low temperatures) regime as we have done [1] for the linear (high temperatures) regime, we find an approximate solution of the photoluminescence intensity:

$$I_{em} \propto \Im \sum_{\lambda} \frac{\int d^3\mathbf{r} \Psi^{\lambda}(\mathbf{r},\mathbf{r}) \sum_{\ell} \int d^3\mathbf{r}' C_{\ell}^{\lambda*} \Phi^{\mu_e}(\mathbf{r}') \Phi^{\nu_h}(\mathbf{r}') f^{\mu_e} f^{\nu_h}}{E^{\lambda} - \hbar\omega - i\gamma}.$$

$\Phi^{\mu_e}(\mathbf{r})$ and $\Phi^{\nu_h}(\mathbf{r})$ are the single-particle envelope functions, $\hbar\omega$ is the photon energy, μ_e (ν_h) symbolize the different electron (hole) states and $\ell = \mu_e \nu_h$. γ is a small damping constant accounting for the coupling with the environment, which in the relaxation time approximation is related to the dephasing time, i.e $\tau = \hbar/\gamma$. $\Psi^{\lambda}(r,r)$ is the excitonic eigenfunction which is expanded in terms of the single-particle states [3].

Our purpose is to investigate the temperature dependence of the photoluminescence in the wide temperature range (8-300) K. The validity of our theoretical analysis is tested by interpreting consistently the experimental findings reported by Dou Xiu-Ming et al. [4] for the temperature dependence of the emission spectra of a single InAs/GaAs self-assembled quantum dot. Our theoretical predictions for the redshift of the emission peak with increasing temperature in the range (10-60) K as well as for the dephasing times caused by acoustic and optical phonon scattering are in a good agreement with the experiment. Furthermore, we interpret the experimental findings reported by Matsuda et al. [5] for the temperature dependence of the emission spectra of a single In_{0.5}Ga_{0.5}As lens-shaped self-assembled quantum dot in the temperature range (8-256) K.

[1] Zora A., Simserides C. and Triberis G., J. Phys.: Condens. Matter 19, 406201 (2007).

[2] Kira M., Jahnke F., Hoyer W. and Koch S. W., Prog. Quantum Electron. 23, 189 (1999); Koch S. W., Meier T., Hoyer W. and Kira M., Physica E 14, 45 (2002).

[3] Simserides C., Zora A. and Triberis G., Phys. Rev. B 73, 155313 (2006).

[4] Dou Xiu-Ming, Sun Bao-Quan, Xiong Yong-Hua, Huang She-Song, Ni Hai-Qiao, and Niu Zhi-Chuan, Chin.Phys.Lett. 25, 3440 (2008).

[5] Matsuda K., Ikeda K., Saiki T., Tsuchiya H., Saito H and Nishi K., Phys. Rev. B 63, 121304(R) (2001).

Preparation and Characterization of Palladium Supported on Zeolites

E. Pavlidou¹, M. Filippoussi¹, D. Zamboulis², N. Vouroutzis¹, A. Filippidis³ and I. Georgiadis³

¹ Department of Physics, Aristotle University, GR-54124 Thessaloniki, Greece

² Department of Chemistry, Aristotle University, GR-54124 Thessaloniki, Greece

³ Department of Geology, Aristotle University, GR-54124 Thessaloniki, Greece

elpavlid@auth.gr

Introduction: Zeolites are three-dimensional, microporous, crystalline solids with well-defined structures that contain aluminum, silicon and oxygen in their regular framework; cations and water are located in pores. Transition metal ions have been deposited by impregnation or by ion exchange onto a variety of supports, such as metal oxides [1], layered clays [2], cages of zeolites X and Y [3-5] followed by reduction to yield small particles. The metal ions were introduced into the support either directly during synthesis or by post-synthesis treatment [6]. The aim of this work was to prepare new forms of ¹⁰³Pd, a low energy x-ray emitter as a new and potentially superior candidate for brachytherapy, based on natural and synthetic zeolites. ¹⁰³Pd can be ion implanted into different materials, designs, and devices either for vascular brachytherapy [7] or for brachytherapy treatment of localized cancers. ¹⁰³Pd has a half-life of 16.99 days and decays by electron capture with the emission of characteristic X-rays of energy 20-23 keV and Auger electrons. The Pd-loading of the zeolites was performed by dry impregnation using palladium chloride.

Experimental details: Natural zeolite crystals (heulandite) were detached from the cavity of the ore and were reduced in size in a mortar. A small quantity of the zeolite was placed in a porcelain boat and dried at 200°C. Following drying 0.2 mL of an acidic PdCl₂ solution (3.33% w/v) in ethylene glycol was added and the mixture was homogenized with a glass rod. The zeolite was then heated again in a muffle furnace at 200°C for about 10 min. During heating the zeolite was dried and palladium ions were reduced to metallic palladium. This procedure was repeated several times depending on the amount of palladium to be deposited on the zeolite. The same procedure was also followed for the synthetic zeolites Na13X and NaY.

Results and discussion: X-ray diffraction (XRD) analysis was performed, initially, on the natural heulandite and on the synthetic zeolites Na13X and NaY to confirm the crystal structure and the mineral identity of the zeolites. Following dry impregnation with palladium chloride and reduction with ethylene glycol the XRD investigations showed the presence of only metallic palladium. In all cases impregnation with palladium chloride provoked a slight amorphization of the zeolite as proved by the XRD spectra due to the hydrochloric acid present in the palladium chloride solution. Moreover, the SEM-EDS investigation revealed sub-microscopic Pd-phases supported on the surface of the interacting zeolite. Atomic Force Microscopy measurements were also carried out.

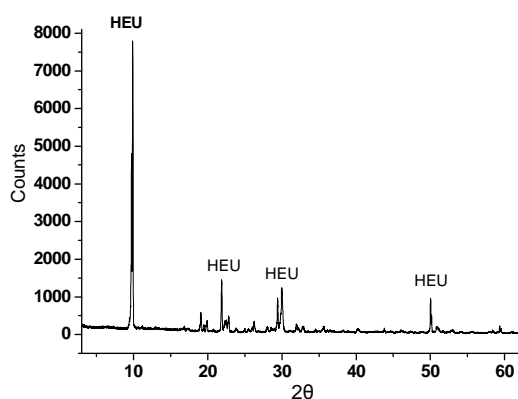


Figure 1. X-ray diffraction pattern of heulandite

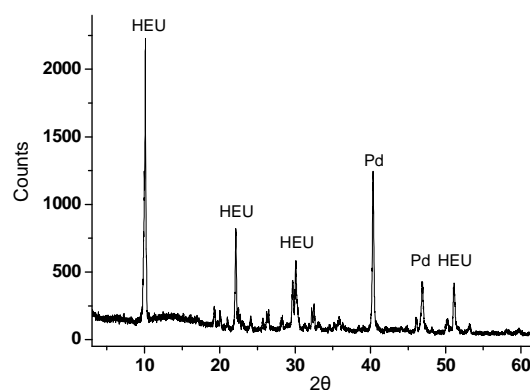


Figure 2. X-ray diffraction pattern of heulandite after dry impregnation with palladium chloride and reduction to metallic palladium

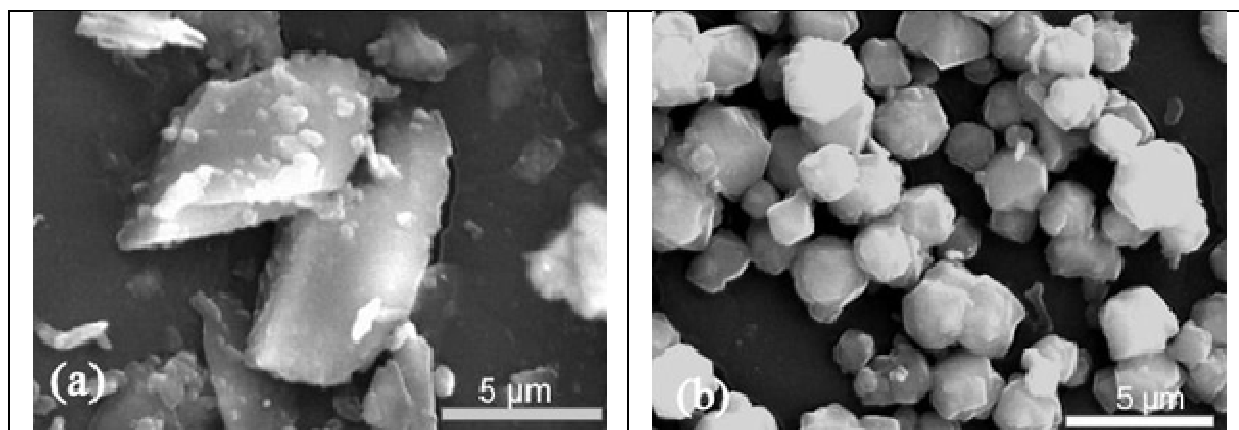


Figure 3. SEM microphotographs of zeolites (a) heulandite, (b) Na13X.

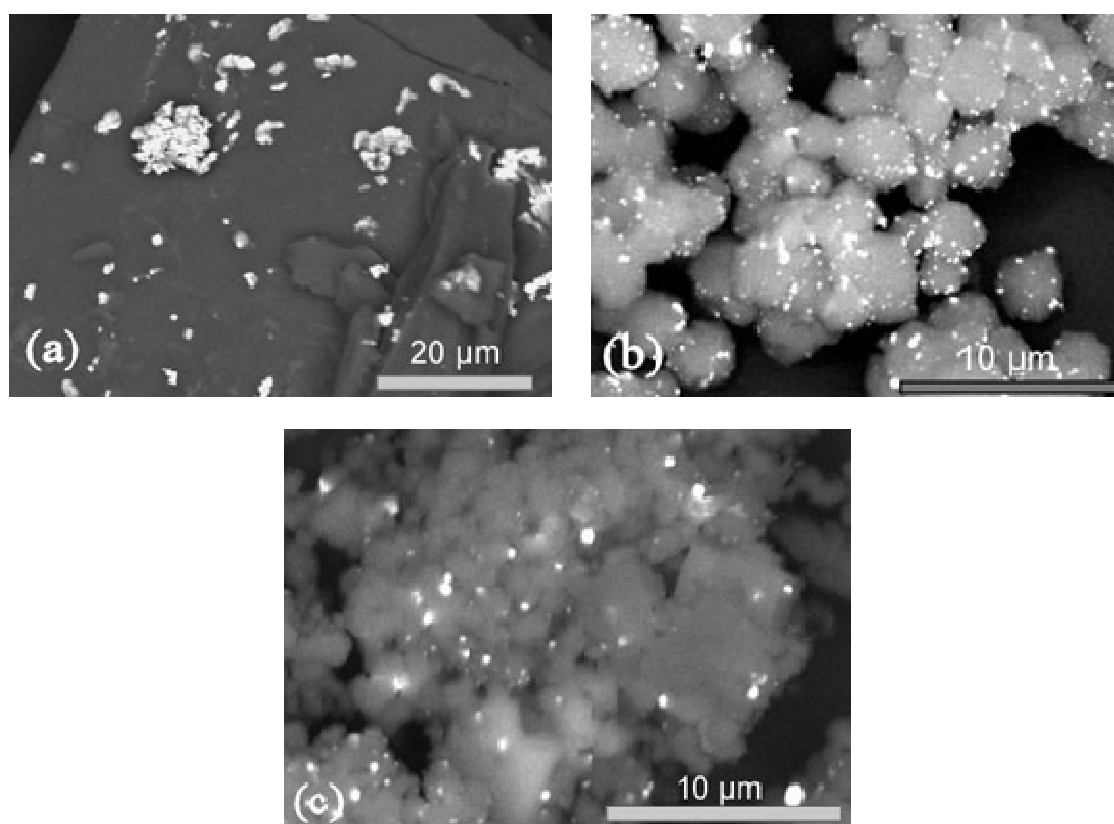


Figure 4. SEM microphotographs (back scattering) of palladium loaded zeolites (a) heulandite, (b) Na13X, (c) NaY

References:

- [1] R. Diaz-Ayala, R. Raptis, C.R. Cabrera, *Rev. Adv. Sci.* 10,375-380 (2005).
- [2] F. Favier, E.C. Walter, M.P. Zach, T. Benter, R. M. Penner, *Science*, 293, 2227 (2001).
- [3] R.M. Penner, *J. Phys. Chem.* 106, 3339 (2002).
- [4] H. Matsumoto, S. Tanabe, *Czech. Chem. Comm.* 57, 4, 817-825 (1992).
- [5] C. Song, *Chemtech* 29, 3, 26-30 (1999).
- [6] A. Fukuoka, N. Higashimoto, Y. Sakamoto, *Catal. Today* 66, 23 (2001).
- [7] Piran Sioshansi and Raymond J. Bricault, Jr., *B.S. Cardiovascular Radiation Medicine*, 278–287 (1999).

Nanomechanical and Structural Properties of Deposited Binary Nitrides Thin Films grown by Pulsed Laser Deposition

C.A. Charitidis^{1*}, A. Skarmoutsou¹, L.E. Koutsokeras², Ch.E. Lekka², P. Zotali¹, P. Patsalas²

¹*School of Chemical Engineering, National Technical University of Athens, 15780 Athens.*

²*Department of Materials Science and Engineering, University of Ioannina, 45110 Ioannina.*

*charitidis@chemeng.ntua.gr

Transition metal (TM) nitrides are well known for their remarkable physical properties including high hardness and mechanical strength, chemical inertness, and electrical resistivities which vary from metallic to semiconducting. As a result, they are widely studied and have become technologically important for applications such as hard wear-resistant coatings, diffusion barriers, decorative coatings, and optical thin films.

The use of transition metal nitride coatings has been successfully explored in the last decades, due to properties like high hardness, biocompatibility, wear and corrosion resistance, and thermal stability [1–5]. The most thoroughly studied among the transition metal nitrides certainly is the titanium nitride. However, zirconium, niobium, and vanadium nitrides, among others, also exhibit similar protection properties.

In this study we investigate the growth of several binary nitrides films grown by a hybrid Pulsed Laser Deposition (PLD) process, which employs an external electric field during growth as described previously [6]. Transition metals of Nb, Hf, Zr, W and Ta were used for the growing nitrides films. The produced nitride films had average thickness of 80 – 120 nm and were studied by X-Ray Diffraction (XRD). XRD spectra revealed an fcc structure of NaCl. The films are, according to Scherrer (row 5) and Williamson-Hall (row 4) analyses [7], nanocrystalline with grain size of the order of 15-10 nm, with the major exception of WN, which exhibits smaller grains.

The indentation analysis was performed using a Hysitron TriboLab® Nanomechanical Test Instrument that is capable of performing indentations. A Berkovich diamond indenter was used with a maximum load of 7000 μN at room temperature. The TriboLab® Nanomechanical Test Instrument employed in this study is equipped with a Scanning Probe Microscope (SPM), in which a sharp probe tip is moved in a raster scan pattern across a sample surface using a three-axis piezo positioner.

The hardness (H) and elastic modulus (E) of nitride films are determined from nanoindentation measurements at loads 100 to 7000 μN. Average values of H and E are presented at Table 1. The film elastic behavior can be analyzed based on a contact analysis for solids of revolution [8], using the Tresca yield criterion and Tabor's relation, according to which, the load at the onset of yielding is proportional to H^3/E^2 . This ratio is indicative of the material elasticity, i.e. high (low) values of H^3/E^2 reflect a predominantly elastic (plastic) behaviour. For the 5d metals HfN film and 4d metals NbN films examined in this work, H^3/E^2 is equal to ~0.25 and ~0.10 respectively, suggesting a relatively high resistance to plastic flow for 5d metals HfN film (Table 1).

Table 1: Average H and E values of nitride films and H^3/E^2 ratio.

Sample	H (GPa)	E (GPa)	H ³ /E ²
NbN	17±2	220±3	0.10
HfN	24,82±2	250±6	0.25
ZrN	19±1,5	248±6	0.11
WN	14,45±1	206±4	0.07
TaN	21,5±1	223±3	0.20

These results are in a good agreement with previous findings [9, 10]. The elastic–plastic behaviour of the 4d, 5d metals films can be interpreted in light of the dependence of plastic deformation on the indentation load. At low loads all coatings revealed an elastic behaviour, with the exception of WN thin film. For higher loads (6000, 7000 and 8000 μN) coatings revealed a plastic behaviour. The almost identical loading and unloading patterns of the indentation curve shown in Fig. 1 (a) indicates that the deformation of the film deposited is essentially elastic. A comparison of Fig. 1 (a) and (b) shows that the slopes of the loading and unloading portions of the indentation curves decrease and the force hysteresis area increases, with increasing valence electron number of the constituent metal. However, detailed *ab-initio* calculation within the density functional theory (DFT), using the *Wien2k* software [11], revealed a significant increase of the bulk modulus with the number of valence electrons of the constituent metal. We should consider that the bulk modulus is an intrinsic atomic property of the material and hardness is a macroscopic property that can be affected by other factors, as well [12,13]. Indeed, we have measured a deterioration of the film density vs. the atomic number of the constituent metal, compared to the corresponding bulk values, which may well explain [12] the experimental findings regarding the mechanical properties of the studied films.

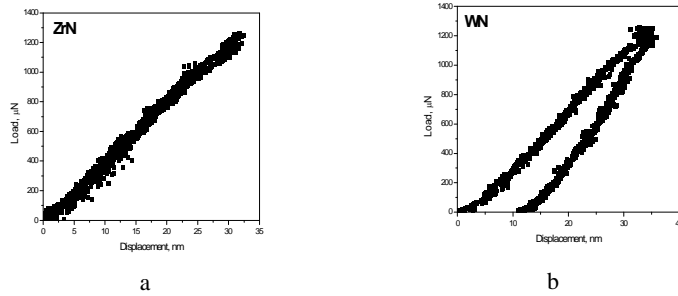


Figure 1: Force vs. indentation depth curves for 4d metals: ZrN (a) and WN (b).

The threshold stress intensity at which the fracture progresses spontaneously is called the critical stress-intensity factor, K_{Ic} , or the fracture toughness of the material. The unit of K_{Ic} is $\text{MPa m}^{1/2}$. Toughness is a measure of the ability of the material to absorb energy up to failure. Materials with higher strength have lower toughness. Fracture always starts at a point of stress concentration. If the stress-intensity factor exceeds K_{Ic} , fracture will occur, even though ultimate strength is not exceeded. The indentation cracking method is especially useful for measurement of fracture toughness of thin films or small volumes. Based on fracture mechanics analysis, Lawn et al. [14] developed a mathematical relationship between fracture toughness and indentation crack length, c , given as [14,15]:

$$K_{Ic} = B \left(\frac{E}{H} \right)^{1/2} \frac{P}{c^{3/2}} \quad \text{Equation 1}$$

where E is the Young's modulus, H is hardness, P is the applied load, B is an empirical constant related to tip geometry and c is the radial crack length. B for a Berkovich tip is ~ 0.016 [16,17]. Fracture toughness measured by Eq.1 for nitride thin films is $\sim 1 \text{ MPa m}^{1/2}$ [15], but there is approximately 10–20% uncertainties in this calculated value (depends on the statistics model and definition of crack length uncertainty used) and it is most likely attributed to the unequal crack length in the three sided Berkovich tip [15]. Note that Eq.1 does not count the effect of residual stress. Once the tensile residual stress is counted, the estimated fracture toughness should be slightly increased.

Generally, materials are preferred to exceed high values of K_{Ic} and resistance to plastic deformation, but this behaviour wasn't noticed for the studied thin films. It was shown that the film's stiffness and resistance to plastic deformation (H^3/E^2) decrease with the increase of fracture toughness, with exception of TaN thin film which revealed an increase of K_{Ic} with the increase of H^3/E .

Finally, further work is needed to determine the effect of crystal orientation on fracture resistance, especially for the case of TaN films, which are highly textured [18].

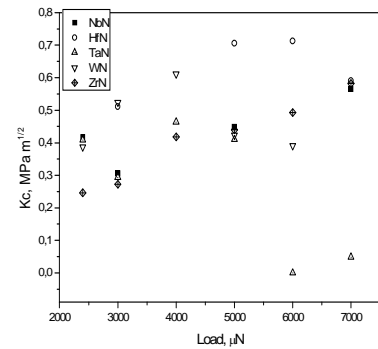


Figure 2: Plot of K_{Ic} vs load

- [1] Honer P., Sanjines R., Levy F., Surf. Coat. Technol. 94/95, 398 (1997).
- [2] Lim J.W., Park J.S., Kang S.W., J. Appl. Phys. 87, 4632 (2000).
- [3] Kang J.H., Kim K.J., J. Appl. Phys. 86, 346 (1999).
- [4] Massiani Y., Crousier J., Fedrizzi L., Cavalleri A., Bonora P.L., Surf. Coat. Technol. 33, 309 (1987).
- [5] Svedberg E.B., Birch J., Ivanov I., Munger E.P., Sundgren J.E., J. Vac. Sci. Technol. A 16, 633 (1988).
- [6] Patsalas P., Kazianis S., Kosmidis C., Papadimitriou D. and Evangelakis G., J. Appl. Phys., submitted.
- [7] Cullity B.D., Elements of X-Ray Diffraction, Addison Wesley, Reading Massachusetts (1978).
- [8] Johnson K.L., Contact Mechanics, Cambridge University Press, Cambridge, UK, (1985).
- [9] Ljungcrantz H., Odén M., Hultman L., Greene J.E., Sundgren J.E., J. Appl. Phys. 80, 6725 (1996).
- [10] Shin C.S., Gall D., Desjardins P., Vailionis A., Kim H., Petrov I., Greene J. E., Appl. Phys. Lett. 75, 3808 (1999).
- [11] Blaha P., Schwarz K., Madsen G.K.H., Kuasnicka D., Luitz J., WIEN2K, Augmented Plane Wave Local Orbitals Program for Calculating Crystal Properties, Vienna University of Technology, Vienna, Austria (2001).
- [12] Patsalas P., Charitidis C., Logothetidis S., Surf. Coat. Technol. 125, 335 (2000).
- [13] Charitidis C., Nanomechanical and Nanotribological properties of carbon based thin films, To be published in International Journal of Refractory Metals and Hard Materials (Special Issue: Tribology of Hard Coating), Elsevier Editorial System (2009).
- [14] Lawn B.R., Evans A.G., Marshall D.B., J. Amer. Ceram. Soc. 63, 574 (1980).
- [15] Anstis G. R., Chantikul P., Lawn B. R., Marshall D. B., J. Am. Ceram. Soc. 64, 533 (1981).
- [16] Ostojic P., McPherson R., Inter J. Fract 33,297 (1987).
- [17] Jackson A P., Vincent J. F. V., Turner R. M., Proc. the Royal Soc. of Lon. Series B, Biolog. Scie. 234, 41540 (1988).
- [18] Matenoglou G.M., Koutsokeras L.E., Lekka Ch.E., Abadias G., Camelio S., Evangelakis G.A., Kosmidis C., Patsalas P., J. Appl. Phys. 104, 124907 (2008).

Mechanical and Electrical Properties of Epoxy Resin Filled With Multi Walled Carbon Nanotubes

C. Georgiou¹, C. A. Charitidis^{1*}, Z. Marioli-Riga², A. Karanika², S. Panagiotopoulos²

¹National Technical University of Athens, School of Chemical Engineering

²The Hellenic Aerospace Industry S.A. (HAI) P.O. Box 23, GR 320 09, Schimatari, Greece

*charitidis@chemeng.ntua.gr

In this study epoxy resin was filled with multi walled carbon nanotubes (MWCNT's) and the mechanical and electrical properties of the composites were investigated. The effects of the MWCNT's dispersion quality on Young's modulus, resistance and electrical conductivity were studied. The results indicate that MWCNT's can be dispersed quite well in the epoxy resin using a dissolver device. A number of experiments performed testing what happens to electrical resistance with the simultaneous elongation of the specimen. Rising up the content of MWCNT's in resin matrix, tensile tests show that the Young's modulus and the electrical resistance have been increased. However, the samples became more fragile and the tensile strength was decreased. This leads to the design of advanced composite materials using MWCNT's, as sensors detecting stress variations, resulting from the combination of electrical resistance with strains.

Among the current studies a research line of particular impact is indeed focused on the manufacturing of single- walled (SWCNT) or multi walled carbon nanotube reinforced polymer matrix composites. By combining the right choice of base materials with the appropriate processing method, the excellent properties of CNT's may be transferred to the polymeric composites. Epoxy resins are actually finding broad applications in a variety of industries and are also an important bulk structural material for demanding aerospace projects. Modification of polymers, using inorganic fillers dispersed at nanoscale, has opened up new perspectives for a wide range of applications. The very appealing physical and mechanical properties of CNT's, such as high Young modulus, as well as remarkable thermal and electrical conductivity, are the focus of extensive studies for a number of applications [1-3]. However, the potential applications of CNT's are hindered by manipulation difficulties due to their insolubility and pure dispersion in polymeric matrices. In order to fully realize the mechanical reinforcement and conduction improvement in polymer- based CNT composites, there are two fundamental and critical issues that have to be resolved. One is the dispersion of CNT's and the other is the interfacial adhesion between CNT's and the polymeric matrix [4]. CNT's have large surface area and possess large Van der Waals forces, so they are difficult to be effectively dispersed in polymeric matrix. Efforts to obtain homogeneous and fine dispersion of CNT's have been undertaken. Aided by applied manufacturing methods such as sonication, dissolver device, torus mill and callander, the quality of dispersion can be improved [5].

As far as the experimental part is concerned, a low-viscosity epoxy resin (Araldite LY 564) combined with a cycloaliphatic polyamine accelerator (Aradur 2954) was the matrix of the composite material. CNT's with diameter 10-15 nm, in concentrations of 0.5%, 1%, 1.5% and 3% w/w were dispersed in the matrix using dissolver device (fig.1) The resin and CNT's compound was stirred in a vacuum container to avoid air inclusions for 36 hours at 60°C. Tensile specimens were prepared in accordance to ASTM standard specification, for each level of CNT's concentration (fig.2). Two cables were put on every dog- bone specimen connected with an electronic polymerizer. A number of tensile tests took place using a Servohydraulic Mechanical testing System. Stress, strain and electrical resistance of all specimens were measured. Scanning Electron Microscope (SEM) was used to examine the dispersion quality of CNT's in the resin (fig.3).



Figure 1: Dissolver device [5].



Figure 2: A mould filled with mixture of resin and CNT's-post curing.

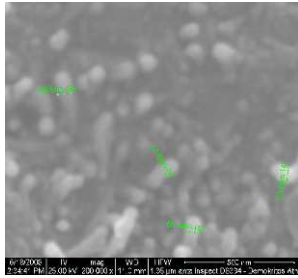


Figure 3: SEM image- dispersion quality of CNT's.

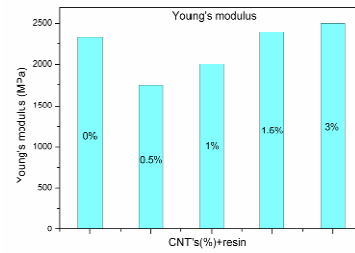


Figure 4: Young's modulus vs. CNT's percentage in resin.

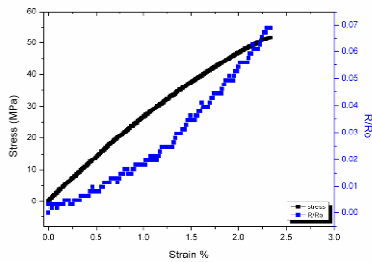


Figure 5: Stress-strain and electrical resistance of specimens.

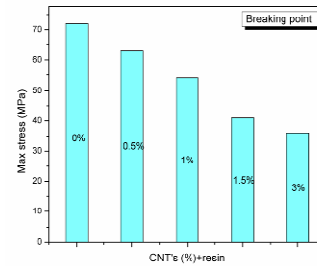


Figure 6: Maximum stress vs. CNT's percentage in resin.

SEM investigation showed a generally homogeneous dispersion with well-dispersed CNT's, distributed in the whole volume of the resin matrix (fig.3). The addition of CNT's in resin increased the Young's modulus. Specimens with 3% CNT's in epoxy resin showed a relative higher Young's modulus value (~2500MPa) (fig. 4).

Moreover, electrical resistance was increased in all specimens reinforced by CNT's. As a result, the electrical conductivity was decreased (fig.5). The specimens became more fragile in contrast to those with 0% w/w CNT's while the tensile strength was decreased (fig.6). The decrease of breaking point is attributed to the dispersion of CNT's. The defects from agglomerates in a number of specimens caused relative poor dispersion. In addition, the inclusion of air bubbles in some specimens made them more fragile and led to failure.

Homogeneous mixture of CNT's-resin is a major issue. Achieving high quality dispersion, leads to considerable improvement in mechanical and electrical properties of the testing specimen. Dispersion and percolation behavior depend on many factors. Shape and size of the dispersed CNT's, shear rate, viscosity and chemical functionalisation influence the resultant dispersion. An efficient exploitation of the CNT's properties is related to their homogeneous dispersion in the resin and to exfoliation of agglomerates. This leads to the design of composite materials with remarkable mechanical and electrical properties. CNT's form a conductive network inside the resin. The break of this network decreases the electrical conductivity. The possibility to measure stress with electrical resistance and the resultant strain can lead to the design of advanced composite materials with MWCNT's for stress-strain sensors.

REFERENCES

- [1] Iijima S., Nature 354, 56-58 (1991).
- [2] Thostenson E.T., Ren Z., Chou T.W., Compos. Sci.Technol. 61, 1899-1912 (2001).
- [3] Ajayan P.M., Zhou O.Z., Applications of Carbon Nanotubes. In: Dresselhaus MS, Dresselhaus G, Avouris P, editor Carbon Nanotubes: Synthesis, Structure, Properties, and Applications 2000 Berlin; Springer: 386-421.
- [4] Saito R., Dresselhaus G., Dresselhaus M.S., London; Imperial College Press 137-221 (1998).
- [5] Kempel F., Schledjewski R., Arana N.M., Fernberg P., Emani-Alagha N., Wichmann M., Tsoira P., 'Selection of optimal processes for CNT's and interleave inclusion', 2005.

Acknowledgments

The authors are grateful to the European Commission for financial support under the contract Aerospace Nanotube Hybrid Composite Structures with Sensing and Actuating Capabilities (NOESIS), Contract No.: 516150, AST4-CT-2005-516150.

Theoretical Investigation of model Non-Platinum Cathode Catalysts for Low Temperature Fuel Cells

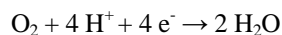
Georgios A. Tritsarlis^{*}, Jan Rossmeisl and Jens K. Nørskov

Center for Atomic-scale Materials Design, Department of Physics, Technical University of Denmark, DK-2800 Lyngby, Denmark

**george.tritsaris@fysik.dtu.dk*

Hydrogen economy stands today as one of the most attractive solutions to the energy demands of the future. Central to this concept are fuel cells. Proton exchange membrane (PEMFC) and direct methanol (DMFC) fuel cells are the ones most suited for mobile applications and for replacing combustion engines in automotive vehicles.

The efficiency and cost of a fuel cell is to a large extent determined by the catalyst used. In present technology, the cathode catalyst is mainly Platinum-based and even though Platinum is the best metal catalyst (and serves its purpose almost flawlessly as an anode for the oxidation of hydrogen), most of the overpotential for a PEM fuel cell originates directly from the cathode due to the sluggish kinetics of the oxygen reduction reaction (ORR), described by the following reaction [1]:



Another major challenge is the storage of hydrogen. This may be circumvented for some portable systems with the use of methanol as fuel instead of hydrogen, as in the case of DMFC, solving the problem with hydrogen storage. However, the selectivity of the cathode catalyst is of great importance, as there will be a competition between the ORR and the combustion of methanol (the so called ‘methanol crossover’ effect) causing a mixed potential on the cathode side which greatly reduces the performance of the fuel cell. Thus, a fundamental aspect in the development of fuel cells concerns the optimization of the electrocatalytic efficiency of the materials used as electrodes, as it has a direct impact on the fuel cell’s power density and overall performance.

A concentrated effort is being made today towards the identification of efficient non-Platinum based cathode catalysts in terms of kinetics, selectivity and cost. In that direction, transition metal chalcogenides including Ruthenium/Selenium alloys have been acknowledged as promising candidates[2]. However, the exact mechanism that provides the selectivity and high specific activity of these materials is still not completely understood.

Using density functional theory (DFT) calculations we probe the performance of Ruthenium/Selenium and other Selenium containing model surface alloys, specifically investigating the atomistic details of the ORR process. On the basis of DFT calculations the complete kinetics of a catalytic reaction may be reconstructed from calculated reaction barriers, reaction energies and entropies. Such theoretical treatment is important not only for fundamental reasons but by identifying descriptors of the catalytic activity, general trends may be deduced, facilitating the rational design of catalytic materials that optimize the catalytic performance and durability of the electrodes[3,4].

The starting point of our study is the calculation of adsorption energies of ORR intermediate species on Selenium-containing Ruthenium model surface alloys. The binding energy of oxygen, for example, serves as an excellent descriptor of the catalytic activity of clean surfaces of transition metals and metal oxides[1,3,4]. This is rather straightforward when taking into account that oxygen is an intermediate species of the ORR process and that correlations have been identified for such surfaces between the binding energy of oxygen and that of other intermediate species, namely hydroxyl or peroxide ion. Fig. 1 illustrates this point. What it shown is the linear correlation between the binding energies of oxygen and hydroxyl molecules, adsorbed in the lowest energy position outside the close-packed surface of different transition metals. The calculated binding energies correspond to the reaction energies of the reactions:



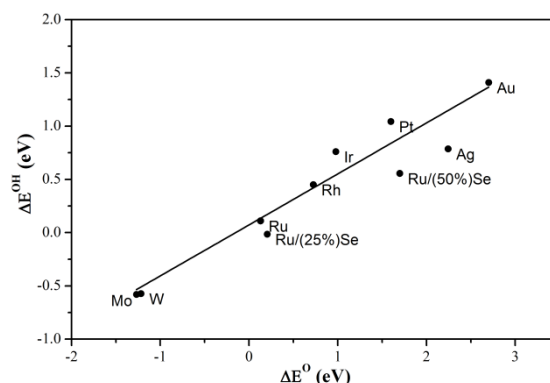


Figure 3. Linear correlation between binding energies of oxygen and hydroxyl molecules adsorbed in the lowest energy position outside the close-packed surface of different transition metals and two Ruthenium/Selenium surface alloys of different Selenium content.

The fact that Platinum is known to be a relatively better, in terms of catalytic activity, catalyst for the ORR compared to the other metals is easily understood by examining Fig. 1. The perfect catalyst, should bind oxygen neither too strongly nor too weakly. For metals that bind oxygen more strongly than optimum the rate is limited by the removal of adsorbed O and OH intermediate species from the surface. On the other hand, if oxygen binds too weakly, depending on the details of the mechanism that the ORR process proceeds, the rate is limited by the dissociation of oxygen molecule on the surface or the transfer of electrons and protons to the adsorbed oxygen. Platinum proves to be the closest to the optimum than the other metals but still overbinding.

This insight provides a basic framework for the study of the performance of Selenium-containing surface alloys. Why Ruthenium is known to be not a good catalyst for the ORR is also reflected on Fig. 1. Its stronger than optimum binding leads to the formation of a Ruthenium oxide. The binding energies of oxygen and hydroxyl for two Ruthenium surface structures of different concentrations of Selenium in the top layer are also shown. Although it is not safe to assume that the behavior of this type of alloys is directly comparable to that of transition metal surfaces (as described above), a carefully designed Ruthenium/Selenium structure is shown to lie closer to Platinum and further from Ruthenium, motivating further research.

Our initial results suggest that a Ruthenium/Selenium skin is the case, as Selenium will always segregate to the surface even in the case of bulk Ruthenium/Selenium alloys. The catalytically active centers are also identified to be as the same as in the case of a pure Ruthenium surface. Thus, it is suggested that Selenium apart from altering the electronic structure of the material towards more favorable energetics, has mainly the role of blocking adsorbents access to the strongly binding adsorption sites of Ruthenium. Similar effects are expected for other Selenium-containing metal surfaces which is the subject of our currently undergoing research.

[1] Nørskov J. K., Rossmeisl J., Logadottir A., Lindqvist L., Kitchin J., Bligaard T., Jónsson H., *J. Phys. Chem. B*, 108 (2004).

[2] Schulenburg H., Hilgendorff M., Dorbandt I., Radnik J., Bogdanoff P., Fiechter S., Bron M., Tributsch H., *J. Power Sources* 155, 47 (2005).

[3] Nørskov J. K., Bligaard T., Rossmeisl J., Christensen C. H., *Nat. Chem.*, 1, 37 (2009).

[4] Stamenkovic V., Moon B. S., Mayrhofer K. J. J., Ross P. N., Markovic N. M., Rossmeisl J., Greeley J., Nørskov J. K., *Angew. Chem. Int. Ed.*, 45, 2897 (2006).

Acknowledgments. Financial support by IGSEE (International Graduate School of Science and Engineering) is gratefully acknowledged. Center of Atomic-Scale Materials Design is funded by the Lundbeck foundation. This work is also supported by the Danish Center for Scientific Computing.

Crystal Growth Model with Stress Development and Relaxation

N. Tsakiris^{1*}, P. Argyrakis¹, I. Avramov²

¹ Department of Physics, University of Thessaloniki – 54124 Thessaloniki Greece

² Institute of Physical Chemistry, Bulgarian Academy of Sciences –1113 Sofia Bulgaria

*ntsak@grid.auth.gr

Crystal growth has been a very challenging topic over the years, mainly due to a very large number of models and approaches that have been developed in the effort to better understand the microscopic mechanisms of growth in detail [[1]-[2]]. Recently, a new model was suggested combining ideas from percolation theory and the glass-forming ability of silicates, [[4]- [7]]. Most glass-forming systems consist of networks in which the network formers, NF, are connected with oxygen bridges. The addition of a different component (Network Modifier) in the network can cause the breaking of the oxygen bridges. The network is “floppy” or “rigid”, depending on the number of broken oxygen bridges (NBO) per NF. If NBO is less than this critical value, the network is “rigid”. However, in “rigid” networks there are still some tiny “floppy” regions. The crystallization process is expected to take place in the floppy regions, where it initially proceeds at a high growth rate. Once the crystal has covered this region, it will start expanding in the adjacent rigid one.

The present investigation [8] aims to describe crystallization in multicomponent systems, which are built using both Network Formers and Modifiers. Our basic starting assumption is that we expect some stress energy to develop during this process, impeding its growth. We developed here a model that describes crystal growth that starts with a small crystal seed and proceeds to a full size crystal based on considerations of the stress energy developed during the process.

Calculations are performed on 2D square lattices, of size NxN. In the initial configuration, just a small fraction of the lattice sites are initially occupied. These sites form a square cluster at the central region, of size nxn. Our assumption is that the central nxn region corresponds to a floppy one, and that the crystallization process has already been initialized, having formed this cluster. All the particles that belong to the cluster are connected through bonds. Since the rest of the region is rigid, we monitor the expansion of the central cluster through it. The crystal grows in size when new particles are added to its periphery, and as a consequence bonds are formed with the existing cluster particles. We expect that the transition from the floppy region to the rigid one will affect the crystal growth rate due to the presence of the stress energy. In the floppy region this rate is very fast and stresses do not develop, while in the rigid one it is comparable to the relaxation rate and the stress energy can not be now neglected ad hoc

At each time step an attachment probability is calculated for each one of the neighboring sites, accounting for the stress energy ε according to the formula

$$P=1-e^{-\frac{mb-\varepsilon}{kT}}$$

where b is the energy of a bond, k is constant Boltzmann and T is the temperature. By m we denote the number of the bonds through which a site can be attached to the cluster. The stress energy is not constant during the simulation and its value depends on whether a site is attached to the cluster, according to the probability P and on the relaxation time. The change $\Delta\varepsilon$ in the stress energy is given by the following formula

$$\Delta\varepsilon = \begin{cases} -\frac{\varepsilon}{\tau} + \varepsilon_0, & \text{if a site is attached} \\ -\frac{\varepsilon}{\tau}, & \text{if no site is attached} \end{cases}$$

where τ is a constant for the relaxation time. By ε we denote the current value of the stress energy and by ε_0 a constant value that is added instantaneously when a new atom is attached to the crystal.

We use Monte Carlo methods to simulate crystallization and a typical picture of the domain evolution is given at fig. 1.

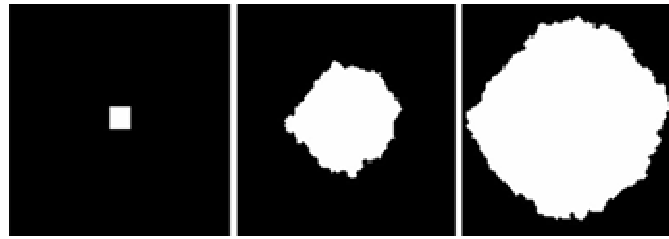


Fig. 1: Snapshots of the crystal growth. Left: initial configuration of the cluster of size $n \times n$, where $n = 3$ at time $t = 0$ (but here shown larger by a factor of 5 for visual purposes). Middle: the grown cluster after $t=250$ Monte-Carlo steps. Right: growth after $t=450$ MC steps. A lattice of size 100×100 was used and the parameters were set as $b=1$, $T=1$, $\varepsilon_0=1$, $\tau=100$.

The model shows a fast initial increase in size of the order of a few nm, which then slows down to a more moderate rate, which is strongly dependent on the relaxation time allowed for the system. We find that the rate of increase of the crystal diameter scales with the relaxation time with a scaling exponent of 0.44. This fast/moderate crossover is also observed experimentally in composite BaF_2 crystals [9].

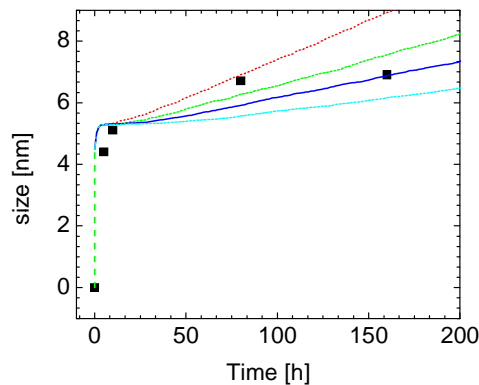


Fig. 9: Size of the crystals in nm versus time in hours. The black squares are the experimental results for the growth of BaF_2 crystals. The lines are the simulation results for relaxation times $\tau = 1000$ (red dot line), $\tau = 2000$ (green dash line), $\tau = 4000$ (solid line), and for $\tau = 10000$ (cyan dash dot line).

In many systems the crystal growth rate remains approximately constant or in some cases even increases during the course of the crystallization. In these systems the components that crystallize are usually silicates or aluminosilicates. This, however, leads to a depletion of the glassy phase near the crystals in network formers which results in a decrease in viscosity. Then the relaxation processes are enhanced. Hence, depending on temperature and the chemical composition of the glasses and the precipitated crystal phases, the crystal growth might be controlled by stress development and stress relaxation or, however, might not depend on such effects.

References

- [1] Mutaftschiev B., *The Atomistic Nature of Crystal Growth*, (Berlin, Springer-Verlag, 2001).
- [2] Vogel W., *Glass Chemistry*, (Springer-Verlag, 2nd Edition, 2002).
- [3] Michely Y., Krug J., *Islands Mounds and Atoms; Patterns and Processes in Crystal Growth Far from Equilibrium*, (Berlin, Springer-Verlag, 2004).
- [4] Avramov I., Keding R., Russel C., *J. Non-Cryst. Solids* 272, 147, (2000).
- [5] Avramov I., Keding R., Russel C., Kranold R., *J. Non-Cryst. Solids* 278 13 (2000).
- [6] Avramov I., Keding R., Russel C. *Glastech. Ber. Glass. Sci. Technol.* 73 C1 138 (2000).
- [7] Keding R., Russel C., *J. Non-Cryst. Solids* 351 1441 (2005).
- [8] Tsakiris N., Argyrakis P., Avramov I., Russel C., Bocker C., *Crystal growth model with stress development and relaxation*, submitted to EPL.
- [9] Bocker C., Russel C., *J. Europ. Ceram. Soc.* 29 1221 (2009).

Percolation Theory and Phase Transitions in Granular Ferromagnets

C. Batistakis* and P. Argyrakis¹

Department of Physics, University of Thessaloniki, 54006 Thessaloniki, Greece

*cbatis@physics.auth.gr

In this work we studied using Monte Carlo simulation the critical phenomena that occur in interfaces between metallic magnetic nanoparticles and insulators where the nanoparticles are randomly distributed and embedded in the insulating matrix. These highly disordered materials have characteristic magnetoresistance curves with many unique fluctuations in critical values of the applied magnetic field.

Magnetic nanoparticles that evaporated in an insulating matrix form islands. As the number of nanoparticles increases, the islands coalesce to larger clusters which create a percolation network. Thus, the conductivity in these highly disordered materials is determined in the terms of percolation theory. According to these behavior, conductivity exists only when the concentration of nanomagnetic grains is higher than a critical density p_c . The width of the materials whose density of islands is above the critical point p_c is called *critical width*. Granular ferromagnets, which are formed near the critical width have characteristic fluctuations in their electrical resistance value when a magnetic field is applied. This is against the classic magnetoresistance definition according to which, the electric resistance of magnetic material decreases when a magnetic field is applied. In order to explain these fluctuations, it is assumed that the total conductivity depends from some bottleneck grains through which almost all the electrical current flows. So the fluctuations are caused by the flip of the magnetic moments of these bottleneck grains.

In order to test this hypothesis, we performed large scale Monte Carlo computer simulations. We constructed a Miller-Abrahams two-dimensional bond-percolating *Random Resistor Network* which has been previously used for the modeling of magnetic materials. The sites of the network are assumed to be nanomagnetic grains with two possible orientations of their magnetic moments (up and down) and the local conductivities are assumed to be the contacts between neighboring pairs of grains. The magnetic moment \mathbf{M}_i of the ferromagnetic grain is assumed to be always parallel or antiparallel to its randomly distributed easy axis. Once a magnetic field is applied, the grain magnetic moment will flip once $\mathbf{M}_i \cdot \mathbf{H} < L(h) = \coth(h) - 1/h$, where $L(h)$ is the Langevin function and $h = M_i H / k_B T$. The value of the local conductivities is assumed to be given by the Strenliker equation $\sigma_{ij} = \sigma_0(\Theta_{ij}) \exp[-\kappa \cdot \text{rand}(ij)]$ [1], where κ can be considered as a measure of the disorder, $\text{rand}(ij)$ is a random number in the range [0,1] and $\sigma_0(\Theta_{ij}) = 1/R_{ij}$. Here $R_{ij} = R_0 [1 - (\delta R / 2 R_0)^2 (1 + \cos \Theta_{ij})^2]$ is the total resistance between a pair of neighbouring ferromagnetic grains, where $R_0 = (R_{\uparrow\downarrow} + R_{\uparrow\uparrow}) / 2$ and $\delta R_0 = (R_{\uparrow\uparrow} - R_{\uparrow\downarrow}) / 2$ according to the “two-current model”.

The total effective resistance R of the network can be calculated by solving the linear Kirchhoff equations in the spanning cluster. In order to allocate the spanning cluster we used the Hoshen-Kopelman algorithm. In Fig.1 we show the experimental magnetoresistance curves obtained for a dilute Ni granular 2D sample as well as theoretical drawings of the quantity $(R(h) - R(0)) / R(0)$ versus h obtained from our computer simulations for different values of the disorder κ ($\kappa=4$ and $\kappa=40$) and for system size $L=80$.

The resistance fluctuations can be clearly seen both from the experimental [2] and the simulation curves. In order to test the impact of the “bottleneck” grains in the system (namely “red bonds” in percolation theory), we removed the specific resistor on which the local current is maximal. From the current distribution it can be clearly seen that after the removal of the critical resistor, the total current transition changes. By measuring the quantity R_{cut} / R (where R is the total resistance and R_{cut} is the total resistance after removing the “bottleneck” resistor) we confirm that it scales as $\kappa^{4/3} / L$ and $\kappa / L^{1/1.3}$ (Fig.2).

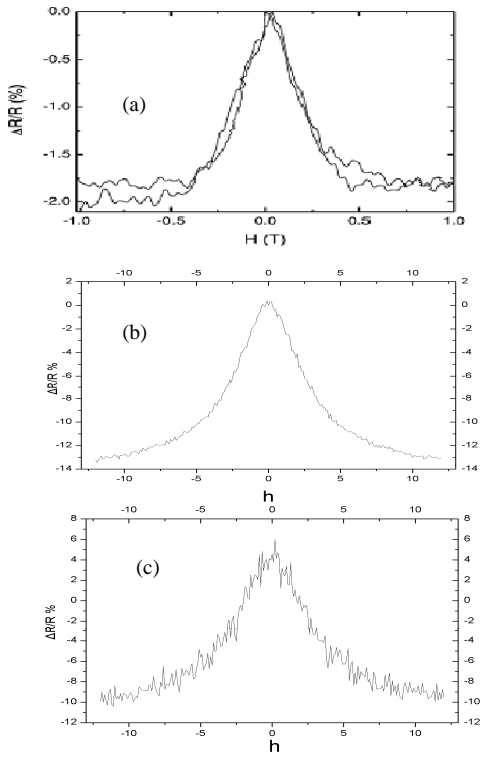


Fig.1 (a) Experimental results of the Magnetoresistant in a granular Ni sample on SiO₂. (b) Simulation results of the quantity $(R(h)-R(0))/R(0)$ versus h for disorder $\kappa=4$ and (c) for $\kappa=40$.

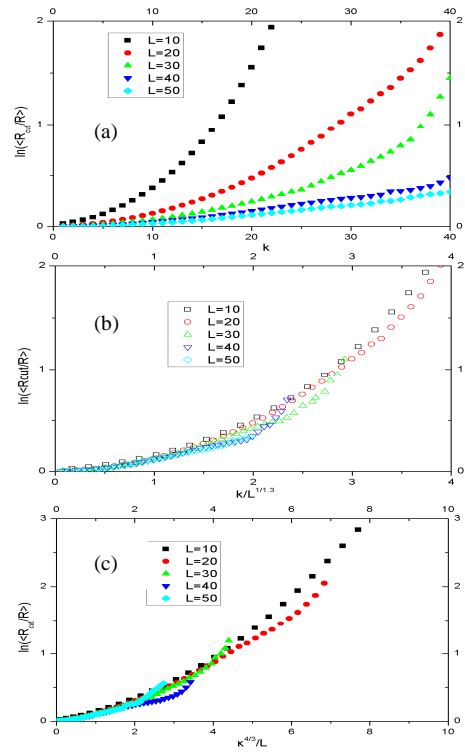


Fig.2 (a) A semilog plot of the mean value of the quantity R_{cutf}/R vs k . (b) A semilog scaling plot of the same quantity versus $k/L^{1/1.3}$ and (c) a semilog plot of the same quantity versus $k^{4/3}/L$

[1] Yakov M. Strelniker, Richard Berkovits, Aviad Frydman, and Shlomo Havlin, PHYS REV E **69**, 065105(R) (2004).
 [2] A.Y Dokow, H.Vilchik, and A.Frydman, phys Rev B **72** (094402) (2005).

Simulation of Non Classical Coarsening Mechanism in Pb/Si

L.Skarpalezos^{1*}, M.Maragakis¹, P.Argyarakis¹ and M.Tringides²

¹ Department of Physics, University of Thessaloniki, 54006 Thessaloniki, Greece

² Department of Physics and Ames Laboratory, USDOE, Iowa State University, Ames, Iowa 50011–9557, USA

*loukas@kelifos.physics.auth.gr

Pb/Si (111) in low temperatures (around 200K) is a system that displays interesting phenomena. Classical kinetics fails to explain the self-organizing uniform height distribution of the resulting Pb islands. Although sufficient evidence has been presented that the kinetics of QSE (Quantum Size Effects) govern this effect [1, 2], no adequate explanation has so far been given about the unusually fast decay of the unstable height islands. The experimentally observed process does not follow the classical Gibbs Thompson coarsening theory [3]. Indeed, as seen from recent experiments [4], most of the results for Pb-Si(111)7x7 do not comply with the corresponding classical prediction and islands with less than 7 layers decay at very fast rates. In order to explain this we propose a biased random walk mechanism that depends on the distance of the diffusing particle from the nearest stable island and make a comparison with the classical isotropic Random Walk process.

In our simulations hexagonal islands were created in random positions throughout a hexagonal 2D lattice. No overlapping of the generated islands was allowed and a minimum distance between the islands was used. We randomly denote some islands as stable and the rest as unstable. The height h of the islands is only modeled by the amount of monomers they contain, which is equal to h times the number of sites of their basis. As in the experiment, in our simulations the islands stability is defined only by its height. Stable islands are represented as having height 7 and unstable ones height 4. The system is therefore considered as a 2-D one and the transfer of the material to other planes is irrelevant. All unstable islands are then treated as sources of monomers. The decay begins at the same time for all unstable islands. Monomers are released from randomly chosen sites of the unstable islands periphery and perform a walk, until they are attached to the periphery of a stable island. Also the growth of the stable islands and the decay of the unstable ones are simulated by adding/removing an external hexagonal shell when the corresponding number of monomers reach/detach from the island. Both isotropic random walk and highly biased random walk towards the nearest stable island were used to simulate the propagation of the monomers from the unstable to the stable islands. We apply a bias to the monomers to move towards stable islands as follows. A monomer can jump to a neighboring site according to a hopping probability given by the following equation:

$$P_{i,j} = \frac{1}{l_j^\alpha}$$

where l_j is the distance of the nearest stable islands facet to site j that the monomer initially in site i is about to jump to, and α is an exponent with value chosen arbitrarily as 10 (to get long range effect of the biased random walk). The probabilities given by the above equation are normalized for all six directions (all six possible j sites). This algorithm is not symmetric, meaning that even for large distances the monomers have a greater probability to go towards the stable islands than to move away from them. The asymmetry also grows as the monomers approach the island facet and l gets smaller. It follows that as the separation l between the monomer and the stable island decreases the movement towards the stable island is accelerated. For example when $l < 3$, the monomer practically goes directly towards the stable island since the probability to move along the line and towards the island is close to 1.

The main result of our simulations is that as expected the biased random walk is much more efficient in material transport from the unstable to the stable islands. This is made clear by plotting the distribution of time for a monomer to be caught for the two types of random walk (fig 1). Not only is the average less for the biased walk but also the width of the distribution is smaller. The capture times have higher probability around the average time for biased than for isotropic random walk. Also the amount of monomers captured by the nearest stable island is higher in the biased case and corresponds to the experimentally observed preferential growing of the nearest stable island. The strong anisotropy and the efficiency of the biased diffusion versus the classical random walk mechanism can be further clarified. To do this we compare the probability to find a particle at every lattice site during the entire process for the two cases. The resulting figure (fig 3) depicts how the particles move in the lattice. In the random walk case they perform normal diffusion giving a “cloudy” image near the basis of each decaying island. In the biased case most of the trajectories are directed along the line terminating at the vertex of an unstable island. This behavior is also due to the topology of the hexagonal lattice. Once the

monomers are released and target the nearest neighboring stable island they diffuse towards it with higher probability. Finally the rate of growth of the stable islands, which is a quantity that can be measured experimentally, is also affected. The curve of this quantity is much more abrupt in the biased case and fits qualitatively better with experimental observations (fig 2).

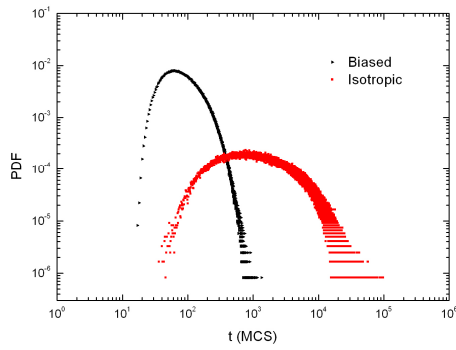


Fig1. Log-log probability density function for biased and isotropic random walk on a 100x100 hexagonal lattice for $\theta=0.064$

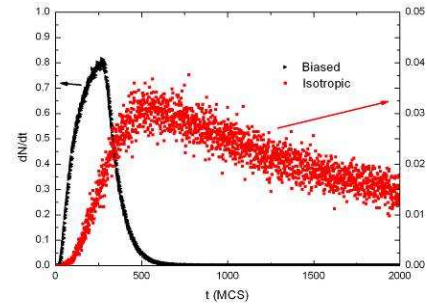


Fig2. Capture rate vs time for stable islands for isotropic random walk (scale to the right) and biased random walk (scale to the left) for $\theta=0.064$

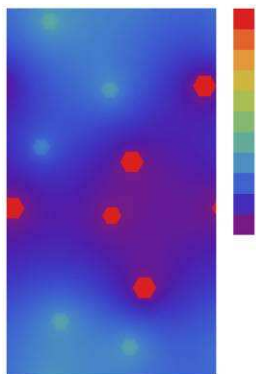


Fig 3a. Probability to find a particle in a lattice site for the all time of the experiment for the RW case (100 runs, $\Gamma=1, \theta=0.064$).

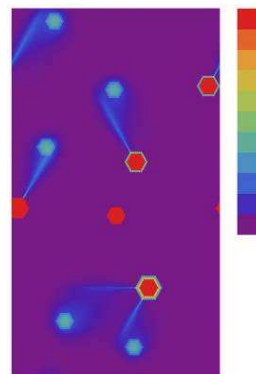


Fig 3b. Probability to find a particle in a lattice site for the all time of the experiment for the Biased Walk case (100 runs, $\Gamma=1, \theta=0.064$).

[1] C.Chan, Z.Wang, M.Hupalo, M.C.Tringides, K.M.Ho PhysRevLett.96.226102(2006).
 [2] Z.Kuntova, M.Hupalo, Z.Chvoj, M.C.Tringides Phys.Rev.B.75.205436(2007).
 [3] L.Kuipers, J. W.M.Frenken, PhysRevLett.70,3907-3910(1993).
 [4] C.A Jeffrey, E.H.Conrad et al, PhysRevLett.96.106105(2006).

Fe₃O₄@Au Core-Shell Nanocrystals: Magnetic and Optical Properties

Konstantinos Brintakis^{1,2*}, Athanasia Kostopoulou^{1,3} and Alexandros Lappas¹

¹ *Institute of Electronic Structure and Laser, Foundation for Research and Technology – Hellas, Vassilika Vouton, 71110 Heraklion, Greece*

² *Solid State Physics Section of Physics Department, Aristotle University of Thessaloniki, 54124 Thessaloniki, Greece*

³ *Department of Chemistry, University of Crete, Voutes, 71003 Heraklion, Greece*

* *kbrin@iesl.forth.gr*

During the last decade we witness a surge of research activities concerning nanotechnology. A lot of effort has been placed in the area of novel nanoparticles. The reason has been that the physical and chemical properties of a material at the nanometer scale are quite different from what we usually meet in the same phase in a bulk form. One project of our team is the synthesis and the characterization of core – shell type nanocrystals (NCs), involving magnetite and noble metals (c.f. gold).

This type of “hybrid” NC has the advantage of extra functionality as the magnetic material is combined with the optical properties that the gold shell offers. Except the size dependent plasmonic properties, gold gives good conductivity and biocompatibility. These features give the opportunity for many applications, including medical treatment, magnetic resonance imaging, materials for magnetic and optical recording, sensors etc. The type of application that such NCs could be implemented into depends on its diameter (size) and consequently on the magnitude of the magnetic moment that it carries.

The core-shell NCs of Fe₃O₄@Au are synthesized with the seeded growth approach [1, 2]. First we synthesize the Fe₃O₄ core with a two steps procedure; the first step produces the nucleus of the Fe₃O₄ and the second step at higher temperature controls the growth and consequently the diameter of the NCs. A monodispersed solution of the Fe₃O₄ is essential in order to continue with the coverage of the core with the Au shell [1, 2, 3]. Carefully selected measurements have been performed both on seeds as well as on the hybrid, core-shell nanocrystal.

The project investigates the structural, magnetic and optical properties of NCs with different diameter. We compare NCs with approximately 10 nm [1, 2] and 100 nm [3] diameters. The structural characterization is performed by X-ray diffraction (XRD) that could give a first idea about the crystallinity and the size of the NCs. Conventional transmission electron microscopy (CTEM) (Fig. 1) and Hi-Resolution TEM (HRTEM) are combined to give a more precise view on the size and shape of the NCs, the interface between the core and the shell and the thickness of the shell. SQUID magnetometry (Fig. 2) is utilized as a probe of the magnetic response (superparamagnetism vs. ferromagnetism) of the NCs in an effort to help us understand how the size of the NCs and the thickness of the shell affect the magnitude of the magnetic moment. These are supported by UV absorbance measurements, which identify the plasmon band (517 nm) [1] of the gold shell and follow its evolution as a function of the diameter of the NCs. On another account, we discuss the perspectives for such hybrid NCs in view of superlattice formation. For this purposes, substrates (Si-based) of varying degree of hydrophobicity are utilized in order to explore the assembly of NCs in multifunctional structures.

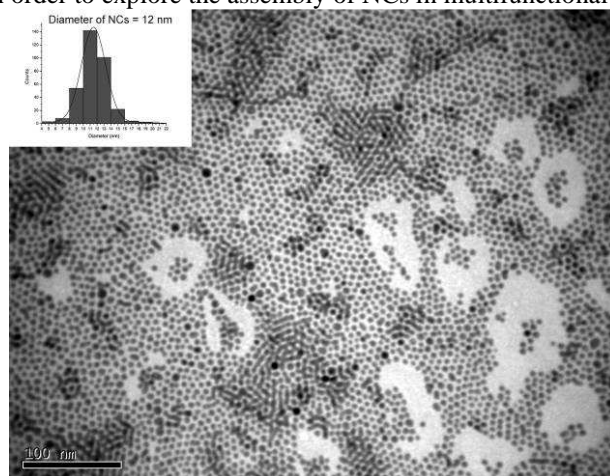


Fig. 4. An image taken with CTEM of the Fe₃O₄@Au core-shell.

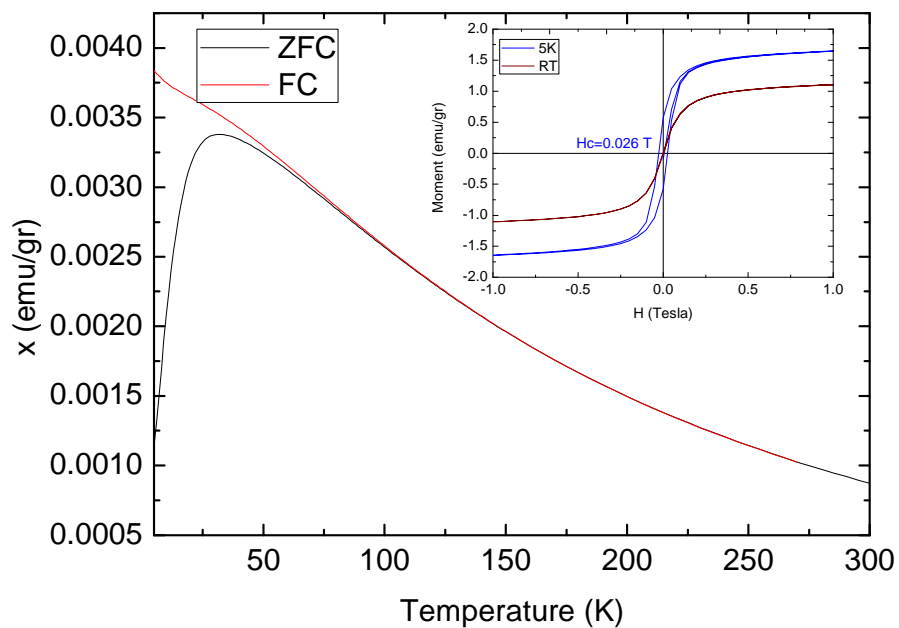


Fig 5. ZFC-FC measurements and Hysteresis Loops at RT and 5 K.

- [1] Wang L., Luo J., Fan Q., Suzuki M., Suzuki I. S., Engelhard M. H, Lin Y., Kim N., Wang J. Q, Zhong C., J. Phys. Chem. B, 109, 21593 (2005).
 [2] Sun S., Zeng H., Robinson D. B., Raoux S., Rice P. M, Wang S. X, Li G, J. Am. Chem Soc., 126 (1), 273 (2004).
 [3] Deng H, Li X., Peng Q., Wang X., Chen J., Li Y., Angew. Chem. Int. Ed., 44, 2782 (2005).

Acknowledgements:

The Marie-Curie Transfer of Knowledge program of the European Commission is acknowledged (“NANOTAIL”, Grant no. MTKD-CT-2006-042459).

Structural and Magnetic Properties of Colloidal Iron Oxide Magnetic Nanoclusters

A. P. Douvalis^{1*}, A. Kostopoulou^{2,3}, A. Lappas² and T. Bakas¹

¹ Physics Department, University of Ioannina, 45110 Ioannina

² Institute of Electronic Structure & Laser, FORTH, Vassilika Vouton, 71110 Heraklion

³ Department of Chemistry, University of Crete, Voutes, 71003 Heraklion

*adouval@cc.uoi.gr

In the last decades the use of Magnetic nanoparticles (MNPs) in several aspects of modern technological and medical applications has established an important trend towards the better understanding of their structural and magnetic properties [1]. In order to be able to design special materials for targeted applications we have to apprehend and control the factors that determine these properties. On the other side the structural and magnetic properties of MNPs are quite strongly interconnected and the investigation of the factors influencing solely one of these properties cannot be easily done without altering the corresponding factors controlling the other remaining properties.

In particular for iron oxide MNPs crucial factors determining their magnetic properties is their chemical composition and morphology, and the most important way to manipulate these factors is by controlling their preparation procedure. In this work we present a study of the structural and magnetic properties of colloidal clusters made of iron oxide MNPs, which have been prepared by a wet chemical preparation route. The preparation is based on a hydrolysis reaction at 220 °C of FeCl₃ metallic precursor, in diethylene glycol (DEG) solvent, with the use of a poly-electrolyte [poly(acrylic) acid (PAA)] as surfactant [2]. The poly-electrolyte serves a dual purpose: on the one hand it assists to the creation of the nanoclusters and on the other it helps on their dilution in water. The stock solution is made of NaOH in DEG and the important parameter which determines the size of the nanoclusters is the quantity and addition rate by which the stock solution is added in the mother solution at 220 °C. We have prepared a number of nanoclusters samples by using different quantities and addition rates of the stock solution and we have characterized them with the use of several experimental techniques like X-ray diffraction (XRD), Transmission Electron Microscopy (TEM), magnetization and magnetic susceptibility measurements and ⁵⁷Fe Mössbauer spectroscopy.

The powder XRD pattern of a characteristic nanoclusters sample is shown in Fig. 1(a). The diffraction peaks correspond to iron oxide spinel, which could be characterized either as magnetite (Fe₃O₄) or maghemite (γ-Fe₂O₃) (this is not clear from this pattern as the two phases have quite similar XRD diagrams and the sample's pattern has rather broadened peaks due to its nanostructured nature). The TEM image of this sample displayed in Fig. 1(b), reveals indeed the presence of the nanoclusters, their morphology and internal structure which is composed of iron oxide MNPs. The size of the nanoclusters, which could be determined from this picture, follows a distribution [see insert of Fig. 1(b)], which is centered on 100 nm. By applying the Scherrer formula [3] to the XRD pattern of Fig. 1(a), the average particle size is estimated to be about 7 nm.

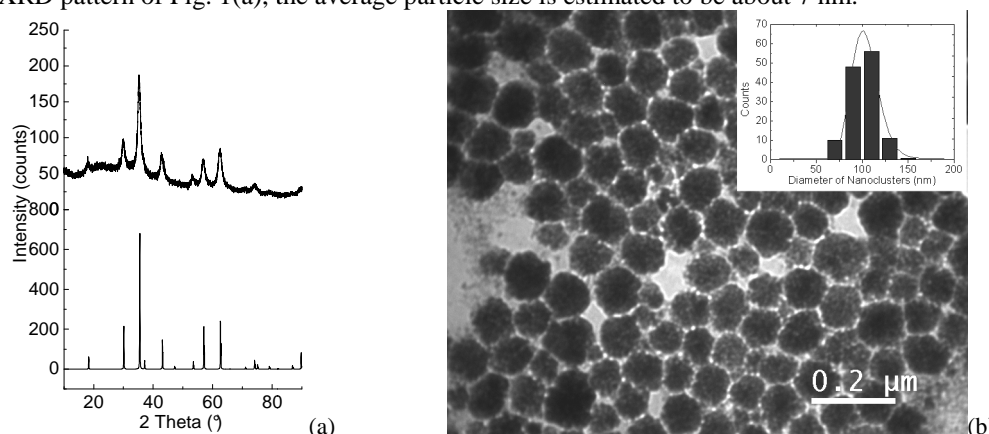


Figure 1. (a) Powder XRD diagram of a characteristic iron oxide nanoclusters sample. The corresponding pattern of bulk magnetite is shown for comparison. (b) TEM image of the same iron oxide nanoclusters sample. The size distribution of the nanoclusters for this sample is shown in the insert.

The TEM analysis of a series of nanoclusters samples prepared by using different quantities and addition rates of the stock solution has allowed us to establish a way to control the average cluster size, which is increased as the quantity and addition rate increases. The magnetization and magnetic susceptibility measurements, shown in Fig. 2 verify this trend, as the samples with the larger average nanoclusters sizes show higher Blocking

temperatures and increased saturation magnetization values. However the average sizes of the iron oxide MNPs which compose the nanoclusters, as estimated from the Scherrer formula, seem to have an opposite trend showing a small decrease, from 11 nm to 9 nm to 7 nm, as the size of the nanoclusters increases from 40 nm to 70 nm to 100 nm respectively.

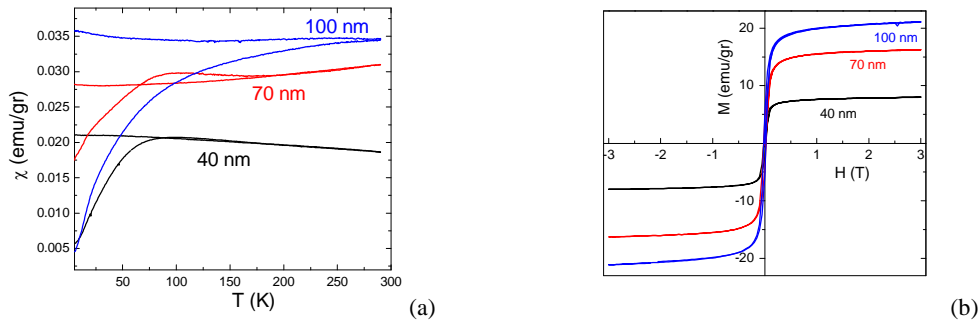


Figure 2. Magnetic susceptibility recorded in an applied field of 200 Oe (a) and magnetization measurements collected at 5 K (b) of characteristic nanoclusters samples with different average cluster sizes assigned to each curve.

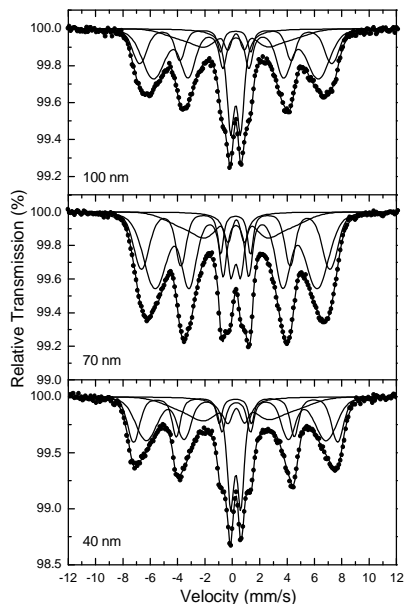


Figure 3. ^{57}Fe Mössbauer spectra of the three nanoclusters samples of different average cluster sizes recorded at room temperature.

The ^{57}Fe Mössbauer spectra of these three characteristic samples collected at room temperature (RT) are shown in Fig. 3. The spectra possess high absorption line broadening, which is a declarative characteristic of the nanostructured nature of the particles. Both magnetically split and superparamagnetic contributions are present in the spectra, indicating a distribution of particle sizes as well as the possible presence of magnetic interparticle interactions between the iron oxide MNPs within the nanoclusters. The Mössbauer parameters reveal the presence of predominantly Fe^{3+} valence states. However minor magnetically split contributions of intermediate valence $\text{Fe}^{2.5+}$ states are resolved at lower temperatures above 120 K (the Verwey transition for magnetite [4]), suggesting that the chemical composition of the iron oxide MNPs is not uniform and could involve non-stoichiometric iron spinel oxide compositions of the $\text{Fe}_{3-x}\text{O}_4$ type, with x ranging between 0 (magnetite) and 0.33 (maghemite). An important characteristic of these spectra is that the sample with the lower average nanocluster size (40 nm) shows the larger hyperfine magnetic field (B_{hf}) values, which is a property that can be attributed either to the increased iron oxide MNPs size or to the adaptation of a composition closer to maghemite for this particular sample, as maghemite usually shows larger B_{hf} than magnetite [5]. The first assumption is in accordance with the results of the XRD and TEM analyses, which show larger average MNPs size for this sample compared to the other two. It is also important to

mention here that the superparamagnetic part of the spectra of all samples retains its absorption area almost intact throughout the whole measuring temperature range from 300 K to 77K, indicating that this part of the MNPs assembly corresponds to particles of very small sizes.

On the other hand having in mind the reduced particle size (7-11 nm), the dominant presence of magnetically split components in the Mössbauer spectra of all samples suggests that the magnetic interparticle interactions experienced by the iron oxide MNPs within the nanoclusters possess enough strength to overcome the superparamagnetic relaxation even at temperatures as high as RT.

References

- [1] Pankhurst Q. A., Connolly J., Jones S. K. Dobson J., J. Phys. D: Appl.Phys. 36, R167 (2003).
- [2] Ge J., Hu Y., Yin Y., Angew. Chem. Int. Ed. 46, 7428 (2007).
- [3] Cullity B. D., Elements of X-ray Diffraction (Reading, MA: Addison-Wesley 1956).
- [4] Walz F., J. Phys.: Condens. Matter 14, R285 (2002).
- [5] Greenwood N. N., Gibb T. C., Mössbauer Spectroscopy (London: Chapman and Hall 1971).

Acknowledgements The Marie-Curie Transfer of Knowledge program of the European Commission is acknowledged (“NANOTAIL”, Grant no. MTKD-CT-2006-042459).

Organomodification of Nanoclays and its Role on the Porous Structure of Polymer Nanocomposites Produced by Supercritical CO₂

A. Tsimpliaraki^{1,2}, I. Tsivintzelis¹, S.I. Marras², I. Zuburtikudis² and C. Panayiotou^{1*}

¹ Department of Chemical Engineering, Aristotle University of Thessaloniki, 54124, Greece

² Department of Industrial Design Engineering, TEI of Western Macedonia, 50100 Kozani, Greece

*cpanayio@auth.gr

Recently, supercritical fluids have been used as foaming agents in various polymers as well as nanocomposite systems. The presence of nanoparticles, such as nanoclays, may enhance cell nucleation, provide foam reinforcement, lower gas escape rate, and result in char formation when foam is exposed to fire (improved fire retardance and better barrier properties) [1,2]. So far, there have been reported many studies on the effect of the filler on the transport of gases in polymers, and especially the role of the loading of fillers [3]. However, the effect of the surfactant type used for the clay modification as well as the role of the cation exchange capacity (CEC) of the clay after modification has not been investigated yet. The scope of this work is to examine the way these two factors affect the final porous structure of the hybrid materials.

Firstly, modification of sodium montmorillonite has been performed resulting in two different series of clay products. One series of modified montmorillonite were prepared using different types of alkylammonium in terms of C atoms (i.e. 4, 8, 12, 16 and 18-ammonium), while the alkylammonium concentration was kept equivalent to 1.5 times the cation exchange capacity (CEC) of the clay. The other series was prepared by using only hexadecylammonium for the modification and by varying the modification level from 50 to 200% of the clay CEC.

Two series of nano-hybrid films were subsequently fabricated from a poly(DL-lactic acid) solution loaded with 3 wt% of organically modified montmorillonite from the two previously prepared series. Porous structures of pure and nanocomposite poly(DL-lactic acid) were prepared with the batch foaming technique (pressure quench) using supercritical CO₂ as blowing agent. The morphological correlation between the dispersed silicate particles and the obtained microcellular porous structure of the foam was investigated using scanning electron microscopy (SEM), and cross-sections of the porous samples are indicatively shown in Fig. 1.

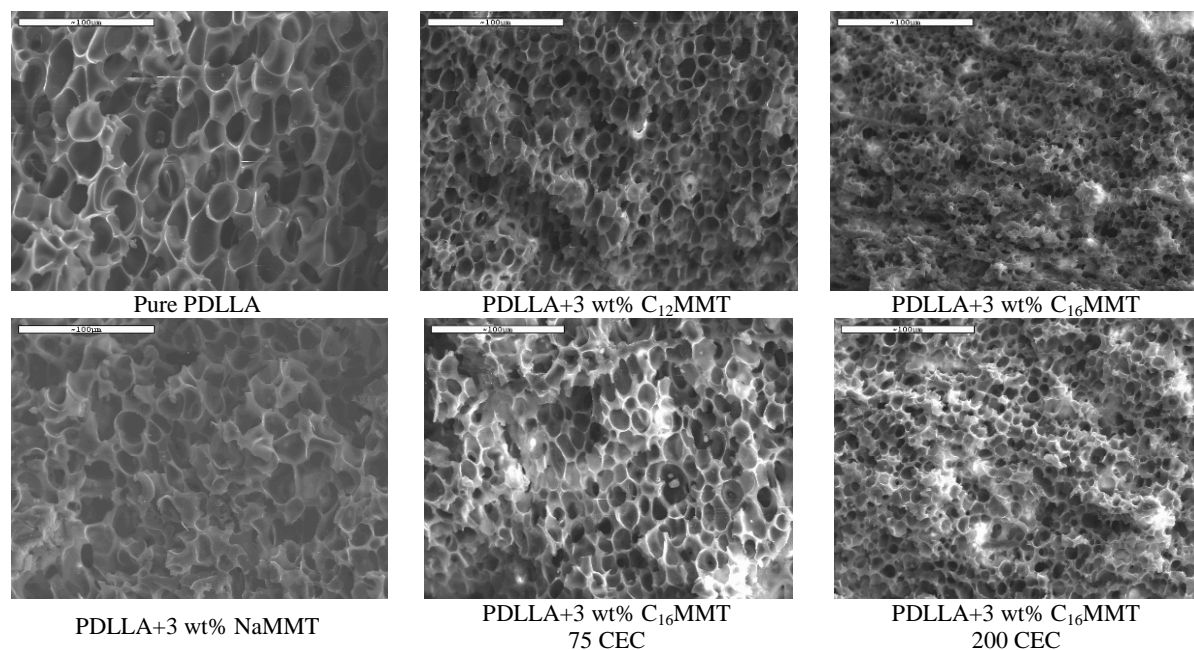


Fig.1. Porous structures of pure PDLLA and PDLLA nanocomposites compared via SEM micrographs; scale bar at 100 μm.

Image analysis revealed that the final cellular structure is strongly related to, both, the type and the CEC of the alkylammonium used for the modification of the filler. The results suggest that the size of the pores decreases with the increase of the surfactant's C atoms and cation concentration, while the bulk foam density does not seem to be affected in neither case.

[1] Ibeh C., *J Cellular plastic*, 44, November (2008).

[2] Tomasko D. L., Han X., Liu D., Gao W., Koelling K. W., Lee L. J, *Current Opinion in Solid State and Materials Science* 7 (2003) 407–412, (2003).

[3] Tsivintzelis I., Marras S.I., Zuburtikudis I., Panayiotou C., *Polymer*, 48, (2007).

Atomic Scale Modelling by the use of a III-species Environment Approach: Implementation on Threading Dislocations and (Al,In)N/GaN Interfaces

J. Kioseoglou¹, E. Kalesaki¹, G.P. Dimitrakopoulos¹, Th. Kehagias¹, Ph. Komninou^{1*}, and Th. Karakostas¹

¹Department of Physics, Aristotle University of Thessaloniki, GR-54124 Thessaloniki, Greece

*komnhnoy@auth.gr

In the present work, an interatomic Tersoff potential is utilized for atomistic calculations of III (Al, Ga, In) - N compound semiconductors in the wurtzite structure. A III-species environment approach is developed for this empirical, bond-order Tersoff interatomic potential, in which the cut-off distance for Al-Al and In-In interactions is tuned, since in the wurtzite structure of AlN and InN the second-neighbour distance is very close to the stable “metallic” Al-Al and In-In distances respectively.

The multiple atomic configurations (5/7, 8, and 4) of the a -edge threading dislocations in III (Al, Ga, In)-N compound semiconductors are studied by the III-species environment approach (Fig. 1). Structural and energy related conclusions are drawn which are attributed to the complexity of the III-III metal type and N-N interactions (bond Ga-Ga < bond Al-Al < bond In-In) in connection with the difference of the lattice parameters ($a_{\text{AlN}} < a_{\text{GaN}} < a_{\text{InN}}$) and the elastic constants. The 5/7 atomic core configuration is calculated as the most energetically and structurally favorable in all three compounds. Having as reference the 5/7 atom model which represents the most stable dislocation structure, the 8-atom core model becomes the next favorable when the lattice parameter increases (a_{InN}) while the 4-atom core model becomes more energetically preferable when the lattice parameter decreases (a_{AlN}).

Moreover the polar (Al,In)N/GaN interfaces are investigated (Fig. 2). HRTEM observations have shown that multiple interfacial structural configurations are present and influence significantly the overall properties of III-N nanostructures. The strain stored in lattice mismatched heterostructures, such as InN/GaN and AlN/GaN, can be relaxed by the formation of misfit dislocations on the corresponding interfaces. In order to get an on-atomic-scale description of III-Nitride heterostructures and determine the preferable interfacial plane (i.e. cutting of single (type 1) or double bonds (type 2) and/or the preferable polarity along the interfaces) we perform first-principles as well as Tersoff interatomic potential calculations for the system of (Al,In)N/GaN interfaces.

Our III-species environment approach calculations reveal that the relaxed AlN/GaN interfaces are dominated by vast areas of “good fit” which resemble pseudomorphic growth of AlN on GaN (Fig. 3). Applying the same criteria we performed *ab-initio* calculations examining three different cases which correspond to three different epilayer – substrate interface reconstructions. In all cases the thin epilayer is pseudomorphically adjusted to the basal-plane lattice parameters of the thick substrate. Concerning the c lattice constant two different approaches are followed. It is either optimized by total energy minimization following the plane strain approach or determined by the biaxial strain. Based on our empirical potential and Density Functional Theory (DFT) calculations we conclude that the III-polarity interfaces of type 1 are energetically favorable. DFT reveals also that the AlN/GaN wurtzite interfacial stacking is preferable in comparison to the zinc blende and the interfacial energy difference ($\Gamma_{\text{wurtzite}} - \Gamma_{\text{zincblende}}$) increases proportionally to the basal lattice constant of the pseudomorphically adjusted thin layers. Finally, the effect of lattice strain on the electronic properties of the AlN/GaN system was investigated. It was found that the band gap of AlN is screened from that of GaN in all cases. Our results suggest that the compressive strain applied in the AlN/GaN system leads to a widening of its band gap; the latter exhibits a linear dependence to the strain. In addition biaxial strain is found to flatten this linear variation considerably.

Acknowledgments Financial support by the European Community's Marie Curie Research Training Network PARSEM (MRTN-CT-2004-005583) is gratefully acknowledged.

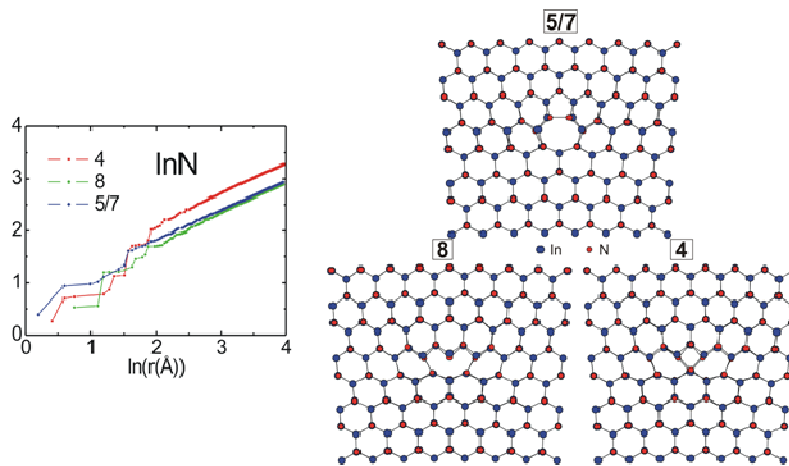


Figure 1. Elastic energy per unit length $E_d(r) = E_{core} + E_{elastic}$ stored in a cylinder of radius r as a function of $\ln(r)$ and the relaxed atomic configurations of the 5/7, 8 and 4 atomic core configurations of $\frac{1}{3}\langle 1\bar{2}10 \rangle$ perfect edge threading dislocations in InN, projected along the [0001] direction. Large and small circles denote In and N atoms respectively.

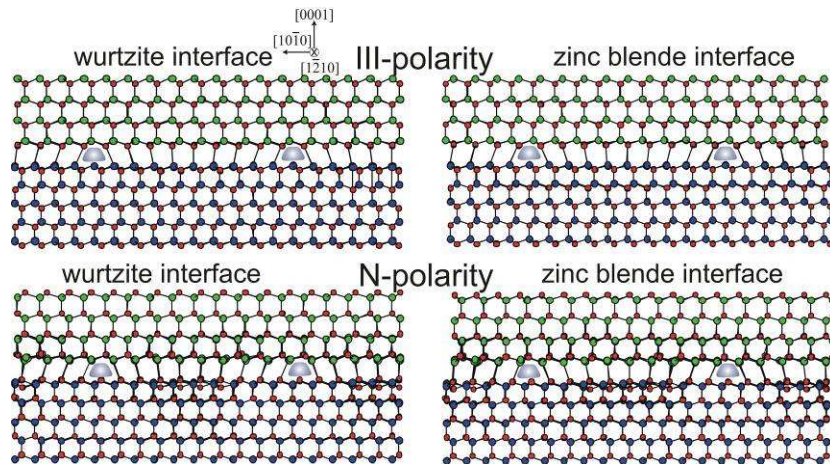


Figure 2. Relaxed InN/GaN type 1 (cutting single bonds) interfaces for wurtzite and zinc blende interfacial structures viewed along $[1\bar{2}10]$.

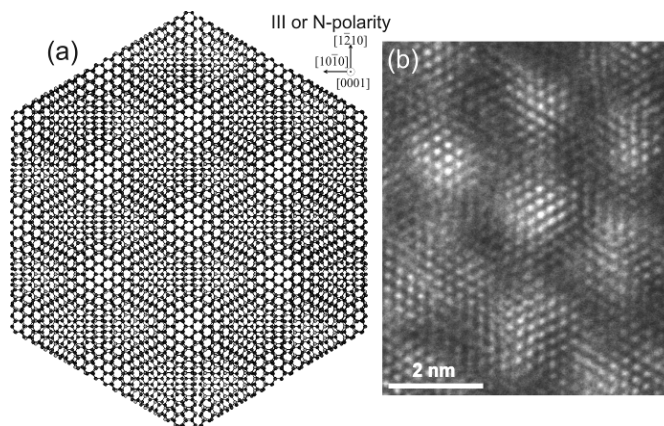


Figure 3. (a) [0001] projection of the relaxed InN/GaN type 1 (cutting single bonds) interface having wurtzite interfacial structure. The two polarities are non distinguishable when viewed along [0001]. (b) HRTEM image along the [0001] direction of InN/GaN interface. The moiré pattern reveals the regions of “good” and “bad” fit.

The Electronic Structure of Ni-Phthalocyanine on ITO/Flexible Interface Studied by Photoelectron Spectroscopies

D.Tsikritzis^{1*}, F. Petraki¹ S. Kennou¹

¹Department of Chemical Engineering, University of Patras and FORTH/ICE-HT, Gr-26504, Patras, Greece

*tsikritzis@chemeng.upatras.gr

The chemical and electronic properties of ITO/PET, as well as the interface that it form with Nickel Phthalocyanines (NiPc) thin films, were studied by X-ray and UV Photoelectron Spectroscopies (XPS, UPS).

Indium Tin oxide is the most widely used, among other transparent conductive oxides, in organic light emitting devices (OLED), liquid crystal displays and solar cells because it exhibits a combination of high electrical conductivity at room temperature and a wide band gap. It is used as a high work function electrode and it determines the energy barrier height with the polymer in contact, which affects the carrier injection in the device [1]. The work function value of the ITO is of great importance in the device performance. Recently, polymer LED fabricated on flexible substrates exhibited promising characteristics compared to those on glass substrates. Phthalocyanines (Pcs) are a family of medium sized organic molecules. These materials are already widely used in gas sensor technology and in electronic devices because of their beneficial properties such as thermal, chemical and photochemical stability, layered like growth mode when deposited onto metallic substrates and advantageous optical and electronic properties. In addition, NiPc is an organic semiconductor with a relatively high mobility value ($\approx 1 \times 10^{-5} \text{ m}^2 \text{ V}^{-1} \text{ s}^{-1}$) compared with the equivalent for other MPcs [3], which makes it a promising candidate for the development of future electronic devices. The aim of this study is to investigate the electronic properties of the interface formed between NiPc films and ITO on flexible (PET) substrate commercially available.

The experiments were carried out in an ultra high vacuum system, which allows the preparation of interfaces with high purity and controlled thickness [2]. Commercial NiPc powder was thermally evaporated in a step wise manner, from a home-made deposition source, on the surface of the ITO/PET substrate and thin NiPc films with a total thickness of 11 nm were prepared. After each deposition step the formed interfaces were investigated by Photoelectron Spectroscopies (XPS ($\text{MgK}\alpha$) and UPS (HeI)).

The chemical composition of the ITO on PET substrate was determined by XPS ($\text{AlK}\alpha$), and according to the wide scan spectrum, which is displayed in figure 1, it is composed of Indium, Tin, and Oxygen atoms. Carbon was also present at the surface due to the exposure of the sample to the atmosphere. No cleaning method was used to remove the contaminants from the substrate in order to investigate the properties of NiPc interface on ITO/PET as it is used in device technology. From the high binding energy cut-off region in the UP spectra, the work function of ITO/PET substrate was determined equal to $4.0 \pm 0.1 \text{ eV}$.

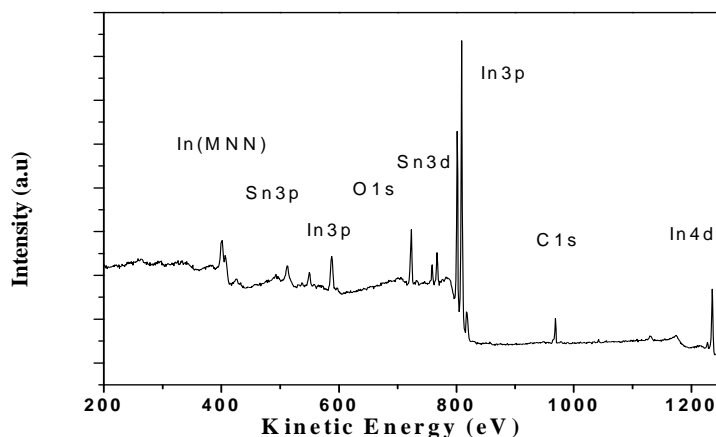


Figure 1: ITO/PET, XPS wide scan ($\text{MgK}\alpha$)

The deposition of NiPc thin films on the surface of ITO on PET showed that the organic molecules form abrupt interfaces with the ITO film. No band bending was observed at the organic energy levels. The valence band structure of the organic overlayer, which is shown in figure 2, consists of four peaks at binding energies

1.50 eV, 3.80 eV, 6.60 eV and 8.85 eV respectively, which are in agreement with previous studies (NiPc/metals [3], NiPc/ITO-glass). The HOMO cut-off position of NiPc is located at 1.00 ± 0.05 eV and due to band bending absence, the hole injection barrier (Φ_{bh}) was found equal to 1.0 ± 0.1 eV similar to that in the case of the NiPc/ITO-glass interface. A small (~ 0.1 eV) reduction of the vacuum level was observed during the interface formation, leading to an interfacial dipole of the same magnitude, which could arise from a net charge transfer from the NiPc molecules to ITO. Thus, the work function of NiPc was determined equal to 3.9 ± 0.1 eV.

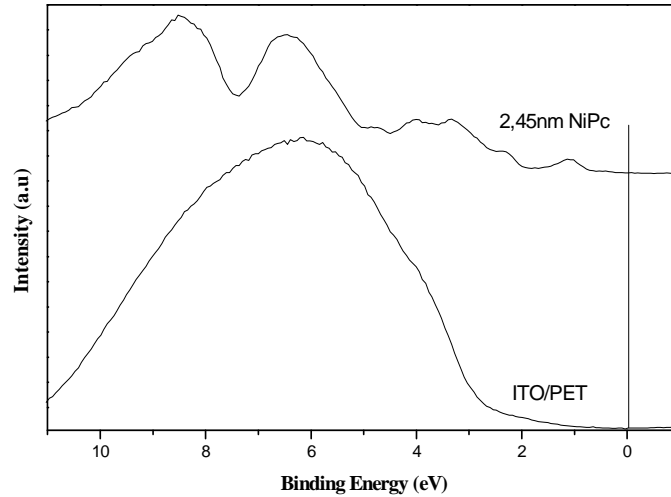


Figure 2: Valence Bands of ITO/PET and NiPc (2.45 nm thick)

References

- [1] K. Sugiyama, H. Ishii, Y. Ouchi and K. Seki, *J. Appl. Phys.* **87**, 295 (2000).
- [2] F. Petraki, S. Kennou and S. Nespurek, *J. Appl. Phys.* **103**, 033710 (2008).
- [3] F. Petraki, V. Papaefthimiou and S. Kennou, *Org. Electron.* **8**, 522 (2007).

Structural characterization of ZnO/Mg_xZn_{1-x}O and ZnO/MgO thin films grown on sapphire by using HRTEM

I. Tsiaoussis^{1*}, V. Petukhov², A.-H. Elshaer², A. Bakin², J. Stoemenos¹, A. Waag²

¹*Physics Department, Aristotle University Thessaloniki, GR-54124 Thessaloniki, Greece*

²*Institut für Halbleitertechnik, Technische Universität Braunschweig, 38106 Braunschweig, Germany*

**tsiaous@auth.gr*

ZnO is a II–VI wide band gap (3.37 eV) semiconductor with a large exciton binding energy of 60 meV, which has attracted considerable attention as a promising candidate for optical and electronic device applications [1]. It is well known that the electrical and optical properties of ZnO films depend on the microstructure, and that the presence of defects and the structure of the film–substrate interface have a crucial role in device performance. [1–6]. Plasma-assisted molecular beam epitaxy (PAMBE) method is typically used for manufacturing of high-quality epitaxial layers, providing excellent control of layer thickness, composition, interface and surface uniformity and sharp dopant profiles. One of the most successful approaches which led to the improvement of the ZnO layer quality is the implementation of a thin MgO buffer layer grown directly on sapphire with a consequent low-temperature ZnO buffer layer [7]. In this work the structural characteristics of the ZnO films grown on Zn_xMn_{1-x}O multilayer templates were studied by Transmission Electron Microscopy (TEM).

The growth of ZnO and Zn_{1-x}Mg_xO layers with Mg contents of 0%–30%, determined by quartz crystal deposition monitor, was done in a modified Varian Gen II MBE system with a base pressure of 10⁻⁸ Torr. In this system, for evaporation of 6N Zn and 4.5N Mg materials, double zone effusion cells were used. Reactive oxygen radicals were produced by an RF-plasma source. 5N oxygen gas was injected in this source through a mass flow controller. The samples investigated in this report were grown on sapphire with conventional double high-temperature-MgO/low-temperature-ZnO buffer. In the case of sample MB368, a Zn_{0.7}Mg_{0.3}O/Zn_{0.8}Mg_{0.2}O template, followed by a ZnO/Zn_{0.8}Mg_{0.2}O multiple quantum-well structure with 10 periods and a Zn_{0.8}Mg_{0.2}O/Zn_{0.7}Mg_{0.3}O covering layer were grown on the buffer. In the case of the sample MB412 we attempted to produce a Zn_{0.8}Mg_{0.2}O/ZnO-supperlattice on a ZnO-template. The structure was then covered with another ZnO layer. The structural investigations performed by using a conventional TEM microscope JEM 100 CX operating at 100 kV, and a JEM 2011 operating at 200 kV with point to point resolution of 0.194 nm.

Low magnification TEM micrographs show the existence of different zones (A, B, C, D, E, F) in the first set of samples (MB368) as it is seen in Fig.1 a. An overall view of the film is shown in low magnification micrographs, where the thickness of the thin film was found to be about 260 nm. It is evident that most of the dislocations are confined in the zone A by bending. The majority of the dislocations that penetrated the zone A were perpendicular to the substrate. The dislocation density was measured in the upper part of the film where the multilayer zone was formed and it was of the order 5×10⁹ cm⁻², quite high but in the same order as described by Vashaei et al. [8]. It is noticed that in some cases pyramids were formed at the surface due to the presence of the threading dislocation. The corresponding electron diffraction patterns have been taken with the incident electron beam parallel to the [2-1-10] direction of sapphire and reveal a good epitaxial growth of the film (Fig.1 b). The epitaxial relationship of the layers are the following: [10-10]_{MgZnO}//[10-10]_{ZnO}// [11-20]_{sapphire} and (0001)_{MgZnO} (0001)_{ZnO}//(0001)_{sapphire}. HRTEM micrographs taken near the interface, shows clearly the existence of dislocations directly at the interface (Fig.1 c). This is due to different lattice spacing between MgO and Al₂O₃. A HRTEM micrograph taken at the upper part of the film shows a ten times repetition of ZnO/Zn_{1-x}Mg_xO quantum wells (QWs) growth along the [0001] direction (Fig.1 d). A detailed investigation of the second set of samples (MB412) by using conventional microscopy shows large precipitates indicated by arrows, as shown in Fig.2a. In the corresponding selected area electron diffraction pattern (SAED), taken with the incident electron beam parallel to the [1100] direction of the ZnO, three sets of spots are evident, these of the ZnO denoted by the letter Z, the spots from the sapphire substrate, denoted by the letter S and spots from the precipitate denoted by the letter M. The spots belonging to the precipitates were indexed and was found that they belong to pure MgO, having the [112] crystallographic direction parallel to the electron beam. The epitaxial relationship of the precipitates are the following: [111]_{MgO}//[0001]_{ZnO}, and the [220]_{MgO}//[1120]_{ZnO}. Therefore the precipitate was in perfect epitaxial relation with the ZnO overgrown. In order to take DF micrographs from the precipitate the (420) diffraction spot was chosen, first because this type of spots are far from the ZnO and the sapphire spots, as is evident in the SAED pattern, and second because this reflection is one of the strongest in MgO (intensity of about 19%). The corresponding DF micrograph shows, MgO precipitates bright in dark background contrast. Actually not only the defined precipitate is diffracting strongly but also all the neighboring precipitates are in contrast revealing that all the MgO precipitates are in a good epitaxial relationship with the matrix. From the TEM micrographs can be deduced that the MgO precipitates are plate-like. HRTEM micrographs have been

taken with the incident beam parallel to the [2-1-10] direction of sapphire. Lattice fringes of the [0001] direction are visible in the ZnO layer close to the precipitate and cross them. The corresponding electron diffraction pattern shows a good epitaxial growth of ZnO/MgO on sapphire (Fig.2b). The reason of the formation of MgO precipitates is attributed to the high temperature annealing ($\sim 700^\circ\text{C}$) during the growth of the superlattice. This step was included in order to improve surface morphology. As the result, MgO clusters were formed destructing the superlattice. The next superlattices were grown without this high-temperature step providing high-quality superlattice formation.

In summary we characterized the structure of QWs ZnO/MgZnO grown on sapphire as well as the morphology of ZnO/MgO/Al₂O₃ thin films. In the first case the structure inside the QWs remains the same as the structure of ZnO, which has a hexagonal structure. A large number of stacking faults is visible inside them due to the misfit between the different unit cells. In the second case plate-like precipitates were formed and the structure of the MgO is cubic. Formation of these MgO inclusions was caused by the introduction of high-temperature annealing step in the growth process in order to improve surface morphology.

References

- [1] Y. Chen, D.M. Bagnall, H.J. Koh, K.T. Park, K. Hiraga, Z. Zhu, T. Yao, J. Appl. Phys. 84 (1998) 3912.
- [2] T. Ohgaki, N. Ohashi, H. Kakemoto, S. Wada, Y. Adachi, H. Haneda, T. Tsurumi, J. Appl. Phys. 93 (2003) 1961.
- [3] El-Shaer, A. Che Mofor, A. Bakin, M. Kreye, A. Waag, Superlattices and Microstructures 38 (2005) 265.
- [4] A. Bakin, A. El-Shaer, A. Che Mofor, M. Kreye, A. Waag, F. Bertram, J. Christen, J. Stoimenos., J. of Crystal Growth, 287 (2006) 7.
- [5] A. El-Shaer, A. Bakin, A. Che Mofor, J. Stoimenos, B. Pécz, and A. Waag, J. Superlattices and Microstructures, 42 (2007) 158.
- [6] B. Pecz, A. El-Shaer, A. Bakin, A.-C. Mofor, J. Stoimenos and A. Waag, J. App. Phys. 100 (2006) 103506.
- [7] K. Miyamoto, M. Sano, H. Kato, T. Yao, J. Crystal Growth 265 34 (2004).
- [8] Z. Vashaei., T. Minegishi, H. Suzuki, M. W. Cho, T. Yao , J. of Physics and Chemistry of Solids 69 497 (2008).

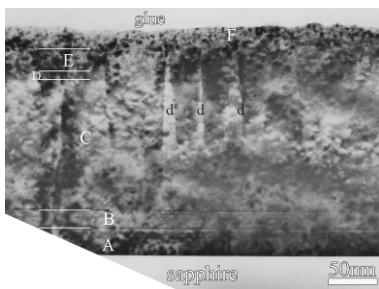


Figure 1a): An overall view of the film is shown in the low magnification micrograph, where the thickness of the thin film was found to be about 260nm.

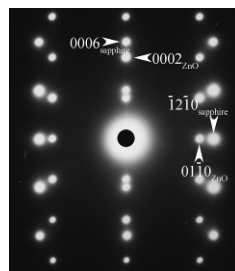


Figure 1b): The corresponding electron diffraction pattern with the incident electron beam parallel to the [2-1-10] direction of sapphire, reveal a good epitaxial growth of the film.

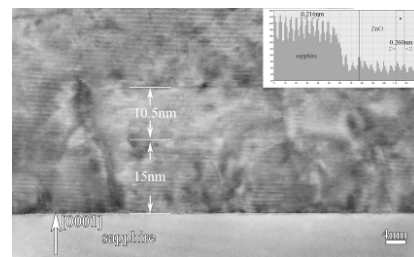


Figure 1c): A HRTEM micrograph taken near the interface shows clearly the existence of dislocations directly at the interface. The inset figure is a line profile at the interface.

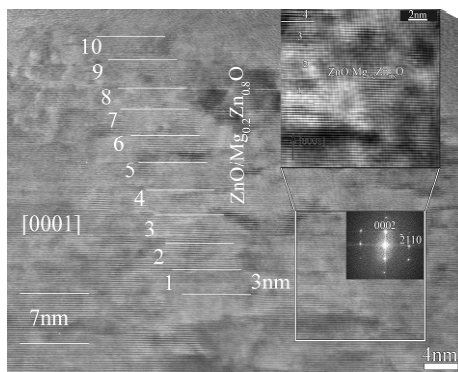


Figure 1d): A HRTEM micrograph taken at the upper part of the film shows the growth along the [0001] direction of ZnO/Mg_{0.2}ZnO_{0.8} QWs.

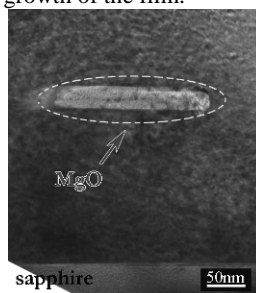


Figure 2a): A LM micrograph shows a MgO precipitate with a plate-like morphology.

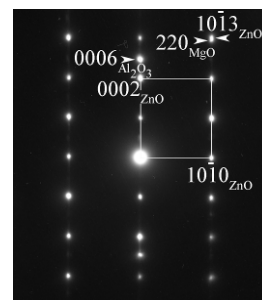


Figure 2b): The corresponding selected area electron diffraction pattern (SAED), taken with the incident electron beam parallel to the [2-1-10] direction of sapphire.

Hydrogen Storage in the Pseudobinary System of $\text{TiMn}_{0.4}\text{Fe}_{0.2}\text{V}_{0.4}$, $\text{TiMn}_{0.1}\text{Fe}_{0.2}\text{V}_{0.7}$ and $\text{Ti}_{0.4}\text{Zr}_{0.6}\text{Mn}_{0.4}\text{Fe}_{0.2}\text{V}_{0.4}$

V. Kouloukis¹, S.S. Makridis^{1*}, E. Pavlidou², A. Ioannidou¹ and E. S. Kikkinides¹

¹ University of Western Macedonia, Kozani, GR 50100, Greece

² Aristotle University of Thessaloniki, Thessaloniki, GR 54124, Greece

*smakridis@uowm.gr

Due to price rise and decrement of fossil fuels, it seems to be necessary finding renewable and clean energy resources. Hydrogen is a potential and renewable fuel for the future [1]. However, one big problem is the economic and safe method to store hydrogen for automotive or other applications.

TiFe is a promising storage material, with low production cost and large hydrogen capacity. However it has some disadvantages, such as high hydrogen pressure, high temperature required for activation and, a large hysteresis gap [2-3]. It reacts with hydrogen to form two hydrides, TiFeH and TiFeH₂. One prosperous way of improving TiFe properties, is by substituting Ti and Fe by other elements, while its inherent advantages remain the same. For example, when Ti is substituted by a small amount of Zr, plateau pressure and hydrogen capacity decreases. This addition of Zr, results to an alloy with good properties [4].

In this research work, TiFe alloys have been developed, according to the stoichiometry $\text{Ti}_{1-x}\text{A}_x\text{Fe}_{1-y}\text{B}_y$ ($\text{A} \equiv \text{Zr}$; $\text{B} \equiv \text{Mn}$, V). The materials were made by arc-melting and the powder was produced by ball milling, under Argon atmosphere, using a high energy planetary ball miller. The crystal structure and microstructural properties of the samples have been studied by using an X-Ray Diffractometer (XRD) and a Scanning Electron Microscopy (SEM), respectively.

Hydrogen activation has been performed on the samples at 150 °C for 2 hours, while absorption and desorption has been measured at 120 °C by using a Sievert-type volumetric apparatus.

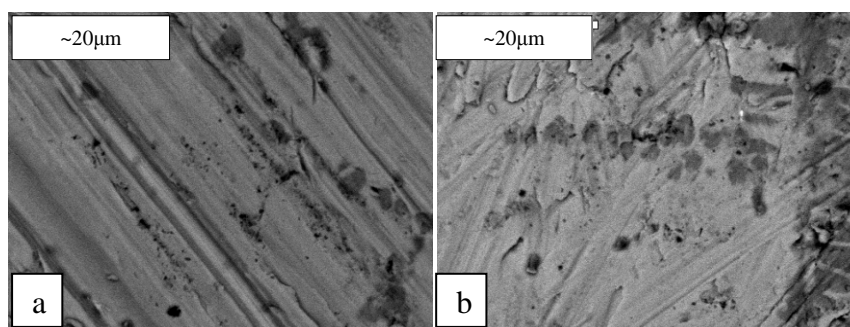


Fig. 1. SEM images of a) $\text{TiMn}_{0.4}\text{Fe}_{0.2}\text{V}_{0.4}$ b) $\text{TiMn}_{0.1}\text{Fe}_{0.2}\text{V}_{0.7}$

[1] Mandal P. and Srivastava O.N., J. Alloys and Compounds 111, 205 (1994).

[2] Sasai T., Oku K., Konno H., Onouwe K. and Kashu S., J. Less Common Metals 281, 89 (1983).

[3] Jang T. H., Han J. I. and Lee Jai-Young, J. Less Common Metals 237, 119 (1986).

[4] Rajalakshmi N., Dhathathrean K.S., J. Hydrogen Energy 625, 24 (1999).

Acknowledgments

This work has been supported by the FP6 Integrated Project NESSHY (Contract no.: SES6-518271)

Structural Properties of the Effect of V Substitution on the Composite Zr-Ti-Cr-V-Ni Intermetallic Hydrides

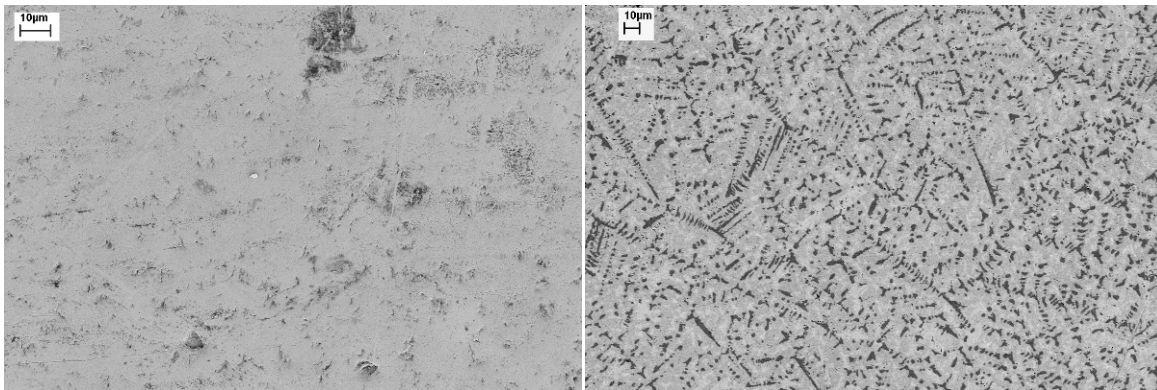
Alexandra Ioannidou^{1*}, Sofoklis S. Makridis¹, Eustathios S. Kikkinides¹ and Athanasios K. Stubos²

¹ Department of Mechanical Engineering, University of Western Macedonia, GR-50100, Kozani, Greece

² Institute of Nuclear Technology and Radiation Protection, NCSR “Demokritos”, Ag. Paraskevi, Athens, GR-15310, Greece

*aioannidou@uowm.gr

There is a growing interest in hydrogen storage and compounds, capable of incorporating reversible larger amounts of this emergent are being intensively studied. Of particular interest are hydrogen storage compounds for low temperature applications. Hydrogen storage in reversible metal hydrides is attractive because it can be stored at relatively low pressures with a high volumetric density. In the present research work have been investigated compounds with nominal compositions $Zr_{0.8}Ti_{0.2}Cr_{1.2}V_{0.4}Ni_{0.4}$ and $Zr_{0.8}Ti_{0.2}Cr_{0.8}V_{0.8}Ni_{0.4}$ that have been prepared by arc-melting under argon atmosphere. The alloys were brittle and silver white in colour. Structural characteristics have been studied by using X-ray powder diffraction while the patterns have been analysed by using the Rietveld analysis. A main hexagonal Laves phase $MgZn_2$ (C14) – type of structure has been found for the powders. The bulk samples have composite microstructures. High resolution scanning electron microscopy (HR-SEM) and energy dispersive X-ray analysis (EDAX) have been used for the morphology and quantitative analysis, respectively. The increasing of the V concentration in the stoichiometry helps the development of a dendritic-type of microstructure. Hydrogenations and dehydrogenations have been obtained after crucial activation procedure. The alloys have been found to be more active under hydrogen while the desorbed amount of hydrogen has been measured in the temperature range of 20 to 120 °C by using a Sieverts-type apparatus. Vant’ Hoff diagrams have been developed from hydrogen absorption-desorption isotherms.



Micrographs for $Zr_{0.8}Ti_{0.2}Cr_{1.2}V_{0.4}Ni_{0.4}$ (left) and $Zr_{0.8}Ti_{0.2}Cr_{0.8}V_{0.8}Ni_{0.4}$ (right) traced by using high resolution scanning electron microscopy (HR-SEM).

Transport properties of flows at the nanoscale

F. Sofos, T.E. Karakasidis* and A. Liakopoulos

*Hydromechanics and Environmental Engineering Laboratory, School of Engineering, University of Thessaly,
38834 Pedion Areos, Volos, Greece*

**thkarak@uth.gr*

In the past decade, nanofluidics has emerged as an important subfield of nanotechnology with applications primarily in the area of biomedical and environmental science and technology. For example, moving minute amounts of fluids at a controlled rate is of great interest in the medical field and presents a challenge in technological terms. In meeting these challenges, experimental studies and fabrication techniques are important but, obviously, studying devices and materials on the smallest possible scale with reliable simulation techniques can provide a useful insight on phenomena that could not be studied experimentally [1]. Molecular dynamics (MD) [2-5] has emerged as the dominant simulation technique at the atomic scale. The main idea behind classical MD is the calculation of the interactions between atoms and the solution of Newton's equations of motion for each particle.

Fluid flows at the nanoscale present various methodological and practical difficulties, since it has been shown that the classical Navier-Stokes equations used at the macroscale are not valid in channels of small widths. At the nanoscale, wall atoms interact with a significant number of fluid atoms inside the channel (at the macroscale the effect of wall atoms is not accounted for) and most fluid properties change. More specifically, density profiles reveal strong oscillations in the number of fluid atoms at layers adjacent to the walls. There exists inhomogeneity of the fluid in the channel, which is not accounted for in the classical hydrodynamics treatment of Poiseuille flow. This inhomogeneity is expected to affect transport properties, such as diffusion coefficient, shear viscosity and thermal conductivity [6-7].

In this work, we present non-equilibrium molecular dynamics simulations of Poiseuille flow of liquid argon. A schematic of the system studied is shown in Fig. 1. Density profiles across the channel are investigated for channels of various widths, h , (in the range 0.9-17.1nm) and the transport properties (diffusion coefficient, shear viscosity and thermal conductivity) are calculated. As far as density profiles are concerned, the fluid is fully ordered in distinct layers. This ordering persists close to the walls even for wider channels while the fluid becomes homogeneous in the central part of the channel (Fig. 2a). Homogeneity inside the channel is reached for $h \gtrsim 6\text{nm}$.

The diffusion coefficient is calculated along the channel in distinct layers and the profile extracted is shown in Fig. 2b. Comparing the values in each channel ($h=0.9-17.1\text{nm}$), we observe that diffusion coefficient is always greater in the inner layers than it is at layers adjacent to the walls. This can be attributed to the fact that near the walls the repulsive solid/fluid effect is strong and fluid mobility in this region is small. Moreover, diffusion coefficient values increase as channel width increases and the bulk value is reached at $h \gtrsim 5-6\text{nm}$. At small channel width we have large values of shear viscosity and its value decreases as the channel width increases to attain the bulk value above $h \gtrsim 5-6\text{nm}$ (Fig. 2c). Finally, thermal conductivity increases as the channel width increases to attain the bulk value at about $h \gtrsim 6\text{nm}$.

To sum up, we found that transport properties exhibit a significantly different behavior than that of the bulk fluid below a critical channel width which in our system seems to be located in the region 5-6nm. The existence of this critical width is attributed to the interaction of the fluid with the walls since at smaller channel widths the effect of the difference of interactions of the walls on the fluid extends practically to the whole range of the fluid modifying considerably its properties in comparison to the bulk. We believe that the results shown are important characteristics of flows in nanochannels and should be taken into account in the design of nanofluidic devices.

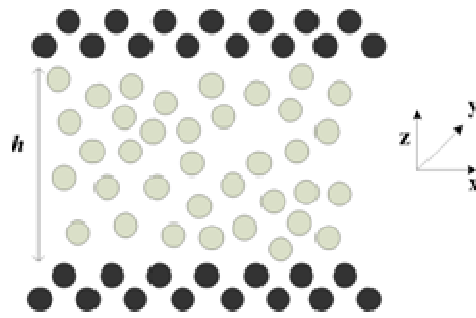


Figure 1: Schematic of the system studied

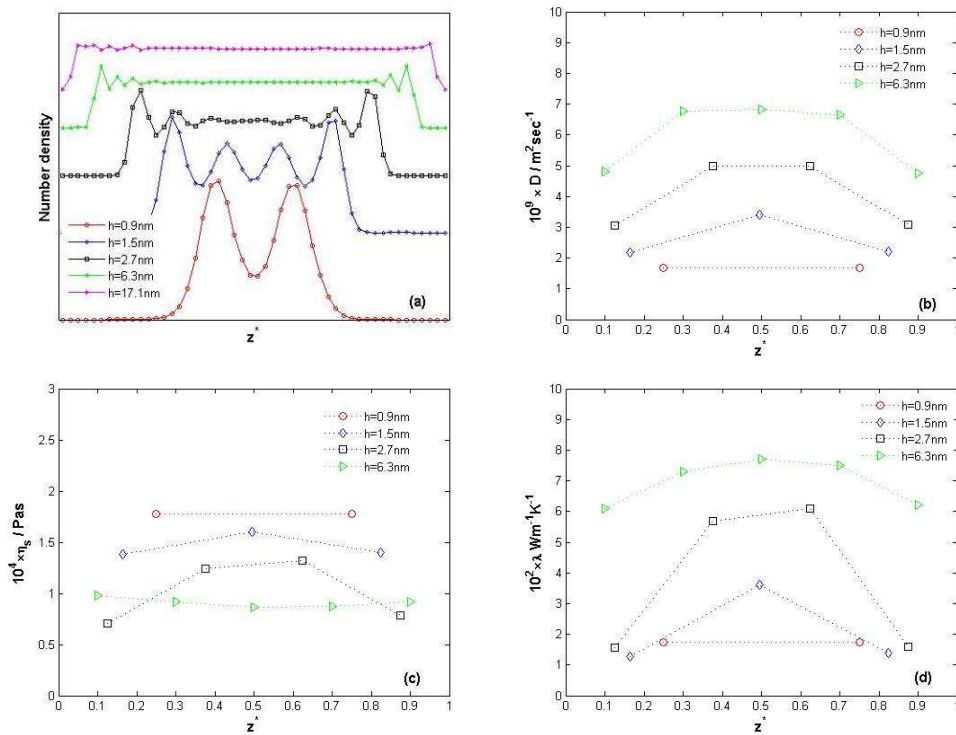


Figure 2: a) density profiles, a) diffusion coefficient profiles, c) shear viscosity profiles and d) thermal conductivity profiles in various channel widths

References

- [1] Allen M.P., Tildesley T.J., *Computer Simulation of Liquids* (Clarendon Press, Oxford, 1987).
- [2] Karniadakis G.E., Beskok A., Aluru N., *Microflows and Nanoflows: Fundamentals and Simulation* (Springer, New York, 2002).
- [3] Nagayama G., Cheng P., *Int. J. Heat Mass Transfer* 47 (2004).
- [4] Koplik J., Banavar J.R., Willemsen J.F., *Phys. Fluids A* 1, 781 (1989).
- [5] Sofos F., Karakasidis T.E., Liakopoulos A., *Cont. Eng. Scienc.* 2 (2009).
- [6] Sofos F., Karakasidis T.E., Liakopoulos A., *Int. J. Heat Mass Transfer* 52 (2009).
- [7] Somers S.A., Davis H.T., *J. Chem. Phys.* 96, 5389 (1991).

Flow in periodically grooved nanochannels studied by computer simulation

D. Kasiteropoulou, T.E. Karakasidis* and A. Liakopoulos

Hydromechanics and Environmental Engineering Laboratory, School of Engineering, University of Thessaly, 38834 Pedion Areos, Volos, Greece

**thkarak@uth.gr*

Fluid flow and heat transfer through low-dimensional grooved channels has attracted research interest in recent years due to the eventual practical applications in many domains [1]. Numerical simulation is a tool that is widely used for the study and understanding of such flows since in many cases conducting experiments at the micro and nanoscale presents several difficulties. Such studies concern the effect of surface roughness on slip flow of gaseous argon in submicron platinum channels by non-equilibrium molecular dynamics [2], studies of nonequilibrium flow of a gas in a two-dimensional grooved channel, due to the motion of the channel wall, based on kinetic [3]. Fluid flow through small channels could also be treated by other mesoscopic simulation methods. Mesoscopic methods are distinguished in grid-based techniques such as lattice gas and lattice Boltzmann gas (LBG) and off-grid particle methods, such as DPD (Dissipative Particle Dynamics, [4]), SPH (Smoothed Particle Hydrodynamics, [5]), DEM (Discrete Element Method, [6]) and FPM (Fluid Particle Model, [7]).

In the present work, we study, flow in nanochannels and seek further insight on the effects of wall roughness on fluid flow. Flow is studied by DPD (Dissipative Particle Dynamics) method which is a mesoscale fluid simulation method and has its firm basis in statistical mechanics [8, 9]. The DPD method combines features from both MD and Lattice Boltzmann methods (LBM). In contrast to MD, DPD can employ much larger particle sizes (up to 10^9 number of atoms, 10^{-9} - 10^{-6} m) and time scales (up to 10^{-9} sec) [10].

Roughness is introduced by periodically placing rectangular protruding elements on the upper channel wall. The length of the protrusions is varied (case $l_{r0}=0$ l_{tot} is the smooth channel, case $l_{r1}=0.5l_{tot}$ corresponds to one rectangular groove in the computational domain, $l_{r2}=0.25$ l_{tot} to two rectangular grooves and $l_{r3}=0.125$ l_{tot} to four rectangular grooves (see Fig.1)), in order to examine the effect of the wall shape on the motion of the fluid particles while the height of the protrusions is constant and equal to 10% of the channel width. Pressure, density, velocity and temperature profiles are calculated. These results, along with an analysis of fluid particle trajectories (see Fig.2b), show that some particles are “trapped” for a significant amount of time inside the cavities formed between the protrusions and that the protrusion length plays an important role on flow properties studied here such as density, velocity, temperature and pressure distributions.

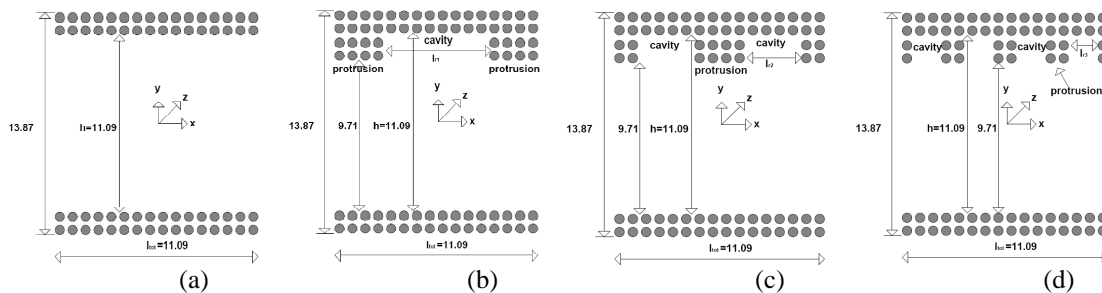


Figure 1. Schematic view of channels studied. a) $l_{r0}=0l_{tot}$, b) $l_{r1}=0.5l_{tot}$, c) $l_{r2}=0.25$ l_{tot} and d) $l_{r3}=0.125$ l_{tot} .

In particular, local density profiles (see Fig.2a) show that as cavities become narrower, the trapping time increases and velocity decreases resulting in a systematic reduction of the flow velocities in the channel (see Fig.3a). Inside the cavities, small flow velocity values are detected while flow velocity profiles are shifted towards the smooth wall. Temperature profiles are of similar shape and have, generally, smaller maximum values compared to the smooth channel indicating a cooling effect due to the presence of cavities (see Fig.3b). Maximum temperature values depend on the protrusion length and their magnitude decreases as the length decreases. This is due to the fact that roughness elements act as a friction factor, which reduce the thermal velocities and thus the fluid temperature. For all channels studied, temperature profiles close to the channel centreline are practically flat.

The effect of wall roughness on density, velocity, pressure and temperature is significant and should be further investigated with different protrusion heights or lengths and different materials for the wall particles and fluid particles. The results are of particular importance in the design of nanochannels for cooling purposes in the nanodevices.

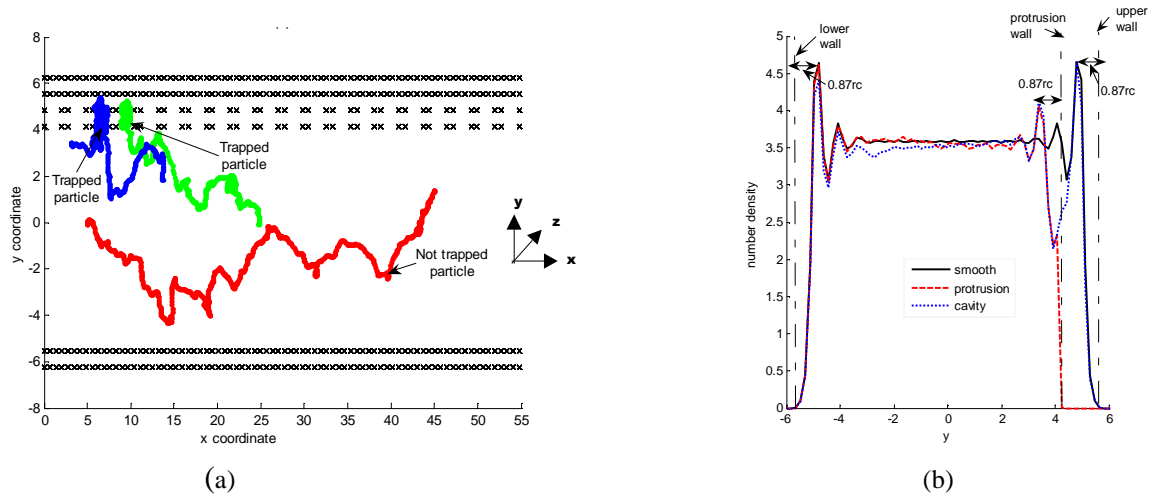


FIG.2. a) Representative trajectories of “trapped” and non-trapped fluid particles in the xy -plane for $l_{r3}=0.125 l_{tot}$. Symbols x denote solid walls. (b) Local number density profiles plotted at the protrusion midpoints and the cavity midpoints for $l_{r1}=0.5l_{tot}$, (y is in r_c units). Dash-dot lines denote solid wall limits.

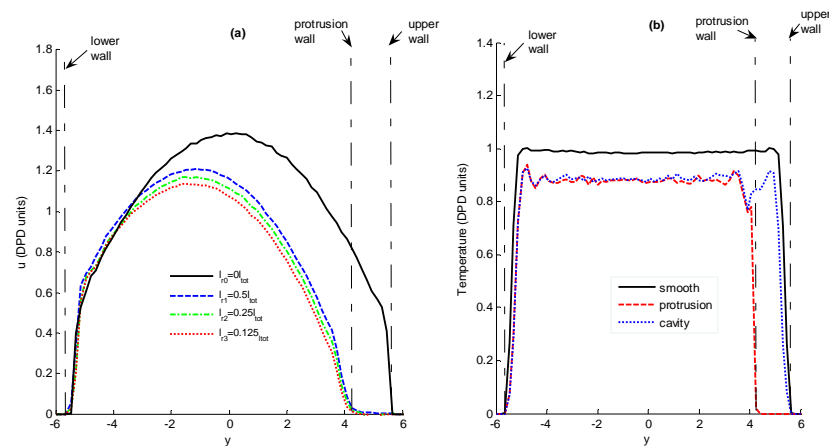


FIG.3. a) Average velocity for cases i) $l_{r0}=0l_{tot}$, ii) $l_{r1}=0.5l_{tot}$, iii) $l_{r2}=0.25 l_{tot}$ and iv) $l_{r3}=0.125 l_{tot}$. Dash-dot lines denote solid wall limits (y is in r_c units). b) Local temperature profiles at the protrusion midpoints and the cavity midpoints for $l_{r2}=0.25 l_{tot}$ (y is in r_c units). Dash-dot lines denote solid wall limits.

References

- [1] C. Herman and E. Kang, *Int. J. Heat Mass Transfer* 45, 3741 (2002).
- [2] B. Y. Cao, M. Chen and Z. Y. Guo, *Int. J. Eng. Sci.* 44, 927 (2006).
- [3] S. Naris and D. Valougeorgis, *Phys. Fluids* 19, 067103 (2007).
- [4] P.J. Hoogerbrugge and J. M. V. A. Koelman, *Europhys. Lett.* 19, 155 (1992).
- [5] J.J. Monaghan, *Annu. Rev. Astronomy Astrophysics* 30, 543 (1992).
- [6] P.A. Cundall and O.D.L. Strack, *Géotechnique* 29, 47 (1979).
- [7] P. Espanol, *Phys. Rev. E* 57, 2930 (1998).
- [8] P. Espanol and P. Warren, *Europhys. Lett.* 30 191 (1995).
- [9] C. Marsh, *Theoretical aspect of dissipative particle dynamics*, Ph.D.thesis, University of Oxford (1998).
- [10] G. Karniadakis, A. Beskok and N.Aluru, *Microflows and Nanoflows, Fundamentals and Simulation*, (Springer, 2005).

ACKNOWLEDGEMENTS

This research project (PENED) is co-financed by E.U.-European Social Fund (75%) and the Greek Ministry of Development-GSRT (25%).

Following the Synthesis of Metal Nanoparticles within pH-Responsive Micelles and Microgels by SAXS

E. Pavlopoulou,^{1,2*} G. Portale,³ V. Katsamanis,^{1,4} K. Christodoulakis,^{1,2} M. Vamvakaki^{1,2} and S. H. Anastasiadis^{1,5}

¹ Foundation for Research and Technology-Hellas, I.E.S.L., Heraklion, Crete, Greece

² Department of Materials Science and Technology, University of Crete, Heraklion, Crete, Greece

³ DUBBLE CRG / European Synchrotron Radiation Facility, Grenoble, France

⁴ Department of Physics, University of Crete, Heraklion, Crete, Greece

⁵ Department of Chemistry, University of Crete, Heraklion, Crete, Greece

*epavl@iesl.forth.gr

Metal nanoparticles display unique desirable properties and characteristics in comparison to bulk materials and, consequently, find applications in many areas of modern technology. In particular, the enormous surface-to-volume ratio of nanoscale particles (about $100\text{--}3000\text{ m}^2/\text{cm}^3$) is a promising feature for their use as catalysts. In the past decade, the use of nanostructured polymeric matrices for nanoparticle synthesis and stabilization has received considerable attention, and a number of polymeric matrices have been shown to provide stabilization and control of the particle growth. Among them, pH-sensitive materials (block copolymer micelles and microgels) is a very promising category of responsive materials, since they can be used as nanoscopic reaction vessels for the in-situ growth of inorganic nanocrystals in water, resulting in hybrid nanocomposite materials.

In our research two types of polymeric matrices have been used for the growth of colloidal Pt nanoparticles: (1) Polymeric micelles formed by the pH-driven self-assembly of amphiphilic poly(hexa(ethylene glycol) methacrylate)-*b*-poly(2-(diethylamino)ethyl methacrylate) diblock copolymers, PHEGMA-*b*-PDEA; at low pH the copolymer is in its “unimer” state, while an increase of the pH results in the formation of micelles. (2) pH-sensitive PDEA-microgels, which exhibit reversible swelling properties in water by adjusting the solution Ph; at low pH the microgel particles are swollen, while an increase of the pH leads to hydrophobic latex particles. Metal nanoparticles were synthesized within both the micellar cores of the diblock copolymers and the microgels by the incorporation of the metal precursor, i.e., H_2PtCl_6 or K_2PtCl_6 and the subsequent metal reduction, at various metal-to-polymer ratios [1-5]. Herein, we report the structural study of aqueous solutions of these systems by Small Angle X-ray Scattering (SAXS) during the three steps of the metal nanoparticle synthesis: the original polymer dispersions in water, the metal – loaded polymer matrices and the metal nanoparticle-containing polymers after reduction. The influence of the metal loading on the polymer characteristics was examined.

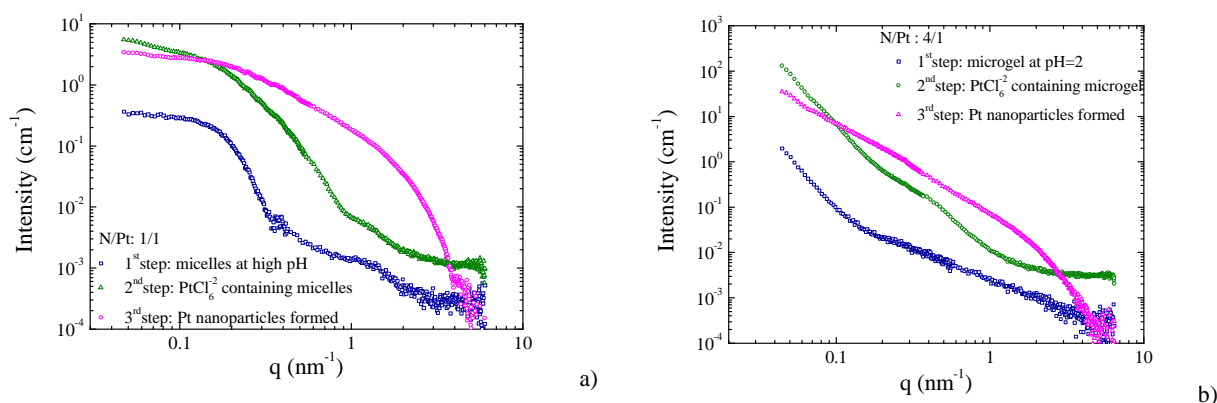


Figure 1: The SAXS intensity profiles for the various synthetic steps followed for the formation of Pt nanoparticles within the PHEGMA-*b*-PDEA micelles (a) and the PDEA microgels (b). K_2PtCl_6 was used as the metal precursor in both cases, while the DEA-to-metal mole ratio was 1/1 for the micelles and 4/1 for the microgels.

SAXS measurements have been carried out at the Dutch-Belgian Beamline (DUBBLE) at the European Synchrotron Radiation Facility (ESRF) in Grenoble, France, covering a very wide scattering vector range, $0.04 < q < 6.4\text{ nm}^{-1}$. The scattered intensity was corrected for background and transmission whereas measurement of a standard sample (Lupolen) was utilized for intensity normalization. For dilute systems like those under study, the q -dependence of the SAXS scattered intensity corresponds directly to the form factor of the scatterers and, thus,

information about the shape, the size and the number density of the polymeric matrices, the metallated phase and the metal nanoparticles can be obtained. The complexity of the final system requires the simultaneous characterization of all three steps, each one providing information for a different structure.

The scattering intensity profiles acquired for the various synthetic steps followed for the formation of Pt nanoparticles within the PHEGMA-b-PDEA micelles are shown in Fig. 1a; K_2PtCl_6 was used as the metal precursor, while the polymer (in terms of monomeric metal binding units) to metal mole ratio was 1/1. The scattering pattern of the pure micellar solution corresponds to the form factor of a core-shell structure, with a core radius of 14.2 nm and a homogeneous shell with a thickness of 1.55 nm. Upon addition of the metal precursor, a scattering profile of a similar shape was acquired, corresponding to a core-shell structure, with much higher intensity in the low q range, which was attributed to the enhanced contrast of the metal loaded core. The form factor analysis revealed a decrease in the core radius with increasing metal loading, while the shell thickness remained unaffected. In the reduced sample, a size of around 2 nm in diameter was estimated for the metal nanoparticles, which was constant for the three different DEA-to-metal mole ratios investigated.

Fig. 1b presents the SAXS intensity profiles for the three synthetic steps followed for the formation of Pt nanoparticles within the PDEA microgels; K_2PtCl_6 was used again as the metal precursor, while the DEA-to-metal mole ratio was 4/1. The scattering profile of the pure microgel dispersion exhibits two contributions: a Porod-like q -dependence arising from the water/microgel interface and a power law q -dependence due to the microgel network. The Porod scattering was still evident after metal incorporation, while a shoulder appeared at higher q values, which was attributed to the condensation of the metal complexes within the microgel particles. Following metal reduction, Pt nanoparticles were formed with size of around 1.5 nm in diameter, which was independent of the metal loading and similar to that obtained for the nanoparticles formed within the micellar matrices.

[1] Vamvakaki et al., *Faraday Discuss.*, 128, 129 (2005).

[2] Bronstein et al., *Langmuir*, 21, 9747 (2005).

[3] Palioura, D.; Armes, S. P.; Anastasiadis, S. H.; Vamvakaki, M., *Langmuir*, 23, 5761 (2007).

[4] S. H. Anastasiadis and M. Vamvakaki, *Int. J. Nanotechnol.* 2009, 6, 46-70.

[5] K. E. Christodoulakis, D. Palioura, S. H. Anastasiadis and M. Vamvakaki, *Top. Catal.* 2009, 52, 394-411.

Acknowledgments: Part of this research was sponsored by the Greek General Secretariat for Research and Technology (ΠENEΔ 2003 program 03EΔ581).

Self-assembly and molecular dynamics of nanographenes

C. Grigoriadis^{1*}, N. Haase², G. Floudas¹, H.-J. Butt² and K. Müllen²

¹*Department of Physics, University of Ioannina, 451 10 Ioannina, Greece
and Foundation for Research and Technology-Hellas (FORTH), Biomedical Research Institute (BRI), Ioannina,
Greece*

²*Max Planck Institute for Polymer Research,*

**chgrigor@cc.uoi.gr*

Discotic liquid crystals are materials where self-assembly is driven by non-covalent intermolecular interactions. The aromatic cores are responsible for the π -stacking whereas the presence of aliphatic chains ensures solubility, processability and a rich thermotropic behavior. During the self-organization process, the disk-shaped molecules organize into columns that further assemble into two-dimensional arrays whereas the alkyl chains fill the intercolumnar space. Highly ordered columnar structures of HBC were found to be very promising as active semiconductors in organic field-effect transistors and photovoltaic devices. The self assembly and molecular dynamics a series of dipole functionalized nanographenes were studied using differential scanning calorimetry (DSC), wide-angle x-ray scattering (WAXS), and dielectric spectroscopy (DS) as a function of temperature. There is a phase transformation from the liquid crystalline (Lc) phase at high temperature to the crystalline phase (Cr) at lower temperature. The effect of dipole substitution is to destabilize the crystalline phase (Cr). All compounds display a strong dipolar relaxation (α -process) reflecting in- and out- of plane disk motion with a strong temperature dependence that conforms to the Vogel-Fulcher Tammann (VFT) equation. The inter- and intra-columnar thermal expansion was studied in a series of dipole functionalized hexa-*peri*-hexabenzocoronenes that undergo a transition from the high temperature liquid crystalline to a crystalline phase at lower temperatures. Within the liquid crystalline phase the intra- and inter-columnar thermal expansions were different but both positive. Within the crystalline phase the inter-columnar thermal expansion is negative. Responsible for the negative thermal expansion is the increase of the tilt angle of the discotic cores with respect to the columnar axis. Similarities and differences with the thermal contraction in graphite and in graphenes are discussed.

Absorption and Diffusion of commercially available cleaning liquids in Epoxy Resin Nanocomposites

A.Z Stimoniari^{1,2} and C.G. Delides^{2*}

¹ Chemistry Department, University of Ioannina

² Laboratories of Physics and Materials Technology, Technological Educational Institute of Western Macedonia, 50100, Kila, Kozani, Greece

*kdelides@yahoo.com

Epoxy resins either pure and/or composites are widely used in applications such as adhesives, casting and tooling, floor, furniture and marine protection coatings etc [1-7]. In every day cleaning uses the epoxy coated surfaces are in close contact with cleaning liquids commercially available in enormous scale. From this point of view it is very important to study the absorption and diffusion behavior of the epoxy coatings, since this strongly affects the physicochemical properties and the life duration. It is well known that the incorporation of nanoparticles into the matrix improves tremendously the physicochemical properties. In the case of epoxy matrix, carbon nanotubes are often chosen to be fillers for composites used in many applications [2,5].

The absorption of commercially available cleaning water solutions in systems consisting of diglycidylether of bisphenol A (DGEBA) with triethylenetetramine (TETA) as curing agent and amino functionalized Multi Walled Carbon Nanotubes(MWCNTs) as fillers is studied. The fillers' modification allows a better dispersion into the matrix, but it also plays an important role to the formation of a secondary crosslinking network, between the amine groups of the nanotubes and the epoxy rings of the prepolymer. The secondary network seems to affect the final properties of the product [3,6].

For the absorption measurements the specimens were immersed at room temperature (~22 °C) in deionized water and commercially available fluids (vinegar, AZAX, Chlorine). These water solutions were chosen together with water because they are widely used in everyday cleaning duties including surfaces coated by epoxy composites and for this reason there is a grate practical interest. Influence of diluents absorption during different periods of time on the glass transition temperature was studied by Differential Scanning Calorimetry (DSC).

The fluids sorption profiles for the pure resin (DGEBA/TETA) and the nanocomposite (DGEBA/TETA/MWCNTs) are shown in Figure 1 (a) and (b) respectively.

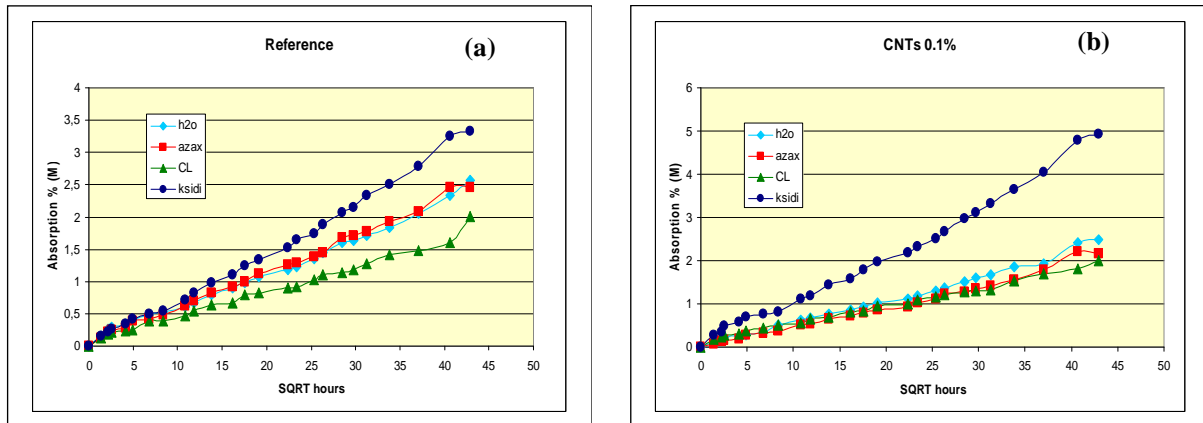


Figure1. Fluid absorption as a function of immersion time): (a) for pure resin and (b) for the nanocomposite.

As shown in Fig. 1 (a) the weight gain for the pure epoxy is strongly affected by the chemical nature of the fluid. In vinegar epoxy matrix shows a faster weight increase than the epoxy resin in the water. This phenomenon indicates that the presence mainly of the acetic acid molecules in the vinegar solution acts catalytically to the diffusion of water molecules through the bulk of polymer network and/or through the hydrogen bonding between hydrophilic groups associated with hydroxyl or amine groups attached to the polymer chains and the water molecules. On the contrary, the absorption rate for chlorine is lower than that for water. This is probably due to the presence of thorium and hydrogen ions preventing the hydrogen bond formation. For the AZAX liquid the absorption is close to the water one. Similar remarks can be extracted for the

composites, as shown in Fig. 1(b). Generally the absorption is higher in the composites indicating that the nanotubes act as plasticizer enhancing the water absorption mechanisms.

A comparison of water absorption to the other solutions is clearly shown in Fig. 2 for the matrix and the composite.

The glass transition temperature is lightly depended from the nature of liquid. In general, is higher in the composites due to the participation of the modified nanotubes to the network formation. In addition, the influence of nanotubes content on the water absorption studied by DSC is presented Figure 3: (a) and (b).

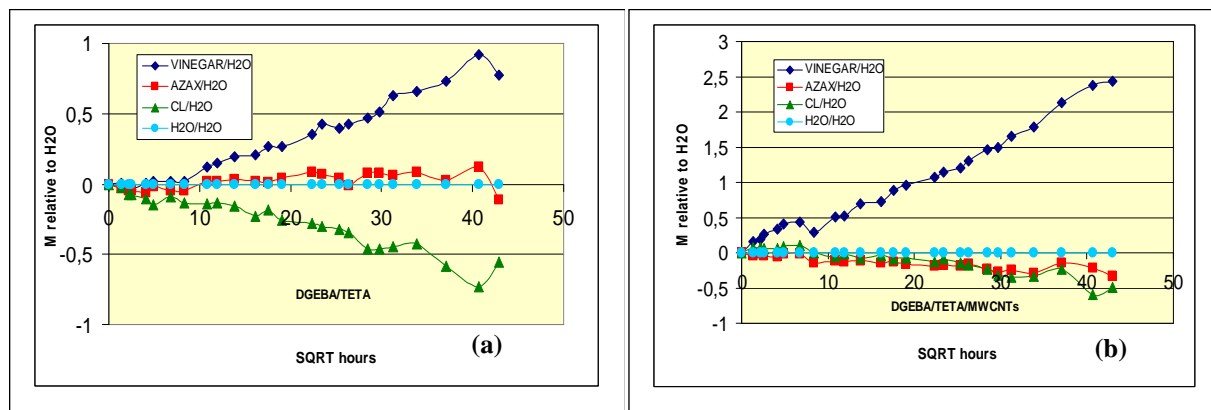


Fig.2. Normalized to water fluid absorption as a function of immersion time): (a) for pure resin and (b) for the nanocomposite.

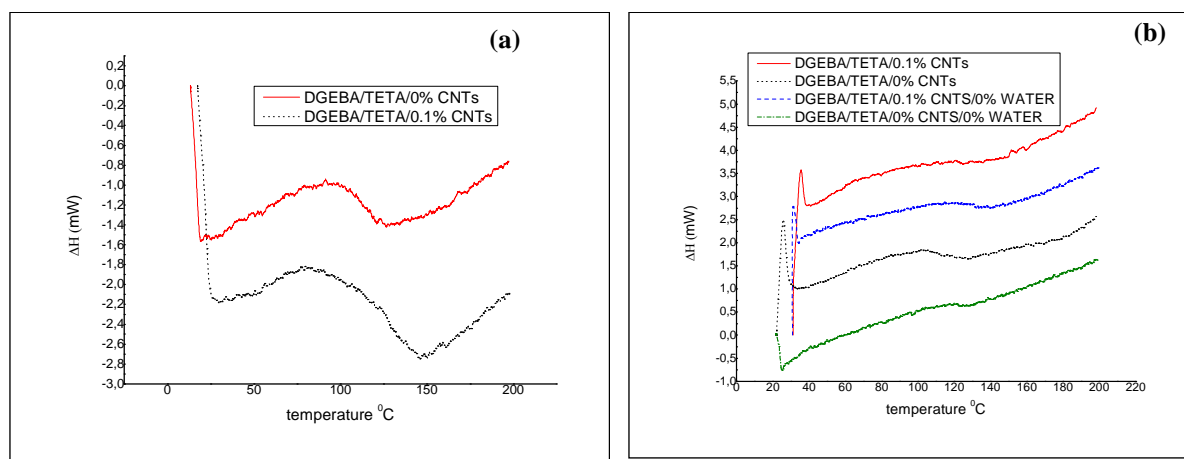


Figure 3. DSC profiles: (a) before immersion and (b). The influence of water absorption after 144 hours of immersion for the nanocomposites.

References

- Papanicolaou G. C., Kosmidou Th. V., Vatalis A.S., Delides C.G., J. Appl. Pol. Sci.,99, 1328-1339, (2006).
 Giacalone F., Martn N., Chem. Rev., 106 (12), 5136-5190 (2006).
 Ming-Jen Chang, Lin-Fen Chang, George J. Jiang, POLYMER COMPOSITES, 390-39 (2007)
 M. Chen, A.S. Ren, J.F. Wang, M.S Lee, L.R Dalton H. Zhang, G. Sun, W.H Steirer, , Polym. Prepr. 40 162. (1999)
 Sala G. Composites, Part B: Engineering 31, 357-373. (2000).
 Han S. O.,Drzal L.T., Europ.Pol. J., 39, 1791-1799. (2003).
 Villanueva M.,Fraga I.,Rodriguez-Anon J.A., Proupin-Castineiras J.,Martin J.L. J. Therm. Anal. & Calorimetry 87 ,205-209 (2007)

Acknowledgements. Acknowledgements are expressed to Professor R.A. Pethrick for the stimulating discussions during this work and to students Eleni Nikolaidou and Xristos Liakopoulos for their contribution to sample preparation.

Fluid Absorption Effects on the Dynamics of Epoxy Resin Nanocomposites

A.Z Stimoniari^{1,2} and C.G. Delides^{2*}

¹ Chemistry Department, University of Ioannina

² Laboratories of Physics and Materials Technology, Technological Educational Institute of Western Macedonia, 50100, Kila, Kozani, Greece

*kdelides@yahoo.com

Epoxy resins are widely used as matrices in different composite systems. The prepolymer is usually mixed with an amine curing agent that generates the formation of the 3D crosslinking network of the final thermoset product.

Carbon Nanotubes are often chosen to be fillers for composites used in many applications [2-7]. The achievement of good filler dispersion into the matrix is difficult because of the nature of the forces developed between the components. In order to improve the dispersion level, the fillers are often subjected to the appropriate modification. Amine modified Multi-Walled Carbon Nanotubes (MWCNTs) are used in the current study, as they are proven to be the most appropriate for epoxy nanocomposites. The formation of the 3D crosslinking network is effected by the existence of the amine groups on the nanotubes[1].

The effect of the network architecture on the thermophysical properties of system consisting of diglycidylether of bisphenol A (DGEBA) with triethylenetetramine (TETA) as curing agent and amino functionalized Multi Walled Carbon Nanotubes as fillers is reported. The fillers' modification allows a better dispersion into the matrix, but it also plays an important role to the formation of a secondary crosslinking network, between the amine groups of the nanotubes and the epoxy rings of the prepolymer. The secondary network seems to affect the final properties of the product [2,3].

The techniques used on the study of this effect were Differential Scanning Calorimetry (DSC) and Dynamic Mechanical Analysis (DMA). The specimens were immersed at room temperature (~22 °C) in deionized water and commercially available fluids (vinegar, AZAX, Chlorine). These diluents were chosen because they are widely used in everyday cleaning duties including surfaces coated by epoxy composites and for this reason there is a grate practical interest. In the DSC measurements the heating rate was 20 °C/min and for DMA measurements the temperature range was from room temperature up to 200 °C and the scanning frequency 10 Hz.

The effect of diluents' absorption on the dynamic mechanical behavior are presented in figures 1 and 2.

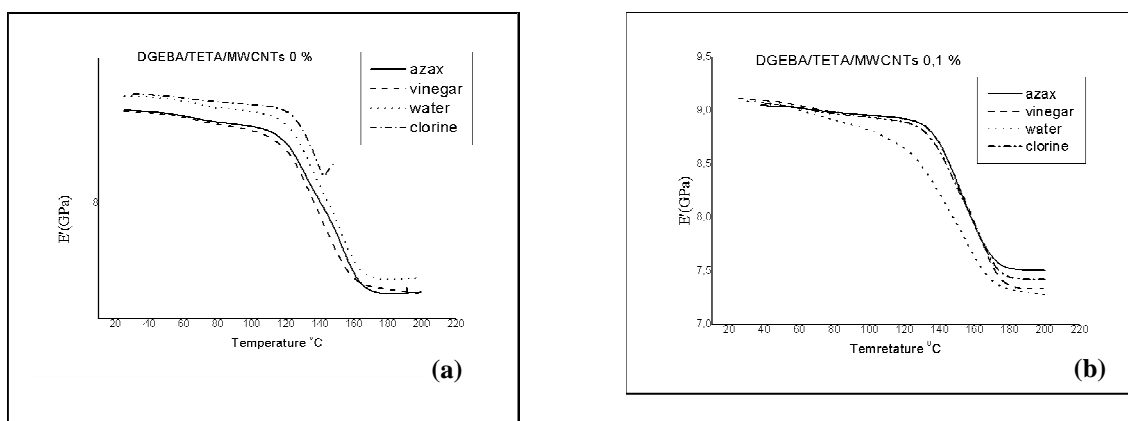


Figure 1. DMA profiles of storage modulus (E'): (a) for pure resin and (b). for the nanocomposite

Figs.1 (a) and (b) show changes in storage modulus (E') for the matrix (a) and the composite (b). In the matrix the values of the modulus for chlorine is larger in comparison to that in water, while for AZAX and vinegar is smaller. On the other hand, in the composite the E' values are larger for the three solutions in comparison to the water. In the epoxy matrix the changes in the modulus are significant both in the glassy and the rubbery state, while in the composite it is more clear in the rubbery state. These results support the hypothesis that the incorporation of the nanotubes contributes to the formation of a complex network with distinguish

behavior in each diluents. These changes of the dynamic mechanical parameters (E' , E'' , and T_g as well) can be related to the complex water absorption mechanism, which is became more complex due to existence of the extra molecules, in the form of ions, of the solutions.

Representative curves for $\tan \delta$ for the matrix and the composite versus temperature are shown in Fig. 2 (a) and (b) respectively.

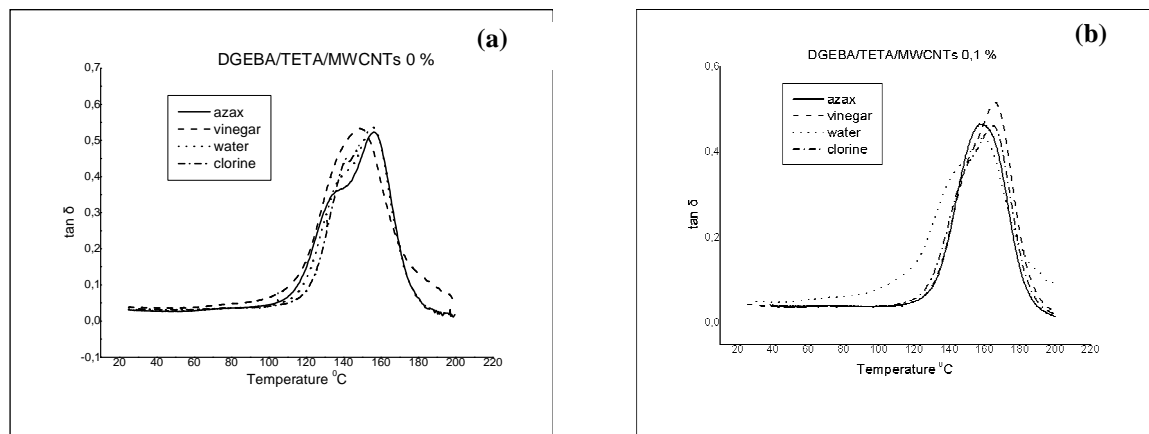


Figure 2. DMA profiles of $\tan \delta$: (a) for pure resin and (b).for the nanocomposite

As it is clearly shown in Figure 2 an additional relaxation is observed (a peak below and close to T_g in the pure resin and in the nanocomposite as well for all diluents. This indicates the existence of two crosslinking mechanisms which act complementary. The first mechanism is caused by the reaction of the crosslink agent with the epoxy groups and the second one appears as a result of the modified nanotubes' participation on the curing reaction, giving in that way the shoulder in α -relaxation [1,8]. The calculated T_g values from $\tan \delta$ curves are presented in Table 1.

Table 1. Glass Transition Temperatures T_g 's detected from the maximum from $\tan \delta$ peaks.

Commercial fluids	DGEBA/TETA/MWCNTs 0 %		DGEBA/TETA/MWCNTs 0,1 %	
	α relaxation (oC)	$\tan \delta$ (peak)	α relaxation (oC)	$\tan \delta$ (peak)
Vinegar	149	0,533	166	0,516
Water	155	0,538	159	0,432
AZAX	157	0,523	159	0,464
Clorine	~ 160	~ 0,55	164	0,463

References

- Papanicolaou G. C., Kosmidou Th. V., Vatalis A.S., Delides C.G., J. Appl. Pol. Sci.,99, 1328-1339, (2006).
 Giacalone F., Martin N., Chem. Rev., 106 (12), 5136-5190 (2006).
 Ming-Jen Chang, Lin-Fen Chang, George J. Jiang, POLYMER COMPOSITES, 390-39 (2007)
 M. Chen, A.S. Ren, J.F. Wang, M.S Lee, L.R Dalton H. Zhang, G. Sun, W.H Steirer, , Polym. Prepr. 40 162. (1999)
 Sala G. Composites, Part B: Engineering 31, 357-373. (2000).
 Han S. O.,Drzal L.T., Europ.Pol. J., 39, 1791-1799. (2003).
 Kim H. J.,Seo D.W., International Journal of Fatigue 28,1307-1314,(2006).
 Th.V.Kosmidou, A.S. Vatalis, C.G. Delides, E. Logakis, P. Pissis, G.C. Papanicolaou' express Polymer Letters 5(2), 364-372 (2008).

Acknowledgements. Acknowledgements are expressed to Professor R.A. Pethrick for the stimulating discussions during this work and to students Eleni Nikolaidou, Xristos Liakopoulos Maria-Anna Kardasi for their contribution to sample preparation.

Epoxy Composites Filled with Amine Modified Carbon Nanotubes: High Voltage Corona Discharge Studies

D. Piromalis¹, D.I. Tseles¹, A. Kanapitsas², H. Zois² and C.G. Delides^{3*}

¹ Technological Educational Institute (TEI) of Piraeus, Department of Automation, Data Acquisition Systems Laboratory, 250 Thivon & P. Ralli, 12244, Egaleo, Attica, Greece

² Technological Educational Institute (TEI) of Lamia, 3rd km Old National Road Lamia-Athens, 35100 Lamia, Greece

³ Technological Educational Institute (TEI) of Western Macedonia, Laboratories of Physics and Materials Technology, 50100 Kila, Kozani, Greece

*kdelidis@yahoo.com

Nanocomposites show different properties than the bulk polymer [1-7] matrix. It is well known that the composite properties can change with the dispersion state, geometric shape, surface properties, particle size and particle size distribution. Epoxy composites filled with Carbon Nanotubes have been shown to undergo substantial improvement in mechanical, electrical and dielectric properties [1-4].

Specimens were prepared from epoxy resin (Diglycidyl ether of bisphenol A (DGEBA)) as matrix material with triethylenetetramine (TETA) as hardener and amine modified Multi Wall Carbon Nanotubes (MWCNTs) as filler. The procedure is fully presented elsewhere [1].

The electrostatic charge retained on the surface of a material influences the useful opportunities presented by static electricity, presented meanwhile some undesirable problems. This is manifested as the surface voltage created by the charge retained. The “suitability” of a material may be judged in terms of the maximum surface voltage created and/or by the time for which this is maintained [2, 3]. The surface discharging effect of the nanocomposites are investigated using the John Chubb Instrumentation (JCI) 155v5 charge decay test unit. A high voltage corona discharge is used to deposit a patch of charge on the surface of the material to be used. A fast response electrostatic fieldmeter measures the voltage generated by the charge. From the measurements the “capacitance loading” experienced by the charge on the surface it easy to be calculated. This “capacitance loading” gives guidance to the maximum surface voltage likely to be created by certain quantities of charge on the surface [4]. A high capacitance loading means that only low surface voltage arise per unit of charge.

If this “capacitance loading” is large then only low surface voltages will occur with practical quantities of charge transfer, and static problems are unlikely to arise from charge retained on the material itself. This approach provides a necessary addition to assessment of materials by the charge decay time, when charge decay times are long.

All experiments were carried out under ambient conditions with temperature and relative humidity 22 °C and 30 %, respectively with an initial voltage charging of 9000 Volts. Two groups of measurements were carried out with positive and negative charging in order to elucidate if there us any difference depending on the sing of the charge. Characteristic values calculated from the measurements for negative and positive charging are presented in the following Table 1.

Table 1: Characteristic values for negative and positive charging of DGEBA/TETA/MWCNTs composites.

Negative charging

CNTs (%)	0	0.01	0.05	0.1	0.2	0.3	0.5	1
V _{start} (Volts)	-1700	-1720	-1800	-1900	-110	-108	-100	-73
t _{1/2} (s)	57000	44000	35000	2.3	15.3	4.1	0.02	29.1
T _{10%} (s)	116000	56000	47000	127.4	114.2	78.2	0.07	813.2
CL	3.52	3.73	4.21	4.62	2130	4400	4520	6753

Positive charging

CNTs (%)	0	0.01	0.05	0.1	0.2	0.3	0.5	1
V _{start} (Volts)	2600	2200	2100	1800	190	121.8	116.2	74.4
t _{1/2} (s)	65700	56400	52030	21.5	0.06	207.2	0.022	15.6
T _{10%} (s)	153600	138140	132300	183.8	0.68	2672.4	0.058	831.7
CL	0.26	2.4	4.1	5.02	1714.5	3367.2	4536.1	8293.4

WE2

P40

The variation of the two main characteristics of the decay of the surface potential (Capacitance Loading, CL and charge decay time, $t(s)$) as function of nanotubes content are shown in Fig. 1 and Fig. 2.

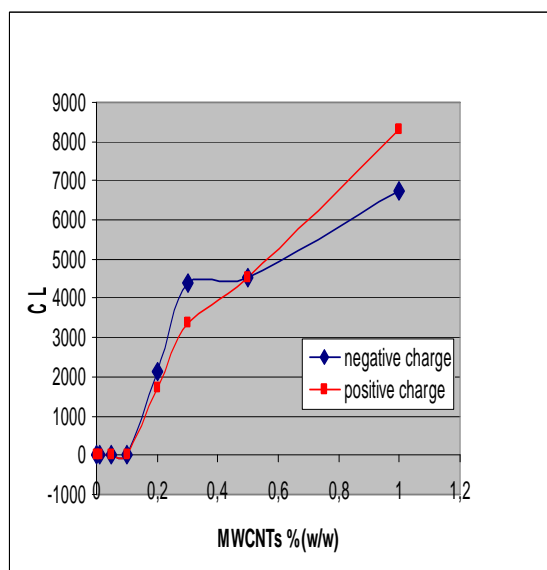


Fig. 1. Variation of Capacitance Loading (CL) corona charging as a function of nanotubes content.

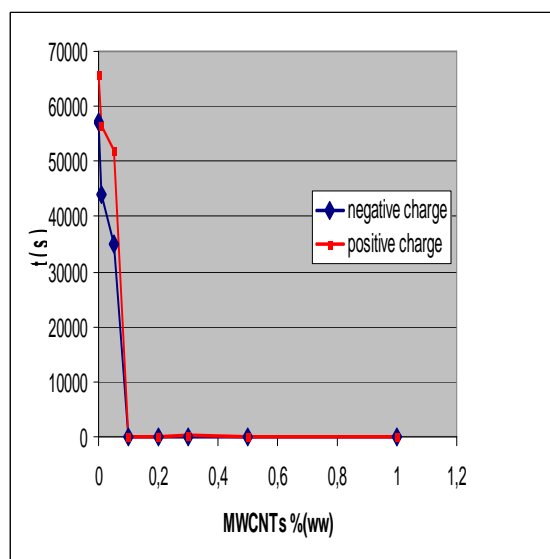


Fig. 2. Variation of charge decay time ($t(s)$) as a function of nanotubes content.

As it is clearly shown from the results there are similarities and some differences with positive and negative charging. A typical discharging behaviour is observed in both ways of charging. The Capacitance Loading increases rapidly with the filler content at a value of about 0.01 % and the sample becomes almost conductive for higher filler loading. Meanwhile, the charge decay time decreases in the same way and reaches very small values after 0.01 % of filler content. The large increase of Capacitance Loading and the rapid decrease of charge decay time is probably attributed to the formation of a percolation structure, which is consistent with dielectric and conductivity measurements [4, 5, 8]. The participation of amine-modified nanotubes to the crosslink procedure may play a dominant role to the formation of a complex network responsible for this charge surface migration.

According to Chubb's suggestion, the suitability of materials for avoiding problems from retained charge in static sensitive applications is judged: (a) by whether the capacitance loading is sufficiently high and/or (b) whether the charge decay time is suitably short. Based on this suggestion, we can conclude that these nanocomposites can be used in static sensitive applications, without problems, for a carbon nanotubes loading higher than 0.01 % w/w.

The next step in this research involves the investigation of discharging effects in epoxy nanocomposites filled with conductive fillers in different environmental conditions, since the epoxy based systems are very sensitive to humidity.

- [1] Th.V. Kosmidou, A.S. Vatalis, C.G. Delides, E. Logakis, P. Pissis, G.C. Papanicolaou' express Polymer Letters 5, 364 (2008).
- [2] J.N. Chubb, IEEE Trans. Ind. Appl. 26, 1182 (1990).
- [3] J.N. Chubb, J. Electrostatics 54, 233 (2002).
- [4] W. Zhang, R.S. Blackburn, A.A. Dehghani-Sanij, J. Mater. Sci. 42, 7861 (2007).
- [5] Z. Xu, L. Zhang, G. Chen, J. Phys. D: Appl. Phys. 40, 7085 (2007).
- [6] R. Schueler, J. Petermann, K. Schulte, H-P. Wentzel, J. Appl. Polym. Sci. 63, 1741 (1977).
- [7] Y.X. Zhou, P.X. Wu, Z-Y. Cheng, J. Ingram, S. Jeelani, express Polymer Letters 2, 40 (2008).
- [8] J. Sandler et al. Polymer.40, 5967 (1999).

Acknowledgements

The financial support from the program "Archimedes II" is gratefully acknowledged. We also thank Prof. Richard Pethrick for helpful suggestions and the students Helen Nikolaidou, Marianna Kardasi and Christos Liakopoulos for their help to sample preparation.

Thermogravimetric Properties of Epoxy Resin/Carbon Nanotubes Nanocomposites

A. Kanapitsas^{1*}, H. Zois¹ and C. G. Delides²

¹ *Technological Educational Institute (T.E.I.) of Lamia, 3rd km Old National Road Lamia-Athens, 35100 Lamia, Greece*

² *Technological Educational Institute (T.E.I.) of West Macedonia, Laboratories of Physics and Materials Technology, 50100 Kila, Kozani, Greece*

*kanapitsas@teilam.gr

Nanocomposites show different properties than the bulk polymer matrix because of the small size of the filler and the corresponding increase in their surface area [1, 2]. It is well known that the composite properties can change with the dispersion state, geometric shape, surface properties, particle size, and particle size distribution. Because of the recent commercial availability of nanoparticles, there is increasing interest in polymer nanocomposites. These composites have been shown to undergo substantial improvements in mechanical properties such as the strength, modulus, and dimensional stability, permeability to gases, water and hydrocarbons, thermal stability, flame retardancy, chemical resistance, and electrical, dielectric, magnetic and optical properties [3, 4].

Carbon nanotubes (CNTs) have received much attention since their discovery by Iijima in 1992 [5]. Extensive research and development efforts have been devoted to the use of CNTs as nanofillers to produce a variety of high-performance polymer nanocomposites for specific applications. Among the advantages of CNTs is their high aspect ratio (as high as 1000), which can induce better adhesion with the polymeric matrix, which is an important factor for effective enhancement of the nanocomposites properties.

The main aim of the present work is to study the thermomechanical properties and thermal stability of nanocomposite materials based on epoxy resin (ER) matrix filled with multi-walled carbon nanotubes. Diglycidyl ether of bisphenol A (DGEBA) with triethylenetetramine (TETA) as hardener was the matrix material, while different amounts of amine-modified multi-walled CNTs were used as filler particles. The filler content was systematically varied from 0.1 to 1 % w/w.

The pre-polymer D.E.R.332 used in this study is diglycidyl ether of bisphenol A (DGEBA) supplied by Fluka SA. The hardener used was triethylenetetramine (TETA) supplied by Sigma Aldrich. The amine-modified multi-walled carbon nanotubes (average diameter 9.5 nm and average length < 1 μm) was supplied by Nanocyl SA. All the components of the system are commercial products and were used without any purification. The DGEBA/TETA/MWCNTs nanocomposites were prepared by the dispersion of the determined amount of carbon in a glass vessel. Prior to that procedure, the pre-polymer was heated at 40 °C in order to decrease the viscosity. The stoichiometric amount of TETA (14 phr) was added, and then the mixture was mechanically stirred for 1 h at 2000 rpm and degassed under vacuum for 15 min. Finally, the mixture was sonicated for 30 min in order to break up the CNTs agglomerates [6] and degassed again. The homogeneous liquid was poured in rectangular shaped molds and the samples were cured at 60 °C for 20 h and at 150 °C for 2 h.

Thermogravimetric and Differential Thermal Analysis analysis was performed on a simultaneous thermal analyzer (TGA/DTA) STA 503 device (BAEHR ThermoAnalyse GmbH, Germany). TGA tests were conducted in temperature range from 20 to 1400 °C under dry nitrogen (N_2) atmosphere at a heating rate of 20 °C/min and the weight loss was monitored.

The effect of CNTs on the thermal stability of the nanocomposites was studied using thermogravimetric analysis (TGA). Relative TGA and derivative (DTGA) curves for neat epoxy and the prepared ER/CNTs nanocomposites are presented in Fig. 1. Similar curves have also been obtained for epoxy resin nanocomposites filled with carbon black (ER/CB) [7]. The results revealed that the samples show good thermal stability for temperatures up to 350 °C with a maximum decomposition temperature higher than 370 °C. The decomposition (thermal degradation) temperature corresponds to the temperature of the peak of the derivative mass loss (DTGA) curve, i.e. the temperature of the maximum weight loss rate. The thermal degradation temperatures of the pure epoxy and the ER/CNTs nanocomposites are similar, within experimental errors (± 1.5 °C).

The temperature corresponding to 5 % initial mass loss (onset of the TGA curve) indicates the thermal stability of the samples. Typical plots are shown in Fig. 2 (left axis). The data reveals that the pure epoxy matrix shows, generally, better thermal stability (i.e. the degradation starts at higher temperatures), compared to the ER/CNTs nanocomposites.

Fig. 2 (right axis) shows the variation of residual mass (char content) of the nanocomposites at 1000 °C as a function of the filler composition. The char content are indicative of the degradation level and the flammability resistance of the samples. The char formation mechanism is, generally, enhanced when adding filler particles,

however the values of the residual mass for the ER/CNTs nanocomposites decrease with increasing filler content.

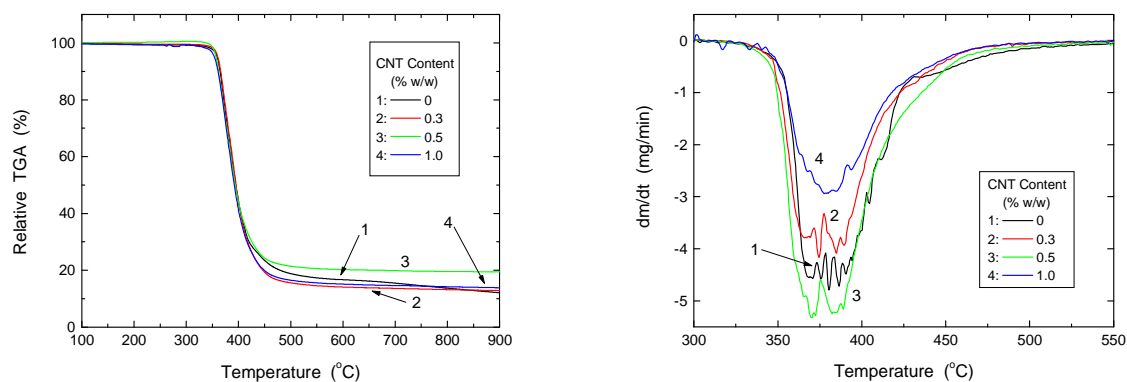


Fig. 1 Comparative relative TGA (left) and DTGA (right) plots for ER/CNTs nanocomposites and various filler contents.

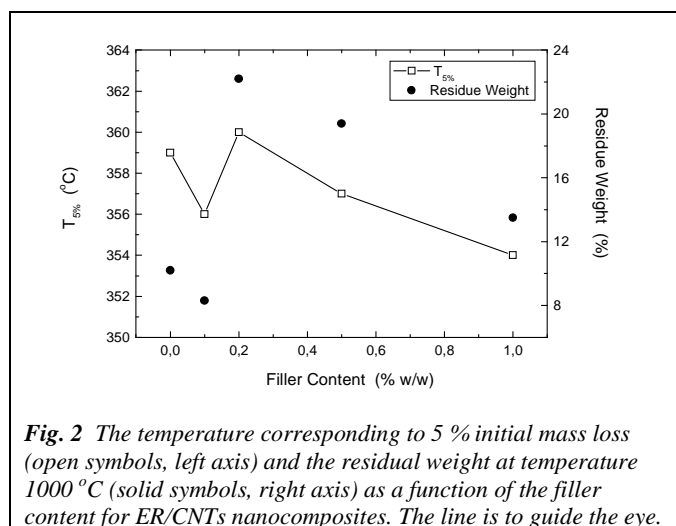


Fig. 2 The temperature corresponding to 5% initial mass loss (open symbols, left axis) and the residual weight at temperature 1000 °C (solid symbols, right axis) as a function of the filler content for ER/CNTs nanocomposites. The line is to guide the eye.

In the following Table 1 the values of the characteristic parameters of TGA measurements for ER/CNTs nanocomposites are summarized.

The reduction observed for the samples with higher CNTs content is probably attributed to the fact that the degradation process of the nanocomposites is hampered by the increased filler concentration, because the interactions between the ER matrix and the CNTs filler particles are stronger. This result is in agreement with DMA measurements and glass transition temperature studies [6]. It should also be mentioned that CNTs were found to have better dispersion within the polymer matrix, compared to ER/CB nanocomposites [7]. A complete comparison of the thermomechanical properties and thermal stability of ER/CNTs and ER/CB nanocomposites can be found in [7]

Table 1 The characteristic values of TGA parameters for ER/CNTs nanocomposites

Filler Content (% w/w)	0	0.1	0.2	0.5	1.0
Maximum weight loss rate (mg/min)	4.8	4.6	5.0	5.2	3.0
Decomposition temperature (°C)	380	379	382	378	379
$T_{5\%}$ (°C)	359	356	360	357	354
Residual mass (%)	10.2	8.3	22.2	19.4	13.5

To conclude, it was found that the addition of carbon nanotubes enhances the thermal properties of the epoxy matrix. The degradation starts at higher temperatures and the char formation mechanism is enhanced when adding filler particles. For higher CNTs content, the interactions between the polymer matrix and the filler particles play an important role and the degradation process becomes slower.

[1] Sun Y., Zhang Z., Moon K.-S., Wong C.P., J. Polym. Sci. Part B: Polym. Phys. 42, 3849 (2004).
 [2] Brown J., Rhoney I., Pethrick R.A., Polym. Int. 53, 2130 (2004).
 [3] Zhou Y.X., Wu P.X., Cheng Z.-Y., Ingram J., Jeelani S., eXPRESS Polym. Lett. 2, 26 (2008).
 [4] Kanapitsas A., Pissis P., Kotsilkova R., J. Non-Cryst. Solids 305, 204 (2002).
 [5] Ijiima S., Nature 354 (1991).
 [6] Kosmidou Th., Vatalis A., Delides C., Logakis E., Pissis P., Papanicolaou G., eXPRESS Polym. Lett. 2, 364 (2008).
 [7] Kanapitsas A., Zois H., Delides C.G., Proc. 9th Med. Conf. Medicta 2009, Marseille, France (2009).

Dielectric and Functional Properties of Polymer Matrix/ZnO/BaTiO₃ Hybrid Composites

G. Ioannou, A. Patsidis, G. C. Psarras*

Department of Materials Science, School of Natural Sciences, University of Patras,
Patras 26504, Hellas

*G.C.Psarras@upatras.gr

Ceramic-polymer composites consisting of ferroelectric and piezoelectric crystal particles, randomly distributed within a glassy polymer matrix represent a novel class of materials. The electrical response of these hybrid materials can be suitably adjusted by controlling the type and the amount of the ceramic inclusions. High tech electronic devices require new high dielectric permittivity materials (known as high-K materials), which should combine at the same time, suitable dielectric properties, mechanical strength and ease processing. Recently, ceramic-polymer composites have been studied in various potential applications including integrated capacitors, acoustic emission sensors and for the reduction of leakage currents [1-3]. Furthermore, composites including ferroelectric and/or piezoelectric particles are expected to exhibit functional properties because of the varying polarization of the ceramic particles [4,5].

In the present study polymer matrix/ZnO/BaTiO₃ composites were prepared, in different filler concentrations. The dielectric response of all samples was studied by means of Broadband Dielectric Spectroscopy (BDS), over a wide temperature (from 30°C to 160°C) and frequency (from 10⁻¹ Hz to 1 MHz) range. Experimental data were analyzed by means of dielectric permittivity and electric modulus formalisms [6-8].

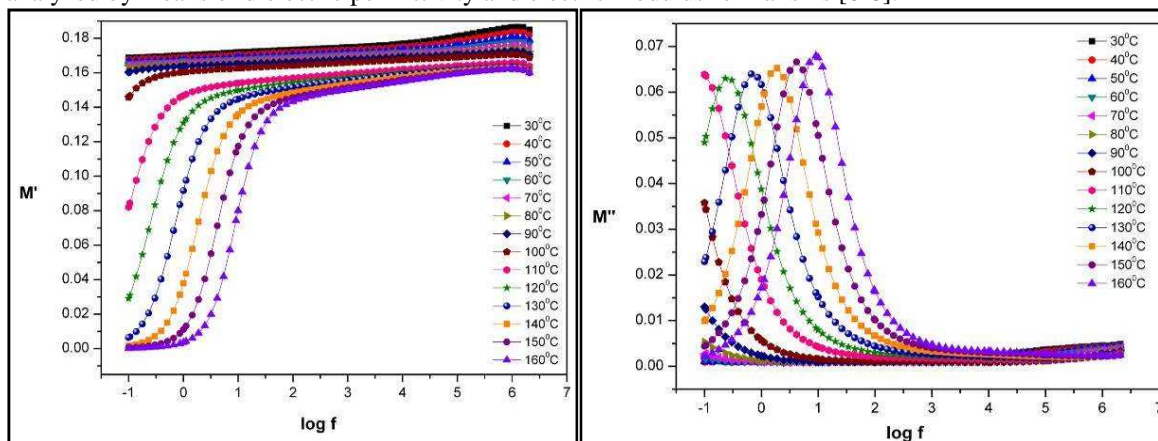


Figure 1: Real and imaginary part of electric modulus for the specimen of pure epoxy resin.

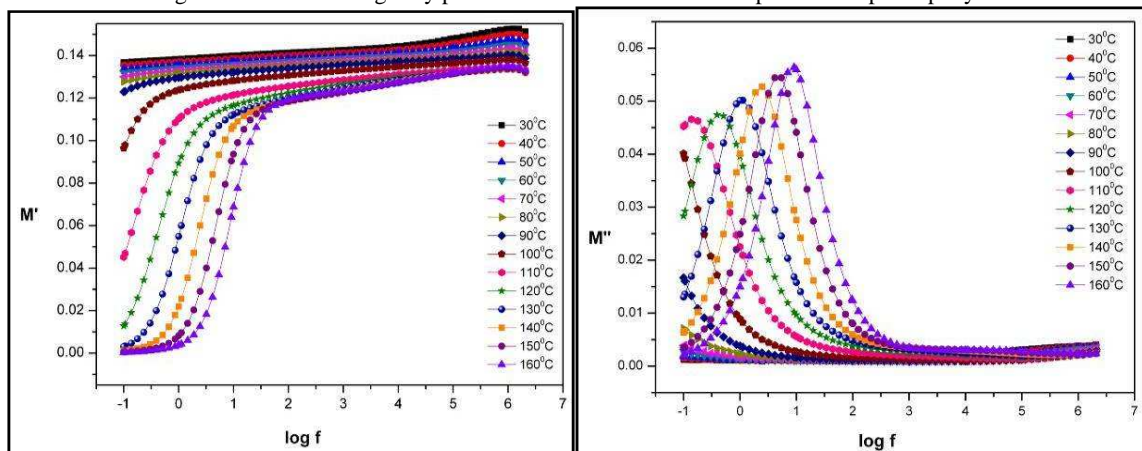


Figure 2: Real and imaginary part of electric modulus for the composite with 20 phr BaTiO₃.

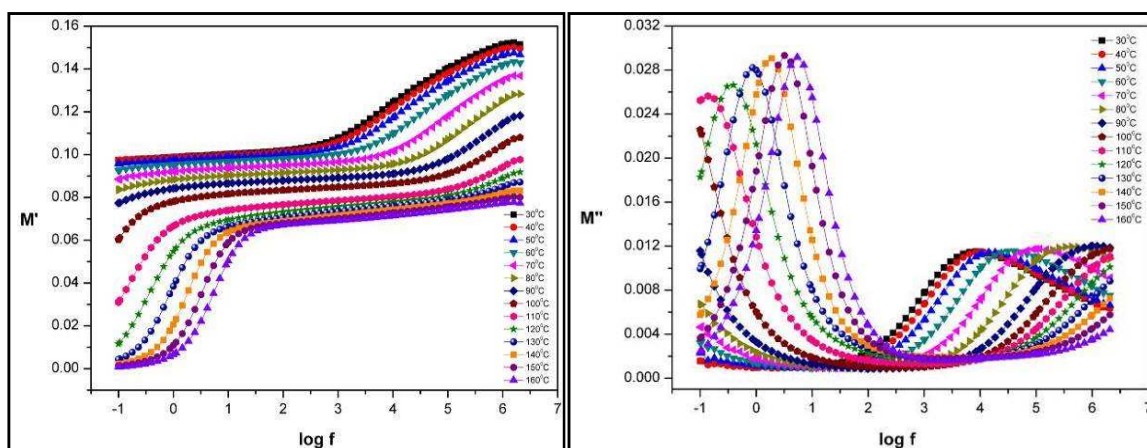


Figure 3: Real and imaginary part of electric modulus for the composite with 20 phr BaTiO₃ and 50 phr ZnO.

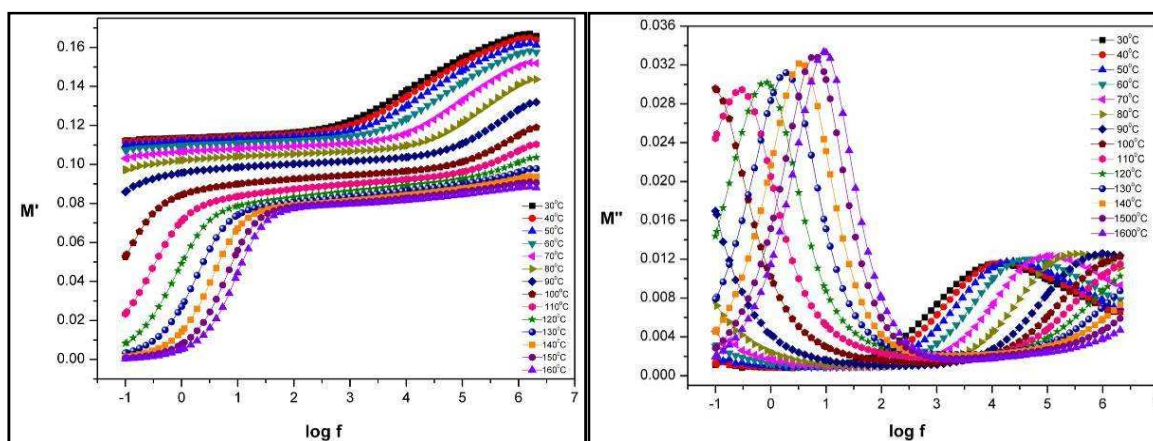


Figure 4: Real and imaginary part of electric modulus for the composite with 50 phr ZnO.

From the conducted analysis results, that the recorded dielectric relaxations are related to both the polymer matrix (glass to rubber transition and reorientation of polar side groups) and the presence of the reinforcing phases. Dielectric permittivity and loss are increasing with ceramic filler and diminishing rapidly with frequency. Composites with ZnO exhibit an intermediate relaxation phenomenon called IDE (Intermediate Dipolar Effect), which is attributed to intrinsic interfacial polarization phenomena within ZnO grains [9]. The functionality of the composite systems is related to the variation of the real part of permittivity, in the vicinity of the characteristic Curie temperature of BaTiO₃, and to the relaxing polarization of the ZnO particles.

References

- [1] Popielarz R., Chiang C. K., Nozaki R., Obrzut J, *Macromolecules*, 34, 5910 (2001).
- [2] Korotkov N., Gridnev S. A., Konstantinov S. A., Klimentova T. I., Barmin Y. V., Babkina I. V., *Ferroelectrics*, 299, 171 (2004).
- [3] Jylhä L., Honkamo J., Jantunen H., Sihvola A., *Journal of Applied Physics*, 97, 104104 (2005).
- [4] Kontos G.A., Soulintzis A.L., Karahaliou P.K., Psarras G.C., Geoga S.N., Krontiras C.A., Pisanias M.N., *Express Polymer Letters*, 1, 781 (2007).
- [5] Patsidis A., Psarras G.C., *Express Polymer Letters*, 2, 718 (2008).
- [6] Tsangaris G.M., Psarras G.C., Kouloumbi N., *Journal of Materials Science*, 33, 2027 (1998).
- [7] Psarras G.C., Manolakaki E., Tsangaris G.M., *Composites Part A*, 33, 375 (2002).
- [8] Psarras G.C., Manolakaki E., Tsangaris G.M., *Composites Part A*, 34, 1187 (2003).
- [9] Soulintzis A., Kontos G., Karahaliou P., Psarras G.C., Geoga S.N., Krontiras C.A., *J Pol Sc B : Pol Phys*, 47, 445 (2009).

Dielectric Response and Functionality of Polymer Matrix BaTiO₃ Nanocomposites

A. Patsidis, G. C. Psarras*

Department of Materials Science, School of Natural Sciences, University of Patras,
Patras 26504, Hellas

*G.C.Psarras@upatras.gr

Polymer matrix composites incorporating, homogeneously distributed, ferroelectric crystal particles constitute a novel class of materials, with several interesting properties. Integrated decoupling capacitors, angular acceleration meters, acoustic emission sensors and electronic packaging are some potential applications [1-4]. Ferroelectric materials exhibit spontaneous polarization and are characterized by a temperature dependent disorder to order transition. Thus, besides all the expected influences (volume fraction, geometrical characteristics, type of distribution etc), the electrical response of ferroelectric particles – polymer matrix composites depends on the ferroelectric to paraelectric transition of the inclusions.

In the present study composite systems of epoxy resin and ceramic BaTiO₃ nanoparticles have been prepared, varying the volume fraction of the inclusions. The dielectric response of the composites was studied in a wide frequency and temperature range. Care was taken in order to include the characteristic disorder to order transition temperature, in the examined temperature range.

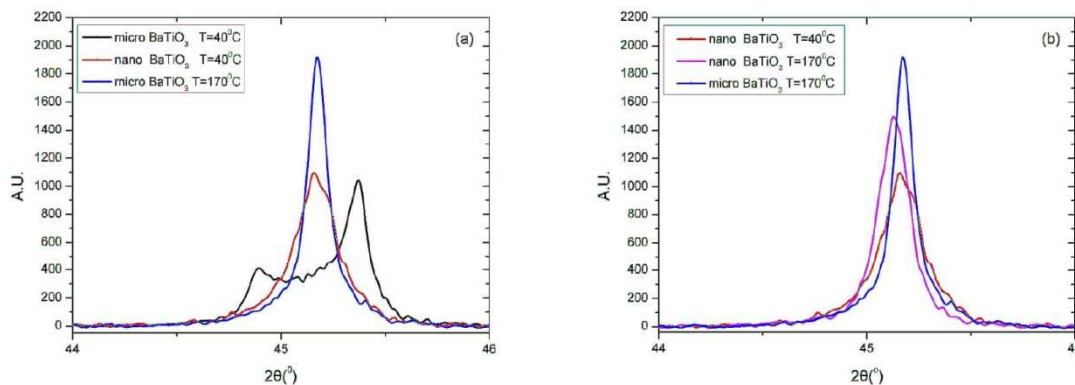


Figure 1: XRD spectra of BaTiO₃ micro and nanoparticles below (40°C) and above (170°C) Curie temperature.

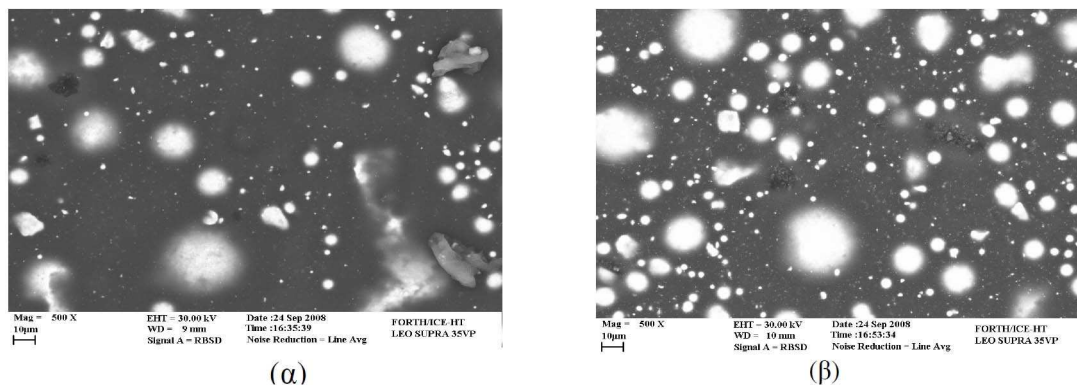


Figure 2: SEM images of the composites with (a) 5 and (b) 10 phr in BaTiO₃ nanoparticles.

Data were analyzed by means of dielectric permittivity and electric modulus formalisms. From the conducted analysis results, that the recorded dielectric relaxations are related to both the polymer matrix and the presence of the reinforcing phase. Dielectric permittivity and loss are increasing with ceramic filler and diminishing rapidly with frequency. XRD spectra indicate that below critical temperature (T_C), BaTiO₃ microparticles acquire tetragonal crystal structure, while above (T_C) transform to cubic. In the case of nanoparticles, a “mixed” structure of tetragonal and cubic lattice appears to exist below critical temperature [4-7].

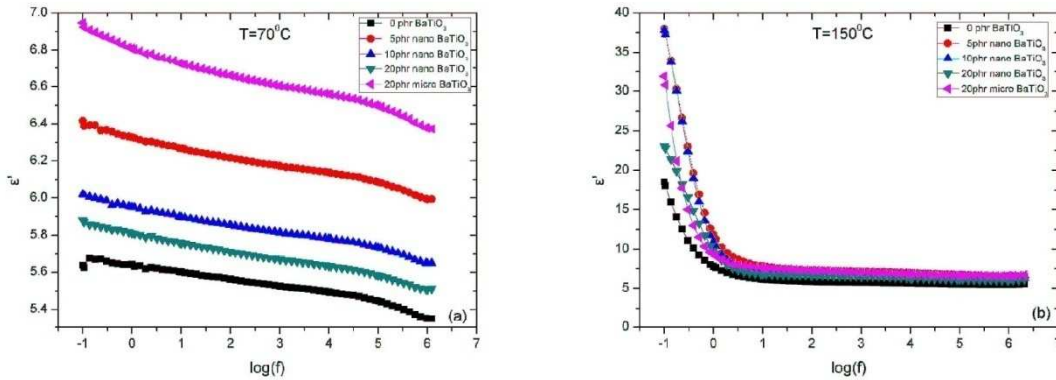


Figure 3: Real part of dielectric permittivity as a function of frequency for all the examined composites.

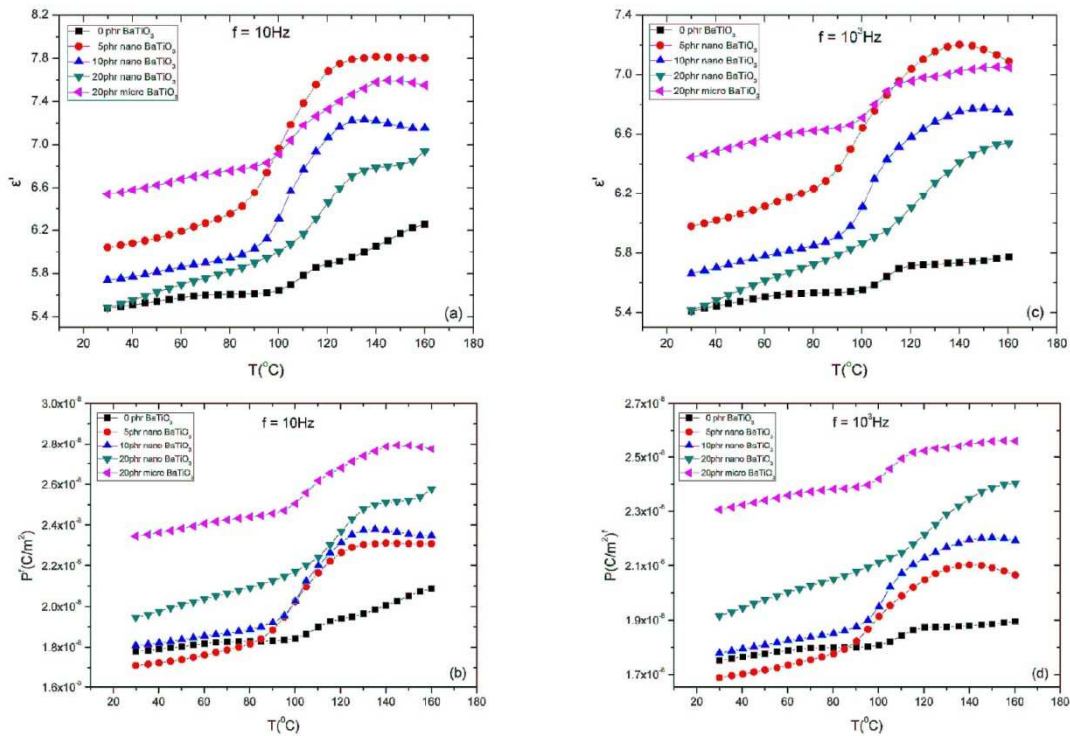


Figure 4: Variation of real part of dielectric permittivity and polarization with temperature for all the examined composites.

In the vicinity of the characteristic Curie temperature of BaTiO₃ an abrupt variation of the real part of permittivity and polarization is observed. The recorded peaks are related [8] to the “disorder to order” or ferroelectric to paraelectric transition of BaTiO₃.

References

[1] Channal C.V., Jog J.P., Exp. Polym. Let., 2, 294 (2008).
 [2] Bade M.G., Comprehensive Composite Materials, 6.01, Elsevier Science Ltd. (2000).
 [3] Psarras G.C., Exp. Polym. Let., 2, 460 (2008).
 [4] Dang Z.-M., Xu H.-P., Wang H.-Y., Applied Physics Letters 81, 4814 (2007).
 [5] Mandal T. K., Materials Letters 61, 850 (2007).
 [6] Smith M.B., Page K., Siegrist T., Redmond P.L., Walter E.C., Seshadri R., Brus L.E., Steigerwald M.L., J. Ame. Chem. Soc. 130, 6955 (2008).
 [7] Baeten F., Derks B., Coppens W., Kleef van E., J. Eur. Cer. Soc. 26, 589 (2006).
 [8] Patsidis A., Psarras G.C., Exp. Polym. Let. 2, 718 (2008).

Development of Metallic Ag Nanowires and Nanoparticles on Mesoporous Silicas: Effect of Pore Structure and Size of the Silica Support

A. Delimitis^{1*}, A. Fotopoulos², K. Matis², and K. Triantafyllidis^{1,2}

¹ *Chemical Process Engineering Research Institute (CPERI), Centre for Research & Technology-Hellas (CERTH), 57001 Thessaloniki, Thessaloniki, Greece*

² *Department of Chemistry, Aristotle University of Thessaloniki, 54124 Thessaloniki, Greece*

*andel@cperi.certh.gr

Ordered mesoporous inorganic materials have exhibited great capability for carrying the unique chemistry of crystalline zeolites to a larger pore regime. Inevitably, this has focused a lot of research work onto their application as chemical reactors, via the inclusion of catalytically active species in the pores [1]. Another area of ongoing interest has been the incorporation of transition elements or semiconductors to give continuous metal 'nanowires' within the channels, where the mesoporous solid acts as a suitable template. A great advantage of template method is that it provides good control over the size and shape of the nanowires and can be used to prepare the nanomaterial with the desired aspect ratio [2].

One of the most important applications is the growth of Ag particles and nanowires using appropriate templates, with applications to heterogeneous catalysis, where Ag can utilize its excellent oxidation properties. The commercial process of ethylene epoxidation for the formation of ethylene oxide, a valuable raw material, uses a catalyst based on Ag supported on low-surface area α -Al₂O₃ [3]. More recently, we showed that the use of ordered, high surface area (ca. 800-1000 m²/g), mesoporous silicas, such as MCM-41 or HMS as a template for Ag, can enhance its dispersion up to relatively high loadings (ca. 40 wt.% Ag), leading to more active epoxidation catalysts [4]. In this work, we report on the characterization of Ag-based catalytic materials supported on mesoporous silica templates using transmission electron microscopy (TEM-HRTEM) techniques. The results revealed the growth of Ag nanoentities with various morphologies, such as nanoparticles and/or nanowires. The dependence of Ag morphology and particle size distribution on the structure and pore size of the silica support, as well as on the Ag loading itself is analyzed.

The types of ordered mesoporous silicas that have been used as supports for the preparation of the Ag nanoentities were: a) MCM-41 silica with 2-dimensional hexagonally arranged tubular mesopores, having a surface area (S) of 895 m²/g and average mesopore size $d=2.9$ nm; b) HMS silica with 3-dimensional wormhole-like mesoporous morphology, with $S=970$ m²/g and $d=2.4$ nm, and c) SBA-15 with 2-dimensional hexagonally arranged tubular mesopores with $S=800$ m²/g and mesopore diameter $d=5.9$ nm. The deposition of Ag on these supports was accomplished by the dry impregnation method in which the silica supports were impregnated under stirring with aqueous solution of AgNO₃; the volume of the AgNO₃ solution was equal to the total pore volume of the silica sample in each case. The impregnated samples were dried under vacuum and subsequently reduced at 350°C for 2 h under a H₂ flow in a tubular quartz reactor. For all samples, the Ag loading was 10 wt%. The samples were examined in a JEOL 2011 high resolution transmission electron microscope operating at 200 kV with a point resolution of 0.23 nm and a spherical aberration coefficient of $C_s = 1$ mm. Complementary characterization data were also provided by N₂ adsorption-desorption measurements at 77 K and X-ray diffraction (XRD).

The HRTEM studies revealed that Ag incorporation in MCM-41 supports results in two distinct morphologies, as depicted in Fig. 1(a) and (b). Both metallic nanoparticles, with sizes up to 50 nm, as well as Ag nanowires co-exist in the same MCM-41 particle. The Ag nanoparticles are mainly distributed on the surface of the support particles and are single crystalline, as confirmed by electron diffraction experiments. On the other hand, the Ag nanowires are quite long and are formed inside the pores of MCM-41; consequently, they are only up to 2.9 nm wide. HRTEM observations revealed that the nanowires do not follow a specific crystallographic orientation, however, their {111} lattice fringes were often revealed. The formation of Ag nanoparticles, in addition to the nanowires, may be also attributed to the high metallic content (10 wt%) in the synthesis.

The dry impregnation of Ag into HMS and SBA-15 led to a single morphology, as illustrated in Fig. 2. In both cases, only Ag nanoparticles are grown, which are distributed on the external surfaces of the two porous supports. The nanoparticles are highly crystalline, as depicted in Fig. 3 and their typical sizes are up to 20 nm for HMS and up to 40 nm for SBA-15. In both cases, no nanowire formation is observed, although SBA-15 exhibits an ordered mesoporous structure similar to MCM-41. This finding enables us to conclude that the 2.9 nm ordered pore opening is ideal for the successful growth of metallic Ag nanowires. Furthermore, the inclusion of silver into the long silica pores can provide an effective way for the production of Ag nanowires, since the dissolution of MCM-41 by a mixture of HF and H₂SO₄ is feasible.

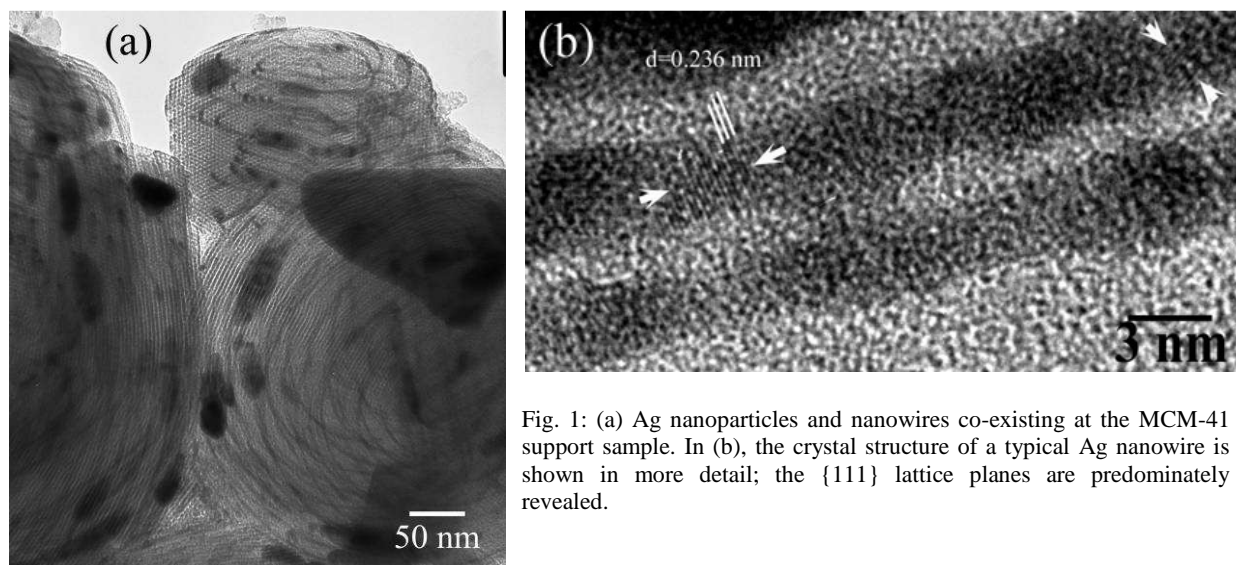


Fig. 1: (a) Ag nanoparticles and nanowires co-existing at the MCM-41 support sample. In (b), the crystal structure of a typical Ag nanowire is shown in more detail; the {111} lattice planes are predominately revealed.

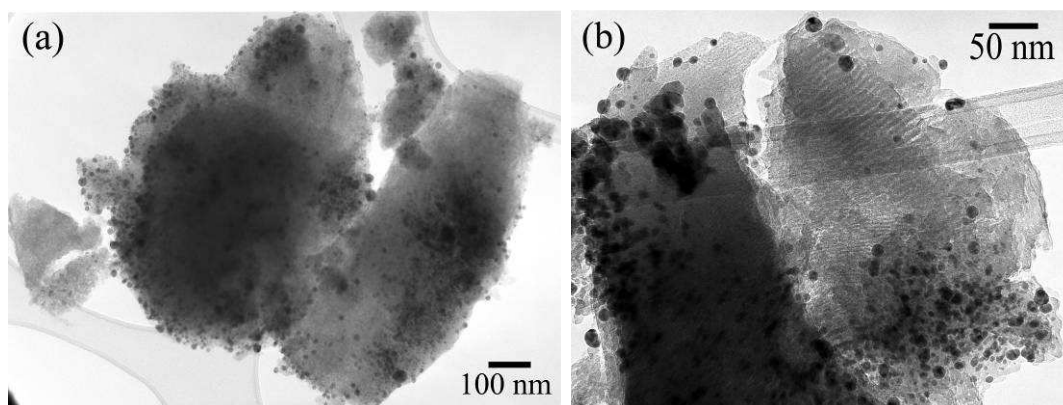


Fig. 2: The Ag nanoparticle formation as a common morphology in two different silica supports, namely (a) HMS and (b) SBA-15.

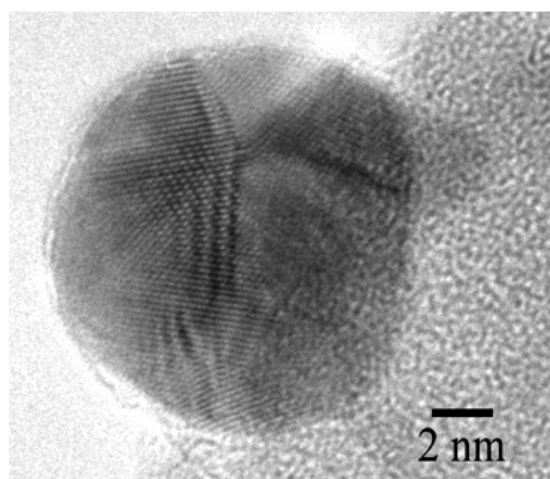


Fig. 3: A single crystalline Ag particle in the SBA-15 supported sample, exhibiting a fivefold {111} twinning.

- [1] Moller K., Bein T., Chem. Mater. 10, 2950 (1998).
- [2] Hornyak G.L., Patrissi C.J., Martin C.R., J. Phys. Chem., B 101 1548 (1997).
- [3] Serafin J.G., Liu A.C., Seyedmonir S.R., J. Mol. Catal. A-Chem. 131 157 (1998).
- [4] Fotopoulos A.P., Triantafyllidis K.S. Catal. Today 127, 148 (2007).

Statistical Distributions of Bubble Lengths in DNA

G. Kalosakas^{1*} and S. Ares²

¹ *Materials Science Department, University of Patras, GR-26504 Rio, Greece*

² *Max Planck Institute for the Physics of Complex Systems, Nothnitzer Str. 38, D-01187 Dresden, Germany, and Grupo Interdisciplinar de Sistemas Complejos (GISC)*

*georgek@upatras.gr

The length distribution of bubbles (large amplitude base-pair openings) in double stranded DNA is discussed in the framework of the Peyrard-Bishop-Dauxois model [1]. In this approach a DNA segment is described through a lattice, where each lattice site corresponds to a particular base-pair of the sequence. Then a continuous variable y_n on each lattice site n represents the corresponding base-pair stretching. Appropriate effective potentials describe in a mesoscopic level both the intra-base-pair interactions between complementary nucleotides and the stacking interactions between adjacent base-pairs. For more details of the model see Refs. [1-3].

Using Monte Carlo simulations we have shown that the numerically obtained distribution $P(l)$ of bubble lengths l in thermal equilibrium can be accurately described by the power-law modified exponential [2]

$$P(l) = W \frac{e^{-l/\xi}}{l^c}. \quad (1)$$

This formula describes the bubble distributions in the whole region starting from small bubble sizes (for $l > 1$) up to lengths of about a hundred base-pairs [2,3].

Fig. 1 shows bubble length distributions in DNA segments of different GC percentages at a fixed temperature (left) as well as for different temperatures at a fixed GC content (right).

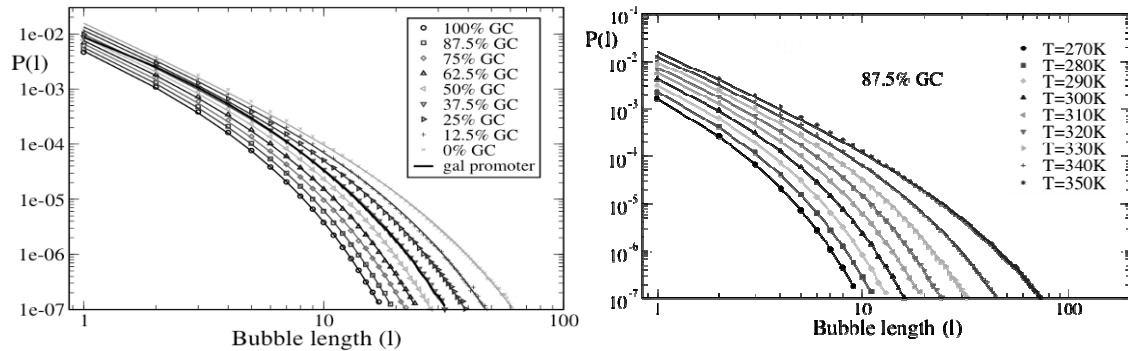


Figure 1. Points show distributions per base-pair, $P(l)$, of bubble sizes l (in number of base-pairs). Lines are fits with the analytical distribution, Eq. (1). *Left:* Distributions are shown at fixed $T=310$ K for random DNA sequences with different GC contents. *Right:* Distributions are shown for different temperatures at random DNA sequences of a fixed GC percentage $x_{GC} = 87.5\%$. In all cases the threshold value of base-pair openings in order to form a bubble is considered as $y_{\text{thres}}=1.5$ A.

We have investigated in detail and quantified the dependence of bubble length distributions on temperature, T , and the GC content, x_{GC} , of the DNA segment [3]. This has led to simple approximate expressions for the dependence of the parameters ξ , c , and W of Eq. (1) on T and x_{GC} :

$$\xi(T, x_{GC}) = a_1 + a_2 \cdot x_{GC} + \frac{a_3 + a_4 \cdot x_{GC}}{a_5 + a_6 \cdot x_{GC} - T},$$

$$c(T, x_{GC}) = b_1 + b_2 \cdot x_{GC} + (b_3 + b_4 \cdot x_{GC}) \cdot T,$$

$$W(T, x_{GC}) = d_1 + d_2 \cdot x_{GC} + (d_3 + d_4 \cdot x_{GC}) \cdot T + (d_5 + d_6 \cdot x_{GC}) \cdot T^2,$$

where a_1, \dots, a_6 , b_1, \dots, b_4 , and d_1, \dots, d_6 are constants independent of T and x_{GC} [3].

Fig. 2 and Fig. 3 show examples of the obtained $\xi(T, x_{GC})$ and $c(T, x_{GC})$ dependences, respectively.

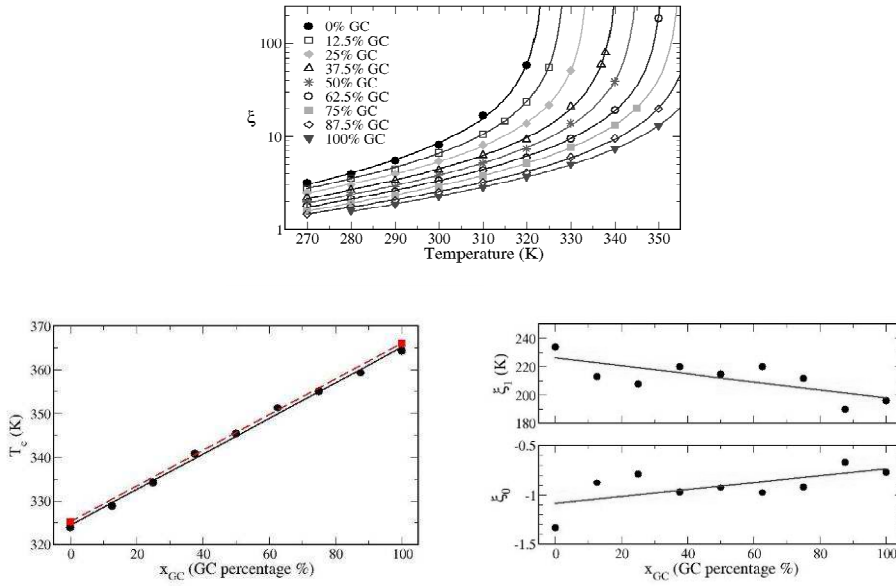


Figure 2. *Top:* Dependence of the decay length ξ of distribution (1) on temperature, for different values of the GC content of the DNA sequence (points). Lines show fits with the function $\xi(T) = \xi_0 + \frac{\xi_1}{T_c - T}$. *Bottom left:* Dependence of the critical

temperature T_c , as obtained from the fitting of the $\xi(T)$ data with the previous equation, on the GC content of the sequence (circles). Solid line represents a least square fit according to a linear dependence. Squares show numerically exact results of the critical temperatures for the homogeneous cases of 0% GC and 100% GC, obtained through the transfer integral method, while the dashed line connects these two points. *Bottom right:* Dependence of the parameters ξ_1 and ξ_0 , as obtained from the fitting of $\xi(T)$ data with the previous equation, on the GC content of the sequence (circles). Solid lines represent linear fits of the corresponding data.

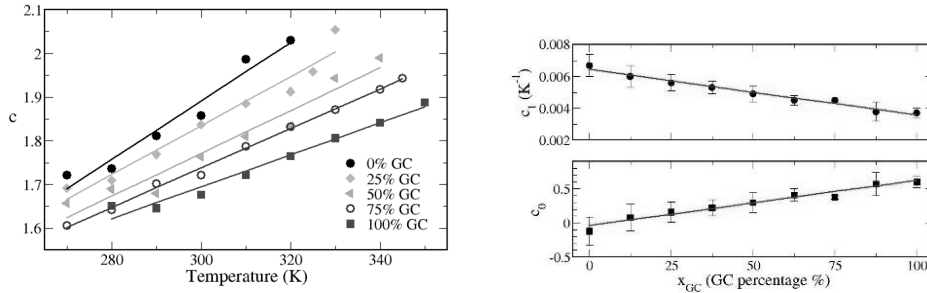


Figure 3. *Left:* Dependence of the exponent C of the distribution (1) on temperature, for different values of the GC content of the DNA sequence (points). Lines show linear fits with equation $c(T) = c_0 + c_1 \cdot T$. *Right:* Dependence of the parameters C_1 and C_0 of the fit of the $c(T)$ data with the previous equation, on the GC content of the sequence (points). Error bars are standard errors resulting from the fitting procedure. Solid lines represent linear fits of the corresponding data.

- [1] Dauxois T., Peyrard M., Bishop A.R., *Phys. Rev. E* 47, 44 (1993).
 [2] Ares S., Kalosakas G., *Nano Lett.* 7, 307 (2007).
 [3] Kalosakas G., Ares S., *J. Chem. Phys.* (2009) in press.

Acknowledgments G.K. acknowledges support from the C. Caratheodory program C155 of University of Patras and S.A. from Ministerio de Educacion y Ciencia (Spain) through grant MOSAICO.

Nanoindentation studies of phase separated glasses: The ternary Ag-As-S system

K.S. Andrikopoulos^{1*}, J. Arvanitidis¹, E. Fournou¹, B. Kargas¹, T. Wagner² and S.N. Yannopoulos³

¹ Department of Applied Sciences, Technological Educational Institute of Thessaloniki, 57400 Sindos, Greece

² Department of Inorganic Chemistry, Faculty of Chemical-Technology, University of Pardubice, Legion's sq. 565, 53210, Czech Republic

³ Foundation for Research and Technology Hellas, Institute of Chemical Engineering and High Temperature Chemical Processes, (FORTH/ICE-HT) P.O. Box 1414, GR-26 504 Patras, Greece

*kandriko@gen.auth.gr

Abstract

The mechanical properties of the ternary $\text{Ag}_x(\text{As}_{0.33}\text{S}_{0.67})_{100-x}$ chalcogenide system ($0 \leq x \leq 25$) are studied by means of a nanoindenter. The mechanical modulus and hardness of the materials is extracted and real time scanned images are captured for a specific sample region and subsequently compared with the modulus-map provided by point-by-point nanoindentation measurements performed on the same sample region. It is shown that the samples are homogeneous for $x \leq 2$ and $x > 20$. On the contrary the samples in the composition range $2 < x \leq 20$ are phase separated on a microscopic scale. Inhomogeneities are droplets of highly symmetric sphere-like domains (Ag-rich phase) dispersed in a Ag-poor phase. For the samples under investigation the mechanical properties of the two phases do not depend upon glass composition, signifying that the structure of the two phases is not altered by addition of silver. The Ag-rich phase has mechanical properties comparable to the $x=25$ sample (smithite-type glass) while the mechanical properties of the Ag-poor phase are close to those of the glassy matrix (AsS_2). The two phases interchange volume fractions with increase of Ag content. This effect was monitored by inspecting the change of the size and density of the spherical domains which leads to a percolation transition of the Ag-rich phase at $x \sim 8\%$.

Introduction

Bulk chalcogenide glasses are candidates for a number of applications arising basically from their semiconductor nature. Bulk silver-doped chalcogenide glasses, in particular, are known to possess increased ionic conductivity and are potential candidates of ionic conductors [1]. In addition, they may be involved in other applications of technological significance such as memory switching and programmable metallization devices [2]. Interest on the silver doped arsenic sulfides has been evoked recently, mainly because the phase separation they show may be interconnected with their ionic conductivity through the percolation limit observed for specific silver concentration. Raman and SEM/EDS studies have already been carried out in order to reveal the structure of these glasses as a function of silver concentration [3]. However, despite the fact that their information is valuable, they may lead to side effects such as photodissolution of silver and electron induced silver mobility [4] whose influence in final results is indistinct. Nanoindentation techniques may play a key role for surface characterization of similar materials as well as for bringing insight to the corresponding mechanical properties that cannot be easily found in the literature, especially for the case of ultra thin films. Moreover, it was shown lately that nanoindentation methods can successfully be applied on the investigations of the so-called photoinduced plasticity in non-crystalline materials [5].

Experimental

Bulk glasses of the ternary system $\text{Ag}_x(\text{As}_{0.33}\text{S}_{0.67})_{100-x}$ were cut into rectangular slabs which were then polished. Details related to sample preparation can be found elsewhere [3]. Nanoindentation measurements were performed by utilization of a Hysitron Tribolab instrument possessing a Berkovich tip. The force application routine was as follows: (i) the force increased linearly from 0 up to 1 mN within a time interval of 20 s, (ii) it was kept constant at 1 mN for 60 s and then (iii) it was reduced linearly down to 0 within 20s. This standard trapezoidal loading function was selected among others after several tests involving different maximum force values and was evidently applied to both extreme stoichiometries i.e. $x=0$ and $x=25$, as well as all the intermediate silver concentrations under investigation. The mechanical properties of the two extreme glasses were studied thoroughly and mean values of modulus and hardness were calculated from statistical measurements (25 equivalent nanoindentations), since these samples served as reference samples for the evaluation of the properties measured for the other silver concentrations. For the mapping of modulus on samples' surface, 42 nanoindentation measurements of $4 \mu\text{m}$ distance one from the other, were performed on a $20 \mu\text{m} \times 24 \mu\text{m}$ domain.

Results and discussion

WE2

P46

The mechanical properties extracted by nanoindentation measurements for the binary AsS_2 and the ternary AgAsS_2 glasses are listed in Table I. The mean values of modulus and hardness (followed by the corresponding standard deviations) are higher for the ternary glass (AgAsS_2). Images captured by scanning the samples' surfaces at microscopic level with the indenter, revealed phase separation for the samples in the composition interval $2 < x \leq 20$. Figure 1(a) depicts an image captured from a $20 \mu\text{m} \times 24 \mu\text{m}$ sample region of the $\text{Ag}_8(\text{As}_{0.33}\text{S}_{0.67})_{92}$ sample. Dark areas correspond to the matrix phase (AsS_2), while the second phase is bound into the light coloured spherical regions. For each glass, there is a distribution of droplet radii which changes with the addition of Ag, showing a percolation transition at $x \sim 8$. Indentations performed in the "dark" areas of all samples exhibiting phase separation, resulted in mechanical properties similar to the AgAsS_2 composition. Similarly, indentations applied in the "light" areas resulted in low values for both modulus and hardness (Table

Table I

Mean values and standard deviations of modulus and hardness for compositions $x=0$ and $x=25$. The respective values for the Ag-poor and the Ag-rich phases of the intermediate compositions $2 < x < 20$ are also given.

Composition	Modulus GPa	Hardness GPa
$x=0$ AsS_2	18.2 ± 0.45	1.56 ± 0.060
$x=25$ AgAsS_2	37.7 ± 0.53	2.27 ± 0.057
Ag – rich phase	37.2 ± 3.46	2.33 ± 0.3
Ag – poor phase	28.3 ± 1.97	1.98 ± 0.15

I). However, the latter values did not match those of the binary AsS_2 system indicating that the second phase possesses appreciable amounts of Ag. These results are in accordance with old phase diagrams and recent combined SEM/EDS and Raman measurements [3], which state that phase separation falls in the range $20 > x > 2$, presenting percolation at $\sim 7\%$ silver concentration; the two phases are glasses of rather steady composition throughout the whole range: one phase is a silver poor phase ($x \sim 4$) while the other is a silver rich phase ($x \sim 25$).

In order to demonstrate the ability of the nanoindenter to provide reliable data, we attempted

to extract the distribution of the modulus values on a sample region and compare it with the scanned-image of the same region. This required a number of sequential nanoindentations on the region of interest and calculation of the modulus for each measurement. The results are presented as a contour map in Fig. 1(b) and reflect reliably the morphology of the scanned image in Fig. 1(a).

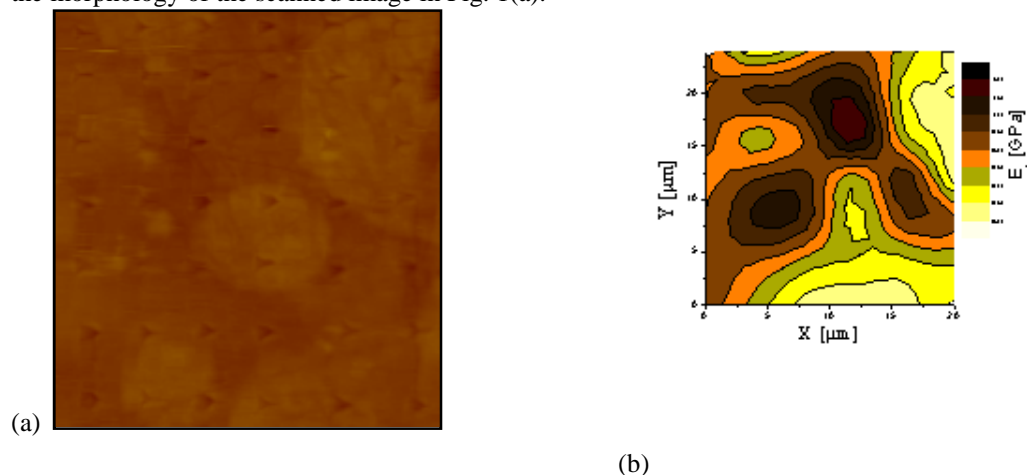


Figure 1. (a) Imaging of a $20 \mu\text{m} \times 24 \mu\text{m}$ sample region (of the $x=8$ composition) after the application of 42 sequential nanoindentations. The indentation marks ($4 \mu\text{m}$ apart one another) can be seen, along with the phase separation of the material (dark background with lighter sphere-shaped shades). (b) Contour mapping of material's modulus in the same region. Coloured scale corresponds to modulus values as shown in the scaling appearing on the right side.

References

- [1] A.V. Kolobov, S.R. Elliott, *Adv. Phys.*, 40, 625 (1991).
- [2] Y. Hirose, H. Hirose, M. Morisue, *Phys. Status Solidi*, 69, K177 (1980); M. N. Kozicki, M. Park, M. Mitkova, *IEEE Trans. Nanotech.*, 4, 331 (2005).
- [3] F. Kyriazis, A. Chrissanthopoulos, V. Dracopoulos, M. Krbal, T. Wagner, M. Frumar and S.N. Yannopoulos, *J. Non-Cryst. Solids*, *in press*.
- [4] T. Wagner, E. Mañriquez, J. Fernández-Pena, J.M. González-Leal, P.J.S. Ewen and S.O. Kasap, *Philos. Mag. B*, 79, 223 (1999).
- [5] M.L. Trunov, *J. Phys. D: Appl. Phys.*, 41, 074011 (2008).

About The Mixed Alkali Effect

A. Angelopoulou^{1,2*}, V. Montouillout^{3,4}, D. Massiot^{3,4} and G. Kordas^{1,2}

¹*Sol-Gel Laboratory, Institute of Materials Science, NCSR "DEMOKRITOS", 15 310 Aghia Paraskevi Attikis, Greece*

²*Department of Materials Science, School of Natural Sciences, University of Patras, 26 500 Patras, Greece*

³*CNRS, UPR3079 CEMHTI, 1D avenue de la Recherche Scientifique, 45071 Orléans cedex2, France*

⁴*Université d'Orléans, Faculté des Sciences, Avenue du Parc Floral, BP 6749, 45067 Orléans cedex 2, France*

*angelopoulou@upatras.gr

Silicate, calcium-silicate, and phosphosilicate glasses of the composition $80 \text{ SiO}_2-(20-x) \text{ Na}_2\text{O}-x \text{ Me}_2\text{O}$ (where $x=0, 10$ and $\text{Me}=\text{Li}$ or K), $48.7 \text{ SiO}_2-26.9 \text{ CaO}-(24.4-x) \text{ Na}_2\text{O}-x \text{ Me}_2\text{O}$ (where $x=0, 12.2$ and $\text{Me}=\text{Li}$ or K), and $46.1 \text{ SiO}_2-2.6 \text{ P}_2\text{O}_5-26.9 \text{ CaO}-(24.4-x) \text{ Na}_2\text{O}-x \text{ Me}_2\text{O}$ (where $x=0, 12.2$ and $\text{Me}=\text{Li}$ or K) have been studied with MAS NMR and MQ-MAS NMR methods. The ^{29}Si MAS NMR analysis of the Na_2O silicate glass revealed two lines attributed to Q_3 and Q_4 . In the $\text{Na}_2\text{O}-\text{K}_2\text{O}$ glass the Q_3 and Q_4 species are preserved while in the $\text{Na}_2\text{O}-\text{Li}_2\text{O}$ glass, three lines were obtained attributed to Q_3 , Q_{4-3} and Q_{4-4} . For the Na_2O calcium-silicate glass, two lines were revealed assigned to Q_2 and Q_1 . In the $\text{Na}_2\text{O}-\text{K}_2\text{O}$ glass, only one line was resolved attributed to Q_2 species while for the $\text{Na}_2\text{O}-\text{Li}_2\text{O}$ glass, two lines were resolved assigned to Q_2 and Q_3 . In the Na_2O phosphosilicate glass, the analysis revealed two lines ascribed to Q_2 and Q_3 . The MQ-MAS NMR in the sodium silicate glass exhibits two Na ionic sites with site 1 ($\delta_{\text{iso}}= 5.1$ ppm, $C_Q= 0.96$ MHz, $\Delta\text{CS}= 20$ ppm), and site 2 ($\delta_{\text{iso}}= 1.9$ ppm, $C_Q= 3.06$ MHz, $\Delta\text{CS}= 20$ ppm). Substitution of Na with Li or K conserves the two sites in these glasses. For the sodium calcium-silicate glass, the analysis revealed only one ionic site which is site 2 ($\delta_{\text{iso}}= 5.4$ ppm, $C_Q= 2.83$ MHz, $\Delta\text{CS}= 17$ ppm). No difference was observed by the substitution of Na with Li or K in these glasses. In the 24.4 Na_2O phosphosilicate glass three ionic sites were obtained (Fig.1) with: site 1 ($\delta_{\text{iso}}= 6.0$ ppm, $C_Q= 1.4$ MHz, $\Delta\text{CS}= 20$ ppm), site 2 ($\delta_{\text{iso}}= 6.8$ ppm, $C_Q= 2.6$ MHz, $\Delta\text{CS}= 20$ ppm), site 3 ($\delta_{\text{iso}}= 6.6$ ppm, $C_Q= 1.2$ MHz, $\Delta\text{CS}= 1$ ppm). The substitution of Na with Li or K resulted in the absence of the third and most ionic site, which is probably associated with the presence of phosphorus in the glassy network.

The existing theories [1-6] on the MAE, consider not only the alkali ions content but they also pay attention on the glassy network. During our work, we studied three different glassy systems. For each one we observed a different structure of the glassy network and for each network we observed a different alkali ion environment. Under these conditions, there should be a different mixed alkali effect theory, to explain the existing ionic environment for each one of the above glassy systems. Since there is only one mixed alkali effect, it should be independent of the glassy structure and depend only on the alkali ion concentration. Moreover, the 2D results (summarized in Table I) for each glassy system illustrate that the ionic environment is, more or less, the same during the substitution of Na^+ by K^+ or Li^+ . In silicate glasses, small changes are observed in C_Q values for each ionic site indicating a similar ionic environment during the substitution of alkali ions with similar charge (Na^+ , K^+ , Li^+) and small deviations ionic radius ($\text{K}^+ > \text{Na}^+ > \text{Li}^+$). In the calcium-silicate glasses the same observation is experienced. As for the phosphosilicate glasses, the mixed alkali effect leads to the absence of ionic site 3 from the Na-K and Na-Li glasses, but the remaining sites 1 and 2 have identical C_Q values indicating a similar ionic environment, as well. This similarity in the ionic environment indicates that alkali migration is not experienced thus, the vacant sites model [7] cannot be used to explain the mixed alkali effect in case of similar (in charge and ionic radius) alkali ions such as Na^+ , K^+ , and Li^+ , since the vacant sites produced from Na^+ ions movement are available both to potassium and lithium ions.

The theoretical simulations (using the G03W and Chem3D) provided a number of different structures (Fig.1) which reproduce the experimental work reasonably, thus resulting in a representation of the silicate, calcium-silicate, and phosphosilicate glassy network of intermediate or median range order. For the calculation of the NMR parameters including isotropic chemical shift δ_{iso} , and quadrupolar coupling constant C_Q , literature reference values were used as well as some new values proposed by this work. The new reference values come from the optimization of $\text{Si}(\text{Q}_n)$ silicate species as well as tetrahedral, hexahedral, and octahedral structures of hydrated Na^+ ions, $[\text{Na}(\text{H}_2\text{O})_4]^+$, $[\text{Na}(\text{H}_2\text{O})_6]^+$, and $[\text{Na}(\text{H}_2\text{O})_8]^+$.

WE2

P47

Table II. Parameters of the ^{23}Na MQ-MAS NMR spectra are resulting from computer simulation.

SAMPLE	δ_{iso} ppm	C_Q MHz	Δcs ppm	%	Na^+ ionic site
Si-Na	5.1	1.0	20	9.2	site 1
	1.9	3.1	20	90.8	site 2
Si-Na-K	6.1	1.4	15	1.5	site 1
	8.7	3.0	15	98.5	site 2
Si-Na-Li	-2.7	1.6	15	9.1	site 1
	-2.9	2.9	15	90.9	site 2
Si-Ca-Na	5.4	2.8	17	100	site 2
Si-Ca-Na-K	10.7	2.99	17	100	site 2
Si-Ca-Na-Li	5.7	2.9	17	100	site 2
45S5-Na	6.0	1.4	20	36.1	site 1
	6.8	2.6	20	62.5	site 2
	6.6	1.2	1	1.4	site 3
45S5-Na-Li	3.3	1.4	20	37.5	site 1
	2.8	2.6	20	62.5	site 2

J. O. Isard, J. Non-Cryst. Solids, 1, 235 (1969).

B. I. Markin, Struct. Glass, 1 209 (1958) .

R. J. Charles, J. Am. Ceram. Soc., 48, 432 (1965).

B. Lengyel and Z. Boskay, Z. Physik. Chem. 203, 93 (1954); 204, 157 (1955); 223 (1963) 49, 186.

G.N. Greaves, K.L. Ngai, J. Non-Cryst. Solids, 172-174, 1378 (1994).

W.A. Weyl and E.C. Marboe, The constitution of glasses, Vol.II Parts I and II (Interscience, New York 1962).

Malcolm D. Ingram, The Mixed Alkali Effect in Glass: A puzzle solved?, Department of Chemistry, University of Aberdeen, Aberdeen, AB24 3UE, UK.

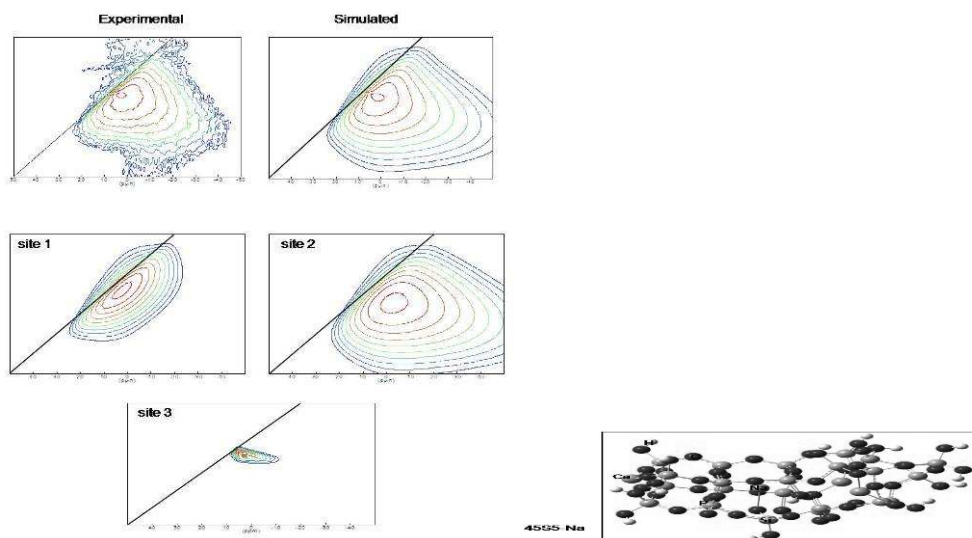


Fig. 1. ^{23}Na MQ-MAS NMR simulated and experimental spectra of the 24.4 mol% Na_2O oxide composition and corresponding theoretical structure.

Modeling Indentation of Porous and Inhomogenous Materials

V. Gountsidou* and H. M. Polatoglou

Physics Department, Aristotle University of Thessaloniki

**ikovou@auth.gr*

There is recently a major interest in the discovery of new materials for industrial and commercial applications and especially for the multifunctional ones. A large range of applications, e.g. athletic equipment, insulation have a cellular structure that optimizes performance for their particular requirements.

Instruments used for the development and study of materials in micro and nanoscale are generally expensive and their utilization is hindered by many unexpected factors.

Indentation is a widely used non-destructive method for examining the mechanical properties of materials. It involves penetration of a specimen by a very small load using a high precision instrument, which records the load and displacement continuously. With computer-aided programs it is possible to achieve virtual indentation. There is a development of analytical models by which the load-displacement data can be used to determine modulus, hardness and other mechanical properties. Structures can be modeled in any desirable shape or dimensions, with one or more layers and with linear or nonlinear materials. Complicated porous bulk crystals [1] and crystals including holes filled with different materials cannot be studied reliably with classical continuum methods. Using finite element analysis one can study a non-random pore geometry varied to achieve different pore shapes and sizes, analyse the effect of the porosity parameters on stress concentrations, improve the mechanical properties of porous structures [2] for better reliability and performance and come to interesting conclusions for the manufacture of products.

In modelling indentation a prescribed load is applied on the upper surface of a spherical indenter which is in contact with the top of the specimen. The depth of penetration (displacement) in the specimen is measured during the application of the load to the indenter. With this process load-displacement curves can be estimated. The bulk crystal is a rectangular containing no hole and the indenter is spherical as shown Figure 1.

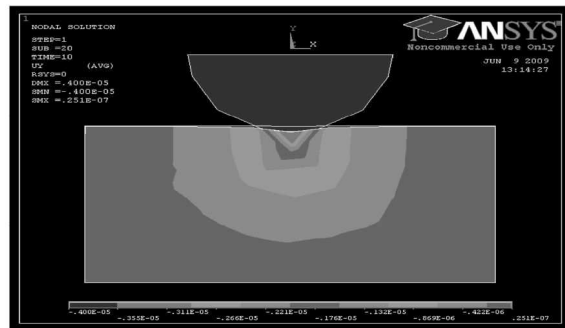


Fig.1. Contour plot of the y-displacement in a model without holes

In the above model a hole can be inserted in the centre of it or in any desired place. In the example beneath this hole is filled with a material harder than that of the bulk crystal as depicted in Figure 2.

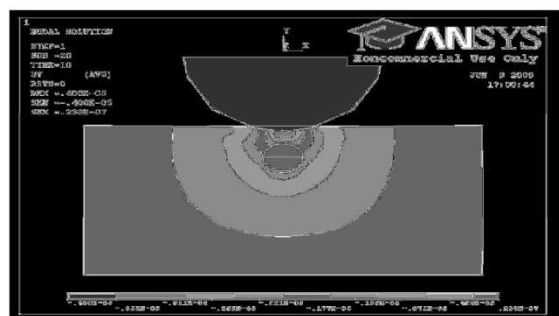


Fig.2. Contour plot of the y-displacement in a model with a hole placed near the top of it filled with a harder material.

For a variety of models according to the number of holes, the nature of the material with which they are filled and the position of them, load–displacement curves can be plotted. The comparison of three of them is depicted in Figure 3. The first plot is for a material with no hole, while the second and the third ones for materials with a hole placed in the centre filled with material harder than that of the bulk crystal. The second one is 5 times harder than the third.

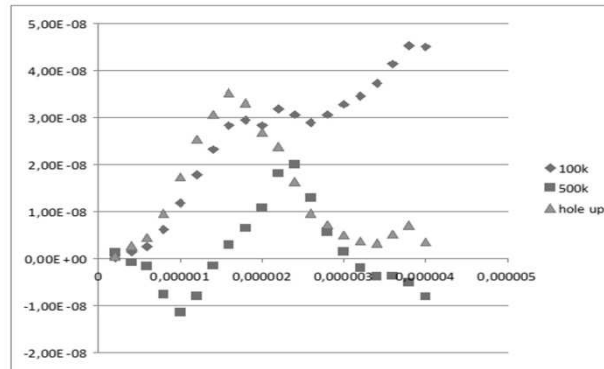


Fig. 3 Comparing the differences in the load-displacement plots

The purpose of the present work is through computer indentation experiments and with the help of careful modeling using the F.E.A. method [3] to reveal specific properties of porous materials or inhomogenous. In particular we obtain the load-displacement curves and examine how the shape reflects the size and the position of the underlying pores and the nature of the material. An extensive F.E.A. analysis and study of the spherical indentation can lead to a creation of a database of load-displacement curves for classes of such materials.

- [1] Gibson, L. J. and Ashby Pergamon Press, Oxford, (1988).
- [2] N. J. Mills and A. Gilchrist, Cellular Polymers 19, (2000) 389-412.
- [3] Chen. Zhangxin, Springer Verlag Berlin Heidelberg (2005).

Mechanical properties of collagen fibrils

T.P. Biros^{*1}, E.C. Aifantis^{1,2}, K.Y. Xu^{3,2}, R. Ballarini⁴, S.J. Eppel⁵

¹ *Laboratory of Mechanics and Materials (LMM) General department, Polytechnic School, AUTH, Greece*

² *College of Engineering, Michigan technological University, Houghton, MI 49931 USA*

³ *Department of Mechanics, Shanghai University, 99 Shanga Road, Shanghai 200444, China*

⁴ *Department of Civil Engineering, Case Western Reserve University, Cleveland, Ohio 44106, USA*

⁵ *Department of Biomedical Engineering, Case Western Reserve University, Cleveland, Ohio 44106, USA*

*birotheo@yahoo.com

Collagen is a unique material. It takes part in the structure of vertebrates and moreover in other species like insects, reptiles, ... so we can say that it is the corner stone of life. Twenty eight known categories until today, with about 80 distinct molecules, create a range of molecules of collagen which combined with other substances construct a diversity of materials unique in properties. Collagen takes part in the construction of bone, eye cornea, skin, teeth, cartilages, arteries and veins. Also it can be found in the species in sea like olothourio, fishes, also in insects, reptiles and others.

It is interesting to build new materials for medicine purposes, like artificial bone, artificial skin, artificial valves or new materials that biomimick the way collagen builds the different tissues, to make new structures in different applications. So it is very important to understand the elastic behavior of collagen.

In this approach, collagen is assumed as continuum material. For all continuum bodies the basic laws of motion, conservation of mass, balance of momentum and energy and principle of entropy, are valid irrespective of internal structure. Different bodies having the same mass and geometry respond differently to identical external effects. These differences in behavior for the same external effects arise from different internal structure. To overcome this problem we should introduce a constitutive law which approximates the physical behavior of a real material under specific conditions. The constitutive equations give the stresses as a function of the deformation history of the body in terms of other field functions, such as strains and temperature.

The constitutive equation for collagen can be obtained by using two different methods; the statistical mechanics approach and the phenomenological approach. The statistical mechanics or molecular approach concern with the microscopic structure of the material, while the phenomenological approach, which concern with the macroscopic nature of the material, try to fit mathematical equations to experimental data.

In this approach used the potential function, which is purely elastic in origin, and is referred in bibliography as strain energy density function or stored energy function. There are two types of strain energy function representation that are commonly used in the literature; one it is expressed in terms of the strain invariants and the other is represented by stretch ratios. Collagen can be obtained as hyper elastic material or Green-elastic material which postulates the existence of a Helmholtz free-energy function Ψ which is defined per unit reference volume rather per unit mass. For the case $\Psi = \Psi(\mathbf{F})$ where \mathbf{F} is the deformation tensor or some other strain tensor the Helmholtz free-energy function is referred to as the strain energy function or stored energy function.

A hyperelastic material is defined as a subclass of an elastic material if the response functions \mathbf{G} and \mathbf{g} have the expressions

$$\mathbf{P} = \mathbf{G}(\mathbf{F}) = \frac{\partial \Psi(\mathbf{F})}{\partial \mathbf{F}} \text{ and } \boldsymbol{\sigma} = \mathbf{g}(\mathbf{F}) = J^{-1} \frac{\partial \Psi(\mathbf{F})}{\partial \mathbf{F}} \mathbf{F}^T \text{ where } \mathbf{P} \text{ is the second Piola Kirchoff tensor and } \boldsymbol{\sigma} \text{ is}$$

the Cauchy stress tensor.

If a scalar valued tensor function is an invariant under rotation, it may be expressed in terms of the principal invariants of its arguments (representation theorem of invariants). So the strain energy function can be expressed as a set of independent strain invariants of the symmetric Cauchy-Green tensors.

Also the strain energy function can be expressed in terms of principal stretches. According to incompressibility and isotropy of material we can obtain a relation between Cauchy stress and strain energy function.

Comparisons of the model with experimental data illustrate the efficiency of the constitutive model and the dependence of the four material parameters.

[1] H.X. Αῦφαντῆς Μηχανικὴ τῶν συνεχῶν μέσῶν Θεσσαλονίκη 2006.

[2] G. A. Holzapfel, Nonlinear Solid mechanics Wiley, 2000.

[3] C. Truesdell, W. Noll The Non-Linear Field Theories of Mechanics ed. S.S. Antman Springer 2004.

- [4] Z.Liu,B.N. Smith, H Kahn, R.Ballarini, S.J. Eppell Mechanical testing of Hydrated collagen nanofibrils Using MEMS technology Nanotechnology, 2006. IEEE-NANO 2006. Sixth IEEE Conference on Volume 1, Issue , 17-20 June 2006 Page(s): 177 – 180.
- [5] Nano Measurements with micro devices : Mechanical properties of hydrated collagen fibrils S.J Eppell, B.N Smith, H Kahn, and R Ballarini J R Soc Interface. 2006 February 22; 3(6): 117–121. Published online 2005 November 29. doi: 10.1098/rsif.2005.0100.
- [6] Logarithmic Strain Measure Model for Constitutive Equations of Hyperelastic Collagen Materials K.Y.Xu & A.C. Aifantis (submitted).

The Influence of Thermal Treatment and Ambient Atmosphere on the Electrical Conductivity of Polypyrrole and Polypyrrole/5%w/w TiO₂ Nanocomposite

K. Emmanouil¹, E. Vitoratos^{1*}, E. Dalas² and S. Sakkopoulos¹

¹Department of Physics, University of Patras, 26500 Patras, Greece

²Department of Chemistry, University of Patras, 26500 Patras, Greece

*vitorato@physics.upatras.gr

Conductive polypyrrole (PPy) is a conjugated polymer, in which π -electrons delocalized along the polymer chains ensure good electric conductivity and interesting optical properties. PPy exhibits high thermal stability and strong absorption along the visible spectrum to near infrared. However, PPy does not have good photoconductive properties for two reasons: the production of free carriers is low and the carrier mobility is low due to the disordered structure of polymers. Hybrid polymer/inorganic nanoparticle systems exhibit interesting electronic and optical properties improving the understanding of the individual characteristics of these two different classes of materials. With the expectation of using these hybrid systems as the active elements in solar cells, the charge separation upon photoexcitation is considered on the basis of the charge transport and transfer to the electrodes to constitute the photocurrent. The mechanisms of charge generation, separation and transport upon optical excitation are different in inorganic nanoparticles and in the disordered polymer chains. The results upon photon absorption in the polymer and (or) in the nanoparticle are shown in Fig.1. [1].

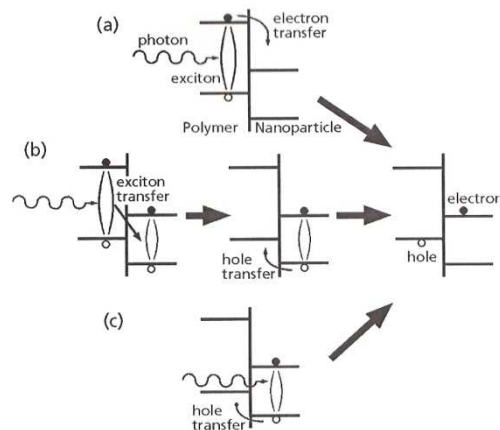


Fig.1. (a) Photon absorption in the PPy is followed by an electron transfer in the TiO₂ nanoparticle (acceptor). (b) absorption in the PPy is followed by an exciton transfer to the TiO₂ nanoparticle, followed by the hole transfer to the PPy and (c) absorption in the TiO₂ nanoparticle is followed by hole transfer to the PPy.

As transport in the polymer is controlled by the chain disorders, which increase with heating in the presence of the oxygen and the moisture of the atmospheric air, the conductivity of pristine PPy and PPy/5% w/w TiO₂ nanocomposite was studied under different heating times at different temperatures in the presence of inert He and atmospheric air.

The main results may be summarized in the following lines:

The slope of conductivity versus temperature curve is lower for PPy/5% w/w TiO₂ samples, than for pure PPy samples. From $(0.020 \pm 0.001) \text{ Scm}^{-1}$ for PPy/5% w/w TiO₂ under ambient atmosphere, becomes $(0.045 \pm 0.001) \text{ Scm}^{-1}$ for PPy samples. A possible explanation is that TiO₂ being a semiconductor of wider energy gap than PPy, makes more difficult the thermal excitation of carriers. On the other hand in He atmosphere the corresponding slopes are $(0.024 \pm 0.001) \text{ Scm}^{-1}$ for PPy/5% w/w TiO₂ and $(0.040 \pm 0.001) \text{ Scm}^{-1}$ for PPy samples. The above experimental results indicate that the factor which differentiates the conductivity trace is the presence of TiO₂ nanoparticles. There is a slight hysteresis as measurements are done from 300 K to 100 K direction and then from 100 K to 300 K.

At prolonged (30 min) stay of the samples at 100 K, under ambient atmosphere, the conductivity exhibits a scattering of the experimental points but it is obvious a tendency of increase. For samples under He atmosphere, the conductivity increases for the first 10 minutes and reaches saturation there after. This behaviour indicates that for prolonged stay at 100 K, the PPy plays the dominant role, which is affected

by the oxygen and the moisture of the air. The increase of the conductivity under He for the first ten minutes, indicates that the “sort range order” of polypyrrole increases.

Conductivity, under prolonged stay (350-700 min) of all the samples at 380 K under ambient or He atmosphere, exhibits also a maximum the first minutes, indicating two competing mechanisms.

Further experimental work may provide useful information about the model of conductivity, the mechanisms that affect the quality of conduction in the polymer/semiconductor nanocomposite, as well as the aging processes of the material[2].

References

- [1] Malhotra Bansi: *Handbook of Polymers in Electronics*, Ch.11: Narayan K.S.: “Nanoparticle-Dispersed Semiconducting Polymers for Electronics”, pp.341-345. Rapra Technology Limited, Shropshire U.K. 2002. ISBN: 1-85957-438-6.
- [2] Sakkopoulos S., Vitoratos E., Dalas E., *Synthetic Metals* 92, 63 (1998).

Acknowledgments

This work was partially financed by the Research Committee of the University of Patras under the frame work of the “Karatheodori” program for basic research strengthening.

Spectroscopic (Mössbauer, XANES and FTIR) and Thermal Investigation of Greek Bauxites from the Parnassos-Ghiona Active Mining Area

P. Gamaletsos^{1*}, A. Godelitsas¹, A. P. Douvalis², J. Göttlicher³, T. Zorba⁴, K. Chrissafis⁴,
K.M. Paraskevopoulos⁴ and T. Bakas²

¹ Faculty of Geology and Geoenvironment, University of Athens, 15784 Zographou, Greece

² Department of Physics, University of Ioannina, 45110 Ioannina, Greece

³ Institute for Synchrotron Radiation (ISS), Synchrotron Radiation Source ANKA Forschungszentrum Karlsruhe, Germany

⁴ Physics Department, Solid State Section, Aristotle University of Thessaloniki, 54124 Thessaloniki, Greece

*platon_gk@geol.uoa.gr

Greece is the 12th largest producer of bauxite in the world (2.2×10^6 tons in 2008 according to U.S. Geological Survey). The exploitation of deposits, hosted in Mesozoic limestones of central Greece [1], is performed by three Greek mining companies (Aluminium of Greece S.A., S&B Industrial Minerals S.A. and ELMIN Hellenic Mining Enterprises S.A.) whereas there is also an Al metallurgical plant owned by Aluminium of Greece S.A.

The mineralogy of Greek bauxites is not particularly variable; diaspore and/or boehmite (AlOOH polymorphs), hematite (Fe₂O₃), goethite (FeOOH) and anatase (TiO₂) are the major phases in the case of typical Fe-enriched (red) bauxite containing 57 wt.% Al₂O₃. Of special interest is the high quality Fe-depleted (white) bauxite composed of diaspore and TiO₂ polymorphs, i.e. anatase and rutile, which contains 80 wt.% Al₂O₃. In this case the partitioning and speciation of the main metal impurities (Fe: 17500 ppm, Cr: 1235 ppm) is critical. Here, we demonstrate the combined application of spectroscopic techniques for the detailed characterization of Greek industrial bauxite.

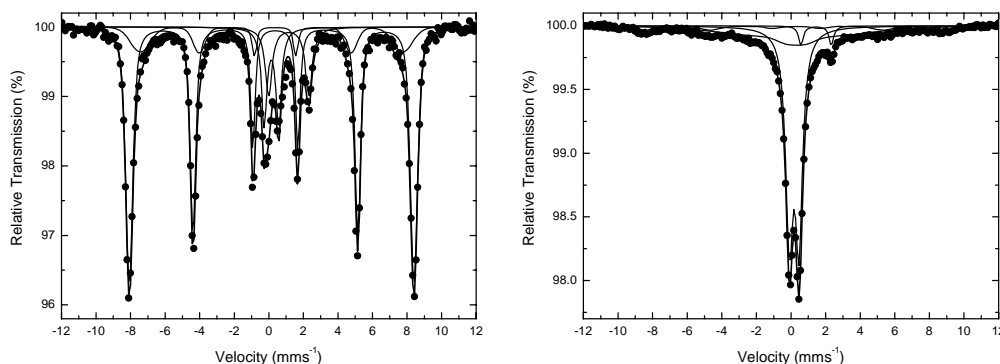


Figure 1. Characteristic ⁵⁷Fe Mössbauer spectra of red (left) and white (right) Greek bauxites recorded at 300 K.

Though bauxite is a quite important industrial material, the number of publications dealing with the determination of the iron mineralogy using ⁵⁷Fe Mössbauer spectroscopy in the literature is rather small and includes mainly investigations on Jamaican bauxite [2] and on geochemical standard bauxite BX-N from Brignoles, France [3]. There are no reports in the literature until now on the examination of the iron mineralogy in Greek bauxites using the ⁵⁷Fe Mössbauer spectroscopy and the relevant reports using other spectroscopic techniques are rather limited as well. In this work a number of red and white bauxite samples, taken from the deposits of central Greece, has been investigated using a set of spectroscopic techniques (⁵⁷Fe Mossbauer, XANES/EXAFS and FTIR) in combination with thermal analyses.

In particular, our investigation using ⁵⁷Fe Mössbauer spectroscopy (Fig. 1) revealed that iron occurs predominantly as Fe³⁺ in hematite and goethite, as well as in the framework of the diaspore and/or boehmite in smaller quantities. On the other hand the presence of Fe²⁺ could be associated with detrital micron-sized Cr-spinel grains as well as with minor aluminosilicate and silicate phases.

Particular emphasis was given to the study of Cr in white (Fe-depleted) bauxite by means of Synchrotron-based X-ray absorption spectroscopy. The corresponding spectra shown in Fig 2 were recorded at the X-ray beamline of the Synchrotron Radiation Laboratory for Environmental Studies (SUL-X) of the synchrotron radiation source ANKA (Forschungszentrum Karlsruhe / D) and confirmed the existence of Cr³⁺, most probably in the structure of the diaspore, in accordance with previous results using Raman spectroscopy [4].

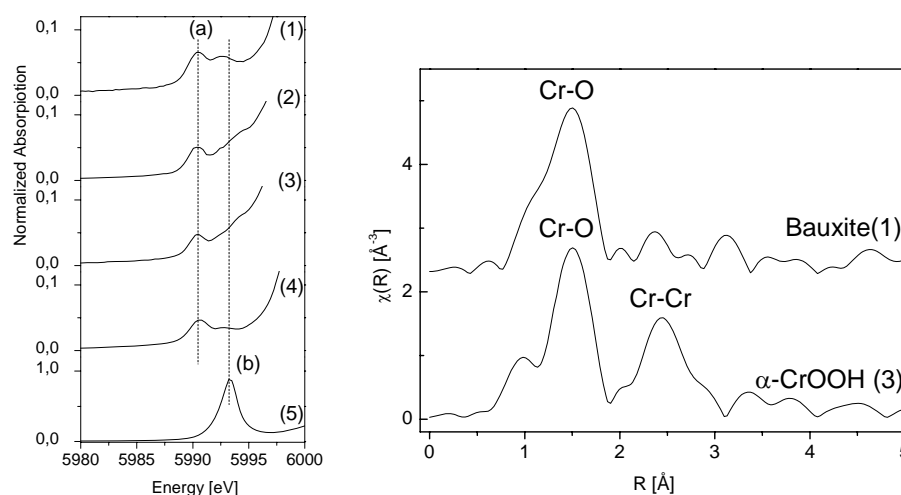


Figure 2. Cr-K edge XANES (1) and reference compounds for Cr(III) (grimaldite α -CrOOH (2), FeCr_2O_4 (3), $\text{Cr}(\text{NO}_3)_3$ (4) and Cr(VI) ($\text{K}_2\text{Cr}_2\text{O}_7$ (5)) as well as the Fourier transform of Cr K-edge EXAFS of white Greek bauxite

Previous studies have been devoted to the investigation of the vibrational properties of diaspore [5], whereas far-infrared spectroscopy (FIR) has been used to distinguish alumina phases [6] as well. The FTIR spectra appearing in Fig. 3 confirmed the abundance of hydrous components, according also to thermal analyses (see Fig. 3), represented mainly by OH⁻ in hydroxylated mineral phases (AlOOH polymorphs and FeOOH) and showed significant differences between Fe-enriched and Fe-depleted bauxite. Differences between the theoretical vibrational spectra of AlOOH polymorphs and the observed ones, can be attributed to metal ion impurities (Fe^{3+} and Cr^{3+} according to Mössbauer and XANES) modifying the AlO_6 octahedra of the structure. The bauxitic diaspore and boehmite show different spectra because they are, in fact, Fe-Cr-containing AlOOH compounds and not pure AlOOH.

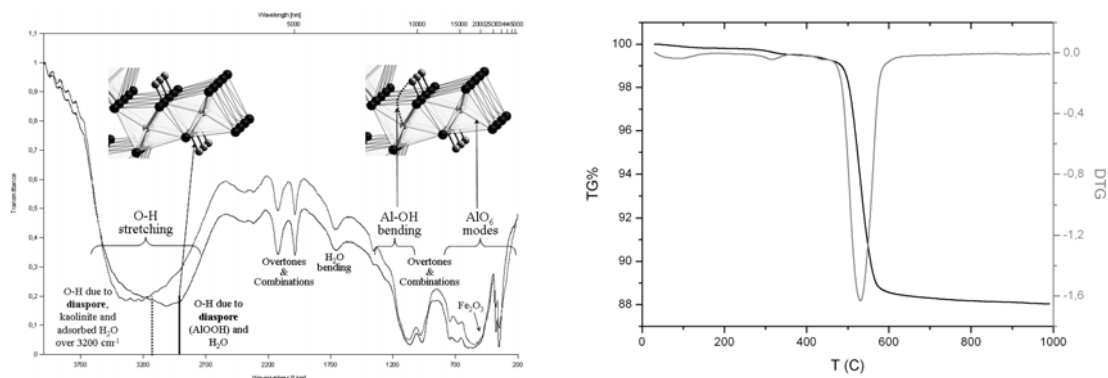


Figure 3. FTIR spectra of red (upper) and white (lower) Greek bauxite, using CsJ pellets, as well as the corresponding thermal analysis of the red bauxite sample (right image)

References

- [1] Valetton I, Biermann M., Reche R. and Rosenberg F., *Ore Geology Rev.* 2, 359 (1987).
- [2] Kirwan L.J., Deeney F.A., Croke G.M. and Hodnett K, *Int. J. Miner. Process.* 91, 14 (2009).
- [3] Murad E., *Miner. Engineer.* 18, 984 (2005).
- [4] Gamaletsos P., Godelitsas A., Chatzitheodoridis E. and Kostopoulos D., *Geol. Soc. Greece Bull.* 40, 739 (2007).
- [5] Demichelis R., Noel Y., Civalleri B., Roetti C., Ferrero M. and Dovesi R., *J. Phys. Chem.* 111, 9337 (2007).
- [6] Ruan H.D., Frost R.L., Klopogge J.T. and Duong L., *Spectrochim. Acta Part A* 58, 265 (2002).

Acknowledgments

The provision of the bauxite samples used for this study from the Greek mining companies Aluminium of Greece S.A., S&B Industrial Minerals S.A. and ELMIN Hellenic Mining Enterprises S.A. is gratefully acknowledged.

Fe Distribution And Speciation In Human Nails

E. Mavromati¹, M. Katsikini^{1*}, F. Pinakidou¹, E. C. Paloura¹, D. Gioulekas², D. Grolimund³

¹ Aristotle University of Thessaloniki, School of Physics, 54124 Thessaloniki, Greece

² Aristotle University of Thessaloniki, Medical School, 54124 Thessaloniki, Greece

³ Swiss Light Source, Paul Scherer Institut, 5232 Villigen, Switzerland

*katsiki@auth.gr

Micro - X Ray Fluorescence (μ -XRF) and Fe-K edge micro-X Ray Absorption Near Edge Structure (μ -XANES) spectroscopies are applied for the study of the distribution and the spatially-resolved bonding environment of Fe in human nails. The main constituent of the nail is the organic matrix which is formed by keratin, a sulphur-rich structural insoluble protein. Human nails contain also small amounts of essential metallic elements like Ca, Fe, Cu, Zn and for this reason they are used to monitor the essential metal concentration in the human body. Lack or excess of some of these elements as well as the local bonding environment of Fe in human tissues has been related to disorders or diseases as well as to environmental and nutritional factors.[1] XRF spectroscopy is a well suited for the quantitative analysis of elements with $Z>11$. On the other hand, XANES spectroscopy is a well-established technique for the investigation of the bonding environment of both metallic and non metallic elements in samples of biogenic nature.[2] The XANES spectra of the Fe containing compounds are often characterized by a peak before the absorption edge (pre-edge peak) which is attributed to forbidden $1s \rightarrow 3d$ electronic transitions.[3] The pre-edge peak is expected to be sensitive to the local geometry changes in the coordination of Fe in the human nail. Additional information can be extracted from the position of the absorption edge (E_{abs}) which is strongly related to changes in the valence and bonding environment of the Fe atom.[4]

The studied samples are nail clippings that are collected at the Pulmonary Clinic of the Aristotle University of Thessaloniki with the patient's consensus. The sample H belongs to a healthy 33-year old female donor, while the samples C1 and C2 belong to male donors 79 and 55 years old, respectively, who suffer from lung cancer. Prior to the measurement the samples were cleaned with acetone, alcohol and deionized water in an ultrasound bath.

The μ -XRF maps and μ -XANES spectra were recorded at the μ XAS beamline of the Swiss Light Source Synchrotron Radiation Facility. The beamline has an undulator source and is equipped with a double Si(111) crystal monochromator. A Kirkpatrick - Baez mirror system focuses the beam to the $2 \times 2 \mu\text{m}$ size. The sample was positioned at 45° to the beam and at 45° to a single element Si detector, on a stage that is moved micrometrically with proper step motors. The μ -XRF maps were recorded using photons of 7150eV excitation energy. The μ -XANES spectra were recorded at the Fe-K edge from sample spots with different iron concentration. The spectra of a hematite (Fe_2O_3) and a magnetite (Fe_3O_4) powder sample, recorded in the transmission mode, were used as reference.

Typical $400 \times 400 \mu\text{m}$ XRF maps from the H and C1 samples, recorded with $2 \mu\text{m}$ step using the Fe K_α fluorescence, are shown in Fig. 1. The maps are normalized to the maximum Fe K_α fluorescence intensity and they reveal the tendency of Fe to segregate. A more detailed $25 \times 25 \mu\text{m}$ map that is recorded with a $1 \mu\text{m}$ step around a local maximum of the Fe concentration is

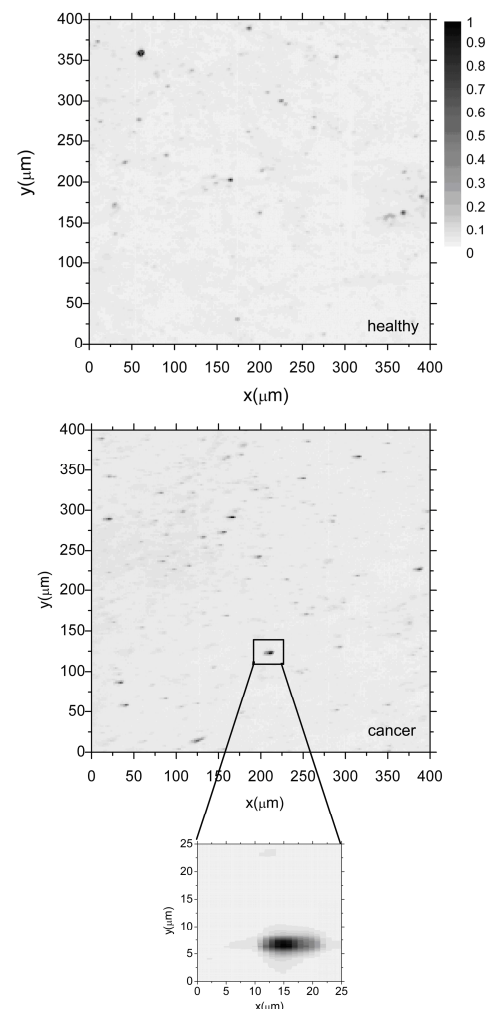


Fig. 1: μ -XRF maps of the distribution of Fe in a healthy nail (sample H) and a nail from a donor who suffers from lung cancer (sample C1). A $25 \times 25 \mu\text{m}$ map recorded with $1 \mu\text{m}$ step around a local maximum of the Fe concentration is shown in the bottom.

WE2

P52

also included in Fig. 1 and reveals that this particular Fe-rich inclusion is about 15 μ m large.

In order to detect any concentration related changes in the bonding environment and valence of Fe, we resorted to μ -XANES spectroscopy. The μ -XANES spectra that were recorded from regions with different Fe concentration, i.e. from a spot with low Fe concentration and from a local maximum (with about 6 times higher Fe concentration) are shown in Fig. 2. All the spectra are characterized by a pre-edge peak (P). The spectra were fitted using a sigmoidal function (its inflection point corresponds to E_{abs}) and a number of Gaussians to simulate transitions to final bound states with p component (above the E_{abs}).[5] An indicative fitting is shown in Fig. 2. In order to isolate the pre-edge peak and reveal its characteristics more clearly, the sigmoidal function was subtracted from the XANES spectra and the peak P was fitted using Gaussian functions. A representative fitting of peak P is shown in the inset of Fig. 2.

The E_{abs} of the spectra recorded from the Fe-rich and Fe-depleted regions of all studied nails, ranges from 7122.1 - 7123.1eV i.e. it exhibits a violet shift compared to the E_{abs} of Fe_2O_3 . Since, the oxidation state of Fe in hematite is +3, the violet shift of E_{abs} cannot be explained by an increase of the valence of Fe rather than a change in its ligation and/or bonding geometry. The most significant variation in E_{abs} is detected in sample H where the E_{abs} of a spectrum recorded from the "Low-Fe" region is found at 7122.1 eV while that of the spectrum recorded from the "High-Fe" region is violet shifted by 0.8eV. Contrary to that, E_{abs} does not vary significantly in the nails C1 and C2 of the cancerous donors. The most striking differences in the μ -XANES spectra recorded from the "High Fe" and "Low-Fe" regions is detected in the pre-edge region. The peak P of μ -XANES spectra of all studied nails was fitted using two Gaussian functions except from the peak recorded from the "Low Fe" region of sample H where three Gaussian functions were necessary for the fitting. The peak P2, that is assigned to Fe^{+3} in distorted or symmetric octahedral sites, is present in the pre-edge peak in the XANES spectra of all studied nails.[3] Octahedrally coordinated Fe^{+2} is detected only in the "Low-Fe" region of the sample H, where the peak P1 that appears at 7111.6eV becomes important. Finally, the peak P3 that appears at 7115.5 eV in all recorded spectra is related to Fe clustering (mixing of 3d orbitals with d orbital of neighboring Fe atoms).[6] Furthermore, the total area under the pre-edge peak (excluding peak P3 which is not related to the immediate ligands of Fe) depends linearly on the E_{abs} indicating that the change of the octahedral environment of Fe towards a more symmetric configuration is possibly related to the change of its ligation.

In conclusion, μ -XRF and μ -XANES were used for the study of human nails. μ -XRF mapping with 2 μ m spatial resolution reveals the tendency of Fe to segregate in Fe-rich regions with about 6 times higher concentration compared to the rest of the sample. The μ -XANES spectra recorded at the Fe-K edge from various sample spots have shown that Fe is trivalent and octahedrally bonded in the cancerous samples while in the healthy sample Fe^{2+} is also detected. Additionally, the decrease in the area under the pre edge peak indicates that the octahedral environment around Fe becomes more symmetric causing a violet shift in the position of the absorption edge that might be related to the presence of divalent Fe and/or to alteration of the Fe ligands.

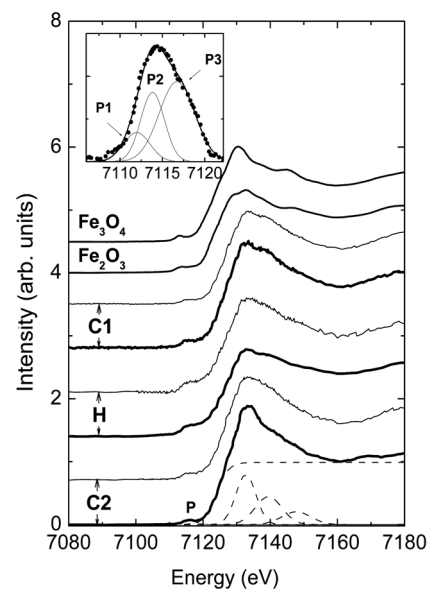


Fig. 2: Fe-K μ -XANES spectra recorded from two different spots with low (thin solid lines) and high (thick solid lines) Fe concentration. The spectra of the reference (Fe_2O_3) and (Fe_3O_4) samples are also shown. A representative fitting of the pre-edge peak (P) is included in the inset.

Acknowledgements The measurements at the SLS were supported by the EC under the 6th FP through the Key Action: Strengthening the European Research Area, Research Infrastructures. Contract n^o: RII3-CT-2004-506008.

References

- [1]. H. C. Hoops, *The Science of the Total Environment*, 7, 71, (1977).
- [2]. S. P. Cramer, *X-ray absorption: Principles, Applications, Techniques of EXAFS, SEXAFS and XANES*, ed. by D. C. Koningsberger and R. Prins, (John Wiley & Sons Inc 1988), ch. 7.
- [3]. T. Westre, P. Kennepohl, J. G. DeWitt, B. Hedman, K. O. Hodgson, E. I. Solomon, *J. Am. Chem. Soc.*, 6297, 119, (1997).
- [4]. S. I. Salem, C. N. Chang, P. L. Lee, V. Serenson, *J. Phys. C: Solid State Phys.*, 11, 4085, (1978).
- [5]. J. Stöhr, *NEXAFS Spectroscopy*, (Springer, Berlin, 1992) p.114.
- [6]. Z. Y. Wu, D.C. Xian, C.R. Natoli, A. Marcelli, E. Paris, A. Mottana, *Appl. Phys. Lett.*, 79, 1918, (2001).

Mechanical Properties of PMMA/Organomodified Montmorillonite Nanocomposites Prepared by *In situ* Bulk Polymerization

A. K. Nikolaidis, D. S. Achilias*, G. P. Karayannidis

Laboratory of Organic Chemical Technology, Department of Chemistry, Aristotle University of Thessaloniki, 541 24, Thessaloniki, Greece

*axilias@chem.auth.gr

Polymer nanocomposites are commonly defined as the combination of a polymer matrix and additives that have at least one dimension in the nanometer range [1]. Polymers reinforced with a small amount of montmorillonite (MMT) clay have attracted a great deal of research interest in the past decade. These nanocomposites exhibit improved mechanical properties, higher thermal stability and better barrier properties. Poly(methyl methacrylate) PMMA/MMT nanocomposites are also of interest due to their reduced flammability, reduced gas permeability and improved thermal and mechanical properties. Moreover, they have good potential to retain excellent optical clarity. Different preparation methods for the PMMA/MMT nanocomposites have been studied, including solution intercalation, *in situ* polymerization, emulsion polymerization, as well as melt intercalation [2]. Among them, dispersing *in situ* polymerization may be the most desirable method for preparing nanocomposites, because the types of nanoparticles and the nature of polymer precursors can vary in a wide range to meet the requirements [3]. In the work reported here, there was an attempt to synthesize PMMA/MMT nanocomposites by *in situ* bulk polymerization. Their structure characteristics were verified by X-ray diffraction analysis (XRD) and FTIR spectrometry. The mechanical behaviour of nanocomposites was comprehensively studied. In particular, tensile properties such as tensile strength, strain at break and tensile modulus were measured. Furthermore, the viscoelasticity of nanocomposites was investigated by measuring storage modulus (E'), loss modulus (E'') and $\tan\delta$, while the glass transition temperature (T_g) was determined from the $(\tan\delta)_{\max}$ value.

For the preparation of the nanocomposites, commercial organically modified montmorillonite clays (OMMTs), Cloisite 15A, Cloisite 25A and Cloisite 30B were used and kindly provided by Southern Clay Products Inc. (Texas/USA). These are MMT modified with a quaternary ammonium salt, which is dimethyl hydrogenated tallow (cationic exchange capacity of 125 meq/100 g clay), dimethyl 2-ethyl hexyl hydrogenated tallow (CEC 95 meq/100 g clay) and methyl tallow bis-2-hydroxyethyl (CEC 90 meq/100 g clay) for Cloisite 15A, 25A and 30B, respectively. In addition, sodium containing natural MMT was used with the trade name Cloisite Na⁺ and CEC = 92.6 meq/100 g MMT. The initial mixture was prepared by dispersing the appropriate OMMT into the monomer methyl methacrylate (MMA) by adequate magnetic and supersonic agitation. The dispersion of the particles in the monomer was homogeneous, as indicated by the high translucency in the visible region. In the final suspension, the initiator benzoyl peroxide (BPO) was added and the mixture was degassed by passing nitrogen and immediately used. Free radical bulk polymerization was carried out by heating each mixture, first at 80 °C for a suitable time period, to get a critical viscosity level. Then the viscous liquid obtained was poured into a mould to finish the polymerization process successively at 40°C for 20h. In each case, standard dumb-bell and rectangular rod-like specimens were prepared by following the afore-mentioned procedure.

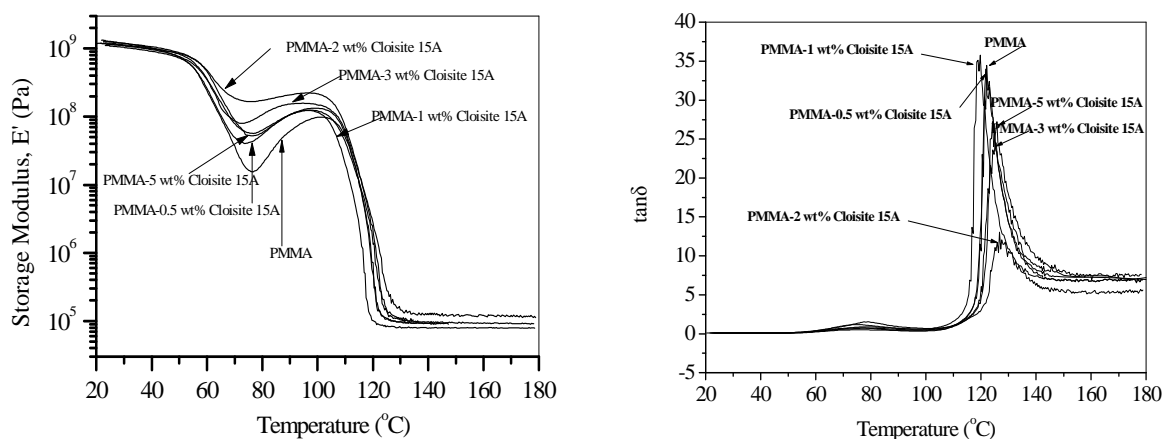
Tensile tests were conducted on an Instron–BlueHill 2 dynamometer at room temperature according to ASTM D638 method. The crosshead speed was set at 5 mm min⁻¹. The effect of the different MMT type and the content of Cloisite 15A on tensile properties such as tensile strength, strain at break and tensile modulus was investigated. The total results of the above study are represented in Table 1. It is obvious that nanocomposites containing Cloisite 15A and Cloisite 25A yielded the maximum values of tensile strength and tensile modulus, probably due to the better compatibility of these MMT types with the organic phase, resulting in a more homogeneous dispersion into the polymeric matrix. Moreover, tensile modulus was increased by increasing Cloisite 15A loading, while both tensile strength and strain at break decreased respectively. These phenomena showed that, although the intercalation of the clay with polymer can increase the stiffness of the hybrid system, the interfacial adhesion between the OMMT and the PMMA molecules is not strong enough to sustain large deformations. As a result, the nanocomposites failed early, and the tensile strength decreased as well.

Thermal mechanical tests were carried out using a Perkin Elmer dynamic mechanical analysis instrument (DMA) in sinusoidal three-point bending mode. The frequency was 1 Hz and the temperature was varied from 25 to 180°C with a scanning rate of 3 °C min⁻¹. The storage modulus (E'), loss modulus (E'') and $\tan\delta$ variations of nanocomposites with temperature were studied, for several MMT types and different amounts of Cloisite 15A.

Table 1. Tensile properties of PMMA/MMT nanocomposites.

Sample	Tensile strength (MPa)	Strain at break (%)	Tensile modulus (GPa)
PMMA	38.06±2.05	4.03±0.36	1.22±0.08
PMMA-1 wt% Cloisite Na ⁺	33.70±2.77	4.07±0.38	1.08±0.05
PMMA-1 wt% Cloisite 30B	38.00±1.81	4.55±0.56	1.25±0.05
PMMA-1 wt% Cloisite 15A	40.00±0.95	3.60±0.29	1.28±0.04
PMMA-1 wt% Cloisite 25A	40.10±0.93	3.90±0.40	1.28±0.03
PMMA-0.5 wt% Cloisite 15A	38.31±1.86	4.51±0.02	1.22±0.19
PMMA-2 wt% Cloisite 15A	32.28±1.19	3.40±0.49	1.28±0.23
PMMA-3 wt% Cloisite 15A	25.38±0.11	2.12±0.18	1.35±0.44
PMMA-5 wt% Cloisite 15A	26.01±0.64	2.20±0.12	1.32±0.38

Fig. 1a reveals that by arising the Cloisite 15A content, at low temperatures, the storage modulus increases as well. The peak observed at the temperature area of 70-80 °C could be attributed to a possible polymerization process of MMA traces remained in specimens, after their preparation. At higher temperatures, the storage modulus rises enough for a content of 2 wt% and 3%wt Cloisite 15A correspondingly. Furthermore, Fig. 1b represents the augmentation of T_g , determined from the $(\tan\delta)_{\max}$ values of nanocomposites, due to the increase of the Cloisite 15A loading.

**Fig. 1.** Storage modulus (E') and $\tan\delta$ of PMMA/MMT nanocomposites containing various amounts of Cloisite 15A.

References

- [1] Mai Y.-W., Yu Z.-Z., Polymer Nanocomposites. (Cambridge England, Woodhead Publishing Limited, 2006).
- [2] Liaw J.-H., Hsueh T.-Y., Tan T.-S., Wang Y. and Chiao S.-M., Polym. Int., 56, 1045 (2007).
- [3] Nese A., Sen S., Tasdelen M.-A., Nugay N., Yagci Y., Macromol. Chem. Phys., 207, 820 (2006).

Bioactivity Studies of Hydroxyapatite based glass-ceramics synthesized by Transferred Arc Plasma (TAP)

E. Roumeli¹, O.M. Goudouri¹, C.P. Yoganand², N. Kantiranis³, V. Selvarajan²,
K.M. Paraskevopoulos^{1*}

¹ Physics Department, Aristotle University of Thessaloniki, 54124 Thessaloniki, Greece
² Plasma Laboratory, Department of Physics, Bharathiar University, Coimbatore-46, India
³ Department of Geology, Aristotle University of Thessaloniki, 54124 Thessaloniki, Greece

*kpar@auth.gr

Bioactive glasses and glass-ceramics have been thoroughly investigated as key materials for bone regeneration, since their bioactivity can be easily controlled by modifying their composition [1]. In the last two decades, remarkable advances in the field of biomaterials have led to the development of bioglasses and bioceramics of various compositions for bone repair and prostheses applications. Plasma technology is an enabling technology, which integrates processes associated with plasma material interaction with manufacturing, adds value to conventional materials and makes new types of materials and material processing techniques possible [2]. The TAP melting method is a process of glass-ceramics preparation in which the raw materials are melted in the plasma and crystallization of the melt occurs while quenching. Such glass-ceramic materials, due to their good mechanical and chemical properties, have been suggested as suitable for biomedical applications. Furthermore, MgO enhances the bioactivity of such materials, yet its excess inhibits the formation of a thick apatite layer during their immersion in SBF [3]. Thus, the aim of the present work was the investigation of the bioactive behavior of the hydroxyapatite/SiO₂-CaO-MgO system as powder and as bulk material.

Hydroxyapatite /SiO₂-CaO-MgO glass-ceramic of the composition 50% hydroxyapatite-50% bioactive glass was produced using the TAP processing method that is extensively described in former papers [2]. In a series of experiments, 50 mg from each sample was compressed to form a 15mm pellet. The in vitro bioactivity assessments were performed by immersing batches of powder and each pellet in c-SBF solution [4] for various immersion periods of time. Fourier Transform Infrared Spectroscopy (FTIR) and Scanning Electron Microscopy (SEM-EDS) were used to characterize all powders and specimens' surfaces before and after the immersion, while XRD studies were also performed.

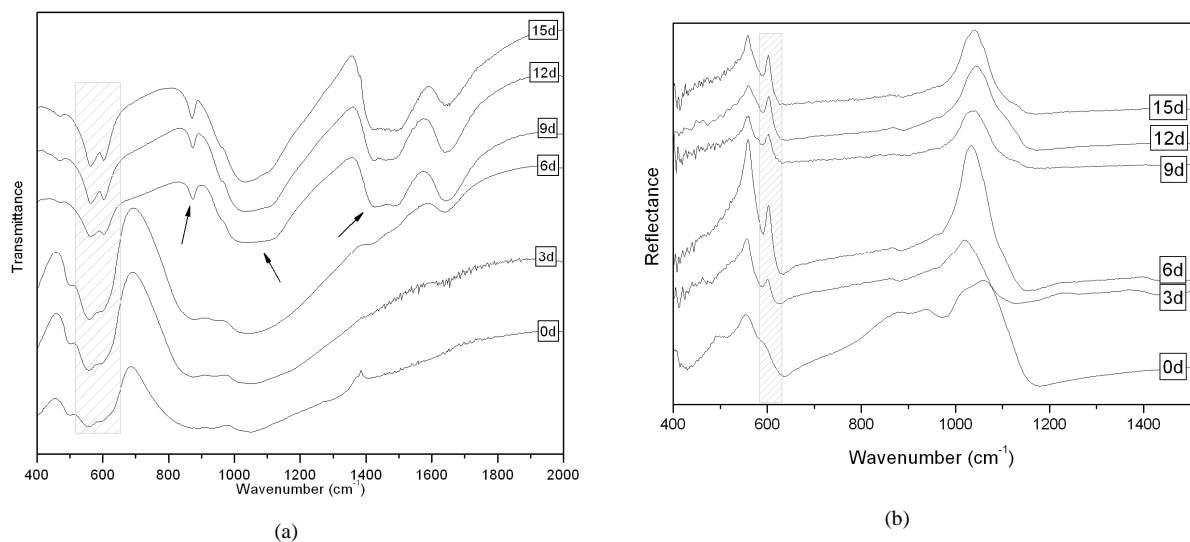
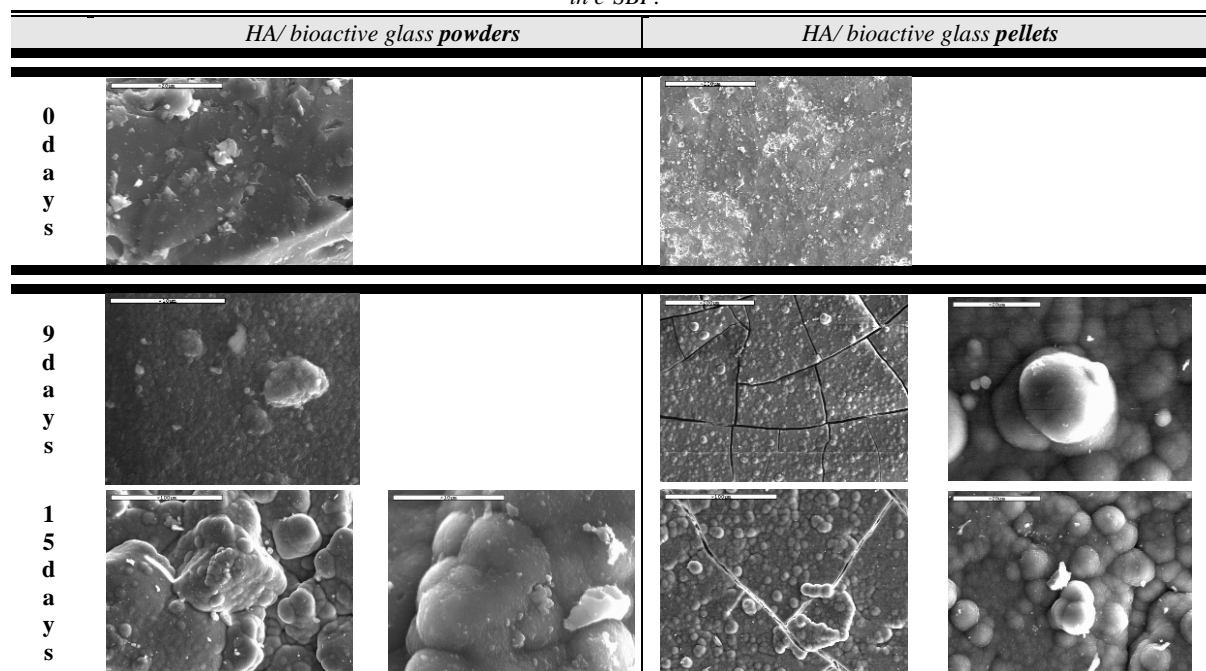


Fig. 1. a) FTIR transmittance and b) reflectance spectra of the HA/bioactive glass as powder and as pellets respectively before and after the immersion in c-SBF for 3-15d.

The *in vitro* bioactivity of the HA/bioactive glass composite as powder and as pellet was studied up to 15 days. In Fig. 1 are presented the FTIR transmittance and reflectance spectra of the composite as powder and as pellet respectively before and after immersion in c-SBF solution. After 6 days of soaking time there is no substantial alteration of the spectra of the powdered samples. However, after 9 days of immersion the spectrum of the composite corresponds to that of pure carbonate hydroxyapatite. In details, the broad peak at 1100-1000 cm^{-1} and the double peak at 604 and 560 cm^{-1} are attributed to the stretching and bending vibrational modes of PO group. Additionally, the double peak at 1500 and 870 cm^{-1} are attributed to CO_3 group of HCAp [5]. Moreover, the FTIR reflectance spectra of the pellets revealed the onset of the apatite formation after the first 6 days of immersion, as there is an enhancement of the peak at 602 cm^{-1} and a significant shifting and the gradual sharpening of the broad peak from 1060 to 1035 cm^{-1} .

Table 1. SEM microphotographs of HA/ bioactive glass composite as powder and as pellet before and after 9 and 15 days in c-SBF.



These findings are confirmed by SEM microphotographs and EDS analysis. The characteristic microphotographs for both powder and pellet samples are presented in Table 1. The surface of the grains of all powdered samples after 9 days of immersion was covered by a rather thin apatite layer, while after 15 days in SBF, SEM microphotographs reveal the development of apatite with spherulitic appearance. Moreover, EDS analysis revealed a molar Ca/P ratio of about 1.89. SEM microphotographs reveal the formation of an apatite layer consisting of spherulitic apatite aggregates on the surface of the pellets even after 9 days in c-SBF. After 15 days the underlying substrate is fully covered of a dense apatite layer and EDS analysis revealed a molar Ca/P ratio of 1.5-1.6, while the peaks attributed to Mg and Al from the substrate have almost disappeared, suggesting a thick and well-formed apatite layer.

In conclusion, as these preliminary results revealed the fast formation of a quite thick apatite layer on transferred arc plasma synthesized HA/SiO₂-CaO-MgO glass ceramics, it is suggested that the use of the TAP processing method is an acceptable alternate method for the fabrication of potentially bioactive glass ceramic materials which can be possibly used as bulk materials.

- [1] Tadashi Kokubo, *Biomaterials* 12, 155 (1991).
- [2] C.P. Yoganand, V. Selvarajan, Luca Lusvarghi, O.M.Goudouri, K.M. Paraskevopoulos, Mahmoud Rouabhia, *Materials Science and Engineering C* 29, 1759 (2009).
- [3] T. Nonami, S. Tsutsumi, *J. Mater. Sci. M* 10, 475 (1999).
- [4] C. Ohtsuki, H. Kushitani, T. Kokubo, S. Kotani, T. Yamamuro, *J. Biomed. Mater. Res.* 25, 1363 (1991).
- [5] E. Kontonasaki, T. Zorba, L. Papadopoulou, E. Pavlidou, X. Chatzistavrou, K.M. Paraskevopoulos, P. Koidis, *Cryst. Res. Technol.* 37, 1165 (2002).

Acknowledgments One of the authors Mhs. O.M Goudouri acknowledges the Greek State Scholarship Foundation (IKY) for the support of this work.

Comparative study of the effect of different nanoparticles on the UV stability of HDPE

I. Grigoriadou¹, K. M. Paraskevopoulos¹, D. Bikiaris^{2*}

¹*Solid State Physics Section, Physics Department, Aristotle University of Thessaloniki, GR- 541 24, Thessaloniki, Macedonia, Greece*

²*Laboratory of Organic Chemical Technology, Department of Chemistry, Aristotle University of Thessaloniki, GR- 541 24, Thessaloniki, Macedonia, Greece*

**dbic@chem.auth.gr*

Abstract

In the present study different series of HDPE nanocomposites were prepared by melt mixing on a Haake-Buchler Reomixer, containing 2.5 wt % of multiwall carbon nanotubes, pristine and modified montmorillonite, surface treated and untreated SiO₂ nanoparticles. Nanocomposites in the form of thin films were exposed to UV radiation at 280 nm at constant temperature (25°C) and constant relative humidity (50%) for several times. From FTIR study and mechanical properties it was found that SiO₂ and organically modified montmorillonite cause a serious effect on UV degradation. Neat HDPE and nanocomposites containing multiwall carbon nanotubes have the highest UV stability.

Introduction

Among the wide number of commercially available thermoplastic polymers, HDPE has been widely used in different packaging applications. This is due to the abundant supply of HDPE and to its combination of low cost and low energy demand for processing. Additionally, the well balanced mechanical properties make HDPE ideal for many industrial applications [1]. Some of these properties can be improved by the addition of inorganic nanoparticles into polymer matrices. Nanocomposites are characterized by the use of a reinforcing agent with nano-dimensions, which is added in small quantities compared to the traditional composites. In the case of HDPE several nanoparticles were used in order to increase its mechanical properties such as tensile modulus and impact strength [2]. SiO₂ nanoparticles, montmorillonite (MMT) and multi-walled carbon nanotubes were used extensively for stiffness enhancement as well as to increase the thermal conductivity of HDPE. However, so far, only limited studies concerning the UV stability of HDPE by the addition of nanofillers, were reported.

Experimental

Materials. Bimodal high density polyethylene (HDPE) appropriate for pipe and fittings production was supplied by TVK Inter-Chemol GmbH (Frankfurt am Main, Germany) under the trade name TIPELIN 7700M. Multi walled carbon nanotubes (MWCNTs) were supplied by Nanothinx (Patra, Greece). Their diameter was between 9-20 nm and their length > 5 μm. The two different types of fumed silica (SiO₂) nanoparticles used for nanocomposites preparation, were supplied by Degussa AG (Hanau, Germany). The first type was hydrophilic silica nanoparticles, under the trade name AEROSIL[®] 200, having a specific surface area of 200 m²/g and SiO₂ content >99.8%, and the second type was the hydrophobic nanoparticles under the trade name AEROSIL[®] R974. The latter were produced by the supplier after treating the hydrophilic nanoparticles with dimethyldichlorosilane (cSiO₂). The two different types of montmorillonite under the trade name Cloisite[®] Na⁺ (pristine) (MMT) and Cloisite[®] 20A (org-MMT), which is modified with a dimethyl, dihydrogenated tallow quaternary ammonium chloride salt, were supplied from Southern Clay Products INC., (Golzaes Texas USA).

Experimental procedure. HDPE nanocomposites were prepared by melt mixing of different nanoparticles (2.5 wt%) with HDPE on a Haake-Buchler Reomixer, at 220°C and 30 rpm for 15 min. Nanocomposites in the form of thin films were exposed to UV radiation at 280 nm at constant temperature (25°C) and constant relative humidity (50%) for several times. Measurements of tensile mechanical properties of the prepared nanocomposites during UV exposure were performed on an Instron 3344 dynamometer, in accordance with ASTM D638, using a crosshead speed of 50 mm/min. FTIR spectra of UV irradiated nanocomposites were obtained using a Perkin-Elmer FTIR spectrometer, model Spectrum 1000.

Results and Discussion

Nanocomposites after exposure to UV radiation at 280 nm were characterized by FTIR spectroscopy in order to evaluate the effect of UV radiation on their photochemical stability. In all the samples after 50h radiation there are no remarkable changes in the recorded spectra. Some alterations became visible after 100h of radiation. New peaks are formed at 920 cm⁻¹ and 1640 cm⁻¹ due to the formation of vinyl groups (>C=C<) and at 3200-3500 cm⁻¹ due to the formation of hydroxyl and peroxide groups. However, the most remarkable differences are recorded in the area 1650-1830 cm⁻¹ (Figure 1). A substantial increase was recorded in the peak at 1714 cm⁻¹ attributed to

the formation of -COOH groups, at 1734 cm^{-1} due to the formation of ester groups (-CO-O-) and at $1780\text{-}1790\text{ cm}^{-1}$ attributed to the formation of anhydride groups (-CO-O-CO-). Comparing the different samples it can be seen that only these containing MWCNTs are stable and no differences can be found during radiation, due to the stabilization effect of MWCNTs absorbing the UV radiation, and thus protecting the HDPE. Neat montmorillonite gives also some protection to HDPE, while in nanocomposites containing SiO_2 and organically modified MMT there is an accelerating effect of these nanoparticles to HDPE decomposition. In the case of organically modified MMT this effect can be attributed to the used ammonium salts while in the SiO_2 nanoparticles to the surface silanol groups.

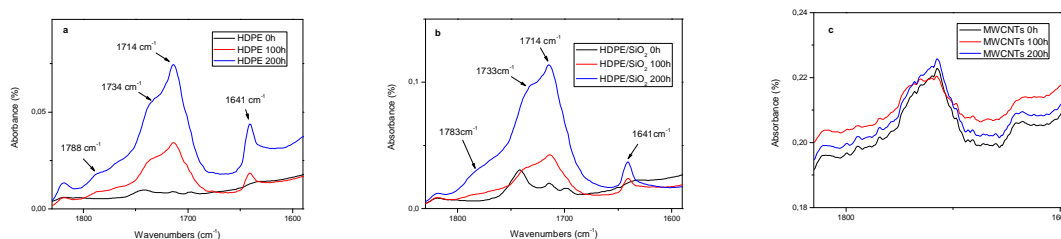


Figure 1. FTIR spectra of nanocomposites during UV radiation for several times a) HDPE, b) HDPE/ SiO_2 nanocomposites and c) HDPE/MWCNTs nanocomposites.

The effect of UV radiation has also affected the mechanical properties of HDPE nanocomposites. As can be seen in Figure 2 Tensile strength at yield point, increases continuously with the increase of the time of UV radiation and only after 100h of radiation there is a small decrease. A similar trend is also recorded to the Youngs' modulus indicating that the samples became stiffer. However, as can be seen from tensile strength at break as well as from elongation at break, the samples from the beginning of UV radiation became brittle and after 70h of radiation are broken immediately. This behavior could be attributed to the formation of cross-linked macromolecules initially while after a certain time a substantial reduction is caused to the HDPE molecular weight therefore, reducing their mechanical properties.

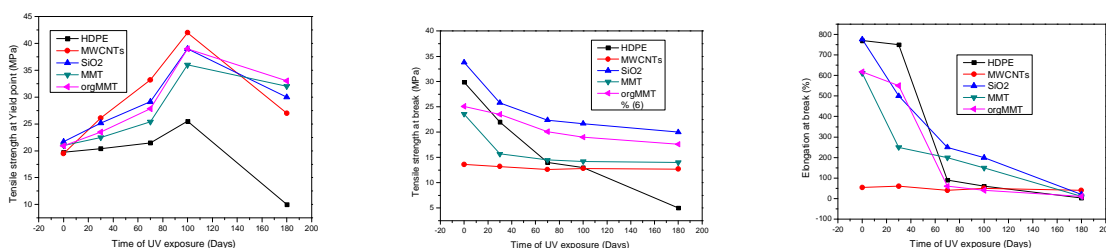


Figure 2. Variation of nanocomposites mechanical properties during UV exposure for several days a) Tensile strength at yield point b) Youngs' Modulus and c) Elongation at break.

References

- [1] Galli P, Vecellio G. *J Appl Polym Sci: Part A: Polym Chem* 42 (2004) 396.
- [2] Chrissafis K, Paraskevopoulos KM, Tsiaoussis I, Bikiaris D. *J Appl. Polym. Sci.*, in press.

Bioactivity Studies of Bioactive glasses in different environments: the case of the 45S5 bioglass

G. Theodorou¹, O.M. Goudouri¹, A. Theocharidou², E. Kontonasaki², X. Chatzistavrou³, L. Papadopoulou³, P. Koidis², K.M. Paraskevopoulos^{1*}

¹Physics Department, ²Department of Fixed Prosthodontics, School of Dentistry, Aristotle University of Thessaloniki, 54124 Thessaloniki, Greece

³Department of Materials, Imperial College London, Exhibition Road, London SW7 2AZ, UK

⁴Department of Geology, Aristotle University of Thessaloniki, 54124 Thessaloniki, Greece

*kpar@auth.gr

Several studies, in the past, have evaluated the biological response of various bioactive glasses in different media, like conventional simulated body fluid (c-SBF), Dulbecco's Modified Eagle's Medium (DMEM) and Tris buffer solution. Both, the onset of apatite formation and the morphology of the developed apatite layer, depend on the immersion media due to the different mechanism of apatite formation in each solution [1]. The aim of the present work was the evaluation of the in vitro bioactivity assessment of the most commonly used bioactive glass -45S5- soaked in DMEM and c-SBF, in order to compare its biological response in organic and inorganic environment. Furthermore, all experiments were carried out under renewal solution conditions, as it has been reported that this method simulate better the in vivo conditions by maintaining the ionic concentration and pH of the solution constant [2].

Melt-derived bioactive glass (SiO₂ 45, Na₂O 24.5, CaO 24.5, P₂O₅ 6 in wt %) was produced as described in literature [3]. The formation of the bioactive glass – in the specific system– was confirmed by Fourier Transform Infrared Spectroscopy (FTIR) and Scanning Electron microscopy with associated energy dispersive spectroscopic analysis (SEM-EDS). The product was sieved to powder of 20-40µm and the in vitro bio-activity of the sample was tested as powder in c-SBF solution prepared as described by Ohtsuki et al [4] and DMEM[®] culture medium (Invitrogen, GIBCO, USA) supplemented with 10% FCS for various immersion times, while the solution was renewed after 6h, 24h and then every 2 days. Fourier Transform Infrared Spectroscopy (FTIR) and Scanning Electron Microscopy (SEM) were used to characterize the reacted powders.

The in vitro bioactivity of 45S5 powder in c-SBF and DMEM solution was studied for 6, 12, 24, 48 hours and 3 days. Even after 6 hours of soaking in c-SBF a broad peak is formed in the spectral area of 550-610cm⁻¹ proving the formation of an amorphous Ca-P phase [6]. After 24 hours a double peak at 562 and 602cm⁻¹ attributed to the bending of P-O vibrational mode is developed indicating the formation of a crystalline HCAp phase on the grains surface [5]. On the surface of the grains immersed for 24 hours in SBF, SEM microphotographs (Table 1) reveal the development of a quite thin apatite layer. However, after 3 days the surface of the grains is fully covered by a rather thick layer.

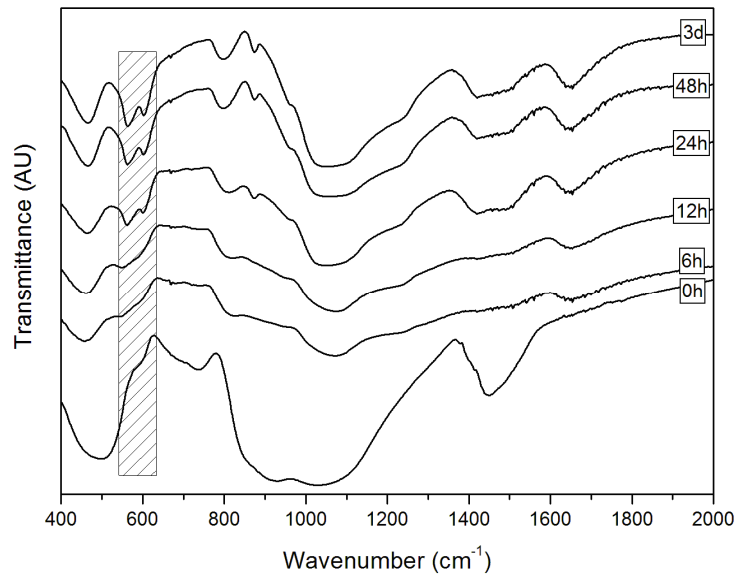
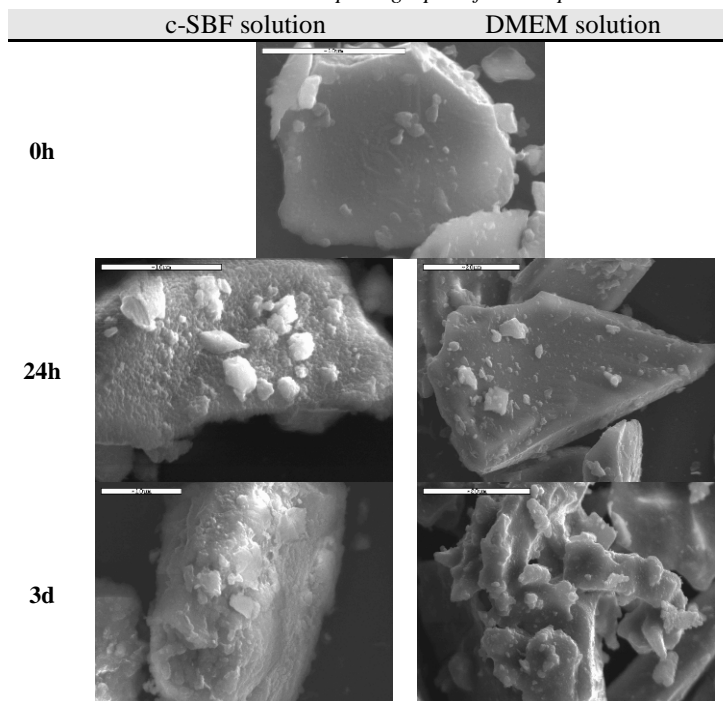


Fig. 1. FTIR spectra of 45S5 powder before and after immersion in c-SBF solution for 6, 12, 24, 48 hours and 3 days.

Table 1. SEM microphotographs of all samples

These findings are further confirmed by EDS analysis, which reveal a mean molar Ca/P ratio of about 1.79 for the sample immersed for 3 days in c-SBF, while the participation of Si from the substrate is dramatically decreased.

For the samples immersed in DMEM solution, the onset of apatite formation on the surface of 45S5 grains was delayed in comparison with the samples immersed in c-SBF solution, as indicated by the FTIR spectra (Fig. 2) that present a broad peak at $500\text{-}610\text{cm}^{-1}$ attributed to an amorphous Ca-P phase even after 3 days of immersion. SEM microphotographs shown in Table 1 indicate that after 3 days of immersion the surface of the grains is only partially covered by an apatite like phase, while EDS analysis present a mean molar Ca/P ratio of about 2. Additionally, EDS analysis proved that, unlikely with the samples immersed in DMEM, the samples immersed in c-SBF for 3 days exhibit a massive decrease of Si and Na from the substrate suggesting a thicker and well-

formed apatite layer.

In conclusion, in the case of 45S5 bioactive glass the renewal conditions promote the onset of apatite formation, while in organic environment the formation of a crystalline apatite layer is prohibited. However, XRD analysis should be performed in order to define the exact apatite phase that has been precipitated and the bioactive behavior of 45S5 bioactive glass should be further examined.

- [1] D. C. Clupper, J. E. Gough, M. M. Hall, A. G. Clare, W. C. LaCourse, L. L. Hench, *J Biomed Mater Res* 67A, 285 (2003)
- [2] J. Zhong, D.C. Greenspan. *J Biomed Mater Res (Appl Biomater)* 53, 694 (2000)
- [3] X. Chatzistavrou, T. Zorba, K. Chrissafis, G. Kaimakamis, E. Kontonasaki, P. Koidis and K. M. Paraskevopoulos, *J. Therm. Anal. Calor.* 85, 253 (2006).
- [4] C. Ohtsuki, H. Kushitani, T. Kokubo, S. Kotani and T. Yamamuro, *J. Biomed. Mater. Res.* 25, 1363 (1991).
- [5] E. Kontonasaki, T. Zorba, L. Papadopoulou, E. Pavlidou, X. Chatzistavrou, K. Paraskevopoulos, P. Koidis, *Cryst. Res. Technol.* 37, 1165 (2002).

Acknowledgments One of the authors Mhs. O.M Goudouri acknowledges the Greek State Scholarship Foundation (IKY) for the support of this work.

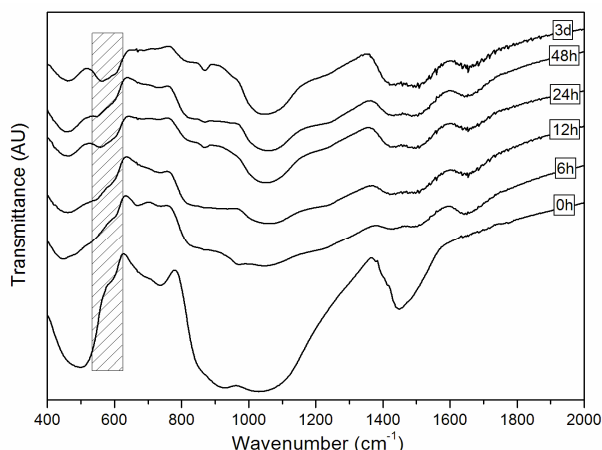


Fig. 2. FTIR spectra of 45S5 powder before and after immersion in DMEM solution for 6, 12, 24, 48 hours and 3 days.

Preliminary TL/OSL Characterization On Synthetic Bioactive Materials

D. Afouxenidis^{1,2,3,*}, X. Chatzistavrou³, G. S. Polymeris¹, N. C. Tsirliganis¹, G. Kitis¹, K.M. Paraskevopoulos³

¹ *Archaeometry Laboratory, Cultural and Educational Technology Institute (C.E.T.I.), R.C. "ATHENA", Tsimiski 58, 67100 Xanthi, Greece*

² *Nuclear Physics Laboratory, Aristotle University of Thessaloniki, 54124 Thessaloniki, Greece*

³ *Physics Department, Solid State Physics Section, Aristotle University of Thessaloniki, 54124 Thessaloniki, Greece*

* *dafouxen@ipet.gr*

In recent years, synthetic bioactive materials have assumed substantial interest and importance because of their osteoinductive and osteoconductive properties, enabling their application in bone tissue engineering. Bioactive glass-ceramics are synthetic substances with high biocompatibility. Due to this specific property, they are extensively used as implant materials in the human body in order to replace and/or to repair diseased or damaged bone in orthopedic, cranio- and maxillofacial and periodontal surgeries as well as a feeling material for human teeth.

Bioactive glasses are mainly used as reactive materials in reconstructive surgeries in order to stimulate the re-growth of new tissue in no load-bearing applications being in contact with soft tissue. On the other hand, synthetic bioceramics like hydroxyapatite are mainly used in contact with hard tissue in orthopaedics and dentistry, because of its chemical and biological similarity to the mineral phase of human bones. The wide spread use of the aforementioned substances for bone grafting purposes, in combination with their chemical composition, constitute two powerful motivations for further investigation of these materials towards their viable use for accidental and retrospective dosimetry purposes.

Within the framework of this objective, specific thermally and optically stimulated luminescence (TL and OSL respectively) features such as TL and room temperature LM-OSL curve shapes, thermal and optical sensitization characteristics, as well as optical bleaching after β irradiation were explored, for two types of bioactive glasses powders and two types of sol-gel derived hydroxyapatite powders. In the former case, the melt-derived bioactive glass 45S5 and the sol-gel derived (bioactive glass) 58S were studied, on the basis that they are well known new type of biomaterials for bone reparation. The two kinds of sol-gel derived hydroxyapatites, separated on the basis of containing or not CaO and Ca(OH)₂, with laboratory codes HAP[E1] and HAP[M] respectively, were selected. Trapping parameters were estimated using Computerized Glow Curve Deconvolution Analysis (CGCDA).

Several quartz-TL features, attributed to the large concentration of SiO₂, such as the 110 °C TL peak and intense sensitization for intermediate doses were revealed for both bioceramics, which yielded different sensitivities, as well as different bleaching and sensitization rates, indicating differences between them. Regarding hydroxyapatites, besides the above-mentioned differences which also stand, it is interesting to note the glow curve shape dependence on the presence of CaO and Ca(OH)₂, providing substantially different glow curves. Implications of these features on their effective use for dosimetry purposes are briefly discussed.

Raman characterization of psoriatic and healthy nails

A. M. Paschou¹, M. Katsikini^{*1}, J. Arvanitidis², S. Ves¹

¹ Aristotle University of Thessaloniki, School of Physics, 54124 Thessaloniki, Greece

² Department of Applied Sciences, Technological Educational Institute of Thessaloniki, 57400 Sindos, Greece

*katsiki@auth.gr

The human nails are formed from dead cells of epithelium and they are rich in keratin. Keratins comprise a large family of proteins that are rich in cysteine (CYS) a sulfur - containing amino acid. The amino acids that are found in highest amount in the nail keratin are the GLU (19mg/g), CYS (17 mg/g), ARG (17mg/g) and SER (5 mg/g) [1]. However, the keratin composition is affected by genetic factors and diseases [2,3,4]. Raman spectroscopy is a well established technique for characterization of molecular materials. It is also applied in the study of biopolymers since it is sensitive to both the amino acid content and the bonding configuration (e.g. tertiary structure of proteins). Here, we explore the use of the Raman spectroscopy for the study of human nails, and its potential application as diagnostic tool.

The studied samples are clippings from two nails, a psoriatic and a healthy, which belong to the same donor. Psoriasis affects both the nails and the skin and in some cases is accompanied by arthritis. The Raman spectra were recorded in the backscattering geometry using a DILOR XY micro-Raman system equipped with a cryogenic charge coupled device (CCD) detector. For excitation, the 514.5 nm line of an Ar⁺ laser was focused on the sample by means of a 100× objective lens with a laser power of ~5 mW. The acquisition time was 300 sec per spectrum and 5 spectra were added for each sample.

The Raman spectra of the two samples, recorded in the frequency range from 400 – 3200cm⁻¹ are shown in Fig. 1. In this range, about 75 peaks were detected, which were fitted using Voigt functions. The detected peaks can be grouped in two categories: (I) Peaks that correspond to vibrational modes of bonds that are characteristic of the amino acids ALA, ASP, ARG, ASN, CYS, CYSCYS, GLN, GLU, GLY, PRO, HIS, SER, ILE, LEU, MET, PHE, TRP, TYR, VAL. The CYSCYS is the cystine that is formed when two CYS (cysteine) are bonded with S-S bonds. These bonds affect the folding of the keratin molecules. (II) Peaks that are affected by the 3 D structure of the keratin and correspond to vibrations of the peptide bond and to vibrations of the C acyclic chain. The ratio of the intensity of the identifiable peaks of the healthy and the psoriatic nail is depicted in Fig. 2, showing different degree of sensitivity. For instance, the CYSCYS content is higher in the healthy nails suggesting dissociation of the S-S disulfide bridging bonds which enhance the nail hardness. Furthermore, the TRP (tryptophan) content in the healthy nail is significantly higher compared to the psoriatic. Finally, psoriasis affects also the keratin folding, as it can be deduced from the significant differences in the intensity of the stretching skeletal C-C modes.

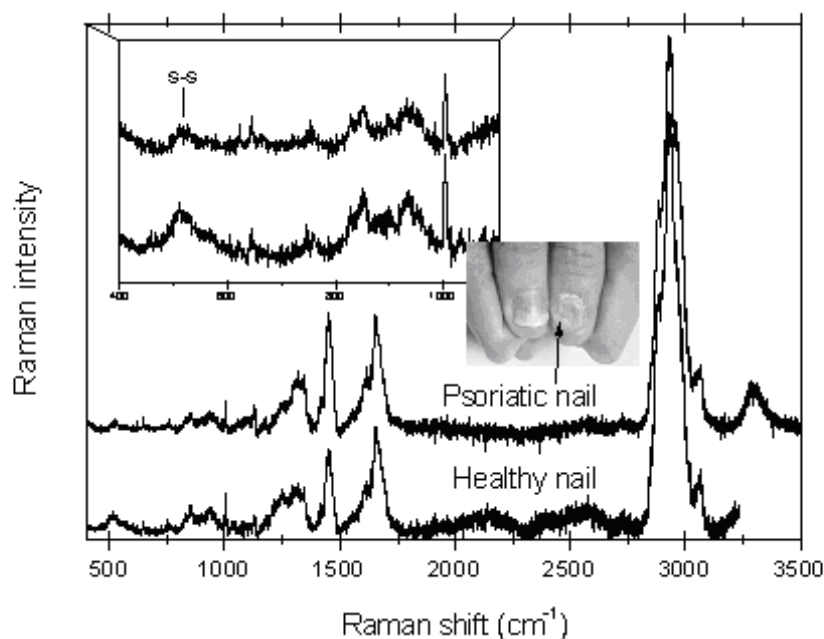


Fig. 1: Raman spectra of the psoriatic and the healthy nail that belong to the same donor. The insets show magnification of the spectrum in the frequency range where the S-S bond vibrations contribute and a photograph of psoriatic nails.

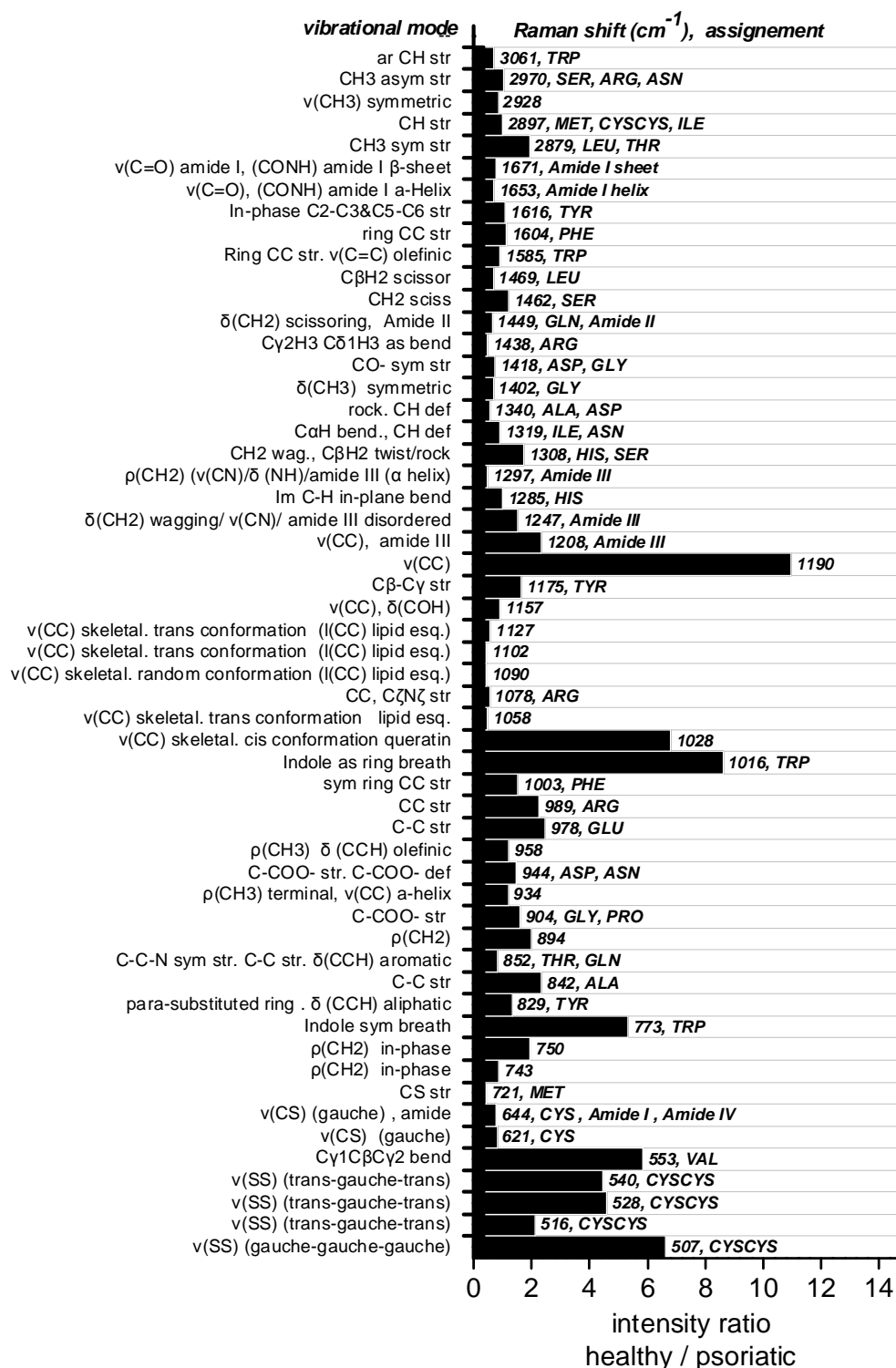


Fig. 2: Ratio of the areas under the peaks that are identified in the healthy and psoriatic nails (v: stretch, δ: deformation, ρ: rock).

References

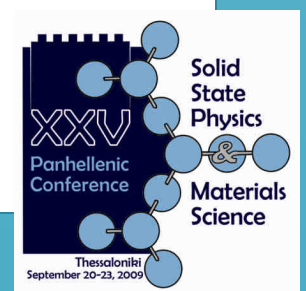
- [1] Mavis S. Greaves and John M. H. Moll, Clin. Chem., 22, 1608, (1976).
- [2] Sheldon A. Payne and William A. Perlzweig, J. Clin. Invest. 12, 899 (1933).
- [3] R. C. Marshall, J Invest. Derm., 75, 264 (1980).
- [4] M. R. Towler, A. Wren, N. Rushe, J. Saunders, N. M. Cummins, and P. M. Jakeman, J. Mater Sci. Mater Med., 18, 759 (2007).

Session WE3

NANOSCALE & SURFACE SCIENCE

PART 1

Wednesday, 23 September 2009, 14⁰⁰-15³⁰



Optical properties of nano-objects: Carbon nanotubes and metallic particles

D. Christofilos

Physics Division, School of Technology, Aristotle University of Thessaloniki, 54124 Thessaloniki, Greece

christof@vergina.eng.auth.gr

Nanoscience and nanotechnology are in the focus of contemporary research regarding the study of physical and chemical properties of matter in the nanoscopic regime and the exploitation of the gained understanding to revolutionize existing applications or invent new ones. Any such attempts can only be accomplished if methods to “see” nanostructures exist. The optical properties of nano-objects are strongly size-dependent due to confinement effects and consequently technologically interesting for tailoring the optical response of devices. Apart from constituting an interesting field of research on their own, they also provide a unique and non-destructive probe for the identification and study of these structures.

Carbon nanotubes belong to the category of one dimensional nanostructures with typical lengths around 1 μm but very small diameters in the range of 1 nm. The nanotube can be considered as a seamlessly rolled single graphitic layer (graphene) along a folding vector, the chiral vector, which uniquely identifies the tube by the vector's integer components (n , m) expressed with respect to the graphene lattice vectors [1]. Consequently, the tube properties can be related to the electronic and phononic properties of graphene being modified by the folding of the Brillouin zone. Concerning their electronic properties, the folding scheme can describe two important properties which depend on the “cuts” of the graphene zones due to folding: (a) the nanotube can be metallic if $2n+m$ is a multiple of three or semiconducting otherwise, (b) van Hove singularities appear in the electronic density of states, the optical transitions between which dominate their absorption and their energy scales with the inverse of the tube diameter as expressed in the so-called Kataura plot [2]. More recently, the observation of strong excitonic effects has complicated this picture [3,4,5]. Among optical properties, the Raman effect is extremely interesting and useful in carbon nanotubes [4,5]. Due to its resonant nature, strong Raman signals are available, originating only from the tubes in resonance with the laser excitation. Furthermore, the radial breathing modes (RBMs) of the tubes, being inversely proportional to the tube diameter can be used to distinguish among the different individual nanotubes that are in resonance [6].

Pressure is a particularly useful external parameter for the study of carbon nanotubes [7]. It results in diameter dependent deformations of the tube cross-section, leading to the loss of resonance and disappearance of the RBMs [8,9]. Our studies with carotene encapsulating carbon nanotubes support the pressure induced structural changes by monitoring the Raman signal of the encapsulated molecular species and demonstrate the pressure screening function of the tube [10]. Bundling can alter the evolution of these effects resulting in less hydrostatic pressure transmitting conditions as indicated by Raman measurements of bundled and individual single-walled carbon nanotubes [11]. In double-walled carbon nanotubes the outer tube provides pressure screening for the inner tube and the internal one, structural support for the outer. Pressure application on the inner tubes is realized through their interaction with the outer ones and consequently it is modulated by the inner-outer tube distance and reflected in the RBM and the tangential modes pressure response [12,13]. The resonant nature of the Raman signal from the inner tubes can be used for a rough estimation of their pressure induced band gap changes [13]. This would be impossible by standard absorption measurements since resonances of the inner and outer tubes overlap in wavelengths and the tube-tube interactions broaden and attenuate the experimental peaks. A simple model of anharmonically coupled anharmonic oscillators provides the basic physical picture of pressure application on the RBMs of double-walled nanotubes and can be generalized for multiwall carbon nanotubes [14] allowing the interpretation of the experimental data in these systems [15]. Finally, the understanding of the pressure response of the RBMs can be used to identify the inner and the outer tube pairs in double-walled nanotubes materials [16].

The optical properties of metallic nanoparticles are by far dominated by the well known surface plasmon resonance (SPR), often referred to as localized SPR (LSPR) for the case of nanoparticles, predominantly studied in particle ensembles both in the linear and the non-linear regime [17,18,19]. Noble metals, silver in particular, provide a convenient material for the study of such effects as the interband absorption is well separated by the SPR feature, whereas in gold, it partially overlaps with the SPR and has to be also taken into account. The SPR absorption originates from dielectric confinement of the metal within a dielectric matrix. When the metal fraction is low, the particles are spherical and well-dispersed and the nanoparticle size considerably smaller than the wavelength of the incident light, it is easy to define an effective dielectric function of the composite medium as a combination of the bulk dielectric functions of its constituents. The result is a pronounced and relatively narrow absorption peak, describing a resonant interaction between the electric field and the collective material

excitations (electron density fluctuations). The effective medium approach is equivalent to keeping the dipolar term in a full Mie scattering treatment of the problem, which is inevitable for large particles, whereas for very small particles, size-confinement has to be considered as well. The use of the pump-probe technique in the study of such effects has been proven fruitful [19]. Size-dependent confinement is evident in electron-electron and electron-phonon interactions, which do not depend on the environment as revealed by measurements in different matrices [20,21]. In order to account for these observations, the “spillover” of electrons outside the particle lattice and the d electron wavefunction localization in the inner region of the particle has to be considered in a core-shell model of the particle. The long time response is dominated by coherent acoustic vibration (breathing vibration) of the particles and energy exchanges with their environment. The frequency of the breathing vibration appears unaffected by the environment, unlike its damping which “probes” the local environment and the pressure induced local alterations of the metal-matrix interface [22,23].

Nevertheless, any results on nanoparticle ensembles include non-homogeneous contributions due to the precise size, shape and local environment of each nanoparticle. Ideally, only the study of individual nanoparticles can confidently elucidate the contribution of each parameter to the observed optical properties, and in this context, we have demonstrated the applicability of a far-field optical technique in the study of individual nano-objects [24]. In the concept of Spatial Modulation Spectroscopy, nano-objects are dispersed so that their surface density is smaller than one particle per square micron on a transparent plate that can be scanned in X-Y. A beam is tightly focused on the surface by an objective and collected from the other side by a similar objective. A small amplitude sinusoidal modulation of the particle position leads to the modulation of the optical transmission signal detected by a silicon photodiode, which can be finally demodulated by a lock-in amplifier. By careful measurement of the experimental parameters (e.g. beam diameter), the *absolute* extinction cross-section of the individual particles can be deduced, as it was demonstrated for gold nanoparticles as small as 5 nm in diameter [24]. Furthermore, polarization dependent measurements can reveal shape distortions and the ellipticity of oval particles can be deduced, as well as the local refractive index of the matrix around the particle, which exhibits deviations [25,26]. Of course, any other nanoscopic object, like gold nanorods, can be detected and studied and their spectra can be used to characterize the particles [26]. This method provides a fast locating method of nanoparticles and therefore it can be combined with other optical techniques using the same optical path to study their non-linear optical properties as well [26]. Currently, the method is being applied for the study of individual nanotubes and semiconductor nanorods.

- [1] M. S. Dresselhaus and P. C. Eklund, *Adv. Phys.* 49, 705 (2000).
- [2] H. Kataura, Y. Kumazawa, Y. Maniwa et al., *Synth. Met.* 103, 2555 (1999).
- [3] F. Wang, G. Dukovic, L. E. Brus and T. F. Heinz, *Science* 308, 838 (2005).
- [4] C. Thomsen, S. Reich, eds. M. Cardona, R. Merlin, *Light Scattering in Solid IX*, *Topics Appl. Phys.* 108, 115 (2007).
- [5] R. Saito et al., eds. A. Jorio, G. Dresselhaus, M. S. Dresselhaus, *Carbon Nanotubes*, *Topics Appl. Phys.* 111, 251 (2008).
- [6] A. M. Rao, E. Richter, S. Bandow et al., *Science* 275, 187 (1997).
- [7] I. Loa, *J. Raman Spectrosc.* 34, 611 (2003).
- [8] U. D. Venkateswaran, A. M. Rao, E. Richter et al., *Phys. Rev. B* 59, 10928 (1999).
- [9] U. D. Venkateswaran, D. L. Masica, G. U. Sumanasekera et al., *Phys. Rev. B* 68, 241406 (2003).
- [10] J. Arvanitidis, D. Christofilos, S. M. Souliou et al., *Phys. Stat. Sol. B* 246, 496 (2009).
- [11] D. Christofilos, J. Arvanitidis, K. S. Andrikopoulos et al., *Phys. Stat. Sol. (b)* 244, 100 (2007).
- [12] J. Arvanitidis, D. Christofilos, K. Papagelis et al., *Phys. Rev. B* 71, 125404 (2005).
- [13] J. Arvanitidis, D. Christofilos, K. Papagelis et al., *Phys. Rev. B* 72, 193411 (2005).
- [14] D. Christofilos and J. Arvanitidis, *J. Phys.: Conf. Series* 121, 162004.1 (2008).
- [15] D. Christofilos, J. Arvanitidis, E. Efthimiopoulos et al., *phys. stat. sol. (b)* 244, 4082 (2007).
- [16] D. Christofilos, J. Arvanitidis, G. A. Kourouklis et al., *Phys. Rev. B* 76, 113402 (2007).
- [17] U. Kreibig and M. Vollmer, *Optical Properties of Metal Clusters*, Springer Verlag, Berlin 1995.
- [18] C.F. Bohren and D.R. Huffman, *Absorption and Scattering of Light by Small Particles*, John Wiley, New-York, 1998.
- [19] C. Voisin, N. Del Fatti, D. Christofilos, and F. Vallée, *J. Phys. Chem. B* 105, 2264 (2001).
- [20] C. Voisin, D. Christofilos, P. A. Loukakos et al., *Phys. Rev. B* 69, 195416 (2004).
- [21] A. Arbouet, C. Voisin, D. Christofilos et al., *Phys. Rev. Lett.* 90, 177401 (2003).
- [22] D. Christofilos, C. Voisin, N. Del Fatti and F. Vallee, *High Press. Res.* 22, 277 (2002).
- [23] C. Voisin, D. Christofilos, N. Del Fatti, F. Vallee, *Physica B* 316-317, 89 (2002).
- [24] A. Arbouet, D. Christofilos, N. Del Fatti et al., *Phys. Rev. Lett.* 93, 127401 (2004).
- [25] O. Muskens, D. Christofilos, N. Del Fatti and F. Vallee, *J. Opt. A: Pure Appl. Opt.* 8, S264 (2006).
- [26] N. Del Fatti, D. Christofilos and F. Vallée, *Gold Bulletin* 41, 147 (2008).

Acknowledgments The hospitality, support and fruitful collaboration in the group of Dr. Fabrice Vallee and Prof. N. Del Fatti in the course of all these years in various laboratories in France is sincerely acknowledged, as well as the harmonic and fruitful collaboration with Dr. J. Arvanitidis and the other members of our research group by Prof. G. A. Kourouklis and Prof. S. Ves.

Thermodynamics and Kinetics of Dislocated Ge/Si and InAs/GaAs Thin Layers

T. Leontiou^{1*}, P. C. Kelires^{1,2}, and J. Tersoff³

¹*Department of Mechanical and Materials Science Engineering,
Cyprus University of Technology, P. O. Box 50329, 3603 Limassol, Cyprus*

²*Department of Physics, University of Crete, P. O. Box 2208, 710 03 Heraclion, Crete, Greece*

³*IBM Research Division, T. J. Watson Research Center, Yorktown Heights, NY 10598, USA*

**theodoros.leontiou@cut.ac.cy*

Epitaxial layers (such as Ge/Si or InAs/GaAs) are under biaxial misfit strain, which is a strong driving force for enhanced interdiffusion. This can be a problem for heterojunction or superlattice devices. However, the misfit strain is usually fully or partially relaxed by dislocations, depending on temperature and other growth conditions. We investigate the thermodynamics and kinetics of intermixing within such dislocated thin layers through simulation and modeling. We show that appropriate injection of misfit dislocations can have the opposite effect, slowing or suppressing interdiffusion. For the simulations we use the continuous-space Monte Carlo method, employing multi-component empirical potentials. The thermodynamic and kinetic models employed rely on a parameterization of the free energy in terms of the elastic energy as given by the linear theory of elasticity.

The results for Ge/Si(001) show a significant reduction in the rate of interdiffusion in the presence of dislocations, leading to substantially less alloyed quantum wells. Note, that the ideal non-dislocated superlattice becomes throughout a random alloy at thermodynamic equilibrium. In the case of the InAs/GaAs(001) superlattice the suppression of interdiffusion in the InAs layer is even more pronounced. This can be explained by the substantially different lattice mismatch between the constituent layers (4% and 7%, respectively). The composition profiles resulting from the semi-analytic thermodynamic model are in agreement with the simulations and aid in the understanding of the underlying physics: in the region between the interfaces the enhanced strain relaxation provided by the dislocations minimizes the elastic energy and reduces entropic mixing.

In actual experimental conditions the thermodynamic equilibrium might be unreachable due to the presence of dislocation-enhanced kinetic barriers in the diffusion process. We provide a measurement of these barriers both through simulation and modeling, thus illustrating the possibility of using dislocations in order to critically damp intermixing.

Synthesis and Characterization of Novel Carbon Nanotubes-Iron Oxide Nanoparticles Hybrids

A. P. Douvalis^{1*}, T. Tsoufis², D. Gournis², P. Trikalitis³ and T. Bakas¹

¹ Physics Department, University of Ioannina, 45110, Ioannina

² Department of Materials Science and Engineering, University of Ioannina, 45110, Ioannina

³ Department of Chemistry, University of Crete, Voutes 71003, Iraklio

*adouval@cc.uoi.gr

Magnetic nanoparticles (NPs) are important materials with a wide range of technological applications, like media for magnetic data storage [1], drug carriers, identifiers as also contrast and hyperthermia agents in biomedicine [2]. On the other hand carbon nanotubes (CNTs) are novel developed versatile materials with extraordinary structural, mechanical, electronic and magnetic properties and possess a high potential to be used in many aspects of modern technical implementations [3]. The joining of the properties of both categories of materials has given rise to new fields of research and dynamic future technological applications [3].

In this work we present a simple and versatile way to synthesize different CNTs-iron oxide NPs hybrid materials. Chemically functionalized CNTs (single- and multi-walled) were used as nanotemplates for the in-situ synthesis of a variety of ferrimagnetic and/or antiferromagnetic iron oxide NPs. The method involves the covalent functionalization of the CNTs, the subsequent adsorption of the nanoparticle precursor on the functionalized nanotube surface followed by the interaction of acetic acid vapors with the derived nanotube-precursor system. The various resulting CNTs-iron oxide NPs hybrid materials were prepared upon pyrolysis of the created iron acetate species under three different atmospheres: air, argon and oxygen.

The characterization of the final hybrid materials with Raman spectroscopy showed that in most cases during the calcinations process, carbon nanotubes retain their initial basic structural characteristics intact. In addition combined X-Ray diffraction, Mössbauer spectroscopy and magnetization measurements revealed that the atmosphere chosen during the thermal treatment affects significantly the nature of the resulting nanoparticles, which were found to be either ferrimagnetic maghemite ($\gamma\text{-Fe}_2\text{O}_3$), magnetite (Fe_3O_4) or antiferromagnetic hematite ($\alpha\text{-Fe}_2\text{O}_3$). Transmission electron microscopy provides information on the formation, size and type of the synthesized iron oxide phases.

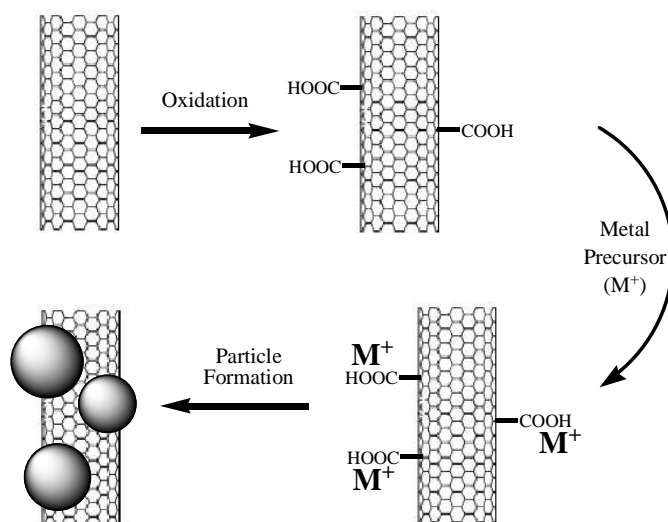


Figure 1. Scheme for the preparation of CNT-iron oxide nanoparticle nanohybrids

References

- [1] Sun S., Murray C. B., Weller D., Folks L., Moser A., Science 287, 1989 (2000).
- [2] Pankhurst Q. A., Connolly J., Jones S. K. Dobson J., J. Phys. D: Appl.Phys. 36, R167 (2003).
- [3] Georgakilas V., Gournis D., Tzitzios V., Pasquato L., Guldi D. M., Prato M., J. Materials Chemistry 17, 2679 (2007).

The nonpolar- semipolar boundaries in III-nitrides: Atomic structure and influence on defect introduction

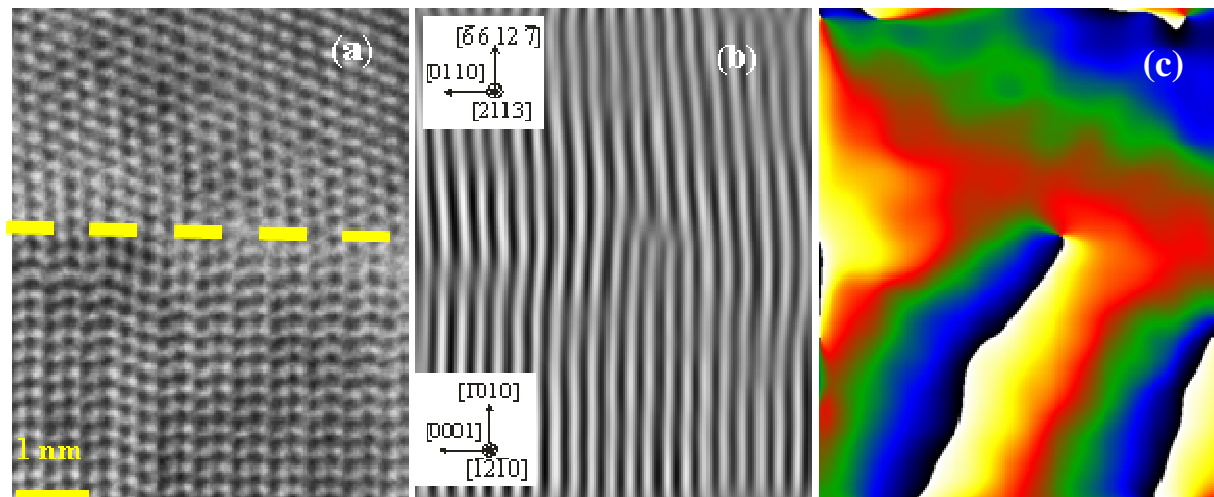
J. Kioseoglou¹, G. P. Dimitrakopoulos¹, J. Smalc-Koziorowska^{1,2}, Ph. Komninou^{1*} and Th. Karakostas¹

¹ Department of Physics, Aristotle University, GR 54124 Thessaloniki, Greece

² Warsaw University of Technology, Department of Materials Science, Poland

*komnhnoy@auth.gr

In III-Nitride compound semiconductor nanotechnology, a lot of emphasis has been placed recently on achieving good quality epilayers grown along nonpolar and semipolar orientations. This is done in order to reduce the polarization-induced internal electrostatic fields and the quantum-confined Stark effect that hamper the quantum efficiency of optoelectronic device active regions. During the growths of both nonpolar or semipolar nitrides on *r*-plane or *m*-plane sapphire respectively, parasitic misoriented nanocrystals are often observed at the epilayer/substrate interface causing introduction of threading dislocations (TDs) [1,2]. This phenomenon is facilitated by the high order of common symmetry conserved by the $90^\circ[11\bar{2}0]$ rotation which characterizes the misorientation between the parasitic nanocrystals and the matrix epilayers. In the present work we characterize by atomistic simulations combined with high resolution transmission electron microscopy (HRTEM) observations the $(10\bar{1}0)/(2\bar{1}\bar{1}2)$ grain boundary (GB) which was found to be important in *a*-plane GaN epilayers grown on *r*-plane sapphire, and to lead to TD introduction. For the atomistic simulations the modified Stillinger –Weber and Tersoff empirical interatomic potentials were employed. Two principal structural configurations were compared, in particular a GB comprising interfacial dislocations and a GB with interfacial disconnections i.e. dislocations exhibiting also step character. It was found that, the dislocated GB exhibits curvature at the points where the interfacial dislocations are located. On the other hand the disconnected GB exhibits no curvature and moreover, appears to explain the HRTEM observations. The Burgers vector of the disconnections is of the $1/6[2\bar{2}03]$ type and was verified on the HRTEM image by using circuit mapping. In agreement with nodal balance requirements, such defects can give rise to TDs emanating into the epilayer. This nanomechanism of defect introduction is in agreement with the experimental observations.



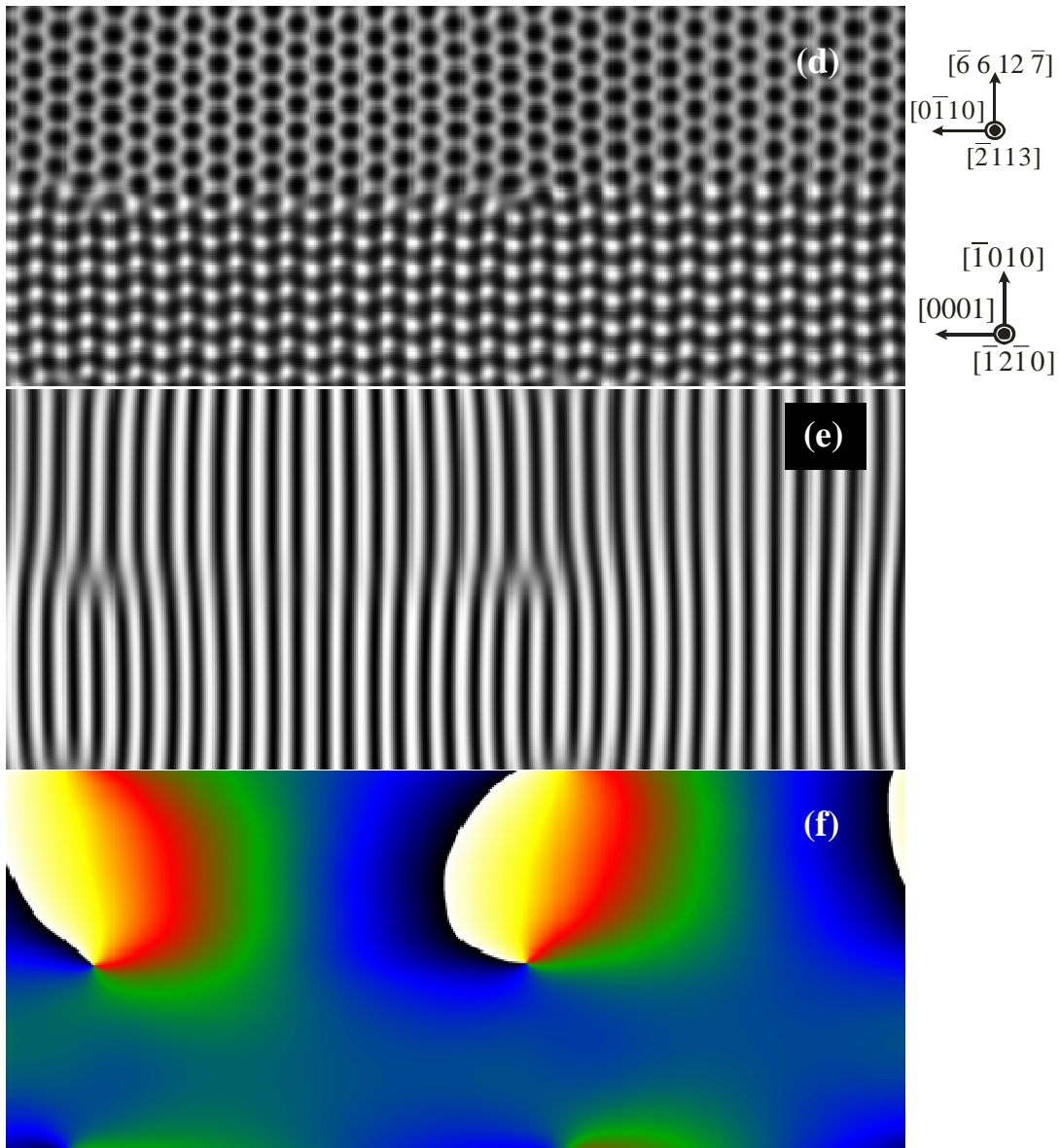


Figure 1. (a) HRTEM image of the $(10\bar{1}0)/(2\bar{1}\bar{1}2)$ GB viewed along the $[\bar{1}2\bar{1}0]/[\bar{2}113]$ directions of the two adjacent GaN domains respectively. (b) the Bragg filtered image and (c) the geometric phase image. (d) The corresponding HRTEM image simulation of the relaxed atomistic configuration of the GB. (e) the Bragg filtered image and (f) the geometric phase image.

[1] J. Smalc-Koziorowska, Ph. Komninou, S.-L. Sahonta, J. Kioseoglou, G. Tsiakatouras, and A. Georgakilas, *phys. stat. sol. (c)* 5, 3748 (2008).

[2] J. Smalc-Koziorowska, G. P. Dimitrakopoulos, S.-L. Sahonta, G. Tsiakatouras, A. Georgakilas, and Ph. Komninou, *Appl. Phys. Lett.* 89, 021910 (2008).

Acknowledgement Support under the 7th European Framework Project DOTSENSE (Grant No. STREP 224212) and the MRTN-CT-2004-005583 “PARSEM” project is gratefully acknowledged.

Nanomechanical Properties of Hydroxyapatite (HA) with DAB Dendrimers (polypropylene imine) Coatings onto Titanium Surfaces

C.A. Charitidis^{1*}, A. Skarmoutsou¹, A. Tsetsekou², D. Tsiourvas³

¹*School of Chemical Engineering, National Technical University of Athens, 15780 Athens.*

²*School of Mining Engineering and Metallurgy, National Technical University of Athens, 15780 Athens*

³*National Centre for Scientific Research "Demokritos", Institute of Material Science, Agia Paraskevi 15310 Athens, Greece.*

*charitidis@chemeng.ntua.gr

Bone is a highly specialised composite consisting of hydroxyapatite (HAP) nanoplates [1], collagen and other proteins, a structure allowing synergistic structure and function during bone mineralization [2]. Implantable biomaterials for bone-grafting must possess characteristics mimicking those of natural bone in order to be successful in their application. As a consequence, the research efforts are now being directed towards biomimetic approaches for the synthesis of HAP crystals of various morphologies, employing polymers such as monosaccharides [3] and related polymers [4] or more recently dendrimers [5-7] to modulate crystal nucleation and growth. It is also known that the use of biomolecules containing specific amino acid residues, such as arginine, lysine or specific peptide sequences, e.g. the RGD sequence, encourages cell attachment, proliferation and differentiation on HA surfaces [8].

In this respect, through the presented work we provide a new route for the formation of functional coatings of HA onto titanium implant surfaces employing a cationic fourth generation diaminobutane poly(propylene imine) dendrimer (DAB) bearing 32 amine end groups for the synthesis of HAP nanorods to increase the coating strength and adhesion and to potentially induce osteogenic cell activity.

Dendrimers exhibit a highly precise architecture [9], as they are highly branched macromolecules composed of a core molecule, a large number of branches regularly extending from the core, and terminal (or surface) groups suitable for further functionalization. They have a definite molecular weight and size, in contrast to the usually broad molecular weight distribution of linear polymers, a near spherical shape for generation numbers larger than 4 and are able to encapsulate metal ions, or organic molecules (e.g. drugs) [10,11]. However, up to now, dendrimer mediated coatings of HAP onto Ti surfaces have not been studied yet.

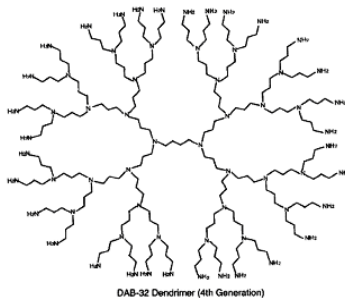


Figure 1: Schematic representation of DAB dendrimer.

For HAP synthesis, aqueous solutions of CaCl_2 (0.1 M; Sigma-Aldrich), Na_2HPO_4 (0.06 M; >99%; Fluka, Buchs, Switzerland) and 1,4-diaminobutane poly(propylene imine) dotriacontaamine dendrimer, DAB (0.2 M; DSM Fine Chemicals,) were prepared with three different calcium:dendrimer molar ratios, viz. 2:1, 1:1, 1:2. The resulting HAP suspensions were either used without any further treatment or hydrothermally treated at 80 °C for 16h, or at 130 °C for 6h. Then the suspensions after several centrifugation and washing steps were employed to coat cpTi coupons 1x1cm (3mm thickness, Aldrich) which had been previously polished with SiC paper for evaluating the nanomechanical properties.

The indentation analysis was performed using a Hysitron TriboLab® Nanomechanical Test Instrument that is capable of performing indentations. The equipment allows the application of loads from 1 to 10.000µN and the recording of penetration depths as a function of applied loads with a high load resolution (1 nN) and a high displacement resolution (0.04 nm). A Berkovich diamond indenter was used with a maximum load of 1000µN at room temperature. Since nanoindentation test results are very sensitive to the quality of the surface of the specimens, samples were first polished before indentation testing.

Coatings of all the three different calcium:dendrimer molar ratios (D, A & B, Table I) synthesized at room temperature or after hydrothermal treatment at 80 or 130 °C were tested at load 1000µN. As a result of the

synthesis conditions the grain size distribution of the coatings as well as their DAB content are different resulting in different H & E values measured. Prior to testing all the different coatings developed, indents were performed at the coating of synthesis D at 130°C on Ti substrates polished with different SiC papers in the range 200-1000. Coatings on Ti substrates ground at 400 grit led to higher H & E values and higher H/E and H3/E2 ratios which measure the coatings resistance in plastic deformation. Thus, polishing at 400 has better adhesion with the coating, since resistance to plastic deformation of the coating has the higher values.

Table I: Concentration and H&E values of three syntheses at each temperature.

Synthesis	Ratio of Ca/dendrimer	T= 20°C		T= 80°C		T= 130°C	
		H(GPa)	E(GPa)	H(GPa)	E(GPa)	H(GPa)	E(GPa)
D	2:1	3,15	118,89	2,76	111,53	2,78	102,03
A	1:1	4,26	147,98	2,38	103,17	3,9	127,5
B	1:2	1,36	91,55	0,992	39,86	1,57	90,15

Nanoindentation analysis of all coatings (A, B & D) revealed a plastic behavior. It is observed (Table 1) that at temperatures 20 and 130°C higher H and E values appear for coating of synthesis A. At temperature 80°C coating of synthesis D appear higher H and E values. It was revealed that higher values of resistance in plastic deformation (H3/E2) had synthesis A at temperatures 20 and 130°C. For temperature 80°C synthesis D had higher value of the ratio (Fig.2a). SEM analysis revealed that all coatings have porosity, with pores almost the size of grains of each coating. At Fig.2b is shown a typical example of a SEM image for synthesis D at 130°C.

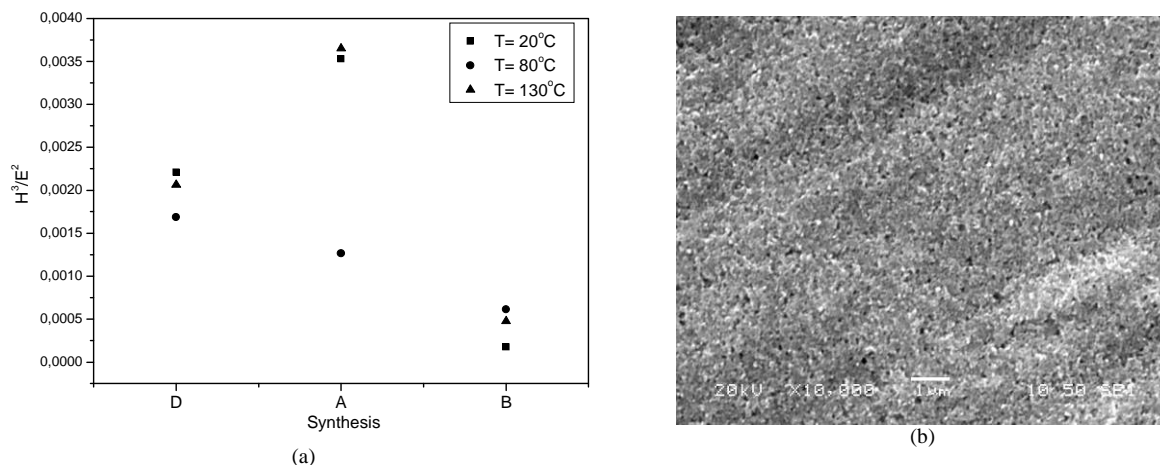


Figure 2: (a) Resistance to plastic deformation vs three different synthesis coatings at different temperatures and (b) SEM image of coating with synthesis D at 130°C.

Concluding with the study, it was shown that a better adhesion property of coatings on Ti substrates has smoothing 400. All coatings have a plastic behavior but higher H & E values have synthesis A, which has for all temperatures the smallest grain size, a medium percentage of polymer mass encapsulated in grain size and smaller pores than coating of synthesis D.

- [1] L.C. Palmer, C. J. Newcomb, S. R. Kaltz, E.D. Spoerke, S.. I. Stupp, Chem. Rev. 2008, 108, 4754-4783
- [2] H. A. Lowenstam, S. Weiner, On Biomineralization, Oxford University Press, Oxford 1989.
- [3] D. Walsh, J. L. Kingstin, B. R. Heywood, S. Mann, J. Cryst. Growth 1993, 133, 1.
- [4] Li, J., Chen, Y., Yin, Y., Yao, F., Yao, K.; Biomaterials, 28 (5), (2007) pp. 781-790.
- [5] J. J. J. M. Donners, R. J. M. Nolte, N. A. J. M. Sommerdijk, Adv. Mater. 2003, 15, 313-6.
- [6] Z.-H. Zhou, P.-L. Zhou, S.-P. Yang, X.-B. Yu, L.-Z. Yang, Mater. Research Bulletin 42 (2007) 1611-8.
- [7] J. M. Oliveira, R. A. Sousa, N. Kotobuki, M.Tadokoro, M. Hirose, J. F. Mano, R. L. Reis, H. Ohgushi, Biomaterials 30 (2009) 804–813.
- [8] G. Balasundaram, M. Sato, T. J. Webster, Biomaterials 27 (2006) 2798-2805.
- [9] J. M. J. Fréchet, D. A. Tomalia, "Dendrimers and Other Dendritic Polymers", in: Wiley Series in Polymer Science, 1st edition, J. Wiley & Sons, New York 2001.
- [10] G. R. Newkome, C. D. Shreiner, Polymer 49 (2008) 1-173.
- [11] Jansen J. J. F. G., De Brabander-van Den Berg, E. M. M., Meijer, E. W. Science 1994, 266, 1226.

Session WE4

NANOSCALE & SURFACE SCIENCE

PART 2

Wednesday, 23 September 2009, 16⁰⁰-17³⁰



Complex conducting nitrides: Synthesis, structure, properties and applications

P. Patsalas

Department of Materials Science and Engineering, University of Ioannina, Ioannina, 45110, Greece

*ppats@cc.uoi.gr

ABSTRACT: The combination of electrical conductivity, chemical and metallurgical stability, refractory character and lattice constants close to those of III-nitrides make transition metal nitrides promising candidates for electronics and device applications. We study the structure, stability and the plasma energy (or conduction electron density) of stoichiometric, transition metal nitrides of similar crystal quality as well as of the widest variety of ternary transition metal nitrides of rocksalt structure ever reported. We identify the factors, which determine the lattice constant of the ternary nitrides. We establish the phase spaces of the plasma energy (6.9-10.5 eV) and the work function (3.7-5.1 eV) of these complex nitrides with their lattice constant (0.416-0.469 nm) and we investigate the limits of their applications.

I. INTRODUCTION

The nitrides of group IVb-VIb transition metals (TMN) exhibit a unique combination of significant electron conductivity, refractory character, high hardness, chemical inertness and a cubic rocksalt structure with a lattice constant close to those of III-nitrides. These properties make them suitable for applications in electronics [1-4]. However, TMN's electronic properties should be combined with the lattice constant in order to match the substrate's lattice and prevent device's degradation and failure due to the formation of misfit dislocations [3]. Therefore, conducting ternary nitrides with tailored lattice constant can be very promising candidates replacing the currently used TiN and TaN [5-7]. In this work we review the ternary nitrides $Ti_xMe_{1-x}N$ and $Ta_xMe_{1-x}N$ (Me=Ti, Zr, Hf, Nb, Ta, Mo, W) over the whole x range ($0 < x < 1$) grown by Pulsed Laser Deposition (PLD), Dual Ion Beam Sputtering (DIBS) and Dual Cathode Magnetron Sputtering (DCMS). We investigate the validity of Vegard's rule and the effect of growth-dependent stresses to the lattice constant. Finally, we present the correlations between their lattice constant and the work function (WF) and the plasma energy E_p .

II. EXPERIMENTAL DETAILS

Ternary $Ti_xMe_{1-x}N$ and $Ta_xMe_{1-x}N$ films, 200-300 nm thick, were grown on Si{001} by reactive Pulsed Laser Deposition (PLD) using the 2nd harmonic of a Nd:YAG laser in flowing N_2 ambient. The sample composition x was changing by using mixed Ti-Me and Ta-Me targets of varying fractions. $Ti_xTa_{1-x}N$ films have been also grown by DIBS and DCMS. The composition of the films was determined by *in-situ* Auger Electron Spectroscopy (AES). The crystal structure was investigated by θ -2 θ X-Ray Diffraction (XRD) in Bragg-Brentano geometry using the $CuK\alpha$ monochromatized line.

III. RESULTS AND DISCUSSION

The XRD patterns of all the studied films exhibited exclusively the characteristic (111) and (200) peaks of the rocksalt structure for all cases without any fine structure, indicating perfect solid solutions over the full range of x ($0 < x < 1$) for all cases, demonstrating the general property of TiN and TaN being fully miscible in every MeN of rocksalt structure, independently of the phase diagram of the constituent metals. The bonding of the metal's d valence electrons with the nitrogen's p electrons [5] makes possible the formation of any rocksalt ternary nitride of the group IVb-VIb metals regardless the valence electron configuration.

The cell sizes (α) were calculated from the (111) interplanar spacings and are displayed in Figs. 1,2. The α vs. the composition x for a very wide variety of $Ti_xMe_{1-x}N$ and $Ta_xMe_{1-x}N$ (Me=Ti, Zr, Hf, Nb, Ta, Mo, W) follow distinct straight lines resembling (but not coinciding) Vegard's rule. In all cases, presented in Fig. 1, the α is expanded compared to the expected values from Vegard's rule; this is exclusively due to in-plane compressive stresses. The amount of stress is process-dependent (see Fig. 2). Thus, values of α for DIBS-grown $Ti_xTa_{1-x}N$ films are more expanded compared to those for PLD-grown $Ti_xTa_{1-x}N$ films due to excessive stress attributed to the contribution of energetic backscattered Ar neutrals. AES spectra revealed that Ar exists in the DIBS-grown films in addition to Ti, Ta and N. AES spectra from a PLD- and a DIBS-grown film, before and after annealing, exhibiting Ta (170-180 eV), Ti and N (360-420 eV) patterns are shown in Fig. 3; the DIBS sample also exhibits the Ar_{LMM} pattern (220 eV), resulting from the entrapment of backscattered Ar reflected from the target surface. After vacuum annealing at 850°C for 3 hours the stress of the films is almost completely relieved and the Ar_{LMM} pattern reduces down to the detection limit of AES, indicating a strong outdiffusion of Ar.

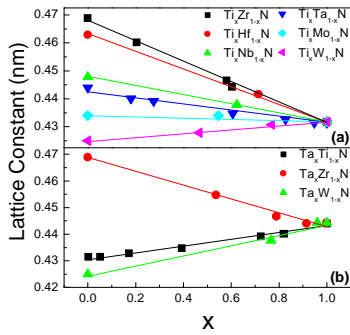


Fig. 1: Experimental demonstration of Vegard's rule for (a) Ti-based, and (b) Ta-based nitrides grown by PLD.

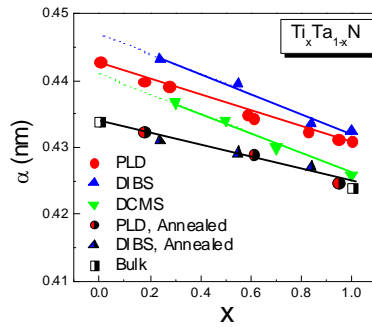


Fig. 2: Variation of the lattice constant with the composition x for ternary $Ti_xTa_{1-x}N$ grown by various techniques.

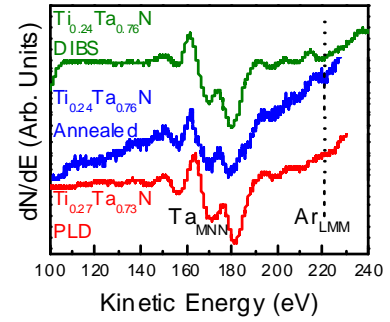


Fig. 3: AES spectra (Ta_{MNN} and Ar_{LMM} peaks) from $Ti_xTa_{1-x}N$ films grown by DIBS (and after annealing) and PLD.

The optical properties were studied using optical reflectance spectroscopy (ORS) and Spectroscopic Ellipsometry, which revealed the typical behavior of conductors, characterized by the plasma energy E_p , which is directly correlated with the conduction electron density N : $E_p = \hbar \sqrt{\frac{Ne^2}{\epsilon_0 m^*}}$. The phase space of E_p^2 with the nitride's

lattice constant has an triangular shape with TiN, ZrN and WN being at the vertices. The form of this phase space reveals that $Ti_xZr_{1-x}N$ is the most versatile system for low-mismatch growth on various semiconductors since it exhibits almost constant E_p^2 (i.e. conduction electron density) and varying lattice constant in the vast range of 0.432-0.469 nm.

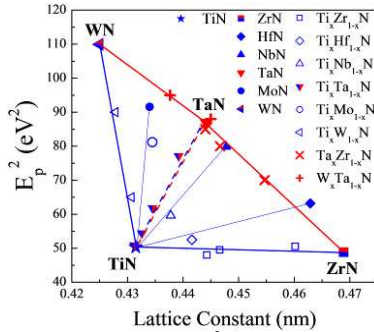


Fig. 4: The phase space of E_p^2 (which is proportional to conduction electron density) vs. the nitride's lattice constant.

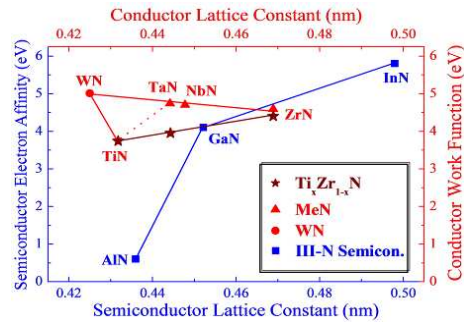


Fig. 5: The variation of WF with the nitride's lattice constant in comparison with the electron affinities and the lattice constants of III-nitrides from (Refs 7,8).

A very important factor for ohmic behavior of a contact is the WF of the conductor. WF values of selected $Ti_xZr_{1-x}N$ samples have been determined by *ex-situ* Kelvin probe measurements and are presented in Fig. 5 along with the values of binary nitrides from Ref. [8], as well as the electron affinities and lattice constants of III-nitride semiconductors. It is evident that $Ti_xZr_{1-x}N$ is structurally and electrically appropriate as growth template or ohmic contact for n -type $In_yGa_{1-y}N$. Taking into account the bandgap values of the III-nitride semiconductors, $W_xTa_{1-x}N$ might be also promising as contact on p -type $Al_yGa_{1-y}N$.

In conclusion, conducting, ternary TMN are stable in the rocksalt structure independently of the valence electron configuration of the two constituent metals and the crystal structure of the constituent binary nitrides. They exhibit a vast range of lattice constants, plasma energy (i.e. conduction electron density) and WF making them suitable for various electronic applications.

- [1] A.E. Kaloyeros, E. Eisenbraun, Annu. Rev. Mater. Sci. 30, 363 (2000).
- [2] P. Ruterana *et al*, Phys. Status Solidi A 176, 767 (1999).
- [3] T. Seppänen, L. Hultman, J. Birch, M. Beckers, U. Kreissig, J. Appl. Phys. 101, 043519 (2007).
- [4] V. Cimalla, J. Pezoldt, O. Ambacher, J. Phys. D: Appl. Phys. 40, 6386 (2007).
- [5] L.E. Koutsokeras *et al*, Appl. Phys. Lett. 93, 011904 (2008).
- [6] G.M. Matenoglou *et al*, J. Appl. Phys. 104, 124907 (2008); G.M. Matenoglou *et al*, J. Appl. Phys. 105, 103714 (2009).
- [7] G.M. Matenoglou, L.E. Koutsokeras, and P. Patsalas, Appl. Phys. Lett. 94, 152108 (2009).
- [8] Y. Gotoh *et al*, J. Vac. Sci. Technol. B21, 1607 (2003); P.-C. Jiang *et al*, Appl. Phys. Lett. 89, 122107 (2006).

Acknowledgments: This is a review of a team work carried out at the University of Ioannina. Therefore, the author is grateful to all co-authors of Refs. 5-7 for their collaboration.

On the Substrate-Driven Oxidation of Ni/NiO(001) by X-ray Photoelectron Spectroscopy and Molecular Dynamics Simulations

E. Symianakis^{1*}, G.A. Evangelakis² and S.Ladas¹

¹Department of Chemical Engineering, University of Patras and ICE/HT-FORTH
26504, Rion, Patras, Greece

²Department of Physics, University of Ioannina, Ioannina 45110, Greece

*manos_simianakis@chemeng.upatras.gr

The reactivity of the substrate plays a critical role in the formation of metallic particles and thin films on oxide substrates, which are related to technological applications, such as gas sensors, metal-oxide contacts, microelectronic and photovoltaic devices, anticorrosion coatings, and oxide supported transition metal catalysts. Certain oxides can oxidize deposited metals at elevated temperatures via oxygen diffusing to their surface from the bulk. This has been reported for Ni and Cr of the order of a few monolayers deposited under UHV on single crystals of yttria-stabilized-zirconia (YSZ), the oxidative capacity of which is due to the known presence of a small bulk concentration of excess non-stoichiometric oxygen [1-3]. This behaviour is not exhibited by α -Al₂O₃ (0001) [1], while Ni deposits on NiO (001) have been also found to oxidize upon annealing in UHV above ~ 750 K [4]. The present work aims in investigating the capacity of NiO (001) single crystal to oxidize deposited Ni in excess of a monolayer, as well as in revealing the origin of the oxygen species involved. The experimental study was done by means of X-ray photoelectron spectroscopy (XPS), while the obtained results were further interpreted with the help of Molecular Dynamics simulations.

Three series of depositions were carried out, resulting in final metallic Ni coverages of 1.6 ML, 3.8 ML and 7.5 ML, as obtained by XPS. Each series was followed by annealing at temperatures ranging from 810K to 940K. When the oxidation of a deposit was completed, the next deposition series took place, whereby only the 7.5 ML deposit could not be fully oxidized within the available experimental time. Figure 1 shows the O1s/Ni2p area ratio, plotted versus the equivalent monolayers of metallic Ni on the surface for the 7.5 ML deposition. The solid line in fig.1 corresponds to the prediction of a model of continuous, amorphous and homogeneous Ni⁰ film completely covering the NiO (001) substrate. The good agreement between the experimental results and the model supports the layer-like character of the deposit even at 550 K, where the XP spectra were taken, meaning that any Ni⁰ clusters formed cover fully the substrate. It also demonstrates the absence of any oxygen that could have been adsorbed on the Ni from the gas phase following deposition.

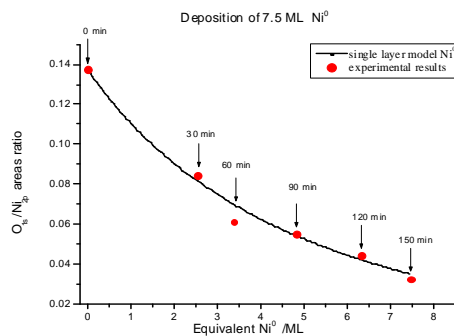


Fig.1 Intensity ratio O1s/Ni2p vs. equivalent ML of deposited Ni⁰ (experimental points) and prediction of a Ni⁰/NiO (100) layer model (solid line) for deposition up to 7.5 ML of Ni⁰.

Annealing above 550 K, up to a maximum of 940 K, results first in a fast, within a few minutes, decrease of the equivalent monolayers of metallic Ni, which is attributed to deposit sintering and secondly to a further gradual decrease of the equivalent monolayers of Ni⁰ which signifies oxidation. The evolution of the interface for sintered Ni⁰ particles partly covering the substrate is described using three limiting models. In model 1 the Ni⁰ particles are oxidized only from the bottom up, in model 2 from the top down and in model 3 from the side only. Figure 2 shows the predictions of the three models for an initial 43% substrate coverage by sintered particles, as derived from the initial fast decrease of the equivalent XPS monolayers upon annealing of the deposited 7.5 ML. As shown in fig.2, the second model, which predicts oxidation from the top, matches best the

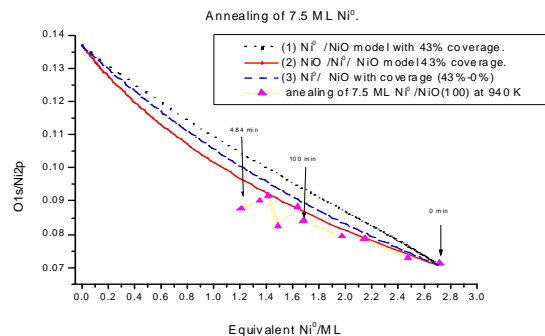


Fig.2 Intensity ratio O1s/Ni2p vs. equivalent ML of remaining Ni⁰ and predictions of three oxidation models upon annealing at 940K of 7.5 ML initially deposited Ni⁰, sintered to a substrate surface coverage of 43%.

experimental results. Furthermore, the plot (not shown) of the remaining quantity of Ni, as deduced from the XPS results in accordance with the model, versus $(\text{time})^{1/2}$ yields a straight line, suggesting that the slow step of the oxidation is the diffusion of oxygen from the bulk towards the Ni particles. The final conclusion is that the metallic Ni particles that are formed after the sintering are covered by NiO, via an oxidation process that proceeds towards their metallic core with oxygen supplied by the substrate. Taking into account the three series of depositions and annealing, at least 6 ML of metallic Ni could be oxidized by the NiO substrate.

The molecular dynamics simulations were carried out in the constant temperature canonical ensemble using the Nose scheme. Slab geometry was used, in which the simulation cell consisted of 1728 ions arranged in 12 planes, each plane containing 72 cations and 72 anions, while in the [001] direction, there was an empty space of four times the length of the slab along the z-direction. The use of periodic boundary conditions resulted in a system with two free surfaces perpendicular to the [001] direction. The equations of motion were integrated by means of Verlet's algorithm and a time step of 10^{-15} s. For the atomic interactions, we adopted a rigid ion potential developed for NiO [5], while the Coulombic contributions were evaluated with the use of the Ewald summation. The system was initially equilibrated for 20 ps, while the simultaneous deposition of Ni ions at adatom positions and the same number of O ions on the other surface of the slab maintained the charge neutrality of the system. These O ions remain at adlayer position over the surface during the simulations. It should be noted at this point that in the simulations the Ni adatoms were let to carry their formal charges (+2). Initial deposits of 8 Ni (0.06ML), 16 Ni (0.11ML) and 32 Ni adatoms (0.22ML) were performed and the evolution of the system was followed for 100000 or 300000 time steps at temperatures corresponding to $0.37T_m$ and $0.57T_m$. The local density distribution function was recorded every 2000 time steps in order to monitor the evolution of the oxygen ions distribution of the slab during each simulation run. By integration of each of the peaks that correspond to each lattice layer the average number of oxygen ions by layer during each simulation can be obtained. Fig. 3 shows the local density distribution function for a simulation of 200000 time steps, whereby 32 Ni ions were placed near the surface at the positive side of the slab and fig. 4 shows the evolution of the average number of anions by layer down to the fourth (layer 5) for 300 000 time steps, expressed as percentage deviation from the perfect lattice, while the solid line displays the deviation from the 32 anions of the fully oxidized adlayer. The deposited Ni ions are initially forming diffusing Ni_xO_y chains, which eventually collide to form non-diffusing NiO ad-islands. The increase of the anions on the surface that occurred between 80000 and 100000 steps coincides with the coalescence of several chains into ad-islands.

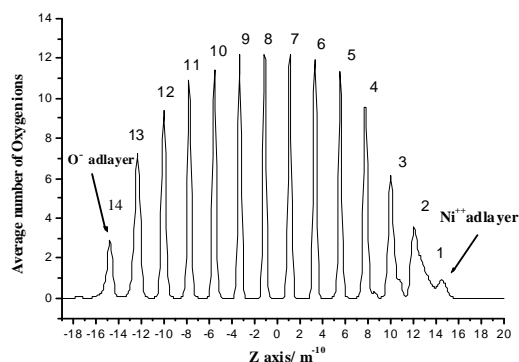


Fig.3 Local density distribution function on the Z axis of the slab, of oxygen ions for deposition of 32 Ni^{++} and 32 O^- ions and after 200 000 simulation steps, (numbers are used to identify lattice layers).

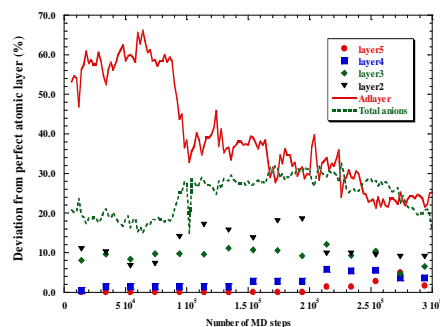


Fig.4 Deviation (%) from the perfect lattice of the average number of oxygen ions per layer (for four layers), after the deposition of 32 Ni^{++} ions during 300 000 simulation steps, total anions line refers to layers 2, 3, 4 and 5.

The simulations demonstrated the capability of the NiO (100) perfect crystal to provide large number of oxygen ions that are bonded to the deposited Ni ions on the surface, with concomitant formation of vacancies in the near-surface layers. This is a possible explanation for the origin and the quantities of the oxygen that is needed for the oxidation of the 6 ML of Ni^0 that was oxidized during the experiment.

- [1] L. Sygellou, S. Zafeiratos, N.Tsud, V.Matolin, S. Kennou, S.Ladas, Surface and Interf. Analysis 34 (2002) 545.
- [2] L.Sygellou, S. Ladas, Surf. Sci., 566 (2004) 698.
- [3] O. Khyzhun, L. Sygellou, S.Ladas, J. Phys. Chem. B., 109 (2005) 2302.
- [4] E. Symianakis, S. Ladas, G.A. Evangelakis, Appl. Surf. Sci. 217 (2003) 239.
- [5] C. Massobrio, M. Meyer, J.Phys.:Condens. Matter 3 (1991) 279.

Magneto-Optical Properties of Iron Oxide Nanoclusters

A. Kostopoulou^{1,2,*} and A. Lappas¹

¹ *Institute of Electronic Structure and Laser, Foundation for Research and Technology-Hellas, Vassilika Vouton, 71110 Heraklion, Greece*

² *Department of Chemistry, University of Crete, Voutes, 71003 Heraklion, Greece*

* *akosto@iesl.forth.gr*

The synthesis of nanostructured magnetic materials has become a particularly important area of research and is attracting a growing interest because of the potential applications in ferrofluids, in biotechnology/biomedicine, such as in directed delivery of drugs and even as contrast agents in magnetic resonance imaging (MRI). Appropriate combination of two different materials in nanoscale range, a magnetic and a metallic, may lead to the development of a multifunctional system that exhibits magnetic and optical (plasmonic) properties at the same time. The key feature for these heterostructures is their solubility in aqueous media, an especially critical property if we wish to achieve optimum functionality in the fields of biology and medicine.

Iron oxide colloidal nanoclusters (CNCs) were synthesized by a high temperature hydrolysis process with glycol as a solvent and FeCl_3 as a metallic precursor [1]. A polyelectrolyte (i.e poly(acrylic) acid, PAA) was used as capping agent. The CNCs have a “flower-like” shape (Fig.1) and are consisted of smaller nanocrystals (5-10nm). The polymer in this reaction has a double role, aids the formation of the CNCs and their solubility into the water. The CNCs are superparamagnetic at room temperature and display soft ferromagnetic-like behaviour below the blocking temperature; the latter is also proved to be a size-depended parameter. These CNCs respond to the application of an external magnetic field and form ordered arrays in aqueous media, while at the same time exhibit unusual optical properties. The wavelength of the reflectance maximum intensity shifts to the blue region as the strength of an external magnetic field increases (Fig. 2).

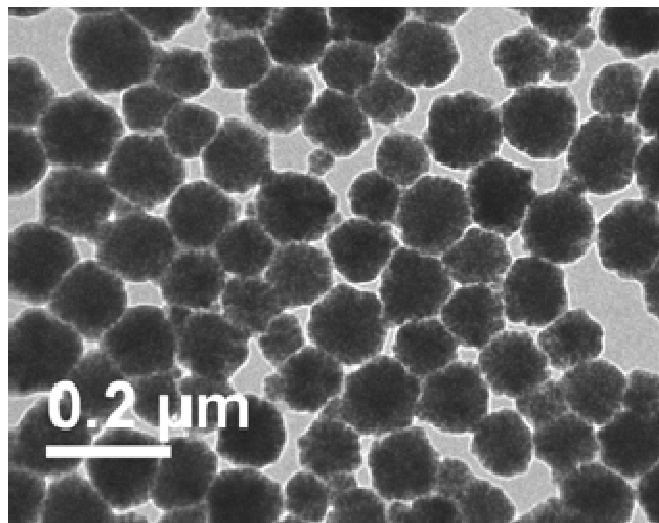


Fig 1. Iron oxide CNCs with mean diameter of ~120 nm.

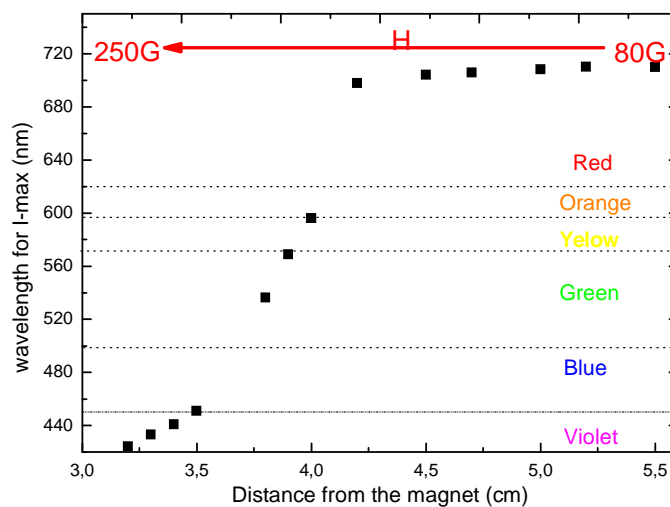


Fig 2. The wavelength (nm) of reflectance maximum intensity as a function of the distance of the sample from the magnetic field.

After the preparation of the heterostructure magnetic component (CNC) there was an effort to use it as seed and grow on it the second component, i.e. the metallic particles. The heterostructure combine the magnetic properties from the CNCs and the plasmonic properties of the metal component. We wanted to investigate the magnetic and the optical properties of the combined system and compare them with those of the pure CNCs.

[1] Ge J., Hu Y., Biasini M., Beyermann W., Yin Y., *Angew. Chem. Int. Ed.* 46, 4342 (2007).

Acknowledgements:

The Marie-Curie Transfer of Knowledge program of the European Commission is acknowledged (“NANOTAIL”, Grant no. MTKD-CT-2006-042459).

Mechanical Properties of Nanocrystalline Copper

N. Galanis, I. N. Remediakis and G. Kopidakis*

Department of Materials Science & Technology, University of Crete, Heraklion, Greece

**kopidaki@materials.uoc.gr*

As most ordinary solids are polycrystalline, the dependence of mechanical and other properties on the size of their grains is a question of fundamental interest for materials science. The hardness of polycrystalline metals increases with decreasing grain size, in accordance to the Hall-Petch law: their hardness is a linear function of d^{-n} , where d is the average grain size and $n > 0$. On the other hand, when the grain size reaches the nanometer range, several metals have been found to exhibit a so-called “reverse Hall-Petch effect”, and become softer at smaller grain sizes. Some very recent experiments show that nanocrystalline ceramics might show the same effect.

In the present work, we present simulations that demonstrate the reverse Hall-Petch effect for a typical metal (Copper). We consider fully three-dimensional model structures, having several grains of random sizes and orientations, and employ state-of-the-art Molecular Dynamics simulations. Samples are created in an automated way using the Voronoi construction method, while the grain size is deduced from sophisticated local order analysis. The properties of the material are themodynamical average values over several different samples.

We calculate structural properties and the full elasticity tensor of the material. We used the determined elastic moduli and Voigt’s formulae in order to estimate the bulk-, shear- and Young’s modulus of the material. Our results compare well with experimental observations. Moreover, we verify that this material becomes softer at small grain sizes. The effect is attributed to the large concentration of grain boundary atoms at smaller grain sizes. Our analysis yields scaling relations for the elastic constants as a function of the average grain size.

Indium Adsorption on the Reconstructed $\text{Si}(111)\sqrt{3}\times\sqrt{3}$ and 4×1 -In Surfaces at Room and Low Temperature

D. Vlachos*, M. Kamaratos and S. Foulas

Surface Physics Laboratory, Department of Physics, University of Ioannina,
PO Box 1186, GR-451 10, Ioannina, Epirus, Hellas

* *dvlachos@cc.uoi.gr*

Abstract

In this work we experimentally study the In adsorption on the reconstructed $\text{Si}(111)\sqrt{3}\times\sqrt{3}$ and 4×1 -In surfaces at room and low temperature. The low energy core levels Si 2p and In 4d as well as the valence band are measured by synchrotron radiation facilities to reveal the structural and the electronic properties.

Introduction

The ability to control the morphology of atomic overlayers on surfaces, is of fundamental importance in nanotechnology. In particular, the shape, the height and the size of the grown nanostructures, affect and ultimately determine the functionality and the performance of the modern micro- and nanoelectronic devices. Therefore, one needs to know the atomistic mechanisms which determine the growth of nanostructures on surfaces, in order to finally achieve selective fabrication of specific nanoscale devices with desirable properties. In the last decade, there is a great research effort in this direction and more particularly in the development of metal/semiconductor epitaxial systems. In this work we investigate the In ultrathin film development on the reconstructed $\text{Si}(111)\sqrt{3}\times\sqrt{3}$ and 4×1 -In surfaces at room and low temperature by using synchrotron radiation facilities.

Experimental

The experiments were performed at BACH beamline in ELETTRA synchrotron radiation center in Trieste in Italy. The sample was a *p* type Si(111) single crystal of resistivity 100 Ωcm , while the indium deposition on the substrate was done in steps of successive doses (1D=10 min) by using a Knudsen cell. An average flux of ~ 0.07 monolayers (ML)/min was estimated throughout the experiments. Low energy electron diffraction (LEED) measurements, were also performed to monitor the In reconstructed $\text{Si}(111)\sqrt{3}\times\sqrt{3}$ and 4×1 -In surfaces. The study is mainly based on the Si 2p and In 4d photoemission spectra as well as on the valence band measurements.

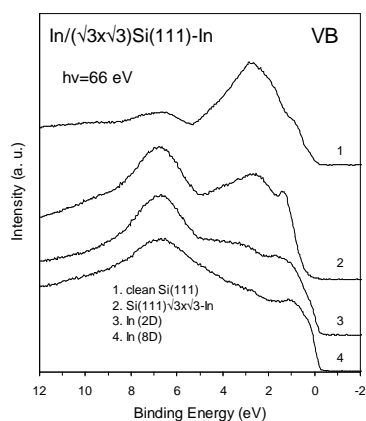


Figure 1. The valence band spectra for In adsorption on the $\text{Si}(111)\sqrt{3}\times\sqrt{3}$ -In surface.

Results and Discussion

Initially the two indium reconstructed silicon surfaces were studied for reference purposes giving consistent results with the literature [1,2]. Next, we started the In deposition on both of the reconstructed Si(111) surfaces. The results show that indium develops in the form of metallic nanoparticles changing the electronic and structural properties of the reconstructed substrate. For example, the semiconducting character of the $\text{Si}(111)\sqrt{3}\times\sqrt{3}$ -In is transformed into metallic as the density of the states increases at the Fermi edge as Fig. 1 shows. The metallic character of the In particles is also indicated from the asymmetric shape of the In 4d doublet at the higher binding energy side as it

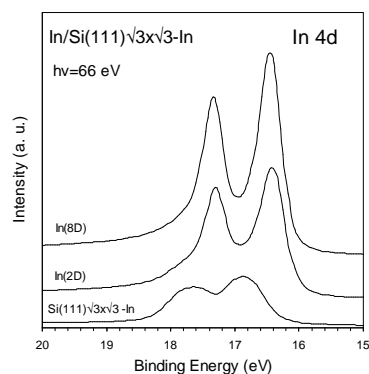


Figure 2. Indium 4d photoemission spectra for In adsorption on the $\text{Si}(111)\sqrt{3}\times\sqrt{3}$ -In surface.

is shown in Fig. 2. This asymmetry is originated by the inelastic collisions of the photoelectrons with the free electrons in the conduction band of the interface. Further investigation was carried out by performing measurements at low temperature to determine how the properties of the In/Si interface are affected by the kinetics at the nanoscale.

Conclusions

Conclusively, as far as it concerns the room temperature experiments, it seems that the different reconstruction of the substrate does not crucially affect the structural and electronic properties of the In overlayer. The low temperature results are still under consideration.

References

- [1] T. Abukawa, M. Sasaki, F. Hisamatsu, M. Nakamura, T. Kinoshita, A. Kakizaki, T. Goto and S. Kono, J. Electr. Spectr. & Relat. Phenom. 80 (1996) 233.
- [2] S. W. Cho, K. Nakamura, H. Koh, W. H. Choi, C. N. Whang, and H. W. Yeom, Phys. Rev. B 67 (2003) 035414.

Acknowledgements: This work was supported by EU through the contract RII3-CT-2004-506008 (IA-SFS).

Session WE5

SPECIAL SESSION ON

*RENEWABLE
ENERGY
RESOURCES
– HYDROGEN*

*Under the auspices of Hellenic Society
for Science and Technology of
Condensed Matter
(H.S.S.T.C.M)*

Wednesday, 23 September 2009, 17³⁰-18³⁰



Solar Thermochemical Water-Splitting for Hydrogen Production: The Hydrosol Process

Athanasios G. Konstandopoulos

Aerosol & Particle Technology Laboratory, CPERI/CERTH, Themi, Greece and Dept. Chemical Engineering, AUTH, Thessaloniki, Greece

We present the Hydrosol process for solar thermochemical hydrogen production via water splitting in monolithic reactors. The reactor concept is adapted from the well-known automotive emission control field, and consists of a multichannel ceramic honeycomb body, coated with nanostructured mixed oxide materials. The coating is able to cycle between a reduced and an oxidized state. The reactor is heated by concentrated solar radiation and is fed with water vapor. The active coating reacts with the water molecule by “trapping” its oxygen and leaving in the effluent gas stream pure hydrogen. In a subsequent step, the oxygen “trapping” material is regenerated, by increasing the amount of solar heat absorbed by the reactor; hence a cyclic reduction-oxidation (redox) operation is established. Monolithic reactors represent a very promising technology for large-scale, emissions-free solar thermochemical hydrogen production.

Perpectives and Challenges of Hydrogen Storage in Metal Hydrides. The Case of the CRES Wind-Hydrogen Plant

Varkaraki E.^{1*}

¹ *Centre for Renewable Energy Sources and Energy Saving*

**evarkara@cres.gr*

In view of a future hydrogen-inclusive economy, there is a great need to develop safe, dense, and cost-effective methods to store hydrogen. Metal hydrides are formed by the reaction of hydrogen with metals, intermetallic compounds and their alloys. The reaction, also called absorption process is reversible, and therefore, it can be used to store hydrogen in a very restricted volume. A wide variety of materials has already been studied for the solid state storage of hydrogen, under various conditions of pressure, temperature and hydrogen density [1].

The main advantages of hydrogen storage in metal hydrides are a high volumetric density, the use of rather low pressures, and the possibility of long term storage without losses. On the other hand, the gravimetric hydrogen density is rather low and limited to less than 3% mass for hydrides operating at near ambient temperature and pressure. While a low gravimetric density is a drawback for transport applications, it is not essential for stationary applications.

If waste heat is available, the metal hydrides can play a dual role for both storing and compressing hydrogen. Hydrogen can be absorbed at low pressure and later recovered at a higher pressure, by supplying more heat than would be necessary for the desorption at a similar pressure. In such a case, the electrical energy needed to run a hydrogen compressor is spared either completely or to some extent, by avoiding the initial, energy-intensive compression stages.

One of the challenges for the development of solid state hydrogen storage is to better understand the interaction of hydrogen with metals, as well as the behavior of impurities present in the hydrogen flow. Metal hydrides can be used for the purification of hydrogen, since only the hydrogen molecule can enter inside the lattice, leaving the impurities in the gas phase or at the surface of the alloy.

At the wind-hydrogen plant of CRES in Keratea, Greece, the metal hydride tanks are based on the AB5 family of intermetallic compounds, which generally crystallize into a hexagonal structure, and can absorb/desorb hydrogen at near ambient temperature. Hydrogen is produced by alkaline electrolysis at a maximum rate of 0.45 kg/h and at 2 MPa pressure. It is stored in six metal hydride tanks with a total capacity of 3.6 kg hydrogen. Hot water for the desorption of hydrogen is supplied by an electrical boiler (4 kW) and cooling water can be provided, if necessary, from a water chiller. Alternatively, hydrogen can be compressed up to 220 MPa in a single-stage compressor, to fill high pressure cylinders. All the components and utilities of the wind-hydrogen system are supplied by wind energy, but only the electrolyser can withstand power variations on a per second basis.

The metal hydride storage consists of 6 water-cooled sub-units, containing a metal alloy based on Lanthanum-Nickel ($\text{La}_{1-x}\text{Ce}_x\text{Ni}_5$). It has been designed by the Frederick Institute of Technology, Cyprus, and manufactured by Labtech SA, Bulgaria. The mass specific hydrogen capacity is 1.28%w for the alloy and 0.66%w for the metal hydride tanks with cooling jackets. There is no pressure or temperature measurement inside the tanks, but the hydrogen pressure is measured on the line after the isolation valves, so it is equal to the pressure in the void space of the hydride tank when the valves are open. The water temperature is measured at the inlet and outlet of the cooling jacket, and therefore, the hydride temperature can be roughly estimated by extrapolation. The eventual presence of "hot spots" inside the tanks cannot be detected.

Hydrogen produced by alkaline water electrolysis generally contains small quantities of oxygen (0.2 to 0.5%v.) and is saturated with water vapour at the pressure and temperature of delivery. It may be purified by passing it through a catalytic deoxidizer, where the oxygen reacts with hydrogen producing more water vapour and a drier, in order to remove the humidity to the residual level desired. The reaction of oxygen and/or water with the intermetallic compound is strongly exothermic and, even if an explosion does not occur at such low concentrations, the hydrogen absorption capacity is expected to decrease. The effect of such impurities is not yet well understood.

In the present case, the oxygen content in hydrogen is approximately 0.2%v. and the humidity content corresponds to an atmospheric dew point of around 12°C. Three of the six hydride tanks are filled with the electrolytic hydrogen without purification, in order to study the effect on their cycling capability. Until now, the tanks have only been subject to a few dozens of absorption/desorption cycles, but the storage capacity has not decreased so far. An absorption experiment is shown in Figure 1.

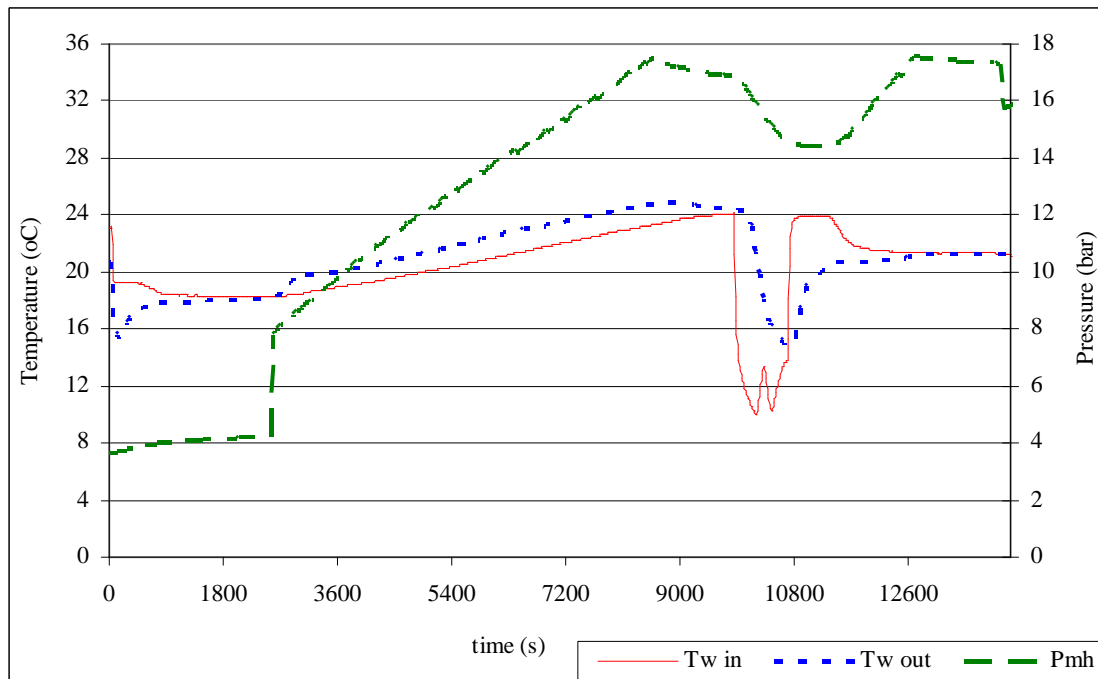


Figure 1. Hydrogen absorption in the metal hydride tanks.

In the experiment of Figure 1, the electrical boiler is not operating, but water from its reservoir is re-circulated in closed circuit, in order to absorb the heat from the hydriding reaction. Initially, the water temperature at the outlet of the cooling jacket is lower than at the inlet, because the temperature in the metal hydride tanks is lower than in the boiler reservoir. Once the water temperatures are stabilized (at around 18°C), the corresponding pressure (0.4 MPa), is considered as the initial equilibrium pressure. The main valve is opened and hydrogen is allowed in the metal hydride tank. The tank pressure increases instantly at the pressure of the hydrogen delivery line (0.8 MPa), because hydrogen fills the void space over the metal hydride. During absorption, the pressure increases gradually, and the heat produced by the reaction of hydride formation is used to heat up the water in the boiler reservoir. After approximately one and a half hours, the tank pressure approaches 1.8 MPa and the main valve is closed. Even without external hydrogen supply, the hydriding reaction continues, because the system is not yet at equilibrium. At some moment, cooling water from the water chiller is injected in the circuit for a few minutes and the system is allowed to reach an equilibrium. When the water temperatures are stabilized again (at around 21°C), the corresponding pressure (1.7 MPa) is considered as the final equilibrium pressure.

At the end of the experiment, the small decrease in pressure (down to 1.6 MPa) is due to a rapid venting (a few seconds) of the hydrogen present in the void space above the hydride tanks. This procedure was adopted, in order to vent the gas phase over the metal hydride, which may be enriched in accumulated impurities. The gas phase over the metal hydride cannot be continuously analysed, but the analysis of the oxygen in hydrogen content during the desorption phase has always shown values below 20-40 ppm. More investigations are necessary for a better estimation of the effect of the impurities on the performance of the hydrogen storage.

To the extent possible, the hydrogen absorption phase should occur without external cooling, in order to reduce the overall energy consumption of the system. In the same way, for the hydrogen desorption phase, it is also important to have a source of waste heat available, in order to avoid the use of an electrical boiler. Hydrogen storage in metal hydride tanks seems particularly interesting when it can be combined with a simultaneous purification and compression of hydrogen.

[1] Sandrock G., Thomas G, Compilation of IEA/DOE/SNL Hydride Databases, IEA Technical Report, (September 1997).

Author index

- Achilias D. S.*, 359
Adamopoulos O., 219
Adikimenakis A., 50
Afouxenidis D., 83, 84, 251, 367
Ahmed Saleh S., 206
Aifantis E. C., 351
Alexandrakis V., 183
Almpanis E., 23
Almyras G. A., 11, 19
Anagnostopoulou E., 209
Anastasiadis S. H., 260, 326
Anastasiou M., 213
Andrianakis A., 35
Andrikopoulos K. S., 45, 345
Andriotis A. N., 231
Angelakeris M., 185, 187, 189, 195, 209, 215
Angelopoulou A., 347
Angelova S., 217
Anne M., 3
Antonakos A., 8
Antoniadis G., 198, 200
Apostolopoulos G., 66, 96, 117
Apostolopoulos P., 131
Arampatzis-Ziamos P., 175
Arapi M., 247
Ares S., 343
Argirusis Ch., 20, 126
Argitis P., 111
Argyarakis P., 202, 203, 249, 302, 304, 306
Arvanitidis J., 12, 33, 345, 368
Aspiroz X., 155
Athanasopoulos G. I., 110
Avramov I., 302
Aydogdu G. H., 8

Bakas T., 183, 310, 355, 376
Bakin A., 318
Ballarini R., 351
Barmparis G. D., 290
Bassiakos Y., 206
Batistakis C., 304
Beltsios K. G., 183
Berdekas D., 67
Biancalana F., 109
Bikiaris D. N., 198, 200, 363
Binns C., 238, 285

Biros T. P., 351
Blackman J. A., 238
Bokas G., 283
Boscherini F., 115
Bösing M., 56
Bras W., 260
Brauckmann J. G., 20
Brintakis K., 308
Brown C. M., 219
Butt H.-J., 328

Calamiotou M., 137, 159
Canard B., 255, 258
Carmi S., 203, 249
Chaliampalias D., 147, 149
Chalkidou A., 215
Chamos A. N., 288
Chapon L. C., 219
Charitidis C. A., 167, 286, 288, 296, 298, 379
Chasoglou D., 267
Chatzidimitriou-Dreismann C. A., 66, 117
Chatzistavrou X., 365, 367
Chrissafis K., 73, 139, 198, 200, 355
Chrissopoulou K., 260
Christodoulakis K., 326
Christofilos D., 33, 373
Civici N., 211, 247
Collaert N., 90
Collings I., 255
Conder K., 159
Constantoudis V., 88
Coutard B., 258
Creatore C., 109
Crisan A. D., 228
Crisan O., 228, 285
Ctistis G., 226

Dalas E., 353
Dallas G. I., 83
Davazoglou D., 111
Delides C. G., 329, 331, 333, 335
Delimitis A., 75, 291, 341
Deliolanis N. C., 58
Dendrinou-Samara C., 185, 195, 215
Desilvestro J., 37
Diamantogiannis G., 235

- Diamantopoulos G.*, 125, 257
Dietl T., 161
Dimakogianni M., 71
Dimitrakopoulos G. P., 50, 60, 64, 94, 314, 377
Dimitriadis C. A., 90
Dimitrijevic M., 41
Dimitropoulos P. D., 80
Dimopoulos T., 183
Dimoulas A., 96
Domingo N., 238
Dooryhee E., 3
Dounos Ch., 235
Douvalis A. P., 310, 355, 376

Economou E. N., 105
Efremidis A. T., 58
Efthimiadis K. G., 129, 173, 175, 177, 181, 193
Efthimiopoulos I., 30, 31, 32
Eickhoff M., 94
Eleftheriou E., 229
Ellis A. M., 285
Elshaer A.-H., 318
Emmanouil K., 353
Emtsev V., 35
Eppel S. J., 351
Erko A., 121
Evangelakis G. A., 11, 19, 283, 385

Falaras P., 37, 39
Fardis M., 125, 167, 257
Farle M., 223
Fessatidis V., 78
Filippaki E., 205, 206
Filippi M., 8
Filippidis A., 294
Filippousi M., 294
Fiorani D., 238
Firsov A., 121
Fitch A. N., 255
Flevaris N. K., 187
Floudas G., 328
Fostiropoulos K., 54
Fotiadou S., 260
Fotopoulos A., 341
Foulias S., 390
Fournou E., 12, 345
Frangeskou F., 195

Frangis N., 119, 280
Frangouli A., 187
Ftikos Ch., 126
Fumagalli P., 226

Gaki A., 191
Galani N., 389
Galata S. F., 96
Galiotis C., 10, 17
Gamaletsos P., 355
Gantis A., 159
Garas A., 202
Gautron E., 258
Georga S. N., 92
Georgakaki D., 278
Georgakilas A., 50
Georgiadis I., 294
Georgiadis J., 185
Georgiadou D. G., 111
Georgiou C., 298
Georgiou D., 54, 56
Ghibaudo G., 90
Gialampouki M., 284
Giannarakis I., 187
Giannouli M., 273
Giapintzakis J., 110
Gidopoulos N., 117
Giersig M., 226
Giesen C., 50
Giot M., 219
Gioti M., 52
Gioulekas D., 357
Gjoka M., 137, 177, 185, 193
Gkinis Th., 189
Glenis S., 169, 171
Godelitsas A., 355
Gogolides E., 88
Göttlicher J., 355
Goudouri O. M., 361, 365
Gountsidou V., 349
Gournis D., 376
Goutziotis Th. A., 43
Grammatikopoulos S., 235
Grattarola M., 153
Gravalidis C., 54, 56
Green M. A., 219
Grigoriadis C., 328
Grigoriadou I., 363
Grolimund D., 357

- Gupta A., 228
 Guskos N., 169, 171

 Haase N., 328
 Habermeier H-U, 8
 Hadjiapostolidou D., 151
 Hadjisavvas G. C., 272
 Hanfland M., 30, 31, 32
 Harikisun R., 37
 Hasapis Th. Ch., 45
 Hatzikraniotis E., 45, 76
 Havlin S., 203, 249
 Hawke L. G. D., 262
 Heuken M., 50, 54, 56
 Hodeau J-L., 3
 Hofmann M., 153
 Holldack K., 121
 Hristoforou E., 129, 173, 224
 Hryha E., 267

 Iliopoulos E., 87
 Ioannidou A., 320, 321
 Ioannou – Sougleridis V., 92
 Ioannou G., 337

 Jancic Heinemann R., 41
 Jansen R. H., 56
 Jimenez C., 155
 Julien F. H., 94

 Kafesaki M., 105
 Kaidatzis A., 236
 Kakali G., 191
 Kalesaki E., 27, 60, 314
 Kalfagiannis N., 280
 Kalisch H., 56
 Kalogirou O., 73, 185, 189, 193, 195, 209, 215
 Kalosakas G., 262, 343
 Kamaratos M., 390
 Kanapitsas A., 333, 335
 Kanatzidis M. G., 119
 Kandaswamy P. K., 94
 Kantiranis N., 361
 Kapaklis V., 75, 226, 235
 Karafiloglou P., 245
 Karafyllidis I. G., 197
 Karahaliou P. K., 47
 Karakasidis T. E., 322, 324
 Karakosta E., 125, 257
 Karakostas Th., 27, 50, 314, 377
 Karanika A., 298
 Karapanagiotis I., 208
 Karavangelis Ch., 191
 Karayannidis G. P., 359
 Kargas B., 12, 345
 Karmakar S., 30, 31, 32
 Karoutsos V., 235
 Kasiteropoulou D., 324
 Kassapoglou Ch., 131
 Kastanis D., 10
 Kastriotou M., 153
 Kataura H., 33
 Katsamanis V., 326
 Katsikini M., 12, 135, 157, 357, 368
 Katsiotis M. S., 257
 Kavouras P., 12, 64
 Kazakopoulos A., 73, 181
 Kehagias Th., 50, 60, 64, 94, 125, 189, 314
 Keiper D., 56
 Kelaidis N., 92
 Kelires P. C., 271, 272, 277, 375
 Kellerman B., 92
 Kennou S., 316
 Keremi Y., 157
 Kiely C. J., 291
 Kikkinides E. S., 320, 321
 Kim J. S., 32
 Kioseoglou J., 27, 50, 60, 314, 377
 Kirmse H., 50
 Kitis G., 83, 84, 251, 367
 Kittas A., 203
 Kleovoulou K. T., 277
 Koidis P., 365
 Komninou Ph., 27, 50, 60, 64, 92, 94, 314, 377
 Konstandopoulos A. G., 395
 Kontonasaki E., 365
 Kontos A. G., 39
 Kopidakis G., 389
 Kordas G., 347
 Koschny Th., 105
 Kosmas K., 129, 173
 Kosmopoulos J. A., 47
 Kostopoulou A., 308, 310, 387
 Kotoulas A., 185
 Kotzamanidi I., 205
 Kouloukris V., 320

- Koumoulis D.*, 165, 167
Koumoulos E. P., 286
Kourouklis G. A., 33
Koutsokeras L. E., 43, 296
Kremer R. K., 30, 32
Kripotou S., 22
Krontiras C. A., 92
Kuncser V., 228
Kunze J., 39
Kypriotis A., 208
Kyratsi Th., 76
Kyriakou A., 213
Kyritsis A., 22

Ladas S., 385
Lafatzis D., 282
Lagogianni A. E., 19
Lagoyannis A., 128
Lahourcade L., 60, 94
Lampakis D., 8, 159
Langbein W., 109
Lantez V., 258
Lappas A., 219, 308, 310, 387
Laskarakis A., 54, 56
Leftheriotis G., 98
Lekka Ch. E., 11, 19, 43, 283, 284, 296
Lemmens P., 31
Leontiou T., 375
Liakopoulos A., 322, 324
Liakos D. G., 256
Liarokapis E., 8, 159
Lidorikis E., 29
Likodimos V., 37, 39, 169, 171
Lin C. L., 169, 171
Lin C. T., 32
Lindla F., 56
Lioutas Ch. B., 48, 119, 280
Lipińska A., 161
Litsardakis G., 177, 179
Logothetidis S., 52, 54, 56, 280
Londos C. A., 35
Lotsari A., 60, 64
Lux-Steiner M. Ch., 54

Majhofer A., 161
Makridis S. S., 320, 321
Manolikas C., 58
Manos M. J., 256
Mantzari M., 62

Maragakis M., 249, 306
Margiolaki I., 159, 255
Marinova M., 62
Marioli-Riga Z., 298
Markou A., 183
Marras S. I., 312
Martinetto P., 3
Martinez-Boubeta C., 195, 215
Massiot D., 347
Matenoglou G. M., 133
Mathioudakis C., 271
Mathis Y.-L., 30, 31
Matis K., 341
Matovic B., 42
Maus-Friedrichs W., 20
Mavromati E., 357
Mavrou G., 96
Mayers J., 117
Menon M., 231
Menu M., 3
Mergia K., 66, 117, 153, 155, 282
Messoloras S., 66, 117, 153, 155
Meyer N., 54, 56
Miltat J., 236
Mirtsou E., 213
Misaelides P., 128
Mitrakas M., 189
Mitrikas G., 68, 100
Mitsas Ch., 278
Monroy E., 60, 94
Montouillout V., 347
Moschou P., 189
Motsanos Ch., 44
Mouchliadis L., 109
Mouis M., 90
Mourdikoudis S., 185, 195, 209
Mousdis G. A., 256
Moussadakos D., 137
Moutis N., 155
Müllen K., 328

Neumann W., 50
Niarchos D., 137
Nikolaidis A. K., 359
Nitschke M., 10
Noli F., 128
Nørskov J. K., 300
Ntallis N., 129, 173
Nyborg L., 267

- Ohyama H.*, 35
Orfanou O., 291
Osborne S., 109
- Palilis L. C.*, 111
Palles D., 8, 256
Paloura E. C., 12, 133, 135, 157, 357
Panagiotaras D., 257
Panagiotopoulos I., 183
Panagiotopoulos S., 298
Panagopoulou A., 22
Panayiotatos Y., 96
Panayiotou C., 208, 312
Pandis P., 126
Panopoulos N., 165, 167
Pantelakis Sp. G., 288
Papadopoulos P. L., 47
Papadopoulou L., 365
Papadopoulou S. K., 208
Papagelis K., 17, 92
Papageorgiou N., 255, 258
Papaioannou E. Th., 226
Papananou H., 260
Papanikolaou N., 23, 107
Papanikolaou P., 245
Papavassiliou G., 68, 100, 125, 165, 167, 257
Papazisis K., 215
Papazoglou M., 147, 149
Pappas S. D., 75, 235
Paraskeva C., 73
Paraskevopoulos K. M., 45, 76, 198, 200, 211, 213, 217, 247, 251, 355, 361, 363, 365, 367
Parthenios J., 17, 92
Paschou A. M., 368
Patoka P., 226
Patsalas P., 29, 43, 64, 133, 296, 383
Patsidis A., 337, 339
Patsis G. P., 88
Pavlidou E., 139, 147, 149, 211, 213, 217, 247, 294, 320
Pavlopoulou E., 260, 326
Pechlivani E. M., 48
Penciu R., 105
Petoussis V. N., 80, 81
Petraki F., 316
Petukhov V., 318
Pinakidou F., 133, 135, 157, 357
- Piromalis D.*, 333
Pissas V., 235
Pistofidis N., 139, 141, 143, 145
Polatoglou H. M., 78, 278, 349
Politis C., 75
Polychroniadis E. K., 62, 181
Polymeris G. S., 83, 84, 251, 367
Pomoni K., 25, 69
Portale G., 260, 326
Posarac M., 42
Poulopoulos P., 75, 187, 235
Prellier W., 8
Psaroudakis N., 256
Psarras G. C., 337, 339
- Rabias I.*, 125
Radaelli P. G., 219
Raghavendra Reddy V., 228
Ramou E., 47
Raptis S., 84
Raptopoulou C. P., 68
Razavi F. S., 30
Remediakis I. N., 44, 290, 389
Rivière J. P., 128
Rohart S., 236
Rossmesl J., 300
Roumeli E., 361
Rusu M., 54
Ruterana P., 94
- Sarafidis C.*, 193
Sahonta S.-L., 50
Sakellari D., 181
Sakellariou E., 217
Sakkopoulos S., 353
Samaras Th., 209, 215, 243
Sanakis Y., 68, 100
Seacrist M., 92
Selvarajan V., 361
Serletis C., 177
Sheetz R. M., 231
Sheloudko N., 193
Shollock B. A., 151
Simeonidis K., 185, 187, 189, 195, 209, 215
Simon F., 10
Simserides C., 161, 262, 293
Siranidi E., 159
Skarlatos D., 92

- Skarmoutsou A.*, 288, 296, 379
Skarpalezos L., 306
Skolianos S., 147, 149
Smalc-Koziorowska J., 377
Sofos F., 322
Sompolos Z., 269
Soras G., 256
Sotiropoulos A., 96
Soukoulis C. M., 105
Souliou S. M., 33
Spanos I., 275
Speliotis T., 155
Stamati F., 247
Stamm M., 10
Stamopoulos D., 125
Stamoulis G., 80
Stathopoulos N. A., 111
Stefanou N., 23, 107
Stergiopoulos T., 37, 39
Stergiou C. A., 179
Stergioudis G., 135, 147, 149
Stimoniaris A. Z., 329, 331
Stock C., 219
Stoemenos J., 318
Strek W., 191
Stubos A. K., 321
Subedi B., 251
Syassen K., 7, 30, 31, 32
Symianakis E., 385
Syrrokostas G., 273

Tasiopoulos A. J., 256
Tassis D. H., 90
Taylor J. W., 219
Tchernycheva M., 94
Tersoff J., 375
Testa A. M., 238
Theocharidou A., 365
Theodorou G., 365
Thiaville A., 236
Todorova N., 25, 69
Trachylis D., 75, 235
Trapalis C., 25, 69
Tresintsi S., 189
Triantafyllidis K. S., 22, 341
Triberis G. P., 71, 293
Trikalitis P., 376
Tringides M., 306
Tritsaris G. A., 300

Trohidou K. N., 161, 163, 238
Tsakaloudi V., 181, 229
Tsakiris N., 302
Tsamis C., 92
Tseles D. I., 333
Tserepi A., 183
Tserkezis C., 23, 107
Tsetsekou A., 379
Tsetseri M., 71
Tsiaoussis I., 195, 318
Tsiberis N. T., 47
Tsikritzis D., 316
Tsimpliaraki A., 312
Tsiourvas D., 379
Tsipas P., 96
Tsirliganis N. C., 83, 84, 251, 367
Tsitrouli D., 125
Tsivintzelis I., 312
Tsormpatzoglou A., 90
Tsoufis T., 376
Tsoutsou D., 96
Tsurkan V., 31
Tulloch G., 37

Vamvakaki M., 326
Vanidhis E. D., 58
Vantarakis G. E., 271
Vargiamidis V., 78
Varkaraki E., 396
Vartzelis-Nikakis K., 22
Vasilakaki M., 163, 238
Vasilopoulou M., 111
Ves S., 12, 33, 58, 368
Viskadourakis Z., 110
Vitoratos E., 353
Vlachopoulou M.-E., 183
Vlachos D., 390
Vlachos P., 197
Voigts F., 20
Volkov Husovic T., 41
Volkov-Husovic T., 42
Vomvas A., 25, 69
von Haefften K., 285
Vourlias G., 135, 139, 141, 143, 145, 147, 149
Vouroutzis N. Z., 48, 211, 280, 294
Voutou B., 209

Waag A., 318

- Wagner T.*, 345
Walter P., 3
Wang X., 30, 31, 32
Watier Y., 255
Wendler E., 12
Wesch W., 12
Wiesner S., 54
Wiglusz R. J., 191
Wirthmüller A., 94
Wright J. P., 255
- Xaplanteris C. L.*, 205, 206
Xidas P. I., 22
Xu K. Y., 351
Yanagi K., 33
- Yannopoulos S. N.*, 45, 345
- Yianoulis P.*, 98, 269, 275
Yioultsis T. V., 179
Yoganand C. P., 361
- Zamboulis D.*, 294
Zaspalis V. T., 181, 229
Zenginoglou H. M., 47
Zhou J., 105
Zois H., 333, 335
Zolnierkiewicz G., 169
Zora A., 293
Zorba T., 211, 213, 217, 247, 355
Zorbas K. T., 76
Zotali P., 296
Zoubos H., 29
Zuburtikudis I., 208, 312

Program at a glance



**MONDAY ,
21 SEPTEMBER 2009**

09⁰⁰-11⁰⁰: Session MO1
(Structural, Mechanical,
Optical Properties)

09⁰⁰ : K. Syassen (Ple2)
10⁰⁰ : A. Antonakos (O1)
10¹⁵ : D. Kastanis (O2)
10³⁰ : Ch. Lekka (O3)
10⁴⁵ : P. Kavouras (O4)

11⁰⁰-11³⁰: Coffee break

11³⁰-13⁰⁰:
Poster Session MO2
(Structural, Mechanical,
Optical Properties, Electronic
Transport, Semiconductors,
Devices, Photonics,
Optoelectronics)

13⁰⁰-14⁰⁰: Lunch break

14⁰⁰-16³⁰: Session MO3
(Electronic Transport,
Semiconductors, Devices,
Photonics, Optoelectronics)

14⁰⁰ : E. Iliopoulos (I1)
14³⁰ : V. Constantoudis (O5)
14⁴⁵ : A. Tsormpatzoglou (O6)
15⁰⁰ : N. Kelaidis (O7)
15¹⁵ : E. Monroy (I2)
15⁴⁵ : S. F. Galata (O8)
16⁰⁰ : G. Leftheriotis (O9)
16¹⁵ : G. Mitrikas (O10)

16³⁰-17⁰⁰: Coffee break

**SUNDAY ,
20 SEPTEMBER 2009**

**17⁰⁰ - 18³⁰
Registration**

**18³⁰ - 19⁰⁰
Opening Ceremony**

**19⁰⁰ - 20⁰⁰
E. Dooryhee (Ple1)**

**20⁰⁰
Welcome Reception**

17⁰⁰-18⁴⁵: Session MO4
(Electronic Transport,
Semiconductors, Devices,
Photonics, Optoelectronics)

17⁰⁰ : M. Kafesaki (I3)
17³⁰ : C. Tserkezis (O11)
17⁴⁵ : L. Mouchliadis (O12)
18⁰⁰ : Z. Viskadourakis (O13)
18¹⁵ : L. Palilis (I4)

**19⁰⁰-21⁰⁰
Round Table**

**TUESDAY,
22 SEPTEMBER 2009**

09⁰⁰-11⁰⁰: Session TU1
(Structural, Mechanical,
Optical Properties)

09⁰⁰ : F. Boscherini (Ple3)
10⁰⁰ : G. Apostolopoulos (O14)
10¹⁵ : Ch. B. Lioutas (O15)
10³⁰ : A. Erko (I5)

11⁰⁰-11³⁰: Coffee break

11³⁰-13⁰⁰:
Poster Session TU2
(Structural, Mechanical,
Optical Properties, Magnetism,
Superconductivity, Cultural
Heritage Materials,
Interdisciplinary Physics)

13⁰⁰-14⁰⁰: Lunch break

14⁰⁰-16³⁰: Session TU3
(Magnetism,
Superconductivity)

14¹⁵ : M. Farle (Ple4)
15¹⁵ : E. Hristoforou (O16)
15³⁰ : E. T. Papaioannou (O17)
15⁴⁵ : O. Crisan (O18)
16⁰⁰ : V. Tsakaloudi (O19)
16¹⁵ : A. Andriotis (O20)

16³⁰-17⁰⁰: Coffee break

17⁰⁰-18⁰⁰: Session TU4
(Magnetism,
Superconductivity)

17⁰⁰ : P. Pouloupoulos (I6)
17³⁰ : A. Kaidatzis (O21)
17⁴⁵ : P. Trohidou (O22)

18⁰⁰-19³⁰: Session TU5
(Cultural Heritage Materials,
Interdisciplinary Physics)

18⁰⁰ : Th. Samaras (I7)
18³⁰ : P. Papanikolaou (O23)
18⁴⁵ : E. Pavlidou (O24)
19⁰⁰ : M. Maragakis (O25)
19¹⁵ : B. Subedi (O26)

21⁰⁰: Conference Dinner

**WEDNESDAY ,
23 SEPTEMBER 2009**

09⁰⁰-11⁰⁰: Session WE1
(Inhomogeneous, Disordered
Materials, Polymers,
Biomaterials)

09⁰⁰ : I. Margiolaki (I8)
09³⁰ : G. Soras (O27)
09⁴⁵ : E. Karakosta (O28)
10⁰⁰ : N. Papageorgiou (I9)
10³⁰ : K. Chrissopoulou (O29)
10⁴⁵ : G. Kalosakas (O30)

11⁰⁰-11³⁰: Coffee break

11³⁰-13⁰⁰:
Poster Session WE2
(Inhomogeneous &
Disordered Materials,
Polymers & Biomaterials,
Nanoscale & Surface Science)

13⁰⁰-14⁰⁰: Lunch break

14⁰⁰-15³⁰: Session WE3
(Nanoscale, Surface Science)

14⁰⁰ : D. Christofilos (I10)
14³⁰ : T. Leontiou (O31)
14⁴⁵ : P. Douvalis (O32)
15⁰⁰ : J. Kioseoglou (O33)
15¹⁵ : A. Skarmoutsou (O34)

15³⁰-16⁰⁰: Coffee break

16⁰⁰-17³⁰: Session WE4
(Nanoscale, Surface Science)

16⁰⁰ : P. Patsalas (I11)
16³⁰ : E. Symianakis (O35)
16⁴⁵ : A. Kostopoulou (O36)
17⁰⁰ : N. Galanis (O37)
17¹⁵ : D. Vlachos (O38)

17³⁰-18³⁰ : Session WE5
(Renewable energy
resources, hydrogen)

17³⁰ : A.G. Konstandopoulos (I12)
18⁰⁰ : E. Varkaraki (I13)

**18³⁰-19⁰⁰:
Awards - Closing Ceremony**
**19⁰⁰-19³⁰:
HSSTCM Annual Meeting**